MODELLING OF SPRAY IMPINGEMENT PROCESSES

by

CHENGXIN BAI

BSc., Msc.

Thesis submitted for the Degree of
Doctor of Philosophy
of the University of London
and for the
Diploma of Imperial College

May 1996

Department of Mechanical Engineering
Imperial College of Science, Technology & Medicine
University of London



ABSTRACT

This thesis is concerned with the development of methodologies for the prediction of the events which occur when a Diesel spray impacts on the walls of the combustion chamber. To this end, an extensive literature survey is first performed on droplet impingement and wall film flow processes. As a consequence of this, seven different impingement regimes are identified; and some useful data are also uncovered concerning regime transition criteria and post-impingement characteristics.

A spray impingement model is formulated on the basis of the literature findings and mass, momentum and energy conservation constraints, using some empirical correlations either taken directly from the literature or further developed therefrom by the author. A random procedure is introduced to determine some of the post-impingement characteristics, in view of the stochastic nature of impingement process.

A mathematical model of wall films formed by spray impingement is constructed. The model takes into account the effects on the film motion of the impingement pressure and tangential momentum imparted by the droplets as well as the gas shear force and capillary pressure. The general transport equations of wall film flow are established in the boundary layer framework, and the general criteria for them to reduce to local equilibrium equations are derived through an order of magnitude analysis. The full film equations are solved by an efficient hybrid integral/finite-volume method, which avoids the cost and complexities of three-dimensional computations.

The models are incorporated into a full two-phase spray simulation procedure in which the gas phase is represented as a continuum and the spray as a statistical sample of discrete droplets with full allowance for interactions between the phases. The gas phase is modelled by the ensemble-averaged conservation equations of mass, momentum and energy and the turbulence is described by the $\kappa - \epsilon$ model. The finite-volume numerical technique is used to solve these equations. The droplet trajectories, mass, velocity and temperature are predicted by solving Lagrangian conservation equations of mass, momentum and energy for each computational droplet.

Assessment of the impingement and film models is performed against several sources of experimental data involving both normal and oblique spray impingement

in test bombs as well as in a cylindrical bowl engine. The calculated impinging spray and wall film characteristics show, in general, satisfactory agreement with experiments.

ACKNOWLEDGEMENT

I am greatly indebted to my Supervisor, Professor A. D. Gosman, whose guidance and insight steered this work to its successful conclusions. He was a constant source of support and inspiration, especially during the troughs of my existence.

I wish to state my appreciation to all members of Professor Gosman's CFD group, who helped me during the course of this work. In particular, my thanks are due to Dr. E. Ikonomou who helped me during the first stages of my research, and to Mr. C. Kralj for some helpful discussions.

I am also grateful to Ms Nicky Scott Knight for her arrangement of many administrative affairs.

Most of all, I would like to express my fondest thanks to my wife, Han Jing, to whom this thesis is dedicated, for her ever-lasting support and encouragement, great patience and sacrifices throughout the course of this work.

Finally, joint financial support from Daimler Benz AG and the Commission of the European Communities is greatly appreciated.

NOMENCLATURE

Roman characters

$\widehat{A}$	coefficient matrix
a_x, a_y	tangential body force components
B_f	heat transfer number
$\mathcal{C}$	curvature
C_r	Courant number
Ca_F	film capillary number
C_d	drag coefficient
$\underline{\underline{D}}$	deformation tensor
$\mathcal{D}$	binary diffusion coefficient
D_d	droplet diameter
D_I	incident droplet diameter
D_N	nozzle diameter
D_I	incident droplet diameter
D_p	particle diameter
D_s	secondary droplet diameter
E_b	probability of bouncing in droplet binary collision
E_c	probability of coalescence
E_k	kinetic energy of incident droplet based
	normal velocity component
e	restitution coefficient; specific internal energy
e_s	specific total energy
$\underline{F}_B$	Basset force on droplet
$\underline{F}_D$	drag force on droplet
F_d	drag force on film
F	integral convection-diffusion flux (subscripted e,w,etc.)
$\underline{F}_L$	Saffman lift force
$\underline{F}_P$	force on droplet due to static pressure gradient in the flow
$\underline{F}_V$	virtual mass force

Fr_F	film Froude number
f	spatial weighting factor
H_w	wall spray height
K	coefficient of thermal conductivity; dimensional parameter defined in Equation (5.40)
K_T	'eddy' conductivity; overall mean kinetic energy or turbulence motion
Ku	phase change number
k	specific mean kinetic energy of turbulence
La	Laplace number
l_c	capillary length
$M_{d,k}$	total mass of droplet parcel K
m_d	single droplet mass
m_I	mass of incident droplet
m_s	mass of total splashing droplets
$\dot{m}_d$	droplet evaporation rate
$\dot{m}_E$	entrainment mass flux
$\dot{m}_{net}$	net mas deposition rate
$\dot{m}_v$	mass of film evaporation rate
N	number of secondary droplets; total number of internal nodes
Nu	Nusselt number
$\underline{n}$	unit vector normal to the surface
P	turbulence energy production term
$\mathcal{P}$	thermodynamic pressure
$P(\sigma_h/\sigma_{h,T})$	viscous sublayer resistance factor
Pe	Peclet number
Pr	Prandtl number
P_T	total gas pressure
$P_{v,\infty}$	partial pressure of fuel vapour
p_d	dynamic impingement pressure
p_{imp}	impingement pressure
p_L	total pressure exerted on liquid film

p_G	gas pressure
p_σ	capillary (or Laplace) pressure
R	gas constant; radius of curvature
Re	Reynolds number
R_w	wall spray radius
r_s	surface roughness
r_i $(i = 1, 2, 3)$	radii of curvature of the i-coordinate lines
Sc	Schmidt number
Sh	Sherwood number
S_P, S_u	integral source terms coefficients
s_P, s_u	differential source terms coefficients
S_ϕ	source term in ϕ-transport equation
$S_{m,d}$	droplet mass source term in gas continuity equation
$S_{u,d}$	droplet source in u-momentum equation of wall film
$S_{v,d}$	droplet source in v-momentum equation of wall film
$S_{\underline{V},d}$	droplet momentum source in gas momentum equations
T_B	Liquid boiling temperature
T_d	droplet temperature
T_g	gas temperature
T_{Leid}	Leidenfrost temperature
T_N	Nakayama temperature
T_{PA}	pure adhesion temperature
T_{PR}	pure rebound temperature
T_s	film interface temperature
T_{sat}	saturation temperature
T_W	wall temperature
t	time
t_b	droplet break time
T_{cyc}	cycle period
U_{inj}	injection velocity
U_s	local gas velocity at the film surface
$\underline{V}$	velocity vector

$\underline{V}_g$	control surface velocity
$\underline{V}_r$	relative velocity between the fluid and control surface
$\underline{V}_{rel}$	relative velocity between a droplet and the fluid
u,v	film velocity components tangential to the surface
u_τ	friction velocity
w	film velocity component normal to the surface
x,y	coordinates tangential to the surface
z	coordinate normal to the surface
V_I	velocity of incident droplet
V_R	droplet rebound velocity
W	droplet weight
We	Weber number
We_c	critical Weber number for splashing
Z	nozzle-to-plate distance (impingement distance)
Z_P	instantaneous piston position

Greek characters

α	heat diffusivity
α_x	angle formed by the injection direction with the x-axis
α_z	angle formed by the injection direction with the z-axis
α_g	angle between the x-axis and the radial grid line in which the injector is located
x-axis	
β	temporal weighting factor
γ	specific heat ratio; momentum equilibrium number of a droplet
γ_{imp}	normalised droplet impact force
Γ	effective transport coefficient
$\Delta(...)$	increment of (...)
δ	film thickness
ϵ	turbulence energy dissipation rate
ϕ	general dependent scalar variable
Λ	film temperature shape factor

λ	wave length
μ	liquid viscousity
μ_T, μ_{eff}	turbulent and effective viscosities, respectively
ν	liquid kinematic viscousity
ζ, ,ξ, ,η	axial-wise, radial-wise and tangential directions, respectively, in gas phase equations; normal and two orthogonally-tangential directions along the wall in film equations
θ_c	spreading droplet or film contact angle
θ_I	droplet incident angle
ρ_L	liquid density
ρ	gas density
σ	liquid surface tension; Schimdt number in gas equation
θ_R	droplet rebound angle
$\underline{\underline{\tau}}$	viscous stress tensor
τ_w	wall shear stress
τ_s	shear stress at the film interface

Subscripts

B	boiling
C	any of E, W, etc.
c	critical
eff	effective
F	film
G	gas
g	grid
J	jet
L	liquid
mix	mixture
s	film surface
sat	saturation
R	Resultant

rel	relative
T	turbulent
W	wall
$-$	vector

Superscripts

k	counter of corrector step
n	new time level
o	old time level
T	transposed
ν	iteration counter

Abbreviations

ASI	after start of injection
ATDC	after top-dead-center
BDC	bottom dead center
CA	crank angle
DI	direct injection engine
E/C	expanding/contracting region
HSDI	high-speed direct injection
IDI	indirect-injection engine
LDA	Laser Doppler Anemometer
PDF	probability distribution function
PIV	particle image velocimetry
SMD	Sauter mean diameter
MMD	mass median diameter
TDC	top dead center

Contents

1 Introduction 29

1.1 Background 29

1.2 The Problem of Wall Impingement 31

1.3 Objectives and Contributions of the Present Study 35

1.4 Thesis Outline 37

2 Literature Review of Impingement Processes and Liquid Film Flows 41

2.1 Introduction 41

2.2 Single Droplet Impingement Process 41

2.2.1 Problem Description 43

2.2.2 Impact Parameters and Their Effect on Droplet Impingement Dynamics 45

2.2.3 Impingement Regimes 59

2.2.4 Post-Impingement Characteristics 67

2.2.5 Summary 88

2.3 Spray Impingement 91

2.3.1 Heat Transfer Characteristics 91

2.3.2 Wall Spray Characteristics 95

2.3.3 Summary 107

2.4 Liquid Film Flow Process 108

2.4.1 Introduction 108

2.4.2 Parameters Influencing Film Dynamics 109

2.4.3 Flow Regimes and Transition Conditions 112

2.4.4 Theoretical Analysis of Different Regimes 118

2.4.5 Droplet Entrainment 124

2.4.6 Films Formed by Impinging Sprays 129
2.4.7 Summary 133

3 Flow and Spray Modelling **135**

3.1 Introduction 135
3.2 The Instantaneous Equations Governing the Gas Phase 136
3.2.1 Mass Conservation Equation 137
3.2.2 Momentum Conservation Equation 137
3.2.3 Energy Conservation Equation 138
3.2.4 Fuel Vapor Mass Conservation Equation 139
3.2.5 The General Transport Equation 139
3.3 The Statistical Approach and the Turbulence Model 140
3.3.1 Ensemble-Averaged Equations 140
3.3.2 The $k-\epsilon$ Turbulence Model 144
3.4 Summary of Averaged Equations 148
3.5 Transport Equations in Moving Coordinate Frame 149
3.6 Transport Equations in Moving Curvilinear Orthogonal Coordinate Frame 150
3.6.1 Expanding/Contracting (E/C) Region 151
3.6.2 Translating (T) Region 155
3.7 Initial and Boundary Conditions 159
3.7.1 Walls 159
3.7.2 Coordinate pole/Axis 163
3.7.3 Cyclic (or Periodic) Boundaries 164
3.7.4 Initial Condition 164
3.8 The Lagrangian Equations Governing the Liquid Phase 166
3.8.1 Atomisation 166
3.8.2 Droplet Motion and Trajectory 178
3.8.3 Droplet Heating and Vaporization 190
3.8.4 Turbulent Droplet Dispersion 194
3.8.5 Droplet breakup 198
3.8.6 Collisions between droplets 208

3.9 Closure 222

4 Development of Mathematical Model for Spray Impingement 223

4.1 Introduction 223

4.2 Impingement Regimes and Transition Criteria 224

4.3 Post-Impingement Characteristics 228

4.3.1 Adhesion (stick/spread) 228

4.3.2 Bounce 228

4.3.3 Splash 229

4.4 Closure 233

5 Formulation of Mathematical Model for Wall Film Flow 235

5.1 Introduction 235

5.2 Modelling Assumptions 236

5.3 Governing Equations 238

5.3.1 Conservation of Mass 239

5.3.2 Conservation of Momentum 239

5.3.3 Conservation of Energy 239

5.3.4 Initial and Boundary Conditions 240

5.3.5 Correlations for Mass Transfer 243

5.4 Local Equilibrium Model 244

5.5 Equations for Film Flows along a General Surface 249

5.5.1 The Coordinate System 249

5.5.2 Differential Equations 250

5.5.3 Integral Equations 251

5.6 Method of Solution 253

5.6.1 Integral Equations 254

5.6.2 Similarity Analysis 254

5.6.3 Analytical Solutions for Simplified Cases 258

5.6.4 Discretisation of Film Equations 261

5.6.5 Solution Procedure 266

5.6.6 Test of the Solution Scheme 271

5.7 Closure 280

6 Numerical Solution Procedure **283**

6.1 Introduction 283

6.2 Discretisation of Gas Phase Equations 284

6.2.1 Discretisation of the General Scalar Transport Equations . . . 286

6.2.2 Discretisation of Momentum Equations 293

6.2.3 Evaluation of Source Terms 297

6.2.4 Final Form of Discretised Equations 307

6.3 Discretisation of Droplet Equations 307

6.3.1 Choice of Droplet Time Step 308

6.3.2 Evaluation of the Local values of Gas-Phase-Related Variables 309

6.3.3 Finite Difference Form of Droplet Equations 309

6.3.4 Evaluation of the Interaction terms 312

6.4 The Numerical Algorithm 314

6.4.1 Initial Bulk Adjustment Step 317

6.4.2 The Predictor Step 318

6.4.3 The Corrector Step 321

6.4.4 Impingement Calculations 323

6.4.5 Final Bulk Adjustment Step 326

6.4.6 The $k-\epsilon$ Predictor-Corrector Procedure 327

6.4.7 Computation of Wall Film 331

6.5 Solution of The Linear Algebraic Equations 331

6.5.1 The Stone Solver 333

6.5.2 Conjugate Gradient Solver 334

6.5.3 Convergence Criteria 336

6.6 Implementation of Boundary Conditions 336

6.6.1 Wall Boundaries 336

6.6.2 Coordinate Pole/Axis 341

6.6.3 Cyclic (or Periodic) Boundaries 343

6.6.4 Injector(s) 344

6.7 Outline of Overall Solution Procedure 347

6.8 Closure 349

7 Validation Studies **353**

7.1 Introduction 353

7.2 Comparison with Experiments of Katsura et al (1989) 354

7.2.1 Introduction 354

7.2.2 Preliminary Parametric Studies 356

7.2.3 Presentation of Results 359

7.3 Comparison with CNPM Normal Spray Impingement Experiments . . 365

7.4 Comparison with Harwell Experiments 375

7.5 Comparison with Experiments of Saito et al 380

7.6 Comparison with CNPM Oblique Spray Impingement Experiments . 385

7.7 Wall Interaction Predictions for a Research Engine 396

7.8 Closure 409

8 Closure **413**

8.1 Main Achievements 413

8.2 Suggestions for Future Work 415

A Relations between Density-Weighted and Unweighted average quantities **419**

B Order of Magnitude Analysis of Film Momentum Equations **421**

List of Figures

1.1 Diagram showing spray impacting on walls 32

1.2 Diagram of wall impingement consequences 33

2.1 Schematic of droplet spreading on impact with a dry wall 43

2.2 Schematic of wall surface roughness 48

2.3 Schematic of typical droplet life time τ_e curve at different wall temperatures T_w. 50

2.4 Schematic of droplet impingement regimes 62

2.5 Overview of droplet impingement regimes and transition conditions . 68

2.6 Variation with time of ratio of sheet spreading velocity to impact velocity for (•) wetted wall covered by a liquid layer 0.5mm in depth and (○) dry wall (adapted from Levin and Hobbs (1971)). 71

2.7 Compression of droplet shape evolution between (a) the model of Harlow and Shannon (1967) with (b) experimental observations of Chandra and Avedisian (1991) during the impact of a droplet on a surface at 24^0C. 72

2.8 Deformation sequence of a water drop with $Re_d = 500$, , $We = 10$ (from Fukai et al. 1993). 74

2.9 Ratio of rebound velocity to impact velocity for droplets impacting onto a hot wall (reproduced from Cumo and Farello 1967). 77

2.10 Diagram showing definition of splash shape parameters. 79

2.11 The total number of splash products, N, resulting from impacts between a drop of 4 mm diameter and targets of varying roughness covered by liquid films of different thickness, θ: (a) medium-rough target; (b) rough target (from Stow and Stainer 1977). 85

2.12 Diagram showing definitions of wall spray height and radius. 96
2.13 Patterns of wall spray and wall film at normal impingement (reproduced from Saito et al. 1993) 101
2.14 Typical pattern of wall spray and film (reproduced from Saito et al. 1993) 101
2.15 Variation of wall spray and film radii with time (reproduced from Saito et al. 1993) 102
2.16 Mean wall film thickness variation with pressure (reproduced from Saito et al. 1993) 102
2.17 Ratio of adhered fuel to total fuel injected variation with impingement distance and angle,and injection pressure (reproduced from Saito et al. 1993) 103
2.18 Behavior of the ratio of upstream and downstream wall spray radii (reproduced from Saito et al. 1993) 104
2.19 Behavior of Spray Sauter mean diameter (reproduced from Saito et al. 1993) 104
2.20 Schematic of film flowing on an inclined plate 115
2.21 Schematic of turbulent film flow. 123
2.22 Schematic of entrainment type. 125
2.23 Distribution of liquid film thickness along the distance from the stagnation point for single water impinging jet (from Siwón 1988). 130
2.24 Distribution of liquid film thickness along the distance from the stagnation point for an air-water two phase impinging spray (from Siwón 1988). 130
2.25 Space-time variation of film thickness along incidence line at (a) $T_w = 240^0C$ and (b) $T_w = 150^0C$ (from Özdemir 1992). 132

3.1 Elevation view of a bowl-in-piston chamber configuration with a protruding valve 151
3.2 The axisymmetric curvilinear orthogonal coordinate system 155
3.3 A constant ξ boundary 163
3.4 An example of a straight walled bowl which is not a volume of a volume of revolution ('square' bowl-in-piston') 165

3.5 Schematic diagram of liquid jet breakup regimes in still gas 168
3.6 Jet breakup regime transitions (Adapted from Faeth 1991) 169
3.7 Sketch of nozzle geometry 173
3.8 Schematic diagram of bag and shear breakup regimes 199
3.9 Drop deformation and breakup regime transition map 200
3.10 Diagram of collision regimes 209

4.1 Diagram showing the cone formed by splashing droplets 230

5.1 Layout of a typical control volume. 262
5.2 Schematic of transient film condensation 272
5.3 Variation with mesh size of the realative error of the steady film thickness between the numerical and analytical solutions 273
5.4 Time taken to reach 99% of the steady state value versus the time step size 274
5.5 Numerical predictions of of film thickness at x=1 m with fixed mesh size (0.05m) and varied time step size: 0.05s, 1s, 5s. 274
5.6 Comparison of numerical and analytical solutions of film thickness at x=1 m. 275
5.7 Coordinate system sketch 275
5.8 Numerical and analytical solutions of film thicknesses at z=1m and $\theta = 0, \pi$. 277
5.9 Variation of the dimensionless film thickness with time 278
5.10 Dimensionless velocity distribution across film thickness 278
5.11 Schematic of drop spreading 279
5.12 Dimensionless droplet spreading profile under the action of capillary pressure 280

6.1 A typical scalar control volume 285
6.2 A typical control volume on three different planes 285
6.3 Control volume for scalar variables 286
6.4 A typical control volume for U-velocity 294
6.5 A typical control volume for V-velocity 295
6.6 A typical control volume for W-velocity 295
6.7 illustration of a droplet moving from one cell to another in one sub-cycling step, with both cells associated with different local coordinate frame 311

6.8 Diagram showing wall boundary 338
6.9 Diagram illustrating grid pole velocity 342
6.10 Diagram showing control volume at a cyclic boundary 344
6.11 Diagram showing injection direction 346
6.12 Illustration of flow chart 350

7.1 Fuel injection history for Case N1 355
7.2 Diagrams showing definitions of (a) radii of wall spray R_w and spray cross section R_c, wall spray height H_w; (b)wall film radius R_f 356
7.3 Effects of grid density change in axial direction on (a) wall spray radius; (b) adhered fuel ratio 358
7.4 Effects of grid density change in radial direction on (a) wall spray radius; (b) adhered fuel ratio 358
7.5 Grid scheme used for Case N1. 359
7.6 Effects of time step size on (a) wall spray radius; (b) adhered fuel ratio . . 360
7.7 Effect droplet parcel introduction rate (a) wall spray radius; (b) adhered fuel ratio 360
7.8 Spray pattern development for Case N1:(a) predictions and (b) image processed spray pattern by Katsural et al (1989) 361
7.9 Predicted and measured temporal evolution of wall spray radius and height for four different impingement distances: (a) Z=24mm, (b)Z=20mm, (c) Z=30mm, and (d) Z=34mm. 362
7.10 Results on (a) temporal evolution of adhered fuel ratio for all four impingement distance; (b) variation with the impingment distance Z of the steady-state adhered fuel ratio; and (c) film thickness spatial distributions for Case N1 at three times after start of injection (note the greatly expanded ordinate scale). 364
7.11 Fuel injection history for Case N2 366
7.12 Predicted development of spray patterns for Case N2 368
7.13 Predicted development of gas velocity fields for Case N2. 370
7.14 Comparison between the predicted and measured droplet peak normal velocities for Case N2 at two locations which are all 2mm height from plate, but differ in radius from the spray axis: (a) r=5mm and (b) r=6mm 371

7.15 Predicted and measured variations with height above the wall for Case N2 of (a) droplet mean tangential velocity; and (b) mean normal velocity at 14mm radius away from the spray axis. 371

7.16 Predicted mean diameter variation with the height above the wall surface at 14mm radius away from the spray axis (Case N2): (a) without Saffman lift forces; (b) predictions with three other practices: (1) with Saffman lift forces included, (2)only bounce and stick regimes assumed, and (3)coalescence assumed to occur for all binary collisions of droplets in the wall spray. 373

7.17 Prediction for Case N2 of (a) temporal evolution of adhered fuel ratio; (b) film thickness distributions at three times after start of injection 375

7.18 Injection history of Harwell experiments 376

7.19 Comparison between predicted and measured temporal variations for Case N3 of (a) wall film radius; and (b) spray cross-section radius at 2mm height above the wall. 377

7.20 Comparison between predicted and measured variations with time of spray cross-section radius at (a) 2mm and (b) 4mm above the wall for Case N4 . 378

7.21 Comparison between predicted and measured variations with time of film radius for Case N4 378

7.22 Predicted film thickness distributions at different times after start of impingement for (a) Case N3 and (b) Case N4 379

7.23 Predicted temporal variations of (a) adhered fuel mass ratio for Cases N3 and N4; (b) evaporated film mass percentage for Case N4 380

7.24 Comparison between predicted and measured (a) wall spray radius and (b) wall spray height 382

7.25 (a) Predicted variation with time (curves in the figure) of adhered fuel ratio for Cases N5, N5 and N7 (the open symbols stand for experimental data for steady value); and (b) predicted and measured steady state adhered fuel ratio versus fuel injection pressure. 382

7.26 Calculated and measured variation with time for Case N5 and N7 of (a) film radii; and (b) mean film thickness 384

7.27 Predicted film thickness distributions at different times for (a) Case N5 and (b) Case N7 384
7.28 Schematics of CNPM oblique impingement cases. 385
7.29 Computational mesh used for Case O1: (a) elevated view (b) plan view . . 387
7.30 Computational mesh used for Case O2: (a) elevated view (b) plan view . . 388
7.31 Predicted development of spray patterns for Case O1 389
7.32 Predicted and measured variations with height above the wall surface for Case O1 of (a) droplet mean tangential velocity; (b) droplet mean normal velocity; and (c) droplet mean size at 14mm radius away from the spray axis. 390
7.33 Predictions for Case O1 at three times of (a) wall film patches (note that point O in the figure denotes the stagnation point); and (b) wall film thickness spatial profiles along the incidence line. 391
7.34 Predicted spray patterns at two times after start of injection for Case O2 392
7.35 Predicted and measured variation with time of film volume wall patch (Case O2). 392
7.36 Wall patch of film thickness measurements. 393
7.37 Predicted and measured variation with time of film thickness at (a) point a; (b) point b; (c) point c; and (d) point d which are located on the selected wall patch (Case O2). 394
7.38 Predicted and measured film thickness distribution along the incidence line at 2.23ms after start of injection for Case O2. 395
7.39 Schematic of the engine used by Guttman (1993) 396
7.40 Fuel injection history for engine case 398
7.41 Computational mesh used for Case O1: (a) elevation view (b) plan view . 399
7.42 Predicted and measured spray tip penetration versus CA for engine case . 400
7.43 Side view of predicted spray patterns 401
7.44 Spray pattern (top view) development for engine case: (a) IMH high speed Schileren-photographs; and (b) predictions. 402
7.45 Calculated gas velocity fields in a vertical plane through spray axis for the engine case 403

7.46 Calculated gas velocity fields in a diametrical plane through the spray stagnation point (4mm above the bowl bottom) for engine case 404
7.47 Predicted relative turbulent intensity contours in an axial plane through spray axis for engine case 405
7.48 Predicted vapour concentration contours in an axial plane through spray axis for engine case 406
7.49 Predicted variation with time of deposited fuel volume on the bowl wall for engine case. 408
7.50 Predicted variations with time of mean film thickness for engine case with (a) static film model; and (b)full film model 408
7.51 Predicted shapes of wall film patch on circumference of cylindrical bowl for engine case. 409

List of Tables

2.1 Some measured values of T_{PA} for different walls and liquids 52

2.2 Summary of Experimental Studies Showing Wall Temperature Effects on Droplet Impingement Outcome 53

2.3 Values of critical Weber number for water drops splashing on 'deep' water layers 65

2.4 Values of S_c corresponding to different r_s 66

2.5 Values of N as a function of impact velocity V_I 83

2.6 Values of parameters in Equation (2.31) 86

2.7 Values of a and b in Eqn (2.32) 87

2.8 Wave onset criteria - theoretical results 116

2.9 Wave onset criteria - experimental results 117

2.10 Critical Reynault number for onset of turbulent film flow 117

3.1 Empirical Coefficients Involved in the Present Turbulence Model . . . 148

3.2 Definition of the Effective Diffusion Coefficients, Γ_ϕ, Gas Source Terms, S_ϕ, and Inter-Phase Exchange Terms, $S_{\phi,d}$, in Equation (3.47) 150

3.3 Definition of Gas Source Terms, S_ϕ, in Equation (3.53) for Expanding/Contracting Region 153

3.4 Definition of Gas Source Terms, S_ϕ, in Equation (3.56) for Translating Region 157

5.1 Definition of g_ϕ, h_ϕ and S_ϕ in Equation (5.88) 258

5.2 Definition of S_ϕ^I and S_ϕ^{II} in Equation (5.131) 265

5.3 Values of parameters in Equation (5.176) 273

6.1 Definition of Gas Source Term Coefficients S_P^ϕ and S_U^ϕ in Equation (6.46) for the Expanding/Contracting region 300
6.2 Definition of Gas Source Term Coefficients S_P^ϕ and S_U^ϕ in Equation (6.46) for the Translating Region 303

7.1 Specification for Case N1 355
7.2 Specification for Case N2 365
7.3 Specifications for Experiments of Saito et al (Cases N5, N6, N7) . . . 381
7.4 Engine Specifications 397

Chapter 1

Introduction

1.1 Background

The growing use of motor-powered vehicles– motorcycles, cars, trucks, buses– has become an important feature of human life. This is mainly due to the increases of population, income and industry throughout the world. There are now almost 400 million passenger cars registered around the world; and this number has doubled in 20 years. In north America there are 50 cars for every 100 people, in Austria the figure is 45, in Europe it is around 40 and in Japan 30. The world average is ten. While motorised vehicles have undoubtedly greatly eased our daily life in that they substantially increase the speed of movement which is entailed by the activities such as work, shopping, social interaction, and distribution of products, they have also caused two major problems that continue to pose formidable challenges to automobile designers. First, exhaust emissions from automobiles have played a significant role in environmental pollution. In industrial countries– and, increasingly, in rapidly growing developing economies–emissions arising from transport constitute a significant share of overall emissions. Within the members of the Organisation of Economic Cooperation and Development, the estimated numbers are 71% of all CO_2 emissions, 49% of NO_X emissions, 39% of unburned hydrocarbon releases, and 50% of atmospheric lead emissions (OECD 1991). NO_X and hydrocarbons are the principal causes of urban smog. These emissions add to acid rain and to the threat of global warming. Consequently, our skys, rivers, lakes, seas and soils are getting increasingly polluted and over-enriched, many species are facing the

danger of extinction, and our health is being threatened as well. Awareness of this has led to more stringent legislation to improve our environmental quality. The US clean act (CAA) amendments of 1990 dictate, among numerous other provisions, a schedule for substantially reducing emissions of the offending gases. Similarly, abatement targets have been mandated within the 12-member European Community, whose council, in 1988, specified national SO_2 and NO_X emission reductions, to be achieved in a staged sequence over the next 10 years. Under such circumstances, improvement of exhaust emissions from automobiles is urgent.

Second, motorised vehicles require the use of fuels that in many cases (especially in the oil-importing countries) must be imported at high cost. The oil shocks of 1970s forced the world community to begin to appreciate the magnitude of the energy-resource-environment problem it faces. Concern is therefore raised regarding long-term availability of petroleum. It is generally believed that at the present rate of consumption, the world's remaining oil resources that can ultimately be recovered amount to less than a 100-year supply (Brown 1976). Although efforts have been made to develop new energy-supply technologies in the longer-term, it is recognised that such efforts would take many decades to result in economically-viable substitute for oil. Thus increased focus has been on the near-term problem, especially on the need to ensure that adequate oil supplies will be available to meet the world's growing fuel requirements during the period of transition to the longer-term sources. Hence pressures are great for substantial improvement in the fuel efficiency of motorised vehicles.

The above discussions highlight the need for automobile industry to develop advanced technologies capable of enhancing the fuel efficiency and reducing the pollutant emissions of future automobiles. Among the important issues that have to be resolved is the improvement of engine performance. This relies on, to a large extent, the quality of injection and mixing of fuel with air in combustion chamber. The Diesel engine, being one of the most efficient devices for converting chemical energy stored in liquid fuels into mechanical work, uses the high temperature generated in the fresh charge of air by compression to heat the fuel above its self-ignition temperature. Compared to petrol engines, Diesel engines posses an attractive feature in that they have high thermal efficiencies resulting from relatively high compression

ratio and substantial higher fuel efficiency. This is the reason why Diesel engines have gain popularity in various kinds of duty vehicles, as well as in passenger cars.

However, Diesel engines produce excessive noise and emissions of particulates, including soot and its precursors. Attempts to mitigate such negative effect have led to a significant amount of research into Diesel engine performance in the past decade.

1.2 The Problem of Wall Impingement

Diesel engines are of two types: direct-injection (DI) or 'open- chamber' engines and indirect-injection (IDI) or 'divided chamber' engines. IDI engines use a variety of divided combustion chamber designs, allowing for much higher injection periods, excellent fuel-air mixing via high swirl rates and high turbulence levels. DI engines employ the direct injection of the fuel into the bulk of the air in the combustion chamber, and operate with a lower intensity of swirl, thereby losing less heat by convection and thus achieving increased fuel efficiency compared to the IDI variety. Hence, from the fuel-efficiency point of view, there appears a trend towards expanding use of DI engines in passenger cars.

However, in small and compact DI engines, the combustion chamber space is rather limited, the spray path is short and its penetration is confined, leading to a more complicated problem– spray/wall impingement. This impingement process may lead to the formation of a wall spray penetrating along the wall, a wall film spreading on wall surface and a gaseous wall jet, as illustrated in Figure 1.1. Such impingement processes are also encountered in petrol engines which employ port-fuel injection system. In such engines, a large amount of injected fuel unavoidably impinges onto the surfaces of intake valves, port and cylinder walls.

The wall spray contains mainly droplets resulting from deflection (by the gas flow), bouncing and splashing upon impingement; whereas the wall film is formed by fuel deposition resulting either from droplets which stick on the wall at low impact energy, or from splashing droplets which leave a proportion of their mass on the surface.

The wall jet created by wall impingement is usually turbulent and contains a

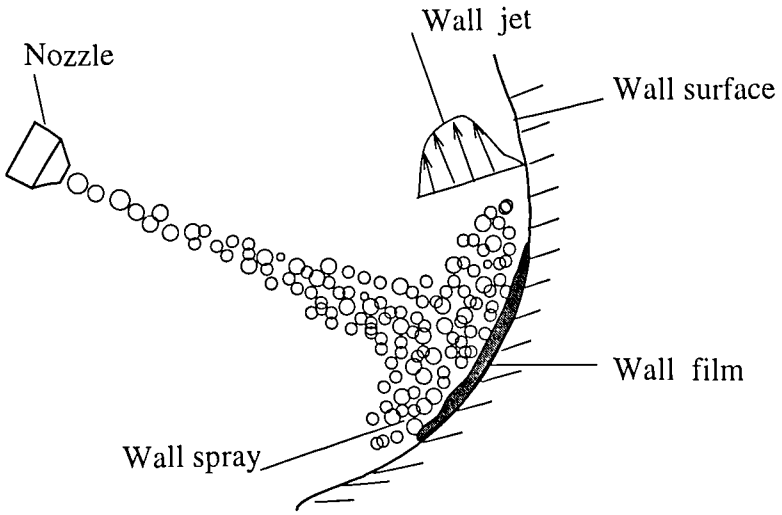


Figure 1.1: Diagram showing spray impacting on walls

leading vortex structure which has been observed experimentally (e.g. Coghe et al 1991; Katsura et al. 1989). These three features –wall spray, wall film and wall jet–are intimately related and fully coupled. Some of the droplets within the wall spray are likely to re-impact on the film surface under the action of collisions and gas flow, causing redeposition of fuel and momentum exchange between the impacting droplets and the wall film. Gas/film interaction results in drag on liquid film, and this drag, if very strong (e.g. in the presence of very strong swirl rate), may cause droplet entrainment from the film surface. The liquid film also add to the complexity of the flow domain by creating a zone which interferes between the shear layer and the solid wall. Its presence also imposes a new boundary for the shear layer which is rough and the degree of roughness depends on the height of the wave crests of the film. Furthermore, this boundary is moving and the shear layer has to be considered as developing along a moving rough wall.

The interaction between the wall jet and the wall spray is evidenced by the following facts. On the one hand, the wall jet plays a role in enhancing mixing via vortex entrainment and turbulent dispersion of wall spray, or altering trajectories of droplets within wall spray by exerting on them some additional forces such as Magnus , Saffman and virtual mass forces. On the other hand, the wall spray drives the wall jet and influences its internal flow patterns and turbulence. A schematic representation of these interactions is depicted in Figure 1.2.

Wall impingement may intensify spray heating and vapourisation for two major

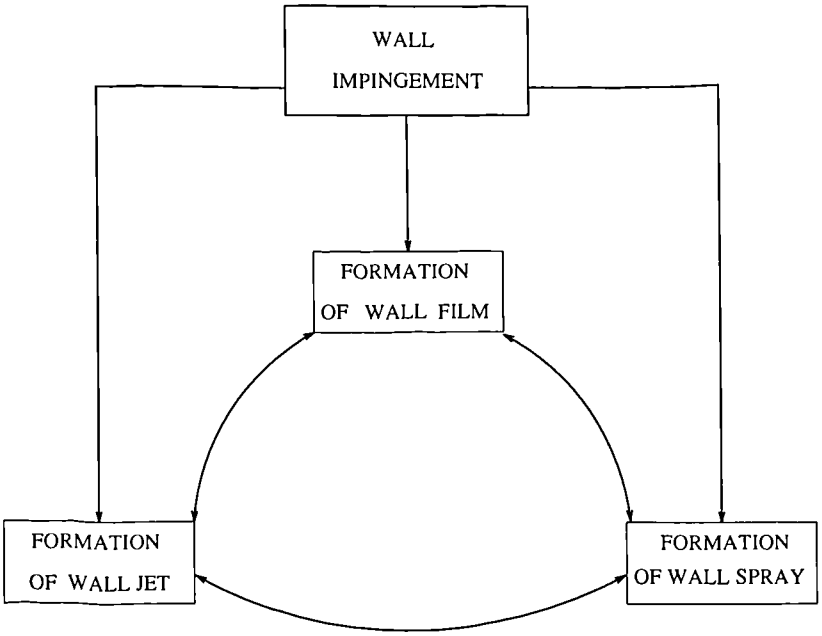


Figure 1.2: Diagram of wall impingement consequences

reasons: (1) secondary fragmentation of droplets may occur in the impingement zone due to splashing or collision-induced breakup between pairs of droplets with high collision energy (as in the case of an outgoing droplet [moving away from the wall] colliding with an incoming droplet [moving towards the wall]), and this contributes to an increase in the total droplet surface area; (2)the directions of rebound droplets and splashing droplets are usually randomly distributed due to the effects of wall surface roughness (dry wall) or irregular film surface (wetted wall), which may be beneficial to droplet dispersion. Also, the wall jet vortex greatly promotes the mixing in wall spray, as evidenced by Katsura et al. (1989). Awareness of this has led to some efforts to achieve a desired fuel evaporation rate, and therefore combustion rate, by deliberate utilisation of wall impingement– such as in M-combustion system (Meurer 1956) –or to promote fuel/air mixing (Kroeger 1986).

Wall film formation, on the other hand, could produce negative effects, because it is likely to enhance soot formation and unburnt hydrocarbon emissions if not burnt completely. Incomplete burning of the wall film will occur when the surrounding gas has a low oxygen concentration, or when the mixing is poor. In this case, film vapourisation will occur without complete combustion, and the fuel vapour will decompose and form unburned hydrocarbons, partial oxidation products, and carbon particles. For this reason, wall impingement has been blamed for enhancing

hydrocarbon emission (Matsui et al. 1981) and for producing smoke at cold start (Tsunemoto et al. 1982).

The study of wall impingement in diesel engines should therefore be concerned with the problems of the following kinds:

- The first problem relates to the development of the wall spray and its vapourisation and mixing with the surrounding gas. It is desired that the wall spray is well-dispersed and sufficiently mixed, and that it contains a large population of small secondary droplets resulting from impingement-induced atomisation so as to increase total spray surface area and thus intensify heating and vapourisation. Wall spray dispersion depends on its interaction with the surrounding gas flow, whereas the impingement-induced atomisation relies on surface conditions as well as arriving droplet sizes and velocities, which in turn depend largely on injection pressures and other factors affecting primary atomisation. The question thus arises as to how to achieve sufficient secondary atomisation and wall spray dispersion by adjusting injection pressure and direction and combustion chamber geometry (such as changing the surface curvatures, or adding protrusions of different shapes and sizes at the impact sites to obtain desirable spray dispersion). The solution to this problem must rely on parametric studies in order to determine which arrangement works best.

- The second problem concerns with achievement of complete burning of the wall film by the end of combustion. In reality, the extent of film burning depends on its vapourisation rate (and also its mixing rate with the surrounding gas), which is in turn determined by many factors including gas and wall temperatures, gas velocity in the near-wall region, wall film motion and its thickness distribution. It is therefore important to identify the major parameters which significantly influence wall film spreading, distribution and evaporation, and hence to determine the optimum operating conditions which will ensure complete wall film evaporation by the end of combustion. This again requires parametric studies.

In designing Diesel engines for which spray impingement is unavoidable, the designers need full knowledge of how different operating conditions and chamber

geometries affect the above two problems before they will be able to condition the impingement event in such a way as to ensure sufficient wall spray dispersion and mixing, and full burning of the fuel wall film. This can be achieved only if the mechanisms governing impingement dynamics are understood and the phenomena can be predicted.

The extreme complexity of the spray impingement makes it difficult to derive information through experimental measurements. For example, the opacity of the highly dense wall spray impedes the use of optical techniques such as LDA (Laser Doppler Anemometer) and PIV (Particle Image Velocimetry) techniques close to the surface. Even if this difficulty is circumvented, experimental approach is not well-suited to performing wide-ranging parametric studies, because they are time-consuming and costly. These considerations have provided the motivation for the present study, which is devoted to the development and assessment of mathematical models of the processes involved in the impingement of Diesel sprays on the walls of the combustion chamber.

1.3 Objectives and Contributions of the Present Study

The objective of the present study is to improve the present Diesel engine modelling through the development of methodologies for the prediction of the formation and evolution of the wall film, the wall spray and wall jet in Diesel engines. To achieve this, an extensive literature survey is first performed to gain insight into the basic physics in sprays, droplet impingement and wall films. Then mathematical models of these processes are constructed and linked together. Finally, these models are incorporated into a full spray simulation procedure, and assessed against experimental data.

The specific contributions are:

1. Evaluation of the mathematical models of the physical processes involved in Diesel sprays, such as atomisation, droplet heating and vapourisation, droplet breakup and collisions, based on the recent findings of the literature survey.

Some deficiencies of the existing submodels have been clarified and possible improvements are suggested.

2. Determination of the full parameters controlling droplet impingement dynamics, including two new characteristic temperatures, termed as the 'pure adhesion' temperature and 'pure rebound' temperature, respectively.

3. Identification of seven droplet impingement regimes for an isolated droplet impinging onto a dry or wetted surface at various conditions. Also uncovered are some useful data on post-impingement characteristics and regime transition conditions.

4. Development of a mathematical model for spray impingement on the basis of the literature findings and conservation constraints of mass, momentum and energy. This impingement model is capable of predicting impingement consequences such as the impingement regimes, the angles and velocities for rebounding droplets, and the numbers, sizes and velocities of secondary droplets resulting from splashing.

5. Construction of a mathematical model for wall films formed by impinging sprays. This model takes full account of impinging droplet contributions in the film momentum equations, addresses film heating and vaporisation, and tracks its moving contact line and deforming interface. The general transport equations of wall film flow are established in the boundary layer framework, and the criteria for them to reduce to local equilibrium equations are derived through an order of magnitude analysis.

6. Development of an efficient numerical scheme for the solution of the film equations. This scheme combines integral and finite volume methods and avoids the cost and complexities of three-dimensional computations. It also provides a procedure for calculating the film interface curvature numerically, which obviates the need to use higher order interpolation function and hence the numerical error associated with this.

7. Incorporation of impingement and film models into a full spray simulation procedure.

8. Validation of the present impingement and film models against experiments by comparing a number of characteristics including wall spray patterns,wall spray height and tip growth; droplet sizes and velocities in the near-wall region; radii of spray sections and wall film; film volume and film thicknesses at some locations, all as a function of time at different gas temperatures and pressures.

1.4 Thesis Outline

The remainder of this thesis is organised as follows.

Chapter 2 is devoted to a review of the previous work on both theoretical and experimental studies on droplet/spray impingement and film flow. First, a unified picture is presented concerning the droplet impingement process, with emphasis on (1) the controlling parameters influencing the impingement dynamics; (2) the various impingement regimes and the associated post-impingement characteristics; (3) the transition criteria between the different regimes.

Second, an overview is presented of the available data on spray impingement. Discussed in detail are two issues: (1) heat transfer between impinging sprays and walls; and (2) characteristics of the wall spray produced by impingement.

The information on liquid film flow is then presented; this includes: (1) major parameters affecting film dynamics; (2) three basic flow regimes and their transition conditions; (3) typical theoretical methods employed for the analysis of different flow regimes; (4) droplet entrainment resulting from gas-induced forces acting on the film surface; and (5) main features of wall films formed by impinging sprays.

In Chapter 3, mathematical models for two-phase spray simulation procedures are described. The Eulerian approach for the gas flow is represented by conservation equations of mass, momentum and energy, with the inclusion of the additional terms to account for the presence of droplet phase. This set of equations is cast into density-weighted ensemble-averaged form, using the k-ε turbulence model to represent turbulence diffusional fluxes. The equations thus obtained are then expressed in a three-dimensional transient orthogonal curvilinear coordinate frame for application in particular engine configurations. Following this, the Lagrangian description of dispersed phase is presented. Droplet trajectory and motion are obtained from

momentum equations which are represented in the same coordinate systems as the gas-phase equations, while droplet vapourisation and heating are computed from mass and energy equations. In addition, the aspects of methodology responsible for droplet breakup due to aerodynamic forces, droplet binary collision resulting from differences of relative velocities and the dense distribution of droplet population, and droplet turbulent dispersion are also discussed.

Chapter 4 is concerned with the assembly of a mathematical model for spray impingement simulation, based on the findings in the literature survey and theoretical analysis. The modeled aspects include impingement regimes and the correlations describing the transition conditions and parameters representing post-impingement characteristics.

Chapter 5 presents the mathematical modelling of wall film dynamics. First, the modelling assumptions are introduced. This is followed by the establishment of governing equations within boundary layer framework, allowing for the impinging droplet dynamic pressure, gas shear, tangential momentum imparted by arriving droplets, and capillary pressure to be accounted for. It is shown that this set of equations can be substantially simplified if local equilibrium occurs and a dimensional analysis is performed to identify the conditions for the applicability of local equilibrium model. An efficient numerical method is subsequently deviced which combines integral and finite volume methods and avoids the cost and complexities of three-dimensional computations. The accuracy of this scheme is then tested against some problems with partial or complete analytical solutions.

Chapter 6 details the numerical solution procedure. The equations for gas and spray phases, along with their discretisation algorithm are first discussed. The EPISO algorithm employed to solve the system of equations and the implementation of boundary conditions is also outlined.

Chapter 7 is concerned with the assessment of the models developed in this study by comparison with experiments. Preliminary test calculations are first carried out to establish requirement of adequate numerical resolution. The models are then assessed against several sources of experimental data for both normal and oblique spray impingement cases, as well as for an engine case. The results obtained and their implications are discussed in detail and a summary of main findings and

conclusions is also presented.

Finally, in chapter 8, main achievements of the present work are outlined. Also suggestions are made for refinements and extensions in future work.

Chapter 2

Literature Review of Impingement Processes and Liquid Film Flows

2.1 Introduction

This chapter is devoted to the collection and review of the previous studies on droplet or/and spray impingement and liquid film flow processes. The purpose is to determine what is known of these processes and what needs to be explored further. The approach regarding spray impingement physics is first to examine single droplet impact, and then under the impingement conditions involving a group of droplets. Thus, in Section 2, the current information on droplet impingement dynamics is first described. This is followed, in Section 3, by a presentation of the knowledge of spray impingement processes including both theoretical and experimental work. Finally, theoretical and experimental investigations on film flow are reviewed in Section 4.

2.2 Single Droplet Impingement Process

The impingement of droplets on a solid or liquid surface occurs frequently in a wide range of situations. These include various types of combustion engines, spray cooling systems, material erosion problems, and many other applications in agriculture, medicine and meteorology. In compression-ignition engines, gas turbines and other liquid-fueled appliances, fuel droplets may frequently hit the walls of combustion chambers. The subsequent hydrodynamics and thermal characteristics of impinge-

ment droplets are important issues requiring fundamental investigations in order to enhance the understanding of combustion.

Droplet impingement is a very complex process, controlled by a variety of parameters. In most practical applications, it involves a number of physical phenomena: droplet fluid flow, heat transport, phase change, liquid evaporation and solidification. A major challenge to the understanding of this process is therefore its inter-disciplinary, non-linear and stochastic nature. Once impingement occurs, the interaction between the droplet and the surface results in a variety of forces, which contribute to determine the subsequent droplet distortion and post-impingement mode. For micrometer-sized droplets, geometric surface and molecular-level forces can be significant. In some instances, the impinging droplet may have a significant charge (Levin and Hobbs 1971), which introduces additional forces into the problem, therefore further compounding its understanding.

Another complication is exemplified by high droplet impact velocity conditions which give rise to extreme deformation of the droplet and the subsequent ejection of secondary droplets, all occurring within very short time scales. Analysis of the associated liquid flow dynamics and the characteristics of secondary droplets (e.g. their sizes and velocities) proves to be very challenging.

In situations involving high wall temperatures, the process is further complicated by the presence of phase change, which may lead to a vapor film between the droplet and the wall, and by the dynamics involved in the heat and mass transfer between the different phases.

The complexities described above seem, in many instances, to have impeded the experimentalist seeking to carefully separate variables and the theorist attempting to accurately model the impingement processes. Consequently, our knowledge of the impingement dynamics has progressed slowly. Nevertheless, a large body of literature on droplet impingement has accumulated. The principal aim of this section is to survey the impingement dynamics of a single droplet (usually water) impinging on a wall. We first outline the problem area and attempt to identify the significant parameters controlling the impingement dynamics. We then examine the various impingement regimes and the associated transition criteria. Subsequently, we integrate the findings on post-impingement characteristics, to provide a basis for

computer modelling of spray impingement. Finally, we present a summary of the main findings and conclusions of this section.

2.2.1 Problem Description

Droplet impingement problem is a process involving three phases: gas, droplet and wall (either dry or wetted). Figure 2.1 illustrates a characteristic spreading stage for a liquid droplet following its impingement onto a plane rigid surface. There is a contact area between the liquid and the solid surface which is delimited by a contact line at which the three phases contact. Each interface has a certain free energy per unit area: σ_{SL} for solid-liquid, σ_{SV} for solid-gas, and σ_{LV} for liquid-gas (the latter for simplicity, will simply be called σ). The contact angle, θ_c, is the angle at which the liquid-gas interface meets the solid plane. The above described parameters are essential in describing liquid wetting dynamics (de Genns 1985). A finite contact angle corresponds to partial wetting, whereas a zero θ_c represents complete wetting. It turns out that it is extremely difficult to determine the moving contact line and the varying contact angle.

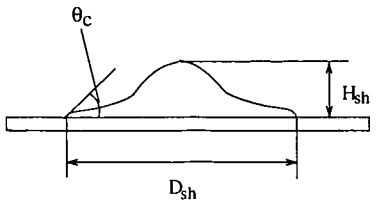


Figure 2.1: Schematic of droplet spreading on impact with a dry wall

For a small liquid droplet spreading on a solid surface at the stage where inertial forces are no longer dominant and interfacial forces are important, the parameter, $e_{dif} = \sigma_{SV} - (\sigma + \sigma_{SL})$ (i.e. the free energy difference between a bare solid, directly in contact with the vapour and a solid covered by a flat liquid layer), is crucial in describing wetting dynamics (De Genns 1985). Clearly, for $e_{dif} > 0$, which is energetically favoured, the drop spontaneously spreads and tends to cover the solid surface. This will lead eventually to complete wetting. The case where $e_{dif} < 0$ represents essentially partial wetting, in this situation the liquid retains a certain shape. Classical capillarity theory predicts the essential features of this shape: if the droplet is small enough that gravity may be neglected, the hydrodynamic pressure

rapidly equilibrates inside the droplet. This enables the drop to assume the shape of a spherical cap in order to obey the Laplace law: $\Delta p = \sigma(1/R_1+1/R_2)$ (Δp being the local pressure difference between the two sides of a curved interface characterised by the two principal radii of curvature R_1 and R_2). The mechanical equilibrium of the contact line then permits the determination of the contact angle through Young's law (Young 1805): $\cos\theta_c = [(\sigma_{SV} - \sigma_{SL})/\sigma]$.

At the early stages of impact, however, the wetting dynamics is negligible compared to the inertial effects, since the droplet experiences rapid spreading and deformation owing to the rapid pressure increase in the drop at the point of impact. This pressure is relieved by the motion of the liquid along the surface principally through formation of a jet at the base of the droplet. Meanwhile, the impinging droplet is typically subject to the following forces: (a) adhesion force: $3\pi\sigma_{SL}D_I(1 + D_{sh}^2/6D_I h_0)$ where h_0 is the distance between the molecules of the drop and the solid surface which are in contact, D_c is the diameter of the contact area and D_I is the incident droplet diameter; (b) contact pressure and wall shear stress; (c) long-range forces due to the presence of ultra-thin liquid zones close to the contact line; and (d)thermally-induced forces resulting from the heat transfer between the wall and the droplet. These forces act to influence the deformation and spreading of the impinging droplet. The outcome is largely determined by the conditions concerning whether or not the spreading flow is stable.

The case of stable flow leads to droplet rebound if the incident kinetic energy is larger than the sum of the dissipated energy and adhesion energy. Otherwise it spreads as a liquid film. In the unstable case, the liquid film may disintegrate, causing the ejection of secondary droplets as well as the deposition of a portion of liquid mass on the wall. Major sources of flow instability are (i) high impact energy ; (ii) surface roughness (Levin and Hobbs 1971); and (iii) a temperature gradient across the spreading droplet film, in situations involving heated walls. Thermal instability for larger drops is of the Rayleigh-Taylor type of the liquid-vapor interface and the dynamics of the bubbles resulting from the periodic instability of the interface. The existence of a dense phase (liquid) supported by a light phase (vapour) is inherently unstable in a gravitational field. Any small perturbation of the interface would be expected to disrupt the interface and lead to bubble formation. However,

for small droplets for which the gravity force is not important in the liquid film spreading, the instability is related to other mechanisms, such as thermocapillarity, vapour recoil (Hickman 1952), and van der Waals attractions (Burelbach et al 1988). The complexity of the thermal instability makes the shattering of the droplets on a hot wall exhibit a variety of patterns.

The above discussions make it apparent that different impingement regimes will occur depending on the conditions of incoming droplets and the wall surface. The purpose of the following subsections is therefore to identify the number of possible impingement regimes and the core parameters that determine these regimes, as well as the post-impingement characteristic quantities. The aim is to be able to predict not only which regime will occur but also the final status of the impingement event once the impact conditions are given.

2.2.2 Impact Parameters and Their Effect on Droplet Impingement Dynamics

As droplet impingement involves typically three physical phases, namely, droplet, wall and gas in the near-wall region, one would naturally expect that the process is generally influenced by droplet geometry, the physical properties of droplet liquid, the droplet impact velocity and the texture and wetting properties of target surface, as well as the characteristics of gas boundary layer in the near-wall region if present. In what follows, we will provide a detailed description of the physical effects of these parameters in determining the impingement dynamics and identify the crucial ones.

1. Droplet liquid properties

a. Density ρ_L. The impact pressure over the contact surface between impinging droplet and target surface is proportional to the liquid density , and thus it contributes to the deformation and spreading processes of droplets.

b. Surface tension σ. This parameter characterises the forces that resist the formation of additional surface area. Thus a droplet with large surface tension is hard to deform and break up. The importance of surface tension in droplet impingement is appreciated by reference to a dimensionless parameter to be defined shortly, the Weber number, which is a measure of the ratio of droplet kinetic en-

ergy to surface energy. This parameter, in all respects, plays a dominant role in determining the impingement characteristics including modes, transition conditions and post-impingement status. Commonly-encountered liquids have surface tensions ranging from $0.073kg/s^2$ for water to $0.027kg/s^2$ for petroleum products. For most pure liquids in contact with air the surface tension decreases with an increase in temperature and is independent of the age of the surface.

c. Viscosity μ_L. The importance of viscosity lies in the fact that it enhances the energy consumption during droplet spreading stage, and also hinders the development of natural instability of the spreading liquid film. The combined effect is to delay secondary disintegration upon impingement. The viscosity of some commonly used liquid ranges from 0.001kg/ms for water to 0.5kg/ms for heavy fuel oil, and generally decreases with an increase in temperature.

2. Droplet size D_I.

Different processes involving droplets may have different ranges of droplet sizes. In natural rain, typical drop size varies from 0.7mm for a rainfall of 0.25 mm/h (drizzle) to 2.0 mm for 25.4mm/h rainfall.(Fyall 1967). For the spray in a diesel engine, droplet size ranges from $1\mu m$ to $100\mu m$ in the near-wall region.

The effect of droplet size on impingement can be appreciated in three ways. Firstly, it is a measure of droplet volume, which in turn determines droplet impact kinetic energy. The latter quantity is crucial in determining the fate of impinging droplet. Secondly, droplet size exerts a direct influence on the deformation and film spreading on the surface upon its collision. This is because the duration of peak impact pressure will decrease with drop size due to the proximity of the free surface of the drop to the center of impact (Brunton and Rochester 1979). The spreading liquid film formed by an impinging droplet plays an important role in determining the details of splash productions such as the number of secondary droplets and their size and velocity distributions. Stow and Stainer (1977) studied the effect of incident droplet size on the number, N, of secondary droplets resulting from splash, using different sizes of water drops with the incident droplet velocity being fixed. Their experimental data suggest that N is approximately proportional to D_I^α ($\alpha > 1$) (a fact which was not noted by them). Droplet size is also shown to have a direct effect on the splashing limit by Stow and Hadfield(1981).

Finally, if droplet size is of the order of 1 μm. forces such as electrostatic and Van der Waals exert an influence which is not negligible(Gillespie & Rideal 1955; Jordan 1954; Brach & Patric 1992). Thus the droplet dynamic behaviour may be different from the case where these forces are negligible. In addition, it is to be expected that the characteristics of droplet impingement in situations where the drop size and surface roughness are comparable will be very different from those where the two parameters are not comparable. This is because of the fact that surface roughness can substantially influence the impingement dynamics, as will be made clear very shortly.

3. Droplet incident velocity V_I.

The impact velocity plays an important role in determining the impingement outcomes. This is because that it determines directly the deformation and radial flow of the droplet on impact, since the order of magnitude of impact pressure inside the droplet after impact which drives the radial flow of liquid is approximately $\rho_L V_{In}^2/2$ (V_{In} being the normal velocity component).

Worthington(1908) observed that for a given droplet impinging on a water surface, it can experience stick, rebound or splash with the increase of impacting velocity. Stow and Stainer found that the number of secondary droplets produced is a linear function of V_I^2. In addition, the parameter D_I/V_I is an important time scale describing the duration of droplet impingement physics.

With increasing impact velocity, Levin and Hobbs (1971) found that the maximum diameter of the sheet and the height of the raised jet increase. Thus, for an impacting drop of a given size, the raised-jet wall may be expected to become thinner at the same time. Consequently, the crown jets will be smaller in diameter,and more smaller droplets should be ejected.

4. Wall surface characteristics

a. Surface roughness r_s. Wall surface roughness is usually characterised by its average height r_s, the standard deviation of the roughness Δr_s, and the mean cycle of roughness, L_s (see Figure 2.2).

It has been observed by a few investigators (e.g. Levin and Hobbs 1971; Mutchler 1970; Stow and Stainer 1977) that surface roughness is a parameter significantly affecting the droplet impingement dynamics. Its effect was first investigated by

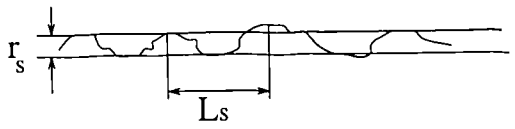


Figure 2.2: Schematic of wall surface roughness

Levin and Hobbs(1971) who noticed that a water drop impacting on a 'smooth ' surface just spreads as liquid film without splashing, while it splashes on a 'rough' surface. Under the same impact conditions, Mutchler (1970) observed that surface roughness affects the ratio of the volume of total secondary droplets to that of *incident droplet*, as well as the size distribution of secondary droplets. Stow and Stainer (1977) observed that as the roughness of the target surface is increased, more secondary droplets were produced, for an impinging droplet 4mm in diameter and Weber number of 607, which is large enough to ensure splashing. Stow and Hadfield (1981) performed a systematic study on the effect of roughness on the splashing limit. They showed that the primary influence of the surface roughness parameter, r_s, is the determination of the condition for the ejection of secondary droplets by the excitation of an instability in the developing watersheet. They further presented evidence to illustrate this point and revealed that the splashing critical velocity (defined as the limit velocity below which droplet does not splash) v_T approaches infinity as $r_s \to 0$, decreases rapidly as r_s increases , and remains nearly as constant when $r_s \geq 12\mu m$.

The profound effects of surface roughness on droplet dynamics are linked to the spreading dynamics of the droplet following its impact with the surface. In fact, during droplet spreading after impact, undulations in the target surface will exert an orographic influence upon the flow which will incur perturbations of wavelength of the same order of magnitude as the dimensions of the undulations. The perturbations so produced will be incoherent and their amplitude may be expected to increase with increasing roughness. On such a basis, the rougher the target surface, the greater will be the amplitude and wavelength of the resonances in the crown which are set up before the splashing event is over. This effect serves to explain an experimentally-observed fact – an increase in splash product size with an increase in surface roughness (Stow and Stainer 1977).

Another effect of surface roughness is to alter the local incidence angle of the

impinging droplet. This effect becomes especially prominent when the droplet size is small compared to the roughness cycle, L_r. Due to the complicated topology structure of the roughness, this variation of the collision angle may be considered as a stochastic process. In addition, in the case of a hot wall,rougher surface tends to enhance the heat transfer rate between the droplet and the wall (Chandra and Avedisian 1992). This is because that surface roughness leads to an increase of the effective area for heat transfer between the surface and the droplet during its spreading process.

b. Wall softness. Mutchler(1970) observed that, for a same water drop splashing on two types of target surface of different softness, the volume of splashing droplets for hard wall is larger than that for softer wall. Wall softness was also found to affect the splashing limit. In engine circumstances, the walls of the combustion chamber is always 'hard', hence we do not need to be concerned with this parameter.

c. Surface curvature. Intuitively, it is clear that a curved surface can alter the droplet spreading rate, and thereby influencing splashing. However, no supporting information could be found in the literature. Nevertheless, Stow and Stainer (1977) made an investigation of the curvature effect on splashing characteristics. They used four values of radius of curvature, R_c, of the impact surface, and the varied ratio D_I/R_C from 0.05 to 0.1. Under the conditions investigated, these authors notice no appreciable effect of R_c on the number N of splashing products. However, it remains to be clarified whether whether this behaviour also holds if D_I/R_c is of order 1.

5. Wall surface temperature T_w.

For fixed droplet impact energy, the surface temperature can effect the impact dynamics by way of heat transfer and energy exchange. As the droplet approaches the wall it may evaporate or condense due to heat transfer between the wall and the droplet. The vapour between the droplet and the wall surface is compressed as the droplet moves closer to the surface, and this may also play an important part in determining the post-impingement modes of the droplet.

Experimental studies have well documented on how wall temperature affects the total vapourisation time of a droplet lying motionless on a surface. Figure 2.3 shows a typical life time as a function of wall temperature. In this figure, points *b*, *c* and

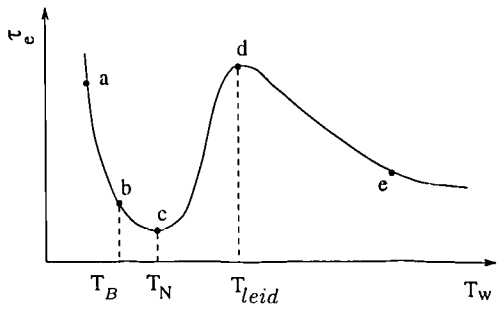


Figure 2.3: Schematic of typical droplet life time τ_e curve at different wall temperatures T_w.

d represent the following three characteristic temperatures respectively: (1) liquid boiling temperature T_B; (2) Nakayama temperature, T_N, at which drops exhibit a maximum evaporation rate; and(3) Leidenfrost temperature, T_{Leid}, which marks the minimum evaporation rate of the droplet. In the following we will demonstrate, by analysing a body of experimental data whose characteristics are summarised in Table 2.2, that two additional characteristic temperatures exist which are useful in describing regime transitions.

Yao and Cai(1985) observed three impingement regimes for a 3mm diameter water drop impacting at a velocity of $0.8m/s$ ($We_n = 27$) normally onto a wall surface whose temperature was varied within a range from around 100 to 400^0C. They are: (1) for $150^0C < T_w < 200^0C$, the drop adheres to the surface and spreads as a film with nucleation occurring beneath the film and bubble forming inside it, (2) when $200^0C < T_w < 260^0C$, rapid boiling occurs inside the drop, causing the formation and breakup of bubbles and eventually its fragmentation; and (3) for $T_w > T_{leid}$, the drop first spreads as liquid film, and then, under the action of the vapour, bounces off the wall without breakup.

The above three regimes have also been observed by Xiong and Yuen (1991) for droplets of hexadecane, heptane, diesel and water, impinging with stainless steel surface whose temperature was varied from 63 to 605^0C. The sizes of the impinging droplets range from 0.068 to 1.8mm, and the Weber number from 1 to 10. The droplet impingement dynamics observed for the different liquids are in essence qualitatively similar: (1) when $T_w - T_B$ is below $20 - 30^0C$, the droplets always adhere to the wall surface and attains a stable lens shape; (2) when T_w is about $50 - 60^0C$ above the boiling point, rapid local boiling at the liquid-solid interface causes droplet

distortion and eventually disintegration; and (3) when T_w exceeds T_N by a certain value (not necessary above T_{Leid}), the droplets bounce off due to the compressed vapour layer.

Similar observations have also been provided by some other investigators, e.g Naber and Farrel (1993); Araki and Moriyama (1982); Seki et al. (1978); Gukhman et al. (1985); and Takeuchi et al (1982). All these results tend to underline the existence of three impingement regimes for a given droplet impinging at fixed impact energy with the wall surface as its temperature is altered, from room temperature to well over Leidenfrost temperature. It therefore follows that there exist two transition temperatures, T_{PA} and T_{PR}, such that a droplet will, following its impact on a dry wall, (a) adhere on the wall for $T_w \leq T_{PA}$; (b) breakup due to rapid liquid boiling for $T_{PA} < T_w < T_{PR}$; and (c) bounce off the wall for $T_w > T_{PR}$. Here T_{PA} and T_{PR} are referred to as the 'pure adhesion temperature' and 'pure rebound temperature' respectively. Like T_N and T_{Leid}, these two new temperatures have also been found to be dependent on wall textures and liquid properties. As an illustration of this, some of the values of T_{PR} extracted from the data of Gukhman et al (1985) are presented in Table 2.1, which exhibits a clear variation of the T_{PA} with both liquid type and surface material. For instance, the T_{PA} for water droplet varied from a value of 160^0C for the copper surface to a value of 310^0C for the lead surface.

It has been further noted that the two new temperatures lie in the range:

$$T_B < T_{PA} < T_N < T_{PR} < T_{leid} \tag{2.1}$$

For instance, for water drops impinging on stainless surface, the results of Makino and Michiyoshi (1984) show that:

$$T_{PR} = 250^0C, \quad T_{PR} - T_N = 95^0C, \quad T_{leid} - T_{PR} = 50^0C$$

Also, the experimental data by Xiong and Yuen (1991) imply that $T_{PA} \leq 155^0C < T_{Leid} \approx 220^0C$ and $T_{PA} \leq 141^0C < T_N \approx 150^0C$ for n-heptane droplets. Further evidence can be found in the data provided by Chandra and Avedisian (1991), who found that $T_{Leid} - T_{PR} > 20^0C$.

Unfortunately, theoretical works which serve to explain and support the above experimental findings are extremely scarce. Nevertheless, the bounce regime observed at the high wall temperature has found theoretical support from a simple

theory proposed by Kazenin and Makeev (1987) who analysed the impingement of a water drop with an isothermal wall heated above T_{Leid} (at low impact energy so that breakup will not occur). They assumed laminar flow, zero gradient of the pressure across the vapour layer, and took into account the temperature dependence of vapour properties. As a consequence of solving the governing equations for the vapour interlayer, Kazenin and Makeev derived an expression for the force F_v acting on the drop by the vapour in the direction away from the wall. This force was found to depend very strongly on the vapour film thickness δ_v and radius of drop spreading R_s. In particular, it was revealed from the expression for F_v that, when the vapour layer is compressed to a certain level (i.e. its thickness δ_v is below a certain value), the droplet stops spreading and begins to contract and move away from the wall.

Theoretical explanations of the other two regimes, i.e., adhesion and boiling-induced breakup could in principle be provided by performing a thermal stability analysis of the liquid and vapour layer, although this has not yet been done.

Table 2.1: Some measured values of T_{PA}
for different walls and liquids

Material of surface	Working liquid	T_{PA} (Measured)
Copper	Water	160
	Alcohol	115
	Acetone	95
Aluminium	Water	175
	Alcohol	120
	Acetone	96
Aluminium oxide	Water	175
	Alcohol	120
	Acetone	96
Iron	Water	190
	Alcohol	126
	Acetone	98
Lead	Water	310
	Alcohol	180
	Acetone	131
Ceramic	Water	260
	Alcohol	150
	Acetone	105

Table 2.2: Summary of Experimental Studies Showing Wall Temperature Effects on Droplet Impingement Outcome

Author(s)	Experimental conditions	Regimes observed (wall or drop temperature ^0C)
Tamura and Tanasawa (1959)	Wall material: fused quartz Liquid: benzene Drop diameter: 2.56 mm Drop Weber number:$\approx$ 0	• Adhesion ($T_W \leq T_B$) • Boiling-induced breakup ($T_W \approx T_N$)
Gukhman et al (1985)	Wall material: copper, aluminium, anuminium oxide, iron, lead, mercury, ceramic Liquids: water, alcohol, acetone Drop diameter: 0.48-2.56 mm Drop velocity:0.7-2.5 m/s Weber number: $10 \leq We < 80$	Adhesion ($T_W < T_{PA}$) Boiling-induced breakup ($T_{PA} < T_W < T_{PR}$) Rebound ($T_W > T_{PR}$)
Seki et al (1978)	Wall material:stainless steel Liquid: water Drop diameter: 2.17mm Drop velocity: 0.63 m/s Weber number: 15	• Adhesion ($T_W = 129$) • Boiling-induced breakup ($T_W = 147$) • Rebound ($T_W = 270$)
Nishio and Hirata (1978)	Wall material: copper Liquid: water Drop diameter: 4.1 mm Drop velocity: 0.77 m/s Weber number: 33	• Boiling-induced breakup ($T_W = 170$) • Bounce ($T_W = 202$)
Inada et al (1988)	Wall material: copper Liquid: water Drop diameter: 2.3mm Weber number: 12-15	• Adhesion ($T_W = 180$, $T_d = 178$) • Boiling-induced breakup ($T_W = 180$, $T_d = 92$) • Bounce ($T_W = 420$, $T_d = 418$)

Table 2.2 (Cont'd)

Author(s)	Experimental conditions	Regimes observed (wall or drop temperature ^0C)
Makino and Michiyoshi (1984)	Wall material: brass, carbonsteel, stainless steel Liquid: water Drop diameter: 3.29 mm Weber number : 0	• Boiling-induced breakup ((i)$T_W = 250$ for stainless still plate; (ii) $T_W = 170$ for brass; (iii) $T_W = 230$ for carbon steel) • Bounce ((i) $T_W = 359$ for steel; (ii) $T_W = 260$ for carbon steel)
Naber and Farrell (1993)	Wall material: Liquid: water Drop diameter: 0.31 mm Drop velocity: 2.4 m/s Weber number: 24	• Adhesion ($T_W = T_B$) • Boiling-induced breakup ($T_B < T_W < T_N$) • Bounce ($T_W = 400$)
Yao and Cai (1985)	Wall material: brass Liquid: water Drop diameter: 3 mm Drop velocity: 0.8 m/s Weber number: 26	• Adhesion ($150 \leq T_W \leq 200$) • Boiling-induced breakup ($200 \leq T_W \leq 260$) • Bounce ($T_W > T_{Leid}$)
Xiong and Yuen (1991)	Wall material: stainless steel Liquid: n-heptane Drop diameter: 0.068-0.314 mm Weber number: $1 \leq We < 10$	• Adhesion($T_W = 95$) • Boiling-induced breakup ($T_W = 141$) • Bounce ($T_W = 155, 605$)
Chandra and Avedisian (1991)	Wall material: steel Liquid: n-heptane Drop diameter: 1.5 mm Drop velocity: 0.93 m/s Weber number: 43	• Adhesion ((i) for dry wall $T_W = 24$, 90, 104, 130; (ii) for wetted wall $T_W = 22$) • Bubbles ($T_W = 154$) • Bounce ($T_W = 180$ for dry wall)
Chandra and Avedisian (1992)	Wall material: ceramic Liquid: n-heptane Drop diameter: 1.5 mm Drop velocity: 0.93 m/s Weber number: 43	• Adhesion ($T_W = 22$, 100) • Boiling-induced breakup ($T_W = 150$) •Bounce ($T_W \approx 200$)

6. Droplet impact angle θ_I.

Jayarantne and Mason(1964) observed that a water drop impacting on a liquid surface with low collision energy will either bounce or coalesce with the water surface. The outcome depends largely on the impact angle, θ_I, formed by the droplet trajectory and the impact surface. In case of rebound, the outgoing velocity is a function of impact angle.

Another effect of θ_I can be appreciated when an impacting droplet hits a liquid film, in which case part or all of drop mass may coalesce with the film depending the impact conditions, as was first observed by Glushkov (1975). He found that this mass exchange between the impinging droplet and the film depends on the impact angle, θ_I. By directing a stream of droplets onto a wetted vertical plate, Clushkov was able to determine the reflection coefficient, $\lambda = 1 - m_c/m_I$, where m_I and m_c are, respectively, the mass of liquid incident on the film and coalescing with it. It was found that there exists a critical range of values (35 to 45^0) of the impact angle θ_I^*, at which λ is at its peak.

Yao & Cai(1985) further noted that, as θ_i departs from its value for normal incidence, a relative tangential velocity between an impacting drop and a wall tends to destabilise the drop upon impact. Accordingly, they claimed that if a droplet does not impact normally to a surface, its tangential velocity contributes to destabilise the spreading film, and hence to enhance fragmentation of the droplet following its impingement. In addition, Yao & Cai(1985) also found that droplet incidence angle can affect the Leidenfrost temperature in case of hot wall.

The effects of impact angle are presumely linked to the asymmetry of spreading liquid sheet resulting from oblique impact. Such asymmetry induces additional instability of the spreading flow.

7. Depth of liquid film covering wall surface

Experimental evidence showing the effect of liquid layer depth δ on droplet impingement dynamics is available mainly for the case of droplet splashing. The fact that the splashing limit depends on δ has been reported by a few investigators (Mutchler 1970; Ghadiri 1978; Macklin and Hobbs 1969). Gregory et al(1959) found that the number of secondary droplets decreases as the depth of liquid layer was increased from 0.2mm to 1.0 mm under the conditions of their experiment. Similar

observations have also been provided by Mutchler (1970) and Stow and Stainer (1977). Levin and Hobbs(1971) noted an order of magnitude difference between the time scales of splashing events for droplets splashing on dry or wetted walls.

The presence of a liquid film also alters the size spectrum of splashing droplets, as noted by some investigators (e.g. Stow and Stainer 1977; Mutchler 1970; and Özdemir 1992). When a water drop splashes onto a thin layer of liquid, water from the layer is incorporated into the jet wall and crown, so that the jet wall may be expected to thicken. As a consequence of this, larger jets will be formed which give rise to larger droplets, yielding in some cases a secondary size distribution with double peaks (cf. Özdemir 1992).

8. Near-wall gas boundary layer characteristics

The effect of a prevailing gas boundary layer on droplet impingement can be attributed to the hydrodynamic forces exerted on the incoming droplets by the gas flow. When a droplet enters a gas boundary layer, it may deform and orient itself with respect to the applied flow; and the shear flow will also lead to an additional lateral velocity of droplet perpendicular to the surface due to Saffman lift force or other aerodynamic lift forces such as the one caused by turbulent 'bursts' (Cleaver and Yates 1973). Saffman(1965) lift results from the velocity gradient in the shear flow. Turbulent 'bursts' are present in turbulent flows and act to move fluid vertically very rapidly from one section of the flow to the other. They are influenced by vortex patterns, among the other things. The bursting activity is not yet fully understood.

With the existence of the drag and lift forces, a droplet which would otherwise stick on a surface upon impact in the absence of a gas boundary layer may be detached from the surface by these forces and therefore result in a change of the outcome of an impinging droplet. This is evidenced by the studies performed by Povarov et al (1975). Their experiments involved a gas boundary layer generated using a rotating disk onto which a 4.2mm diameter water drop is allowed to strike at incident velocities in the range of 8-20 m/s (giving Weber number range of $3682 \leq We \leq 23014$). Normally, with such high impact energy, the droplet will splash if a gas boundary layer is not present, since its Weber number range is well beyond the critical Weber number for splashing (which is typically of the order of 100). But, the experimental photographs provided by Povarov et al (1975) revealed a totally

different picture: the water drop is first greatly retarded and deformed under the influence of the boundary layer, then strikes the wall and spreads over the surface, and eventually 'flys up' from the surface due to the aerodynamic forces. Moreover, the measurements disclosed that the reversed velocity of the reflected drop exceeds its initial incident velocity. This fact could, from the present author's point of view, be explained by the law of energy conservation. The arriving droplet, prior to impingement, will acquire rotational motion since the aerodynamic volume force is not applied to its center of gravity, and some of this rotational energy must then be converted into translation kinetic energy during impingement, resulting in a larger translational velocity magnitude upon the completion of impact. This suggests the importance of droplet rotation phenomenon within a gas boundary layer.

A way of appreciating the boundary layer effects is to examine how the droplet trajectory is altered. For this purpose, Wenglarz (1982) introduced the momentum equilibrium number γ of a droplet as follows:

$$\gamma = \frac{\tau_d f_D}{\tau_r} \tag{2.2}$$

where $f_D = Re_d C_d/24$ and $\tau_d = \rho_d D_d^2/18\mu f_D$. Here τ_r is a characteristic flow time scale, defined by

$$\tau_r = L_c/|\underline{U}_f| \tag{2.3}$$

in which L_c and $\underline{U}_c$ are a characteristic length and a mean fluid velocity scale, respectively. Clearly, the parameter γ is an important descriptor of the ability of a droplet to respond to changes in fluid velocity and so alter its trajectory. Droplets with $\gamma \gg 1$ are highly inertial and very slow to respond to changes in fluid velocity. In contrast, droplets with $\gamma \ll 1$ follow the flow faithfully.

If, in the definition of γ in Equation (2.2), we substitute for the characteristic length the boundary layer thickness, b, and for the mean velocity of the fluid phase the component of particle velocity normal to the surface, V_N, evaluated at $y = b$, we get

$$\beta = \frac{b}{s} = \frac{b}{V_N D_d^2 \rho_d/18\mu} \tag{2.4}$$

The quantity s in Equation (2.4) is referred to as the particle stopping distance. It is a conservative estimate of the maximum distance a droplet is expected to travel at constant mean speed V_N in the direction normal to the surface– starting at the

edge of the boundary layer along that surface–before it adjusts to the local mean velocity, which (within the boundary layer) is primarily aligned to the surface. Only for values of $\beta < 1$ will particle penetrate a boundary layer deeply enough to strike a surface.

Wenglarz (1982) also showed that: (1) the presence of a boundary layer always decreases particle impact speed and impact angle (relative to the tangential direction of the surface); and (2) these two effects are significant only for boundary layers containing particles with $\beta > 0.4$

Summary

To summarise, the influential parameters described above may be combined to yield the following dimensionless parameters essential to the modelling of impingement processes. They are

1. Weber number

$$We = \frac{\rho_L V_{I_n}^2 D_I}{\sigma}$$

This represents a measure of relative importance of droplet kinetic energy and surface energy.

2. Laplace number

$$La = \frac{\rho_L \sigma D_I}{\mu_L^2}$$

This parameter measures the relative importance of surface tension and viscous forces acting on the drople.

3. Incidence angle θ_I: This measures the effect of droplet tangential velocity which usually contributes to the destabilisation of the spreading liquid film. This implies that droplet with larger tangential velocity is more likely to get fragmented, given the normal velocity fixed.

4. Temperature ratios: a number of these may be important, namely,

$$\frac{T_d}{T_B}, \frac{T_W}{T_B}, \frac{T_W}{T_{PA}}, \frac{T_W}{T_N}, \frac{T_W}{T_{PR}}, \frac{T_W}{T_{Leid}}$$

$$T_B < T_{PA} < T_N < T_{PR} < T_{Leid}$$

Here T_B is the liquid boiling temperature, T_N is the Nakayama temperature at which a droplet reaches its maximum evaporation rate, T_{Leid} is the Leidenfrost temperature, or the minimum evaporation temperature. T_{PA} and T_{PR} are referred to 'pure adhesion temperature' and 'pure rebound temperature', respectively.

5. Relative wall film thickness: δ/D_I. This parameter is believed to be of order 1 in Diesel engine case, where the estimated maximum wall film thickness is not in excess of $60\mu m$.

6. Relative wall surface roughness: r_s/D_I. The order of magnitude of this parameter can be estimated for a real Diesel engine if its wall roughness is provided. For instance, if r_s is of the order of $1\mu m$, r_s/D_I would be in the range 0.1~1.

7. Parameters characteristic of a boundary layer: several of these may be important, such as (a) dimensionless boundary-layer thickness, b/D_I or β defined by Equation (2.4); and (b) normalsed droplet impact force:

$$\gamma_{imp} = \frac{1}{2}\rho_L V_{In}^2/F_{Ln} \tag{2.5}$$

which measures the relative importance of the droplet impact force and Saffman lift force in the normal direction within the gas boundary layer.

2.2.3 Impingement Regimes

This subsection is concerned with the description of the fate of a droplet following its impact with a dry/wetted surface. The literature on droplet impingement enables the identification of the following different impingement regimes, which are schematically represented in Figure 2.4.

1. 'Stick'—in which the droplet remains on the wall in nearly spherical form. This occurs when the impact energy is very low and the wall temperature is below the adhesion temperature T_{PA} (Xiong and Yuen 1991). In this regime, wetting dynamics are important and the wetting spreading is driven by Laplace pressure (Diez et al. 1994). In most spray modelling, droplets which reach the wall surface are all assumed to be in this regime. Subsequent attention

is focused on the calculation of droplet heating and vapourisation on the wall surface.

2. 'Spread'– where the droplet spreads out to form a liquid film on the wall surface (Xiong and Yuen 1991; Gukhman et al. 1985; Chandra and Avedisian 1991,1992; Yao and Cai 1985; Naber and Farrel 1993; Inada et al. 1988; Seki et al. 1978). Here, the topic of major concern is the deformation behavior of the film involving the contact angle, the spreading velocity, and the maximum diameter of the spreading film of the disk shape.(cf. Paddy 1992; Good 1992; Shikhmurzaev 1991; Leger and Joanny 1992)

3. 'Rebound'–in which droplet bounces back after impact. This regime is observed for two cases: (i) on a dry wall: the contact between the liquid droplet and the hot surface($T_w \leq T_{PR}$) is prevented by the intervening vapour film resulting in bounce (e.g. Wachters and Westerling 1966; Moureau and Giot 1979; Yao and Cai 1985; Chandra and Avedisian 1991, 1992 Araki and Moriyama 1982; Gukhman et al. 1985; and Xiong and Yuen 1991); (ii) On a wetted wall, when the impact energy is low, the air film trapped between the droplet and the liquid film causes low energy consumption and results in bouncing (Jayarante and Mason 1964; Rodriguez and Mesler 1985; Zhbankova and Kolpakov 1991; Ching et al. 1984; Schotland 1960).

4. 'Rebound with break-up'–where the droplet bounces off a hot surface($T_w \leq T_{PR}$, accompanied by break-up into two or three droplets (e.g. Wachters and Westerling 1966; Moureau and Giot 1979; Yao and Cai 1985; Chandra and Avedisian 1991, 1992 Araki and Moriyama 1982; Gukhman et al. 1985; Xiong and Yuen 1991; and Takeuchi et al 1982).

5. 'Boiling-induced breakup'– in which the droplet, even at very low collision energy , disintegrates due to rapid liquid boiling on a hot wall whose temperature lies near the Nakayama temperature, T_N. (e.g. Seki et al 1978; Inada 1988; Nichio and Hirata 1978; Naber and Farrel 1993; Inda et al. 1989; Makino and Michiyoshi 1984; Xiong and Yuen 1991; and Gukhman et al. 1985)

6. 'Break-up'– where the droplet first undergoes a large deformation to form a radial film on the hot surface ($T_w > T_{PA}$), then the thermo-induced instability within the film causes the fragmentation of liquid film in a random manner.(cf. e.g. Wachters and Westerling 1966; Moureau and Giot 1979; Yao and Cai 1985; Naber and Farrel 1993; Araki and Moriyama 1982; Gukhman et al. 1985; Xiong and Yuen 1991; and Takeuchi et al 1982)

7. 'Splash'– in which, following the collision of a droplet with the surface at a very high impact energy, a crown is formed, jets develop on the periphery of the crown and the jets become unstable and break up into many fragments (e.g. Worthington 1876, 1877, 1908; Engel 1955; Mutchler 1967, 1971; Ghadiri 1978; Loehr and Lasek 1990; Levin and Hobbs 1971; Stow and Stainer 1977; and Walzel 1980). In this regime, we are mostly interested in the quantitative information on the secondary droplet size and velocity distribulations, and the number of fragmented droplets and their ejection angles. Unfortunately, studies of such aspects are very scarce.

If we consider j parameters, $X_1, X_2, X_3, ..., X_j$, controlling the impingement dynamics, then in the space of the parameters $X_1, ..., X_j$, the loci which separates the different impingement regions are of great interest to us, because they define the transition conditions from one regime to another as the parameters $X_1, ..., X_j$ change. The equations describing these loci will be generally of the mathematical form

$$F_i(X_1, X_2, X_3, ..., X_j) = 0, \quad i = 1, 2, ..., n \tag{2.6}$$

where n is the number of boundaries separating different regimes. In particular, if we replace $X_1, X_2, X_3, ..., X_j$ by the specific parameters involved in droplet impingement process, we have

$$F_i(We, La, \frac{T_w}{T_d}, \frac{r_s}{D_I}, \frac{\delta}{D_I}, \beta, \gamma_{imp}, ...) = 0 \quad i = 1, 3, ..., n \tag{2.7}$$

in which β and γ_{imp} are defined by (2.4) and (3.103), respectively; and ... denotes other possible parameters not yet identified.

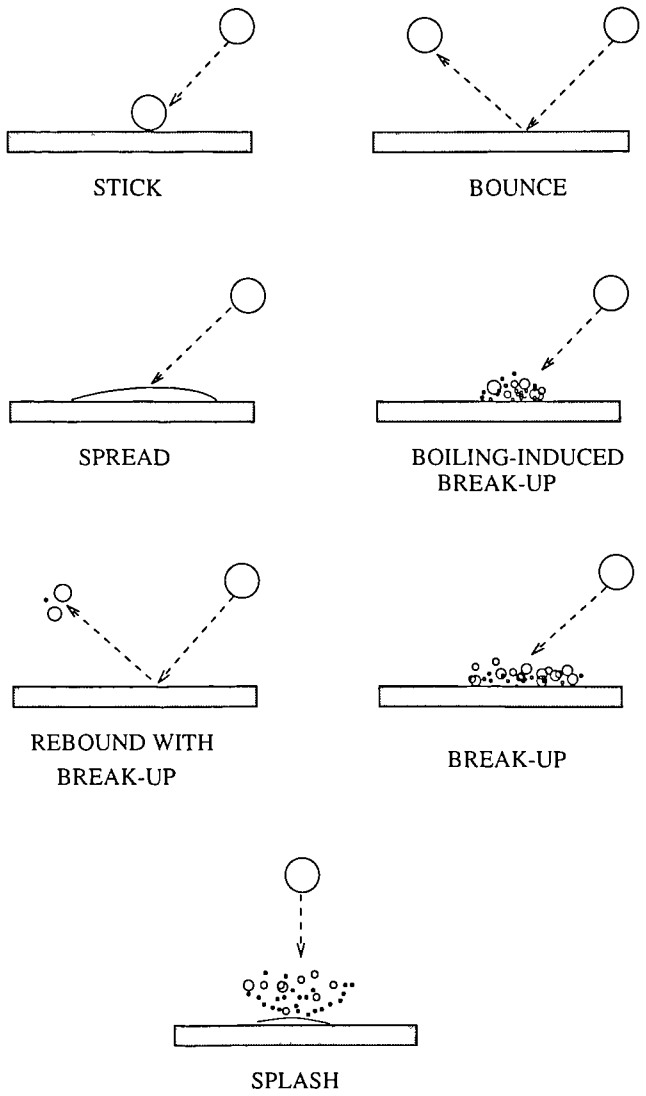


Figure 2.4: Schematic of droplet impingement regimes

Equation (2.7) is a general transition function in terms of seven parameters, namely , Weber number, Laplace number, dimensionless wall temperature, relative wall surface roughness and wall film thickness, relative gas boundary layer thickness and the ratio of droplet inertial force to the lift force in the boundary layer.

The determination of these criteria is difficult, but necessary to enable the prediction of which regime will occur in given circumstances. It is often convenient to establish the criteria, either theoretically or experimentally, by assuming that all controlling parameters, save one, are kept constant, while the chosen one is continuously varied. We then should pass from one regime to another when the particular parameter we are varying takes a certain critical value.

Thus far, there is no theoretical description that would enable the accurate determination of any kind of transition conditions from the initial parameters, nor has there been any adequate experimental investigation on this aspect. The transition function information uncovered so far is restricted to a limited range of conditions and is summarised as follows.

1. Wetted wall (covered with liquid of depth δ)

When an impinging droplet approaches a liquid surface, the gas film trapped between the droplet and the liquid surface has to be ruptured if the droplet is to adhere with the target liquid. According to Kolpakov et al. (1985), the breakdown of the gas film can be achieved if (i) the droplet, during the interaction, is able to approach target within a distance equal to the radius of the intermolecular forces h_k (Jayarante and Mason 1964); or (ii) the impact energy corresponds to the conditions in which the recovery of the deformation surface is accompanied by the development of a cumulative rim, whose energy is sufficient to rupture the gas film. In the former case, stick or coalescence occurs if

$$We \approx 1 \tag{2.8}$$

In the latter case, the criterion for adherence can be written:

$$We \geq 4 \tag{2.9}$$

The above results also support the view that the occurrence of impingement regimes for a wetted wall is, in the order of increasing Weber number, as follows:

$$\text{Stick} \rightarrow \text{bounce} \rightarrow \text{spread} \rightarrow \text{splash}$$

Schotland (1960) investigated collisions between electrically neutral drops of diameter 200-800 μ and a hemisphere target, and observed that droplet coalesces with the target occurred for $We > 3$, whereas bounce occurred at lower speeds.

Jayarante and Mason (1964) found that for droplets greater than 250 μm diameter colliding with a plane water surface there was a critical impact speed above which coalescence would occur and below which bounce took place. They presented their data in a plot which links the droplet sizes with the critical normal impact velocities above which coalescence occurs. From these data we can calculate that the critical Weber numbers from bounce to coalescence lie between 4 to 5.

Zhbankova and Klpakov (1991) revealed that, for water drops impacting onto a plane water surface, the outcomes of the collision observed are stick, bounce, spread and splash. However, they found that no sharp boundaries exist between these regimes and there are regions in which any outcome: bounce, stick and spread can occur. The transition conditions were therefore described by Zhbankova and Klpakov (1991) in terms of coalescence (or adherence) probability.

Rodriguez and Mesler (1984) produced data indicating that when $We > 5$, the incoming droplet spreads on the target liquid surface. They also found that there is no sharp transition from spread to splash for water drops striking a water pool. They uncovered a limited range of data on critical Weber numbers for splashing, as listed in Table 2.3. The average value of these critical values of Weber number is about 60.

Walzel (1980) carried out a detailed experimental investigation on the critical conditions for splashing by allowing droplets of a few liquids (water, water-glue etc.) to impact on a liquid film with $\delta/D_I = 0.1$ and $T_w < T_B$. His data was found to be fitted well by the following correlation:

$$We = 2500La^{-0.2} \tag{2.10}$$

To summarise, the transition criteria can be combined to give:

(a) 'Stick' → 'Bounce':

$$We \approx 1 \tag{2.11}$$

(for water droplet on water surface, $\delta/D_I \gg 1, \theta_I = 90^0$,)

(b) 'Bounce' → 'Spread'

$$We \approx 5 \tag{2.12}$$

(for water droplet on water surface,$\delta/D_I \gg 1, \theta_I = 90^0$)

(c) 'Spread' → 'Splash'

$$We \approx 60 \tag{2.13}$$

(water droplet on deep water layer$\delta/D_I \ll 1$;from Rodriguez & Mesler 1985)

$$We = 2500La^{-0.2}$$

(water and water-glue droplet on liquid film,$T_w/T_B < 1$;$\delta/D_I = 0.1$ from Walzel 1980)

Table 2.3: Values of critical Weber number
for water drops splashing on 'deep' water layers

D_I (diameter mm)	V_I (velocity m/s)	We_c (critical Weber number for splash)
3.1	1.13	55
4.9	0.86	51
2.5	1.22	52
1.23	2.20	81
1.22	2.07	71
1.96	1.64	72
2.77	1.22	56
4.38	0.97	56

2. Dry wall

'Cold' wall ($T_w < T_B$). The most detailed study on splashing criterion for this case is due to Stow and Hadfield(1981) who examined a series of impacts between

a given target and a drop of a given diameter for various values of impact velocity, V_I. In all circumstances, it was found that a critical velocity V_c existed below which splashing was not evident. Moreover, they obtained the following criterion for the onset of splashing:

$$D_I V_c^{1.69} = S_c \tag{2.14}$$

where S_c is a parameter dependent on target surface roughness r_s. D_I is measured in mm and V_c in m/s. Some values of S_c are listed in Table 2.4 for a few values of r_s.

Table 2.4: Values of S_c corresponding to different r_s

r_s (μm)	0.05	0.14	0.84	3.10	12.0
S_c	25-26	23.8	14.4	12.2	8.4

Unfortunately, Equation (2.14) is not widely applicable because of its dimensional form. A generalised expression for this will be proposed later in Chapter 4.

'Hot wall' ($T_W > T_{PA}$). Quite a few workers have provided quantitative data on regime transition conditions for this case (e.g. Wachters and Westerling 1960; Moureau and Giot 1979; Araki and Moriyama 1982; Yao and Cai 1985; Naber and Farrel 1993). In general, these data can be expressed in terms of critical Weber numbers as follows:

$$\text{Rebound} \rightarrow \text{rebound with breakup}: \quad We = C_I$$

$$\text{Rebound with breakup} \rightarrow \text{Breakup}: \quad We = C_{II}$$

The data by Watchers and Westerling (1966) suggest that $C_I \approx 30$ and $C_{II} \approx 80$ for water drops impinging on a polished stainless steel surface heated at 400^0C. This was subsequently confirmed by Moureau and Giot (1979) whose experiments also involved water drops but covered a much wider range of wall temperature, ranging from 600 to 1200^0C. Naber and Farrel (1993) found that C_I varied from 30 to 46, and C_{II} from 70 to 80.

The most detailed study on the values of C_I and C_{II} is due to Araki and Moriyama (1982). Their experiments covered droplets of several different liquids

impinging on a chromium-plated copper surface. They found that (i) $20 \leq C_I \leq 60$, $105 \leq C_{II} \leq 120$ for ocetic acid droplet; (ii) $25 \leq C_I \leq 40$, $80 \leq C_{II} \leq 120$ for benzene droplet; (iii)$20 \leq C_I \leq 65$, $105 \leq C_{II} \leq 125$ for ethanol droplet; and (iv)$25 \leq C_I \leq 60$, $140 \leq C_{II} \leq 180$ for isobutyl droplet. Here it can be seen that for different liquid, C_I and C_{II} scatter in different ranges, suggesting that the Weber number alone is not adequate to describe transition conditions.

Yao and Cai (1985) appear to be the only investigators who investigated the effect of impact angle. They proposed that

$$C_I = 12.89 + 0.85\theta_I - 0.0053\theta_I^2 \tag{2.15}$$

where θ_I is measured in degrees. This relation gives a value of 45 for C_I at normal incidence, i.e., $\theta_I = \pi/2$.

The only effort expended on the establishment of transition condition from breakup to splash when $T_w > T_{PA}$ is due to Walzel (1980) who provided the following transition criterion:

$$We = 7.9 \cdot 10^{10} La^{-1.4} \tag{2.16}$$

For a given Laplace number, $La = 1000$, which is typical of Diesel droplets, the above correlation gives $We_c \approx 4.985 \times 10^6$, which is so high that splashing is virtually impossible. This casts doubts on the validity of this criterion.

Figure 2.5 shows for the dry wall case a qualitative picture for the impingement regimes and the associated transition regions(shaded area) in a two-dimensional space with Weber number and wall temperature as the space variables. The boundaries in this diagram are not necessarily straight lines in the real situation, although they are plotted so for the illustrative purposes.

2.2.4 Post-Impingement Characteristics

This subsection describes the limited information uncovered on the post-impingement characteristics First, the data on the features of droplet spreading on the wall surface are presented, since they are essential to the understanding of several issues involved in the post-impingement modes of other impingement regimes. Attention is then directed to the heat transfer characteristics between the impinging droplet

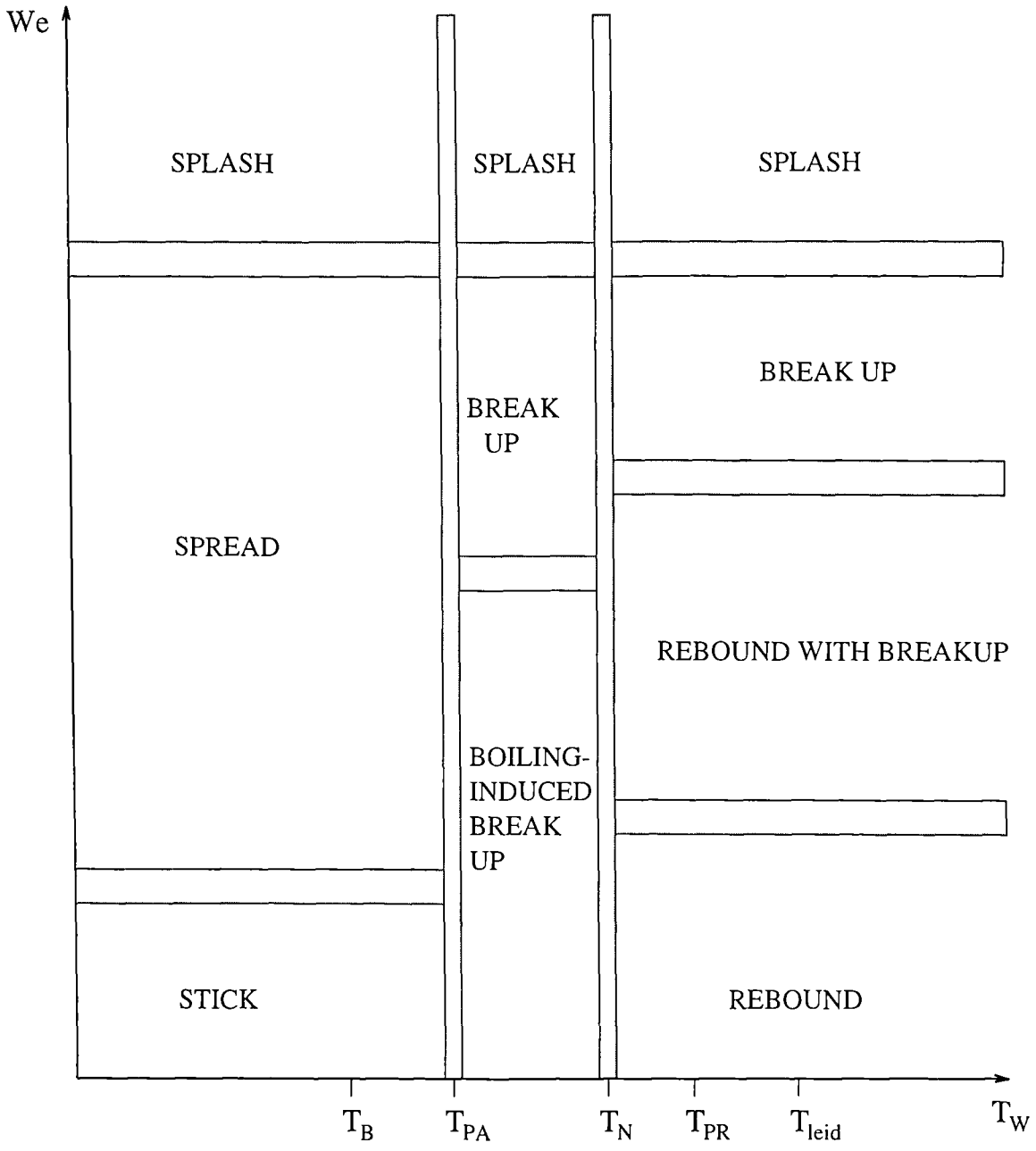


Figure 2.5: Overview of droplet impingement regimes and transition conditions

and the wall surface. Following this, detailed descriptions are given on the post-impingement behaviours for the following regimes: (i) bounce; (ii) splash; and (iii) breakup. Discussions about the rebound-with-breakup regime and boiling-induced-breakup regime are not attempted because of the lack of the data.

I. Spreading dynamics

Spreading is a physical phenomenon occurring at the very early stages of the interaction between an impinging droplet and the wall surface. The hydrodynamics involved in spreading are important in understanding the subsequent impingement outcomes. In the course of spreading, the spreading sheet is of the form of crown (see Figure 2.1), the height H_{sh} and the diameter D_{sh} of which are changing with time. The characteristics of spreading may therefore be described by the following parameters : (a) the spreading factor, $\xi = D_{sh}/D_I$; (b) the dimensionless height of the sheet, $\bar{H} = H_{sh}/D_I$, (c) the ratio of spreading velocity to the impact velocity, $(d\xi/dt)/V_I$; and (d) the time scale, t_{sp}, required for the parameter ξ to reach a maximum. In this subsection, investigations concerning these parameters are reviewed

Qualitative observations of the impact of liquid drops on dry solid surfaces have been described by Engel (1955), Savic and Boult (1957), Levin and Hobbs (1971) and Stow and Stainer (1977). Engel's experiments involved water drops impacting on different wall materials, such as metal, glass sheet and filter-paper. In the case where water drops fall onto a filter-paper, it showed that the water at the base of the impacting droplet flowed to the the periphery in a number of radial arms similar to those observed in the classical experiments of Worthington (1876, 1908). In a typical impact with a glass plate, at 8.2 m/s, a drop of diameter $D_I = 5.8mm$ (with $t^* = D_I/V_I \approx 0.7ms$) was observed to splash completely within 1.2 ms, the accompanying impact force decaying rapidly to zero within approximately 1 ms. The initial velocity of radial flow was found to be at least five times the impact velocity, dropping to a fraction of the impact velocity within 1 ms thereafter. Engel noted further that deformation of the crown of the drop did not commence until some time after impact and that no crown or spray developed when the target surface was highly polished. She explained her observation of high radial flow velocities in terms of the propagation of the acoustic waves within the drop. While she was able

to predict an initial flow of 8.6 times the impact velocity , Engel was constrained to postulate an effectively instantaneous deceleration of the drop crown to a velocity of $0.6V_I$ at a moment approximately 10 μs after impact.

Savic and Boult (1957) derived expressions for the velocity potential within a drop composed of an incompressible, inviscid liquid colliding with a solid surface. Unlike Engle, their theory predicted that no deceleration of the drop crown should occur until the impact is well advanced and the deformation of the drop appreciable. Their experiments gave generally good support to their predictions with the exception of their forecast of infinite initial impact pressure.

Levin and Hobbs (1971) employed a target made of copper in the form of a roughened hemisphere of radius of 2.5 mm. Although their interest was primarily in the formation of well developed crowns and in electrical effects associated with the ejection of secondary droplets, they confirm the findings of Savic and Boult concerning the motion of the drop crown after impact: for a drop of radius 1.47 mm impacting at a velocity of 2.81 m/s, no substantial deceleration of the drop crown occurred until approximately 0.5 ms elapsed after first contact. In agreement with Engel (1955), Levin and Hobbs observed radial velocities at the base of forming crowns of between five and nine times the velocity of impact. As an illustration of the radial velocity variation with time, the results obtained by Levin and Hobbs is replotted in Figure 2.6, which clearly exhibits a rapid deceleration of the base flow at the early stages.

Stow and Hadfield (1981) attempted to describe in detail the influence of the impingement surface on water drop impact dynamics. They showed that deceleration of the drop crown does not commence until $t > 0.3(D_I/V_I)$, contrary to the prediction of Engel (1955) but in good agreement with that of Savic and Boult (1957). Close examination of the very early stages of impact suggests strongly that the so-called watersheet originates at a moment $t' = (tV_I/D_I) = 0.005$ after first contact, regardless of the absolute values of D_I, V_I, or r_s; the initial normalised watersheet velocity is about 5. Where there is ejected mass, its normalised velocity at the moment of ejection is of the order of 20 % greater than that of the watersheet substrate. Savic and Boult (1957) performed simple calculations which also suggest that initial fluid velocities greater than $10V_I$ are required immediately before the

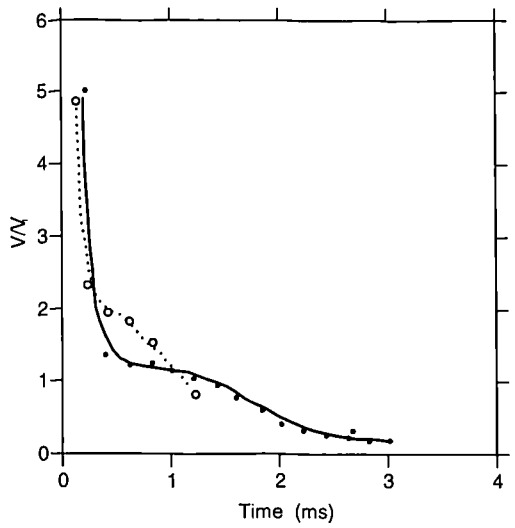


Figure 2.6: Variation with time of ratio of sheet spreading velocity to impact velocity for (•) wetted wall covered by a liquid layer 0.5mm in depth and (○) dry wall (adapted from Levin and Hobbs (1971)).

initiation of the watersheet ($t' < 0.005$). Impacts at speeds considerably greater than the appropriate terminal fall speed in air show no deviations in character from those investigated at much lower speeds.

Chandra and Avedisian (1991) observed that the spreading factor ξ and the spreading rate are independent of surface temperature in the early period of impact. This result is in qualitative agreement with theoretical predictions of Savic and Boult (1955) in which viscous and surface tension effects were neglected. Chandra and Avedisian attempted to explain the result by arguing that inertial effects dominate the spreading dynamics at early stages and produced evidence by performing an order of magnitude analysis that viscous and surface tension forces are indeed negligible at the early stages compared to the stagnation pressure in the droplet which drives the spreading flow.

A number of workers, for example, Harlow and Shannon (1967), Huang et al. (1973), Tan et al (1989), Trapaga and Szekely (1991), and Fukai et al. (1993) have performed numerical studies to predict the evolution of the shape of droplets impacting on solid surface.

Neglecting liquid compressibility, surface tension and viscosity, the predicted droplet shapes were shown to have a universal form independent of liquid properties.

The droplet shape is only a function of a dimensionless time, $(V_I t/D_I)$. Harlow and Shannon (1967) calculated these universal shapes (the calculated shapes are cross sectional images) which compare favourably with the experimental observation by Chandra and Avedisian (1991), as shown in Figure 2.7. This agreement occurs only in the early stage of spreading, where the inertial effect is dominant (hence the surface tension and viscosity are negligible). Indeed, the calculations by Harlow and Shannon produced a constant liquid sheet spreading velocity 1.6 times greater than the initial droplet speed, which implies that the spreading process never stops. This latter feature is physically unacceptable and can be attributed to the neglect of viscosity and surface tension.

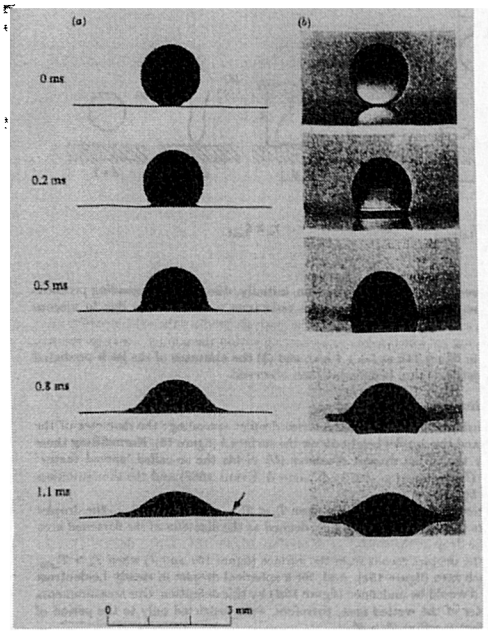


Figure 2.7: Compression of droplet shape evolution between (a) the model of Harlow and Shannon (1967) with (b) experimental observations of Chandra and Avedisian (1991) during the impact of a droplet on a surface at 24^0C.

Trapaga and Szekely (1991) presented a more comprehensive numerical analysis of droplet deformation process by solving the Navier-Stokes equation for a droplet, treating the flow within it as axisymmetric. Their analysis takes into account both viscous and surface tension effects, but involves assuming the value of contact angle, θ_c. The main results predicted by the calculations are :

1. The liquid-sheet spreading velocity is at least 3 times the value of the initial droplet impact speed, during the early stages of impingement, and subse-

quently decreases asymptotically. This result is reminiscent of the experimental observations mentioned above.

2. Thc spreading factor, ξ, is a function of droplet Reynolds number $Re_d(= \rho_L V_I D_I/\mu_L)$. In particular, the maximum values of ξ_m calculated for various Reynolds numbers, are in good agreement with the asymptotic solution developed by Medjeski (1976) who established that

$$\frac{3\xi_m^2}{We} + \frac{1}{Re_d}\left(\frac{\xi_m}{1.2941}\right)^5 = 1 \tag{2.17}$$

3. The final sheet thickness was found to be less than 5 percent of the initial droplet diameter. The spreading time scale, t_{sp}, for the liquid sheet diameter to reach a maximum value was identified to be of the same order as D_I/V_I.

4. A general trend was revealed that inertial effects dominate at the very early stages of spreading, while viscous effects become more important as the spreading continues, and the surface tension becomes an important factor toward the end of the spreading process.

More recently, Fukai et al. (1993) employed deforming finite elements to simulate rather accurately the large deformations, as well as the domain nonuniformities characteristic of the spreading process. Their calculations, which do not assume contact angle θ_c, documented the effects of impact velocity, droplet diameter, surface tension, and material properties on the fluid dynamics of the deforming droplet. It was shown that the occurrence of droplet recoiling and local mass accumulation around the edge of the spreading film were defining features of the flow field (see Figure 2.8 which is cited from Fukai et al.). Also, their calculations confirmed that the liquid sheet initially advances outward with velocities far exceeding the impact velocity of the droplet. This advancement is retarded and finally halted by the action of surface tension and viscosity. Subsequently, flow reversal is observed and the main flow is diverted toward the axis of symmetry.

II. Heat transfer characteristics

In circumstances involving droplets striking hot walls, heat transport between the droplet and the wall is an important phenomenon requiring fundamental investi-

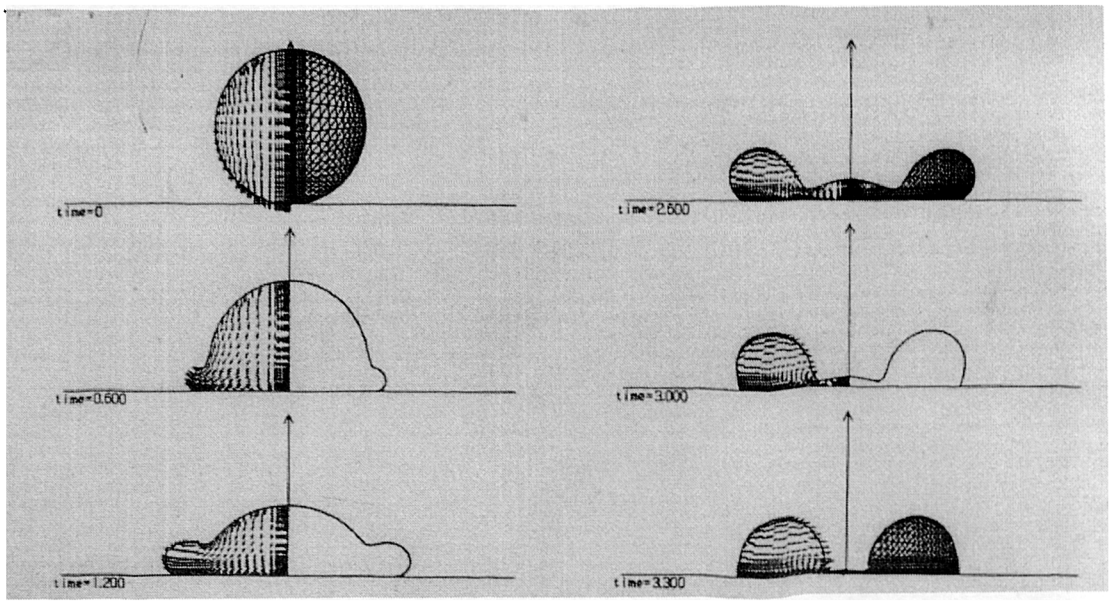


Figure 2.8: Deformation sequence of a water drop with $Re_d = 500$, , $We = 10$ (from Fukai et al. 1993).

gation. The major interests have been attached to: (1) heat energy transferred to the droplet per unit time; (2) wall surface temperature variation in response to the droplet contact; (3) life time of impinging droplet as a function of wall temperatures; and (4) key parameters influencing heat transfer characteristics.

Kazenin and Makeev (1987) proposed a simple theory for the thermal and dynamic processes of collision between a droplet (with impact Weber number less than its critical value for breakup) and a wall heated above the Leidenfrost temperature. As a result, they established that the heat transfer to the drop from the wall per unit contact time is given by

$$Q = \left[\rho\rho_L^2\sigma^{-1}D_I^{11}h_{fg}\mu^1 k^3(T_W - T_{sat})^4\right]^{1/4} F(We) \tag{2.18}$$

where $F(We)$ is a function of droplet Weber number, k is the thermal conductivity, and T_{sat} is the saturation temperature.

Labeish and Pimenov (1984) conducted a detailed experimental study of impinging droplet heat transfer characteristics. They concluded that: (i) the time of contact of the liquid phase with the wall before a vapour layer appears is about 10^{-9} seconds; (ii) in the range $We_n > 80$, i.e., in the breakup regime, the heat removed by a droplet is approximately proportional to its mass; (iii) the effect of the impact velocity is twofold: on the one hand, an increase in V_I intensifies heat exchange with

the surrounding air and forced convention to the liquid, leading to a larger wetted area, whereas on the other hand, an increase in V_I decreases the time of contact of the drop with the wall; (iv) when $T_w > T_{leid}$, an increase in velocity leads to a decrease in heat removal, which contradicts Pedersen's data (1970); and (v) when a droplet of temperature $T_d < T_w$ comes into contact with a hot wall, the wall temperature first drops abruptly, then goes up steadily untill the wetted area dries up, and eventually reeaches an almost constant level.

McGinnis and Holman (1969) investigated the heat transfer characteristics of water, acetone and alcohol droplets impinging on a hot wall at velocities that ensure either rebound or breakup . The effects on heat transfer of (a) droplet size; (b) droplet impact velocity; and (c) droplet impact angle were examined. It was found that heat transfer per drop exhibits a maximum at a temperature excess (i.e. $T_w - T_{sat}$) of approximately 300^oF and a correlation for this maximum was given. Peak heat transfer is proportional to the the drop diameter to a power slightly greater than three. The heat transfer to the drop increases in direct proportion to impact velocity until some critical velocity is reached, above which it begins to decrease. This behaviour was explained by the opposing effect of increasing contact area but decreasing the contact time due to the increase of droplet impact velocity: at some critical velocity the effect of decreased contact time exceeds the effect of increased area, thereby resulting in a reduction of total heat transfer even if the velocity is further increased. Investigation of the impact angle effect showed that the normal component of velocity is the important factor describing heat transfer characteristics.

Leidenfrost temperature is an important parameter describing the droplet thermal dynamics, and it has been shown that (e.g. Penderson 1967; Kendall 1978; Yao and Cai 1985) the higher the incoming Weber number of droplets the higher the Leidenfrost temperature. This is because the vapour film between the drop and the surface can be more readily squeezed out at high impact energy.

There have been many research efforts devoted to the determination of the evaporation rate of an impinging droplet. Wachters et al. (1966b) made an attempt to do this analytically by neglecting the effect of radiation and invoking simplified balance equations of mass, momentum and energy. The calculated evaporation rates were found to be in qualitative agreement with the experimental results.

The study of Satcunanathan (1968) revealed that for liquid droplets evaporating in the 'spheroidal' state on a hot surface upon impact with the wall at very low impact energy, the evaporation rate is given by:

$$D^{1.25} = D_I^{1.25} - C_e t \tag{2.19}$$

where D is the diameter of droplet at instant t, D_I the initial diameter, and C_e the evaporation constant.

Xiong and Yuen (1991) presented comprehensive data on the life time of impinging droplets for several liquids on a hot stainless plate. The droplet sizes investigated ranged from 0.07 to 1.8 mm, and the wall temperatures were varied from 63 to 605^0C. It was shown that the droplet life time curve as a function of wall temperature is qualitatively similar for all droplet sizes. The maximum heat transfer rate occurs $56 - 60^0C$ above the boiling temperature for all pure liquids, and the Leidenfrost heat transfer rate occurs at about 120^0C for pure fuels and 180^0 for water above the boiling temperature.

It should be remarked that the above information is relevant to the 'hot' wall case where the wall temperature is typically above the liquid boiling temperature. Although this condition is out of range for the present study, which is concerned with the 'cold' wall case, the above information may be useful if spray impingement in indirect-injection Diesel or petrol engines is to be examined. This would be a natural extension of the present study in the future.

III. Rebound

In this regime, we are concerned with the data on the following quantities: (a) rebound velocity magnitude V_R and rebound angle θ_I; (b) residence time of a droplet on the surface before rebound, t_R. These data are necessary for solving the equations governing the trajectories of the droplets bouncing from a surface which may subsequently strike the surface again.

For heated dry walls, several investigators (e.g. Wachters and Westerling 1966; Cumo and Farello 1967; Moureau and Giot 1979; Araki and Moriyama 1982; and Ueda et al. 1979) have confirmed that t_R is of the magnitude of the first order

oscillations of a free oscillating droplet, that is

$$t_R = \pi\sqrt{\frac{\rho_l d_I^3}{16\sigma}}$$

Experimental data on the ratios V_R/V_I and θ_R/θ_I were provided by Cumo and Farello (1967) for water drops hitting a heated dry wall for $T_w > T_B$, with a roughness value of $r_s = 13\mu m$. For various diameters, the average values of V_R/V_I are shown in Figure 2.9 as a function of the wall temperature, T_w. It can be seen that this ratio can be as high as 90% and for the most part higher than 50%. In general, V_R/V_I increases with wall temperature T_w, indicating a better elastic recovery at high wall temperatures. This behaviour may be explained by the forces exerted by the vapor film– the higher the temperature, the faster the vapour forms and hence the greater the upward-pushing forces by the vapour to the droplet. From Figure 2.9, it is also clear that influence of droplet diameter on V_R/V_I is profound but nonmonotonic. V_R was further observed to increase with the impact velocity V_I up to a moderate value of V_I, above which it remains constant. However, according to Cumo and Farello (1967), the ratio V_R/V_I is virtually independent of wall temperature, varying in the range of 0.5-1.0. Unfortunately, correlations for both of these two parameters, V_R/V_I and θ_R/θ_I were not attempted by these authors, nor can they be found elsewhere.

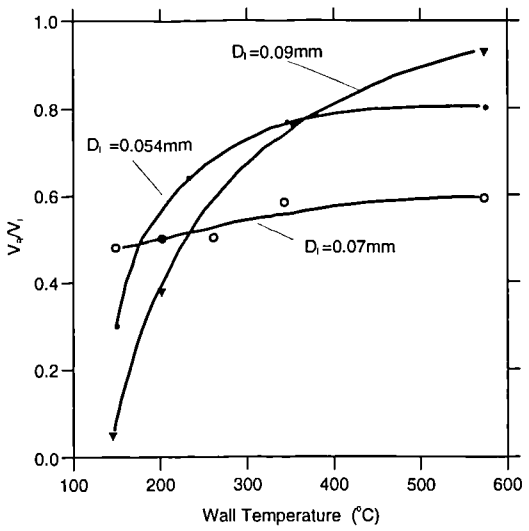


Figure 2.9: Ratio of rebound velocity to impact velocity for droplets impacting onto a hot wall (reproduced from Cumo and Farello 1967).

In the situation where a droplet bounces off a 'deep' water layer, Jayarante and Mason(1964) obtained the following correlation

$$\frac{V_R}{V_I} = \sqrt{1 + 0.95 \sin^2 \theta_I} \tag{2.20}$$

by fitting the measured data of the fraction of the initial kinetic energy lost by the drop on impact, which is expressed as $(V_I^2 - V_R^2)/V_R^2$. This correlation is also supported by a theoretical analysis performed by Jayarante and Mason (1964). Clearly, Equation (2.20) predicts a minimum value of $V_R/V_I = 0.22$ at normal incidence, which is substantially lower than the average of V_R/V_I for the case of a droplet impinging normally onto heated dry wall as disclosed by Cumo and Farello (1967). No data concerning θ_R/θ_I have been located for the water layer case.

In reality, V_I and θ_I are usually not sufficient to determine uniquely the values of V_R and θ_R, for the latter may be affected by a number of other factors. These include: (a) variations in droplet shape, size, and rotational velocity at the time of impact; (b) variations in the topology and properties of the impact surfaces; (c) uncontrollable phenomena, such as droplet fragmentation, droplet-droplet collisions, changes in properties of droplet liquid owing to sudden localised temperature increases; and (d) variations in near-surface fluid flow conditions, which significantly affect droplet trajectories if the parameter γ defined in (2.2) is less that 1. It is therefore clear that, if the effects of the above factors cannot be accounted fully, V_R and θ_R may have statistical distributions for fixed values of V_I and θ_I. In such circumstances a statistical analysis should be invoked in evaluating V_R and θ_R.

IV. Splash

A. *Characteristic parameters describing splash shape*

Figure 2.10 illustrates the definitions of some characteristic parameters of the splash phenomenon. The dry-wall case and wetted-wall cases are different in that in the latter there is crater formation and the sheet is larger than the dry-wall case. The splash angle θ_s indicates the direction of the secondary droplets as they leave the surface at a particular instant. The parameter H_{sh} is a measure of the mean splash height as measured normal to the wall surface. The sheet diameter D_{sh} characterises the extent of the splash sheet.

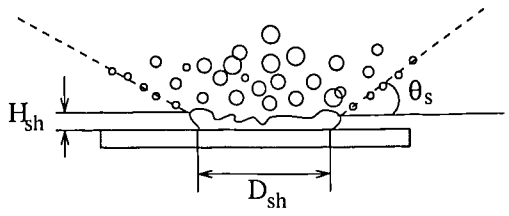


Figure 2.10: Diagram showing definition of splash shape parameters.

The splash angle θ_s is determined by several parameters such as surface roughness and softness, and the thickness of the liquid film covering the surface. Rochester and Brunton (1974) noted that the value of θ_s is around 11 degrees for a drop impacting on a hard smooth surface, whereas it takes a value of about 49^0 for a drop splashing on a soil-paste surface as noted by Ghadiri and Payne (1979). Ghadiri (1978) recorded that θ_s varies over a range of $20^0 - 60^0$ for fine soil surfaces. The angle of ejection of droplets from splashes on wetted horizontal surfaces tends to increase with the depth of liquid. For instance, increasing the water depth from 0.1 to about 5 mm over sand surfaces increases the splash angle from 35 to about 85 degrees, and over smooth glass from about 50 to 90 degrees (Mutchler 1967).

Mutchler (1967) also provided observation of temporal variation of θ_{st} (the ejection angle of droplets ejected at time t) and other parameters for a 5.6 mm water drop impacting at its terminal velocity on a 0.5 mm thick water layer. It was found that θ_{st} increases with time. This indicates that: (i) droplets ejected earlier have smaller values of θ_{st} than droplets ejected later; and (ii) all droplets ejected lie within a cone with ejection lines of the first ejected droplets forming the bounding surfaces. In addition, peak values of θ_{st} observed range from 80^0 to 85^0, suggesting that the ejection angles are likely to extend to the axis of the cone. However, whether all angles are equally probable remains to be established. Ghadiri (1978) also confirm these two features in his experiments. Thus the most important requirement for determining the ejection cone is to find correlations for θ_s, which stands for the smallest ejection angle, as a function of surface roughness and liquid layer depth, etc.

B. *Features of secondary droplets*

Sizes of secondary droplets. Ghadiri (1978) noticed that the ejection of secondary droplets in a splash takes place over a finite time, with droplets of smaller sizes

ejected earlier and those with larger sizes later. His data allowed him to plot the sizes of the ejected droplets as a function of time, which were found to be a nonlinear increasing function.

Mutchler (1971) measured the size distribution of secondary droplets resulting from splashing of water drops impacting at terminal velocity onto water layers of various depths on a smooth glass. He concluded that size distribution on a volume basis followed a normal distribution. This enabled the use of the median droplet diameter, D_{50} (the droplet diameter for which 50% of the splash volume consists of larger droplets), in describing the size distribution. He found that for an incident drop with diameter of 4 mm, D_{50} was about 0.4 mm near zero layer depth, reached a maximum size of 1.5 mm at $\delta/D_I = 0.5$, and therefrom decreased to a constant size of 1.3 mm for $\delta/D_I > 3$. In Mutchler's description, however, D_{50} and the standard deviation σ of the distribution are only correlated with one parameter δ/D_I, with no information on the most important parameter, We. Thus, Mutchler's description is of limited practical use.

Levin and Hobbs (1971) measured the size distribution of secondary droplets from a water drop 2.5 mm in diameter impacting at a velocity of 4.2 m/s onto a carbon hemisphere. They did not confirmed Mutchler's results: instead, they found that the size distribution is log-normal, which is mathematically expressed as:

$$f(\tilde{d}) = \frac{1}{\tilde{d}n2\pi} exp\left[-\frac{1}{2n^2}(ln\tilde{d} - m)^2\right] \tag{2.21}$$

where m and n are respectively, the mean value and variance of the droplet diameter $\tilde{d}$. As shown by Aitdrison and Brown (1957), the distribution of Equation (2.21) has a new set of mean α' and variance β'^2 given by:

$$\begin{aligned} \alpha' &= \exp\left(m + \frac{1}{2}n^2\right) \\ \beta'^2 &= \alpha'^2\left(e^{n^2} - 1\right) \end{aligned}$$

Stow and Stainer (1977) performed exhaust tests which confirmed Levin and Hobbs's findings (1971) over a wider range of conditions. They also quantified the dependence of the log-normal parameters, i.e., m , n , α' and β' on a number of controlling parameters, such as target radius of curvature, the thickness of liquid film covering the wall surface, and velocity of impact. They found that the mean

size of the ejected droplets increases with incident droplet size, surface roughness and depth of liquid film, but decreases with increasing impact velocity and with a reduction in surface tension. However, they did not attempt to correlate these parameters in terms of dimensionless quantities such as, We, La, r_s/D_I and δ/D_I

Velocities of secondary droplets. Allen (1988) measured the velocities of ejected droplets resulting from a water drop 4 mm in diameter impacting at a velocity of 6 m/s (We = 1793) onto a liquid surface of 1 mm depth. It was found that the magnitudes of ejection velocities are always less than that of the incident droplet, varying over a range of 1−5 m/s. The ejection angles fall within a rather narrow band, ranging from 50^0 to 70^0.

Ghadiri (1978) performed a comprehensive set of experiments on ejection velocities. He investigated a large number of drops impacting on a range of target materials. He found that droplets ejected immediately after impact have velocities much higher than that of the impacting drop and the velocities of succeeding droplets are progressively smaller. It was also found that droplets ejected earlier have smaller ejection angles than those ejected later. Although Gharidi (1978) did not present any explanation for these observations, it is evident that they are linked to the radial velocity of the liquid sheet during its evolution. As discussed earlier, the radial velocity of the sheet is larger than the impact velocity immediately after impact, and decreases monotonically with time. This trend must also be followed by the ejected droplets, since they are released directly from the liquid sheet. The behaviour of the sheet also provides an explanation for the ejection direction distribution−droplets ejected earlier have larger tangential velocity components and hence travel at smaller angles with the impact surface. In addition, size-time relation for secondary droplets disclosed by Gharidi (1978) can be linked with the liquid sheet flow. In the early stages the high flow rates produce surface waves of shorter wave length, which in turn leads to ejection of droplets of smaller sizes. Also, the fact that the spreading liquid periphery contains less mass at the early stages adds to the explanation to this phenomenon.

From the data on the variation of the droplet sizes and velocities with ejection time, Ghadiri (1978) was able to present plots depicting the relationship between the sizes and velocities of secondary droplets for four different cases involving different

impact velocities and incident droplet sizes. The graphically-illustrated relation for each case can be mathematically described by:

$$lnD_s = A_0^{'}V_s + B_0^{'} \tag{2.22}$$

In the plots presented by Ghadiri (1978), it is clear that the slope $A_0^{'}$ is the same for each case, while B_0 changes. In particular, $A_0^{'}$ is determined by the present author from the plots as:

$$A_0^{'} \approx \begin{cases} -3.3, & \text{if } V_s \leq 1(m/s) \\ -0.27, & \text{if } V_S > 1(m/s) \end{cases} \tag{2.23}$$

Unfortunately, Ghadiri did not attempt to plot the above relation in terms of dimensionless parameters. Nevertheless, from the above information, it is not difficulty to infer that, a general size-velocity correlation may be described by

$$ln\frac{D_s}{D_I} = A_0^{'}\frac{V_s}{V_I} + B_0^{'} \tag{2.24}$$

General expressions for $A_0^{'}$, $B_0^{'}$ remain to be established.

In chapter 5, where the spray impingement model is developed, Equation (2.24) is used to assist in the determination of the secondary droplet velocities.

Number of secondary droplets produced per splash. Mutchler (1970) obtained numerous data on the number N of secondary droplets produced by water drops splashing onto liquid layers. He varied the ratio δ/D_I in the range from 0 to over a value of 3.0, and drop diameter from 2.9 to 6.0 mm. For each case examined, the impact velocity was adjusted such that the impacting drop yielded splashing only when $\delta > 0$. The values of N obtained ranged from 4381 at $\delta = 0.1$ mm to 823 at $\delta = 3$ mm for a 5.59 mm diameter water drop, indicating a dependence of N on δ/D_I. Mutchler attempted to fit his experimental data using the equation

$$N/W = f(\delta/D_I) \tag{2.25}$$

in which W stands for the incident droplet weight. The equation predicts a maximum number of droplets at a depth δ of 0.02 drop diameters and a decreasing number for deeper depths. It also predicts that larger incident drops produce more secondary droplets.

Mutchler (1970) further noticed the profound effects of surface roughness and softness on the quantity N. For instance, he noted that, for the same impinging drop

and δ/D_I , twice as many as secondary droplets were produced on a rough surface than on a smooth surface. He also found that half as many droplets were ejected on a soft surface than on a hard surface. Unfortunately, Mutchler did not attempt to quantify these effects. He also did not attempt to take into account the effect of Weber number or to make Equation (2.25) nondimensional.

In their systematic studies of drop splashing events, Stow and Stainer (1977) measured N for a wide range of impact conditions. In particular, they allowed 4-mm water drops to impact onto a cold dry wall of 'medium' roughness at velocities ranging from 2.0 to 8.4 m/s, and recorded the number of secondary droplets produced. The results are summarised in Table 2.5.

Table 2.5: Values of N as a function of impact velocity V_I

V_I	2.0	2.8	3.5	4.0	4.6	5.8	7.2	8.4
N	27	147	267	332	552	768	1298	1999

It is evident that N has a strong dependence on drop impact velocity V_I: an increase in V_I by a factor of two produces more than an order of magnitude increase in N. The best straight-line fit to these data, according to Stow and Stainer, is given by:

$$N = 26V_I^2 - 63 \tag{2.26}$$

where V_I is measured in metres per second. The limitations of this correlation are also evident: it is linked only to the impact velocity and is of dimensional form. A subsequent attempt to refine this correlation was made by Stow and Hadfield (1981), who invoked the condition that $N = 0$ at the onset condition of splashing and derived the following expression:

$$N = \alpha E_k - F \tag{2.27}$$

where

$$\alpha = \alpha(r_s/D_I) > 0$$
$$F = F(D_I)$$

and E_k is the kinetic energy of incident drop. In particular, for $r_s = 3.4\mu m$, the data of Stow and Hadfield gives a specific form of Equation (2.27):

$$N = 0.406 D_I^3 V_I^2 - 5.041 D_I^{1.82} \tag{2.28}$$

Equation (2.28) still has its limitations, as will be pointed in Chapter 4, where the present impingement model is described and a new correlation for N is derived.

That N is strongly dependent on surface roughness has also been observed but not quantified by Stow and Stainer (1977). They found that: a 4-mm diameter water drop impacting on a dry wall at a velocity 4.6 m/s breaks up into 7 droplets when it is a smooth surface ($r_s \approx 0.89\ \mu m$) and 552 droplets when it is 'medium rough' ($r_s \approx 12\ \mu m$). They further revealed that the number of secondary droplets increases with incident droplet size, but decreases with a reduction in surface tension of the impinging droplet.

In the case where a 4mm water drop is allowed to impinge on liquid layers of different depths at the conditions that ensure the occurrence of splashing, Stow and Stainer (1977) recorded a dependence of N on the depth δ of the liquid layer covering the wall surface. Their experimental data are presented in Figure 2.11, which exhibits a non-monotonical dependence of N on δ. When δ is less than a value of around 0.03 mm, N decreases monotonically and reaches a minimum at $\delta \approx 0.03mm$. Beyond this N increases and reaches a maximum at a depth of about 0.06 mm. Thereafter, N decreases again in a nearly-linear fashion. For this linear dependence region, Stow and Stainer (1977) fitted their data by the following correlations:

$$N = 670 - 700\delta \qquad \text{(for surface of medium roughness)} \tag{2.29}$$

$$N = 539 - 571\delta \qquad \text{(for surface of larger roughness)} \tag{2.30}$$

The above correlations are of dimensional form and therefore are not valid for general circumstances.

Stow and Stainer (1977) also noted that at large values of δ the properties of the splashing becomes more or less independent of surface texture. The reason for this was however not explained. A probable explanation for this would be that when δ is larger than a critical value, the droplet energy consumption in crater formation

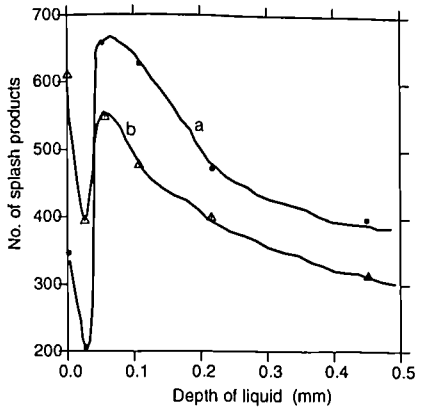


Figure 2.11: The total number of splash products, N, resulting from impacts between a drop of 4 mm diameter and targets of varying roughness covered by liquid films of different thickness, θ: (a) medium-rough target; (b) rough target (from Stow and Stainer 1977).

remains virtually the same and the subsequent processes are not sensitive to wall effects.

Mass ratio of splashing droplets m_s to the incident droplet m_I, i.e.,m_s/m_I. In a splashing event, the incident droplet mass splits into two parts: one consists of the mass of ejected secondary droplets, and the other remains on the wall. It is therefore important to determine the quantity, m_s/m_I. Apparently, $m_s/m_I \leq 1$ for a dry wall. However, for a wetted wall, it is possible that $m_s/m_I > 1$ (Mutchler 1970), since in this case the liquid sheet contains both the incident droplet and some wall film (Allen 1988). Also, in the case of a wetted wall there is a mass exchange between the liquid film and the impacting droplet, such that the ejected droplets contain some of the film mass whilst the film absorbs some mass from the impacting droplet.

Studies to quantify m_s/m_I are only available for the wetted wall case. Mutchler and Larson (1971) investigated this ratio for various depths of water layer covering glass plates, with water drops impacting at their terminal velocities. For the conditions investigated, they found that the quantity m_s/m_I can take a value larger than 2. Moreover, they derived the following correlation:

$$\frac{m_s}{m_I} = A + B\left(\frac{\delta}{D_I} - \frac{\delta}{0.4}\right) \tag{2.31}$$

where A and B are known functions of δ/D_I. The above correlation predicts that splash is zero at $\delta/D_I = 0$ and increases to a maximum at δ/D_I of 1.4 and 2.0 mm

for $D_I = 5.59$ and 2.96mm, respectively. The correlation, however, suffers from the same limitations as Equation (2.25).

A few investigators have carried out experimental studies on the mass transfer between the wall film and impinging droplets (eg. Glushkov 1975; Shrayber et al. 1992). These studies include not only splash regime but also the rebound and stick or spread regimes. Shrayber et al. (1992) studied the quantity $\Pi = m_c/m_I$, where m_c is the mass of impinging droplet which coalescences with the liquid film. To measure this, they allowed monodispersed droplets to impact obliquely ($\theta_I < 10^0$) onto a horizontal wall covered with a liquid film. The working fluid was aqueous glycerol solutions. Droplets diameters were varied over a range from 0.3 to 1 mm, the impinging velocity from 6 to 22 m/s, and the film thickness δ from 0.3 to 2 mm. The experimental results showed that Π is inversely related to the impact angle θ_I and the liquid viscosity. It also exhibits a complicated relation with the parameter $L = \delta/D_I$. At large L, Π increases strongly with δ/D_I, but at low L this quantity is virtually independent of L. Accordingly, Shrayber et al. (1992) proposed the following correlation for Π:

$$\Pi = B\left(1 - 0.884La^{-0.027}e^{-0.188/La}\right)We^{\xi}\left(\frac{\delta}{D_I}\right)^{\eta}\theta_I^{\zeta} \tag{2.32}$$

where the coefficients B, ξ and ζ are given in Table 2.6

Table 2.6: Values of parameters in Equation (2.32)

L^*	Region	B	ξ	η	ζ
1.2	$L < L^*$	0.73	0.046	0.008	1.45
	$L > L^*$	0.130	-0.027	0.257	1.35
1.4	$L < L^*$	0.07	0.045	0.027	1.43
	$L > L^*$	0.115	-0.300	0.341	1.39

It was shown that the rms deviation of experimental points from this relationship is of the same order of magnitude as the error of the measurements, ranging from 0.12 to 0.14. Equation (2.32) is apparently the 'best of its kind' thus far uncovered in the sense that it is dimensionless and contains several dominant parameters, i.e.,

droplet Weber number, Laplace number, impact angle and the relative thickness of the wall film.

V. Breakup

In an experiment involving water droplets impinging onto a heated wall, Takeuchi et al (1982) documented some data on the characteristics of breakup regime. The breakup time t_{br} was found to be related to the droplet Weber number and the dimensionless time scale, D_I/V_I. Therefore, t_{br} is correlated as: $t_{br} = g(We_n)D_I/V_I$. Another parameter examined by Takeuchi et al. (1982) is the Sauter mean diameter of secondary droplets, D_{32}. It was shown that this has a strong dependence of droplet Weber number as well as wall temperature. Linear-scale plots were presented showing the dependence of D_{32}/D_I on Weber number We_n at different values of wall temperature ($T_W = 400°C$, $300°C$, $200°C$). These plots are, however, not very useful for seeking a suitable correlation between these two variables. The present author replotted these data in a log-log coordinate system. It was found that they fall approximately on a set of straight lines for different wall temperatures. This allows D_{32}/D_I to correlated in terms of We as:

$$\frac{D_{32}}{D_I} = aWe^{-b}, \quad We \geq We_c \tag{2.33}$$

where $a, b > 0$ are dependent on the temperature ratio T_W/T_B (T_B being the droplet boiling temperature). Some values of a and b at different T_W/T_B are listed in Table 2.7.

Table 2.7: Values of a and b in Eqn (2.33)

T_W/T_B	a	b
4	69.417	0.976
3	151.36	1.2
2.5	38.9	0.875
2	18.62	0.83

A more recent experimental examination by Naber and Farrell (1993) has provided further data on secondary droplet behaviour in the breakup regime. They

observed that, for a drop 105 μm in diameter impacting at 7.1 m/s ($We_n = 74$, $D_I/V_I = 0.015ms$) onto a heated dry wall ($T_w = 400°C$), the mean ejected diameter was 42 μm; the mean normal and tangential ejection velocities were, respectively, $V_{bn} = 0.51$ m/s and $V_{bt} = 0.31m/s$ (with $V_{bn}/V_I = 0.072$ and $V_{bt}/V_I = 0.044$) ; and the number of secondary droplets was $N = 8.8$. It was noted that a group of larger droplets between 70-90 μm were ejected nearly normal to the surface, while smaller ejected droplets with sizes between 20-55 μm were ejected with considerable tangential velocities and have smaller ejection angles. This behaviour is consistent with that observed by Ghadiri (1978) for the splash regime, as described earlier. Similar results were obtained for a water drop with smaller velocity (5.2 m/s) but larger size (303 μm in diameter) and Weber number ($We_n = 74$). In this case, for instance, a single large droplet (around 260 μm) was observed to leave the surface in a normal direction with a velocity of 0.75 m/s. Furthermore, Naber and Farrell (1993) presented a secondary droplet size distribution histogram which looks very similar to those presented by Stow and Stainer (1977) for splashing droplets. This suggests that size distribution of secondary droplets for the breakup regime may well be log-normal, although Naber and Farrell did not attempt to provide any mathematical expression to fit their data.

It is interesting to note here that, although the fragmentation mechanism of breakup regime is different from that of the splash regime, the characteristics of the secondary droplets appear to follow the same trend. However, more experimental data are needed to confirm this for the breakup regime.

2.2.5 Summary

In this section the impingement dynamics of single droplets has been reviewed. The main emphasis has been on the key parameters that control the impingement process, the impingement regimes and the associated transition criteria, as well as post-impingement characteristics.

A set of parameters has been determined to describe the impingement dynamics. These parameters include: droplet Weber number, Laplace number, impact angle, pure adhesion temperature and pure rebound temperature, dimensionless surface roughness and thickness of liquid layer covering the wall surface. In addition, it

has also been demonstrated that gas boundary layer acts to play an important role in effecting droplet impingement outcomes and the parameters representing the boundary-layer effects have yet to be established. It would be of great use for such parameters to be included in evaluating regime transition criteria and post-impingement quantities.

Seven impingement regimes have been identified as a consequence of assembling and analysing the available experimental data. Further, it has been noted that there are no sharp boundaries between various regimes, due to the stochastic nature of the droplet impingement process. It has also been stressed that there is currently very scant knowledge of the regime transition criteria, although some useful though limited data have been uncovered. The establishment of general transition criteria still poses substantial future challenges.

It is worth pointing out that, even for the simplified regime transition criteria established in this section, application to engine circumstances contains many uncertainties, since they were derived from data for impinging droplets at room temperature and in air at atmospheric pressure and room temperature. In engine circumstances, the droplet is usually surrounded by a vapour layer due to the strong evaporation. This layer may act to prevent the droplet from contacting the wall and result in bouncing even for the 'cold' wall case, for which the present transition criteria would predict an adhesion outcome instead of bouncing. It will therefore be of interest in the future to reexamine experimentally the impingement outcomes for the situations where the impinging droplet is already surrounded by a vapour layer prior to impingement.

Experimental data on post-impingement characteristics for most of the impingement regimes have been collectively presented. The following issues have been discussed in detail:

1. Droplet spreading dynamics. This is a phenomenon that occurs at the early stages whatever the impingement regime. The main findings on this can be summarised as: (1) the spreading velocity at the early stage is several times larger than the droplet impact velocity, implying that the film velocity is of the same magnitude of the incoming velocity at the stage where the impingement process is well underway; (2) the time scale for the completion of the

spreading is of the order of D_I/V_I; and (3) the early spreading stage is controlled by inertial effects, whereas the later spreading stage is marked by the dominance of the surface tension and viscosity and the wetting dynamics here are important.

2. Heat transfer characteristics. The heat transfer rate between the impinging droplets and the wall surface has been identified to be mainly dependent on droplet size, impact velocity and impact angle. The evaporation life time for all impinging droplets has been shown experimentally to exhibit the same pattern irrespective of the liquid type and the surface material. The Leidenfrost temperature of impinging droplets has however been found to be affected by the impact velocity.

3. The quantities V_R/V_I and θ_R/θ_I for the rebound regime. A well-established correlation is available only for the case where an impinging droplet bounces off a deep water surface. For the dry-wall case, these quantities have not been well correlated either experimentally or theoretically, although graphical representation is available for droplets bouncing on a dry wall. The data on θ_R/θ_I is even more scarce, and no single correlation has yet been located.

4. Features of secondary droplets for both splash and breakup regimes. The size distribution of the secondary droplets for the splash regime has been shown to be approximately log-normal, and this also appears to be the case for breakup regime as suggested by the limited data available. Further efforts are needed to quantify in a general manner the two key parameters involved in this log-normal distribution function, namely the mean diameter and the standard deviation.

   A common feature has been unveiled for both regimes: the larger secondary droplets are released later, move more slowly and at a steeper angle with the wall than the smaller secondary droplets that are released earlier. However, quantitative information on velocity distribution of the secondary droplets still remains elusive. Although some correlations have emerged for splash regime for describing the number of secondary droplets N, and the proportion of the mass deposited on the wall surface, most of these are, unfortunately, not very

useful because they do not take into account the effects of an adequate number of controlling parameters or because they are in dimensional form.

2.3 Spray Impingement

The process of spray impingement, involving multiple droplets, not surprisingly proves to be much more complicated than that of a single droplet. This is because in the former process, each impinging droplet may interact with the neighbouring droplets, and it is this mutual interference that proves extremely difficult to clarify. Consequently, our detailed understanding of the spray impingement process remains quite poor. Available experimental studies on this process have been focused mainly on: (i) heat transfer between impinging sprays and walls, and (ii) characteristics of the wall spray which is formed by droplets resulting from deflection (by the gas flow), bouncing and splashing upon impingement. Each of these two topics will now be addressed.

2.3.1 Heat Transfer Characteristics

In the framework of spray/wall heat transfer studies, three basic modes of heat transfer have been identified, depending on the wall surface temperature and spray mass flux (see, for example, Grissom and Wierum 1981). They are: (i) the 'dry-wall' mode–in which the surface is so hot that it vapourises all of the impinging spray (Bonacina et al 1975); and (ii) the 'Leidenfrost' mode– in which the impinging droplets are deflected from the surface by a thin vapour film after impact; and (iii) the 'flooded' mode–where the spray forms a thin liquid film on the surface. Of these modes, the dry-wall one has been most studied. In this mode, the heat flux is found to be directly related to the impinging spray mass flux. The Leidenfrost mode exhibits very poor heat transfer (similar to film boiling). The flooded mode, which occurs at relatively lower wall temperature, involves essentially heat transfer within a liquid film, the liquid being supplied only incidentally by a spray.

A description of the transition conditions between the three modes can be found in the work of Grissom and Wierum (1981). Qualitatively, it can be described as follows. When the wall temperature is low or the mass flux is large so that the mass

vapourised is less than the mass arriving, liquid mass accumulates on the wall to form a film which in turn hinders the overall heat transfer through the surface and thereby increases still further the rate of mass accumulation. The result will be the flooded state. In this situation, the liquid film plays a dominant role in determining the wall heat flux. Also, the heat transfer rate depends on the surface geometry and the gas boundary characteristics in the near-wall region. In typical high speed direct-injection diesel engines, the wall temperature is usually less than the fuel boiling temperature, thus spray/wall heat transfer is most probably in the flooded mode or in the intermittent flooded mode. This makes it possible, from the point of view of CFD, to address the heat transfer problem by solving film momentum and energy equations, taking the wall heat flux or wall temperature as the boundary conditions, provided that an appropriate film model is available. Meanwhile, the heating and vapourisation of the droplets in the vicinity of wall film can be calculated in the same manner as those droplets suspended in the bulk flow. This is because the wall heat flux has been mainly absorbed in the liquid film, so the heating of droplets by the wall is therefore negligible.

If the wall temperature is increased or spray mass flux is decreased such that mass evaporation rate is fast enough to prevent film formation, then the dry-wall mode is realised. For a given mass flux, there is obviously a transition temperature, T_f, from flooded mode to dry-wall mode. In a spark-ignition engine, the heat transfer process between the impinging spray and the intake valve surface is perhaps in the dry-wall mode. Here, in the computer simulations, the conventional calculation of droplet heating and vapourisation have to be modified to accommodate the effect of the wall heat flux. This flux has to be provided by appropriate correlations.

At a sufficiently high wall temperature, $T_w = T_{Leid}$, which marks the initiation of the Leidenfrost state, any impinging droplet begins to vapourise as it approaches the surface, as already mentioned in Section 2.2. This vapour quickly spreads into a layer which decreases the surface heat flux so dramatically that initiation of the Leidenfrost state on the surface would lead quickly to a flooded surface with film boiling. The Leidenfrost mode, though seldom occurring in Diesel and spark ignition engines, is popular in the metallurgical industry and in nuclear reactor safety devices for cooling of very hot materials at beyond the Leidenfrost temperature.

Some quantitative data on the transition temperatures T_f and T_v ($T_f < T_v$) have been provided by Grissom and Wierum (1981).They also found that, in the dry-wall mode, the heat flux is essentially a linear function of the impinging spray mass flux.

Deb and Yao (1989) performed an analysis of impinging spray heat transfer in the Leidenfrost state. They distinguish two cases: (i) dilute sprays in which heat transfer interaction among droplets is negligible, and (ii) dense sprays in which significant interaction exists. In the former case, heat transfer analysis is pursued by decomposing the mechanisms into three identified subprocesses, namely, drop contact heat transfer, bulk air convective heat transfer, and radiative heat transfer. This enables the evaluation of the heat fluxes for each subprocess which are then summed to obtain the total heat flux.

In dense spray circumstances, the effect of droplet interaction on the heat transfer cannot be neglected, which further complicates the analysis. For instance, Hoogendoom and Hord (1974) noticed that (a) the spray heat transfer data show a strong drop interaction effect when compared with single drop data; and (b) the Leidenfrost temperature strongly increases with spray density. This interaction effectively decreases the heat transfer to each droplet, as argued by Deb and Yao (1989). To enable analysis for dense sprays, these authors adopted the following approach: first analyse and predict the limiting or asymptotic conditions of a dense spray; and then evaluate wall heat flux for the intermediate region as combination of dense and dilute extreme conditions. The heat flux for the intermediate case is given by the empirical relation:

$$q_{\text{dense}}^{-0.86} = q_{\text{dilute}}^{-0.86} + q_{\text{pool}}^{-0.86} \tag{2.34}$$

Arcoumanis and Chang (1993) performed an experimental study on the heat-flux distribution in the vicinity of the impingement point when a transient impinging spray impacts onto a hot wall whose temperature ranges from $150 - 250^0C$ (always less than the Leidenfrost temperature but sometimes above T_B). In their work, they examined the effects of several parameters including the impingement distance, the injection frequency, the injected fuel volume and the wall temperature. This allowed them to cover both flooded and dry-wall modes, as the conditions alter. Their measurements demonstrated a clear dependence of the heat transfer rate on the spray characteristics prior to impingement: as might be expected, the higher

the arriving velocities of the droplets, the higher the heat transfer. In the light of the experimental findings, the authors developed a correlation for spray/wall heat transfer, given by:

$$Nu = a_1 R_e^{b_1} Pr^{c_1} We^{d_1} \tag{2.35}$$

where the coefficients a_1, b_1 and c_1 are determined experimentally, and:

$$\begin{aligned} Nu &= \frac{hD}{k} \\ Re &= \frac{\rho V D}{\mu} \\ Pr &= \frac{C_p \mu}{k} \end{aligned}$$

in which D and V are respectively droplet characteristic size and velocity.

The correlation (2.35) has two major limitations. Firstly, it does not account for the effect of a wall film, which may be effective in the flooded mode. In this case, the surface topology and material properties are also influential. Secondly, the arriving mass flux, which is important in the dry-wall mode (according to Grissom and Wierum (1981)), does not appear in the correlation.

Some experiments have been conducted under conditions likely to be encountered in DI diesel engines. For example, Kamimoto et al. (1982,1992) and Wolf and Cheng (1989) examined the spray/wall heat transfer with and without combustion in rapid compression machines. Under the conditions investigated, both groups noted an interesting phenomenon: for short spray penetration distances ($\leq$ 30mm which is typical of small DI engines), the heat transfer rate at the impact point is identical for both combustion and non-combustion cases. This, according to Wolf (1988), can be attributed to the fact that the spray was not burning at the impact point duc to the rich local equivalent ratio. Additionally, Kamimoto et al. (1982) also observed that the heat transfer rate for the 45^0 impingement angle case was hardly different from that at normal incidence. Moreover, the influence of the distance between the nozzle and wall surface on the heat flux was small within the examined range (28-40mm). Wolf (1988), however, observed a different behaviour: the heat transfer at the impact point in the non-combusting case exhibited an inverse square dependence on the spray-wall separation distance. The reason for this contradiction is, however, not clear.

2.3.2 Wall Spray Characteristics

Attention is now turned to surveying the studies on the characteristics of the wall spray (as defined in Chapter 1) and wall jet resulting from wall impingement.

Experimental Investigations

Taylor and Walsham (1970) studied the behaviour of sprays in a constant volume bomb and in relatively large combustion chambers of medium-speed engines, using Schlieren and direct photographic techniques. Their results showed that deliberately ensuring impingement in open-bowl and 'Hesselman' pistons enhances fuel-air mixing.

Idoum et al (1985) utilised a hydraulic analogue technique to simulate Diesel injection processes, with particular emphasis on the development of the wall spray and wall gas jet. Mixing phenomena in the wall spray region were studied both experimentally and theoretically in quiescent and swirling flows. They observed that the spray jet was deflected under cross-flow conditions, with the volume of the downstream wall spray expanding faster than that of upstream wall spray. They also produced evidence that better mixing can be achieved through combinations of jet velocities and swirl speed, which yielded substantial improvement over the quiescent case. Beyond a certain swirl rate, however, the effect of impingement on fuel-air mixing was found to be marginal.

An interesting result was obtained by Karimi (1989) in his investigation of spray and combustion events using a four-cylinder Perkins engine and also a constant-volume combustion bomb. He observed that, in the piston cavity at which the sprays were directed, turbulence is so strong that it not only enhances fuel-air mixing but also prevents the spray from hitting the wall. This finding suggests that it is possible to reduce, if not avoid, fuel deposition by altering the flow pattern in the impingement region.

Recently, more experimental studies have emerged on the wall spray characteristics (e.g. Kuniyoshi et al. 1980; Fugimoto et al. 1988; Sakane et al. 1988; Katasura et al. 1989; Saito et al. 1991; Miraz 1991; Saito et al. 1993; Kavamura and Saito 1993). The main features examined in these studies included: (1) wall spray radius R_w and height H_w, as defined in Figure 2.12 for both normal and oblique

impingement; (2) temporal development of the wall spray structure; (3) droplet concentration and distribution within the wall spray; (4) amount of fuel deposited; and (5) wall film footprint and mean film thickness.

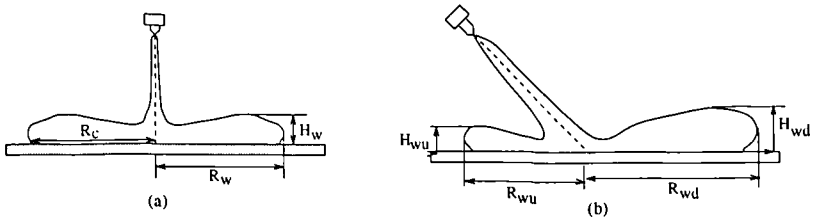


Figure 2.12: Diagram showing definitions of wall spray height and radius.

Fujimoto et al. (1988) conducted an experimental study on Diesel sprays impinging normally onto a flat plate at room temperature, various ambient gas densities and different distances between the nozzle and the wall. Spray patterns were presented as photographs obtained with transmitted light and scattered light. The wall spray looks like a disc at the beginning in the vicinity of its axis, while its height rises. Subsequently, the wall spray forms waves on its free surface. Their results also showed that, when chamber gas density is increased, the wall spray penetrates faster in the vertical direction and slower in the tangential direction. This is because the higher gas density presents larger resistance force to the spray, which tends to push droplets upward more strongly and to reduce the radial penetration rate of the wall spray. Additionally, measurements were made of the total amount of the fuel deposited on the wall as a liquid film for different gas densities. It was found that, for a fixed nozzle-wall distance, the amount of adhered fuel remains almost constant for gas densities up to approximately $18\,kg/m^3$, above which it decreases.

Fujimoto et al. (1988) also performed calculations of the temporal and spatial distribution of the droplet volume density, defined as volume of drops per unit volume in space, within the wall spray from the data obtained by the laser light extinction method. They found that the density is higher near the wall and in the peripheral region of the wall spray. This local high density was explained by the authors as follows. Upon impingement, fuel droplets first travel along the wall and

then are pushed upwards by the resistance of the ambient gas. During this process, some of the fuel droplets cling to the wall and as a consequence a film is formed on the wall.

Similar experiments were carried out by Katsura et al. (1989) who paid particular attention to the spray pattern and the temporal and spatial distribution of droplet density. Their experiments involved variations in injection pressures ranging from 0.2 to 19.5 MPa, injection duration from 1.03 to 1.38ms, fuel quantity from 9.7 to $11.1mm^3$, ambient density from 6.15 to 28.1 kg/m^3 and impingement wall distance from 20 to 34mm. A single-hole nozzle of 0.3 mm diameter and 2.0mm orifice length was used to inject light diesel-oil into a high pressure chamber, charged with air or CO_2 gas, enabling normal impingement of the spray onto the wall.

Their results confirmed the effect of gas density variation on the wall spray behaviour identified by Fugimoto et al (1988), as mentioned earlier. In addition, they investigated the effect of the injection pressure. It was found that, as the injection pressure is increased, the wall spray radius and height also increase. At the earlier stages of impingement, the tangential penetration rate of the wall spray is essentially not affected by the change in the injection pressure, whereas the normal penetration rate clearly increases with increase of the injection pressure. There are two reasons proposed by the investigators. Firstly, the arriving droplets, which lose their momentum due to the resistance of the surroundings, are pushed upward by the droplets which are immediately behind them, and the pushing forces become stronger at higher injection pressures. Secondly, high injection pressure also enhances air entrainment, creating an even stronger wall jet vortex (see its definition in Chapter 1) which has been observed clearly by the authors. This in turn increases the region of low droplet density (higher air/fuel ratio). In the present author's opinion, another important reason might be that higher injection pressure gives rise to higher impingement velocities, thereby causing more intensified splashing. This not only leads to better mixing but also produces more secondary droplets which leave the wall in the near-normal directions as was pointed in Section 2.2.

Katsura et al (1989) established the following correlations from their experimental data of wall spray radius and height in terms of some key operation conditions:

$$R_w = 3.87\Delta P^{0.89}\rho^{-0.24}t_{rel}^{0.48} \tag{2.36}$$

$$H_w = 1.23\Delta P^{0.5}\rho^{0.048}t_r^{0.35} \tag{2.37}$$

Here ΔP (MPa) is the pressure drop between the injection pressure and ambient pressure; ρ (kg/m^3) is the ambient gas density and t_r (ms) is the time from the onset of impingement.

Although these correlations are in good agreement with the experimental data from which they were deduced, they cannot be extended to condition outside of the experiments with confidence. The reason is that (2.36) and (2.37) are not non-dimensional. Also the effects of the injection direction, the gas cross flow and wall impingement distance are not included.

The first detailed study of the effect of a cross flow on spray impingement appears to be due to Miraz (1991). In his wind tunnel experiments, a single-hole nozzle was used to inject a diesel spray at either 0^0 or 30^0 with the normal direction to the wall, and the nozzle was placed at 31mm above the impingement surface. The cross-flow is in the direction parallel to the wall. Measurements of the following characteristics are presented and discussed: (i) impingement time, t_{imp}, which is defined as the time required to reach the impingement wall;(ii)wall spray radius; and (iii) wall spray height. For each of the parameters measured above, correlations were given and compared with experiments. They are cited below:

Impingement time t_{imp}

(without cross flow)

$$t_{imp,\alpha} = \frac{(Z/cos\alpha)^2}{C_t^2}\left[\frac{\Delta P}{\rho}\right]^{-0.5} D_N^{-1}\left(1 + 2.7\times 10^{-4}\left(\frac{Z}{cos\alpha}\right)^{-2}\right) \tag{2.38}$$

Here C_t is an empirical coefficient set to be 3.8, Z is the wall impingement distance, ΔP is the pressure drop between the injection pressure and ambient pressure, and α is the angle between the injection direction and the normal direction to the wall. Unfortunately, in this correlation the cross flow effect is not accounted for.

Downstream Spray radius

This parameter R_{wd}, together with downstream spray height H_{wd}, is schematically defined in Figure 2.12b.

(i) Without cross-flow

$$R_{wd} = 1.23(\cos\alpha + 0.79\sin\alpha)\left[\frac{\Delta P}{\rho}\right]^{0.25} D_N^{0.5} t_r^{0.5} \tag{2.39}$$

(ii) with cross-flow

$$R_{wd} = 1.23(cos\alpha + 0.79sin\alpha)\left[\frac{\Delta P}{\rho}\right]^{0.25} D_N^{0.5} t_r^{0.5}(1 + 19\left[\frac{W_G cos\alpha}{U_{inj}}\right]^{1.33} \tag{2.40}$$

Here t_r stands for the time from the onset of the impingement, W_G is the gas cross-flow velocity which is uniform and constant, and U_{inj} is the injection velocity.

Downstream spray height

(i) Normal Impact ($\alpha = 0^0$)

$$\frac{H_w}{D_N} = 0.087[We_J]^{0.52}\left(\frac{\rho}{\rho_L}\right)^{0.52}\left(\frac{t_r}{t_b}\right)^{0.365}\left[1 - 8.41\left(\frac{W_G}{U_{inj}}\right)^{1.5}\right] \tag{2.41}$$

(ii) Oblique impact ($\alpha = 30^0$)

$$\frac{H_{wd}}{D_N} = 0.075[We_J]^{0.52}\left(\frac{\rho}{\rho_L}\right)^{0.52}\left(\frac{t_r}{t_b}\right)^{0.48}\left[1 - 17.8\left(\frac{W_G}{U_{inj}}\right)^{2}\right] \tag{2.42}$$

Here t_r/t_b= ratio of the time from the onset of wall impaction to the characteristic jet breakup time (0.25 ms),and $We_J = \rho_L U_{inj}^2 D_j/\sigma$ is the jet Weber number (D_j being the equivalent jet diameter).

Miraz's findings on the wall spray radius and height can be summarised as follows:

- For a given ambient pressure, an increase in cross-flow velocity, which is in the downstream direction, results in an increase of downstream wall spray radius, but a decrease of downstream wall spray height.
- Both spray radius and height increase as cross-flow turbulence intensity becomes larger and larger.
- As the gas pressure increases, the spray radius decreases whilst the spray height increases.
- In oblique impingement circumstances, both downstream wall spray radius and height exhibit larger values compared to normal impingement cases for the same conditions.

Recently, a more comprehensive investigation has been carried out by Saito et al (1993) of impinging spray characteristics at the conditions of high injection pressures. Their studies involved both normal and oblique spray impingement in test bombs. A single-hole nozzle of 0.25mm was used. The bomb was charged with N_2 of pressure 2.1 MPa. Parameters varied include:(a) fuel pressure (30, 55 and 120 MPa); (b)wall impingement distance (15, 25 and 35mm); and (c) impingement angle (45^0, 60^0, 75^0 and 90^0). Measurements were made of the following kinds: (1) wall spray radius and height as a function of time; (2)spray Sauter mean diameter before and after impingement at different fuel pressures;(3) photographs of spray and wall film patterns; (4) mean thickness of wall film and its radius variation with time; (5)ratio of adhered fuel to total fuel injected; and (6) droplet density distribution within the wall spray.

To gain some insight into their results, a few examples have been reproduced here. Figures 2.13 and 2.14 show the typical spray and wall film patterns in the case of normal impingement. The boundaries of wall film are rather irregular, exhibiting a certain kind of fractal structure. It is clearly evident that the film radius is smaller than the wall spray radius. A comparison is made in Figure 2.15 which shows variations with time the radii of both the wall film and the wall spray. The mean film thickness decreases with increasing injection pressure as show in Figure 2.16 , for a given ambient pressure. It can also be seen from this figure that the higher the ambient pressure, the lower the mean film thickness. Figure 2.17 shows that the larger the injection pressure the smaller the amount of deposited fuel on the wall. This behaviour, as we suggest, can be explained by two possible mechanisms. Firstly, higher injection pressure results in better atomisation, making the sizes of arriving droplets smaller. This in turn yields more droplets being deflected by the wall gas jet, which also exhibits stronger turbulence intensity than in the case of the low injection pressure. Secondly, as the wall gas jet becomes more violent, the turbulence bursts mentioned earlier may play a role in reducing fuel deposition.

Figure 2.17 also shows a linear dependence of the adhered fuel amount on impact angle, with normal impingement giving the maximum value. The reason for this was not explored by Saito et al. (1993). We believe it is due in part to the fact that as the injection direction is more oblique with the impingement surface, both the

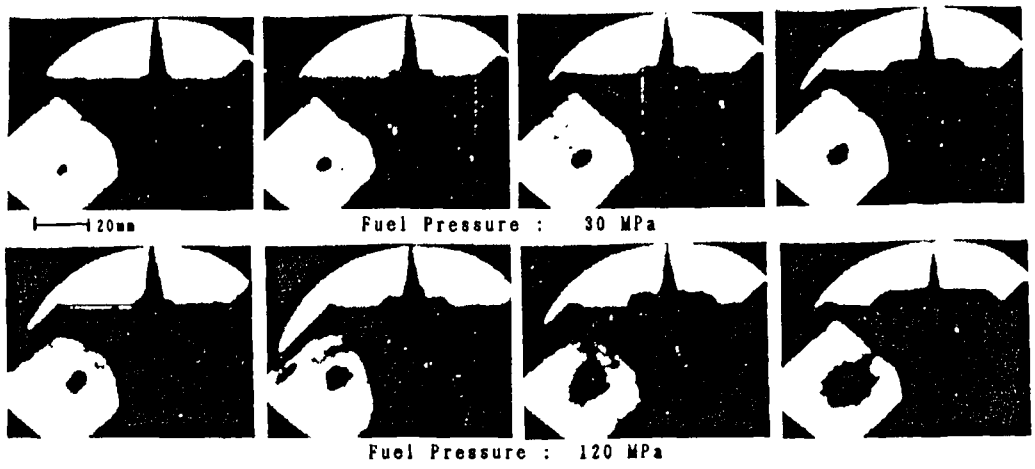


Figure 2.13: Patterns of wall spray and wall film at normal impingement (reproduced from Saito et al. 1993)

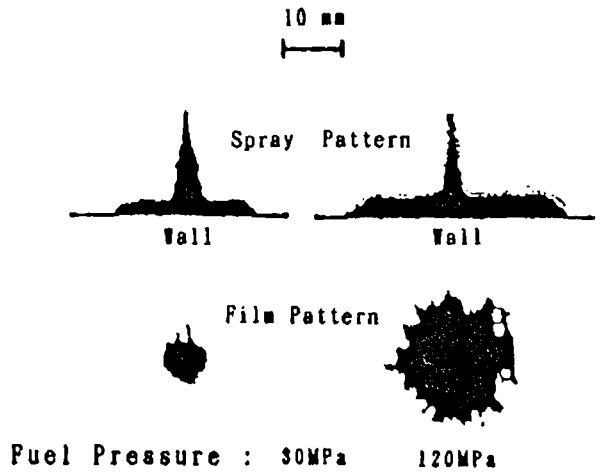


Figure 2.14: Typical pattern of wall spray and film (reproduced from Saito et al. 1993)

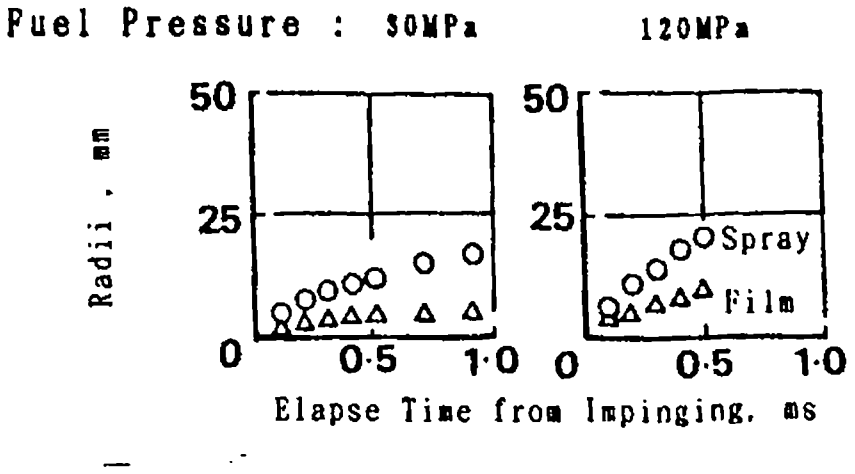


Figure 2.15: Variation of wall spray and film radii with time (reproduced from Saito et al. 1993)

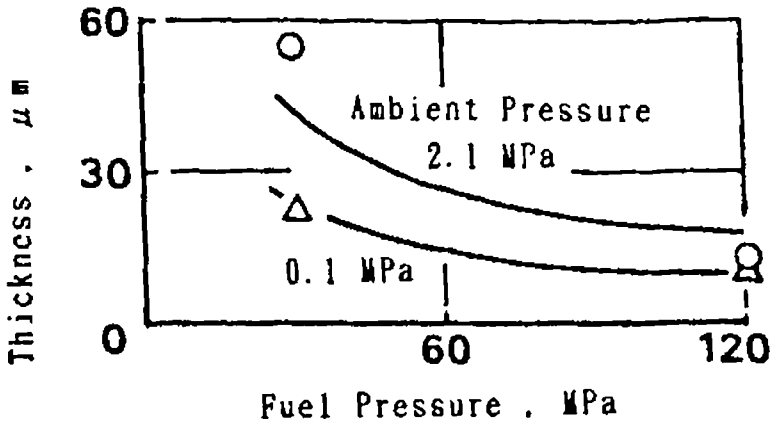


Figure 2.16: Mean wall film thickness variation with pressure (reproduced from Saito et al. 1993)

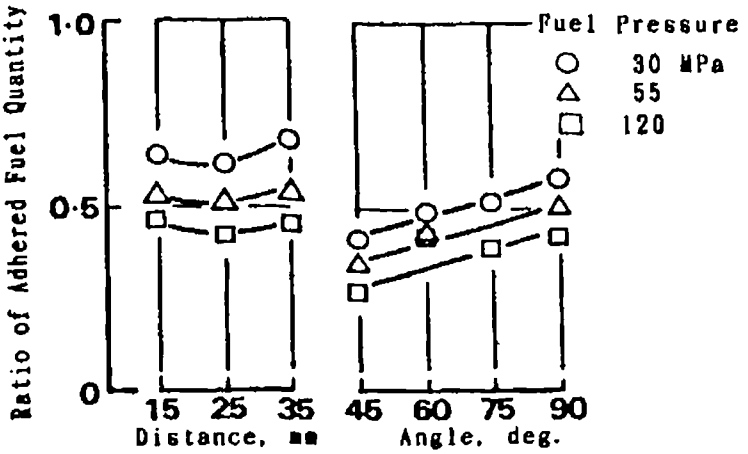


Figure 2.17: Ratio of adhered fuel to total fuel injected variation with impingement distance and angle,and injection pressure (reproduced from Saito et al. 1993)

arriving droplets and gas jet possess more tangential momentum which cause more droplets to slide along the wall, thereby reducing fuel deposition.

A linear dependence on impact angle also exists for the ratio of upstream and downstream wall spray radii, as evidenced in Figure 2.18. The reason for this is almost self-evident– the larger the impact angle, the larger the tangential momentum of the wall spray and jet in the downstream region.

Figure 2.19 illustrates the behaviour of the entire spray Sauter mean diameter, which becomes smaller after impingement due to impingement-induced atomisation. The difference between the Sauter mean diameters before and after impact is most profound at low fuel injection pressure. However, as the injection pressure is increased, this difference becomes smaller and smaller. The reason may be that when the injection pressure is above a certain level, atomisation is so strong such that wall-impingement-induced breakup is not evident.

While most of investigators have concentrated on wall spray height and radius as well as droplet density in the wall spray, few attempts have been made to measure the local droplet size and velocity distributions. These data are necessary if the computational models of wall spray impingement are to be more rigorously tested and developed. Coghe et al. (1992) have obtained some experimental data of this kind. They employed a single-hole nozzle and a transient fuel mass flow rate involving a peak injection pressure of 600 bar. The nozzle-to-plate (perpendicular)

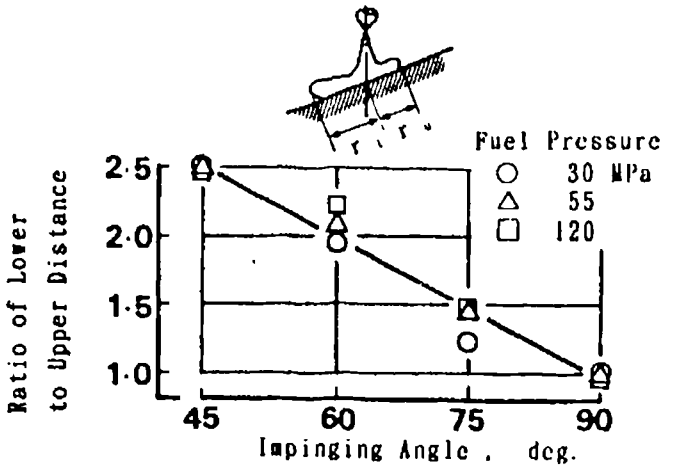


Figure 2.18: Behavior of the ratio of upstream and downstream wall spray radii (reproduced from Saito et al. 1993)

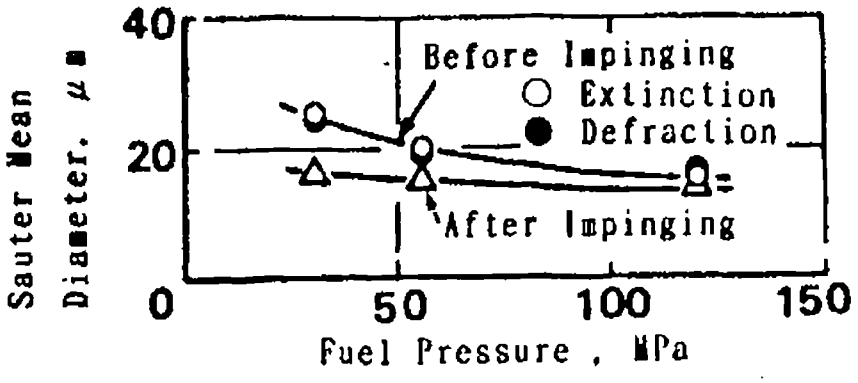


Figure 2.19: Behavior of Spray Sauter mean diameter (reproduced from Saito et al. 1993)

distances are 25 and 20mm respectively for normal and oblique (with inclination angle 45^0) cases. A technique of LDV was used to measure the following quantities: (i) temporal variations of droplet peak normal velocities at specific locations in the near-wall region; (b)ensemble-averages over 1 millisecond duration of droplet diameter, normal and tangential velocities at 14mm from the stagnation point and various heights from the wall surface for both normal and oblique spray impingement events in quiescent chambers. Their results will be discussed in more detail and compared with the calculations in Chapter 7, where the models developed in this study are assessed.

Computational Modelling

Some attempts have been made to develop mathematical models of spray wall impingement, using computational techniques. An early attempt was that of Naber and Reitz (1988), who developed a model for spray impingement which they embodied in the KIVA code. In their model, a droplet which reaches the wall is assumed either to stick on the wall in a spherical form ('stick' model), reflect elastically ('reflect' model), or move tangentially along the surface like a jet, with the same velocity magnitude as that before impact ('jet' model). There are three limitations of this model: (1) the conditions for the occurrence of each regime are not specified in the light of experimental data; (2) the phenomenon of droplet shattering, which occurs at high collision energy and can be important in effecting wall spray dispersion and vapourisation, is ignored; and (3) the energy and momentum losses of the impinging droplets are not accounted for.

While this model has been found to work reasonably well in cases involving relative large injector-wall distances (larger than around 60 mm), it has proven less satisfactory when the wall is in closer proximity. For instance, Naber et al (1988) examined a case where the impact wall is positioned only 6.4mm from the injector, such that the impingement-induced droplet breakup is important. They found that the model had to be modified in such a way as to account for this behaviour. To do this, they imposed a normal velocity component on the ejected droplets randomly chosen to be 0-34% of the incident velocity, in order to achieve reasonable agreement with the experimental data. However, this modified version was found to be unsat-

isfactory in the study by Alloca et al (1990), where the calculated spray pattern was appreciably different from the experimental pattern.

Watkins and Wang (1990) later proposed a model which differs that of Naber and Reitz in two ways. Firstly, a droplet which hits the wall is assumed to suffer one of the two consequences: namely rebound or breakup, depending on the impact energy. The transition criterion between these two regimes is described by a critical Weber number, $We_c \approx 80$, which was deduced by Wachters and Westerling (1966) from their experimental data on water drops impinging with a very hot wall whose temperature is above the Leidenfrost temperature. This criterion, as was made clear in the preceding section, is not applicable to a wall whose temperature is below the fuel boiling point as is usually the case in Diesel engines. Secondly, the modelling of post-impingement behaviour is different in the following ways. For the 'rebound' regime, the rebound angle is assumed to be equal to that of the incidence angle, but the magnitude of the rebound velocity is determined from an energy loss correlation proposed by Jayarante and Mason(1964) for a water drop impinging on a 'deep' water layer. For the 'breakup' regime, the ejected droplets are assumed to move tangentially to the wall at a velocity equal to the incident droplet tangential velocity; and the sizes of the ejected droplets are assumed to be one-quarter of the incident ones. An obvious weakness of this treatment is that it fails to reflect the physics that the secondary droplets usually leave the wall at an angle with it and fall within a cone, and that they follow a distribution of sizes and velocities.

The model of Watkins and Wang was initially found to significantly underpredict wall spray dispersion (and hence wall spray volume as well) when compared to experimental data (Watkins and Wang 1990). In order to achieve better agreement, these authors modified the droplet binary collision model of O'Rourke and Bracco (1980) so that the colliding droplets are caused to move along the direction of maximum local void fraction gradient. As a consequence of this, better prediction of the wall spray dispersion was achieved, but still the calculated wall spray volume appears to be appreciably smaller than that of the experiment.

From the above discussion it is clear that theoretical modelling of spray impingement is still at its infant stage, and there is clear need to develop the methodology further.

2.3.3 Summary

In this section an overview has been provided of the information presently available on spray impingement dynamics. Two major issues have been tackled. Firstly, on the side of heat transfer between the impinging spray and the walls, three basic operation modes have been identified which are determined by spray mass flux and the wall temperature. Some correlations on heat transfer have been presented and critically examined. It has been stressed that these correlations are each limited to a specific set of conditions and are therefore not suitable for general use in CFD simulations.

Secondly, on the side of the wall spray characteristics, experimental data are mostly available for wall spray radius and height. These data are undoubtedly useful for model assessment; but they are by no means adequate for the full validation of the model, since it is quite possible for predicted and measured wall sprays to have closely matched wall spray extents but very different local droplet size and velocity distributions. This latter information is more important in reality, for it is closely linked to the spray evaporation rate. Unfortunately, experimental data of this kind is extremely limited; there is therefore a further need for the experimental investigators to provide local data on the size and velocity distributions of the droplets within the wall spray.

2.4 Liquid Film Flow Process

2.4.1 Introduction

Liquid film flow occurs in a wide range of practical applications. The literature on the subject is therefore extremely rich. The focus here is on those papers which address aspects that are mostly likely to be encountered in diesel engine wall film flows. It is therefore useful to have a physical picture of what occurs within diesel engine films while impingement is underway. In the present author's opinion, three stages may be distinguished in the film evolution:

1. 'Inception stage'-where the deposited fuel mass resulting from those droplets which either adhere or splash is at first scattered on the wall surface in the form of discrete disks or domes of very small size. As time goes on, more and more mass accumulates and a continuous liquid layer begins to form. This *stage corresponds to the very early period* of the impaction process.

2. 'Development stage'- which covers the period from the onset of continuous liquid layer to the end of fuel injection. In this stage, the liquid film continues to build up as more and more fuel mass is deposited, and spreads outward under the action of gas drag and the bombardment of incoming droplets. Here, film spreading is characterised by its deforming interface and moving contact line which delimits the area covered by the wall film. Meanwhile, as the gas is compressed by the piston, its temperature increases which in turn causes film evaporation. The film surface is subjected to the disturbances by the impinging droplets and the gas drag, causing wave formation and evolution at its surface. These waves have been observed by Özdemir (1992) who studied the behaviour of wall films formed by impinging sprays in a test bomb, as will be reviewed shortly. The waves may break up, resulting in droplets being torn off from the film surface, a phenomenon called droplet entrainment. This occurs if the gas drag is very strong– as when there exists a strong swirl flow. The mean film thickness during this stage is believed to be in the range of a few microns or a few tens microns in the light of the experimental data. (eg. Özdemir 1992; Síwon 1988; Ereaut et al 1992), in which case long-range

molecular or ionic forces are negligible.

3. 'Thinning stage'-Shortly after termination of fuel injection, mass deposition ceases, therefore film continuously becomes thinner due to evaporation. This thinning process eventually leads to an ultra-thin film regime followed by dry-out.

In typical high speed direct-injection diesel engines, the mass flux in the impingement zone may be high enough so that the time required for the formation of a continuous liquid layer is very short, whereas the time scales for the following stages appear to be much longer. For this reason, it is justifiable to view that a continuous layer of liquid patch is formed immediately after the commencement of impingement.

In what follows, a review is made of the literature that are relevant to the processes involved in the 'development stage'(data on other stages are extremely limited and will not be discussed here). First, core parameters affecting film dynamics are discussed in Section 2.4.2. This is followed in Section 2.4.3 by a brief discussion of flow regimes and the corresponding transition conditions. Subsequent attention is then devoted, in Section 2.4.4, to theoretical methodologies used for analysing different flow regimes. In Section 2.4.5, detailed discussion of droplet entrainment is presented. Finally in Subsection 2.4.6, a brief discussion is provided of the characteristic features of wall films formed by liquid deposition of impinging sprays.

2.4.2 Parameters Influencing Film Dynamics

The film dynamics are governed by a number of parameters representing the conditions of liquid film itself, the surrounding gas, droplets, and the wall along which the film flows. Consequently, there are a variety of forces acting on the films. These forces include:

Body forces. These my be due to gravity or the wall acceleration– as occurs in internal combustion engines. If the typical film thickness is less than the capillary length $l_c = (\sigma/\rho_L g)^{1/2}$ which is usually of the order of 1 mm, the gravity force is negligible. In typical high speed direct-injection engines, the peak body force due to wall acceleration is of the order $100N/m^3$. Therefore, these forces are to be accounted for in this study.

Capillary (or Laplace) pressure. This, as indicated clearly by its expression, $(-\sigma\mathcal{C})$, represents the combined action of liquid surface tension σ and film surface curvature $\mathcal{C}$. This force drives fluid surface toward a minimal energy state characterised by a configuration of minimum surface area, and its largest magnitude appears in the fluid medium on the concave side of the interface–since it is directed towards the center of the curvature of the interface. It has been demonstrated that (eg. Kocamustafaogullari 1984) the capillary pressure produces a stabilising effect on film flows.

Viscous (or friction) force. This is closely linked with the liquid viscosity and the local velocity gradients within the film. It dissipates film energy and hinders the development of natural instability of the film.

Interfacial shear force. This results from the relative velocity between the liquid film and the surrounding gas. It enables momentum exchange between the gas and the film, produces disturbances on films which may generate surface waves (e.g. Hanratty & Engen 1957; and Van Rossum 1959), and causes changes in local film velocity and thickness. Moreover, when this force is very strong, it may lead to surface wave breakup and liquid removal from the film in the form of droplets, a phenomenon called droplet entrainment. Evidence of this has been provided by the experimental data of Wallis (1962), and Zuber (1962) for annular film flows, and by Shin et al (1994) for gasoline engines with port injection systems. This latter case will be described in more detail in a subsequent subsection.

Forces due to impinging droplets and gas jets. These arise in situations where impinging droplets and/or gas jets strike the film surface and thus impart normal and tangential momenta to the film. No attempts appear to have been made in the previous studies to incorporate these forces into a film flow analysis. However, according to an order of magnitude analysis made in the present study, the impingement-induced forces are dominant in the impingement zone. It is therefore necessary to include these forces in the present study, as will be described later in Chapter 5.

Vapour recoil. This is a pressure force which results from film vaporisation (Hickman 1952). Because mass must be conserved, the change in fluid density during evaporation results in a discontinuity in both the fluid velocity normal to the inter-

face and the rate of transport of linear momentum across it. On the other hand, momentum must also be conserved. Thus, the discontinuity in velocity results in a downward force, p_v^* on the interface, called 'vapour recoil', which increases with evaporation rate and with an increase in the density ratio between the liquid and gas, as can be seen from its expression given below:

$$p_v^* = \dot{m}_v^2 \left(\frac{1}{\rho_G} - \frac{1}{\rho_L} \right) \tag{2.43}$$

where $\dot{m}_v$ is the film vaporisation rate which is dependent on the film surface temperature and the surrounding gas temperature, among other factors.

According to Bankoff (1971), who performed an analysis of evaporating films draining down an inclined heated plate, vapour recoil destabilises film flows.

In addition, the following parameters characterising wall conditions are also important.

Wall roughness. This parameter, as discussed earlier in Section 2.1, is crucial in influencing the dynamics of the liquid film formed during droplet impact. It also has a substantial influence on liquid films, and its main effects which have been found are: (i) roughness tends to increase the heat transfer rate between the film and its surroundings due to the fact that it facilitates the formation of surface waves (e.g. Bressler 1960); and (ii) it tends to cause the film flow to become turbulent more readily, since roughness gives rise to additional disturbances in the laminar films. Evidence of this has been provided by the work of Vouyoucalos (1961), Saveanu et al (1962), and Brauer (1956).

Wall temperature. This not only has a direct effect on film heating (cooling) and mass transfer, but also plays a role on the stability of film flows. The latter is evidenced by the stability studies of Marschall & Lee (1973), Unsal & Thomas (1978), Spindler (1982), and Goussis and Kelly (1985), each of which tends to reveal that wall heating ($T_W < T_L$, T_L being liquid temperature) destabilises the film flow while wall cooling ($T_W > T_L$) stabilises it.

The relative importance of the above-described forces and parameters can be measured by estimating the following dimensionless parameters:

(a) Film Reynolds Number: $Re_F = \rho_L \bar{u} \bar{\delta} / \mu_L$. This measures the relative importance of inertial and viscous forces.

(b) Film Weber number: $We_F = \rho_L \bar{u}^2 \bar{\delta}/\sigma$. This represents the ratio between the inertial force and surface tension force.

(c) Film Froude number: $Fr_F = \bar{u}/(g\bar{\delta})^{1/2}$

(d) Capillary number: $Ca_F = \mu_L \bar{u}/\sigma = We_F/Re_F$.

(e) Phase change numbers: $Ku = c_p(T_W - T_s)/h_{fg}$, $Ku_G c_p(T_G - T_s)/h_{fg}$. These two parameters characterise the ratios of the available enthalpy in the wall and in the surrounding gas, respectively, to the heat required to evaporate film. Thus, they represent the driving force for the evaporation/condensation processes.

(f) Prandtl number: $Pr = \nu_L/\alpha$. This is a measure of relative importance of the momentum transport ability and the thermal diffusivity ability.

(g)Dimensionless gas shear at the interface: $\tau_s^* = \tau_s \bar{\delta}/\sigma$. This measures the relative importance of gas shear force and surface tension force. It is an important parameter in describing droplet entrainment, as will be discussed later.

(h) Ratio of film thickness to wall roughness : $\bar{\delta}/r_s$

In the above $\bar{u}$ stands for mean film velocity, $\bar{\delta}$ is the mean film thickness, g is the gravitational acceleration, τ_s is the interfacial shear, and T_s is the film surface temperature.

2.4.3 Flow Regimes and Transition Conditions

According to experimental observations, three basic flow regimes can be distinguished. They are briefly described as follows:

1. *Smooth laminar film flow* - which exhibits smooth film surface and regular flow pattern. This occurs at low film flow velocity where external disturbances caused by gas drag or wall roughness and thermal effects are usually absent or not appreciable.

2. *Laminar wavy film flow* - in which different types of surface waves can appear including gravity type or capillary type, mixed capillary-gravity type or other types (cf. Yarin & Oron 1993). The specific type of surface waves depends on the nature of external disturbances that are dominant. In this regime, the parameters characterising the wave structure such as wave speed, lengh,

and amplitude are important quantities in analysing film interface transfer processes. It is, however, very challenging to determine them.

3. *Turbulent film flow* - where flow field becomes irregular and turbulent, and eddy diffusity features in transport processes. This occurs at high flow velocity, and the film surface can be either smooth or rough depending on the flow conditions. In most circumstances, turbulent films also have surface waves. However, in situations where films are relatively thick and free of gas shear, there may not be appreciable waves at the interface (cf. Levich 1948). As will be made clear later, the turbulence structure of films with surface waves is different from that without, and the modelling methodology for both classes of turbulent film flows should be different.

As with the problem of droplet impingement, it is of practical importance to identify which flow regime will occur given that the flow conditions are known. For instance, it is important to know when surface waves exist on with non-isothermal films. This is because that the rates of heat and mass transfer to or from such films can be significantly affected by surface waves (see the evidence of this provided by Zotikov and Bronskii (1962), and Labuntsov (1956), Zhavoronkov et al. (1951), and Kamei and Oishi (1955)).

The transitions between different flow regimes are determined by the parameters described in the preceding section. However, due to the extreme complexity involved in this problem, most of the studies now available in this aspect appear to be incomplete in that the transition criteria obtained are not general, but are only applicable to a very limited range of working conditions. As will be shown below, most correlations obtained for the onset of wavy flow or turbulent flow are functions of film Reynolds or Froude number only, with other parameters being neglected.

Onset of waves in film flows - Determination of the criteria for this onset has been attempted both theoretically and experimentally by numerous investigators. On the theoretical side, a general way of analysing the problem is to impose small perturbations on the governing flow equations (usually the Navier-Stokes equations or the simplified boundary-layer type equations or the Nusselt equations), leading to an equation of Orr-Sommerfeld type, which is then solved by various approximate

means to determine the conditions for stability to exist.

Most of theoretical studies have been confined to isothermal films on vertical or inclined walls with shear-free interface. For example, Benjamin (1957) and Yih (1963) performed linear stability analysis; while Benney (1966), and Gjevik (1970) conduced nonlinear stability studies. The stability problems of non-isothermal films have recently been tackled by Bankoff (1971), Goussis and Kelly (1985), Hwang and Weng (1987), and Kocamustafaogullari (1984). The analysis of Kocamustafaogullari appears to be the best of its kind, as it takes into account of a few more parameters in addition to film Reynolds number in the wave onset equation. These include phase change number Ku, Prandtl number, dimensionless surface tension, film thickness and gravity force. Detailed discussions of the above works are beyond of the scope of the present thesis, therefore only a summary of the typical results is presented in Table 2.8. In this, all the films considered are laminar flows and the works of Goussis and Kelly (1985) and Kocamustafaogullari (1984) are not included due to their complexity. Also included in this table is the work of Craic (1966) who examined the stability problem due to gas shear under isothermal conditions.

On the experimental side, by considering only one parameter and fixing other parameters for simplicity, some investigators have provided observations that when film Reynolds number (or Froude number) is below a critical value the film surface is smooth, otherwise waves will appear at the interface. For vertically falling liquid films, experimental studies of the onset of undulatory motion have been reported by Brauer (1956), Binnie (1957), and Belkin(1959). For films flowing down plates inclined at angle θ (See Figure 2.20 for the definition), observations of wave inception have been provided by Binnie (1959) and Fulford (1962) among others. Typical experimental results are summarised in Table 2.9.

Onset of turbulence in film flows - Studies concerning this issue have been virtually all carried out experimentally in terms of only the Reynolds number Re_F, other parameters being ignored. There are quite a few reports in the literature of a critical Reynolds number at which film flows become turbulent. These values of Re_{Fcrit} are usually determined from the discontinuities which appear in the curves of film thickness, surface velocity of the film, heat or mass transfer coefficients in the film, etc., when plotted against Re_F. Some of the critical values of Re_F obtained

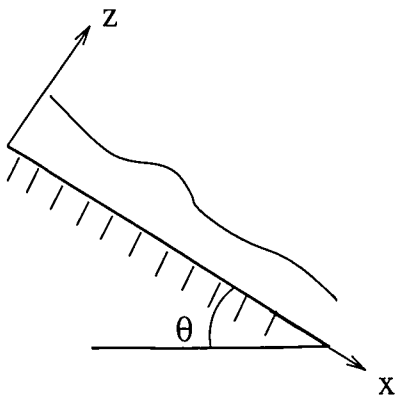


Figure 2.20: Schematic of film flowing on an inclined plate

by some investigators are presented in Table 2.10, in which the relative experimental conditions are not included here due to space limitation. It is clear that there is no single sharply defined critical Reynolds number for the transition to turbulence in a thin film, and the measured values scatter in the range 144-1000. One reason why the critical value of Reynolds number cannot be precisely defined is that the onset condition depends also on several other parameters (as described in Section 2.4.2) which were, unfortunately, not accounted in the above studies. Another reason is the difficulty in controlling experimental conditions.

Table 2.8

Wave onset criteria – theoretical results

Investigator(s)	Remarks	Wave onset conditions
Shibuya (1951)	stability analysis of films on the outer surface of a vertical tube, neglecting surface tension	$Re_F = 7$
Yih (1954)	Stability analysis of films on a vertical wall	$Re_F = 1.5$
Ishihara et al (1952)	stability analysis of laminar flow in open channel	$Fr_F = 0.58$
Benjamin (1957)	theoretical study of wave formation in laminar flow down an inclined plane	$Re_F = \frac{5}{6} cot\theta$
Ishihara et al (1961)	analysis of wave formation of film flows in open channels	$Re_F = cos\theta$
Kapitza (1948)	stability analysis of viscous liquid films in open channels	$Re_F = 0.61 \left(\frac{\mu_L^4 g}{\rho_L \sigma^3} sin\theta \right)^{-1/11}$
Hanaratty &Hershman	study of stability for films flowing in open channels	$\frac{cos\theta}{Fr_F^2} = 3 - n^2 We_F^2$ $n = 2\pi\bar{\delta}/\lambda$
Bankoff (1971)	stability analysis of evaporating films draining down an inclined heated plate	$Re_F = \frac{cot\theta}{6/5 + 23\beta}$ β: dimensionless wall heat flux parameter
Craic (1966)	stability analysis of horizontal films under the action of gas shear forces (Π and Σ are dimensionless normal and shear surface stresses)	$\Pi_r + \frac{3\Sigma_i}{2n} = \frac{n^2}{We_F} + \frac{1}{Fr_F}$ $n = 2\pi\bar{\delta}/\lambda$ (λ being the wave length)

Table 2.9

Wave onset criteria – experimental results

Investigator(s)	Remarks	Wave onset conditions
Brauer (1956)	experimental observation of wave inception in water films outside a vertical tube	$Re_F \approx 3.5$
Binnie (1957)	experimental determination of the onset of waves in water films outside a vertical tube	$Re_F \approx 4.5$
Belkin et al (1959)	obsevation of wave onset for thin films outside a tube	$Fr_F \approx 1$
Bennie (1959)	wave inception observation of water films in channels	$Re_F \approx 29,\ \theta \approx 3^0$ $Re_F \approx 34,\ \theta \approx 1.5^0$
Fulford (1962)	wave onset observation for water films in channels at slopes $7 - 90^0$	$Re_F \approx 6.5,\ \theta = 90^0$ $Re_F \approx 8,\ \theta = 62^0$ $Re_F \approx 9,\ \theta = 44^0$ $Re_F \approx 10,\ \theta = 16^0$ $Re_F \approx 20,\ \theta = 7^0$
Portalski (1960)	observation of wave inception for aqueous glycerol solutions	$Re_F \approx 1.6$

Table 2.10

Critical Reynault number for onset of turbulent film flow

Investigator(s)	Critical Reynault number (Re_F)
Hopf (1910)	250 - 230
Fulford (1962)	260 - 330
Grigull (1952)	310 - 450
Belkin et al (1959)	325 -400
Kutataladze & Styrikovich (1958)	100 - 400
Horton et al (1934)	500 - 750
Zhivaikin & Volgin (1961)	400 - 1000

2.4.4 Theoretical Analysis of Different Regimes

This section presents a brief description of previous theoretical investigations of thin film flows.

1. Laminar Smooth Film Flow.

In this regime the capillary pressure is usually ignored, due to the fact that film has a smooth surface whose curvature is usually very small. Some basic theoretical methods used in tacking this regime are now briefly reviewed.

Nusselt theory- This is a simple but useful method first employed by Nusselt (1916) for analysing smooth laminar film flows. He assumed that local equilibrium occurs within the film, which means that acceleration terms are negligible and viscous forces are simply balanced by gravity. Nusselt also postulated a linear temperature profile, which amounts to neglecting convective terms in the energy equation. As a consequence, the film velocity profile can be obtained analytically, and analytical expressions can also be obtained for some other characteristic quantities including film temperature, film thickness, mean flow velocity, volumetric flow rate, wall shear stress, and heat transfer rate.

For smooth film flow, the Nusselt theory found support from the experimental data of Friedman & Miller (1941), and Wilkes & Neddermann (1962). Also, as will be described in more detail later, the theoretical results of Sparrow and Gregg (1959) showed that, for condensate films, the Nusselt theory works well for $Pr > 1$. They reached this conclusion by solving the full steady boundary layer type equations and comparing the results with those obtained by the Nusselt theory.

Similarity analysis - This is the technique widely used in the analysis of boundary layer flows. It assumes self-similar solutions, which means that the differential equations and the associated initial and boundary conditions can, in two-dimensional cases, all be expressed in terms of a single independent variable. The problem is thereby reduced to the solution of an ordinary differential equation with appropriate boundary conditions.

Sparrow and Gregg (1959) applied this method to the study of a steady 2-D

laminar film flow which is governed by the following equations:

$$\frac{\partial u}{\partial x} + \frac{\partial w}{\partial z} = 0 \tag{2.44}$$

$$\rho_L \left(u\frac{\partial u}{\partial x} + v\frac{\partial w}{\partial z} \right) = g(\rho_L - \rho) + \mu_L \frac{\partial^2 u}{\partial z^2} \tag{2.45}$$

$$\rho_L c_p \left(u\frac{\partial T_L}{\partial x} + w\frac{\partial T_L}{\partial z} \right) = k_L \frac{\partial^2 T_L}{\partial z^2} \tag{2.46}$$

which are subject to the following boundary conditions:

$$z = 0; \quad u = w = 0,\ T_L = T_w$$

$$z = \delta; \quad \frac{\partial u}{\partial z} = 0,\ T_L = T_{sat}$$

Here u and w are respectively the stream-wise cross-film velocities along the x and z directions, respectively; and T_{sat} is the saturation temperature.

By introducing a stream function ψ, defined by:

$$u = \frac{\partial \psi}{\partial z},\ w = -\frac{\partial \psi}{\partial x} \tag{2.47}$$

and a similarity variable, η, given by:

$$\eta = \frac{cz}{x^{1/4}},\ c = \left[\frac{g c_p (\rho_L - \rho)}{4 \nu_L k_L} \right]^{1/4} \tag{2.48}$$

Sparrow and Gregg (1959) obtained the following ordinary differential equations:

$$F''' + \frac{1}{Pr}\left[3F''F - 2(F')^2 \right] + 1 = 0 \tag{2.49}$$

$$\theta'' + 3F'\theta' = 0 \tag{2.50}$$

where the dependent variables F and θ are defined by:

$$F(\eta) = \frac{\psi}{x^{3/4}} \frac{1}{4\alpha c}, \quad \theta(\eta) = \frac{T_L - T_{sat}}{T_w - T_{sat}} \tag{2.51}$$

The boundary conditions are transformed into:

$$\eta = 0; \quad F = F' = 0,\ \theta = 1$$

$$\eta = \eta_\delta; \quad F'' = \theta = 0 \tag{2.52}$$

where η_δ is the value of η corresponding to $z = \delta$.

Sparrow and Gregg noted that , if local equilibrium occurs, Equation (2.49) becomes:

$$F''' + 1 = 0 \tag{2.53}$$

which can be solved analytically.

On the other hand, Equation (2.53) can also be obtained from (2.49) by taking $Pr \rightarrow \infty$. This means that the local equilibrium model is also valid for very large *Prandtl* number.

In addition, by solving numerically (2.49) and (2.50), Sprrow and Gregg was able to further conclude that linear film temperature profile assumption is justified if $Ku \gg 1$. The present author will, in Chapter 5, derive general conditions which cover this as a special case.

Integral methods - These exploit similitudes of flow variables in the direction normal to the principal flow direction, thereby reducing the order of governing equations. The methods are approximate in that they do not attempt to exactly satisfy the film equations at every location; instead, the equations are satisfied only on an average extended over the depth of film.

Examples of applying integral methods to the study of two-dimensional steady film flow condensation can be found in the works of Koh (1961), Nakayama et al (1982), and Nakayama and Koyama (1984, 1986). Their approaches are similar to each other and can be summarised as: (i) derivation of integral form of momentum, energy equation and energy balance equation at the interface, (ii) postulation of the velocity and temperature profiles, (iii)insertion of the assumed profiles into the conservation equation to obtain the ordinary differential equations, and (iv) transformation of the differential equations into algebraic equations which are then solved numerically.

In the present study, we will employ an extended integral method, coupled with finite-volume numerical method, to solve full three-dimensional transient film equations of the boundary layer type, as will be detailed in Chapter 5.

There are also some other theoretical methods which are, however, not so typical as those outlined above. One of these is the so called perturbation method employed by Chung (1963) for the study of two-dimensional unsteady film flows where the inertial terms were included and the vapour shear force at the interface was also considered. Detailed treatment of this will not be described here, but the main result obtained is that, at low Prandtl numbers ($Pr < 1$), the vapour shear force and the inertial terms all play an important part in effecting film heat transfer

dynamics.

2. Laminar wavy film flows

For this class of flows, the capillary pressure gradient is normally not negligible because of the occurrence of surface waves, and the unsteady and inertial terms are also important because of the motion of surface waves. Thus, it is necessary to solve the full boundary-layer type equations involving pressure gradient terms.

Kapitza (1948) made the first attempt to analyse the isothermal laminar wavy film flow in the absence of gas shear on an inclined plate at an angle θ. The governing equations are given by:

$$\frac{\partial u}{\partial x} + \frac{\partial v}{\partial y} = 0 \tag{2.54}$$

$$\frac{\partial u}{\partial t} + u\frac{\partial u}{\partial x} + w\frac{\partial u}{\partial z} = -\frac{1}{\rho_L}\frac{\partial p_\sigma}{\partial x} + \nu_L\frac{\partial^2 u}{\partial z^2} + g sin\theta \tag{2.55}$$

where $p_\sigma = -\sigma\partial^2\delta/\partial x^2$ and δ is the film thickness.

By using an integral method and assuming a semiparapolic velocity profile:

$$u = \frac{g}{\nu_L} sin\theta \left(\delta z - \frac{z^2}{2}\right) \tag{2.56}$$

Kapitsa recast the above equations into the following depth-average ones:

$$\frac{\partial \delta}{\partial t} + \frac{(\partial \bar{u}\delta)}{\partial x} = 0 \tag{2.57}$$

$$\frac{\partial \bar{u}}{\partial t} + \frac{9}{10}\bar{u}\frac{\partial \bar{u}}{\partial x} = \frac{\sigma}{\rho_L}\frac{d^3\bar{\delta}}{dx^3} - \frac{3\nu_L\bar{u}}{\delta^2} + g sin\theta \tag{2.58}$$

where $\bar{u}$ is the depth-average film velocity.

It is then further assumed that the waves are long compared to the film thickness δ, so that the latter can be expressed as:

$$\delta = \bar{\delta}(1 + \phi) \tag{2.59}$$

where $\bar{\delta}$ is the mean film thickness and ϕ is the local deviation from the mean. The mean velocity and thickness are then referred to the new variable $(x - ct)$, where c is the phase velocity of the waves. Thus, upon insertion of (2.59) into (2.58) and making necessary rearrangement, the following equation, to a first-order approximation, is obtained:

$$\frac{\sigma}{\rho_L}\frac{d^3\phi}{dx^3} - (c - \bar{u})\left(\frac{9\bar{u}}{10} - 10\right)\frac{d\phi}{dx} - \frac{3\nu_L}{\left(\bar{\delta}\right)^2}(c - 3\bar{u})\phi + g sin\theta - \frac{3\nu_L\bar{u}}{\delta^2} = 0 \tag{2.60}$$

In order for an undamped periodic solution to exit it is necessary that the constant term in this equation and the coefficient of ϕ both be equal to zero, thus yielding

$$\bar{u} = \frac{\left(\bar{\delta}\right)^2 g sin\theta}{3\nu_L} \tag{2.61}$$

$$c = 3\bar{u} \tag{2.62}$$

Equation (2.61) can also be obtained using the Nusselt theory for the same problem, as noted in the first part of this section. This suggest that, to a first approximation, the film mean velocity is not affected by the waviness of the flow.

With the aid of (2.61) and (2.62), Equation (2.60) becomes

$$\frac{\sigma\bar{\delta}}{\rho_L}\frac{d^3\phi}{dx^3} + 4.2\bar{u}^2\frac{d\phi}{dx} = 0 \tag{2.63}$$

for which the function ϕ defining the surface shape (2.59) is

$$\phi = nsin\left[\bar{u}\left(\frac{4.2\rho_L}{\sigma\delta}\right)^{1/2}(x - ct)\right] \tag{2.64}$$

where $n = 2\pi\bar{\delta}/\lambda$ is the dimensionless wave number (λ being the wave length).

In the second approximation, the equation analogous to (2.60) contains terms to the second order in ϕ. The detailed results turn out to be much more complicated; so we will not discuss them here.

3. Turbulent flows

Earlier studies on turbulent flows were confined to smooth films with no interfacial shear forces. Levich (1948, 1959) conducted his pioneer studies on fully-developed turbulent film flows under such conditions, using a diffusivity model which allows for the decrease of eddy diffusivity near the interface. He deduced that the scale of turbulence and the turbulent velocity normal to the interface must be proportional to the distance from the interface, so that all turbulent pulsations must disappear at the interface itself, leaving there a nonturbulent layer of thickness

$$\delta' \propto \delta/(Re_F)^{3/4}$$

Levich also obtained the mean film velocity as

$$\bar{u} = \sqrt{\frac{g\delta\sin\theta}{K}}\ln\left[\frac{\delta}{\nu}\sqrt{\frac{g\delta\sin\theta}{K}}\right] \tag{2.65}$$

where K is a constant which, according to Fulford (1962), is in the region of 1/9.

The presence of the gas shear and therefore waves at the interface further complicates the turbulent flow structure, as evidenced by air-water experiments of Chien and Ibele (1964), Ueda and Tanaka (1974), and Ueda and Nose (1974) for two-phase annular flows. Their results indicate that the liquid film can be divided into two layers (see Figure 2.21 in which δ denotes time-average film thickness): (i)the continuous liquid layer of thickness δ_b which is in direct contact with the wall; and (ii) a disturbed wave layer of thickness $(\delta_c - \delta_b)$ (δ_c being the thickness of wave crests) where irregular motion of surface waves play an important role in the evolution of film dynamics.

Most of the investigators of turbulent film flows, e.g., Dukler (1960), Hewitt (1961), Davis et al (1978), failed to recognise the fact that there is difference in turbulence structure between the above-mentioned two layers. They simply assume that the turbulence structure within the whole layer is similar to that of single-phase pipe flow in the sense that the dimensionless value u^+ is a unique function of the dimensionless distance from the wall y^+. Thus, their analysis involves the use of either eddy diffusivity models of Deissler, Von Karman and Van Driest, or universal velocity profiles. The results thus obtained turned out to over-estimate appreciablely the film thickness and heat transfer rates when compared with experimental data.

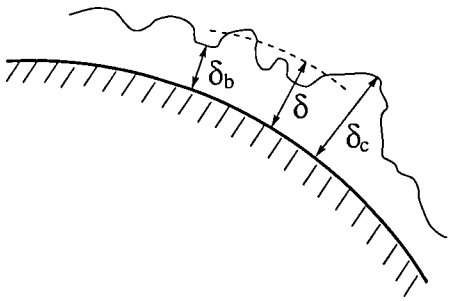


Figure 2.21: Schematic of turbulent film flow.

Subsequent improvements have been made by Dobran (1983) who used an alternative approach which allows for different treatments of the continuous and wave layers of the film. In this approach, the single-phase turbulence structure is assumed to be valid for the continuous layer, whereas appropriate modifications are introduced to the turbulence structure in the wave layer. More specifically, the

following universal velocity profiles are assumed for the continuous layer:

$$u^+ = y^+ \qquad \text{for } 0 \leq y^+ \leq 5 \text{(laminar sublayer)} \tag{2.66}$$

$$u^+ = -0.35 + 5.0 \ln y^+ \qquad \text{for } 5 \leq y^+ \leq 30 \text{(buffer layer)} \tag{2.67}$$

$$u^+ = 5.5 + 2.5 \ln y^+ \qquad \text{for } 30 \leq y^+ \leq \delta_b^+ \text{(turbulent zone)} \tag{2.68}$$

where

$$u^+ = u/u^* \qquad \text{(dimensionless velocity)} \tag{2.69}$$

$$y^+ = yu^*/\nu_L \qquad \text{(dimensionless distance from wall)} \tag{2.70}$$

$$\delta_b^+ = \delta_b u^*/\nu_L \qquad \text{(dimensionless film thickness)} \tag{2.71}$$

$$u^* = (\tau_w/\rho)^{1/2} \qquad \text{(friction velocity)} \tag{2.72}$$

In the wave layer, the eddy viscosity is assumed to be proportional to the thickness of this layer. Thus, the following expression for the velocity within the wave layer is obtained:

$$u^+ = u^+(\delta_b^+) + \frac{(y^+ - \delta_b^+)}{\left(\frac{\mu_{eff}}{\mu_L}\right)_{wl}} \left[1 - \left(1 - \frac{\tau_s}{\tau_w}\right) \frac{y^+ + \delta_b^+}{2\delta^+}\right] \tag{2.73}$$

where $(\mu_{eff}/\mu_L)_{wl}$ is the effective diffusivity for the wave layer. The viscosity ratio $(\mu_{eff}/\mu_L)_{wl}$ is related to the quantity $(\delta^+ - \delta_b^+)$ via an empirical formula:

$$\left(\frac{\mu_{eff}}{\mu_L}\right)_{wl} = 1 + C_1(\delta^+ - \delta_b^+)^n \tag{2.74}$$

in which $C_1 = 1.6 \times 10^{-3}$ and $n = 1.8$ are empirical constants introduced by Dobran (1983).

Dobran also derived an correlation for the substrate film thickness, δ_b, which is a function of the Reynolds number based on the pipe diameter and mean film flow velocity. In different circumstances, such as engine wall film flows, his correlation may not be applicable. Nevertheless, Dobran's method produced results which are in appreciably better agreement with the experimental data than other models for the case of annular turbulent film flows.

2.4.5 Droplet Entrainment

We now return to discussing in more detail the phenomenon of droplet entrainment, which is in essence caused by the breakup of surface waves under the action of

gas hydrodynamic forces. The forces acting on the wave crests depend on the flow pattern around them as well as the shape of the interface. Thus far a few different basic entrainment mechanisms have been observed, two of which are most studied and are believed to be the most relevant to engine film flows. They are briefly described as follows (see Figure 2.22):

1. Tearing of the liquid bulk (or rolls wave mechanism) - where capillary (or roll) waves (Diagram (a)) are torn or sucked away in regions of high shear (e.g. Hanratty and Woodmansee 1965; Brodkey 1967; Hewitt & Hall-Taylor 1970; Kataoka et al 1983). For relatively high film Reynolds number ($Re_F > 160$), droplet entrainment is due to this mechanism (Ishii and Grolmes 1975)

2. Wave 'undercutting' mechanism (Diagram (b))- in which the gas shear acts on the wave crest of the film and undercut it (e.g. Hewitt and Hall-Taylor 1970). This occurs at relatively low Reynolds number.



Figure 2.22: Schematic of entrainment type.

The mechanisisms of mass, momentum and energy transfer between the film and the gas are significantly affected by entrainment. It is therefore of particular importance to have an understanding of the conditions leading to droplet entrainment, and the rate of entrainment. Studies on these two major issues are now briefly reviewed.

1. *Droplet Entrainment criteria.* These have been mostly investigated in experimental studies of annular flows in tubes. Reviews of data and correlations for the onset of entrainment have been given by Zuber (1962); Hewitt and Hall-Taylor (1970); Wallis (1969); Kutateladze (1972); and Ishii and Grolmes (1975). These works also revealed that the available correlations exhibit some appreciable discrepancies, and in some cases there are conflicting results.

An early study of Woodmansee and Hanratty (1969) concerned the critical conditions and the mechanism of atomisation for the co-current flow of air and liquid.

Their work involved both experiments and theoretical analysis. Their theoretical work suggested that droplet removal is due to the imbalance between the pressure variations in the air flowing over wavelets and the stabilising forces of gravity and surface tension. This is essentially a Kelvin-Helmholz instability. To establish the droplet inception criteria, these authors measured the local mean air velocities,U_s, at which droplets are first observed to be removed from flowing water film. This allowed them to describe the critical conditions for entrainment in terms of a Weber number:

$$We_E = \rho(U_s - C)^2\delta_0/\sigma$$

which is defined in terms of the difference between the local gas velocity U_s, and surface wave velocity C, the gas density ρ, the surface tension σ, and a characteristic liquid film thickness δ_0. The experimental data disclosed that, if δ_0 is taken to be the height of the roll waves, then the critical We_E is around 5.5. If the height of the base film is used, a critical We_E of 1.5 is obtained. The critical conditions given here are not convenient for practical use, because the Weber number involves the wave velocity which is itself unknown a priori and has to be determined from theory or experiment.

For the wave-cut entrainment type, van Rossum (1959) showed that his data for the inception of entrainment can be well correlated by the film Weber number defined by

$$We_{FG} = \frac{\rho(U_s - \bar{u})^2\bar{\delta}}{\sigma} \tag{2.75}$$

The inception criterion can be expressed as:

$$We_{FG} \geq We_{FG_c} \tag{2.76}$$

in which the critical Weber number We_{FG_c} was shown by van Rossum to be around 17, below which no entrainment exists.

Use of (2.76) requires that the mean film thickness $\bar{\delta}$ be evaluated a *priori*. This can be done either analytically, numerically or empirically. In annular film applications, $\bar{\delta}$ is usually evaluated using empirical correlations. Such correlations were provided by van Rossum (1959), and Hweitt and Hall-Taylor (1970), among others.

Ishii and Grolmes (1975) took the critical Weber number as $We_{FG_c} = 22$ in Equation (2.76) which is the value determined by Hinze (1955) for droplet breakup onset. Based on the work of Hweitt and Hall-Taylor (1970), they proposed another correlation for $\bar{\delta}$ which is given by:

$$\bar{\delta} = \frac{\mu_L}{\sqrt{8\rho_L \tau_s}} Re_F^{1/2} \tag{2.77}$$

With the aid of (2.77), Ishii and Grolmes (1975) recast Equation (2.76) into the following specific form:

$$\frac{\mu_L U_s}{\sigma}\sqrt{\frac{\rho}{\rho_L}} \geq \frac{3}{4} Re_F^{-1/2} \tag{2.78}$$

This was found in satisfactory agreement with their experimental data when: (i) $Re_F < 1/2$ for a vertical downward film; and (ii) $Re_F < 40$ for a horizontal or vertical upward flowing film flow. Outside of this range of conditions, the entrainment is of roll wave type, and the entrainment criteria are described by different correlations, as will be presented shortly.

Zuber (1962) appears to be the first to study the conditions of roll-wave entrainment inception. He proposed the following form of the inception criterion:

$$F_d \geq F_\sigma \tag{2.79}$$

where F_d is the drag force resulting from the shear of gas acting on the wave crest, and F_σ stands for the retaining force of surface tension. Under the action of the gas shear, the wave form cannot retain its original form, thus leading to the deformation of the wave crest and its breakup.

Using Equation (2.79), Ishii & Crolmes (1975) derived specific inception criteria for roll-wave type entrainment which are valid when $Re_F > 1/2$ for vertical film flow and $Re_F > 40$ for horizontal film flow. These are given below:

$$Ca_F \frac{U_s}{\bar{u}}\sqrt{\frac{\rho}{\rho_L}} = \begin{cases} 7.421\left(\frac{\bar{\delta}}{l_c} We_F\right)^{0.4} Re_F^{-1.133} & \frac{\sqrt{We_F}}{Re_F}\sqrt{\frac{\bar{\delta}}{l_c}} \leq \frac{1}{15}; \\ 0.85 Re_F^{-1/3} & \frac{\sqrt{We_F}}{Re_F}\sqrt{\frac{\bar{\delta}}{l_c}} > \frac{1}{15} \end{cases} \tag{2.80}$$

Here dimensionless parameters Ca_F, We_F etc. are defined in Section 2.4.2; and the capillary length l_c is defined by:

$$l_c = \sqrt{\frac{\sigma}{g(\rho_L - \rho)}} \tag{2.81}$$

Kataoka et al. (1983) also derived a criterion for roll-wave entrainment using Equation (2.79), which is expressed by a critical Weber number given by:

$$We_{FG_c} = \frac{8}{C_d} \tag{2.82}$$

where C_d is the drag coefficient related to interfacial shear stress, τ_s, an expression for which can be found in Kataoka et al. (1983).

2. *Correlations for droplet entrainment rate*

Once droplet entrainment occurs, the droplet entrainment rate, $\dot{m}_E$, is an important quantity which needs to be determined. Hutchinson and Whalley (1973), Ueda (1979) and Kataoka and Ishii (1982) have provided representative expressions for this quantity.

The correlation given by Hutchinson and Whalley (1973) for wave-cut mechanism is a function of a dimensionless gas shear, τ_s^* $(= \tau_s \bar{\delta}/\sigma)$, and was derived based on a force balance at the wavy interface between the liquid film and gas. Their correlation, however, showed substantial scatter in comparison with the experimental data.

A similar correlation was later proposed by Ueda (1979), of the form:

$$\dot{m}_E = 3.54 \times 10^{-3} \left[\frac{\tau_s}{\sigma} \left(\frac{\bar{u}}{\sigma} \right)^{0.6} \right]^{0.57} \quad \left(\text{for } \frac{\tau_s}{\sigma} \left(\frac{\bar{u}}{\sigma} \right)^{0.6} \geq 120 \right) \tag{2.83}$$

Although the above relation agrees well with Uede's experimental data, it can not be extrapolated with confidence outside of the experimental conditions, since it is not in dimensionless form.

In his attempt to extend the above efforts to account for the roll wave mechanism, Sugawara (1990) derived a correlation which takes into account the effects of the density ratio between the vapour and liquid film, and of the hydrodynamic equivalent wave height which is an average measure of the film surface roughness. His correlation reads:

$$\dot{m}_E = 1.07 \tau_s^* Ca_F \left(\frac{\Delta h_{eq}}{\bar{\delta}} \right) \left(\frac{U_s}{\bar{u}} \right) \left(\frac{\rho_L}{\rho} \right)^{0.4} \tag{2.84}$$

where

$$\Delta h_{eq} = k_s \; (Re_G > 10^5) \tag{2.85}$$

$$\Delta h_{eq} = k_s[2.136log_{10}(Re_G) - 9.86] \; (Re_G \leq 10^5) \tag{2.86}$$

$$k_s = 0.57\bar{\delta} + 21730\bar{\delta}^2 - 38.8^6\bar{\delta}^3 + 56.68^9\bar{\delta}^4 \tag{2.87}$$

with k_s being the hydrodynamic equivalent wave roughness.

Equation (2.84) was claimed to be applicable for a wide range of pressure and mass velocity.

Wang and Street (1978) derived a correlation for $\dot{m}_E$ in terms of the Reynolds number:

$$R_\sigma = u_* h_c/\nu$$

where u_* is the gas friction velocity (τ_s/ρ), h_c is the local r.m.s interface elevation and ν is the gas kinematic viscosity. The correlation is based on air/water experiments, and it is necessary to determine the interfacial stress and wave amplitudes before it can be used.

2.4.6 Films Formed by Impinging Sprays

In this subsection, a review is presented of the film characteristics measured under the spray impingement conditions.

Siwoń (1988) appears to be the first to study experimentally the behaviour of a liquid film formed by an impinging spray. In his experiments, a steady water spray issued from an atomizer was directed vertically onto a horizontal flat surface. Measurements were then made of the area covered by the resulting thin liquid film and the film thickness at some points along a diametrical line passing through the stagnation point was determined using the electro-chemical method.

Experimental data were obtained for different air $(\dot{m}_g)$ and liquid $(\dot{m}_l)$ flow rates, revealing that for a fixed $\dot{m}_l$ the area covered by the liquid film increases with $\dot{m}_g$.

The main results concerning the film thickness distribution are shown in Figures 2.23 and 2.24. Figure 2.23 displays the result for the case where a single liquid jet, with no air injection, is directed onto the plate at two different flow rates. It is clear that two regions can be distinguished. In the inner region which corresponds to impingement zone, the liquid film apparently has smallest thickness. In the outer region, which is outside the impingement zone, the thickness clearly increases. For both cases presented in Figure 2.24, the values of film thickness is in the range of

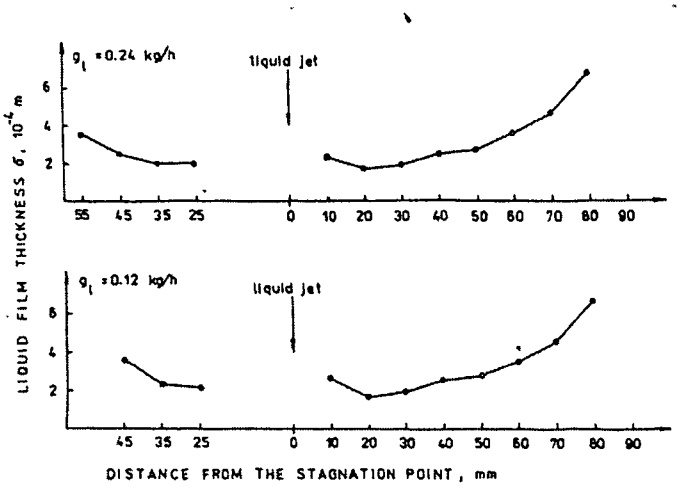


Figure 2.23: Distribution of liquid film thickness along the distance from the stagnation point for single water impinging jet (from Siwón 1988).

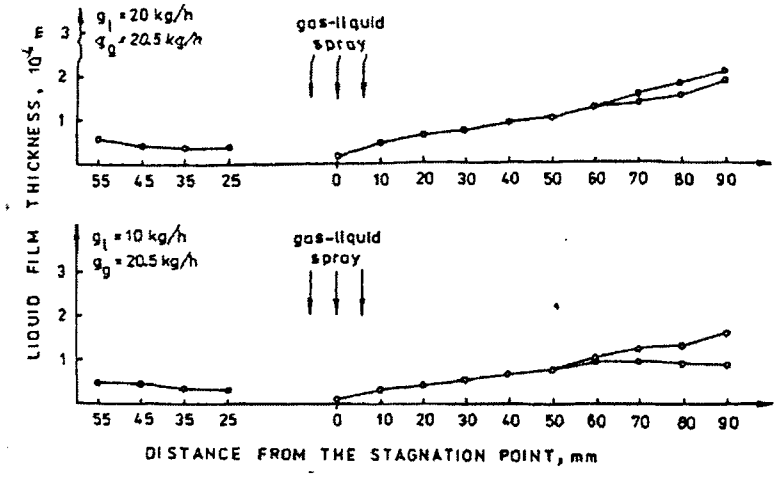


Figure 2.24: Distribution of liquid film thickness along the distance from the stagnation point for an air-water two phase impinging spray (from Siwón 1988).

0.2-0.6 mm. Siwoń did not attempt to explain this result, but we believe that the dynamic impingement pressure produced by the jet is the main factor responsible for causing the spreading and thinning of the liquid film in the impingement zone.

The results for a two-phase jet are shown in Figure 2.24, which shows that film thickness becomes smaller as the air flow rate is increased. This is because the gas phase exerts a two-fold effect on the liquid film. Firstly, it contributes to breakup the droplets and carry away the smaller droplets from the impingement region, causing less mass deposition. Secondly, the gas jet also plays a role in spreading the liquid film owing to its drag effect on the film. The latter explanation is also consistent with the observation that the film area increases with an increase of the air flow rate. Another noteworthy feature is that, in the presence of the gas , the minimum film thickness occurs around the stagnation point, taking values of 10 to 50 μm. Note that at the right-hand side of the stagnation point in Figure 2.24 , there are two lines in the region outside of the impingement zone: one is the maximum film thickness, and the other the minimum thickness.

The experiments results discussed above seem to suggest that thinner film, which is desirable in Diesel engine combustions, could be attained either by increasing gas flow rate or by producing finer droplets through liquid breakup.

A more recent experimental study of the characteristics of liquid films formed by impinging sprays was performed by Özdemir (1992). He developed a dynamic technique for the measurement of unsteady component of the film thickness. The technique makes use of frequency modulated signal analysis of light intensity variations. Özdemir (1992) applied his technique to the measurement of film thickness for diesel sprays impinging obliquely onto a plane heated wall ($T_w > T_B$) in a test bomb.

Typical results are presented in Figure 2.25, which illustrates the space-time structure of the liquid film for two wall temperatures, $T_w = 150^0$, 240^0 along the incidence line which is the intersection between the impingement plane and the plane formed by the nozzle axis and the injection direction. It is seen that the film exhibits similar features in both cases. The plots confirm the findings of Siwoń (1988) in that the film remains thin in the impingement region and increases rapidly in thickness at large radial distances from the stagnation point. At both wall temperatures, an

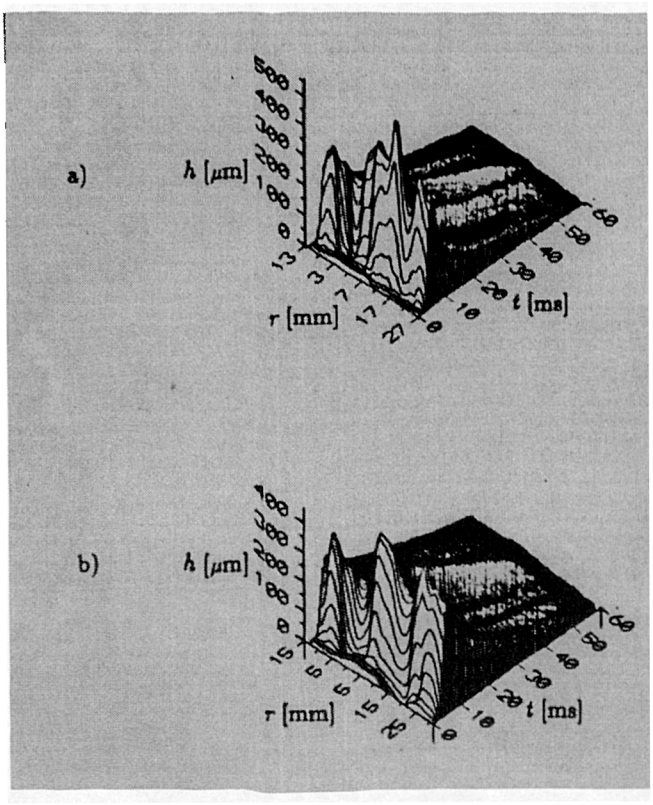


Figure 2.25: Space-time variation of film thickness along incidence line at (a) $T_w = 240^0C$ and (b) $T_w = 150^0C$ (from Özdemir 1992).

apparent wave structure can be observed at the film interface. The film has three regions of large unsteady thickness variation, two at large radial distances and one in the impingement zone. The wave pattern is apparently more significant in the case with higher wall temperature, presumably because of the stronger thermal gradient across the film. This strong wave pattern leads to better heat and mass transfer rate—which is desirable in Diesel engines. Another feature that can be noted is that mean film thickness is in general smaller at high wall temperature. This is because: (i) the droplets at the near-wall regions evaporate fast and cause less mass deposition when they coalescence with the film; and (ii) the film also exhibits a fast evaporation rate at higher wall temperature.

Ereaut et al (1992) at Harwell Laboratory in U.K. developed a fluorescence/length of line technique for the measurement of wall film characteristics under spray impingement circumstances. They applied this technique to the measurements for the cases involving normal spray impingement in pressure chambers at different gas temperatures and pressures. They found that even for the cases where fuel evapo-

ration is negligible, maximum wall film thickness is always below $50\mu m$, indicating the feature of very small film thickness. Their data on film characteristics will be discussed in more detail in Chapter 7, where comparisons between the predictions and measurements are made.

Coghe et al (1992) used the same technique developed by Ereaut et al (1992) to measure film thickness characteristics for an oblique impingement case which involves a spray impinging at an angle of 60^0 onto the side wall of a cylindrical quiescent chamber whose radius and height are respectively 50 and 60 mm. They measured the following quantities: (i)spatial distribution of film thickness; (ii) temporal variation of film thickness at specific locations; and (iii)film volume over a specific wall area as a function of time. These data will also be compared with our calculations in Chapter 7.

As mentioned earlier in Subsection 2.3.2, Saito et al (1993) also investigated experimentally the wall film characteristics at normal impingingment conditions closely approximating those in Diesel engines. In particular, they measured the following quantities: (a) mass deposited on the wall after termination of injection, (b)penetration of film edge; and(c) temporal variation of mean film thickness. These data will also be used to assess the present models to be discussed in subsequent chapters.

As for the modelling of dynamic characteristics of wall films formed by impinging sprays, the only published work that deals with the modelling of the impingement-induced wall film flows appears to be that of Siwón and Ennaoui (1991), who investigated steady and isothermal wall films formed by impinging water sprays. However, in their study, they confined their attention to two-dimensional films, which spreads in one direction, and also neglected the important droplet momentum sources in the film equations. In addition, no treatment was given for simulating film spreading process. For these and other reasons, their method is not applicable to the present problem.

2.4.7 Summary

The survey presented in this section has considered several aspects regarding liquid film flow processes. First, major parameters that govern film dynamics have been

described including various forces acting on films and wall characteristics, and these have been further grouped into different dimensionless parameters including film Reynolds number, Weber number, Froude number, Scaled interfacial stress and wall roughness, and phase change numbers.

Second, three basic flow regimes (i.e., laminar smooth flow, wavy flow and turbulent flow) have been identified and their main characteristics have been outlined. Also, a very limited range of data has been uncovered on the onset conditions for surface waves and turbulent flows from the literature, which were mainly derived based on one or two parameters (e.g. film Reynolds number or Froude number). They are closely related to the film flow instability which are caused by several sources: (i) high flow velocity; (ii) interfacial shear stress; (iii)flow properties of the vapour that adjoins the liquid film; and (iv) the excess temperature of the wall over the film. In particular, the data on flow transition to turbulence have evidenced that there is no sharp boundary between the laminar (or wavy) and turbulent flows.

Next, some theoretical methods for analysing two-dimensional film characteristics in each regime have been discussed, although none of them can be used for the prediction of wall films form by impinging sprays where the moving contact line has to be tracked and droplet momentum source terms have to be accounted for. Nevertheless, the integral method, which has been widely used, will be further developed and applied in the present study.

Subsequently, particular attention has been paid to a special case corresponding to the flow instability and surface wave breakup due to strong gas interfacial shear. This is the so called droplet entrainment phenomenon. Two major issues were discussed: (i) inception criteria of entrainment; and (ii) entrainment mass flux. Some empirical correlations these were presented and discussed. The importance of entrainment in engine environment, however, has yet to be established via experimental observations.

Finally, some experimentally-observed characteristics have been summarised of wall films formed by impinging sprays. The main features to be noted are that this type of film flows, typically with mean thickness of a few ten microns, exhibit wave flow patterns; and the flow behaviour is clearly affected by the injection flow rate.

Chapter 3

Flow and Spray Modelling

3.1 Introduction

In Diesel engines, a liquid spray undergoes several physical processes before it hits the walls of combustion chamber. These include the primary atomisation of the liquid jet emerging from the nozzle, droplet breakup due to aerodynamic forces, droplet-droplet collisions and coalescences resulting from the velocity differences between the droplets, droplet vapourisation and heating, and the interaction between the sprays and the gas through the exchange of mass, momentum and energy. These phenomena determine the impingement conditions and therefore influence the impingement processes. The purpose of this chapter is therefore to highlight the fundamental concepts, laws and equations describing these processes.

Section 3.2 presents the instantaneous Navier-Stokes equations for the gas phase in the framework of Eulerian approach. These equations are subsequently recast into their ensemble-average forms in Section 3.3, using the two-equation $k-\epsilon$ model to close the system. Section 3.5 assembles the transport equations for an Eulerian frame, which are then transformed, in Section 3.5, into a frame which moves in accord with the reciprocating motions of the piston and valve. Further to this, the equations are expanded, in Section 3.6, into a curvilinear orthogonal frame to accommodate a range of relatively complex engine geometries. The formulation of the gas phase model is completed with the specification of suitable initial and boundary conditions which are necessary to advance the solution in time.

The Lagrangian model for liquid phases is presented in Section 3.8. Discussed

in detail are the equations governing droplet mass, momentum and energy conservations, along with the important issues concerning spray atomisation, droplet breakup, droplet-droplet collisions and coalescences, and droplet dispersion due to turbulence.

3.2 The Instantaneous Equations Governing the Gas Phase

The mathematical description of the state of the in-cylinder gas flow interacting with the spray phase consists of the differential equations representing the conservation of mass, momentum and energy for a given elementary volume, regarding the gas phase as a continuum.

The major physical variables involved in these equations are fluid velocity (three components), mass fraction of fuel vapour resulting from droplet heating and vapourisation (a single-component liquid is assumed), and three thermodynamic quantities pertaining to the fluid, i.e. pressure, density and temperature—which are related by the equation of state. These variables are functions of time and space, and the ultimate purpose is to evaluate their temporal and spatial distributions.

The presence of a liquid phase induces two major effects on the gas phase which have to be accounted for in the gas equations. Firstly, there are transfers of mass, momentum and energy between the phases, introducing additional source/sink terms into the gas phase equations. Secondly, the liquid phase occupies a volume not available to the gas phase, causing local displacement of the gas. To account for these effects, it is convenient to introduce first some definitions. Let ρ be the material density of the gas, which is the mass per unit volume in a volume that includes only gas. Let ρ_b be the gas bulk density, which is the mass of the gas in a volume that includes both gas and liquid. Furthermore, θ is defined as the void fraction of the gas which is the ratio of the equivalent volume of gas to a given volume of a gas and liquid mixture. It follows that

$$\rho_b = \theta\rho$$

Therefore the displacement effect can be accommodated by introducing ρ_b (or θ) into the gas equations, and treating their unknowns as continuous field variables.

In reality, θ results from the spatially discrete droplet volumes, and is not strictly continuous.

In the following, the vector-tensor form of the instantaneous equations governing the gas phase are first given in an Eulerian frame of description, in which the fundamental physical principles are applied to an elementary control volume fixed in space.

3.2.1 Mass Conservation Equation

Application of the law of mass conservation to an fixed elementary control volume results in the following gas continuity equation (e.g. Tabrizi 1991):

$$\underset{\substack{\text{rate of mass}\\ \text{increase of gas}\\ \text{per unit volume}}}{\frac{\partial \rho_b}{\partial t}} + \underset{\substack{\text{mass efflux of gas}\\ \text{per unit volume}}}{\nabla \cdot (\rho_b \underline{V})} = \underset{\substack{\text{net rate of droplet}\\ \text{mass transfer to}\\ \text{the gas phase by}\\ \text{means of evaporation}\\ \text{per unit volume}}}{S_{m,d}} \tag{3.1}$$

Here t and $\underline{V}$ stand for time and gas instantaneous velocity vector, respectively; and $S_{m,d}$ represents the evaporation rate of the droplets.

3.2.2 Momentum Conservation Equation

Applying Newton's second law to an elementary control volume, and regarding droplets as sources/sinks of momentum to the conveying gas, the following gas motion equations can be obtained (e.g. Tabrizi 1991):

$$\underset{\substack{\text{rate of increase}\\ \text{of gas momentum}\\ \text{per unit volume}}}{\frac{\partial}{\partial t}(\rho_b \underline{V})} + \underset{\substack{\text{gas momentum}\\ \text{efflux by}\\ \text{convection per}\\ \text{unit volume}}}{\nabla(\rho_b \underline{V}\,\underline{V})} = \underset{\substack{\text{rate of}\\ \text{gas momentum}\\ \text{gain due to}\\ \text{internal stresses}\\ \text{per unit volume}}}{-\theta \nabla P + \nabla \cdot (\theta \underline{\underline{\tau}})} + \underset{\substack{\text{net rate of}\\ \text{droplet momentum}\\ \text{exchange with}\\ \text{the gas per}\\ \text{unit volume}}}{S_{\underline{V},d}} \tag{3.2}$$

where P and $\underline{\underline{\tau}}$ denote the gas thermodynamic pressure and viscous stress tensor, respectively. The stress tensor $\underline{\underline{\tau}}$ is given, for a simple compressible Newtonian flow,

by

$$\underline{\underline{\tau}} = 2\mu\underline{\underline{D}} - \frac{2}{3}\mu\nabla\cdot\underline{V}\,\underline{\underline{I}} \tag{3.3}$$

where μ is the gas molecular viscosity, and $\underline{\underline{D}}$ is the deformation tensor given by:

$$\underline{\underline{D}} = \left[\nabla\underline{V} + (\nabla\underline{V})^T\right]/2$$

Note that in the gas momentum equations, the void fraction,θ, is set to lie outside the pressure gradient term, rather than within it (i.e. $-\nabla(\theta P)$). This is because that in the latter case, the equation would fail to represent static equilibrium for an inhomogeneous distribution of the dispersed phase (Harlow & Amsden 1975).

3.2.3 Energy Conservation Equation

The principle of energy conservation for a control volume requires

$\frac{\partial}{\partial t}(\rho_b e_s)$	$+$	$\nabla\cdot(\rho_b\underline{V}e_s)$	$=$	$\nabla\cdot\left(\gamma\frac{\mu}{\sigma_h}\theta\nabla e_s\right)$
rate of gain of gas energy per unit volume		efflux of gas energy per unit volume		rate of gas energy input by conduction per unit volume

$-\theta\nabla\cdot(P\underline{V})$	$+$	$S_{e,d}$
rate of work done on gas per unit volume by pressure forces		net rate of droplet total energy exchange with the gas per unit volume

(3.4)

where the specific total energy $e_s = e + \frac{1}{2}\underline{V}\cdot\underline{V}$, e is the specific internal energy $(= c_v T)$, the quantity σ_h is the molecular Prandtl number, and γ is the gas heat specific ratio, defined as:

$$\gamma = \frac{c_p}{c_v} \tag{3.5}$$

in which c_p and c_v are the gas specific heats at constant pressure and volume, respectively.

In engine applications, it is reasonable to assume perfect gas behaviour. Thus, the temperature, density and pressure are linked by the equation of state:

$$P = \rho RT \tag{3.6}$$

where R and T are the gas constant and absolute temperature, respectively.

In the above energy balance, the term representing molecular shear work, $\nabla \cdot (\underline{V} \cdot \theta \underline{\underline{\tau}})$, has been dropped due to its small contribution to energy balance in engine circumstances.

3.2.4 Fuel Vapor Mass Conservation Equation

Application of the principle of mass conservation to the fuel mass vapour fraction, m_f, requires only a slight generalisation of the development for the conservation of the total mass of the gas phase in Section 3.2.1. We must now allow for a mass flux of the vapour by diffusion as well as by convection. Thus, the conservation equation of the fuel vapour mass fraction reads (e.g. Beshay 1985):

$$\underbrace{\frac{\partial}{\partial t}(\rho_b m_f)}_{\substack{\text{rate of increase} \\ \text{of fuel} \\ \text{per unit volume}}} + \underbrace{\nabla \cdot (\rho_b \underline{V} m_f)}_{\substack{\text{efflux of fuel} \\ \text{per unit volume}}} = \underbrace{\nabla \cdot \left(\frac{\mu}{\sigma_f} \theta \nabla m_f \right)}_{\substack{\text{rate of fuel input} \\ \text{by diffusion} \\ \text{per unit volume}}} + \underbrace{S_{m,d}}_{\substack{\text{net rate of} \\ \text{evaporation of} \\ \text{fuel within} \\ \text{a unit volume}}} \tag{3.7}$$

where σ_f is the Schmidt number.

3.2.5 The General Transport Equation

Inspection of the foregoing conservation equation reveals that all the dependent variables of interest here obey the common conservation form:

$$\frac{\partial}{\partial t}(\rho_b \phi) + \nabla \cdot (\rho_b \underline{V} \phi) = \nabla \cdot (\Gamma_\phi \theta \nabla \phi) + S_\phi + S_{\phi,d} \tag{3.8}$$

where ϕ is the dependent variable in question, Γ_ϕ is the 'diffusion coefficient'. The first three terms are, respectively, the unsteady term, the convection term, and the diffusion term, whereas the forth term, S_ϕ, represents the additional 'gas-related source' term, and the fifth term, $S_{\phi,d}$ stands for the terms associated with the inter-phase exchange.

3.3 The Statistical Approach and the Turbulence Model

The in-cylinder flow field of an operating reciprocating engine is invariablely turbulent and non-stationary, and the temporal and spatial variations in the dependent variables encompasses such a widely-disparate set of length and time scales as to preclude the direct numerical solution of the governing equations. Consequently, the effect of turbulence is simulated in this study using a common approach– a statistical averaging procedure– in which the dependent variables are decomposed into mean and fluctuating components by use of a suitable averaging procedure, and the resulting equations are averaged to convert them into statistical equations describing the evolution of mean quantities. The appropriate averaging procedure will depend on the nature of the flow: for a statistically steady flow this will be a time average; for a statistically homogeneous one, a volume averaging; and for the non-stationary flows, as those encountered in engines, ensemble averaging, or phase averaging in periodic flows (Reynolds 1980). However, the averaged equations are not closed due to a loss of information resulting from averaging process, and additional unknowns are introduced. A turbulence model is therefore employed to provide the additional relationships necessary for the closure of the problem.

3.3.1 Ensemble-Averaged Equations

In general, the ensemble average of a local variable, ϕ, can be defined as the weighted arithmetic mean over many identical experiments (hence, the averaged quantity may be time dependent):

$$\breve{\phi}(\underline{x},t) = \lim_{N\to\infty} \frac{\sum_{i=1}^{N} g(\underline{x},t+iT_0)\phi(\underline{x},t+iT_0)}{\sum_{i=1}^{N} g(\underline{x},t+iT_0)} \tag{3.9}$$

where $\underline{x}$ denotes the location of the measurement, i is the number of observations (e.g engine cycles), t is the time after the start of each cycle of period T_0, and g is a chosen weighting function. Different choices of g will result in different ensemble-averaging procedures, two of which are most frequently employed for deriving averaged equations. They are:

- Conventional Reynolds averaging (or unweighted average). This corresponds to the case where g = constant in Equation (3.9). The instantaneous value of ϕ can then be represented as:

$$\phi = \bar{\phi} + \phi' \tag{3.10}$$

where the Reynolds mean component $\bar{\phi}$ is given by

$$\bar{\phi}(\underline{x}, t) = \lim_{N\to\infty} \frac{1}{N} \sum_{i=1}^{N} \phi(\underline{x}, t + iT_0) \tag{3.11}$$

and the Reynolds 'fluctuating' component, ϕ', satisfies the condition:

$$\bar{\phi'} = 0 \tag{3.12}$$

- Favre-averaging (or density-weighted averaging). This involves the choice of the weighting function g in Equation (3.9) as the density ρ. Thus, the variable, ϕ, is decomposed into its Favre mean, $\tilde{\phi}$, and Favre 'fluctuating', ϕ'', components as follows:

$$\phi = \tilde{\phi} + \phi'' \tag{3.13}$$

where in general $\phi'' \neq 0$, and $\tilde{\phi}$ is given by:

$$\tilde{\phi} = \frac{\overline{\rho\phi}}{\bar{\rho}} \tag{3.14}$$

Favre averaging was first suggested by Favre (1969) in the study of high speed turbulent flows in which the density variations are due to viscous heating and mean pressure variations. This procedure is generally advantageous to studying processes involving density variations, as in the case of combusting, compressible or two-phase flows, since it reduces the number of the additional terms that would otherwise appear and provides a clearer physical interpretation of the individual terms (Jones 1979; Libby and Williams 1980).

In the case of the in-cylinder gas-droplet flow, Favre averaging can be further extended to account for the local temporal variation of void fraction by taking the bulk density as the weighting function in Equation (3.9). When this is done, the Favre mean, $\tilde{\phi}$, takes the form:

$$\tilde{\phi} = \frac{\overline{\rho_b\phi}}{\bar{\rho}_b} = \frac{\overline{\rho\theta\phi}}{\overline{\rho\theta}} \tag{3.15}$$

By use of definitions (3.10), (3.12), (3.13) and (3.15) the following relations can be obtained between weighted and unweighted average quantities (see Appendix A for details):

$$\begin{aligned}
\bar{\phi}'' &= -\frac{\overline{\rho_b' \phi'}}{\bar{\rho}_b} \\
\overline{\rho_b \phi''} &= 0 \\
\bar{\rho}_b \tilde{\phi}'' &= -\overline{\rho_b' \phi''} \\
\overline{\rho_b' \phi''} &= \overline{\rho_b' \phi'}
\end{aligned} \tag{3.16}$$

With the definitions of the Reynolds averaging and Favre averaging procedures, the conservation equations can be recast in terms of the Reynolds averaged quantities and Favre averaged ones. In the following, two types of ensemble-averaged equations are provided: Reynolds averaged equations and Favre averaged ones. The formers are derived by use of Reynolds decomposition (3.10) and subsequent application of the Reynolds averaging procedure to all components of equations; while the latters are obtained by adopting the following practice. First, we distinguish two types of dependent variables: (i) those which appear together with the bulk density ρ_b in the same terms (e.g. velocities), and (ii) those which do not. For the first type of variables we apply the Favre decomposition (3.13) to them, since this will result simpler form of averaged equations. For the other variables the Reynolds decomposition is used. Thus, the relation (3.13) is applied to the bulk density, void fraction, pressure, the stress tensor, and droplet-related source terms. Second, Reynolds averaging procedure is applied to the resulting decomposed equations.

The results are given below:

Continuity

Reynolds averaging yields:

$$\begin{aligned}
\frac{\partial}{\partial t}(\bar{\rho}\bar{\theta} + \overline{\rho'\theta'} + \nabla \cdot (\bar{\rho}\bar{\theta}\underline{\bar{V}} + \bar{\rho}\overline{\theta'\underline{V}'} + \overline{\rho'\bar{\theta}\underline{V}'} + \overline{\rho'\theta'}\underline{\bar{V}} + \overline{\rho'\theta'\underline{V}'}) \\
= (\overline{\bar{S}_{m,d} + S'_{m,d}})
\end{aligned} \tag{3.17}$$

Favre decomposition followed by Reynolds averaging gives:

$$\begin{aligned}
\frac{\partial}{\partial t}(\rho_b) + \nabla \cdot (\rho_b \underline{\tilde{V}} + \rho_b \underline{V}'') &= (\bar{S}_{m,d} + S'_{m,d}) \\
\frac{\partial}{\partial t}(\bar{\rho}_b) + \nabla \cdot (\bar{\rho}_b \underline{\tilde{V}}) &= (\overline{\bar{S}_{m,d} + S'_{m,d}})
\end{aligned} \tag{3.18}$$

Momentum

Reynolds averaging yields:

$$\begin{aligned}
&\frac{\partial}{\partial t}(\tilde{\rho}\bar{\theta}\underline{\bar{V}} + \bar{\rho}\overline{\theta'\underline{V'}} + \overline{\rho'\bar{\theta}\underline{V'}} + \overline{\rho'\theta'}\underline{\bar{V}} + \overline{\rho'\theta'\underline{V'}}) + \\
&\nabla\cdot(\bar{\rho}\bar{\theta}\underline{\bar{V}}\,\underline{\bar{V}} + \bar{\rho}\bar{\theta}\overline{\underline{V'}\underline{V'}} + \bar{\rho}\overline{\theta'\underline{\bar{V}}\,\underline{V'}} + \bar{\rho}\overline{\theta'\underline{V'}}\,\underline{\bar{V}} + \bar{\rho}\overline{\theta'\underline{V'}\underline{V'}} + \overline{\rho'\bar{\theta}\underline{\bar{V}}\,\underline{V'}} + \\
&\overline{\rho'\bar{\theta}\underline{V'}\,\underline{\bar{V}}} + \overline{\rho'\bar{\theta}\underline{V'}\,\underline{V'}} + \overline{\rho'\theta'}\underline{\bar{V}}\,\underline{\bar{V}} + \overline{\rho'\theta'\underline{\bar{V}}\,\underline{V'}} + \overline{\rho'\theta'\underline{V'}}\underline{\bar{V}} + \overline{\rho'\theta'\underline{V'}\,\underline{V'}} \\
&= -(\bar{\theta}\nabla\bar{P} + \overline{\theta'\nabla P'}) + \nabla\cdot(\bar{\theta}\bar{\underline{\tau}} + \overline{\theta'\underline{\tau}'}) + (\overline{\bar{S}_{\underline{V},d} + S'_{\underline{V},d}})
\end{aligned} \tag{3.19}$$

Favre decomposition followed by Reynolds averaging gives:

$$\begin{aligned}
&\frac{\partial}{\partial t}(\rho_b\tilde{\underline{V}} + \rho_b\underline{V''}) + \nabla\cdot(\rho_b\tilde{\underline{V}}\,\tilde{\underline{V}} + \rho_b\tilde{\underline{V}}\,\underline{V''} + \rho_b\underline{V''}\,\tilde{\underline{V}} + \rho_b\underline{V''}\,\underline{V''}) \\
&= -(\bar{\theta}+\theta')\nabla(\bar{P}+P') + \nabla\cdot(\bar{\theta}+\theta')(\bar{\underline{\tau}} + \underline{\tau}') + (\bar{S}_{\underline{V},d} + S'_{\underline{V},d})
\end{aligned}$$

$$\begin{aligned}
&\frac{\partial}{\partial t}(\bar{\rho}_b\tilde{\underline{V}}) \quad + \quad \nabla\cdot(\bar{\rho}_b\tilde{\underline{V}}\,\tilde{\underline{V}} + \overline{\rho_b\underline{V''}\,\underline{V''}}) \quad = \\
&-(\bar{\theta}\nabla\bar{P} + \overline{\theta'\nabla P'}) + \nabla\cdot(\bar{\theta}\bar{\underline{\tau}} + \overline{\theta'\underline{\tau}'}) + (\overline{\bar{S}_{\underline{V},d} + S'_{\underline{V},d}})
\end{aligned} \tag{3.20}$$

Scalar Transport

Reynolds averaging yields:

$$\begin{aligned}
&\frac{\partial}{\partial t}(\tilde{\rho}\bar{\theta}\bar{\phi} + \bar{\rho}\overline{\theta'\phi'} + \overline{\rho'\bar{\theta}\phi'} + \overline{\rho'\theta'}\bar{\phi} + \overline{\rho'\theta'\phi'}) + \\
&\nabla\cdot(\bar{\rho}\bar{\theta}\underline{\bar{V}}\bar{\phi} + \bar{\rho}\bar{\theta}\overline{\underline{V'}\phi'} + \bar{\rho}\overline{\theta'\underline{\bar{V}}\phi'} + \bar{\rho}\overline{\theta'\underline{V'}\phi'} + \bar{\rho}\overline{\theta'\underline{V'}\phi'} + \overline{\rho'\bar{\theta}\underline{\bar{V}}\phi'} \\
&+\overline{\rho'\bar{\theta}\underline{V'}\bar{\phi}} + \overline{\rho'\bar{\theta}\underline{V'}\phi'} + \overline{\rho'\theta'}\underline{\bar{V}}\bar{\phi} + \overline{\rho'\theta'\underline{\bar{V}}\phi'} + \overline{\rho'\theta'\underline{V'}}\bar{\phi} + \overline{\rho'\theta'\underline{V'}\phi'}) \\
&= \quad \nabla\cdot[\bar{\Gamma}_\phi(\bar{\theta}\nabla\bar{\phi} + \overline{\theta'\nabla\phi'}] + (\overline{\bar{S}_\phi + S'_\phi}) + (\overline{\bar{S}_{\phi,d} + S'_{\phi,d}})
\end{aligned} \tag{3.21}$$

Favre decomposition followed by Reynolds averaging gives:

$$\begin{aligned}
&\frac{\partial}{\partial t}(\rho_b\tilde{\phi} + \rho_b\phi'') + \nabla\cdot(\rho_b\tilde{\underline{V}}\phi'' + \rho_b\tilde{\underline{V}}\phi'' + \rho_b\underline{V''}\tilde{\phi} + \rho_b\underline{V''}\phi'') \\
&= \nabla\cdot[\Gamma_\phi(\bar{\theta}+\theta')\nabla(\tilde{\phi}+\phi'')] + (\tilde{S}_\phi + S''_\phi) + (\bar{S}_{\phi,d} + S'_{\phi,d})
\end{aligned}$$

$$\begin{aligned}
&\frac{\partial}{\partial t}(\bar{\rho}_b\tilde{\phi}) \quad + \quad \nabla\cdot(\bar{\rho}_b\tilde{\underline{V}}\tilde{\phi} + \overline{\rho_b\underline{V''}\phi''}) \quad = \\
&\nabla\cdot\bar{\Gamma}_\phi[\bar{\theta}\nabla\tilde{\phi} + \bar{\theta}\nabla\bar{\phi''} + \overline{\theta'\nabla\phi''}] + (\overline{\tilde{S}_\phi + S''_\phi}) + (\overline{\bar{S}_{\phi,d} + S'_{\phi,d}})
\end{aligned} \tag{3.22}$$

Inspection of the above set of equations reveals that:

- Both averaging procedures introducing a number of new correlations involving fluctuating properties, although the Favre formulation, which eliminates most correlations involving density fluctuations, provides much simpler forms of averaged equations;

- Neither procedure produces equations of closed form, so additional effort is required to determine the correlations involving, for instance, the void fraction fluctuations, velocity fluctuations, and fluctuating properties of the droplet field, e.g., $\overline{S_{\phi,d}}$, $\overline{S'_{\phi,d}}$.

To ease the task of tackling the new correlation terms emerging from the averaging procedure, the Favre-averaged equations are used in this study. Further, the correlations involving void fraction fluctuations and those involving fluctuating properties of the droplet field are omitted. Additionally, in view of the fact that characteristic Reynolds number based on the length scales over which the mean flow properties change will always be large in our applications, the effects of molecular diffusion terms, $\nabla \cdot (\bar{\theta}\bar{\underline{\underline{\tau}}} + \bar{\theta}'\underline{\underline{\tau}}')$ and $\nabla \cdot \bar{\tau}(\bar{\theta}\nabla\tilde{\phi} + \bar{\theta}\nabla\bar{\phi}'')$, on the right hand side of Equations (3.20) and (3.22) will be neglected. Thus, the set of Favre-average equation reduces to:

$$\begin{aligned}
\frac{\partial}{\partial t}(\bar{\rho}_b) \quad + \quad \nabla \cdot (\bar{\rho}_b \tilde{\underline{V}}) &= \bar{S}_{m,d} \\
\frac{\partial}{\partial t}(\bar{\rho}_b \tilde{\underline{V}}) + \nabla \cdot (\bar{\rho}_b \tilde{\underline{V}}\,\tilde{\underline{V}} + \overline{\rho_b \underline{V}''\,\underline{V}''}) &= -\bar{\theta}\nabla\bar{P} + \bar{S}_{\underline{V},d} \\
\frac{\partial}{\partial t}(\rho_b \tilde{\phi}) + \nabla \cdot (\bar{\rho}_b \tilde{\underline{V}}\tilde{\phi} + \bar{\rho}_b \overline{\underline{V}''\,\phi''}) &= \tilde{S}_\phi + \bar{S}_{\phi,d}
\end{aligned} \tag{3.23}$$

and the gas state equation reads:

$$\bar{P} = \bar{\rho} R \tilde{T} \tag{3.24}$$

3.3.2 The $k - \epsilon$ Turbulence Model

To close the system of equations (3.23), it is necessary either to relate those extra correlation terms directly to the mean quantities, or to supply additional equations from which they can be derived. The latter method may lead to an infinite set of equations, if no special treatment is invoked. To illustrate this, the instantaneous equations can be manipulated to generate transport equations for new correlations

containing triple correlations, for which further transport equations can be obtained involving forth order correlations, etc. It follows that manipulation for each order of moment of the momentum equations will produce higher order equations, thus eventually leading to infinite number of correlations. To avoid this problem, a turbulence model is employed to close the problem at a certain level, and the optimum level of closure seems to be second-order as far as physical interpretation and potential applicability is concerned.

In this study, the well known $k-\epsilon$ turbulence model is chosen for the closure purpose. This model belongs to eddy viscosity class and still provides the best option in practical engine calculations (see, for example, the discussion in Ahmadi-Befrui (1985)). The basic assumptions providing the framework of the $k-\epsilon$ model are now discussed.

First, in eddy viscosity closures, the turbulent fluxes are assumed to be proportional to the mean flow strain rate. This is based upon the observation that the main effect of turbulence is to increase transport of the conserved properties and dissipation effects with respect to the laminar state. As for laminar flows, these processes are controlled by viscosity of fluid flow, it becomes natural to represent the turbulence in terms of an increasing viscosity, associated with the seemingly chaotic motion on the turbulence length scale (hence the use of the term 'eddy'). With this assumption, a mathematical relationship of the Newtonian type can be written (Launder & Spalding 1972):

$$-\overline{\rho_b \underline{V}'' \underline{V}''} = 2\mu_t \bar{\theta}[\underline{\underline{\bar{D}}} - \frac{1}{3}\nabla \cdot \tilde{\underline{V}}\,\underline{\underline{I}}] - \frac{2}{3}\bar{\rho}_b k \underline{\underline{I}} \tag{3.25}$$

where μ_t is the turbulent or eddy viscosity of the gas, which is, in general, a function of the properties of the flow field rather than of the fluid– as is the case for the molecular viscosity μ.

Second, in analogy with the concept of eddy viscosity, a concept of eddy diffusion is also introduced in order to relate the second order correlations of velocity and scalar fluctuations, $\overline{\rho_b \underline{V}'' \phi''}$, to the gradients of the mean variables. Thus,

$$-\overline{\rho_b \underline{V}'' \phi''} = \Gamma_{\phi,t} \bar{\theta} \nabla \tilde{\phi} \tag{3.26}$$

in which $\Gamma_{\phi,t}$ is the gas turbulence (eddy) diffusivity and is evaluated from the

relation (Launder & Spalding 1972)

$$\Gamma_{\phi,t} = \frac{\mu_t}{\sigma_{\phi,t}} \tag{3.27}$$

where $\sigma_{\phi,t}$ is the turbulent Prandtl/Schmidt number for variable ϕ.

The $k-\epsilon$ model involves the evaluation of μ_t from:

$$\mu_t = C_\mu \bar{\rho} \frac{k^2}{\epsilon} \tag{3.28}$$

where C_μ is an empirical coefficient (usually taken as a constant with a value 0.09), k is the specific kinetic energy of the gas turbulence, defined as

$$k = \frac{1}{2} \frac{\overline{\rho_b \underline{V}'' \cdot \underline{V}''}}{\bar{\rho}_b} \tag{3.29}$$

and ϵ is the turbulence energy dissipation rate of the gas, defined as:

$$\epsilon = \frac{1}{\bar{\rho}_b} \overline{\theta \underline{\underline{\tau}}'} : \nabla \underline{V}'' \tag{3.30}$$

Transport equations for k and ϵ can be derived from the momentum equations with the aid of assumptions and empiricism. According to Tabrizi (1991), the equations read:

$$\underbrace{\frac{\partial}{\partial t}(\bar{\rho}_b k)}_{\text{rate of change}} + \underbrace{\nabla \cdot (\bar{\rho}_b \tilde{\underline{V}} k)}_{\text{convective transport}} = \underbrace{\nabla \cdot (\Gamma_k \bar{\theta} \nabla k)}_{\text{diffusive transport by turbulent and molecular means}} + \underbrace{\bar{\theta}\mathcal{P}}_{\text{generation by mean shear with gas flow}}$$

$$\underbrace{-\bar{\rho}_b \epsilon}_{\text{dissipation by viscous forces}} + \underbrace{\bar{S}_{k,d}}_{\text{interaction of droplets with gas turbulence}} \tag{3.31}$$

and

$$\underbrace{\frac{\partial}{\partial t}(\bar{\rho}_b \epsilon)}_{\text{rate of change}} + \underbrace{\nabla \cdot (\bar{\rho}_b \tilde{\underline{V}} \epsilon)}_{\text{convective transport}} = \underbrace{\nabla \cdot (\Gamma_\epsilon \bar{\theta} \nabla \epsilon)}_{\text{diffusive transport by turbulent and molecular means}} + \underbrace{C_{\epsilon_1} \frac{\epsilon}{k} \bar{\theta}\mathcal{P}}_{\text{generation by shear and the self stretching action of turbulence}}$$

$$\underbrace{-C_{\epsilon_2} \bar{\rho}_b \frac{\epsilon^2}{k}}_{\text{viscous destruction}} + \underbrace{C_{\epsilon_3} \bar{\rho}_b \epsilon \nabla \cdot \tilde{\underline{V}}}_{\text{additional generation/ destruction due to comppressibility}} + \underbrace{\bar{S}_{\epsilon,d}}_{\text{interaction of droplets with gas turbulence}} \tag{3.32}$$

where Γ_k and Γ_ϵ are the effective diffusivity coefficients of k and ϵ, respectively, defined by:

$$\begin{aligned} \Gamma_k &= \frac{\mu_{eff}}{\sigma_k} \\ \Gamma_\epsilon &= \frac{\mu_{eff}}{\sigma_\epsilon} \end{aligned} \tag{3.33}$$

in which σ_k and σ_ϵ denote the turbulent Prandtl numbers (usually regarded as constants) for the k and ϵ, respectively, and μ_{eff} represents the effective viscosity, given by:

$$\mu_{eff} = \mu + \mu_t \tag{3.34}$$

The variable $\mathcal{P}$ is expressed as:

$$\mathcal{P} = -\overline{\rho_b \underline{V}'' \underline{V}''} : \nabla \tilde{\underline{V}} \tag{3.35}$$

and C_{ϵ_1}, C_{ϵ_2} and C_{ϵ_3} are the gas turbulence model coefficients; their values are taken from Ahmadi-Befrui (1985) and presented in Table 3.1.

The droplet interaction terms, $\bar{S}_{k,d}$ and $\bar{S}_{\epsilon,d}$ represent additional dissipation of turbulence energy by the passage of droplets through the eddies. They can be evaluated by considering the work done by droplets on the turbulent eddies. The following relations are due to Amsden et al. (1985):

$$\begin{aligned} \bar{S}_{k,d} &= -\int\int\int f \bar{\rho}_b \frac{\pi}{12} D_d^3 \overline{\underline{F}\,\underline{V}''} dD_d dU_d dT_d \\ \bar{S}_{\epsilon,d} &= C_\epsilon \frac{\epsilon}{k} \bar{S}_{k,d} \end{aligned} \tag{3.36}$$

where f is the number density function of droplets of diameter D_d, velocity U_d, temperature T_d, and specific acceleration $\underline{F}$ in the physical space at time t; and the empirical coefficient, C_ϵ, is taken to be 1.5. The validity of relation (3.36) has, however, not been adequately established. Therefore, the effects of $\bar{S}_{k,d}$, and $\bar{S}_{\epsilon,d}$ are ignored in this study.

A limitation of the $k-\epsilon$ equations is that they assume local isotropy. Even so, this model has proven capable of approximately predicting a large range of complex flows.

Table 3.1: Empirical Coefficients Involved in the Present Turbulence Model

C_μ	C_{ϵ_1}	C_{ϵ_2}	C_{ϵ_3}	$\sigma_{h,t}$	$\sigma_{f,t}$	σ_k	σ_ϵ	k_ν	E
0.09	1.44	1.92	-0.373	0.9	1.0	1.0	1.22	0.4187	9.793

3.4 Summary of Averaged Equations

This section provides a summary of the closed set of averaged gas-phase equations assembled thus far. Thus, we have:

Mean flow equations

$$\frac{\partial}{\partial t}(\bar{\rho}_b) + \nabla \cdot (\bar{\rho}_b \underline{\tilde{V}}) = \bar{S}_{m,d} \tag{3.37}$$

$$\frac{\partial}{\partial t}(\bar{\rho}_b \underline{\tilde{V}}) + \nabla \cdot (\bar{\rho}_b \underline{\tilde{V}}\,\underline{\tilde{V}}) = -\bar{\theta}\nabla\bar{P} + \nabla \cdot [2\mu_{eff}\bar{\theta}(\underline{\underline{\tilde{D}}} - \frac{1}{3}\nabla \cdot \underline{\tilde{V}}\,\underline{\underline{I}}) - \frac{2}{3}\bar{\rho}_b k \underline{\underline{I}}] + \bar{S}_{\underline{V},d} \tag{3.38}$$

Mean scalar equations

$$\frac{\partial}{\partial t}(\bar{\rho}_b \tilde{e}_s) + \nabla \cdot (\rho_b \underline{V}_r) = \nabla \cdot [\gamma \frac{\mu_{eff}}{\sigma_{h,eff}} \bar{\theta} \nabla \tilde{e}_s] - \bar{\theta}\nabla \cdot (\bar{P}\underline{\tilde{V}}) + \bar{S}_{e,d} \tag{3.39}$$

$$\frac{\partial}{\partial t}(\bar{\rho}_b \tilde{f}) + \nabla \cdot (\bar{\rho}_b \underline{\tilde{V}} \tilde{f}) = \nabla \cdot [\frac{\mu_{eff}}{\sigma_{f,eff}} \bar{\theta} \nabla \tilde{f}] + \bar{S}_{m,d} \tag{3.40}$$

Turbulence equations

$$\frac{\partial}{\partial t}(\bar{\rho}_b k) + \nabla \cdot (\bar{\rho}_b \underline{\tilde{V}} k) = \nabla \cdot (\frac{\mu_{eff}}{\sigma_k} \bar{\theta} \nabla k) + \theta \mathcal{P} - \bar{\rho}_b \epsilon \tag{3.41}$$

$$\frac{\partial}{\partial t}(\bar{\rho}_b \epsilon) + \nabla(\bar{\rho}_b \underline{\tilde{V}} \epsilon) = \nabla \cdot (\frac{\mu_{eff}}{\sigma_\epsilon} \bar{\theta} \nabla \epsilon) + C_{\epsilon_1} \frac{\epsilon}{k} \bar{\theta} \mathcal{P} - C_{\epsilon_2} \bar{\rho}_b \frac{\epsilon^2}{k} + C_{\epsilon_3} \bar{\rho}_b \epsilon \nabla \cdot \underline{\tilde{V}} \tag{3.42}$$

in which:

$$\mathcal{P} = [2\mu_{eff}(\underline{\underline{\tilde{D}}} - \frac{1}{3}\nabla \cdot \underline{\tilde{V}}\,\underline{\underline{I}}) - \frac{2}{3}\bar{\rho} k \underline{\underline{I}}] : \nabla \underline{\tilde{V}} \tag{3.43}$$

Finally, the equation of state of the gas is:

$$\bar{P} = \bar{\rho} R \tilde{T} \tag{3.44}$$

Hereafter, the averaging overbars will be omitted for convenience.

3.5 Transport Equations in Moving Coordinate Frame

The foregoing equations have been obtained for an arbitrary fixed elementary volume and are therefore valid for an Eulerian coordinate frame. In this section, general equations will be provided for an elementary volume which is both moving and deforming arbitrarily. These are needed for engine applications where the flow domain contracts and expands in accord with the piston and valve motions.

The task can be accomplished by either performing an moving elementary control volume analysis (White 1979) or by applying to the individual terms of Equations (3.37) to (3.42) general transformation formulae relating the derivatives between the two coordinate systems (see, for example, Watkin 1977; Johns 1980). The resulting equations read:

$$\frac{1}{\mathcal{V}}\frac{\partial}{\partial t}(\rho_b \mathcal{V}) \quad + \quad \nabla \cdot (\rho_b \underline{V}_r) \; = \; S_{m,d} \tag{3.45}$$

$$\begin{aligned} \frac{1}{\mathcal{V}}\frac{\partial}{\partial t}(\rho_b \mathcal{V}\underline{V}) \quad + \quad \nabla \cdot (\rho_b \underline{V}_r \underline{V}) \; = \; -\theta \nabla P \\ +\nabla \cdot [2\mu_{eff}\theta(\underline{\underline{D}} - \frac{1}{3}\nabla \cdot \underline{V}\,\underline{\underline{I}}) - \frac{2}{3}\rho_b k \underline{\underline{I}}] + S_{\underline{V},d} \end{aligned} \tag{3.46}$$

$$\frac{1}{\mathcal{V}}\frac{\partial}{\partial t}(\rho_b \mathcal{V}\phi) + \nabla \cdot (\rho_b \underline{V}_r \phi) = \nabla \cdot [\Gamma_\phi \theta \nabla \phi] + S_\phi + S_{\phi,d} \tag{3.47}$$

where $\mathcal{V}$ is the instantaneous elementary volume, and $\underline{V}_r$ is the relative velocity between the fluid and the local coordinate frame, defined by:

$$\underline{V}_r = \underline{V} - \underline{V}_g \tag{3.48}$$

in which $\underline{V}$ and $\underline{V}_g$ are, respectively, the fluid and the local coordinate frame velocities relative to an Eulerian coordinate system. The quantities, Γ_ϕ, S_ϕ and $S_{\phi,d}$ are defined in Table 3.2.

As can be easily noted, the equations in moving coordinate frame differ from their counterparts for a fixed frame in the following two aspects: (i) the unsteady term involves the rate of change of the control volume; and (ii) the convective term contains the relative velocity, $\underline{V}_r$.

Table 3.2: Definition of the Effective Diffusion Coefficients, Γ_ϕ, Gas Source Terms, S_ϕ, and Inter-Phase Exchange Terms, $S_{\phi,d}$, in Equation (3.47)

ϕ	Γ_ϕ	S_ϕ	$S_{\phi,d}$
e_s	$\gamma\frac{\mu_{eff}}{\sigma_{h,eff}}$	$-\theta\nabla\cdot(P\underline{V})$	$S_{e,d}$
f	$\frac{\mu_{eff}}{\sigma_{f,eff}}$	0	$S_{m,d}$
k	$\frac{\mu_{eff}}{\sigma_k}$	$\theta P-\rho_b\epsilon$	0
ϵ	$\frac{\mu_{eff}}{\sigma_\epsilon}$	$C_{\epsilon_1}\frac{\epsilon}{k}\theta P-C_{\epsilon_2}\rho_b\frac{\epsilon^2}{k}+C_{\epsilon_3}\rho_b\epsilon\nabla\cdot\underline{V}$	0

3.6 Transport Equations in Moving Curvilinear Orthogonal Coordinate Frame

Equations (3.45) to (3.47) are independent of coordinate system used, since they are given in the vector-tensor form. To effect numerical solution, they will now be expressed in terms of a particular coordinate frame.

The choice of a coordinate system is largely determined by the extent to which the geometric complexities are addressed of engine combustion chambers. If the full complexities are to be coped with, a general non-orthogonal coordinate system has to be used, in which case, the expanded form of equations is very complicated, and the effort involved in the numerical solution is substantial. Following Begleris (1987), a simpler curvilinear orthogonal coordinate system is employed in this study, which involves less complexity and still allows calculations for relative complex geometries. Begleris (1987) has derived and discussed in detail the form of the gas-phase transport equations in a general curvilinear orthogonal coordinate system. There is therefore no need for a repetition of this exercise here; so only a brief outline is given, by reference to the particular engine configuration of Figure 3.1, which depicts an offset bowl-in-piston geometry with a protruding inlet/exhaust valve.

The solution domain for this example of Figure 3.1 can be divided into two zones: (a) an expanding/contracting (E/C) region between the piston surface and the cylinder head; and (b) a translating (T) region in the bowl. For the sake of simplicity,

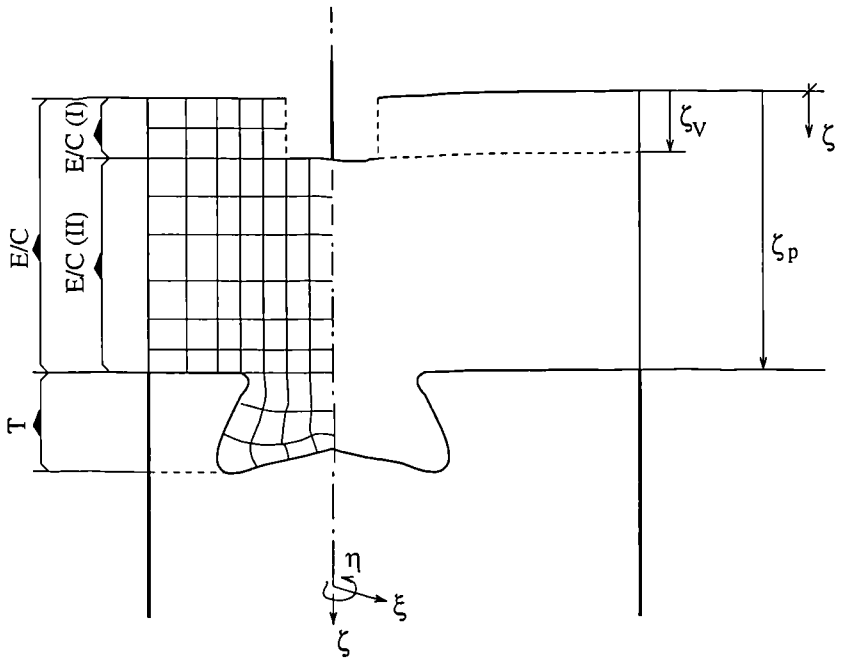


Figure 3.1: Elevation view of a bowl-in-piston chamber configuration with a protruding valve

a general curvilinear orthogonal grid is not used in all planes. Instead, each region is fitted with a grid that is arbitrarily- orthogonal in one set of planes only, with the coordinate in the third direction being either rectilinear or circumferential, in which case the planes containing the orthogonal curvilinear coordinate form a body of revolution.

The coordinate system for the solution domain is defined by the axial, radial and circumferential directions, represented, respectively, by ζ-, ξ- and η- coordinates. In what follows, the transport equations for each region will be presented, following a brief discussion of the characteristic features of the region.

3.6.1 Expanding/Contracting (E/C) Region

This region possesses two major features: (i) the direction ζ is rectilinear; and (2) the arc lengths $\Delta\xi$ and $\Delta\eta$ are invariant with ζ; and $\Delta\zeta$ is invariant with ξ and η. In addition, the coordinate motion is defined to be:

$$\underline{V}_g = (W_g, 0, 0) \tag{3.49}$$

where the local axial coordinate velocity, W_g, is a specified function of axial position and time, i.e.

$$W_g = W_g(\zeta, t) \tag{3.50}$$

It is useful to treat the moving piston and valve surfaces separately. To allow for this, the E/C region is further divided into two subregions, namely, E/C(I) between the cylinder head and the valve face, and E/C(II) between the valve face and the piston crown (Figure 3.1). Furthermore, W_g is assumed to vary linearly: (i) in E/C(I) between zero at the cylinder head and the valve velocity V_v, at the valve face; and (ii) in E/C(II) between V_v and the piston velocity, V_p. Thus:

$$W_g = \begin{cases} \dfrac{\zeta}{\zeta_v} V_v, & \text{for } 0 \le \zeta \le \zeta_v \\ \\ (1-f)V_v + fV_p, & \text{for } \zeta_v < \zeta \le \zeta_p \end{cases} \tag{3.51}$$

in which

$$f = \frac{\zeta - \zeta_v}{\zeta_p - \zeta_v} \tag{3.52}$$

where $\zeta_v = \zeta_v(t)$ and $\zeta_p = \zeta_p(t)$ are the instantaneous distances of the valve face and piston crown from the cylinder head where $\zeta = 0$.

The above described features enable the transport equations for E/C region to be expressed as (Begleris 1987):

$$\begin{aligned} &\frac{1}{\mathcal{V}}\frac{\partial}{\partial t}(\rho_b \mathcal{V}\phi) + \frac{\partial}{\partial \zeta}(\rho_b W_r \phi) + \frac{1}{\Delta\eta}\frac{\partial}{\partial \xi}(\rho_b \Delta\eta U \phi) + \frac{1}{\Delta\xi}\frac{\partial}{\partial \eta}(\rho_b \Delta\xi V \phi) \\ &= \frac{\partial}{\partial \zeta}(\Gamma_\phi \theta \frac{\partial \phi}{\partial \zeta}) + \frac{1}{\Delta\eta}\frac{\partial}{\partial \xi}(\Gamma_\phi \theta \Delta\eta \frac{\partial \phi}{\partial \xi}) + \frac{1}{\Delta\xi}\frac{\partial}{\partial \eta}(\Gamma_\phi \theta \Delta\xi \frac{\partial \phi}{\partial \eta}) + S_\phi + S_{\phi,d} \end{aligned} \tag{3.53}$$

where W, U and V are the components of the gas velocity vector, $\underline{V}$, in the axial (ζ-), radial (ξ-) and circumferential (η-) coordinates, respectively; $W_r = W - W_g$; and the elementary volume, $\mathcal{V}$, is given by:

$$\mathcal{V} = \Delta\zeta \Delta\xi \Delta\eta \tag{3.54}$$

in which $\Delta\zeta$, $\Delta\xi$, and $\Delta\eta$ are the arc lengths in ζ-, ξ- and η- directions, respectively. ϕ represents any dependent variable of W, V, U,... etc. In particular, the continuity equations can be obtained by selecting $\phi = 1$, Γ_1 and S_1, both to zero and $S_{1,d} = S_{m,d}$. The Γ_ϕ and $S_{\phi,d}$ expressions are given in Table 3.2; and the corresponding expressions for S_ϕ are defined in Table 3.3.

Table 3.3 Definition of Gas Source Terms, S_ϕ, in Equation (3.53) for Expanding/Contracting Region

ϕ	S_ϕ
W	$-\theta\frac{\partial P}{\partial \zeta}+\frac{\partial}{\partial \zeta}[\mu_{eff}\theta\frac{\partial W}{\partial \zeta}-\frac{2}{3}(\rho_b k+\mu_{eff}\theta\nabla\cdot\underline{V})]+\frac{1}{\Delta\eta}\frac{\partial}{\partial \xi}(\mu_{eff}\Delta\theta\eta\frac{\partial U}{\partial \eta})+\frac{1}{\Delta\xi}\frac{\partial}{\partial \eta}(\mu_{eff}\theta\Delta\xi\frac{\partial V}{\partial \zeta})$
U	$-\theta\frac{\partial P}{\partial \xi}+\frac{\partial}{\partial \eta}(\mu_{eff}\theta\frac{\partial W}{\partial \xi})+\frac{1}{\Delta\eta}\frac{\partial}{\partial \xi}\{\Delta\eta[\mu_{eff}\theta(\frac{\partial U}{\partial \xi}+\frac{2V}{\Delta\xi}\frac{\partial\Delta\xi}{\partial \eta})]\}-\frac{\partial}{\partial \xi}[\frac{2}{3}(\rho_b k+\mu_{eff}\theta\nabla\cdot\underline{V})]$ $+\frac{1}{\Delta\xi}\frac{\partial}{\partial \eta}[\Delta\xi\mu_{eff}\theta(\frac{\partial V}{\partial \xi}-\frac{U}{\Delta\xi}\frac{\partial\Delta\xi}{\partial \eta}-\frac{V}{\Delta\eta}\frac{\partial\Delta\eta}{\partial \xi})]+\frac{1}{\Delta\eta}\frac{\partial\Delta\eta}{\partial \xi}[\rho_b V^2-2\mu_{eff}\theta(\frac{\partial V}{\partial \eta}+\frac{U}{\Delta\eta}\frac{\partial\Delta\eta}{\partial \xi})]$ $-\frac{1}{\Delta\xi}\frac{\partial\xi}{\partial \eta}[\rho_b UV-\mu_{eff}\theta(\frac{\partial V}{\partial \xi}-\frac{U}{\Delta\xi}\frac{\partial\Delta\xi}{\partial \eta}+\frac{\partial U}{\partial \eta}-\frac{V}{\Delta\eta}\frac{\partial\Delta\eta}{\partial \xi})]$
V	$-\theta\frac{\partial P}{\partial \eta}+\frac{\partial}{\partial \zeta}(\mu_{eff}\theta\frac{\partial W}{\partial \eta})+\frac{1}{\Delta\eta}\frac{\partial}{\partial \xi}[\Delta\eta\mu_{eff}\theta(\frac{\partial U}{\partial \eta}-\frac{U}{\Delta\xi}\frac{\partial\Delta\xi}{\partial \eta}-\frac{V}{\Delta\eta}\frac{p\Delta\eta}{\partial \xi})]+\frac{1}{\Delta\xi}\frac{\partial}{\partial \eta}\{\Delta\xi[\mu_{eff}\theta(\frac{\partial V}{\partial \eta}+\frac{2U}{\Delta\eta}\frac{\partial\Delta\eta}{\partial \xi})]\}$ $-\frac{\partial}{\partial \eta}[\frac{2}{3}(\rho_b k+\mu_{eff}\theta\nabla\cdot\underline{V})]+\frac{1}{\Delta\xi}\frac{\partial\Delta\xi}{\partial \eta}[\rho_b U^2-2\mu_{eff}\theta(\frac{\partial U}{\partial \xi}+\frac{V}{\Delta\xi}\frac{\partial\Delta\xi}{\partial \eta})]$ $-\frac{1}{\Delta\eta}[\rho_b UV-\mu_{eff}\theta(\frac{\partial V}{\partial \xi}-\frac{U}{\Delta\xi}\frac{\partial\Delta\xi}{\partial \eta}+\frac{\partial U}{\partial \eta}-\frac{V}{\Delta\eta}\frac{\partial\Delta\eta}{\partial \xi})]$

Table 3.3 (continued)

ϕ	S_ϕ
e_s	$-\theta\nabla\cdot(P\underline{V})$
f	0
k	$\theta P-\rho_b\epsilon$
ϵ	$C_{\epsilon_1}\theta P\frac{\epsilon}{k}-C_{\epsilon_2}\rho_b\epsilon^2/k+C_{\epsilon_3}\rho_b\epsilon\nabla\cdot\underline{V}$

where:

$$P = \mu_{eff}g_t-\frac{2}{3}\nabla\cdot\underline{V}(\rho k+\mu_{eff}\nabla\cdot\underline{V})$$

in which,

$$\begin{aligned} g_t = {} & 2\left[\left(\frac{\partial W}{\partial\zeta}\right)^2+\left(\frac{\partial U}{\partial\xi}+\frac{V}{\Delta\xi}\frac{\partial\Delta\xi}{\partial\eta}\right)^2+\left(\frac{\partial V}{\partial\eta}+\frac{U}{\Delta\eta}\frac{\partial\Delta\eta}{\partial\xi}\right)^2\right] \\ & +\left(\frac{\partial U}{\partial\zeta}+\frac{\partial W}{\partial\xi}\right)^2+\left(\frac{\partial V}{\partial\zeta}+\frac{\partial W}{\partial\eta}\right)^2+\left(\frac{\partial V}{\partial\xi}-\frac{U}{\Delta\xi}\frac{\partial\Delta\xi}{\partial\eta}+\frac{\partial U}{\partial\eta}-\frac{V}{\Delta\eta}\frac{\partial\Delta\eta}{\partial\xi}\right)^2 \end{aligned}$$

and:

$$\nabla\cdot\underline{V} = \frac{\partial W}{\partial\zeta}+\frac{1}{\Delta\eta}\frac{\partial}{\partial\xi}(\Delta\eta U)+\frac{1}{\Delta\xi}\frac{\partial}{\partial\eta}(\Delta\xi V)$$

3.6.2 Translating (T) Region

This region is characterised by its axisymmetrical geometry, since it represents a body of revolution. Thus the coordinates for this region are axisymmetric curvilinear-orthogonal, with the coordinate axis coinciding with the bowl axis. It follows that all variables in the η- direction of geometric (but not flow) quantities defined on a constant -η surface can be assumed to be zero.

Figure 3.2a represents the intersections of the constant -ζ surfaces with a constant -η surface (which is a place through the symmetry axis). Figure 3.2b depicts a plane normal to the symmetry axis: planes of constant η appear on it as straight lines radiating from the point of symmetry, while circles drawn with this point as centre are lines of intersection of the mutually orthogonal constant -ζ and constant -ξ surfaces.

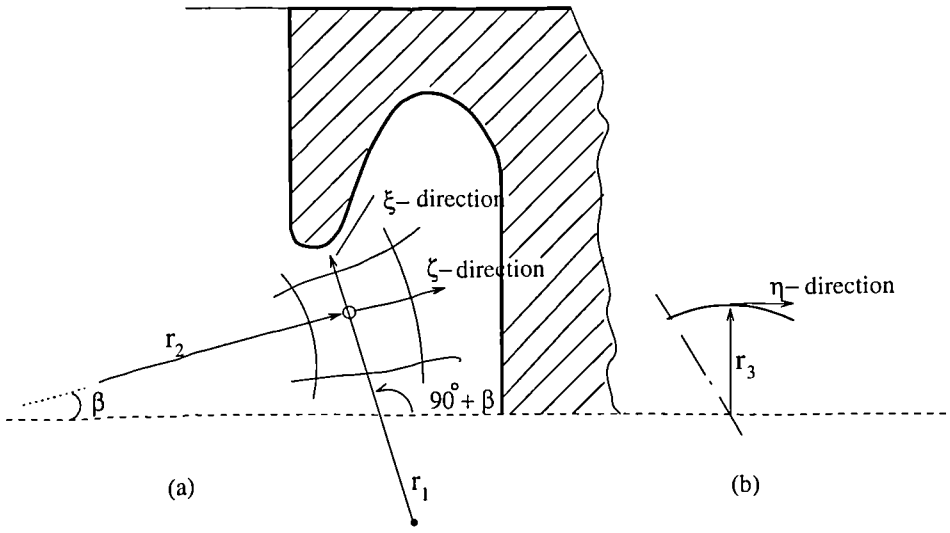


Figure 3.2: The axisymmetric curvilinear orthogonal coordinate system

For each point inside the bowl, whose local coordinate frame is characterised by three radii of curvature: r_1, r_2 and r_3, sufficient information is provided by a knowledge of: ζ- direction orientation, specified by defining the angle β between the ζ-direction and the axis of symmetry; and the radii of curvature r_1, r_2 and r_3. The significance of the radii of curvature is best perceived from Figure 3.2: r_1 and r_2 are , respectively, the radii of curvature of the ζ- and ξ- coordinate lines on a plane through the symmetry axis; r_3 is the distance of the point from the symmetry axis. Each of these radii will vary, in general, from point to point, but the variations have

to conform to certain geometrical rules (Begleris 1987).

The local coordinate velocity vector is expressed as:

$$\underline{V}_g = (V_p \cos\beta, -V_p \sin\beta, 0) \tag{3.55}$$

where V_p is the instantaneous piston velocity.

According to Begleris (1987) , the transport equations for the translating region is given as:

$$\frac{\partial}{\partial t}(\rho_b \phi) + \frac{1}{\Delta\xi\Delta\eta}\frac{\partial}{\partial\zeta}(\Delta\xi\Delta\eta\rho_b W_r \phi) + \frac{1}{\Delta\eta\Delta\zeta}\frac{\partial}{\partial\xi}(\Delta\eta\Delta\zeta\rho_b U_r \phi) + \frac{\partial}{\partial\eta}(\rho_b V \phi)$$
$$= \frac{1}{\Delta\xi\Delta\eta}\frac{\partial}{\partial\zeta}(\Delta\xi\Delta\eta\Gamma_\phi \phi\frac{\partial\phi}{\zeta}) + \frac{\partial}{\partial\eta}(\Gamma_\phi\theta\frac{\partial\phi}{\partial\eta}) + S_\phi + S_{\phi,d} \tag{3.56}$$

where the fluid velocities relative to the local coordinate frame, W_r and U_r, are defined as:

$$\begin{aligned} W_r &= = W - V_p \cos\beta \\ U_r &= U + V_p \sin\beta \end{aligned}$$

The quantities Γ_ϕ and $S_{\phi,d}$ are defined in table 3.2; and the gas source terms, S_ϕ, for each variable are given in Table 3.4.

Table 3.4 Definition of Gas Source Terms, S_ϕ, in Equation (3.56) for Translating Region

ϕ	S_ϕ
W	$-\theta\frac{\partial P}{\partial \zeta}+\frac{1}{\Delta\xi\Delta\eta}\{\Delta\xi\Delta\eta[\mu_{eff}\theta(\frac{\partial W}{\partial \zeta}+\frac{2U}{r_1})]\}-\frac{\partial}{\partial \zeta}[\frac{2}{3}(\rho_b k+\mu_{eff}\theta\nabla\cdot\underline{V})]+\frac{1}{\Delta\eta\Delta\zeta}\frac{\partial}{\partial\xi}[\Delta\eta\Delta\zeta\mu_{eff}\theta(\frac{\partial U}{\partial \zeta}-\frac{W}{r_1}-\frac{U}{r_2})]$ $+\frac{\partial}{\partial\eta}(\mu_{eff}\theta(\frac{\partial V}{\partial \zeta}-\frac{V\sin\beta}{r_3})]+\frac{1}{r_2}[\rho_b U U_r-2\mu_{eff}\theta(\frac{\partial U}{\partial\xi}+\frac{W}{r_2})]$ $+\frac{\sin\beta}{r_3}[\rho_b V^2-2\mu_{eff}\theta(\frac{\partial V}{\partial\eta}+\frac{W\sin\beta+U\cos\beta}{r_3})]-\frac{1}{r_1}[\rho_b W_r U-\mu_{eff}\theta(\frac{\partial W}{\partial\xi}-\frac{W}{r_1}+\frac{\partial U}{\partial \zeta}-\frac{U}{r_2})]$
U	$-\theta\frac{\partial P}{\partial\xi}+\frac{1}{\Delta\xi\Delta\eta}[\Delta\xi\Delta\eta\mu_{eff}\theta(\frac{\partial W}{\partial\xi}-\frac{W}{r_1}-\frac{U}{r_2})]+\frac{1}{\Delta\eta\Delta\zeta}\frac{\partial}{\partial\xi}\{\Delta\eta\Delta\zeta[\mu_{eff}\theta(\frac{\partial U}{\partial\xi}+\frac{2W}{r_2})]\}\frac{\partial}{\partial\xi}[\frac{2}{3}(\rho_b k+\mu_{eff}\theta\nabla\cdot\underline{V})]$ $+\frac{\partial}{\partial\eta}[\mu_{eff}\theta(\frac{\partial V}{\partial\xi}-\frac{V\cos\beta}{r_3})]+\frac{1}{r_1}[\rho_b W W_r-2\mu_{eff}\theta(\frac{\partial W}{\partial \zeta}+\frac{U}{r_1})]$ $+\frac{\cos\beta}{r_3}[\rho_b V^2-2\mu_{eff}\theta(\frac{\partial V}{\partial\eta}+\frac{W\sin\beta+U\cos\beta}{r_3})]-\frac{1}{r_1}[\rho_b W U_r-\mu_{eff}\theta(\frac{\partial W}{\partial\xi}-\frac{W}{r_1}+\frac{\partial U}{\partial \zeta}-\frac{U}{r_2})]$
V	$-\theta\frac{\partial P}{\partial\eta}+\frac{1}{\Delta\xi\Delta\eta}[\Delta\xi\Delta\eta\mu_{eff}\theta(\frac{\partial W}{\partial\eta}-\frac{V\sin\beta}{r_3})]+\frac{1}{\Delta\eta\Delta\zeta}\frac{\partial}{\partial\xi}[\Delta\eta\Delta\zeta\mu_{eff}\theta(\frac{\partial U}{\partial\eta}-\frac{V\cos\beta}{r_3})]$ $+\frac{\partial}{\partial\eta}[\mu_{eff}\theta(\frac{V}{\eta}+2\frac{W\sin\beta+U\cos\beta}{r_3})-\frac{2}{3}(\rho_b k+\mu_{eff}\theta\nabla\cdot\underline{V})]$ $-\frac{1}{r_3}\{\sin\beta[\rho_b W V-\mu_{eff}\theta(\frac{\partial V}{\partial \zeta}+\frac{\partial W}{\partial\eta})]+\cos\beta[\rho_b U V-\mu_{eff}\theta(\frac{\partial V}{\partial\xi}+\frac{\partial U}{\partial\eta})]+\mu_{eff}\theta\frac{V}{r_3}\}$

Table 3.4 (continued)

ϕ	S_ϕ
e_s	$-\theta\nabla\cdot(P\underline{V})$
f	0
k	$\theta P-\rho_b\epsilon$
ϵ	$(C_{\epsilon_1}\theta P-C_{\epsilon_2}\rho_b\epsilon)\frac{\epsilon}{k}+C_{\epsilon_3}\rho_b\epsilon\nabla\underline{V}$

where:

$$P = \mu_{eff}g_t-\frac{2}{3}\nabla\cdot\underline{V}(\rho k+\mu_{eff}\nabla\cdot\underline{V})$$

in which,

$$\begin{aligned} g_t &= 2\left[\left(\frac{\partial W}{\partial\zeta}+\frac{U}{r_1}\right)^2+\left(\frac{\partial U}{\partial\xi}+\frac{W}{r_2}\right)^2+\left(\frac{\partial V}{\partial\eta}+\frac{W\sin\beta+U\cos\beta}{\rho_3}\right)^2\right] \\ &\quad+\left(\frac{\partial V}{\partial\zeta}+\frac{\partial W}{\partial\eta}-\frac{V\sin\beta}{r_3}\right)^2+\left(\frac{\partial U}{\partial\zeta}+\frac{\partial W}{\partial\xi}-\frac{W}{r_1}-\frac{U}{r_2}\right)^2+\left(\frac{\partial V}{\partial\xi}-\frac{\partial U}{\partial\eta}-\frac{V\cos\beta}{r_3}\right)^2 \\ \nabla\cdot\underline{V} &= \left(\frac{\partial W}{\partial\zeta}+\frac{W}{r_2}\right)+\left(\frac{\partial U}{\partial\xi}+\frac{U}{r_1}\right)+\frac{1}{r_3}(W\sin\beta+U\cos\beta)+\frac{\partial V}{\partial\eta} \end{aligned}$$

3.7 Initial and Boundary Conditions

The above described equations apply to any fluid flow. To obtain the particular solutions for a given practical problem, specification is required of the initial and boundary conditions for each dependent variables. The operative boundaries for a practical engine consist of inlets or outlets, solid walls, coordinate pole/axis, a cyclic (or periodic) boundaries. The mathematical representation of these is detailed in this section.

3.7.1 Walls

The presence of a wall alters the nearby flow pattern and therefore causes additional complexities. Firstly, the no-slip condition at the wall surface requires the turbulence intensity in the near-wall region to fall from its maximum value to zero over a very thin layer, resulting very steep gradients of the flow properties. Secondly, the suppression of the normal component of turbulent intensity by the wall induces the 'damping' of the eddy viscosity, thus resulting in a strong anisotropic turbulence structure. Thirdly, the presence of a viscous sublayer, where turbulent effects are much smaller than viscous transport and the mean velocity profile is therefore linear, exerts substantial influence on the production, diffusion and dissipation of turbulent energy (Tennekes & Lumley 1980). These factors pose substantial modelling problems, because the viscous sublayer has to be adequately modelled, whereas turbulence models are often developed based on the assumption of high Reynolds number, which does not take into account near-wall effects. It is for these reasons that special practices are needed for the treatment of the near-wall region flows.

The main point of the near-wall treatment is to modify the high Reynolds number form of the equations within the viscous sublayer. Two different approaches are usually used to account for the viscous sublayer.

The first approach involves the use of modified equation for calculating turbulence kinetic energy and dissipation within the viscous sublayer (Jones and Launder 1973; Chien 1982). In this approach, damping functions are typically added to the source terms in the dissipation equations. In reality there is a dramatic change in the behaviour of the dissipation from the fully turbulent region to the viscous sub-

layer, which cannot be completely predicted by the modelled dissipation equation. Consequently, many investigators solve for a nonphysical dissipation within the viscous sublayer and modify the kinetic energy equations appropriately to account for this and to allow eddy viscosity to damp exponentially as the wall is approached.

The second approach involves the use of the wall function method to bridge the viscous sublayer, enabling the linkage of the flow properties within the viscous sublayer with those outside it (Launder & Spalding 1972). This method obviates the need to solve equations for the flow within the viscous sublayer. One problem with this approach is that it depends heavily on the validity of the adopted wall functions. The commonly-used wall functions of Launder and Spalding (1972) may not be accurate for complex flows, since they are only strictly valid for one dimensional turbulent Couette flows. The inaccuracy thus induced affects not only the turbulent quantities but also the mean flow predictions since a wall boundary condition for the streamwise momentum equations comes directly from the wall functions. Another deficiency of the method occurs when grid points lie within the viscous sublayer, in which case the standard $k-\epsilon$ equations are not valid and spurious boundary conditions will be obtained. Nevertheless, the wall function approach is employed in this study because it still offers the best compromise for engine calculations. A description of the wall function approach is now presented.

Wall functions are in essence equations relating a dimensionless velocity, U^+, and temperature, T^+, to a dimensionless distance, Y^+, normal to the wall. These dimensionless parameters are defined as:

$$\begin{aligned} Y^+ &= \frac{\rho u_\tau Y}{\mu} \\ U^+ &= \frac{U_R}{u_\tau} \\ T^+ &= \frac{\rho u_\tau c_p (T_W - T)}{\dot{q_W}} \end{aligned} \tag{3.57}$$

where U_R is the magnitude of the resultant tangential velocity relative to the wall at a distance Y along the normal to the wall, T_W is the wall temperature, $\dot{q_W}$ is the wall heat flux, and u_τ is the fluid friction velocity given by:

$$u_\tau = \sqrt{\frac{\tau_W}{\rho}} \tag{3.58}$$

in which τ_W is the resultant wall shear stress.

The wall functions employed here have their origin from one dimensional Couette flow analysis which involves the following assumptions:(i) the wall layer is divided into the viscous (or linear) sublayer where viscous forces are dominant, and the inertial sublayer where turbulent eddy interaction predominates, with the cross-over point from one region into the other taken to occur at $Y^+ = 11.63$; (ii) the mean properties obey, respectively, linear and logarithmic laws in the viscous and inertial sublayers; (iii) constant shear stress and heat flux prevail across the wall layer. (These assumptions are strictly valid only for an impermeable wall, with negligible streamwise pressure gradient); (iv) in the inertial sublayer ($Y^+ > 11.63$), the characteristic velocity is the friction velocity, u_τ, and the the eddy length scale is therefore assumed to vary in proportion to the distance from the wall, thus yielding:

$$\mu_t = k_v \rho u_\tau Y \tag{3.59}$$

in which the parameter, k_v, is the von Karman constant which assumes the value of 0.4187; and (v) turbulence is assumed to be in local equilibrium in the inertial sublayer, resulting in:

$$P_k \approx \rho\epsilon \tag{3.60}$$

where P_k is the total turbulence energy production.

With the above assumptions, the velocity and temperature profiles can be expressed as follows.

For the viscous sublayer ($Y^+ \leq 11.63$):

$$U^+ = Y^+ \tag{3.61}$$

$$T^+ = \sigma_h Y^+ \tag{3.62}$$

For inertial sublayer ($Y^+ > 11.63$):

$$U^+ = \frac{\ln(EY^+)}{k_v} \tag{3.63}$$

$$T^+ = \sigma_{h,t}\left[\frac{1}{k_v}\ln(EY^+) + P(\frac{\sigma_h}{\sigma_{h,t}})\right] \tag{3.64}$$

where the P-function is the viscous sublayer resistance factor expressing the contribution of the viscous sublayer to the total resistance and is given for smooth walls by (Jayatillaka (1966)):

$$P(\frac{\sigma_h}{\sigma_{h,t}}) = 9.0(\frac{\sigma_h}{\sigma_{h,t}-1})(\frac{\sigma_h}{\sigma_{h,t}})^{-\frac{1}{4}} \tag{3.65}$$

in which $\sigma_h(=0.7)$ and $\sigma_{h,t}(=0.9)$ are the laminar and turbulent Prandtl numbers, respectively.

Furthermore, the above equations can be employed to obtain explicit expressions for the wall shear stress, τ_w, and the wall heat flux, q_w, respectively, in terms of the velocity, U_R, and the temperature, T, of a point within the wall layer. These are given by:

$$\tau_w = -\mu_{eff}\frac{U_R}{Y} \tag{3.66}$$

$$\dot{q_w} = -K_{eff}\frac{T-T_W}{Y} \tag{3.67}$$

where the parameters, μ_{eff} and K_{eff} are expressed as follows:

$$\mu_{eff} = \begin{cases} \mu & \text{for } Y^+ \leq 11.63 \\ \dfrac{C_\mu^{1/4} k_v \rho k^{1/2} Y}{\ln(EY^+)} & \text{for } Y^+ > 11.63 \end{cases} \tag{3.68}$$

and:

$$K_{eff} = \begin{cases} \dfrac{\mu c_p}{\sigma_h} & \text{for } Y^+ \leq 11.63 \\ \dfrac{\mu c_p}{\sigma_{h,t}} Y^+ \dfrac{1}{k_v}\ln(EY^+) + P(\dfrac{\sigma_h}{\sigma_{h,t}}) & \text{for } Y^+ > 11.63 \end{cases} \tag{3.69}$$

The tangential velocity relative to the wall, U_R, is the resultant of either $(U-U_W)$ and $(V-V_W)$ or $(W-W_W)$, depending on whether the boundary under consideration is a constant-ζ or constant-ξ surface (see Figure 3.3). Here, (W_W, U_W, V_W) are the components of the wall or wall film (if present) velocity vector in the ζ, ξ and η directions, respectively. For a constant-ξ boundary illustrated in Figure 3.3, U_R is given by :

$$U_R = \sqrt{(W-W_W)^2 + (V-V_W)^2} \tag{3.70}$$

Accordingly, the resultant shear stress, τ_w, evaluated from (3.66), can also be resolved into the two directions as:

$$\begin{aligned} \tau_{\xi\eta} &= \tau_w \frac{W-W_W}{U_R} = -\mu_{eff}\frac{W-W_W}{Y} \\ \tau_{\xi\eta} &= \tau_w \frac{V-V_W}{U_R} = -\mu_{eff}\frac{V-V_W}{Y} \end{aligned} \tag{3.71}$$

in which $\tau_{\xi\eta}$ and $\tau_{\xi\eta}$ are the shear stress components in the ζ and η directions at a constant-ξ solid boundary.

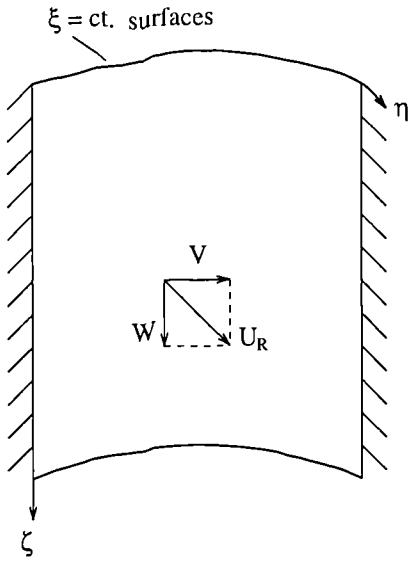


Figure 3.3: A constant ξ boundary

Finally, It is also necessary to impose wall boundary conditions on the $k-\epsilon$ equations. According to Launder & Spalding (1972), the sink term $\rho\epsilon$ in the $k-$equation must be modified to allow for the steep variation of ϵ in the Couette layer, yielding:

$$\rho\epsilon = \begin{cases} \dfrac{C_\mu^{3/4}\rho k^{3/2}Y^+}{Y} & \text{for } Y^+ \leq 11.63 \\ \dfrac{C_\mu^{3/4}\rho k^{3/2}}{ln(EY^+)/(k_vY)} & \text{for } Y^+ > 11.63 \end{cases} \tag{3.72}$$

In addition, the correct evaluation of the shear stress, τ_w, must be ensured in the near-wall region. This can be achieved by suitable modification of the production term. Also, the wall boundary conditions for ϵ can be described by:

$$\epsilon = \frac{C_\mu^{3/4}k^{3/2}}{k_vY} \tag{3.73}$$

This relation links the value of ϵ to that of k at the edge of the Couette flow region, and is obtained by the use of the assumption that balance exists between production and viscous dissipation of k near the wall.

3.7.2 Coordinate pole/Axis

The coordinate system chosen in this study may have a pole, which is specified to coincide with the chamber axis when the geometry and the drop-gas flow field are

axisymmetric. In this case, all the gas phase properties are assumed to have zero gradient, and the radial velocity component set to be zero.

However, for a general three-dimensional droplet-gas flow field, the coordinate pole is not an axis of flow symmetry, in which case the unknown values of the gas phase variables at the pole are calculated by area-weighted interpolations, between surrounding gas field values in the physical plane, as will be documented in Chapter 6.

3.7.3 Cyclic (or Periodic) Boundaries

Cyclic boundaries are associated with circumstances where the flow repeats itself cyclically in identical sectors in plan view. To illustrate this, let us consider an example of an engine with a 'square' bowl-in-piston, for which it is desired to predict, during the compression stroke, the dynamic evolution of sprays injected into the combustion chamber for a four-hole injector, positioned at the center of the cylinder head (see Figure 3.4). In diametrical view in Figure 3.4, the flow field can be divided into four sectors, each of which containing sprays injected from one nozzle hole. It is apparent that the droplet-gas flow in each sector will exhibit the same pattern, provided the air motion from induction possesses symmetric properties. The flow condition on these planes are identical and hence they are called cyclic (or periodic) boundaries.

However, on these boundaries, the values of the variables and their fluxes have to be determined as part of the solution, since they are not known *a priori*. The procedure for treating cyclic boundaries is presented in Chapter 6. This allows the solution domain to be confined in one sector, such as AOB in Figure 3.4, in which case the axial planes OA and OB are the two coordinate surfaces bounding the domain in the circumferential directions

3.7.4 Initial Condition

Where necessary, the initial conditions for the gas flow field, have to be set in a manner as to be consistent with the state equation. Calculations can start with the piston at any position provided the distribution of the velocity components,

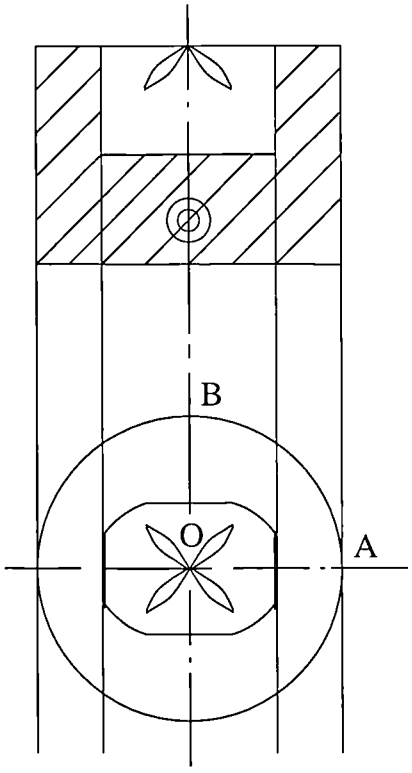


Figure 3.4: An example of a straight walled bowl which is not a volume of a volume of revolution ('square' bowl-in-piston')

pressure, temperature, density and the turbulent kinetic energy and its dissipation rate at that position are known.

The initial conditions of the injected droplet parcels are the subject of the next section, in which a whole subsection is devoted to the description of the atomisation model, which involves the determination of the initial sizes and velocities of the droplet parcels introduced near the nozzle.

3.8 The Lagrangian Equations Governing the Liquid Phase

In Diesel engines the fuel is introduced via the nozzle in the form of a high-velocity jet, which rapidly disintegrates into drops of varying sizes. Thus in this study the liquid phase is viewed as a dispersed or discrete phase. Furthermore, the Lagrangian approach is employed to mathematically model the spray dynamics. In this, the liquid phase is represented by discrete 'computational droplets' which interact with the gas phase. Each such 'droplet' represents a group or parcel of real droplets possessing the same physical properties (eg. size, velocity, temperature, etc.) and nominal location. The Lagrangian conservation equations of mass, momentum and energy for each computational droplet are solved to obtain the trajectories, masses, velocities and temperatures of the parcels.

Additionally, submodels are introduced to address each of the following processes: (i) liquid primary breakup resulting from atomisation, (ii) droplet secondary breakup due to aerodynamic forces, and (iii) droplet collisions and the resulting coalescence, bouncing or separation.

3.8.1 Atomisation

(a) Introduction

Atomisation is a process in which the liquid fuel is transformed into drops through disintegration of the liquid jet emerging from a nozzle. Basically, it can be considered as a disruption of the consolidatory influence of surface tension by the action of internal and external forces. Breakup occurs when the magnitude of disruptive force just exceeds the consolidatory surface force.

The parameters that control this process include mainly nozzle geometry and jet exit velocity, liquid surface tension which tends to pull liquid into the form of a sphere, and liquid viscosity which exerts a stabilising influence by opposing any change in shape. Two important dimensionless parameters are usually used to characterise the atomisation process, namely, the jet Weber number based on gas density:$We_J = \rho D_N U_{inj}^2/\sigma$, and the jet Laplace number $La_J = \rho_L \sigma D_N/\mu_L^2$.

The importance of atomisation lies in the fact that it directly determines the

initial spray structure in the near-nozzle region and the subsequent evolution of spray size distribution and mixing dynamics. In order to clarify the structure of the spray in the near-nozzle region, it is important to determine the jet breakup regimes and the associated transition criteria. Several jet breakup regimes have been identified in quiescent surroundings (Scheele & Meister 1968; Ranz 1956, 1958; Ohnesorge, 1936; Miesse 1955; Reitz 1978; Sterling and Sceicher 1975). They are:
(i) 'Nonjetting' or 'drip' - this occurs at very low flow rates with $We_{JL} < 3 - 4$. Here the jet momentum is not large enough to overcome surface tension forces at the passage exit(Scheele and Meister,1968).
(ii) 'Stable liquid jet' - which occurs for $La_J < 1/16 - 1/4$, where viscous forces are large enough to damp all disturbances that would lead to breakup.
(iii) 'Rayleigh breakup' - in which interactions between liquid inertia and surface tension cause jet breakup, yielding drop diameters somewhat larger than the injector diameter with jet breakup length increasing with increasing flow rate.
(iv) 'First wind-induced breakup' - where a twisting and helical instability of the liquid column results in jet breakup, yielding drops with diameters comparable to the injector diameter.
(v) 'Second wind-induced breakup' - which is caused by both surface and helical instabilities of the liquid column, yielding a wide range of drop sizes extending to the injector diameter.
(vi) 'Atomisation breakup' - which occurs at very high flow rates, involving breakup at the liquid surface right at the injector exit, producing drops that are generally smaller than the injector diameter.

The drip and stable jet regimes are of no importance in practical applications, since they do not produce sprays. The latter four breakup regimes, occurring in order of increasing jet flow rate, are illustrated in Figure 3.5. Of particular importance here is the atomisation breakup regime which usually produces a dense spray region, sometimes consisting of a liquid core, like the potential core of a single-phase jet, surrounded by a developing multiphase mixing layer consisting of entrained gas and droplets. Since practical sprays in engines require small drops for adequate mixing and vapourisation, the use of small injector hole sizes (typically 0.2-0.5mm diameter) and high injection velocities (of the order of 200m/s) is common such that

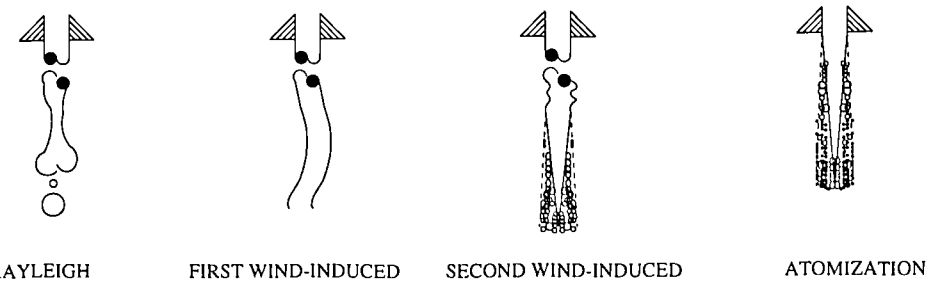


Figure 3.5: Schematic diagram of liquid jet breakup regimes in still gas

the atomisation breakup regime is realised. Thus the topography of atomisation breakup is most important, and deserves more study.

Several investigators (e.g. Castman 1932, Phinney 1973; Hiroyasu et al. 1982; Chehroudi et al. 1985) have provided observation that the liquid jet requires a finite distance to atomise fully. This distance is referred to as the 'breakup length', and in some cases may be comparable to the distance from the nozzle to the position at which impingement may occur on the piston wall(as evidenced by Yule and Filipovic 1992). To describe this phenomenon, Castman (1932) proposed a concept of gradual atomisation process, which fundamentally opposes the once widely-received concept of 'instantaneous atomisation' at the orifice proposed by Haenlein (1932) and others. In the present author's opinion, neither of these concepts can cover all circumstances, instead each of which corresponds only a certain range of injection conditions. It is therefore important to clarify the conditions under which whether the liquid core exists or not.

Transition conditions between the breakup regimes are necessary for the purpose of theoretical modelling of atomisation process and the realisation of particular breakup regimes by adjusting nozzle operating conditions. Transition maps can be plotted in a variety of ways, depending on the choice of parameters as the coordinate variables. A convenient transition map is given by Faeth (1990), as illustrated in Figure 3.6, which is plotted in terms of We_J and La_J.

The following features can be noted in this Figure:

- The transition from the drip regime is related to the density ratio, since at transition $We_{JL} = (\rho_L/\rho)We_J = 4$. This implies a progressively narrower Rayleigh breakup regime as ρ_L/ρ decreases.

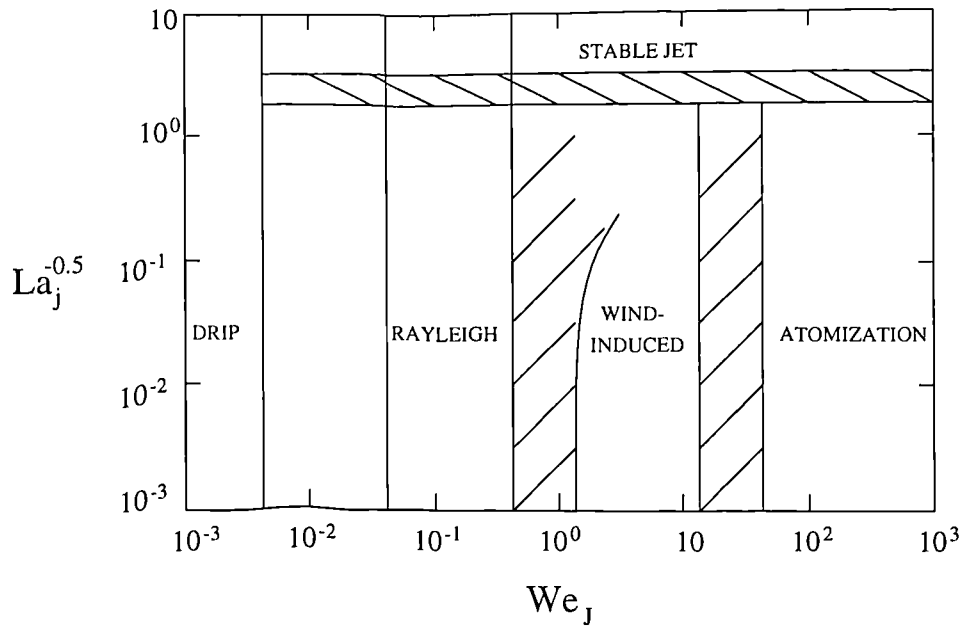


Figure 3.6: Jet breakup regime transitions (Adapted from Faeth 1991)

- The transition boundary from Rayleigh to wind-induced breakup is approximately a straight vertical line at high La_J, and becomes more dependent on La_J at low La_J. Indeed, Ranz (1958), suggests a transition Weber number as $We_J \approx 0.4$ for high La_J, while Sterling & Sleicher (1975)observe transition at $We_J = 1.2 + 3.41 La_J^{-0.45}$ for $La_J \geq 6.25$.

- The transition between first and second wind-induced breakups is gradual and a transition criterion has not yet been found.

- Transition to atomisation breakup involves nearly constant We_J. However, uncertainties exist concerning this critical value, as can be seen from Figure 3.6. Ranz (1958) and Miesse (1955) suggest respectively $We_J \approx 13$ and $We_J \approx 40$.

- Little data have been uncovered about the transition to the stable jet regime.

It is clear that there are still uncertainties in all transitions at low La_J, i.e. when the liquid is of high viscosity. This is important for heavy fuels at high ambient pressures– a case which is likely to be encounted in marine Diesel engines. Under these circumstances La_J becomes smaller as the thermodynamic critical point of the liquid surface is approached. Therefore more study of low La_J transitions is needed. In addition, both liquid cavitation and gas phase turbulence affect breakup (Hinze

1955, Ruff et al 1989), and their influence on breakup regime transition needs to be quantified.

Available measurements by Ruff et al. (1989) and Ruff & Faeth (1990) on the structure of the multiphase mixing layer using double-flash holograms of water sprays revealed some interesting features. Their results, at $x/D_N = 25$ (D_N being the nozzle diameter), for atomisation breakup and nonturbulent jet exit conditions showed that: large, irregular, ligament-like elements are located in the region near the liquid surface, while smaller round drops exit in the dilute spray region near the edge of the flow (direct evidence of important effects of secondary breakup near the surface). These findings appear to support the conventional picture of atomisation within dense sprays: primary breakup followed by secondary breakup into small round drops. This conflicts with another hypothes, based on computational studies, that small drops are formed at the liquid surface and then collide and coalesce to create larger drops within the multiphase mixing layer (Reitz and Bracco 1984). Additional measurements are needed to resolve this controversy.

Drop sizes along the liquid surface are larger for turbulent exit conditions (Ruff et al. 1989). In spite of the effects of secondary breakup and liquid turbulence, the ratio of the mass mean diameter MMD and the Sauter mean diameter SMD was roughly 1.2 everywhere, which agrees with Simmons (1977a,b) for a wide variety of nonevaporating dilute sprays. Furthermore, drop-size distributions for all conditions also satisfied Simmons universal root-normal distributions for this MMD/SMD ratio. This is helpful, since the entire drop size distribution can be related in a simple manner to the SMD. However, an explanation of this behaviour and more evidence concerning its generality for dense sprays are needed.

The above experiments also shed some light on the distributions of drop velocities in the near-nozzle region. They vary substantially with drop diameter at each point in the flow. Near the liquid core, the largest drops have velocities comparable to liquid injection velocities; however, velocities decrease with drop size and radial distance. A surprising feature is that gas velocities (which approximate the velocities of the smallest drops) are low and nearly constant across the mixing layer. This implies relatively ineffective momentum exchange between the phases, since the large drops contain most of the momentum and respond slowly to drag forces.

As for turbulent jet exit conditions, Lee and Spencer (1932, 1933) provided early observations that much larger drops resulted from primary breakup at low ambient pressure. This breakup mechanism has also been confirmed recently by Ruff and Faeth (1990), who argued that this mechanism is due to turbulent distortion of the liquid surface, stabilised by surface tension. According to Ruff and Faeth (1990), the outcomes of turbulent breakup can be estimated by considering the momentum required to overcome surface tension forces when forming a drop, using the relationship between velocity fluctuations and eddy size within the inertial region of the turbulence spectrum (Hinze 1975). This yields a correlation for the range of drop sizes that can be formed, which seems to support the above evidence. However this breakup mechanism was investigated under the conditions involving nozzles with larger diameters (5.0-9.5mm), and its applicability to Diesel engines is doubtful, since in such circumstances the sizes of injectors are smaller, and the length-to-diameter ratios are also small such that liquid turbulence may not be as fully developed as in the situations examined by Ruff and Faeth (1990).

(b) Atomisation model

As already stated, numerical modelling of the spray dynamics requires the resolution of the atomisation phenomenon in order to specify the initial drop sizes and velocities in the near-nozzle region. In response to this need, some models have emerged to represent the atomisation process. The model of Reitz and Diwakar (1987) involves the concept that atomisation of the injected liquid and the subsequent breakup of drops are indistinguishable processes within a dense spray. In this model, the liquid is injected as discrete parcels of drops or 'blobs'. The size of injected drop decreases with time due to breakup and the size is specified using experimental drop breakup correlations. It is demonstrated that this model predicts a core region near the nozzle which contains large drops, and length of the core agrees with core length measurements in dense sprays. However, it also predicts a negligible fuel vapour in the core region, which does not reflect the experimental behavior. Subsequently, Reitz (1987) proposed an improved atomisation model, known as wave breakup model which differs from the previous model in that the size of the drops produced is determined from the wave length of unstable waves on the surface

of the blobs, instead of from experimental correlations. Here, the determination of the wave length is based on a stability analysis for liquid jets issuing from a circular orifice into a stationary incompressible gas. For this purpose, an infinitesimal axisymmetric surface displacement is imposed on the initially steady motion, yielding small axisymmetric fluctuating pressures, and axial and radial velocity components in both the liquid and gas phases. These fluctuations are described by the continuity equation and the equation of motion, which are solved to give a dispersion equation for the wave growth rate and wavelength (Reitz and Bracco 1984). A distinct feature of this model is that it covers a number of jet breakup regimes ranging from Reyleigh breakup to atomisation. It also produces finely-atomised drops which are seen at the spray edge near the nozzle in photographs of high-pressure sprays.

In this study, the atomisation is modelled following the approach of Huh and Gosman (1991) for the atomisation jet breakup regime occurring at high jet Reynolds number. The model starts with the identification of the dominant mechanisms that control spray atomisation. An order of magnitude analysis of the possible relevant forces in the jet breakup has revealed that atomisation is mainly controlled by two mechanisms: aerodynamic forces and jet internal stresses induced by the turbulence. Accordingly, the atomisation process is envisaged to take place in two stages. Firstly, as supported by the work of Ruff and Faeth (1990), turbulence is developed inside the nozzle due to the high injection velocity, inducing initial perturbations on the jet surface when it leaves the nozzle. Secondly, once these perturbations have reached a certain level, where the turbulence effect becomes less evident due to its decay, the perturbations are further driven by aerodynamic forces, growing exponentially by Kelvin-Helmholtz instabilities until they become detached as liquid droplets.

The model is then devoted to the determination of the length and time scales of atomisation by analyzing the corresponding characteristic scales involved in the above two stages. These time and length scales are finally used to simulate the basic elements involved in the atomisation process. Detailed features of this model are now discussed.

Nozzle flow turbulence

Turbulence in nozzle flow is mainly caused by the high injection velocity, as well

as some other factors such as nozzle wall surface roughness, imperfections in the nozzle geometry, abrupt changes in cross-sectional area. In order to analyse the effect of this turbulence on liquid atomisation, a first step is to evaluate the values of the exit mean turbulence kinetic energy, K_{avg}, and its dissipation, ϵ_{avg}. This is pursued by considering energy and force balances inside the nozzle hole (taking the nozzle volume as a control volume). First, a force balance of the liquid in the nozzle requires, under steady-state conditions that

$$\pi D_N L \tau_{wall} = \frac{\pi D_N^2}{4} \Delta P_N \tag{3.74}$$

where D_N is the nozzle diameter, L is the nozzle length, and τ_{wall} is the shear stress applied on the liquid by the nozzle wall surface. The pressure drop ΔP_N is expressed (from the Bernoulli equation) as:

$$\Delta P_N = \frac{\rho_L U^2}{2} \left[\frac{1}{c_d} - K_c - (1 - s^2) \right] \tag{3.75}$$

in which ρ_L is the liquid density; U is a time averaged injection velocity with respect to the injection duration; K_c and c_d are the form loss coefficient and discharge coefficient, respectively; and $S = D_0^2/D_N^2$ is the area ratio (see Figure 3.7). Substitution

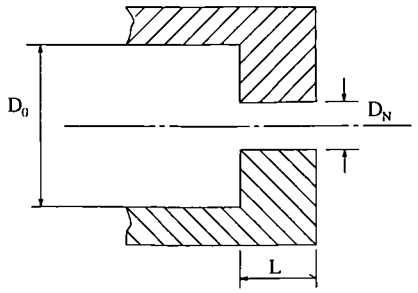


Figure 3.7: Sketch of nozzle geometry

of (3.75) into (3.74) leads to

$$\tau_{wall} = \frac{\rho_L U^2}{8L/D_N} \left[\frac{1}{c_d^2} - K_c - (1 - s^2) \right] \tag{3.76}$$

Use of (3.76) and an energy balance equation in the hole gives

$$K_{avg} = \frac{U^2}{8L/D_N} \left[\frac{1}{c_d^2} - ((1 - s^2) - K_c) \right] \tag{3.77}$$

$$\epsilon_{avg} = K_\epsilon \frac{U^3}{2L} \left[\frac{1}{c_d^2} - ((1 - s^2) - K_c) \right] \tag{3.78}$$

where K_c is the form loss coefficient, set to be 0.45. K_ϵ is an empirical coefficient which is tuned to be 0.27 by Huh through comparison with multidimensional flow field calculations.

The turbulence length and time scales are defined by:

$$L_t^0 = C_\mu^{3/4} \frac{K_{avg}^{3/2}}{\epsilon_{avg}} \tag{3.79}$$

$$\tau_t^0 = C_\mu^{3/4} \frac{K_{avg}}{\epsilon_{avg}} \tag{3.80}$$

where $C_\mu = 0.09$ is a constant taken from the $k - \epsilon$ turbulence model, and the subscript $_{avg}$ refers to the average value.

The above values of L_t^0 and τ_t^0 are assigned as initial values to each injected parent droplet at the exit of injector. However the internal turbulence of the parent droplets decays with time as they travel downstream, since there is no turbulence generation within them. An analysis is therefore performed for a parent droplet using the $k - \epsilon$ model and assuming homogeneous isotropic turbulence within the droplet. This leads to the following decaying expressions:

$$L_t(t) = L_t^0 \left[1.0 + (C_2 - 1.0)\frac{t}{t_t^0}\right]^{xenp} \tag{3.81}$$

$$\tau_t(t) = \tau_t^0 + (C_{20} - 1.0)t \tag{3.82}$$

where t is the time after the injection of the parent droplet, $C_{20} = 1.92$ is a constant from the $k - \epsilon$ model, and the exponent $xenp$ is set to be 0.4565.

Aerodynamic disturbance

As mentioned earlier, the liquid jet surface, upon exposure to the gas phase, possesses initial perturbations, the amplitude of which increases under the action of the aerodynamic forces. The evolution of the perturbated waves can be described by the period equation of Taylor (1958) for a viscous liquid

$$(\alpha + 2\nu k^2)^2 + \frac{\sigma k^3}{\rho_L} - 4\nu^2 k^3 \left(k^2 + \frac{\alpha}{\nu}\right)^{1/2} + (\alpha^2 + i\nu k)^2 \frac{\rho}{\rho_L} = 0 \tag{3.83}$$

where ν is the kinematic liquid viscosity, k is the wave number which is related to the detached droplet size, D_d, by $k = 2\pi/D_d$, i denotes the imaginary unit, and α is the complex frequency. The wave growth rate is evaluated from the real part of α, i.e., $Re(\alpha)$, and the wave growth time scale, t_w, is obtained as the inverse of $Re(\alpha)$.

At this point, estimation of atomisation time and length scales can be made based on two postulates:

(i) The length scale of atomisation, L_A, is mainly controlled by the turbulence length scale,L_t, and they are related by

$$L_A = C_1 L_t \tag{3.84}$$

The surface wave length, L_w, is linked to L_A by

$$L_w = \frac{L_A}{C_2} \tag{3.85}$$

where C_1 and C_2 are empirical constants. C_1 is set to 2.0 by putting the atomisation length scale equal to the dominant eddy diameter, which is twice the integral length scale of the turbulence, while C_2 is set to equal to 0.5 from the conceptual picture that half the surface wave will be detached as a secondary drop from the jet.

(ii) The atomisation time scale, t_A, is taken a linear combination of the turbulence and wave growth time scales. This yields

$$\tau_A = C_3\tau_t + C_4\tau_w = \tau_{spn} + \tau_{exp} \tag{3.86}$$

in which τ_{spn} is the time scale associated with the nozzle turbulence effect which initialises the instability of the emerging liquid jet, and is therefore termed the spontaneous growth time; whereas τ_{exp} is the time scale linked to the aerodynamic-driven wave growth behaviour which is represented by an exponentially-varying function, and hence called the exponential growth time. The empirical coefficients C_3 and C_4 have been tuned by Huh to be 1.0 and 3.0, respectively, by reference to data on spray angle, discharge coefficient and breakup length data, using a trial and error method.

Liquid injection and breakup

Liquid injection is effected by introducing parcels of parent droplets, or blobs, with size equal to the nozzle diameter. The number of blobs injected in unit time is determined from the mass flow rate. Each blob is given an initial axial velocity component,U_t, and a radial velocity component, $V = U_t \tan(\theta/2)$, where U_t is the instantaneous injection velocity and θ is assumed to be uniformly distributed between 0 and the spray angle, Θ, which is given by:

$$\tan\left(\frac{\Theta}{2}\right) = \frac{L_A^0/\tau_A^0}{U} \tag{3.87}$$

in which $L_A = C_1 L_t^0$ and $\tau_A = C_3 \tau_t^0 + C_4 \tau_w$, and U is the time averaged injection velocity.

Atomisation of the blobs proceeds in two steps. First, each blob is allowed to decrease in size during atomisation period as a consequence of detachment of secondary droplets. The rate of change of primary droplet size is described using the following rate equation:

$$\frac{dD_d/2}{dt} = -\frac{L_A}{K_A \tau_A} \tag{3.88}$$

where K_A is an empirical constant which is determined by fitting experimental data such as the breakup length or tip penetration. This size-decreasing procedure continues until the spontaneous time scale becomes larger than the exponential time scale.

Secondly, there is a need to determine the size of new droplets detached from the blob. This is pursued by assuming a probability density function (pdf) for the atomised droplets, which is defined as the volume fraction of the total atomised droplet volume, V_d, occupied by the droplets with size x per interval dx,

$$p(x) = \frac{1}{V_d}\frac{dV_d}{dx} \tag{3.89}$$

Construction of $p(x)$ is based on the assumption of isotropic turbulence in the liquid phase and the following four hypotheses concerning the number density of the atomised droplets:

- the number of droplets of size x is inversely proportional to the atomisation time scale τ_A,
- the number of droplets of size x is proportional to the jet-droplet surface area ratio, D^2/x^2,
- the number of droplets with size x is proportional to the turbulence energy spectrum $\Phi(x)$, which is given by Equation (3.91).
- the number of droplets in the range $(x, x+dx)$ is proportional to the unit size interval, dx/x.

Use of the above hypotheses leads to

$$p(x) = C\frac{\Phi(x)}{\tau_A(x)} \tag{3.90}$$

where C and Φ are the normalisation constant and the dimensionless turbulence energy spectrum, respectively. The latter is estimated, according to Hinze (1955), by:

$$\Phi(x) = \frac{[\kappa(x)/\kappa_e]^2}{[1+(\kappa(x)/\kappa_e)^2]^{11/6}} \tag{3.91}$$

where the peak wavenumber $\kappa_e = 2\pi/L_e$, and $L_e = L_t/0.75$. The length scale L_e can be interpreted as the average size of the energy-containing eddies.

The cumulative distribution function, $F(x)$, is calculated as:

$$F(x) = \int_{x_{min}}^{x} p(x)dx \tag{3.92}$$

in which the minimum droplet size, x_{min} , is calculated, according to the Kelvin-Helmholtz instability theory, by:

$$x_{min} = 2\pi \frac{(\rho_L + \rho_G)\,\sigma}{\rho_L\,\rho_G\,U^2} \tag{3.93}$$

Finally, the size of atomised droplets, x_a ,is determined in a random manner such that:

$$\int_{x_{min}}^{x_a} p(x)dx = Y_r \tag{3.94}$$

where Y_r is a randomly-chosen number in the range $(0,1)$. The number, N_a of droplets with size x_a is evaluated from the mass balance for the liquid:

$$N_a = \frac{(D_d)^3 - (D_d^n)^3}{x_a^3}\,, \tag{3.95}$$

where a superscript ^{n} denotes the condition after breakup.

(c) Discussion

According to what has been described in the preceding subsection, the atomisation model of Huh and Gosman is only applicable to the jet atomisation regime which involves high jet velocity and relatively fully-developed nozzle flow turbulence. Uncertainty may arise if the nozzle length is small, in which case the nozzle turbulent flow is not developed to such an extent as to ensure the dominant role of jet internal stresses. For instance, in intermittent injections systems there are a period at the beginning of each injection when the velocity is rising from zero and a corresponding period at the end when it falls again to zero, during which the flow

may well be either laminar or semiturbulent and the above atomisation model is therefore not completely applicable.

Other uncertainties associated with the model may be linked with some empirical coefficients involved in the determination of atomisation length and time scales. In addition, the size distribution function of the atomised droplets in this model is constructed on the basis of physical intuition. Further validation or improvement of the constructed distribution function may be made by reference to the experimental data of Ruff et al. (1989) who claim that the drop size distribution satisfies Simmon's universal root-normal distributions for MMD/SMD=1.2, as mentioned earlier.

3.8.2 Droplet Motion and Trajectory

The droplet motion equation can be established by applying Newton's second law to a droplet traveling in a flow field, as follows:

$$m_d \frac{d\underline{U}_d}{dt} = \underline{F} \tag{3.96}$$

where m_d is the mass of droplet parcel, U_d is the droplet velocity vector, and $\underline{F}$ is the resultant force applied on the droplet which, in general, includes:

1. *The aerodynamic drag force which comprises skin friction and form drag.* This has the form:

$$\underline{F}_D = \frac{1}{2} A_d V_{rel} (\underline{V} - \underline{U}_d) C_d \tag{3.97}$$

where A_d, is the projected area of the droplet in the direction of the flow, and the drag coefficient, C_d, is defined as

$$C_d = \frac{|\underline{F}_D|}{(\pi/4) D_d^2 (\rho V_{rel}^2/2)} \tag{3.98}$$

A detailed discussion of the drag coefficient will be given shortly.

2. *The force due to the static pressure gradient in the flow.* This is given by

$$\underline{F}_P = -\frac{\pi}{6} D_d^3 \nabla P \tag{3.99}$$

This force, as evidenced by an order of magnitude analysis of Williams (1962), is often negligible for sprays.

3. *The virtual mass force due to the inertia of the fluid displaced by the motion of the droplet.* This is expressed as:

$$\underline{F}_V = \frac{\pi}{12} D_d^3 \rho C_I \frac{d(\underline{V} - \underline{U}_d)}{dt} \tag{3.100}$$

where C_I is the virtual mass coefficient, which is set to be 1 in most cases. The virtual mass force can be neglected if the liquid-to-gas density ratio is large. In engine-related spray calculations, $\rho_d/\rho \geq 20$ is a typical condition. It is therefore reasonable to ignore this force.

4. *The Basset force which corrects for temporal variations in the relative velocities.* The expression for this force is given by:

$$\underline{F}_B = \frac{3}{2} D_d^2 (\pi \rho \mu)^{1/2} C_B \int_{t_0}^{t} \frac{\frac{d}{dt^*}(\underline{V} - \underline{U}_d)}{(t - t^*)^{1/2}} dt^* \tag{3.101}$$

in which C_B is the Basset coefficient.

Ormancey and Martinon (1984) provided evidence to show that negligence of Basset force is reasonable for low turbulence intensities and moderate departures from homogeneity. However, for highly-turbulent flow, this force is non-negligible according to Hansell et al. (1992) who performed numerical calculations under typical combustor conditions of 20 bar and 1500K. Their results showed that neglect of both Basset force and virtual mass force can induce an error up to 25% for particles travelling in a highly-turbulent flow. More studies are needed to establish the conditions under which the Basset force is effective. Nevertheless, the Basset force is not considered in the present study and its calculation will be attempted as a future task.

5. *Magnus and Saffman lift forces.* Magnus forces are associated with droplet rotation, whereas Saffman forces are induced by shear flow gradients. In the bulk of a flow, rotation of droplet, if present, is expected to be damped rapidly by viscous dissipation, making it possible to neglect the Magnus forces. As for the Saffman forces, Faeth (1983) showed that they are at least an order of magnitude smaller than the drag force, if the droplet is located in the region of $x/D_N > 10$ (here D_N is the nozzle diameter and x denote the distance from the droplet to the nozzle). Thus, neglecting Magnus and Saffman forces may

be reasonable in the bulk flow, apart from very near the nozzle. However, in the near-wall region where strong fluid shear is induced and droplets acquire appreciable rotation by virtue of wall impingement and shear flow, the magnitudes of these terms may be significant relative to the drag term. For instance, we can show that there is a subregion contained in the near-wall region, in which Saffman lift forces are at least of the same order of the drag forces. To this end, let us consider a two-dimensional case and denote by x the direction parallel to the wall and by y the direction normal to the wall. The Saffman lift force is given by (Saffman 1965):

$$F_L = K\mu D_d^2 \left(\frac{1}{\nu}\frac{dU}{dY}\right)^{1/2} (U - U_d) \tag{3.102}$$

where K was obtained from numerical integration and its value was corrected from 20.3 to 1.615 by Saffman (1968); U and U_d are respectively the gas and droplet velocity in the x direction; and Y is the distance normal to the wall.

We now consider first the ratio between the lift force and the drag force in the x direction, which is given by:

$$\frac{|\underline{F}_L|}{|\underline{F}_{Dx}|} = \frac{K}{3\pi}\left[D_d^2 \frac{dU}{dY}\frac{\rho}{\mu}\right]^{1/2} \tag{3.103}$$

where ρ and μ are respectively gas density and viscosity. To evaluate the term dU/dy, we use the log-law wall function (3.63) (here we only consider those droplets located in the inertial layer). This yields:

$$\frac{dU}{dy} = \frac{u_\tau}{k_v y} \tag{3.104}$$

Substitution of (3.104) into (3.103) gives:

$$\frac{|\underline{F}_L|}{|\underline{F}_{Dx}|} = 0.171 \left(\frac{Y^+}{k_v}\right)^{1/2} \frac{D_d}{y} \tag{3.105}$$

where Y^+ is defined in (3.57) which satisfies the relation $Y^+ \geq 11.63$ in the inertial region. Thus

$$\frac{|\underline{F}_L|}{|\underline{F}_{Dx}|} \geq 1.05 \frac{D_d}{y} \tag{3.106}$$

which yields

$$\frac{|\underline{F}_L|}{|\underline{F}_{Dx}|} \geq 1; \qquad \text{if } \frac{D_d}{y} \geq 0.98 \tag{3.107}$$

The above implies that if$D_d/2 \leq y \leq 1.02D_d$, the magnitude of Saffman lift force is not less than that of the drag force in the x direction.

To compare the ratio between the lift force and the drag force in the normal direction, we can also write:

$$\frac{|\underline{F}_L|}{|\underline{F}_{Dy}|} = \frac{K}{3\pi}\left[D_d^2\frac{dU}{dy}\frac{\rho}{\mu}\right]^{1/2}\left(\frac{U-U_d}{V-V_d}\right) \tag{3.108}$$

In the linear layer of the wall, the fluid velocity U is linear in Y in the linear sublayer, whereas V is proportional to Y^2—a requirement of the no-slip condition (Hinze 1975). Thus the ratio $(U-U_d)/(V-V_d)$ varies as $1/Y$ and hence its magnitude increases as it approaches the wall. On the other hand, the magnitude of $(D_d^2/\nu)(dU/dY)$ should be bounded in order to satisfy the condition for which Equation (3.102) was derived. It follows that the ratio $|\underline{F}_L|/|\underline{F}_{Dy}|$ becomes much greater than unity.

This concludes that in the near-wall region, it is indeed the case that the lift force is at least of the same order of magnitude of the drag force.

6. *Gravity and other body forces.* In most spray-related problems, gravity is the only body force which can be shown, through an order of magnitude analysis, to be negligible in comparison to the drag force if droplet sizes are less than 1 mm in diameter and the drop-gas relative velocity is beyond 1 m/s. The latter conditions are usually satisfied for diesel sprays, since the diameters of injector holes are typically $0.1 \sim 0.4$ mm and the injection velocity of fuel is usually of the order of 100 m/s. Thus, it is reasonable to neglect gravity in engine spray calculations.

From the above discussions, it seems justifiable, in this study, to retain only the drag force in the droplet momentum equations, while including the Saffman forces for the droplets moving in the near-wall region. Thus, in the bulk flow, we have the following droplet motion equation:

$$\frac{d\underline{U}_d}{dt} = \frac{3}{4}C_d\frac{\rho}{\rho_d}\frac{V_{rel}}{D_d}(\underline{V}-\underline{U}_d) \tag{3.109}$$

and in the near-wall region, we have

$$\frac{d\underline{U}_d}{dt} = \frac{3}{4}C_d\frac{\rho}{\rho_d}\frac{V_{rel}}{D_d}(\underline{V}-\underline{U}_d) + \frac{3}{4}\frac{F_L}{\rho_d D_d^3} \tag{3.110}$$

The droplet position vector x_d is governed by:

$$\frac{d\underline{x}_d}{dt} = \underline{U}_d \tag{3.111}$$

Drag Coefficients

We return now to the drag force, which is determined by the specification of the drag coefficient, C_d. This, however, poses an extremely challenging problem, for it requires a full knowledge of the flow pattern around the droplet which is complex. Thus far theoretical analysis of the drag coefficient has only met with success for flows at low Reynolds numbers. In this case, Stokes (1901) derived the following expression:

$$C_d = \frac{24}{Re_d} \tag{3.112}$$

where

$$Re_d = \frac{\rho_L V_{rel} D_d}{\mu}$$

is the droplet Reynolds number. The C_d given by Equation (3.112) is called the 'Stokes' drag, valid strictly for $Re_d < 1$.

For higher Reynolds numbers, however, the drag coefficients differ from Stokes law for two main reasons. First, the inertial forces become significant and the drag force may be increased due to the formation of a wake and possible detachment of energy-consuming vortices. Second, the presence of a boundary layer around the droplet induces additional complexity which also makes the drag coefficient depart from the Stokes drag. Recognition of these factors has led to numerous correlations which incorporate correction factors to Stokes drag. Most of these are based on the analysis of experimental data, and are limited to a single spherical particle or droplet. A commonly used 'standard' drag coefficient relation is given by (Wallis 1969):

$$\begin{aligned} C_d &= \frac{24}{Re_d}\left(1 + 0.15 Re_d^{0.687}\right) \qquad 0 < Re_d < 1000 \\ C_d &= 0.44 \qquad\qquad\qquad\qquad\qquad\quad Re_d > 1000 \end{aligned} \tag{3.113}$$

The term 'standard' here refers to the conditions in which a single spherical particle/droplet moves steadily in a non-turbulent flow field at low temperature (thus the nature of momentum transfer is a quasi-steady state). In diesel engines, however, the droplets usually experience a drag that differs from the standard drag, since the

flow pattern around the droplet is considerably different from that for which the standard drag law is derived. In what follows, some major factors affecting C_d are discussed.

(i) Effect of relative flow unsteadiness on drag coefficient

In a diesel spray environment, it is often the case that the droplets are accelerated by the gas flow if the gas velocity is higher that the droplet velocity, or decelerated if the gas velocity is lower than the droplet velocity. Thus the effect of unsteadiness on the drag coefficient is always present, although for low accelerations the drop drag coefficient approaches the steady-state value.

Ingebo (1956) conducted experiments to investigate the drag coefficients of liquid and solid spheres accelerating in airstreams for various of airstream pressures, temperatures and velocities. The following relation is found to describe well the drag coefficients of isooctane, water, and trichlorethylene and solid spheres (magnesium and calcium silicide):

$$C_d = \frac{27}{Re_d^{0.84}} \qquad (for \quad 6 < Re_d < 400) \tag{3.114}$$

which lies between the Stokes drag and the standard drag, according to Ingebo (1956).

Briffa (1981) also examined experimentally the unsteady relative motion effect on droplet drag, using a water spray decelerating in an airstream. His results showed that the drag coefficients were quite different from the standard drag curve. More recently, Choi and Lee (1992) provided further observation that the droplet drag coefficient is much lower than the standard one during a severe droplet deceleration process; however, when this deceleration rate is reduced rapidly by increasing gas velocity, the trend is reversed. Unfortunately, no attempt has been made to incorporate a parameter, which is characteristic of droplet/gas relative motion unsteadiness, into the drag coefficient correlations.

(ii) Effect of droplet interaction on drag coefficient

Since sprays normally involve a large number of droplets, the flow pattern around a particular droplet may be affected by the presence of its neighbouring droplets. Thus its drag coefficient may also be affected. Recently, this effect has been studied by some investigators,(e.g. Rowe and Henwood 1961; Raju and Sirignano 1990),

although they confine themselves to the situations involving droplets in tandem(e.g. Rowe and Henwood 1961; Raju and Sirignano 1990) or side-by-side in parallel (e.g. Dandy and Dwyer 1990; and Kim et al 1992).

Mulholland et al. (1988) studied experimentally the influence of droplet spacing on the drag coefficient. A horizontal stream of non-evaporating, equal-sized drops was introduced into quiescent ambient gas, yielding a range of the Reynolds number (Re_d) of 90 to 290, and droplet spacing to diameter ratio (L/D_d) of 1.7– 1700. They obtained the following correlation for droplet drag coefficient as a function of Re_d and L/D_d:

$$[C_d(Re_d, L/D_d)]^{-n} = [C_{d,0}(Re_d, L/D_d)]^{-n} + [C_{d,\infty}(Re_d)]^{-n} \tag{3.115}$$

where $n = 0.378 \pm 0.7$ is a parameter obtained by experiment; $C_{d,\infty}$ is the standard drag given by (3.113); and $C_{d,0}$ is expressed by:

$$[C_{d,0}(Re_d, L/D_d)]^{-n} = C_{d,0'}(Re_d) + a(Re_d)^{-1}(L/D_d - 1) \tag{3.116}$$

in which $C_{d,0'}$ is evaluated from:

$$[C_{d,0'}(Re_d)]^{-n} = \left[\frac{0.755}{Re_d}\right]^{-n} - [C_{d,\infty}(Re_d)]^{-n} \tag{3.117}$$

Equation (3.115) implies that L/D_d has an appreciable effect on C_d: closely spaced tandem droplets have a much lower drag coefficients than widely spaced droplets. This trend has also been confirmed by Choi and Lee (1992), who proposed that, for closely spaced tandem droplets with $L/D_d < 4$, the drag coefficient be estimated by their empirical correlation:

$$C_d = \frac{2.3}{Re_d^{0.37}}, \qquad 20 \leq Re_d \leq 110 \tag{3.118}$$

which does not however contain the parameter L/D_d.

In the dense portion of spray, droplet interaction is much more complicated than the case discussed above, thus the use of standard drag coefficient (3.113) or even Equation (3.115) is inappropriate, and modified drag coefficients are required. Unfortunately, current information is not adequate for this purpose.

(iii) Effect of droplet deformation on drag coefficient

As mentioned above, the standard drag expression (3.113) is valid for rigid spherical particles or spherical droplets. However, when a droplet travels in a gas stream

with a sufficiently large relative velocity, it deforms and is no longer spherical due to the aerodynamic forces, a feature which has been observed experimentally by many researchers, e.g., Ranger and Nicholls (1969), Hinze (1955), Hsiang and Faeth (1992). At the Reynolds number (Re_d) and Weber number ($We_G = \rho D_d V_{rel}/\sigma$) levels indicative of the onset of droplet oscillation and deformation, the drag coefficient for the droplet was observed to suddenly depart from the standard drag curve and increase with increasing Reynolds number (c.f. Hu and Kintner 1955, Klee and Treybal 1956, Greene et al. 1993, Hsiang and Faeth 1992). Thus there is a critical Weber number, $We_{G,crit}$ above which the droplets begin to deviate from the standard drag law. Greene et al. (1993) found that this limiting value is around 8.21 for a single liquid droplet setting in a tall column of another lighter immiscible liquid. According to Greene et al. (1993), the drag coefficient upon deformation can be correlated by

$$\frac{C_d}{C_{d,crit}} = \frac{Re_d}{Re_{d,crit}} \tag{3.119}$$

where $C_{d,crit}$ and $Re_{d,crit}$ are, respectively the critical values of C_d and Re_d at the onset of drop oscillatory deformation; and $Re_{d,crit}$ is related to $We_{G,crit}$ by:

$$Re_{d,crit} \cdot We_{G,crit} = 165 \tag{3.120}$$

However, Hsiang and Faeth (1992) found that for a liquid droplet suspended in an air stream ($La = \rho_l \sigma D_d/\mu^2 > 100$), the above limiting Weber number is approximately 3, which shows a substantial difference from that determined by Greene (1993). This may be due to the fact that in the latter case, the viscosity of the continuum in which the droplet travels plays a non-negligible role. Hsiang and Faeth (1992) observed that when $We_G > We_{G,crit} = 3$, the droplet drag increases as the deformation intensifies, but they provided no specific drag correlations.

The necessity of appropriately modelling the dynamic change of droplet drag coefficient with the drop deformation has been illustrated recently by Liu et al. (1993), who performed numerical studies of the dynamic effects of drop drag on fuel spray characteristics. Assuming linear variation with drop deformation of the drag coefficient from the lower limit of a rigid sphere (no distortion) to an upper limit of a disk (maximum distortion), these authors presented some interesting results of calculations. In particular, it was shown that, although spray tip penetration is

relatively insensitive to the value used for the drop drag coefficient, the distribution of droplet sizes within the spray (thus also spray vapourisation) is clearly influenced. This feature is not difficult to perceive: changes in drag result in changes in drop-gas relative velocity which plays a crucial role in determining spray size distribution and evolution through its influence on droplet breakup rate and drop binary-collision outcomes.

(iv) Effect of Evaporation on drag coefficient

Diesel sprays often involve elevated temperatures, where the effect of evaporation on drag must be considered. Yuen and Chen (1976) found that evaporation affects droplet drag in two ways. First, the temperature and concentration gradients between the drop surface and the ambient gas cause substantial reductions in the absolute viscosity of the gas, thereby decreasing friction drag. Second, the mass transfer associated with evaporation induces the so called 'blowing' effect, which reduces friction drag and increases form drag. To account for both variable properties and blowing associated with evaporation, Reunksizbulut and Yuen (1983) proposed the following correlation for the drag coefficient:

$$C_d = \frac{24}{Re_m}\left(1 + 0.2Re_m^{0.63}\right)(1 + B_f)^{-0.2} \qquad 10 < Re_d < 300 \tag{3.121}$$

where Re_m and B_f are the Reynolds number and the mass transfer number at the film conditions, respectively. The latter quantity is defined as:

$$B_f = \frac{c_{pf}(T_\infty - T_s)}{h_{fg}} \tag{3.122}$$

in which h_{fg} is the latent heat of vapourisation of the drop at surface temperature T_s and c_{pf} is the specific heat of the vapour and air mixture at the film condition. The mean kinematic viscosity, ν, contained in Re_m, is equal to μ_f/ρ_∞, where ρ_∞ is the density of the gas at temperature T_∞ at infinity, and μ_f is the absolute viscosity of the vapor and gas mixture at film condition.

A limitation of Equation (3.121) is that it is derived by fitting to the the experimental data of Yuen and Chen (1976) and Eisenklan et al. (1967), which involve free-falling single droplets, so the gas/droplet momentum transfer was quasi-steady state. This casts doubts on its validity for unsteady evaporating single droplets, since there is evidence that the drag coefficients of unsteady evaporating single droplets

differ appreciablely from those for the non-evaporating steady state condition, according to Dwyer and Sanders (1984) who performed a numerical analysis for the unsteady case.

(v) Effect of wall on drag coefficient

Faxen (1923) noticed that the presence of the wall increases the drag coefficient of the sphere in the near-wall region as compared to that in the case of unbounded flow. To account this effect, Faxen (1923), Brenner (1961) and Maude (1961) have introduced correction factors to the standard drag force. For a small particle moving parallel to the wall with a Reynolds number less than 1, Faxen (1923) derived the following expression of the correction factor to the stokes drag as a function of D_p/Y:

$$C_{w\tau} = \left[1 - \frac{9}{16}\left(\frac{D_p}{2Y}\right) + \frac{1}{8}\left(\frac{D_p}{2Y}\right)^3 - \frac{45}{256}\left(\frac{D_p}{2Y}\right)^4 - \frac{1}{16}\left(\frac{D_p}{2Y}\right)^5\right]^{-1} \tag{3.123}$$

where Y is the normal distance between the particle and the wall, and D_p is the particle (or droplet) diameter. Equation (3.123) shows that the drag force parallel to the wall for a particle increases as the droplet nears the wall. For instance, according to (3.123), for the case of $D_p/Y = 0.5$, the drag for a particle is about 1.2 times its value in an unbounded flow. As for the case involving a small particle moving normal to the wall, Brenner (1961) and Maude (1961) independently determined the following modification to the drag force, C_{wn}, which was also found to be a function of D_p/Y:

$$C_{wn} = -\left(1 + \frac{9}{16}\frac{D_p}{Y}\right) + O\left(\left(\frac{D_p}{Y}\right)^2\right) \tag{3.124}$$

For small Y, Cox and Brenner (1967) used lubrication theory to show that the drag force approaches infinity as the gap between the wall and the particle becomes small:

$$C_{wn} = -\frac{1}{r}\left[1 + \frac{r}{5}\ln\left(\frac{1}{r}\right) + 0.971214r\right] \tag{3.125}$$

where $r = (2Y - D_p)/D_p$.

Equation (3.125) indicates that, because the drag force becomes infinitely large as the wall is approached, it is impossible for a particle to reach a wall in a finite amount of time. This is however physically unrealistic. The reason for this is that the shear stress in the gas produces the singular behaviour in (3.125). In reality, for particles moving through a gas, the continuum approximation breaks down when

the distance between the surface of the particle and the wall becomes comparable with the molecular mean-free-path (m.f.p.) of the gas. One effect of this breakdown is, according to Cunningham (1910), that the continuum model overpredicts the magnitude of the shear stress on the surface of the particle in the gap. Dahneke (1974) suggested the following modification of the drag law to incorporate the effects of molecular slip:

$$C_{wn} = \frac{1 + \dfrac{D_p}{2Y - D_p}}{1 + \dfrac{2.8\lambda}{2Y - D_p}} \tag{3.126}$$

where λ is the molecular m.f.p. Results of simulations using the drag correlation in (3.126) has been reported by Kallio (1989).

The above information indicates a need to modify the drag coefficients of the droplets in the near-wall region if accurate predictions of the wall impingement characteristics are to be achieved.

Summarising, it can be stated that at present there is no single expression for droplet drag coefficient that applies to all conditions. Available correlations of drag coefficient which accounts for the effect of droplet interaction, deformation and unsteady loading are not conclusive. Thus, we will use in this study Equation (3.113) for low gas temperatures and (3.121) for high temperatures. It should be recognised that this practice will give rise to certain uncertainties in the prediction of real spray dynamics, according to the above discussions.

Equations of Droplet Motion in Moving Coordinate Frame

Equations (3.109) and (3.111) are independent of coordinate frame. They can be expressed, in the same velocity and coordinate systems as the gas phase equations, as

$$\frac{d\underline{U}_{d,r}}{dt} = \frac{\underline{V}_r - \underline{U}_{d,r}}{\tau_m} - \frac{d\underline{V}_g}{dt} + S_{\underline{U}_{d,r}} \tag{3.127}$$

where $\underline{U}_{d,r}$ is the relative velocity between the droplet and the local coordinate frame–$O\xi\eta\zeta$:

$$\underline{U}_{d,r} = \underline{U}_d - \underline{V}_g \tag{3.128}$$

in which $\underline{U}_d$ and $\underline{V}_g$ are the droplet and local coordinate frame velocities relative to an Eulerian coordinate system. The quantity τ_m is referred to as the response time,

or the time available for momentum transfer due to drag, and is given by

$$\tau_m = \frac{4}{3}\frac{\rho_d D_d}{\rho V_{rel} C_d} \tag{3.129}$$

The vector $S_{\underline{U}_{d,r}}$ contains terms representing the centrifugal and Coriolis forces.

The trajectory equation is given in terms of the droplet position relative to the local coordinate frame, $\underline{x}_{d,r}$, by:

$$\frac{d\underline{x}_{d,r}}{dt} = \underline{U}_{d,r} \tag{3.130}$$

If we write

$$\begin{aligned}
\underline{U}_{d,r} &= (U_{d,r}, V_{d,r}, W_{d,r}) = (U_d - U_g, V_d - V_g, W_d - W_g) \\
\underline{x}_{d,r} &= (\xi_{d,r}, \eta_{d,r}, \zeta_{d,r}) \\
S_{\underline{U}_{d,r}} &= (S_{V_{d,r}}, S_{U_{d,r}}, S_{W_{d,r}})
\end{aligned}$$

an expanded form of Equations (3.127) and (3.130) is

$$\begin{aligned}
\frac{dW_{d,r}}{dt} &= \frac{W_r - W_{d,r}}{\tau_m} - \frac{dW_g}{dt} + S_{W_{d,r}} \\
\frac{dU_{d,r}}{dt} &= \frac{U_r - U_{d,r}}{\tau_m} - \frac{dU_g}{dt} + S_{U_{d,r}} \\
\frac{dV_{d,r}}{dt} &= \frac{V_r - V_{d,r}}{\tau_m} - \frac{dV_g}{dt} + S_{V_{d,r}}
\end{aligned} \tag{3.131}$$

and

$$\begin{aligned}
\frac{d\zeta_{d,r}}{dt} &= W_{d,r} \\
\frac{d\xi_{d,r}}{dt} &= U_{d,r} \\
\frac{d\eta_{d,r}}{dt} &= V_{d,r}
\end{aligned} \tag{3.132}$$

where $W_{d,r}$, $U_{d,r}$ and $V_{d,r}$ are the components of the droplet relative velocity, $\underline{U}_{d,r}$, in the axial (ζ-), radial (ξ-) and circumferential (η-) coordinates, respectively; W_d, U_d and V_d are the corresponding components of the droplet velocity, $\underline{U}_d$; W_g, U_g and V_g are the corresponding components of the local coordinate frame, $\underline{V}_g$; and $S_{W_{d,r}}$, $S_{U_{d,r}}$ and $S_{V_{d,r}}$ are the corresponding components of $S_{\underline{U}_{d,r}}$, whose expressions are given below for expanding/contraction region (in which $U_g = V_g = 0$) and translating region (in which $V_g = 0$), respectively.

Expanding/Contracting region

$$
\begin{aligned}
S_{W_{d,r}} &= 0 \\
S_{U_{d,r}} &= \underset{centrifugal}{V_d^2 \frac{1}{\Delta\eta}\frac{\partial(\Delta\eta)}{\partial\xi}} - \underset{Coriolis}{U_d V_d \frac{1}{\Delta\xi}\frac{\partial(\Delta\xi)}{\partial\eta}} \\
S_{V_{d,r}} &= \underset{centrifugal}{V_d^2 \frac{1}{\Delta\xi}\frac{\partial(\Delta\xi)}{\partial\eta}} - \underset{Coriolis}{U_d V_d \frac{1}{\Delta\eta}\frac{\partial(\Delta\eta)}{\partial\xi}}
\end{aligned}
\tag{3.133}
$$

Translating region

$$
\begin{aligned}
S_{W_{d,r}} &= \underset{centrifugal}{\frac{U_d U_{d,r}}{r_2} + \frac{V_d^2 \sin\beta}{r_3}} - \underset{Coriolis}{\frac{U_d W_{d,r}}{r_1}} \\
S_{U_{d,r}} &= \underset{centrifugal}{\frac{W_d W_{d,r}}{r_1} + \frac{V_d^2 \cos\beta}{r_3}} - \underset{Coriolis}{\frac{W_d U_{d,r}}{r_2}} \\
S_{V_{d,r}} &= \underset{centrifugal}{\frac{V_d W_d \sin\beta + U_d V_d \cos\beta}{r_3}}
\end{aligned}
\tag{3.134}
$$

The quantities r_1, r_2, r_3 and β appearing inthe above have been defined in Section 3.6.

3.8.3 Droplet Heating and Vaporization

When there is a temperature difference between a droplet and its surrounding gas, as occurs in Diesel engines, simultaneous heat and mass transfer processes take place. As the heat is transferred to the drop surface (or possibly released from it, depending the ambient gas conditions and the initial fuel temperature) by conduction and convection from the surrounding hot gas, the vapour is also transferred by convection and diffusion into the gas stream. A full knowledge of the rates of heat and mass transfer is central to the understanding of combustion process which depends on the production of a combustible mixture of air and fuel vapour.

During droplet vapourisation, the droplet size is continually changing due to loss of mass, which is governed by the droplet mass conservation:

$$
\frac{dm_d}{dt} = \dot{m}_d \tag{3.135}
$$

where $\dot{m}_d$ is the rate of droplet vapourisation.

The variation of the droplet temperature associated with the heat transfer is governed by the droplet energy conservation equation. The total heat transferred from the hot gas to the droplet, Q, splits into two parts: one part produces the phase change by overcoming the latent heat of vapourisation; the remainder is transferred into the droplet interior, raising its temperature. Thus:

$$Q = m_d \frac{d(c_p T)_d}{dt} - h_{fg}\dot{m}_d \tag{3.136}$$

where c_{p_d} is the droplet specific heat at constant pressure, h_{fg} is the latent heat of vapourisation, and T_d represents the droplet temperature which is assumed uniform (the reason for this will be discussed shortly). Thus, the temperature of droplet, T_d, is governed by:

$$m_d \frac{d(c_p T)_d}{dt} = Q + h_{fg}\dot{m}_d \tag{3.137}$$

We now proceed to assemble expressions for the vapourisation rate, $\dot{m}_d$, and the total heat flux Q. The correlations for these quantities are first established for the limiting case where there is no relative motion between the droplet and the gas, and where a spherically symmetric field exists for the gas field surrounding the droplet and for the liquid field. The results are then extended to convective vapourisation circumstance by introducing correction factors.

Spherically-symmetric droplet

In this case, the droplet does not move relative to the gas as vapourisation occurs. Therefore, heat and mass transfer in the liquids occur due only to diffusion with a moving boundary but without convection. To develop a theory of droplet vapourisation for this case, certain simplifying assumptions are usually employed. The Mach number is considered small, so that kinetic energy and viscous dissipation are negligible. Gravity effects, droplet deformation, radiation, Dufour energy flux, and mass diffusion due to pressure and temperature gradients are all neglected. In addition, the droplet heating time is assumed to be short compared to its life time. This implies that the droplet interior is quickly heated since a thermal wave diffuses from the droplet surface to its center in a short time compared to the lifetime. As a consequence, a nearly uniform liquid temperature is established quickly. Thus the droplet temperature can be assumed to be uniform. This assumption is justified,

according to El Wakil et al (1954), if the so called resistance ratio $2k_L/h_cD_d$ ($2k_L$ being liquid thermal conductivity and h_c a coefficient of heat transfer to the liquid droplet based on the portion of heat transferred to the liquid droplet that appear as sensible heat) is 6 or over.

Derivation of the droplet vapourisation rate equation is usually pursued by neglecting thermal diffusion and assuming that the driving force for species is a concentration gradient in the direction of the diffusion path. The expression for $\dot{m}_d$ is given by [detailed derivations are provided in the publications of Faeth (1977), Goldsmith and Penner (1954), Spalding (1955) and Williams (1976)]:

$$\dot{m}_d = -\pi D_d^2 P_T k_g \ln\left(\frac{P_T - P_{v,\infty}}{P_T - P_{v,s}}\right) \tag{3.138}$$

where P_T is the total gas pressure, $P_{v,\infty}$ is the partial pressure of the fuel vapour away from the droplet, $P_{v,s}$ is the partial vapour of the fuel vapour at the droplet surface, and k_g is the mass diffusion coefficient, determined from :

$$Sh = \frac{k_g D_d R_m T_m}{\mathcal{D}_m} \tag{3.139}$$

In this $\mathcal{D}$ is the diffusion coefficient, and the subscript $_m$ denotes the mean film properties. Substitution of (3.139) into (3.138) yields

$$\dot{m}_d = -2\pi D_d \frac{\mathcal{D}_m SH}{R_m T_m} P_T \ln\left(\frac{P_T - P_{v,\infty}}{P_T - P_{v,s}}\right) \tag{3.140}$$

in which the Sherwood number is given by

$$Sh = 2 \tag{3.141}$$

Evaluation of the heat transferred from the gas to the droplet is made using the following expression derived by El Wakil et al. (1954):

$$Q = \pi D_d^2 h \frac{z}{(e^z - 1)}(T - T_d) \tag{3.142}$$

where h is the heat transfer coefficient in the absence of mass transfer, and the factor $z/(e^z - 1)$ represents a correction factor to the heat transfer coefficient to account for mass transfer from the droplet. The quantity z is defined by

$$z = -\frac{c_{p_v}\dot{m}_d}{\pi D_d k_m Nu} \tag{3.143}$$

in which c_{p_v} is the fuel vapour specific heat at constant pressure, and Nu is the Nusselt number which is given by

$$Nu = \frac{hD_d}{k_m} = 2 \tag{3.144}$$

Thus use of Equation (3.144) yields the final form for Q:

$$Q = \pi D_d k_m Nu \frac{z}{(e^z - 1)}(T - T_d) \tag{3.145}$$

Convective droplet vapourisation

In Diesel applications, the spray droplets move at a relative velocity to the surrounding gas. The droplet is therefore surrounded by convective boundary layers and separated near wakes, which enhance the heat and mass transfer rates over the values for the spherically-symmetric case. As a result, vapourisation rates increase with increasing Reynolds number, whose value varies throughout the lifetime of the droplet since neither the droplet diameter nor the droplet relative velocity remains constant.

Awareness of the above facts has led to some attempts to introduce different correction factors for the Sherwood number and Nusselt number to evaluate $\dot{m}_d$ and Q according to Equations (3.138) and (3.145). One commonly used approach is due to Ranz and Marshall (1952) who derived the following correlations:

$$Sh = 2.0\left(1.0 + 0.3Re^{1/2}Sc^{1/3}\right) \tag{3.146}$$

$$Nu = 2.0\left(1.0 + 0.3Re^{1/2}Pr^{1/3}\right) \tag{3.147}$$

where Sc and Pr are respectively Schmidt number and Prandtl number, defined by:

$$Sc = \frac{\mu_m}{\rho \mathcal{D}_m} \tag{3.148}$$

$$Pr = \left(\frac{c_p \mu}{k}\right)_m \tag{3.149}$$

The above correlations are based on certain quasi-steady, constant radius, porous wetted sphere experiments. Similar correlations are reported by Frossling (1938). Those experiments do not account for transient heating, regressing interface, and internal circulation. In addition, Equations (3.146) and (3.147) may overestimate the transfer rate at low Reynolds number (eg. $Re \leq 10$), since we have $\partial Nu/\partial Re =$

$0.3Pr^{1/3}Re^{-1/2}$ which approaches ∞ as $Re \to 0$. Thus, they predict a physically incorrect oversensitivity of the heat transfer rate to the small velocity fluctuations near $Re - 0$. Despite this, (3.146) and (3.147) are used in this study, since more sophisticated correlations have not been well developed or fully assessed. Therefore, the working version of equations describing the change of droplet size and temperature are written as:

$$\frac{dm_d}{dt} = -2\pi D_d \frac{\mathcal{D}_m Sh}{R_m T_m} P_T \ln\left(\frac{P_T - P_{v,\infty}}{P_T - P_{v,s}}\right) \tag{3.150}$$

$$m_d \frac{d(c_p T)_d}{dt} = \pi D_d k_m Nu \frac{z}{(e^z - 1)}(T - T_d) + h_{fg}\dot{m}_d \tag{3.151}$$

where Sh and Nu are evaluated from (3.146) and (3.147), respectively.

The above equations can be recast into the following simpler forms:

$$\frac{dm_d}{dt} = -\frac{m_d}{\tau_v} \tag{3.152}$$

$$\frac{dT_d}{dt} = \frac{1}{\tau_T}\frac{z}{e^z - 1}(T - T_d) - \frac{1}{c_{p_d}\tau_v} h_{fg} \tag{3.153}$$

where τ_v and τ_T are, respectively, the vapourisation and heat transfer relaxation time scales, defined respectively by:

$$\tau_v = \frac{m_d}{\pi D_d \mathcal{D}_m Sh \rho \ln \dfrac{P - P_{v,\infty}}{P - P_{v,s}}} \tag{3.154}$$

$$\tau_T = \frac{m_d c_{p_d}}{\pi D_d k_m Nu} \tag{3.155}$$

It should be pointed out that Equations (3.150) and (3.151) are derived for isolated droplets. However, sprays involve a large number of droplets such that the interactive processes contribute to alter the heat and mass transfer rates from those of the isolated droplet. Thus additional correction factors are strictly needed for the droplet vapourisation rate to account for the effects of neighbouring droplets. Studies have been made of the aspect, but no suitable corrections have been developed yet. (see the review of Annamalai and Ryan (1992))

3.8.4 Turbulent Droplet Dispersion

The governing equations described in Section 3.8.2 are valid when the gas turbulence intensity is negligible. However in Diesel engines, the gas flow is always strongly

turbulent. In this case a droplet experiences fluctuations in gas-phase properties (such as velocity, temperature and vapour concentration), which in turn may induce fluctuations of the droplet motion, vapourisation rate, etc. Accordingly, the droplet follows a somewhat random walk which deviates from the mean trajectory (which is essentially deterministic) determined only by the ensemble mean velocity of the gas-phase. The extent of such deviations depends on the inertial properties of the droplet and the gas-phase turbulence among other quantities. In modelling this phenomenon, the main difficulties lie in the fact that usually only the ensemble mean properties are obtained from the solution of the governing equations of the gas phase, and the fluctuations have to be extracted from the turbulence model. A reasonable simplification is to consider only the gas velocity fluctuations, and to neglect the effect of fluctuations in other properties of the gas phase, which are usually of secondary importance.

Thus far two approaches have been proposed to estimate gas instantaneous velocity of the gas. One, which is the most commonly used in spray work, takes this velocity as the sum of the local mean value and a random velocity, sampled from a selected probability distribution function. A second approach in which the flow-field velocity is determined by solving a stochastic differential equation has emerged from efforts to compute atmospheric dispersion.

In this study, we will follow the stochastic approach of Gosman and Ioannides (1981) to model the effect of the turbulence on droplets. One feature of this model lies in its stochastic representation of the gas-phase turbulence, which is assumed to be isotropic. The fluctuating velocity here is postulated to possess a Gaussian probability distribution with zero mean and a standard deviation, σ_{sd}, given by

$$\sigma_{sd} = \left(\frac{2k}{3}\right)^{1/2} \tag{3.156}$$

The fluctuating part of gas velocity, $\underline{V}_r''$ is sampled randomly from this distribution as follows:

$$\underline{V}_r'' = \sigma_{sd} sign(1, \gamma) Erf_c(|\chi|) \tag{3.157}$$

in which χ and γ are random variables having uniform distributions in the range $-1 < (x, \gamma) < 1$, and Erf_c is the complementary error function.

Another feature of the model is the manner in which the droplet is assumed

to interact with the turbulence. This is envisaged as a process in which a droplet interacts with a succession of individual turbulent eddies which are assumed to have characteristic integral scales larger than those of the droplet. Fluid dynamic properties within a particular eddy are taken to be uniform. The instantaneous velocity of this eddy is determined by the sum of the local mean value $\underline{V}_r$ and a random fluctuating part $\underline{V}_r''$ which is obtained from (3.157). During the interaction of the droplet with a particular eddy, the droplet drag, vapourisation and temperature change are calculated as if the droplet moved in the gas flow with the velocity $(\underline{V}_r + \underline{V}_r'')$. Thus, the motion of the droplets is computed from a modified version of Equation (3.109) in which the mean gas velocity $\underline{V}_r$ is replaced by its 'instantaneous ' value $(\underline{V}_r + \underline{V}_r'')$:

$$\frac{d\underline{U}_{d,r}}{dt} = C_d \frac{\rho}{\rho_d} \frac{V_{rel}}{D_d} \left(\underline{V}_r + \underline{V}_r'' - \underline{U}_{d,r} \right) - \frac{d\underline{V}_g}{dt} + S_{\underline{U}_{d,v}} \tag{3.158}$$

where the relative velocity between the two phases takes the form

$$V_{rel} = |\underline{V}_r + \underline{V}_r'' - \underline{U}_{d,r}| \tag{3.159}$$

The time duration available for the interaction between the droplet and an eddy is evaluated as the minimum of either the eddy life time, t_e, or the transit time, t_R, required for the droplet to traverse the eddy. These time scales are estimated under the further assumption that the characteristic size of the randomly-sampled eddy is the dissipation length scale, L_e, given by

$$L_e = \frac{C_\mu^{1/2} k^{3/2}}{\epsilon} \tag{3.160}$$

The eddy life time is then estimated as

$$t_e = \frac{L_e}{\underline{V}_r''} \tag{3.161}$$

The transit time is simply given by

$$t_R = \frac{L_e}{V_{rel}} \tag{3.162}$$

The above-described model, however, neglects the effect of the droplets on the gas turbulence. In reality, the interaction between the droplets and the turbulence proceeds in a coupled manner: the turbulence affects the droplet dispersion whilst

the droplets in turn modify the structure of the turbulence, either enhancing or reducing the turbulence level of the carrier fluid depending on the characteristics of the particle and of the turbulent flow. Available experimental data show that droplets may increase or decrease turbulence kinetic energy of the carrier fluid. For example, in some experiments, the injection of fine droplets or solid particles (with diameter less than 250μ) into a free turbulence jet reduces the turbulence intensity, thus lowing the spreading rate of the half-width of the jet (Hestsroni and Sokolov 1971, Popper et al. 1974, Modarress et al. 1984, Fleckhaus et al. 1987, Tsuji et al. 1988). Other experiments (Levy and Lockwood 1981) show that the addition of large particles (with diameter larger than 500μ) increases the turbulence intensity in a free jet, whereas small particles (with diameter less than 250μ) suppress it. However, there is a lack of the insight into mechanisms responsible for this increase or decrease. More studies are needed to clarify this two-way coupling mechanism and future theoretical work should accommodate this coupling effect.

One limitation of the model is that it produces a fluctuating velocity which is discontinuous in time, since a sampled velocity fluctuation remains fixed until the eddy time t_e has elapsed. This means that when a droplet moves from a region of high turbulence intensity to one of low turbulence intensity, within a single eddy life time, information has been passed directly from the high intensity to the low intensity region.

Further limitations of the model lie in the fact that it assumes the turbulence is isotopic, the turbulent eddies are large compared to the droplet size, and the droplet remains in the same eddy for its lifetime. In reality, the 'jet'-like flows characteristic of sprays usually have anisotropic turbulence properties, and the eddy sizes may range from below the droplet size to above it. In this situation, the turbulence affects the droplet in two ways: the eddies with size larger than that of the droplet contribute to transport the droplet, whereas the eddies with size less than that of the droplet tend to 'penetrate' into the droplet and may split it into fragments, yielding another mechanism of droplet breakup (see the evidence of Nambiar et al. 1992)

3.8.5 Droplet breakup

(a) Introduction

Many of the larger drops produced in the initial disintegration process are unstable due to further perturbations by aerodynamic forces, and therefore undergo secondary disruption into smaller droplets. Thus the final range of drops produced in a spray depends not only on the drop sizes produced by atomisation but also on the extent to which these are further disintegrated. It is important, therefore, to examine the various ways in which a single drop of liquid can break up under the action of aerodynamic forces, and to construct theoretical models for the representation of such breakup physics.

Different breakup regimes have been observed, two of which have received much attention. The first type, referred to as 'bag breakup' (see Figure 3.8a) is observed at the onset of the aerodynamic breakup. It occurs when the drop is subjected to a steady stream of air of gradually increasing velocity. When a critical velocity is reached, the drop is blown downstream as a balloon-like structure attached to a heavy rim, until it eventually bursts. Here, the shape of the drop is determined by the nature of the aerodynamic pressure distribution around it. The lower pressure in the equatorial region provides the pull for flattening. The pressure being higher on the upstream surface than in the wake, the drops flattens much more there, eventually developing a concave depression.

The second type of breakup, the shear type (see Figure 3.8b), is observed at higher relative velocities in experiments where the drop is suddenly exposed to a high-speed blast of air such as behind a strong shock wave. The drop is deformed into a plano-convex lenticular body, due to its acceleration, with the convex surface facing the blast. In contrast to the bag breakup mechanism, here breakup occurs by stripping of secondary drops from the periphery of the lenticle. It is believed that the edges of the saucer-shaped body are drawn into a thin sheet by the strong viscous stresses due to the high-speed air flow, and then into fine filaments, which break up into droplets. It is believed that in the shear breakup, equilibrium is lost at the rim, and elsewhere, when the viscous shear stress due to the air flow overcomes surface tension locally, whereby the edge is drawn out into a sheet.

Other breakup regimes are found to exist between the bag and shear breakup

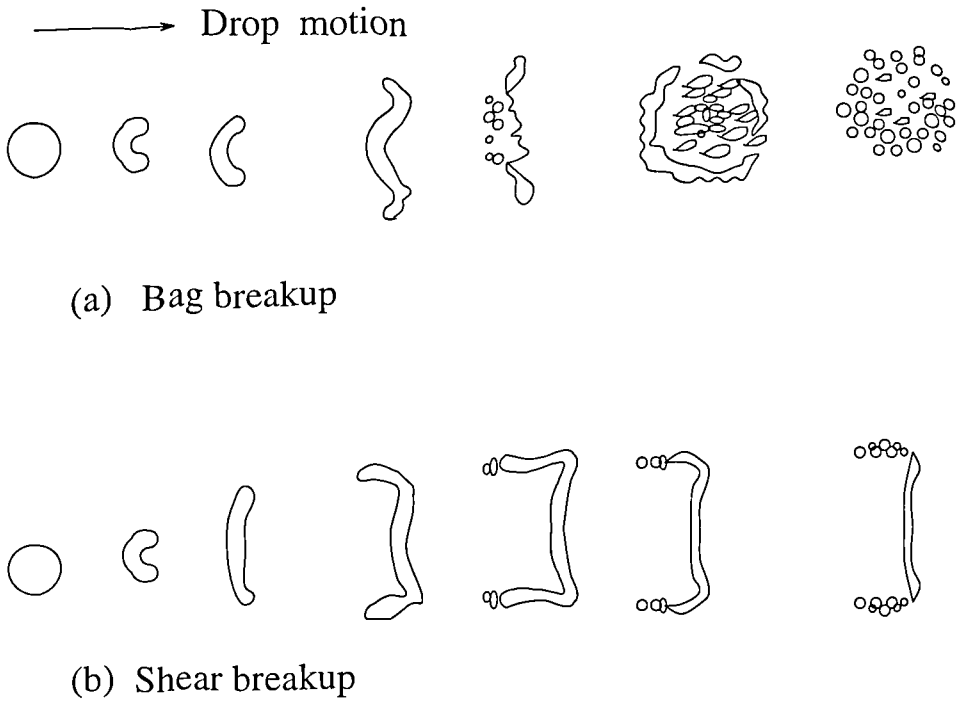


Figure 3.8: Schematic diagram of bag and shear breakup regimes

regimes. They are termed, in the order of increasing relative velocity, parachute breakup, chaotic breakup, bag jet breakup, and transition breakup etc. (see e.g. Krezeczkowski 1980; Hsiang & Faeth 1992). These regimes are also termed *multi-mode breakup* for the convenience.

In general, the breakup of a drop in a flowing stream is controlled by dynamic pressure, surface tension, and viscous forces. They may be grouped to form two dimensionless parameters, namely, the Weber number $We_G = \rho D_d V_{rel}^2/2\sigma$, and the Laplace number $La = \rho_L D_d \sigma/\mu_L^2$, which are measures of relative importance of drag and liquid viscous forces to surface tension forces, respectively. The Weber number is the most crucial controlling parameter: the higher the Weber number, the larger are the deforming external pressure forces compared with the restoring surface tension. The Laplace number effect is weak unless it is less than about 100, i.e., for the higher viscousity liquids. Hinze(1955) found that progressively larger disturbances (i.e. larger We_G) are required for the onset of breakup as La is decreased, because the viscous forces in the liquid tend to inhibit drop deformation.

Conditions for the onset of various breakup regimes have been defined reasonably well by Krzeczkowski (1980) who established a regime transition map in terms of We_G and La. This has been confirmed very recently by Hsiang & Faeth (1993)

in their drop-breakup experiments involving a practical range of conditions, and has been further extended by them to include droplet deformation regimes prior to breakup, which are useful for addressing the problem of drag modification of the drop in the deformation period (see Figure 3.9), as already discussed in Section 3.8.2. However, measurements of transition between breakup regimes have been limited to liquid/gas density ratios, $\rho_L/\rho > 500$, and Reynolds number $Re_G > 500$, which are not characteristic of Diesel engines where typical values of ρ_L/ρ are around 20 and of Re_G are about 300.

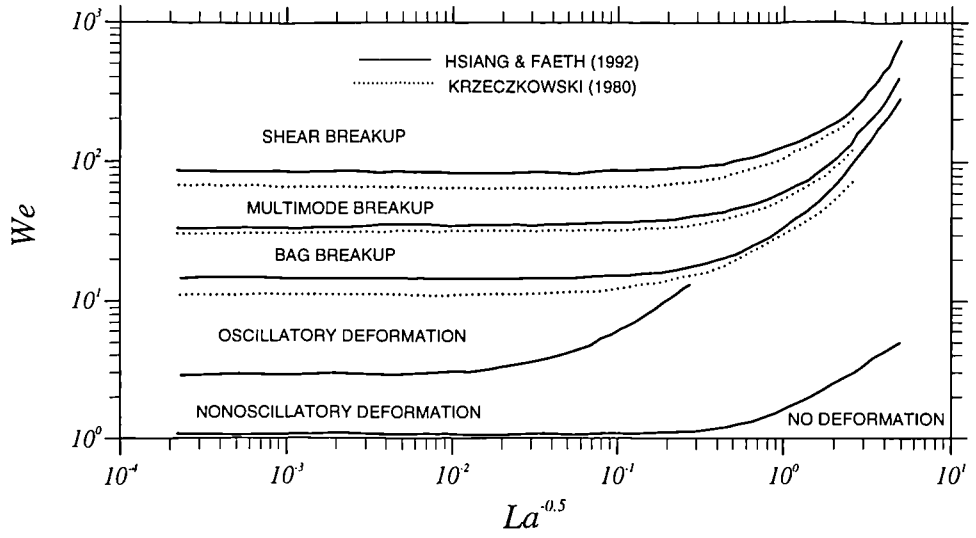


Figure 3.9: Drop deformation and breakup regime transition map

Another important parameter characteristic of breakup is the time required for the completion of the process. Measurements of the breakup time were made by several investigators, eg., Engel (1958), Ranger and Nicholls (1969), Reinecke and Waldman (1970), and Hsiang and Faeth (1992). Their results show that the break time, t_b, normalised by the characteristic length time for shear breakup, $t^* = D_d(\rho_L/\rho)^{1/2}/V_{rel}$ (defined by Ranger & Nicholls 1969), is a function of the Weber number We_G and the Laplace number La. On the one hand, when $La > 100$ which involves low liquid viscosity, the above measurements revealed that the quantity t_b/t^* varies very little even when We_G varies over a large range (roughly $10 - 10^6$). In such circumstances,

the breakup time correlation of Ranger and Nicholls (1969)

$$\frac{t_b}{t^*} = 5.0 \tag{3.163}$$

provides a reasonably good fit to most of the experimental data obtained. On the other hand, for more viscous fluids involving $La < 100$, the data of Hsiang and Faeth (1992) show that t_b/t^* increases with decreasing La in a manner which can be described by the following correlation:

$$\frac{t_b}{t^*} = \frac{5}{1 - \frac{1}{7La^{0.5}}}; \qquad We_G < 10^3,\ La < 100 \tag{3.164}$$

Equation (3.164) is based on relatively few data, and it still remains to be established whether it can be used at conditions outside of the experimental range.

Available information on the post-breakup characteristics of droplets are rather limited. Nevertheless, measurements of droplet size distributions for shock-wave disturbances at $\rho_L/\rho > 500$ have been reported by Dubrovksii et al (1991) and Hsiang and Faeth (1992, 1993). The experiments by Dubrovksii et al (1991) involved drops with ranges of diameters from 3.2-5.9mm, viscosities from 0.00375 to 0.0365 Pa.s, and Weber numbers in the range of $We_G \approx 1 - 30$. They analyzed about 14000 fragments and found that for the drops breaking up in the range of conditions investigated, the size distribution of the fragments is described well by a log-normal law:

$$n(\gamma) = \frac{1}{\sqrt{2\pi}\gamma \ln \Sigma} exp\left[-\frac{(ln\gamma - ln\bar{\gamma})^2}{2ln^2\Sigma}\right] \tag{3.165}$$

Here $\gamma = D_d/D_{d_0}$, where D_d and D_{d_0} denote respectively the secondary and primary droplet sizes. The quantities $\ln\bar{\gamma}$ and $\ln\Sigma$ are mean values of the distribution function which were found to be (in the range of conditions investigated):

$$ln\bar{\gamma} = \text{-}2.2, \quad ln\Sigma = 0.66$$

However, the most recent measurements of Hsiang and Faeth(1993) did not confirm the above findings. Instead they found that, like primary breakup, the droplet size distributions after secondary breakup also follow Simmons' (1977) universal root normal distribution. Shear breakup however, is an exception to this regular behavior, due to the presence of the core drop, which is the remaining portion of the original drop after the stripping of smaller drops has terminated, and whose size contributes

to a distortion of the universal root normal distribution. This problem was later resolved by Hsiand and Faeth (1993) by removing the core drop from the whole drop population and treating it separately. Thus drop sizes after breakup in all breakup regimes can be described by universal root normal distribution with ratio of the mass median diameter to the Sauter mean diameter, $MMD/SMD = 1.2$. This type of distribution involves only two parameters, therefore, after fixing MMD/SMD, drop sizes are fully specified by the SMD only. Moreover, according to Hsiang and Faeth (1992), the SMD for all breakup regimes could be correlated as

$$\frac{\rho SMDV_{rel}^2}{\sigma} = C_s \left(\frac{\rho_L}{\rho}\right)^{0.25} \left(\frac{\mu_L}{\rho_L D_d V_{rel}}\right)^{0.5} We_G \tag{3.166}$$

where C_s is a coefficient determined experimentally. Hsiang and Faeth set C_s to be $C_s = 6.2$ according to their experimental data. Their investigations involved several liquids including water, glycerol solution, n-heptane, ehtyl alcohol and mercury, with Weber numbers of $0.5 - 1000$, Lapace numbers of $0.0625 - 2.8 \cdot 10^6$, and liquid/gas density ratios of $580 - 12000$.

The only work on measurements of droplet velocities during and after breakup is due to Hsiang and Faeth (1993). They observed a substantial reduction of droplet velocities during breakup (30-70%, depending on drop size). This effect is due to the enhancement of the drag coefficients during the drop deformation stage and the associated viscous dissipation. An attempt to quantify this velocity reduction in the course of breakup was made using a simplified phenomenological theory, yielding useful information for theoretical modelling.

(b) Breakup model

Rigorous theoretical modelling of breakup process would demand an exact knowledge of the distribution of aerodynamic pressure on the drop and its detailed deformation history. This is, however, not possible at the current stage. Thus, in the present study, a semi-analytical model proposed by Reitz and Diwakar (1987) is employed to model the breakup of droplets due to aerodynamic forces. The method, as outlined below, concerns itself with only bag and shear breakup regimes and involves three major steps: (1) determination of the conditions of the onset of the two breakup regimes; (2) determination of post-breakup size of droplet; (3) determination of post-breakup droplet velocity using conservation constraints.

First, the postulated breakup criteria are:

- Bag breakup occurs if

$$We_G > A_b \tag{3.167}$$

- Shear (or stripping) breakup occurs if

$$\frac{We_G}{\sqrt{Re_G}} > A_s \tag{3.168}$$

where A_b and A_s are empirical coefficients determined from experimental data. They are ascribed the values: $A_b = 6, \quad A_s = 0.5$ respectively following Reitz and Diwakar (1987). However, as will be discussed later, these values are uncertain to a certain extent.

Calculation of the droplet breakup process is carried out in the following manner. For each computational droplet, the criteria (3.167) and (3.168) are checked in each time step. If either of the two criteria is met, the breakup is modeled by reducing the unstable droplet size continuously with time according to the following rate equation (Reitz & Diwakar 1987)

$$\frac{dD_d}{dt} = -\frac{D_d - D_s}{t_b} \tag{3.169}$$

where D_s is referred to as stable diameter (below which the droplet remains stable under the same conditions), which can be calculated from Equations (3.167) and (3.168), thus

$$D_s = \begin{cases} \dfrac{2A_b\sigma}{\rho V_{rel}^2} & \text{for bag breakup;} \\ \\ \dfrac{4A_s\sigma^2}{\rho V_{rel}^2 \mu} & \text{for shear breakup} \end{cases} \tag{3.170}$$

Here t_b is the breakup time, or the life time of unstable droplet, which is calculated from:

$$t_b = \begin{cases} C_b\sqrt{\dfrac{\rho_L D_d^3}{16\sigma}} & \text{for bag breakup;} \\ \\ \dfrac{C_s D_d}{V_{rel}}\sqrt{\dfrac{\rho_L}{\rho}} & \text{for shear breakup} \end{cases} \tag{3.171}$$

Here, the bag breakup time, is assumed to be proportional to the droplet natural frequency, with the constant $C_b = \pi$. The coefficient C_s in the shear breakup time

follows from some available empirical correlations (cf. Borisov et al 1981; Ranger and Nicholls (1969), with a representative value of 10, as suggested by Reitz and Diwakar(1987). However, the experimental data actually suggests values in the range 1-10, as noted by Reitz and Diwakar (1986,1987). Moreover, C_s is frequently observed to be around 5, according to Ranger and Nicholls 1969; Gel'fant et al 1975; Liang et al. 1988; and Hsiang and Faeth 1992.

Conservation of mass, momentum and energy during the above breakup process is considered by Reitz and Diwakar (1987) through the following practices:

- The number of secondary droplets in the parcel is adjusted to conserve the mass

$$N_f D_f^3 = N_i D_i^3 \tag{3.172}$$

  where N is the number of droplets in the parcel and the subscripts i and f denote conditions after and before breakup, respectively.

- During breakup, droplet surface energy increases as a result of increased number of droplets, whilst droplet kinetic energy also changes in order to conserve energy. This is simply represented by the following energy equation:

$$M_d(\underline{U}_{d,r} \cdot \underline{U}_{d,r})/2 + \pi\sigma D_d^2 N = const \tag{3.173}$$

  where M_d is the total parcel mass, and $\underline{U}_d$ is the droplet velocity vector. The above equation implies that, to conserve energy, each of droplet's three velocity components should be reduced by an amount δU:

$$\delta U = 1 - \frac{3}{2}\left(\frac{D_i}{D_f} - 1\right)\frac{\sigma}{\rho_L D_i}\frac{1}{\underline{U}_{d,r} \cdot \underline{U}_{d,r}} \tag{3.174}$$

- The momentum lost by the droplet during this process, $M_d[(\underline{U}_{d,r})_f - (\underline{U})_{d,r})_i]$, is inparted to the gas, as a momentum source.

It should be pointed out that Equation(3.173) is not strictly valid during the breakup process, since droplet obviously experiences external work done by the gas drag forces and dissipates energy due to deformation (although the latter effect is probably small). Thus two additional terms should be included in the above energy equations to give:

$$\frac{dE_k}{dt} + \frac{dE_s}{dt} + \frac{dE_d}{Dt} = \frac{dE_e}{dt} \tag{3.175}$$

in which E_k, E_s, E_d and E_e are, respectively, the total parcel kinetic energy, surface energy, dissipation energy and external work due to drag forces. The right-hand side term in the equation (3.175) can be written as

$$\frac{dE_e}{dt} = \underline{F}_{drag} \cdot \underline{V}_{rel}$$

To illustrate the deficiency of the Equation (3.173), let us consider a simple example. Assume that, at the instant $t = 0$, a droplet with initial diameter D_i and velocity $U_{d,i} = 0$, is suddenly exposed to a uniform gas flow of velocity V which is high enough to ensure the strip breakup. Thus, according to (3.173), we have

$$E_{k,f} = \sigma\pi(N_i D_i^2 - N_f D_f^2) < 0 \tag{3.176}$$

which implies that the kinetic energy after breakup, $E_{k,f}$, is negative. This is obviously wrong, because in no circumstances would the droplet kinetic energy be less than zero. In fact, for this case, the broken droplets absorb kinetic energy due to the external work done by the gas drag forces, as represented by E_e in (3.175).

In view of the above arguments, in this study we only employ Equation (3.172) for mass conservation. We do not use (3.173) or (3.175) for energy conservation, since the former is not strictly valid, whereas the latter involves the evaluation of E_d and E_e, an issue yet needed to be resolved. Instead, we use the following relation

$$M_d(\underline{V}_{rel} \cdot \underline{V}_{rel})/2 + \pi\sigma D_d^2 N = const \tag{3.177}$$

to calculate droplet velocity after breakup. This relation is obtained from (3.173) by replacing droplet velocity with relative velocity $\underline{V}_{rel}$.

(C) Evaluation

In the preceding subsection, the breakup model used in this study was described. We now proceed to discuss in somewhat more detail the uncertainties or deficiencies associated with this model. As the model involves three major equations, namely, (3.167), (3.168), and (3.169), we investigate each of them separately.

Bag breakup criterion. The main uncertainty with Equation (3.167) lies in the fact that it contains an empirical coefficient A_b, which varies in the wide range of 1.1 to 49.8, according to Wierzba (1990). To clarify the reason for this, the present author made a literature survey which revealed that: the possible causes are:

1. Different experimental methods and facilities (Wierzba 1990), which include towers and vertical wind tunnels for free fall experiments, vertical and horizontal tunnels, suction orifices, horizontal shock tubes, convergent nozzles, and venturi scrubes. As a result of this, droplet experiences different loading conditions, or different histories of aerodynamic forces.

2. The way in which A_b is determined experimentally. In some experiments, A_b is taken as the local value of We corresponding to the moment of breakup(Palatnik 1981). This gives too high a value of A_b, if the breakup occurred with increasing V_{rel}, or too low a value in the opposite case.

3. Neglect of Laplace number(or liquid viscosity) effect in the definition of critical conditions. Thus, relatively wide range of A_b was found in experiments with liquids of different viscosities. Piltch and Erdman(1987) argue that liquid viscosity effects are not negligible if La is less than 100. They proposed the following empirical correlation

$$A_b = 6(1 + 1.077La^{-0.8})$$

to accommodate the Laplace number effect.

4. Neglect of the rate of change of aerodynamic forces during breakup process in determining the critical conditions. Due to the complexity involved in the breakup process, Dubrovskii et al. (1991) argued that Weber and Laplace numbers are not adequate to characterise the breakup criterion. At least one additional parameter, such as the rate of the change of aerodynamic forces, G(defined below), has to be included. In their experiments, they observed a significant effect of G on the critical conditions, and established the following correlation:

$$A_b = 6.75 - 0.22P - (4.75 - 0.22P)\exp\left[(90.005P - 0.25)G\right]$$

$$P = \ln La$$

This applies for G and La in the ranges $3 \leq G \leq 97$ and $5.3 \leq La \leq 3.5 \cdot 10^5$, in which

$$G = \frac{dWe_G}{d(t/t_{osc})}, \quad t_{osc} = 0.83\sqrt{\frac{\rho_L d^3}{\sigma}}$$

Here t is the instantaneous time measured from the onset of breakup. In the present author's opinion, the effect of G may alternatively be represented by the well known Eötvös number, $Eo = a|\rho_L - \rho|D_d^2/\sigma$, in view of the fact that the rate of the change of aerodynamic forces can be described by the drop acceleration, a, which is due to gas motion relative to the drop.

In addition, the measured values of A_b may also be affected by unexpected factors due to the difficulty in controlling the experimental conditions. Thus, further experimental studies are needed to determine the probability distribution of A_b over the scatter range. Before this is available, however, it appears more sensible that the value of A_b should be randomly sampled over the range which is frequently observed in the experimental data, instead of being giving a fixed value.

Shear breakup criterion. The accuracy of Equation (3.168) is very sensitive to the value of A_s if the Reynolds number Re_G is very large, since in this case, a small change of A_s results in an appreciable change of the critical Weber number corresponding to the onset of shear breakup. The values found from experiments involving a small range of gas density variations are close to 0.5. For instance, Rabin et al. (1960), Dickerson and Coultas (1966), Borisov et al. (1970), and Gel'fand et al. (1974) have all confirmed that $A_s = 0.5$. But for a wider range of gas densities, Gel'fand et al. (1975) noted a dependence of A_s on gas pressure. They obtained the following expression for drops experiencing shear breakup in a gas stream with a range of pressures from 1 to 50 bar.

$$A_s = 1.5 \left(\frac{\rho_L}{\rho}\right)^{1/4} \sqrt{\frac{\mu}{\mu_L}} \tag{3.178}$$

This equation gives $A_s \approx 0.8$ at 1bar gas pressure, and $A_s \approx 0.3$ at 20 bar pressure for their experimental conditions. In diesel engines, droplet breakup occurs typically at higher pressures. Thus errors might occur if a fixed value of A_s is used.

Another limitation of Equation (3.168) is that the Reynolds number in it is based on gas viscosity, which however was not appreciably varied by the proposers of (3.168) in their experiments. This casts doubts concerning its applicability outside of their experimental conditions. For this reason, the present author made an attempt to clarify the conditions for the applicability of (3.168). As it is known that the

condition for the onset of bag breakup represents the transition from non-breakup to breakup(Krezeczkowski 1980, Hsiang & Faeth 1992, and Wierzba 1990) , it follows that the critical Weber number obtained from (3.168) must be much larger than that from (3.167), because shear breakup occurs at much higher levels of aerodynamic disturbance. This requirement leads to the following condition

$$We_G > 0.5\sqrt{Re_G} > A_b, \quad or, \quad Re_G > 4A_b^2 \tag{3.179}$$

for the application of (3.168). Recall that all available experiments on shear breakup are for conditions giving $Re_G > 500$, which ensures the satisfaction of (3.179) even if A_b takes the largest value of 49.8.

We now illustrate that violation of (3.179) will result in inconsistency. Consider, for example, an n-dodecane droplet , $1\mu m$ in diameter, moving at a relative velocity of 120 m/s in the air which is at 1 atmospheric pressure and 550K temperature. Under such conditions, we have

$$We_G = 0.9216, \quad Re_G = 2.69, \quad \frac{We_G}{\sqrt{Re_G}} = 0.56 > 0.5$$

This means , according to (3.168), that a droplet at such a low Weber number (0.92) will undergo shear breakup - a self-contradicting result- since it is not supposed to break up according to (3.167).

It appears therefore more logical (and also more convenient) if we use (3.167) only to determine the so called stable droplet size in modelling breakup process. This will avoid any inconsistency that might arise. This argument seems to be supported by the work of O'Rourke and Amsden' (1987). They developed a new breakup model, known as TAB model, in which a droplet is viewed to be analogous to a mass-spring system, whose oscillation is represented by a second-order ordinary differential equation. The droplet is assumed to breakup solely when deformation exceeds a certain extent. They demonstrated that TAB model predicted very similar stable drop sizes to those of Reitz and Diwarkar's model.

3.8.6 Collisions between droplets

(a) Introduction

Collision between droplets is a phenomenon commonly encountered in nature and in many industrial processes. In Diesel engines, it occurs most frequently in the dense portion of the spray near the injector, and the resulting coalescence or breakup can significantly affect the spray size evolution and other characteristics. Thus there is a clear need to study, both experimentally and theoretically, the effect of droplet collision on spray dynamics.

Most experimental studies on the collision dynamics of interacting droplets have been reported by investigators in the atmospheric sciences (Adam et al. 1968, Gunn 1965) and the thermodynamics of wet steam turbines (Ryley and Wood 1966, Ryley and Bennett-Cowell 1967). These studies, motivated mainly by the need for knowledge about the exact growth mechanism of water droplets, have been mainly devoted to: (a) identification of the droplet collision regimes and their characteristics; and (b) determination of parameters and their values which define the boundaries between different types of collisions.

The interactions observed for two water drops can be categorised into five different regimes, as show in Figure 3.10 and described below.

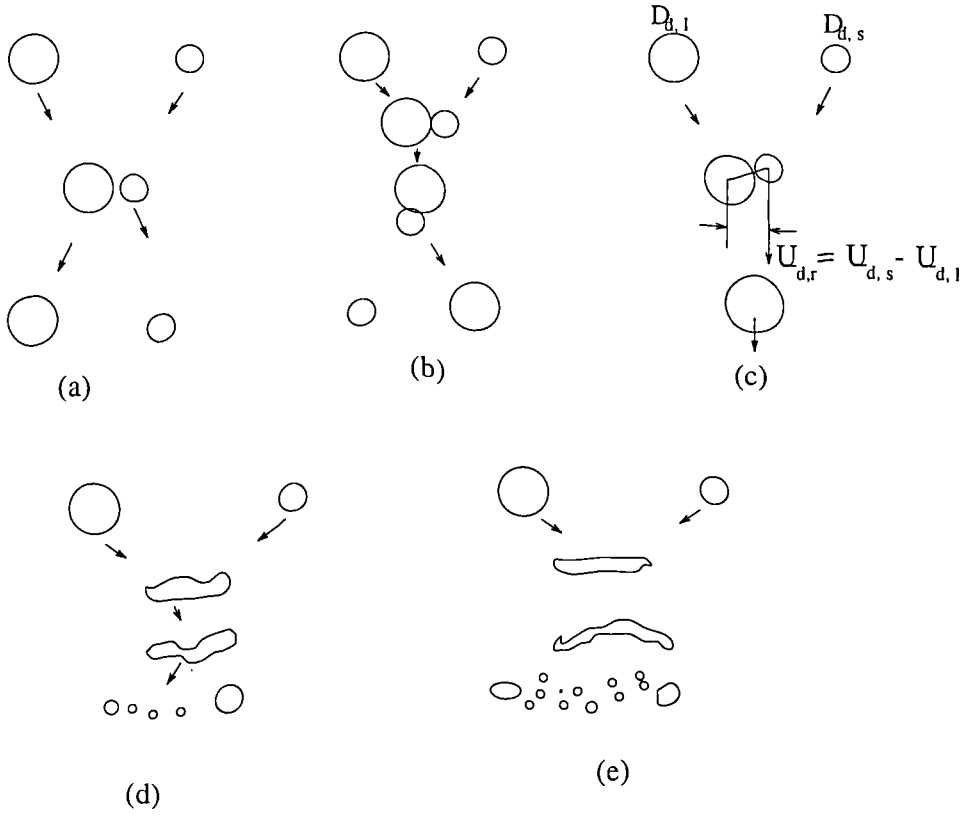


Figure 3.10: Diagram of collision regimes

(a) Bouncing – where the contact of the the two droplet is prevented by the intervening air film, resulting in bouncing after the collision. This occurs at low collision energy, which is not sufficient to rupture the air film trapped between the droplets. (Figure 3.10a)

(b) Grazing bouncing – in which the droplets just slightly touch one another without coalescence. This occurs at nearly normal collision angles. The latter is the angle formed between the relative velocity and the line connecting the centers of the two colliding droplets. (See Figure 3.10b)

(c) Permanent coalescence – where the droplets coalescence permanently and produce a single droplet.(Figure 3.10c)

(d) Separation – in which droplets coalesce to form an unsteady droplet which subsequently splits into two major droplets, with or without satellite droplets. (Figure 3.10d)

(e) Breakup – which occurs at very high collision energies, producing numerous small secondary droplets. (Figure 3.10e)

The above collision regimes have also been observed for collisions of normal-alkane droplets by Jiang et al. (1992), and for n-hexane droplets by Ashgriz and Givi (1987). The occurrence of a particular collision outcome depends a number of parameters such as the droplet density, viscosity, surface tension, diameters and velocities of two droplets, relative velocity of the two droplets, and the impact parameter, b, which is defined as the distance from the centre of one droplet to the relative velocity vector placed on the centre of the other droplet (see Figure 3.10c). By dimensionless analysis, these can be grouped into four dimensionless parameters, namely, Laplace number La_l, Weber number based on smaller droplet We_s, droplet diameter ratio γ, and non-dimensional impact parameter x, which are defined as follows:

$$La_l = \frac{D_l \rho_L \sigma}{\mu_L^2}, \quad , We_s = \frac{|U_{d,l} - U_{d,s}|^2 \rho_L D_s}{\sigma}, \quad , \gamma = \frac{D_{d,l}}{D_{d,s}}, \quad , x = \frac{2b}{D_{d,l} + D_{d,s}}$$

Here $D_{d,s}$ and $D_{d,l}$ are diameters of smaller and larger droplets respectively.

Also for colliding water drops, some quantitative experimental data have emerged to define the boundaries between the different regimes. The first useful measure-

ments of this kind were those of Adam et al. (1968). They made a careful investigation of the effect of varying the impact parameter,x, and obtained the boundary between coalescence and separation for a pair of equal-size drops with 120μ and 600 μ diameters. More detailed studies by Park (1970), Brazier-Smith et al. (1972), Arkhipov et al. (1978), and Ashgriz and Poo (1990) have been conducted on the collision of water drops with different size ratios. They have reported the critical parameters for which bouncing, coalescence and separation regimes occur. The experiment by Arkhipov et al. (1978) was a cinematographic investigation of two colliding water droplets, with size ratios in the range of $0.37 < \gamma < 0.91$, and a Laplace number of about $La_l = 10^5$. They observed that for $We_s < 2.0$, droplets bounces; for $2 < We_s < 15$, coalescence occurs; for $15 < We_s < 50$, separation occurs; and for $We_s > 50$, shattering ensures. The experiment by Brazier-Smith et al. (1972) covered ranges of size ratios from 1.5 to 2.5, Weber numbers (We_s)from 0.4 to 18.5, and x from 0 to 1. They established an equation describing the transition condition from coalescence to separation by comparing the kinetic energy of rotation of the droplets formed by coalescence and the difference between the surface energies of this drop and the original droplets before the collision. These equation, as will be described later, involves a few parameters such as We_s, x, and γ, and will be used for theoretical modelling in this study.

The experiment of Ashgriz and Poo (1990) involved the investigation of binary collision dynamics of water drops for a range of size ratios of 0.5-1.0, and the Weber number of 1 to 100. They identified two types of separation. The first type, referred to as reflexive separation, is found to occur for near head-on collisions. The second, known as stretching separation, occurs for large impact-parameter collisions. They determined, both experimentally and theoretically, the boundaries between both of the separating and coalescence collisions, which are functions of We_s and γ.

Unfortunately, there is inconsistency regarding the regime transitions in the above mentioned experimental results. For instance, while Arkhipov et al. (1978) claimed that transition conditions between different collision regimes are solely determined by the Weber number We_s. However, Brazier-Smith et al. (1972) showed that the Weber number alone cannot characterise the process of droplet collision: there is a critical collision parameter x_{cr}, above which they stay coalesced. Such in-

consistencies may be linked with the complex, stochastic nature of droplet collisions. This complexity may be best explained by the fact that once two droplets are set to collide, several simultaneous processes occur: the pressure rise in the inter-droplet space, droplet deformation which is essentially nonlinear, and the drainage or rupture of the compressed air film trapped between the surfaces of the two droplets (note that coalescence can occur only when the intervening film is ruptured). The latter process is in itself a very complicated one, since drainage rate and rupture mechanism of the intervening air film are governed by hydrodynamics, Van der Waals and other pertinent forces. For this reason, and in view also of the extreme difficulty in controlling and measuring all the governing parameters, it seems more appropriate and illuminative to introduce a probability analysis in describing the onset conditions of each collision regime. This requires determination of the probability of occurrence of a particular type of collision. Experimental data of this respect do exist, but are only confined to the probability of coalescence. For instance, Low and List (1982, a, b), and Ashgriz and Givi (1989) have found the probability of coalescence, i.e., coalescence efficiency, for water and fuel drops respectively.

The above data on transition conditions, however, are not completely applicable to typical sprays, since there are still no concrete conclusions on the effect of all the important nondimensional parameters characterising the dynamics of collision. These results are also not completely valid for describing the collision dynamics of typical hydrocarbon fuel, under the influence of combustion.

In comparison to other collision regimes, shattering collision is the least studied. The most detailed experimental investigation on this regime has been reported by Podvysotsky and Shraiber (1984). They provided correlations for the onset of collision-induced breakup, and both the size and velocity distributions of secondary droplets resulting from the collision-induced breakup. These are very useful in formulating a numerical model for the prediction of post-collision characteristics of secondary droplets.

(b) Droplet collision model

Theoretical studies of droplet collision dynamics have mostly been concerned with spatially-homogeneous droplet clouds involving coalescence. Within this con-

text, kinetic equations have been derived describing the change with time of the droplet size probability density function. The expression for droplet collision rates in these kinetic equations incorporates a collection kernel, which is calculated from the expected droplet relative velocity and the collision efficiency. Gillespie (1975) has rigorously derived a Monte Carlo procedure for modelling the stochastic coalescence process, employing collection kernels. Also, kinetic equations and numerical methods have been developed for the calculation of droplet size distribution in homogeneous clouds, taking into account the droplet breakup and rebound in collisions (Gillespie and List 1979). Brown (1985) proposed finite-difference schemes for solving a coalescence-breakup equation for rain drops in the atmosphere, where the drops were assigned terminal falling velocities.

However, only a few studies have considered inhomogeneous flows of droplets undergoing collisions. Tambour (1985) and Greenberg et al. (1986) analyzed the droplet size distribution in an evaporating spray with droplet coalescence by the sectional method. In this method the droplet size domain is divided into sections and in each section the evolution of only one integral quantity is considered (e.g. number, surface area or volume of droplets in the section). This method correctly predicts the droplet size and spatial distributions in a turbulent fuel spray with vapourisation and combustion. Another collision model, which is used in this study, has been developed by O'Rourke (1981) for numerical simulation of dense sprays in the framework of the Lagrangian approach. In this model, random processes are applied for calculating the collision probability and the outcome of the collision processes for the pair of computational droplet parcels considered. The change of the particle velocity is determined by the impulse equations. Details of this model is described below.

Postulates

In O'Rourke's model, the binary collision of two droplet parcels is defined as a process in which all the droplets in the parcel with larger diameter, called 'collectors', undergo collisions with smaller droplets, called 'droplets', in the other parcel, satisfying the condition that the number of parcels after collision either remains the same or is reduced by one if the droplets are all absorbed by the collectors. The major assumptions invoked are:

(a) A given parcel may collide with another parcel only if these two parcels lie in the same computational cell. This avoids the calculations involving collisions between a parcel in one cell and another parcel in a neighbouring cell. If the time step is very small, the droplet will travel a very short distance in a time step and will thus still remain in the same cell (note that the cell size should be at least a few times larger than the typical droplet sizes to allow for the void fraction to be treated as a continuous variable). In this case, the assumption is appropriate.

(b) The droplets in each parcel are considered to be uniformly distributed throughout the computational cell in which they are located. This assumption is introduced for the purpose of applying concepts similar to those used in the kinetic theory of gases.

(c) The binary collision dynamics of two parcels is not affected by the presence of the other parcels in the same computational cell. This assumption is made in order to simplify the analysis, because reliable measurements of the effect of neighbouring droplets on the binary collisions do not seem to have been made. In reality, drop collision is often affected by the neighbouring droplets in a highly dense spray. More experimental studies are needed to resolve this effect.

(d) The effect of rotation resulting from off-center collision on the post-collision moving directions of drops is neglected. This assumption can not be justified. Nevertheless, this effect, if required, can be readily accommodated provided the collision time scale is known.

Collision Probability

To facilitate the description, we will use subscripts 1 and 2 to refer, respectively, to the properties of collectors and droplets, and call a collector (with larger size) as 'drop 1' and a droplet as 'drop 2'. The probability of a collision between drop 1 and drop 2, in a short time Δt, is defined as the ratio of the collision volume to the volume of a computational cell. The collision volume, in the absence of the influence of gas flow, is that of a cylinder of diameter $D_{d,1} + D_{d,2}$ and length $|\underline{U}_{d,1} - \underline{U}_{d,2}|\Delta t$, in view the fact that during the interval Δt, the center of drop 1 will, in the frame of

reference of drop 2, follow a straight line of length $|\underline{U}_{d,1} - \underline{U}_{d,2}|\Delta t$, and drop 2 would collide with drop 1 if and only if its center lay within a distance $(D_{d,1} + D_{d,2})/2$ of this straight line. In reality however, the drops undergo deflection due to gas drag as they near each other, and the actual collision volume is a distorted collision cylinder. Thus, another parameter E_{12}, called collision efficiency, has been introduced to account for the fact that the drops do not follow straight line trajectories, but instead are deflected due to their interaction with the surrounding gas flow, yielding the following expression for the collision probability:

$$\nu^0 \Delta t = \frac{\pi}{4} \frac{E_{12} |\underline{U}_{d,1} - \underline{U}_{d,2}| (D_{d,1} + D_{d,2})^2 \Delta t}{\Delta V} \tag{3.180}$$

Here ν^0 is the collision frequency, or the collision probability per unit time, and ΔV is the volume of the computational cell in which both drop 1 and drop 2 are located. To obtain an expression for E_{12}, Lagmirur (1948) investigated the trajectories of droplets around collectors by assuming that the presence of droplets does not affect the flow characteristics around the collector, and found that E_{12} is essentially determined by a dimensionless parameter K,

$$K = \frac{\rho_{d,2} |\underline{U}_{d,1} - \underline{U}_{d,2}| D_{d,2}^2}{\mu_{eff} D_{d,1}} \tag{3.181}$$

which represents the ratio between the so-called stopping distance of the droplet (assuming it has an initial velocity $(U_{d,1} - U_{d,2})$ relative to the gas) to the diameter of the collector. According to Langmuir (1948), E_{12} can be expressed as:

$$E_{12} = \frac{K^2}{(K + 0.5)^2} \quad (Re_{d,1} \gg 1) \tag{3.182}$$

$$E_{12} = \left[1 + \frac{3}{4} ln \frac{2K}{(K - 1.214)}\right]^{-2} \quad K > 1.214 \quad (Re_{d,1} \ll 1) \tag{3.183}$$

$$E_{12} = 0 \quad k \leq 1.214 \quad (Re_{d,1} \ll 1) \tag{3.184}$$

The collision frequency, ν, of a collector drop with all droplets in the other parcel, is, from (3.180), given by

$$\nu = \frac{\pi}{4} \frac{N_{d,2} E_{12} |\underline{U}_{d,1} - \underline{U}_{d,2}| (D_{d,1} + D_{d,2})^2 \Delta t}{\Delta V} \tag{3.185}$$

The probability, P_n, that a collector undergoes n collision with droplets during a time step Δt is assumed to follow a Poisson distribution (O'Rourke 1981):

$$P_n = e^{-\bar{n}} \frac{\bar{n}}{n!} \tag{3.186}$$

with mean value $\bar{n} = \nu\Delta t$. (Strictly speaking, this assumption is valid provided ν^0 is small and $N_{d,2}$ is large). Thus, the probability of no collision is:

$$P_0 = e^{-\bar{n}} \tag{3.187}$$

To determine whether collision take place between the drops in parcels 1 and 2 , a random number, X, is chosen in the interval (0,1). If $X < P_0$, then no collision occurs.

Collision regimes and transition criteria

If collision occurs, i.e., if $X \geq P_0$, five different types of collision regimes will be possible, as mentioned earlier, but in this model, only three of them are accounted for. They are: (i) grazing bounce; (ii) permanent coalescence; and (iii) separation. The transition conditions, as described below, are mainly extracted from the results of Brazier-Smith et al. (1972). The controlling parameters involved in these transition criteria are the collision Weber number, We_s, the size ratio, γ, and collision parameter, x, which is treated as a random variable taking values in the interval (0,1) for a given pair of colliding parcels.

The transition criterion from permanent coalescence to separation has been established by Brazier-Smith et al. (1972). This was achieved by treating the condition of zero kinetic energy as an equilibrium one, and assuming that separation occurs if rotation energy exceeds the surface energy required to reform the two drops from a coalesced nominal drop with diameter of $(D_{d,1} + D_{d,2})^{1/3}$. Based on this criterion, the following relation was obtained

$$We_s E_c = 2.4 f(\gamma) \tag{3.188}$$

where $f(\gamma) = \gamma^3 - 24\gamma^2 + 2.7\gamma$ and E_c is referred to as the probability of coalescence given that collision has occurred. E_c is defined to be

$$E_c = \left(\frac{2b_{c1}}{D_{d,1} + D_{d,2}}\right)^2 = x_{c1}^2 \tag{3.189}$$

or

$$x_{c1} = \sqrt{E_c} \tag{3.190}$$

where x_{c1} is the critical value of the dimensionless impact parameter. From Equation (3.188), and in view the fact that E_c can not exceed 1, it can be evaluated from

$$E_c = min\left[1, \frac{2.4 f(\gamma)}{We_s}\right] \tag{3.191}$$

The boundary between coalescence and separation is therefore determined by

$$Y = x_{c1} \tag{3.192}$$

In other words, coalescence occurs if $Y < x_{c1}$, and separation occurs otherwise.

It should be pointed out that (3.188) has been erroneously viewed (c.f. Bradley and Stow 1978) as a representation of an equilibrium state by Brazier-Smith et al. (1972). It actually represents an unstable state of coalescenced drop-pair, according to Bradley and Stow (1978), who obtained the same equation as (3.188) in their stability analysis using a parametric method.

Brazier-Smith et al. (1972) observed grazing bouncing when equaly-sized water drops collide at low relative velocity ($We_s < 2.12$) with values of x close to unity. This means that its onset condition is described by a critical Weber number We_{s_c} (below which grazing is only possible) and a critical collision parameter x_{c2}, above which grazing bouncing is only possible. The value of We_{s_c} is given as 2.12 by Brazier-Smith et al., but x_{c2} was not given by them. In order to determine x_{c2}, a similar equation to (3.188) has been derived as (Tabrizi 1991)

$$E_b^3 = \frac{We_s}{2.4f(\gamma)} \tag{3.193}$$

in which the bouncing efficiency E_b, is defined, similar to E_c, to be

$$E_b = \left(\frac{2b_{c2}}{D_{d,1} + D_{d,2}}\right)^2 = x_{c2}^2 \tag{3.194}$$

or

$$x_{c2} = \sqrt{E_b} \tag{3.195}$$

where x_{c2} is the critical collision parameter above which grazing bounce occurs. Furthermore, E_b can be expressed as

$$E_b = min\left[1, \left(\frac{We_s}{2.4f(\gamma)}\right)^{\frac{1}{3}}\right] \tag{3.196}$$

Thus grazing bounce collision occurs if

$$We_s < 2.12, \quad Y > x_{c2} \tag{3.197}$$

Post-collision properties

No expermental data are available concerning the post-collision properties of the collision regimes described above. An analysis for this purpose is therefore performed by O'Rourke using conservation equations of mass, momentum and energy.

(1) *Coalescence.* In this regime, we first need to determine the number of droplets, n, which collide with each collector, from

$$\sum_{k=0}^{n-1} \frac{P_k}{P_0} \leq \frac{X}{P_0} \leq \sum_{k=0}^{n} \frac{P_k}{P_0} \tag{3.198}$$

where the P_ks are given by the Poisson distribution (3.186). For each collector drop, n_0 droplets are removed from their associated parcel, where n_0 is the minimum of n and n_1, and n_1 is a number such that $n_1 N_{d,1} = N_{d,2}$. In case where $n_0 = n_1$, i.e., there is an insufficient number of droplets to have n coalescences with each collector, the parcel associated with the droplets is deleted. The properties of the collector drops are then modified to conserve mass, momentum and energy, thus:

$$m_d^{coll} = m_{d,1} + n m_{d,2} \tag{3.199}$$

$$(m\underline{U})_d^{coll} = (m\underline{U})_{d,1} + n(m\underline{U})_{d,2} \tag{3.200}$$

$$(mc_pT)_d^{coll} = (mc_pT)_{d,1} + n(mc_pT)_{d,2} \tag{3.201}$$

where the superscript ^{coal} denotes a value after coalescence.

Separation. In this regime, no mass is assumed to exchange between the drops. Thus, we are left to determine only the post-collision velocities of drops. Following O'Rourke (1981), the conservation equations of linear momentum, angular momentum and energy are used to determine these velocities. In an Eulerian frame of reference, they are expressed by:

$$\underline{U}_{d,1}^{coll} = \frac{(m\underline{U})_{d,1} + (m\underline{U})_{d,2} + m_{d,2}\left(\underline{U}_{d,1} - \underline{U}_{d,2}\right)\left(\dfrac{Y - \sqrt{E_c}}{1 - \sqrt{E_c}}\right)}{m_{d,1} + m_{d,2}} \tag{3.202}$$

$$\underline{U}_{d,2}^{coll} = \frac{(m\underline{U})_{d,1} + (m\underline{U})_{d,2} + m_{d,2}\left(\underline{U}_{d,2} - \underline{U}_{d,1}\right)\left(\dfrac{Y - \sqrt{E_c}}{1 - \sqrt{E_c}}\right)}{m_{d,1} + m_{d,2}} \tag{3.203}$$

in which E_c is evaluated from (3.191), and the superscript ^{coll} denotes a value after collision.

Grazing bounce. The post-collision velocities of drops for this regime is obtained by

replacing E_b for E_c in Equations (3.202) and (3.203), yielding

$$\underline{U}_{d,1}^{coll} = \frac{(m\underline{U})_{d,1} + (m\underline{U})_{d,2} + m_{d,2}\left(\underline{U}_{d,1} - \underline{U}_{d,2}\right)\left(\frac{Y - \sqrt{E_b}}{1 - \sqrt{E_b}}\right)}{m_{d,1} + m_{d,2}} \tag{3.204}$$

$$\underline{U}_{d,2}^{coll} = \frac{(m\underline{U})_{d,1} + (m\underline{U})_{d,2} + m_{d,2}\left(\underline{U}_{d,2} - \underline{U}_{d,1}\right)\left(\frac{Y - \sqrt{E_b}}{1 - \sqrt{E_b}}\right)}{m_{d,1} + m_{d,2}} \tag{3.205}$$

where E_b is evaluated from (3.196).

The above expressions for the post-collision velocities for separation and grazing bounce were derived for a collision between two individual droplets. They cannot be applied directly to a collision between two parcels, because in this case both separation and grazing collisions are calculated between N pairs of drops, where N is the minimum of $N_{d,1}$ and $N_{d,2}$. This means that if $N_{d,1} \neq N_{d,2}$, then there must be $|N_{d,1} - N_{d,2}|$ droplets undergoing no collision in the parcel with a larger number of droplets. Nevertheless, for the parcel with the least number of droplets, the above expressions can be used to obtain their post-collision velocities, since each droplet in this parcel will undergo a collision. However for the other parcel, (if $N_{d,1} \leq N_{d,2}$ is assumed), only $N_{d,1}$ droplets will undergo a collision, and $(N_{d,2} - N_{d,1})$ droplets will not. This leads to two groups of droplets in this parcel, each possessing a different velocity. In order to prevent creating new droplet parcel upon collision (and thus also avoid flooding the computer storage), the parcel after collision is assigned a velocity obtained as a weighted mean:

$$\left(\underline{U}_{d,2}^{coll}\right)_{final} = \frac{N_{d,1}\underline{U}_{d,2}^{coll} + (N_{d,2} - N_{d,1})\underline{U}_{d,2}}{N_{d,2}} \tag{3.206}$$

(c). Evaluation

The collision model described above was developed about a decade ago. Ever since then, it has been used in the numerical predictions of spray-related systems. Despite this, the model has not, however, been fully validated. For example, no study seems to have been made that directly assesses the model against existing solutions (note that examples of such solutions can be found in droplet coagulation and fragmentation in homogeneous gas-spray suspensions, for which the results are known concerning the evolution of the droplet size distribution (c.f. Saffman and

Turner 1956, Gillespie and List 1979, Bajpai et al. 1988)). Nevertheless, Bracco (1985) and Reitz (1987) claim that the collision model contributes to the prediction of increasing average droplet size with downstream distance from the injector, a feature that has also been observed in the experiments. This agreement, however, is not conclusive, since several other mechanisms could cause this behavior. These include: (1) the longer wavelength disturbances on the liquid jet will take a longer Lagrangian time to grow and to yield larger droplets; (2) smaller droplets vapourise faster leaving the larger droplets; and (3) condensation may occur in the cold, vapour-rich, dense spray region near the injector. Therefore, reliable validation of the collision model is still needed.

There are at least two limitations of the model. The first is that it is simply a representation of experimental data on water drop collisions at atmospheric pressure and temperature conditions. This casts doubts on its full applicability to Diesel sprays which not only possess different liquid properties but occur at high temperature and pressure. There is evidence showing that the collision behavior of fuel drops is quite different from that of water drops. For instance, Jiang et al (1992) made an experimental study of the collision behavior of both equal-sized water drops and normal-alkane drops, with diameters of around 300 μm, at a Weber number of order 1. In the parametric range investigated their results show that the behavior of hydrocarbon droplet is significantly more complex than that of water droplets. They observed that, for head-on collisions, while permanent coalescence always occurs for water droplets, the outcome is quite non-monotonic for the hydrocarbon droplets in that, with increasing droplet Weber number, collision can result in permanent coalescence, bouncing, permanent coalescence again, and separation. Similar complexities exist for off-centre collisions. Jiang et al. (1992) noted that for hydrocarbon droplets, viscosity did play a role in affecting the collision outcomes, and provided some data on collision regime transitions which are, however, different from those for water drop collisions by Brazier-Smith et al. (1972).

Even for the same liquid, different gas conditions can also result in appreciable difference in collision behavior. Ashgriz and Givi (1987) performed an experimental study on the collision dynamics of equal-sized n-hexane fuel droplets under different gas temperatures. They observed that, for nonburning droplets, the collision type

can be burning, grazing, separation, or permanent coalescence, but for burning droplets with the same initial conditions, only permanent coalescence and separation occur.

Thus, more experimental studies are needed on droplet binary collisions at conditions most likely to be encounted in the Diesel engines, in order to develop a collision model most suitable to the study of Diesel spray dynamics.

The second limitation is linked with the ignorance of three collision regimes, i.e., bouncing, reflexive separation and collision-induced breakup. It can be implied from the transition criteria described in the model that the former two regimes, both of which occur at nearly head-on collisions, are treated as coalescence, whereas the latter is treated as separation. This obviously leads to an over-prediction of the coalescence phenomenon (thus also the average size of the whole spray). On the other hand, it is not difficult to perceive that, in Diesel engines, high-velocity collision can occur in both the atomisation and wall impingement (if present) zones so that collision-induced breakup could be important. In the former case, this occurs when there exists a rapid change in liquid jet injection velocity history; while in the latter case, this is due to the fact that two groups of droplets are present in the near-wall region where impingement occurs. The first group consists of the droplets resulting from bouncing or splashing, moving away from the wall, whilst the second group consists of the droplets coming directly from the nozzle, moving towards the wall. Thus when a droplet from the first group collides with a drop from the other group, the collision energy could be high enough to result in breakup. For instance, in typical HSDI diesel engines, typical relative velocities of droplet collisions of this kind are above 20 m/s, producing resulting collision Weber numbers We_s well above 100, which exceeds the expected limiting Weber number for collision-induced breakup according to the data given by Arkhipov et al. (1978). Also, in this case, the off-center collision-induced rotation of colliding droplets is expected to be profound. This not only contributes to alter the directions of colliding droplets, but also produces lift forces on them (Magnus lift forces). These lift forces in turn influence the wall spray flow patterns.

3.9 Closure

In this chapter, the vector-tensor form of instantaneous equations governing the gas phase in a gas/spray system were Favre-averaged and the $k-\epsilon$ turbulence model was used to close the problem. The averaged equations were then extended to a moving coordinate system, and the expanded forms of these equations were provided in a curvilinear orthogonal coordinate system for particular engine configurations. Subsequently, the boundary conditions for the gas phase, in particular, the treatments of walls, coordinate pole/axis, cyclic boundary and the initial conditions were discussed in detail.

The Lagrangian equations governing the motion of droplets were assembled in the same coordinate frame as that of the gas phase. These equations have been supplemeted by the presentation of the methodologies accounting for the such physical phenomena as droplet dispersion under the action of gas-phase turbulence, droplet breakup by aerodynamic forces, together with droplet heating and vapourisation, collisions between droplets. Uncertainties associated with the spray sub-models have been discussed. In particular, it has been pointed out that the correlations of drag coefficient, Nusselt number and Sherwood number have ignored the effects of neighbouring droplets. An appropriate future improvement would be to extract correction factors for these parameters from the existing studies involving droplets which travel in tandem or side-by-side in parallel.

Up to this point, We have only presented the models that can predict what happens for a spray-gas system when the droplets are suspended in the bulk flow. Nothing has yet been said about the treatment of physics processes involved in the spray impingement on tha walls, namely, spray impingement and wall film flow. These are the subjects of the next two chapters.

Chapter 4

Development of Mathematical Model for Spray Impingement

4.1 Introduction

In Chapter 2, it has been made clear that current theoretical work on spray impingement modelling is still very limited. The existing models for spray impingement involve too-restrictive simplifying assumptions and rather crude treatments of impingement outcomes and post-impingement characteristics. Their deficiencies may be attributed to the lack of a sound experimental basis and theoretical analysis. Thus there is a need to develop a more general impingement model in order to assist engine design.

The work described in this chapter represents a further step towards developing a full computation model which can describe, with reasonable accuracy, the interactions between the spray, the wall and the gas flow in conditions typical of the high speed direct-injection engine. This is achieved through the construction of a mathematical model for spray impingement on the basis of the literature findings and mass, momentum and energy conservation constraints, using empirical correlations either taken directly from the literature or further developed therefrom by the author. Section 2 is devoted to the determination of the impingement regimes and the associated transition criteria, for the conditions considered in this study. Methodology is then developed in Section 3 for the determination of quantities representing post-impingement characteristics, such as rebound velocity and direction for bounc-

ing droplets and the sizes, velocities and ejection angles of secondary droplets, and proportion of mass deposited for the 'splash' regime.

4.2 Impingement Regimes and Transition Criteria

This study will be confined to the situation where the impingement wall surface temperature is below the liquid boiling temperature. This often seems to be the case in direct-injection engines with metal combustion chamber materials, since for such engines, the limit wall temperature is around 250^0C and the fuel boiling point is well above this. Evidence to justify this can be found in the work by Assanis & Heywood (1986). They performed calculations of mean gas temperature and piston surface temperature distribution as a function of crank angle for a turbocompunded DI diesel engine and found that the mean piston surface temperature was always below 500K with the peak temperature less than 20K above the mean value.

In order to simplify the analysis, we ignore the effects of droplet interactions and droplet impingement frequency on the droplet impingement dynamics. This is equivalent to assuming that the time scale required for the completion of an impingement event for a single droplet is negligible compared to the time scale corresponding to the droplet impingement frequency. This may not be true in the real situation, but the available information does not allow a more elaborate treatment. In addition, we neglect the changes in droplet shape during collision which are due to droplet oscillation before impingement. This may be justified if the droplet impact Weber number is large. To illustrate this, let us make an evaluation of the relative time scale ratio between the impingement time scale $t_i = D_I/V_I$ and the oscillation time (cf. Wachters 1966) (fundamental mode) $t_{os} = \pi\sqrt{\rho D_I^3/(16\sigma)}$. This yields

$$\frac{t_i}{t_{os}} = \frac{4}{\pi\sqrt{We}} \tag{4.1}$$

which is usually less than 0.1 when We is more than 100.

No other restrictions are imposed in this study. This implies that the wall surface, which may be either dry or wetted by an already-deposited film, can be of arbitrary roughness; and the droplet impingement conditions are arbitrary.

The relevant impingement regimes can now be readily determined by reference to the findings in Chapter 2. They are (in order of increasing Weber number):

1. **Dry wall: stick→ spread → splash.**

2. **Wetted wall: stick→ bounce→ spread→ splash.**

At this point, we need to determine the transition criteria in order to predict which regime will occur for a given incident droplet, given its size, velocity, temperature and liquid properties. Ideally, quantitative transition criteria should be non-deterministic to a certain extent, because there are actually no clear demarcations between the various regimes. This implies that an appropriate statistical analysis should be introduced in describing these criteria. Also, they should be functions of all the relevant parameters including Weber number, Laplace number, droplet incidence angle, wall temperature, surface roughness, and wall film thickness, if present. However, existing knowledge is insufficient for this purpose, so in this study we will simplify the analysis by: (a)using a deterministic approach, i.e, assuming sharp boundaries between the different regimes; and (b) ignoring the effects of some parameters when there is no alternative. The simplified formulations are outlined below.

1. Dry wall

   In the situation envisaged here, a droplet which reaches the wall will adhere to it and form local film for both 'stick' and 'spread' regimes. Thus for simplicity the latter two regimes are treated as one regime called 'adhesion' in this study. This avoids the need to determine the transition condition between these two regimes, information on which is not available.

   We propose the following expression for the transition criterion from 'adhesion' to 'splash':

$$We_c = A \cdot La^{-0.183} \tag{4.2}$$

   Here the coefficient A depends on surface roughness r_s. This expression is derived from Stow and Hadfield's correlation(1981)

$$V_c^{1.69} D_I = S_c \tag{4.3}$$

where S_c depends only on surface roughness. Rewriting (4.3) in the form

$$(D_I V_c)^{0.31}(D_I V_c^2)^{0.69} = S_c \tag{4.4}$$

yields

$$La^{0.155} We_c^{0.845} = \Lambda \tag{4.5}$$

in which Λ is a function of surface roughness only. Equation (4.5) can be rearranged to give the form (4.2)

Some typical values of A, as a function of r_s can be evaluated from Stow and Hadfield's data and are listed below:

$r_s(\mu m)$	A
0.05	5264
0.14	4534
0.84	2634
3.1	2056
12	1322

The above table clearly indicate that the parameter A is a decreasing function of surface roughness. This means that surface roughness is conducive to splashing event. This is because surface roughness is the main instability source for the spreading droplet liquid film.

2. Wetted wall

In this case, the wall surface is covered with a wall film whose thickness is expected to exert an influence on the transition criteria. The magnitude of this influence is probably a function of the ratio of the local wall film thickness to the incident droplet diameter. In diesel engine circumstances, this ratio is typically of order 1, as already mentioned previously in Chapter 2. However, in this study this parameter will not be considered, because quantitative data on its effect are,unfortunately, extremely scarce. In some cases we even have to neglect the effect of Laplace number, for the same reason. The simplified transition expressions are :

(a) Stick → bounce:

$$We_c \approx 1 \tag{4.6}$$

(b) Bounce → spread:

$$We_c \approx 5 \tag{4.7}$$

(c) Spread → splash:

$$We_c = A \cdot La^{-0.183} \tag{4.8}$$

in which it is proposed to set $A = 1320$, corresponding a very rough wall.

The transition conditions (4.7) is extracted , in an average way, from the existing data on water drops impinging on a deep water layer, while the correlation (4.8) is taken from the splashing criterion established for water droplets impinging on a very rough wall with a roughness value of 12 μm. The argument for this is that the film surface will likely become irregular due to the bombardment by the incoming droplets,and may therefore behave as a rough wall in its effect on the droplet impact dynamics.

In view of the fact that the critical transition Weber number from stick to bounce is very low and that Diesel spray impingement invariablely involve a gas boundary layer which tends to detach the sticked droplets from the surface, it is reasonable to forget about the stick regime in the wetted wall case. Thus, we are here concerned with the following regime transitions:

$$Bounce \rightarrow Spread \rightarrow Splash$$

It should be borne in mind that the above criteria are derived from data for isolated droplets impinging on a liquid surface. In situations involving a group of droplet impinging successively or simultaneously, the above transition conditions will be modified by the interference of the neighbouring droplets. This phenomenon has been noted by Ching et al(1984) in their experimental studies on water drops impacting on liquid surfaces. Unfortunately, quantitative descriptions of this effect are not available.

4.3 Post-Impingement Characteristics

This section presents the quantitative treatment of the post-impingement modes for the three impingement regimes, ie., 'adhesion', 'bounce' and 'splash'.

4.3.1 Adhesion (stick/spread)

Here the arriving droplets are assumed to coalesce to form a local film. The normal component of droplet kinetic energy prior to impingement is assumed to transform into a dynamic pressure represented by $\frac{1}{2}\rho_d U_{in}^2$, while the original droplet tangential momentum act to increase the local film tangential momentum.

4.3.2 Bounce

In this regime, we need to determine the rebound velocity and its direction, which are affected by the irregular film thickness and the surface shape. One way of achieving this is to follow Watkin & Wang's(1990) treatment and use a correlation developed by Jayarantne and Mason(1964) for the kinetic energy loss of rebound droplet,

$$\frac{V_I^2 - V_R^2}{V_I^2} = 0.95 sin^2(\theta_I) \tag{4.9}$$

to determine the rebound velocity magnitude, while assuming that the rebound angle is equal to the incident angle relative to the impact surface. This correlation however, was derived for water drops impacting on a deep water layer ($\delta/D_I \gg 1$), where most of the lost kinetic energy is expended in the process of crater formulation. Thus it will probably overpredict the energy loss for a droplet bouncing from a very thin film surface. This is because in the latter case, firstly $\delta/D_I \leq 1$ and secondly a droplet will frequently encounter a pre-existing cavity in the film surface. It must therefore perform less work in crater formation and thus retain more kinetic energy in bouncing. Another limitation associated with the use of (4.9) to determine rebound velocity is that one has to assume rebound angle θ_R. A usual practice is to set θ_R the same value as that of θ_I. This practice does not allow for a rebound droplet to take different rebound directions due to surface roughness or other factors. As an alternative, we choose the following relations developed for a solid particle bouncing on a solid wall (Mastumoto and Saito 1970) to determine the bouncing velocity

components.

$$u_{dR} = \frac{5}{7}u_d \tag{4.10}$$

$$v_{dR} = \frac{5}{7}v_d \tag{4.11}$$

$$W_{dR} = -ew_d \tag{4.12}$$

where u_d and v_d are the tangential incident droplet velocity components, w_d is the normal velocity component; and u_{dR}, v_{dR} and w_{dR} are the corresponding components of the rebound velocity. The quantity e is the 'restitution coefficient', which is assumed to follow the relation below obtained by Grant & Tabakoff (1975) for the rebounding particles whose rotation effects are negligible:

$$e = 0.993 - 1.76\theta_I + 1.56\theta_I^2 - 0.49\theta_I^3 \tag{4.13}$$

where θ_I is the incident angle with the wall surface and is measured in radians.

4.3.3 Splash

In this regime, we need to determine the quantities such as the proportion of incident droplet mass deposited as a liquid film, and the sizes, velocities and ejection angles of secondary droplets. In the models developed earlier either by Naber and Reitz(1988) or Watkins and Wang(1990), the deposited mass was ignored, and the secondary sizes and velocities were given fixed values. Such treatment is not able to represent the fact that both the sizes and velocities of secondary droplets are each distributed over a certain range. In this study, we take a different avenue in modelling these quantities and adopt the following approaches:

1. Random determination of the total secondary to incident droplet mass ratio m_s/m_I.

2. Determination of secondary droplet sizes using mass conservation and a correlation for the number of secondary droplets per splash.

3. Determination of secondary droplet velocities using energy and tangential momentum conservation, while randomly choosing the ejection angles.

In addition, the following assumptions are invoked:

1. Each droplet parcel produces two secondary parcels with equal mass $m_s/2$, and different sizes D_1, D_2, and velocities $\underline{\tilde{U}}_1 = \underline{U}_1 + \underline{U}_1^{'} = (u_{1n}, v_{1\tau}) + (0, v_{1\tau}^{'})$, $\underline{\tilde{U}}_2 = \underline{U}_2 + \underline{U}_2^{'} = (u_{2n}, v_{2\tau}) + (0, v_{2\tau}^{'})$. Here the subscript n and τ refer to, respectively, the normal and tangential directions; and the symbols $\underline{U}$ and $\underline{U}^{'}$ stand for the velocities caused by the normal and tangential components of incident velocity, respectively.

2. The ejected droplets randomly fall wihtin a cone, as shown in Figure 4.1, for both normal and oblique impingement. The ejection angle for a particular droplet can be sampled such that it is within the cone.

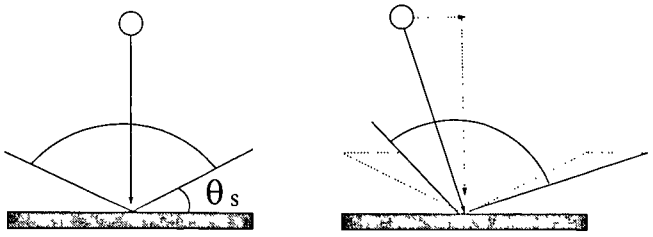


Figure 4.1: Diagram showing the cone formed by splashing droplets

It will become clear shortly that the first assumption is appropriate to produce a kind of distribution, from a statistical point of view, of secondary droplet sizes and velocities, while the latter one is intended to ensure a reasonable wall spray dispersion.

The detailed formulations are now presented:

1. **Mass ratio: $\mathbf{m_s/m_I}$**

   The ratio m_s/m_I is believed to be influenced by a number of parameters, such as We, La, r_s/D_I and δ/D_I. Since no correlations are available in terms of these, we make the following approximations:

$$\frac{m_s}{m_I} = \begin{cases} 0.2 + 0.6\alpha, & \text{for dry wall} \\ 0.2 + 0.9\alpha, & \text{for wetted wall} \end{cases} \tag{4.14}$$

   where α is a random number distributed uniformly in the interval (0,1). For a dry wall, the sampled range is given by Equation (4.14) which corresponds to the range observed experimentally (e.g. Stow and Stainer 1977; Levin and

Hobbs 1971) for a wetted wall the ratio m_s/m_I is allowed to assume values larger than 1, since splashing droplets may entrain liquid from the wall film, as observed experimentally (Mutchler 1970).

It is worthing mentioning that although Mutcheler(1970) proposed a correlation for the mass ratio in terms of one parameter, i.e. D_I/δ_0, only (see Equation (2.21) in Chapter 2), it is based, as discussed in Section 2.2.4, on too-restrictive conditions, and therefore will not be used here.

2. **Secondary droplet sizes $\mathbf{D_1}, \mathbf{D_2}$**

Mass conservation requires that

$$N_1 D_1^3 + N_2 D_2^3 = r_m D_I^3 \tag{4.15}$$

in which, N_1, N_2 are the numbers of droplets with size D_1, D_2, respectively. The quantity $r_m = m_s/m_I$ is the mass ratio and

$$N_1 + N_2 = N \tag{4.16}$$

Here N is the total number of secondary droplets per splash, an expression for which will be given shortly. We randomly choose N_1 such that $1 \leq N_1 \leq N$, and get N_2 by $N_2 = N - N_1$. Then, according to the first assumption, D_1 and D_2 can be determined from the requirements

$$N_1 D_1^3 = \frac{r_m}{2} D_I^3 \tag{4.17}$$

$$N_2 D_2^3 = \frac{r_m}{2} D_I^3 \tag{4.18}$$

In the formulation outlined above, the random determination of N_1 and N_2 under the constraint condition (4.16) makes it possible for D_1 and D_2 to take values in a certain range. This may better represent the fact that the secondary sizes follow a distribution which is usually described by a PDF function (e.g. Equation (2.21)). Unfortunately, the mean value and the variance of this function, which vary with the relevant impingement parameters (e.g. *We*, *La*, r_s), have not been well defined.

We now develop a correlation for N based on the empirical one by Stow and Stainer(1977) which reads

$$N = 0.406 d_i^3 v_I^2 - 63 \tag{4.19}$$

This correlation has two drawbacks. Firstly, it is not in dimensionless form, so its applicability to other conditions is therefore questionable. Secondly, surface roughness effects are not taken into account. To overcome these deficiencies, we propose an alternative expression for N of the form

$$N = a_0 \left(\frac{We}{We_c} - 1 \right), \qquad We \geq We_c \tag{4.20}$$

in which $a_0 \approx 5$, is obtained by fitting Stow and Stainer's data (1977). This implicitly incorporates surface roughness effects through the critical Weber number We_c, which is a function of r_s. In addition, it exhibits a linear dependence on the square of incident droplet velocity v_I^2 as does Equation (4.19) of Stow and Stainer and meets the critical condition that N=0 when $We = We_c$.

3. **Secondary velocity components:$\mathbf{u_1^n, v_1^\tau; u_2^n, v_2^\tau}$**

Determination of secondary velocity components is pursued in three steps. First, conservation of energy based on normal incident velocity component requires that

$$\frac{1}{4} m_s (U_1^2 + U_2^2) + \pi\sigma(N_1 D_1^2 + N_2 D_2^2) = E_{k,s} \tag{4.21}$$

in which

$E_{k,s} = E_k - E_{k,c}$: is the splashing energy

E_k: is the kinetic energy of incident droplet based on normal velocity component

$E_{k,c}$: is the critical kinetic energy, below which no splashing occurs. The last-named can be evaluated from the critical Weber number We_c, given by the relevant regime transition condition(s), as follows:

$$E_{k,c} = \frac{We_c}{12} \pi\sigma D_I^2 \tag{4.22}$$

The approach adopted here comes from the view that the total kinetic energy of an impinging droplet can be split into two parts. The first part is expended on deformation, dissipation, and on producing liquid film energy. This is evaluated, as proposed by the present author, as the critical energy corresponding to the critical splashing Weber number. The remainder of the energy is transferred to the splashing droplets.

Next, from Equation (2.24), which was deduced by the present author from the data on the size-velocity correlation of secondary droplets provided by Ghadiri (1978) for water drops splashing on walls of different materials, we have

$$\left(\frac{U_1}{U_2}\right) = \frac{A_0 \ln\left(\frac{D_1}{D_I}\right) + B_0}{A_0 \ln\left(\frac{D_2}{D_I}\right) + B_0} \tag{4.23}$$

Since B_0 has yet to be decided, we can make a further approximation by setting $B_0 = 0$, thus yielding:

$$\left(\frac{U_1}{U_2}\right) = \frac{\ln\left(\frac{D_1}{D_I}\right)}{\ln\left(\frac{D_2}{D_I}\right)} \tag{4.24}$$

The main implication of this relation is that the larger the sizes of secondary droplets, the smaller the magnitudes of their velocities.

Finally application of the tangential momentum conservation law produces

$$U_1 \cos\theta_1 + U_2 \cos\theta_2 = 0 \tag{4.25}$$

$$u'_{1\tau} = u'_{2\tau} = c_f V_{I\tau} \tag{4.26}$$

Where $V_{I\tau}$ denotes incident tangential velocity, and c_f is the friction coefficient, which is set to be in the range of $0.6 \sim 0.8$ by reference to the values used for a water drop splashing on a soil surface (Wright, 1986); The quantities θ_1, θ_2 are ejection angles of the two droplet parcels. We randomly choose θ_1 such that it lies somewhere in the ejection cone and determine θ_2 from equation (4.25). Thus, the following equations (4.21), (4.24) and (4.25), along with

$$u_{1n} = U_1 sin(\theta_1), \quad u_{1\tau} = U_1 cos(\theta_1) \tag{4.27}$$

$$u_{2n} = U_2 sin(\theta_2), \quad u_{2\tau} = U_2 cos(\theta_2) \tag{4.28}$$

enable the determination of $u_{1,n}, v_{1,\tau}$ and $u_{2,n}, v_{2,\tau}$

4.4 Closure

In this chapter, an impingement model has been developed. Main features of this model are that: (i) it recognises the different regimes and uses the estimated transition criteria for both dry and wetted walls; (ii) it introduces random procedures to

model some of the post-impingement characteristics; and (iii) it exploits literature data in quantifying secondary droplet sizes, velocities and ejection angles, aided by mass, momentum and energy conservation constraints, thereby reducing empiricism. However, the model is nevertheless based on a rather restricted range of data, which is unavoidable at the present stage.

The major input parameters for this impingement model are size, velocity, temperature and incidence angle of an arriving droplet. These parameters can be extracted either by experimental measurements or the computational simulations using a two-phase CFD code which can provide detailed data on droplet behavior in the gas field. In the present work, the model is implemented in the EPISO-SPRAY code, a computer program capable of simulating the in-cylinder gas and spray dynamics in internal combustion engines or allied devices. The mathematical models involved in this code have been described in Chapter 3. The numerical solution scheme involved will be detailed in Chapter 6 and the calculated results are presented in Chapter 7.

It should be pointed that, although the present model exhibits improved features compared to the earlier ones, it still suffers the limitation that it is based largely on the data and correlations for isolated water drops impinging on walls at atmospheric conditions. Numerous effects must be properly taken into account in the future when the experimental data become available. These effects include: (1) neighbouring impinging droplets; (2) gas boundary layer in the near wall region; (3) elevated gas pressure and temperature; and (4) range of fluid properties.

Chapter 5

Formulation of Mathematical Model for Wall Film Flow

5.1 Introduction

In Chapter 2, it was pointed out that previous studies reported in the literature regarding the modelling of film dynamics are mainly focused on film condensation and evaporation, where no droplet/film surface impingement processes occur. The resulting mathematical models are therefore not applicable to the prediction of wall films formed by impinging sprays. Such a film possesses the following typical features: (i) initially its mass accumulates as fuel is deposited on the walls; (ii) the surface area it covers increases continuously as a consequence of film spreading, characterised by its moving contact line, and its continuously deforming and moving interface, under the action of a number of forces, including the shear force on the film surface due to gas swirl, body force due to wall acceleration (if present), and the tangential momentum and impact pressure due to the impinging gas jet and arriving droplets, which are especially important in the impingement region and (iii) it exchanges heat with the walls and the surrounding gas and consequently vapourises and mixes with the gas.

The purpose of this chapter is therefore to develop a wall film model which takes full account of impinging droplet contributions in the film momentum equations, addresses film heating and vapourisation, and tracks its moving contact line and deforming interface.

A major challenge to the modelling of the wall film behaviour is the need to cope with the interface between the liquid and the gas, and to track the moving contact line. Thus far, this interface has been viewed in two ways. One, which has been traditionally employed, is to view it as a surface of discontinuity which is two-dimensional. In this macroscopic view, the local balance laws at any point on the interface are no longer formulated in terms of partial differential equations, but in terms of jump conditions which relate the values of the fundamental quantities on both sides of the interface.

Another, microscopic, view treats the interface as a three-dimensional transition region. Thus, the relevant continuum fields are assumed to vary continuously throughout the entire space, although there exist rapid changes along the direction normal to the interface in material properties in the transition regions which represent the interface. This microscopic view is quite useful in examining the problem of interface mass transport (Slattery 1967), but it involves more complicated mathematical manipulations.

In this study the macroscopic view of the interface is adopted because of its relative mathematical simplicity and the fact that the jump conditions arising from this provides boundary conditions in a straightforward way for problems involving dynamic phase changes.

The organisation of this chapter is as follows. In Section 2 , we discuss the basic assumptions invoked in this study for the film modelling. Section 3 is then devoted to setting up the film governing equations within the boundary-layer framework in terms of a Cartesian coordinate system. In Section 4, the full conditions for the validity of a local equilibrium model are established by performing an order of magnitude analysis. Section 5 presents the general equations for film flow on a curved surface. Finally, methods of solution of film equations are presented and assessed initially in Section 6.

5.2 Modelling Assumptions

To enable the formulation of the film transport equations, the following assumptions regarding the wall film behaviour have been made:

1. The film is thin enough for the boundary layer approximations to apply, i.e., the spatial gradients of the dependent variables tangential to the surface are negligible compared to those in the normal direction. (Appendix B presents an order of magnitude analysis for the full film momentum equations and shows that the condition of very small film thickness does indeed lead to the boundary-layer type equations). The 'thin' film assumption can be justified by an estimation made in the present study, which reveals that the maximum film thickness is around $400\mu m$ for conditions typical of HSDI engines, even under the assumption that all the arriving droplets adhere to form a static film.

2. The incident droplets cause a local build-up of film thickness and impact pressure $p_d = (1-\theta)\alpha_d \rho {U_{In}}^2 (0 < \alpha_d < 1)$ at the interface, where U_{In} is the normal component of the incident droplet velocity and θ is the local void fraction of the gas phase. The pressure p_d is due to the loss of droplet normal momentum caused by interaction with the surface. The impacting gas also induces an impact pressure, $p_g = 1/2\rho V_{gn}^2 \theta$. In addition, there is another normal force present at the interface, namely the capillary (or Laplace) pressure p_σ which arises from surface tension σ and the interface curvature $\mathcal{C}$ and is expressed as:

$$p_\sigma = -\sigma \cdot \mathcal{C} \tag{5.1}$$

where $\mathcal{C}$ is given by:

$$\mathcal{C} = \frac{1}{R_1} + \frac{1}{R_2}; \quad \text{or} \qquad \mathcal{C} = \nabla \cdot \underline{n} \tag{5.2}$$

Here R_1 and R_2 are the principal curvature radii of the film interface; and $\underline{n}$ is the unit outward normal vector to the interface. The second expression of $\mathcal{C}$ in Equation (5.166) is more convenient to use in practice. In view of the fact that the capillary force may be important at the late film spreading stages, we include it here for the sake of completeness of our formulation.

Thus, the liquid film is locally subject to a total pressure, i.e., $p_L = p_d + p_g + p_\sigma$ at the interface. Under the boundary-layer approximations, the local pressure within the film can be taken constant across the film depth, equal to p_L.

3. The tangential momentum lost by the incident droplets provides a source of tangential momentum to the wall film.

4. Film motion is caused by spatial variations in the tangential directions in the total pressure p_L, shear at the film interface, tangential momentum sources provided by incoming droplets, and body forces.

5. The mass flux due to incident droplets may be represented by a spatially smoothly varying function, so that conventional differential operations apply.

6. The thermal radiant and Dufour energy flux in the energy equation, as well as the pressure and thermal diffusion flux in the species equations, are negligible.

7. The gaseous mixture of air and fuel-vapour behaves like an ideal gas. This means that the ratio of the partial pressure of vapour to the total pressure is equal to the mole fraction of vapour.

8. Physical equilibrium prevails at the gas/film interface, and variations along film depth of thermodynamic properties of the liquid phase are negligible.

9. The film is laminar, though it may have waves on its surface.

5.3 Governing Equations

We now proceed to set up the governing equations for wall films based on the above assumptions. For the sake of simplicity and clarity, we work mainly in terms of a Cartesian coordinate system, though our modelling covers also a general orthogonal curvilinear coordinate system, for which case we only present basic equations. To this end, we represent two orthogonal coordinates tangential to the surface by x and y, and the coordinate normal to the surface by z. The film velocity components relative to the wall motion in the x, y and z directions are designated respectively by u, v and w.

5.3.1 Conservation of Mass

For any point inside the film domain, the local mass balance is expressed by the continuity equation:

$$\frac{\partial u}{\partial x}+\frac{\partial v}{\partial y}+\frac{\partial w}{\partial z}=0 \tag{5.3}$$

Since the mass exchange between the liquid film and other phases occurs mainly at the interface due to droplet mass flux and phase changes, it is important to establish mathematical relation of mass balance at the interface. This will be done shortly.

5.3.2 Conservation of Momentum

Application of boundary-layer approximations and relevant assumptions presented in the foregoing section leads to the following film momentum conservation equations:

$$\frac{\partial u}{\partial t}+u\frac{\partial u}{\partial x}+v\frac{\partial u}{\partial y}+w\frac{\partial u}{\partial z}=-\frac{1}{\rho_L}\frac{\partial p_L}{\partial x}+a_x+\nu_L\frac{\partial^2 u}{\partial z^2}+\frac{S^L_{u,d}}{\rho_L} \tag{5.4}$$

$$\frac{\partial v}{\partial t}+u\frac{\partial v}{\partial x}+v\frac{\partial v}{\partial y}+w\frac{\partial v}{\partial z}=-\frac{1}{\rho_L}\frac{\partial p_L}{\partial y}+a_y+\nu_L\frac{\partial^2 v}{\partial z^2}+\frac{S^L_{v,d}}{\rho_L} \tag{5.5}$$

in which $S^L_{u,d}$, $S^L_{v,d}$ are source terms resulting from droplet tangential momentum loss; p_L represents the sum of the impact pressure and capillary pressure. The latter can be approximated by:

$$p_\sigma=-\sigma\mathcal{C}=-\sigma\nabla\cdot\underline{n}\approx\sigma\nabla^2\delta \tag{5.6}$$

where δ is the local film thickness, if the terms $(\partial\delta/\partial x)^2$ and $(\partial\delta/\partial y)^2$ are negligible. This is usually true under the thin film assumptions.

5.3.3 Conservation of Energy

The energy equation of film flow is given by:

$$\rho_L c_p\left(\frac{\partial T_L}{\partial t}+u\frac{\partial T_L}{\partial x}+v\frac{\partial T_L}{\partial y}+w\frac{\partial T_L}{\partial z}\right)=k_L\frac{\partial^2 T_L}{\partial z^2} \tag{5.7}$$

in which T_L stands for film temperature. Here the terms involving second derivatives of T_L with respect to x and y have been dropped under the boundary-layer approximation.

5.3.4 Initial and Boundary Conditions

The solutions of the above equations are fully determined when initial and boundary conditions are specified. These are now discussed as follows.

Initial conditions - The film initial conditions are specified at the time at which impingement commences. Here we assume that there is an immediate formation of a film patch which has an area A_i determined by the positions of either adhesion or splashing droplets (see the definition for this in Chapter 4). The film thickness is assumed to be uniform over this area, and it is determined by the total volume of the deposited fuel divided by the area. The film temperature is also assumed to take a uniform value which is the average temperature of the impinging droplets that deposit mass on the wall. The initial liquid layer is assumed to possess no inertia, but has the momentum sources imparted by the droplets, and is subject to the impact pressure as well.

Gas/film interface conditions - Proper evaluation of the local properties at the interface where complex phenomena take place is important in determining the overall behaviour of wall films. The conditions at the interface can be derived from principles of continuity, conservation, thermodynamic equilibrium, and jump conditions (see e.g. Delhaye 1974). These result in the following equations.

1. The jump mass balance equation:

$$\rho_L \left(\underline{V}_L - \underline{V}_s\right) \cdot \underline{n} = \rho \left(\underline{V}_G - \underline{V}_s\right) \cdot \underline{n} - \dot{m}_{net} \tag{5.8}$$

where ρ_L and ρ are fuel and liquid density respectively; $\underline{V}_L = (u, v, w)$, $\underline{V}_G = (u_G, v_G, w_G)$ and $\underline{V}_s = (u_s, v_s, w_s)$ are, respectively, film velocity vector, gas velocity vector and interface velocity vector; $\underline{n}$ is the unit outward normal vector to the interface; $\dot{m}_{net}$ is the net mass flux due to impinging droplets. With the aid of continuity equation (5.3), the left hand side term in the above equation can be expressed as

$$\rho_L \left(\underline{V}_L - \underline{V}_s\right) \cdot \underline{n} = -\frac{\rho_L}{|\nabla F|} \left(\frac{\partial \delta}{\partial t} + \frac{\partial}{\partial x} \int_0^\delta u dz + \frac{\partial}{\partial y} \int_0^\delta v dz\right) \tag{5.9}$$

in which $F = z - \delta(x, y, t)$ which is used to define the unit outward normal as $\underline{n} = \nabla F / |\nabla F|$.

On the assumption that $(\partial\delta/\partial x)^2$ and $(\partial\delta/\partial y)^2$ are very small, we have

$$|\nabla F| = \sqrt{1 + (\partial\delta/\partial x)^2 + (\partial\delta/\partial y)^2} \approx 1 \tag{5.10}$$

Thus, Equation (5.8) can be recast into:

$$\rho_L \left(\frac{\partial \delta}{\partial t} + \frac{\partial}{\partial x} \int_0^\delta u dz + \frac{\partial}{\partial y} \int_0^\delta v dz \right) = \dot{m}_v + \dot{m}_{net} \tag{5.11}$$

where $\dot{m}_v = -\rho \left(\underline{V}_G - \underline{V}_s \right) \cdot \underline{n}$ stands for fuel vapour mass flux and takes a negative value in case of vapourisation.

2. The jump energy balance equation:

$$\begin{aligned} \dot{m}_v \left\{ h_{fg} + \underline{\frac{1}{2}\left[\left(\underline{V}_G - \underline{V}_s \right) \cdot \underline{n} \right]^2 - \frac{1}{2}\left[\left(\underline{V}_L - \underline{V}_s \right) \cdot \underline{n} \right]^2} \right\} \\ + k_L \nabla T_L \cdot \underline{n} - k_G \nabla T_G \cdot \underline{n} + 2\mu_L \left(\underline{\Sigma}_L \cdot \underline{n} \right) \cdot \left(\underline{V}_L - \underline{V}_s \right) \\ 2\mu_G \left(\underline{\Sigma}_G \cdot \underline{n} \right) \left(\underline{V}_G - \underline{V}_s \right) = 0 \end{aligned} \tag{5.12}$$

where h_{fg} is the latent heat of vapourisation, k and T stand for heat conductivity and temperature respectively; $\underline{\Sigma}$ is the rate of deformation tensor; and the subscript $_L$ and $_G$ refer, respectively, to the liquid and the gas.

In Equation (5.12), the two terms underlined and multiplied by the mass flux represent the net work done by the 'vapour recoil' pressure which, according to Palmer (1976), becomes effective only at very low gas pressures (around or below atmosphere pressure). Thus they can be neglected in engine circumstances. Furthermore, we neglect the terms involving Σ_G and Σ_L for simplicity. Hence, we obtain the following simplified interfacial energy balance equation:

$$\dot{m}_v h_{fg} + k_L \nabla T_L \cdot \underline{n} = k_G \nabla T_G \cdot \underline{n} \tag{5.13}$$

3. Fuel-vapour mass balance at the interface:

$$\dot{m}_v Y_{Ls} - \rho \mathcal{D} \left. \frac{\partial Y_L}{\partial n} \right|_s = \dot{m}_v \tag{5.14}$$

in which Y_L is the fuel-vapour mass fraction, and $\mathcal{D}$ is fuel-vapour/air binary diffusion coefficient. The subscript $_s$ represents the value at the film surface.

4. Phase equilibrium condition:

$$T_s = T_s(P_v) \tag{5.15}$$

which relates the interface temperature T_s to the vapour partial pressure P_v. A commonly-used expression is that of Clausius-Clapeyron (Lefebvre 1989) which is given by:

$$P_v = exp(a - \frac{b}{T_s - 43}) \tag{5.16}$$

Values of a and b depend on the liquid.

5. Continuity of temperature and shear stresses:

$$T_L = T_s = T_G \tag{5.17}$$

$$\left(\mu_L \frac{\partial u}{\partial z},\ \mu_L \frac{\partial v}{\partial z}\right) = (\tau_{sx},\ \tau_{sy}) \tag{5.18}$$

Here the gas shear stress components τ_{sx}, τ_{sy} in the x and y directions, respectively, are calculated from Equation (3.66) by treating the film surface as a moving wall. Thus, we have

$$(\tau_{sx}, \tau_{sy}) = \left(\mu_{eff} \frac{u_G - u_s}{Y}, \mu_{eff} \frac{v_G - v_s}{Y}\right) \tag{5.19}$$

where u_G and v_G are the gas velocity components along film coordinates x and y respectively at a distance Y along the wall normal; and μ_{eff} is defined in (3.68).

Wall boundary conditions - Within the liquid-wall contact area (note that contact line is excluded), the following conditions are imposed:

1. Continuity of temperature:

$$T_L = T_W \tag{5.20}$$

2. No-slip condition:

$$(u - u_W) = (v - v_W) = (w - w_W) = 0 \tag{5.21}$$

3. Reduced momentum equations:

$$-\frac{1}{\rho_L}\frac{\partial p_L}{\partial x} + a_x + \nu_L \frac{\partial^2 u}{\partial z^2} + \frac{S^L_{u,d}}{\rho_L} = \frac{\partial u_W}{\partial t} \tag{5.22}$$

$$-\frac{1}{\rho_L}\frac{\partial p_L}{\partial y} + a_y + \nu_L \frac{\partial^2 v}{\partial z^2} + \frac{S^L_{v,d}}{\rho_L} = \frac{\partial v_W}{\partial t} \tag{5.23}$$

Equation (5.22) and (5.23) come directly from the application of the momentum equations at the wall which, in engine circumstances, has spatially-uniform velocity components u_w, v_w and w_w. The wall velocity is that of moving piston (in diesel engines) or valves and inlet port (in gasoline engines with port injection system), depending on the types of engines and specific wall area considered. It is thus clear that the derivatives of u_w and v_w with respect to x and y becomes zero, these conditions enables the vanishing of the inertial forces at the wall. These two equations are later used to assist in the determination of the coefficients appearing in the integral method of solution adopted in this study.

5.3.5 Correlations for Mass Transfer

From Equation (5.14), it follows that film evaporation rate at the interface is given by:

$$\dot{m}_v = \frac{\rho \mathcal{D} \left. \frac{\partial Y_L}{\partial n} \right|_s}{1 - Y_{Ls}} \tag{5.24}$$

If the film is static and the gas motion effect is negligible, the evaporation rate will then be driven by concentration gradient, and Equation (5.24) can be integrated across the local vapour layer to yield:

$$\dot{m}_v = \frac{\rho \mathcal{D}}{\delta_{vr}} ln \left(\frac{1 - Y_{Ls}}{1 - Y_{f\infty}} \right) \tag{5.25}$$

where δ_{vr} is the local vapour thickness at the location $r(x, y)$ along the surface.

In engine situations, however, there is invariably a strong convective gas boundary layer which interacts with the film surface and exerts significant shear forces on it. This will in general results in more intensified heat and mass transport than the case with negligible gas motion. Furthermore, the shear force at the interface incurs surface waves which could in turn promotes both heat and mass transfer (c.f. Zotikov and Bronskii 1962). As a consequence, film vapourisation increases with increasing local Reynolds number.

To account for the above effects, we now define mass transfer coefficient β_r as

follows:

$$\rho\mathcal{D}\left.\frac{\partial Y_L}{\partial n}\right|_s = \beta_r(Y_{L\infty} - Y_{Ls}) \tag{5.26}$$

where the subscript $_\infty$ indicates local mean values.

Substitution of (5.26) into (5.24) gives:

$$\dot{m}_v = \frac{\beta_r(Y_{L\infty} - Y_{Ls})}{1 - Y_{Ls}} \tag{5.27}$$

For a given value of T_s, the value of Y_{Ls} is obtained through the phase equilibrium relation (5.15). Thus, to enable evaluation of $\dot{m}_v$, we need to estimate β_r which is in turn related to the local Sherwood number Sh_r, defined by:

$$Sh_r = \frac{\beta_r r}{\rho\mathcal{D}} \tag{5.28}$$

Here r is the radial distance measured from a reference position P_0(in the present study this is chosen as the stagnation point). In the absence of better choice, Sh_r is evaluated from Rose's (1982) correlation which was developed for two-dimensional condensations under forced-convection conditions. It is:

$$Sh_r = \Phi Re_r^{1/2} \tag{5.29}$$

where

$$\Phi = \frac{\Psi}{1 + 0.941\dot{M}^{1.14}Sc^{0.93}} + \dot{M}Sc \tag{5.30}$$

$$\Psi = Sc^{1/2}\left(27.8 + 75.9Sc^{0.306} + 657Sc\right)^{-1/6} \tag{5.31}$$

$$Sc = \frac{\nu_G}{\mathcal{D}}; \quad \dot{M} = \frac{\dot{m}_v r}{\mu_G Re_r^{1/2}}; \quad Re_r = \frac{V_{G\infty} r}{\nu_G} \tag{5.32}$$

where $V_{G\infty}$ is the local tangential gas mean velocity magnitude; and Sc is the Schmidt number.

It should be pointed out that T_s and $\dot{m}_v$ are determined together by solving mass transfer equation (5.27) and heating equtaion (5.13) simultaneously.

5.4 Local Equilibrium Model

It is evident that analysis of wall film behaviour by solving Equations (5.4), (5.5), (5.7) and (5.11) is by no means easy, since it involves solution of four simultaneous

equations. Nevertheless, a method for achieving this will be presented later in Section 5.6. However, it is useful to note that the problem will be greatly simplified if we can neglect the convective terms in the momentum and energy equations and also assume quasi-steady state behaviour. Once this is done, it is easy to derive that the temperature profile is linear and the velocity profile is parabolic; thus we need only to solve an integral mass balance equation. As mentioned in Section 2.4.4, Sparrow & Gregg(1959) investigated, to some extent, the conditions for such simplifications. They invoked a special similarity transformation for 2-D steady film flow to obtain a new system of equations, in which the inverse of Prandtl number($Pr = \nu/\alpha$) enters the convective terms as a common factor. Accordingly, they claimed that these terms can be neglected at large Prandtl number, which was supported by their numerical calculations. However, they did not study the conditions under which both the unsteady and convection terms in the energy equation can be ignored. In this section an analysis is made to identify the full conditions for the applicability of the local equilibrium model for general transient film flows, covering a wide-range of practical applications, including film condensation/evaporation, and wall films formed by impinging sprays. This is pursued by performing an order of magnitude analysis on the boundary-layer equations.

A key issue in the order of magnitude analysis is to make appropriate choice of scaling parameters and to ensure that all the dimensionless variables employed are of the order of unity. The two length scaling parameters are easy to determine– one is the typical film thickness, δ_0, while the other is a typical longitudinal dimension, l_0; but the choice of time scaling parameter, t_0, needs some additional effort. For the purpose of determining t_0, we make use of the mass balance equation at the interface, i.e., Equation (5.11), which is now rewritten as:

$$\underset{I}{\frac{\partial \delta}{\partial t}} + \underset{II}{\frac{\partial}{\partial x}\int_0^\delta u dz} + \underset{III}{\frac{\partial}{\partial y}\int_0^\delta v dz} = \underset{IV}{\frac{\dot{m}_v}{\rho_L}} + \underset{V}{\frac{\dot{m}_{net}}{\rho_L}} \tag{5.33}$$

Since terms I, II and III are all of the order δ_0/t_0, where t_0 is the film growth time scale, it follows that t_0 is of the order:

$$t_0 = \delta_0 / \left(\frac{\dot{m}_v}{\rho_L} + U^* \right) \tag{5.34}$$

where $U^* = \dot{m}_{net}/\rho_L$, which can be estimated by the mass balance equation of spray:

$$\beta U_{inj} \frac{\pi D_N^2}{4} = U^* A_{imp} \tag{5.35}$$

in which $\beta (0 < \beta \leq 1)$ is used to account for the fact that not all the injected liquid reaches the wall due to evaporation, droplet bouncing and splashing, or the deflection of droplets by the gas flow; U_{inj} is the mean fuel injection velocity, D_N is the nozzle diameter, and A_{imp} is the area of the impingement zone.

With the time scale determined, the choice of remaining scaling parameters is quite straightforward and we arrive at the following dimensionless variables:

$$\begin{aligned}
(\bar{x}, \bar{y}, \bar{z}, \bar{t}) &= \left(\frac{x}{l_0}, \frac{y}{l_0}, \frac{z}{\delta_0}, \frac{t}{t_0}\right) \\
(\bar{u}, \bar{v}, \bar{w}) &= \left(\frac{u}{l_0/t_0}, \frac{v}{l_0/t_0}, \frac{w}{\delta_0/t_0}\right) \\
(\bar{p}_\sigma, \bar{p}_{imp}) &= \left(\frac{p_\sigma t_0^2}{\rho_L l_0^2}, \frac{p_{imp}}{\rho_L U_{dn}^2}\right) \\
\left(\bar{S}_{u,d}, \bar{S}_{v,d}\right) &= \left(\frac{S_{u,d}}{\rho_L U_{dx}^2 l_0}, \frac{S_{v,d}}{\rho_L U_{dy}^2 l_0}\right) \\
(\theta, \bar{a}_x, \bar{a}_y) &= \left(\frac{T_L - T_s}{\Delta T_0}, \frac{a_x \delta_0^2 t_0}{l_0 \nu_L}, \frac{a_y \delta_0^2 t_0}{l_0 \nu_L}\right)
\end{aligned} \tag{5.36}$$

where p_{imp} is the droplet impingment pressure ($p_{imp} + p_\sigma = p_L$); U_{dn}, U_{dx} and U_{dy} are typical impinging droplet velocity components in the normal and tangential directions, respectively; and $\Delta T_0 = [T_W - T_s]_0$ stands for the initial temperature difference between the wall and film surface.

Substitution of (5.36) into equations (5.4) to (5.5) gives:

Momentum

$$\begin{aligned}
&\frac{K}{Pr}\left(\frac{\partial \bar{u}}{\partial \bar{t}} + \bar{u}\frac{\partial \bar{u}}{\partial \bar{x}} + \bar{v}\frac{\partial \bar{u}}{\partial \bar{y}} + \bar{w}\frac{\partial \bar{u}}{\partial \bar{z}} + \frac{\partial \bar{p}_\sigma}{\partial x}\right) = \\
&-\frac{U_{dn}^2 \delta_0^2 t_0}{l_0 \nu_L}\frac{\partial \bar{p}_{imp}}{\partial x} + \bar{a}_x + \frac{\partial^2 \bar{u}}{\partial \bar{z}^2} + \frac{\bar{S}_{u,d} U_{dx}^2 \delta_0^2 t_0}{\nu_L}
\end{aligned} \tag{5.37}$$

$$\begin{aligned}
&\frac{K}{Pr}\left(\frac{\partial \bar{v}}{\partial \bar{t}} + \bar{v}\frac{\partial \bar{v}}{\partial \bar{x}} + \bar{v}\frac{\partial \bar{v}}{\partial \bar{y}} + \bar{w}\frac{\partial \bar{v}}{\partial \bar{z}} + \frac{\partial \bar{p}_\sigma}{\partial y}\right) = \\
&-\frac{U_{dn}^2 \delta_0^2 t_0}{l_0 \nu_L}\frac{\partial \bar{p}_{imp}}{\partial y} + \bar{a}_y + \frac{\partial^2 \bar{v}}{\partial \bar{z}^2} + \frac{\bar{S}_{v,d} U_{dy}^2 \delta_0^2 t_0}{\nu_L}
\end{aligned} \tag{5.38}$$

Energy

$$K\left(\frac{\partial\theta}{\partial\bar{t}}+\bar{u}\frac{\partial\theta}{\partial\bar{x}}+\bar{v}\frac{\partial\theta}{\partial\bar{y}}+\bar{w}\frac{\partial\theta}{\partial\bar{z}}\right)=\frac{\partial^2\theta}{\partial\bar{z}^2} \tag{5.39}$$

where

$$K=\frac{\delta_0^2}{t_0\alpha},\quad Pr=\frac{\nu_L}{\alpha} \tag{5.40}$$

The implications of the above scaled equations are almost self-evident: (1) if $K/Pr \ll 1$, the momentum equations reduce to a local equilibrium model, which means that viscous forces are simply balanced by body forces; and (2) if $K \ll 1$, Equation (5.39) implies that film temperature varies linearly between the wall and interface values. Clearly, if $Pr \geq 1$-which is typical of diesel fuels and most hydrocarbons, condition (2) covers condition (1).

Physical interpretation of these two conditions can be provided by comparing the relevant time scales. It is a known fact that the time needed to develop the velocity and temperature profiles is of the order of the time constant for cross-stream diffusion. Thus, for a film with a typical thickness, δ_0, the time constant for cross-stream diffusion of heat is of the order $t_h = \delta_0^2/\alpha$, and the time for cross-stream momentum transport is of the order $t_m = \delta_0^2/\nu$, and the film growth constant time t_0 is given by Equation (5.34). Thus:

$$\frac{t_m}{t_0} = \frac{\delta_0^2/\nu_L}{t_0}=\frac{K}{Pr} \tag{5.41}$$

$$\frac{t_h}{t_0} = \frac{\delta_0^2/\alpha}{t_0}=K \tag{5.42}$$

It is therefore apparent that $K/Pr \ll 1$ implies that the time required to develop the velocity profile is significantly shorter than the time constant for film growth, whereas $K \ll 1$ means that the time needed to develop the temperature profile is sufficiently shorter than the time constant for film growth.

It is obvious from Equation (5.40) that, for a given liquid film, whether the parameters K and K/Pr are both sufficiently small is largely dependent on the time scale t_0, which in turn depends on the mass condensation/evaporation velocity $U^h = \dot{m}_v/\rho_L$ and droplet deposition velocity U^*,as can be seen from (5.34). In particular, large magnitudes of U^h and U^* will cause the violation of the above conditions. For instance, if we assume that both U^h and U^* are of the order of

unity, then t_m/t_0 is of the order δ_0/ν_L and t_h/t_0 of the order δ_0/α. In this case, if we take δ_0 to be of the order of $1\mu m$ or larger-which is typical in Diesel engines, then for an n-dodecane liquid film at the conditions typical of HSDI engines, we have the following estimation:

$$\frac{K}{Pr} = \frac{t_m}{t_0} \geq 1, \quad K = \frac{t_h}{t_0} \geq 10$$

which means that local equilibrium model is not valid if the magnitude of either U^h and U^* is of the order 1 or higher.

It is of interest to consider two particular cases which are of importance in practical applications. The first is the one in which the film thickness growth (or reduction) is dominated by heat flux term IV, and term V can be neglected– as frequently encountered in the film evaporation/condensation. In this case, the heat transfer between the vapour and the film is usually neglected and the parameters K and t_0 read:

$$K = \frac{c_p|T_S - T_W|_0}{h_{fg}}, \quad t_0 = \frac{\delta_0^2}{K\alpha}$$

Thus the condition for local equilibrium of momentum, $K/Pr \ll 1$, covers that derived by Sparrow and Gregg(1959), which does not include the parameter K. In addition, the present analysis predicts that a linear temperature profile occurs when

$$\frac{c_p|T_s - T_W|_0}{h_{fg}} \ll 1 \tag{5.43}$$

which is in agreement with the calculated results of Sparrow and Gregg (1959). Numerical examples will be provided later to verify the above criteria.

The second case is the one in which the film growth is dominated by the droplet mass deposition rate so that heat flux term IV in Equation (5.33) is negligible, as is true of impingement zone. In this case, we obtain:

$$K = \frac{U^*\delta_0}{\alpha}, \quad \frac{K}{Pr} = \frac{U^*\delta_0}{\nu_L} \tag{5.44}$$

which illustrates that the droplet deposition velocity, which is determined by the fuel injection rate, plays an important part in justifying whether the local equilibrium model is applicable. According to what was briefly discussed before, the local equilibrium model is not applicable when U^* is of the order of 1 m/s, which is however a typical condition in the impingement zone at the injection conditions typical

of HSDI engines. In fact, if we assume $\beta = 1$ (which means that all liquid reaches the wall) and take typical values of nozzle diameter $D_N = 0.3mm$, spray cone angle $\beta = 12^0$, fuel mean injection velocity $U_{inj} = 100m/s$, and impingement distance $Z = 20mm$, we can easily estimate from Equation (5.35) that U^* is of the order 1 m/s. So strictly speaking, local equilibrium does not apply in the impingement zone.

5.5 Equations for Film Flows along a General Surface

This section is devoted to the derivation of general equations for thin film flows along a general curved surface, $\mathcal{S}$, which possesses no geometrical singularities, in an appropriate coordinates system .

5.5.1 The Coordinate System

The feature of very small film thickness makes it clear that body-fitted coordinate system, though containing curvature terms, is more appropriate to the description of the film governing equations for general applications involving curved surfaces. The reason is that this will allow us to use surface-tangential-oriented velocity components and reduce the three dimensional equations into two dimensional ones with the aid of boundary layer approximations and integral method, as will be made clear shortly. As a consequence of this, we avoid three-dimensional calculations. In addition, it is convenient to choose a body-fitted orthogonal coordinate system to avoid the additional complexities involved with general non-orthogonal curvilinear coordinates.

We denote the equation of the given surface, $\mathcal{S}$, along which the film flows by

$$\zeta(x, y, z) = 0 \tag{5.45}$$

This surface together with all parallel surfaces constitutes a Lamé family of surfaces (Weatherburn 1927):

$$\zeta(x, y, z) = const. \tag{5.46}$$

It follows that there exist two families of surfaces

$$\xi(x,y,z) = const., \quad \eta(x,y,z) = const. \tag{5.47}$$

such that the three families ξ, η, ζ form a triply orthogonal family (Weatherburn 1927).

If $\underline{r}$ is the position vector of point P in space, and h_1, h_2, h_3 are the length elements in the chosen coordinate system, then

$$h_1 = \left|\frac{\partial \underline{r}}{\partial \xi}\right|, \qquad h_2 = \left|\frac{\partial \underline{r}}{\partial \eta}\right|, \qquad h_3 = \left|\frac{\partial \underline{r}}{\partial \zeta}\right| \tag{5.48}$$

and it is obvious that h_3 is a function of ζ only. We can, without loss of generality, take it to be unity, ζ then represents distance measured normal to $\mathcal{S}$.

5.5.2 Differential Equations

In terms of these coordinates, we denote by u, v, w the corresponding velocity components in ξ, η, ζ directions, and make the usual boundary layer assumptions. We then have the following boundary layer-type film equations:

Continuity

$$\frac{1}{h_1}\frac{\partial u}{\partial \xi} + \frac{1}{h_2}\frac{\partial v}{\partial \eta} + \frac{\partial w}{\partial \zeta} - \mathcal{C}_\xi u - \mathcal{C}_\eta v = 0 \tag{5.49}$$

Momentum

$$\begin{aligned}\frac{\partial u}{\partial t} + \frac{u}{h_1}\frac{\partial u}{\partial \xi} + \frac{v}{h_2}\frac{\partial u}{\partial \eta} + w\frac{\partial u}{\partial \zeta} - \mathcal{C}_\eta uv + \mathcal{C}_\xi v^2 \\ = -\frac{1}{\rho_L h_1}\frac{\partial p_L}{\partial \xi} + a_\xi + \nu_L \frac{\partial^2 u}{\partial \zeta^2} + S^L_{u,d}\end{aligned} \tag{5.50}$$

$$\begin{aligned}\frac{\partial v}{\partial t} + \frac{v}{h_1}\frac{\partial v}{\partial \xi} + \frac{v}{h_2}\frac{\partial v}{\partial \eta} + w\frac{\partial v}{\partial \zeta} - \mathcal{C}_\xi uv + \mathcal{C}_\eta u^2 \\ = -\frac{1}{\rho_L h_1}\frac{\partial p_L}{\partial \eta} + a_\eta + \nu_L \frac{\partial^2 v}{\partial \zeta^2} + S^L_{v,d}\end{aligned} \tag{5.51}$$

Energy

$$\rho_L c_p \left(\frac{\partial T_L}{\partial t} + \frac{u}{h_1}\frac{\partial T_L}{\partial \xi} + \frac{v}{h_2}\frac{\partial T_L}{\partial \eta} + w\frac{\partial T_L}{\partial \zeta} \right) = k_L \frac{\partial^2 T_L}{\partial \zeta^2} \tag{5.52}$$

In the above, $\mathcal{C}_\xi$ stands for the principal curvature on the surface $\xi = const.$ in the direction of the parameter η and $\mathcal{C}_\eta$ for the principal curvature on the surface $\eta = const.$ in the direction of the parameter ξ. They are expressed as:

$$\mathcal{C}_\xi = -\frac{1}{h_1 h_2}\frac{\partial h_2}{\partial \xi}, \quad \mathcal{C}_\eta = -\frac{1}{h_1 h_2}\frac{\partial h_1}{\partial \eta} \tag{5.53}$$

In view of the thin film assumption, it is reasonable to further assume that the film thickness is far less than the principal curvature radii $R_\xi = 1/|\mathcal{C}_\xi|$ and $R_\eta = 1/|\mathcal{C}_\eta|$ of $\mathcal{S}$, thus yielding:

$$\frac{\delta}{R_\xi} \ll 1; \quad \frac{\delta}{R_\eta} \ll 1 \tag{5.54}$$

Under the condition (5.54), the curvature terms in the above equations can be neglected when solving film equations, as will be made clear in the next subsection.

5.5.3 Integral Equations

The purpose of this subsection is twofold. Firstly, the differential equations are transformed into their integral counterparts which serve as a starting point for the numerical solution scheme adopted in this study. Secondly, theoretical justifications are provided for the omission of curvature terms in the film equations.

Using the jump condition (5.8), the integral continuity equation can be obtained as:

Continuity

$$\frac{\partial \delta}{\partial t} + \frac{1}{(h_1 h_2)_s}\left(\frac{\partial}{\partial \xi}\int_0^\delta u h_2 d\zeta + \frac{\partial}{\partial \eta}\int_0^\delta v h_1 d\zeta \right) = \frac{\dot{m}_v}{\rho_L} + \frac{\dot{m}_{net}}{\rho_L} \tag{5.55}$$

in which the subscript $_s$ refers to the interface values

Here, the length elements h_1 and h_2 are assumed to take their values at the solid surface, $\mathcal{S}$, because of very small film thickness. Thus, for example, the term $(h_1 h_2)_s$ can be replaced by $(h_1 h_2)_w$ (here the subscript w refers to the values at

the solid surface). They can further be considered not to be dependent on the film-cross coordinate ζ when performing intergration across the film depth. With such approximations, the integral momentum and energy equations can be assembled in the following.

First, the integral momentum equations are obtained by integrating equations (5.50) and (5.51) with respect to cross-film coordinate ζ with the use of continuity equation (5.49):

Momentum

$$\frac{\partial}{\partial t}\int_0^\delta u d\zeta + \frac{1}{h_1}\frac{\partial}{\partial \xi}\int_0^\delta u^2 d\zeta + \frac{1}{h_2}\frac{\partial}{\partial \eta}\int_0^\delta uv d\zeta - \int_0^\delta \mathcal{C}_\xi(u^2 - v^2)d\zeta - \int_0^\delta \mathcal{C}_\eta 2uv = -\frac{1}{\rho_L h_1}\frac{\partial p_L}{\partial \xi}\delta + \bar{a}_\xi\delta + \frac{1}{\rho_L}(\tau_{s\xi} - \tau_{w\xi}) + \frac{\tilde{S}^L_{u,d}}{\rho_L} \tag{5.56}$$

$$\frac{\partial}{\partial t}\int_0^\delta v d\zeta + \frac{1}{h_2}\frac{\partial}{\partial \eta}\int_0^\delta v^2 d\zeta + \frac{1}{h_1}\frac{\partial}{\partial \xi}\int_0^\delta uv d\zeta - \int_0^\delta \mathcal{C}_\eta(v^2 - u^2)d\zeta - \int_0^\delta \mathcal{C}_\xi 2uv = -\frac{1}{\rho_L h_2}\frac{\partial p_L}{\partial \eta}\delta + \bar{a}_\eta\delta + \frac{1}{\rho_L}(\tau_{s\eta} - \tau_{w\eta}) + \frac{\tilde{S}^L_{v,d}}{\rho_L} \tag{5.57}$$

where $\tilde{S}^L_{u,d}$ and $\tilde{S}^L_{u,d}$ stand for the integration of droplet momentum source components over the film thickness; and $\bar{a}_\xi$ and $\bar{a}_\eta$ are depth-average body force components, defined by:

$$\bar{a}_\xi = \frac{1}{\delta}\int_0^\delta a_\xi d\zeta; \qquad \bar{a}_\eta = \frac{1}{\delta}\int_0^\delta a_\eta d\zeta \tag{5.58}$$

Next, the energy equation (5.52) is integrated with respect to ζ, using also the continuity equation (5.49), to yield:

Energy

$$\frac{\partial}{\partial t}\int_0^\delta (T_L - \tilde{T}_s)d\zeta + \frac{1}{h_1}\frac{\partial}{\partial \xi}\int_0^\delta u(T_L - \tilde{T}_s)d\zeta + \frac{1}{h_2}\frac{\partial}{\partial \eta}\int_0^\delta v(T_L - \tilde{T}_s)d\zeta - \int_0^\delta \mathcal{C}_\xi(T - \tilde{T}_s)ud\zeta - \int_0^\delta \mathcal{C}_\eta(T - \tilde{T}_s)vd\zeta = \alpha\left(\left[\frac{\partial T_L}{\partial \zeta}\right]_{\zeta=\delta} - \left[\frac{\partial T_L}{\partial \zeta}\right]_{\zeta=0}\right) \tag{5.59}$$

in which $\tilde{T}_s$ is time-and-space averaged interface temperature given by:

$$\tilde{T}_s = \frac{1}{\mathcal{T}}\frac{1}{A_f}\int_0^{\mathcal{T}}\int_{A_f} T_s dt dA \tag{5.60}$$

where $\mathcal{T}$ is the elapsed time, and A_f is the area covered by the wall film at time $\mathcal{T}$. The purpose of introducing the $\tilde{T}$ parameter will be made clear in the next subsection.

In the light of the above integral equations, the problem of neglecting curvature terms can now be examined. Let us focus, for example, on the fourth term on the left side of Equation (5.56), the magnitude of which can be rewritten, with the aid of the mean-value theorem, as:

$$\left|\int_0^\delta C_\xi(u^2 - v^2)d\zeta\right| = \left|\frac{\delta}{R_\xi}\right| \left|\overline{(u^2 - v^2)}\right| \tag{5.61}$$

where $\overline{(u^2 - v^2)}$ denotes a mean value of $(u^2 - v^2)$ within the film depth. Since, $\delta/R_\xi \ll 1$, according to the assumed condition (5.54), it follows that the above term is negligible. The same conclusion also holds for all other curvature terms. Thus, under thin film assumptions, the need to deal with curvature terms is eliminated, which is also true with general curvilinear coordinate system. This allows for additional improvement of numerical efficiency in the film calculations when curved surfaces are involved.

5.6 Method of Solution

For the general case, the aformentioned film equations preclude analytical solution and recourse must therefore be made to numerical methods. In what follows solution of the film equations is to be sought using a combination of integral and numerical methods. This avoids the need for discretisation of a three-dimensional domain, thus also avoiding the need to adjust the grid to follow the moving and deforming film interface. It also enables the reduction of the order of the governing differential equations and thereby facilitate simple numerical or analytical solutions. In the following, we will first develop the integral solution part with reference to the governing equations in a Cartesian coordinate system. The procedure can easily be extended to the orthogonal coordinate system.

5.6.1 Integral Equations

As a starting point, the intergral momentum and energy equations are presented in the Cartesian coordinate system by reference to those presented in Section 5.5.3 for general orthogonal curvilinear coordinate system. They are given below:

Momentum

$$\frac{\partial}{\partial t}\int_0^\delta u dz + \frac{\partial}{\partial x}\int_0^\delta u^2 dz + \frac{\partial}{\partial y}\int_0^\delta uv dz = -\frac{1}{\rho_L}\frac{\partial p_L}{\partial x}\delta + \bar{a}_x\delta + \frac{1}{\rho_L}(\tau_{sx} - \tau_{wx}) + \frac{\tilde{S}^L_{u,d}}{\rho_L} \tag{5.62}$$

$$\frac{\partial}{\partial t}\int_0^\delta v dz + \frac{\partial}{\partial y}\int_0^\delta v^2 dz + \frac{\partial}{\partial x}\int_0^\delta uv dz = -\frac{1}{\rho_L}\frac{\partial p_L}{\partial y}\delta + \bar{a}_y\delta + \frac{1}{\rho_L}(\tau_{sy} - \tau_{wy}) + \frac{\tilde{S}^L_{v,d}}{\rho_L} \tag{5.63}$$

Energy

$$\frac{\partial}{\partial t}\int_0^\delta (T_L - \tilde{T}_s)dz + \frac{\partial}{\partial x}\int_0^\delta u(T_L - \tilde{T}_s)dz + \frac{\partial}{\partial y}\int_0^\delta v(T_L - \tilde{T}_s)dz = \alpha\left(\left[\frac{\partial T_L}{\partial z}\right]_{z=\delta} - \left[\frac{\partial T_L}{\partial z}\right]_{z=0}\right) \tag{5.64}$$

It is clear that the above-obtained integral equations contain no terms involving w or the derivative terms with respect to the film-cross coordinate z, thus reducing the three-dimensional original conservation equations to two-dimensional ones. This feature is also retained in the integral equations for general orthogonal coordinate system, given in Section 5.5.3. The task now remains to cast them further into equations for depth-average velocities and temperatures which will be solved numerically. This is the topic of the next subsection.

5.6.2 Similarity Analysis

Assuming similitude of the flow variables in the direction normal to the surface allows introduction of the following types of velocity and temperature profiles for the boundary-layer type film equations:

$$\frac{u}{u_\delta} = f(\eta); \quad \frac{v}{v_\delta} = g(\eta); \quad \theta = \theta(\eta) \tag{5.65}$$

where $\eta = z/\delta$; $\theta = (T_L - \tilde{T}_s)/(\tilde{T}_w - \tilde{T}_s)$; and u_s and v_s are velocity components at the interface. Here, like $\tilde{T}_s$, $\tilde{T}_w$ stands for time-and-space averaged wall temperature. These averaged temperatures are introduced to aid in the determination of the particular form of $\theta(\eta)$, which is then used to determine the local T_L by setting $(T_L - T_s)/(T_w - T_s) = \theta(\eta)$.

With the aid of (5.65), Equations (5.11), (5.62), (5.63) and (5.64) can be recast into the following forms:

$$\frac{\partial \delta}{\partial t} + \frac{\partial}{\partial x}(\bar{u}\delta) + \frac{\partial}{\partial y}(\bar{v}\delta) = \frac{\dot{m}_v}{\rho_L} + \frac{\dot{m}_{net}}{\rho_L} \tag{5.66}$$

$$\frac{\partial}{\partial t}(\bar{u}\delta) + \frac{\partial}{\partial x}(\alpha_1 \bar{u}\bar{u}\delta) + \frac{\partial}{\partial y}(\alpha_2 \bar{u}\bar{v}\delta) = \frac{1}{\rho_L}\left(-\delta\frac{\partial p_L}{\partial x} + \tau_{sx} - \tau_{wx} + \tilde{S}_{u,d}\right) + \bar{a}_x \tag{5.67}$$

$$\frac{\partial}{\partial t}(\bar{v}\delta) + \frac{\partial}{\partial x}(\alpha_2 \bar{u}\bar{v}\delta) + \frac{\partial}{\partial y}(\alpha_3 \bar{v}\bar{v}\delta) = \frac{1}{\rho_L}\left(-\delta\frac{\partial p_L}{\partial y} + \tau_{sy} - \tau_{wy} + \tilde{S}_{v,d}\right) + \bar{a}_y \tag{5.68}$$

$$\frac{\partial}{\partial t}(\alpha_4 \delta) + \frac{\partial}{\partial x}(\alpha_5 \bar{u}\delta) + \frac{\partial}{\partial y}(\alpha_6 \bar{v}\delta) = \alpha_7 \frac{\alpha}{\delta} \tag{5.69}$$

where

$$\begin{aligned} \bar{u} &= \frac{1}{\delta}\int_0^\delta u dz, & \bar{v} &= \frac{1}{\delta}\int_0^\delta v dz \\ \alpha_1 &= \frac{\int_0^1 f(\eta)^2 d\eta}{\left(\int_0^1 f(\eta) d\eta\right)^2}, & \alpha_3 &= \frac{\int_0^1 g(\eta)^2 d\eta}{\left(\int_0^1 g(\eta) d\eta\right)^2} \\ \alpha_2 &= \frac{\int_0^1 fg d\eta}{\left(\int_0^1 f d\eta\right)\left(\int_0^1 g d\eta\right)}, & \alpha_4 &= \int_0^1 \theta d\eta \\ \alpha_5 &= \frac{\int_0^1 \theta f d\eta}{\int_0^1 f d\eta}, & \alpha_6 &= \frac{\int_0^1 \theta g d\eta}{\int_0^1 g d\eta} \end{aligned} \tag{5.70}$$

$$\alpha_7 = \frac{\theta'(1) - \theta'(0)}{\Delta T}$$

Here the parameter $\Delta T = \tilde{T}_w - \tilde{T}_s$. The wall shear stress components τ_{wx} and τ_{wy} can be expressed as:

$$\tau_{wx} = \beta_1 \mu_L \frac{\bar{u}}{\delta}; \quad \tau_{wy} = \beta_2 \mu_L \frac{\bar{v}}{\delta} \tag{5.71}$$

in which the positive parameters β_1 and β_2 are given by:

$$\beta_1 = \frac{f'(0)}{\int_0^1 f(\eta)d\eta}; \quad \beta_2 = \frac{g'(0)}{\int_0^1 g(\eta)d\eta} \tag{5.72}$$

Specific forms for $f(\eta)$, $g(\eta)$ and $\theta(\eta)$ can be assumed with certain flexibilities, provided they satisfy the following boundary conditions :

At the interface ($\eta = 1$):

$$f(1) = g(1) = 1 \tag{5.73}$$

$$f'(1) = \alpha_8 \frac{\tau_{sx}\delta}{\mu_L \bar{u}}; \quad g'(1) = \alpha_9 \frac{\tau_{sy}\delta}{\mu_L \bar{v}} \tag{5.74}$$

$$\theta(\eta) = 0 \tag{5.75}$$

where prime denotes the derivative with respect to η; and α_8, α_9 are given by:

$$\alpha_8 = \int_0^1 f(\eta)d\eta; \quad \alpha_9 = \int_0^1 g(\eta)d\eta \tag{5.76}$$

At the solid surface ($\eta = 0$):

$$f(0) = g(0) = 0 \tag{5.77}$$

$$f''(0) = \alpha_8 \frac{\delta^2}{\mu_L \bar{u}} \left[\frac{\partial u_w}{\partial t} + \frac{\partial p_L}{\partial x} - S_{u,d} - a_x \right] \tag{5.78}$$

$$g''(0) = \alpha_9 \frac{\delta^2}{\mu_L \bar{v}} \left[\frac{\partial v_w}{\partial t} + \frac{\partial p_L}{\partial y} - S_{v,d} - a_y \right] \tag{5.79}$$

$$\theta(0) = 1; \ \theta'(0) \neq 0 \text{ (for non} - \text{isothermal case)} \tag{5.80}$$

In the present study, we adopt the following profiles:

$$f(\eta) = a_1\eta + a_2\eta^2 + a_3\eta^3 \tag{5.81}$$

$$g(\eta) = b_1\eta + b_2\eta^2 + b_3\eta^3 \tag{5.82}$$

$$\theta = 1 + \Lambda\eta - (1 + \Lambda)\eta^3 \tag{5.83}$$

in which a_1, a_2, a_3, b_1, b_2, b_3 and Λ are each functions of the variables x, y and t. It is evident that (5.81) and (5.82) automatically satisfy no-slip conditions, and (5.83) satisfies (5.75) and (5.80). The coefficient Λ is the temperature shape factor and is to be determined in the course of solution, while the other six parameters can be determined by boundary conditions (5.73), (5.74), (5.78) and (5.79) to yield:

$$\begin{cases} a_1 + a_2 + a_3 = 1 \\ a_1 + 2a_2 + 3a_3 = \alpha_8 \dfrac{\tau_{sx}\delta}{\mu_L \bar{u}} \\ 2a_2 = \dfrac{\alpha_8 \delta^2}{\mu_L \bar{u}} \left[\dfrac{\partial u_w}{\partial t} + \dfrac{\partial p_L}{\partial x} - S_{u,d} - a_x \right] \end{cases} \tag{5.84}$$

$$\begin{cases} b_1 + b_2 + b_3 = 1 \\ b_1 + 2b_2 + 3b_3 = \alpha_9 \dfrac{\tau_{sy}\delta}{\mu_L \bar{u}} \\ 2b_2 = \dfrac{\alpha_9 \delta^2}{\mu_L \bar{v}} \left[\dfrac{\partial v_W}{\partial t} + \dfrac{\partial p_L}{\partial y} - S_{v,d} - a_y \right] \end{cases} \tag{5.85}$$

Using the above assumed temperature profile (5.83), Equation (5.69) can be rewritten in terms of Λ as:

$$\begin{aligned} &\frac{\partial}{\partial t}(\Lambda\delta) + \frac{\partial}{\partial x}(F_1 \Lambda \bar{u}\delta) + \frac{\partial}{\partial y}(G_1 \Lambda \bar{v}\delta) = \\ &2\frac{\partial \delta}{\partial t} + \frac{\partial}{\partial x}(F_2 \bar{u}\delta) + \frac{\partial}{\partial y}(G_2 \bar{v}\delta) + \frac{3\Lambda\alpha}{\delta} \end{aligned} \tag{5.86}$$

where

$$\begin{aligned} F_1 &= P(a_1, a_2, a_3); \qquad G_1 = P(b_1, b_2, b_3) \\ F_2 &= Q(a_1, a_2, a_3); \qquad G_2 = Q(b_1, b_2, b_3) \end{aligned} \tag{5.87}$$

$$P(x, y, z) = \frac{4\left(\frac{2}{15}x + \frac{1}{12}y + \frac{2}{35}z\right)}{\frac{1}{2}x + \frac{1}{3}y + \frac{1}{4}z}$$

$$Q(x, y, z) = \frac{\left(\frac{1}{6}x + \frac{1}{12}y + \frac{z}{20}\right)}{\frac{1}{2}x + \frac{1}{3}y + \frac{1}{4}z}$$

Equations (5.66), (5.67), (5.68), and (5.86) can now be solved simultaneously by numerical methods to obtain the discrete values of δ, $\bar{u}$, $\bar{v}$ and Λ for general case. doing this will be described in the next section.

For numerical analysis, it is convenient to write the above four equations in a general form as:

$$\frac{\partial}{\partial t}(\phi\delta) + \frac{\partial}{\partial x}(g_\phi \phi \bar{u}\delta) + \frac{\partial}{\partial y}(h_\phi \phi \bar{v}\delta) = S_\phi \tag{5.88}$$

where ϕ stands for dependent variables 1, $\bar{u}$, $\bar{v}$ and Λ; g_ϕ and h_ϕ represent coefficients associated with ϕ arising from integration, and S_ϕ is a 'source' term. The latter three quantities are defined in Table 5.1, in which F_1, F_2, G_1 and G_2 are given in Equation (5.87).

It is interesting to note that Equation (5.88) exhibits a very similar form to the general gas phase transport equation, if we view the film thickness δ as a 'density' function, although it contains no diffusion terms.

Table 5.1: Definition of g_ϕ, h_ϕ and S_ϕ in Equation (5.88)

ϕ	g_ϕ	h_ϕ	S_ϕ
1	1	1	$\frac{\dot{m}_v + \dot{m}_{net}}{\rho_L}$
$\bar{u}$	$\frac{\int_0^1 f(\eta)^2 d\eta}{\left(\int_0^1 f(\eta) d\eta\right)^2}$	$\frac{\int_0^1 f g d\eta}{\left(\int_0^1 f d\eta\right)\left(\int_0^1 g d\eta\right)}$	$\frac{1}{\rho_L}\left(-\delta\frac{\partial p_L}{\partial x} + \tau_{sx} - \beta_1\mu_L\frac{\bar{u}}{\delta} + \tilde{S}^L_{u,d}\right) + \bar{a}_x\delta$
$\bar{v}$	$\frac{\int_0^1 f g d\eta}{\left(\int_0^1 f d\eta\right)\left(\int_0^1 g d\eta\right)}$	$\frac{\int_0^1 g(\eta)^2 d\eta}{\left(\int_0^1 g(\eta) d\eta\right)^2}$	$\frac{1}{\rho_L}\left(-\delta\frac{\partial p_L}{\partial y} + \tau_{sy} - \beta_2\mu_L\frac{\bar{v}}{\delta} + \tilde{S}^L_{v,d}\right) + \bar{a}_y\delta$
Λ	F_1	F_2	$2\frac{\partial\delta}{\partial t} + \frac{\partial}{\partial x}(F_2\bar{u}\delta) + \frac{\partial}{\partial y}(G_2\bar{v}\delta) + \frac{-3(1+\Lambda)\alpha}{\delta}$

5.6.3 Analytical Solutions for Simplified Cases

When the local equilibrium model for the momentum equations is invoked, the need to solve equations (5.67) and (5.68) is eliminated, and this not only enables substantial simplification of the problem but also allows for the analytical solution for some particular cases. Before particular cases are considered, the equilibrium equations will be assembled first.

Equilibrium Equations

The expressions for the velocities u and v from the local equilibrium equations as follows:

$$u = \frac{1}{2\mu_L}H_1 z^2 + \frac{z}{\mu_L}(\tau_{sx} - H_1\delta) \tag{5.89}$$

$$v = \frac{1}{2\mu_L}H_2 z^2 + \frac{z}{\mu_L}(\tau_{sy} - H_2\delta) \tag{5.90}$$

where

$$H_1 = \frac{\partial p_L}{\partial x} - \rho_L a_x - S^L_{u,d} \tag{5.91}$$

$$H_2 = \frac{\partial p_L}{\partial y} - \rho_L a_y - S^L_{v,d} \tag{5.92}$$

The mean film velocities are given by:

$$\bar{u} = -\frac{1}{3\mu_L}H_1\delta^2 + \frac{1}{2\mu_L}\tau_{sx}\delta \tag{5.93}$$

$$\bar{v} = -\frac{1}{3\mu_L}H_2\delta^2 + \frac{1}{2\mu_L}\tau_{sy}\delta \tag{5.94}$$

The set of local equilibrium equations (5.66) and (5.69) now read:

$$\frac{\partial\delta}{\partial t} + \frac{\partial}{\partial x}(\bar{u}\delta) + \frac{\partial}{\partial y}(\bar{v}\delta) = \frac{\dot{m}_v}{\rho_L} + \frac{\dot{m}_{net}}{\rho_L} \tag{5.95}$$

$$\frac{\partial}{\partial t}(\mathcal{W}\delta) + \frac{\partial}{\partial x}\left(\bar{\mathcal{U}}\delta\right) + \frac{\partial}{\partial y}\left(\bar{\mathcal{V}}\delta\right) = \frac{3\alpha\Lambda\Delta T}{\delta} \tag{5.96}$$

where

$$\Delta T = T_w - T_S, \qquad W = \frac{3+\Lambda}{4}\Delta T \tag{5.97}$$

$$\bar{\mathcal{U}} = (\bar{u} + \bar{u}_1 + \bar{u}_2)\Delta T, \quad \bar{\mathcal{V}} = (\bar{v} + \bar{v}_1 + \bar{v}_2)\Delta T \tag{5.98}$$

in which

$$\bar{u}_1 = \Lambda\left(-\frac{5H_1}{24\mu_L}\delta^2 + \frac{\tau_{sx}}{3\mu_L}\delta\right) \tag{5.99}$$

$$\bar{u}_2 = -(1+\Lambda)\left(-\frac{7H_1}{60\mu_L}\delta^2 + \frac{\tau_{sx}}{5\mu_L}\delta\right) \tag{5.100}$$

$$\bar{v}_1 = \Lambda\left(-\frac{5H_2}{24\mu_L}\delta^2 + \frac{\tau_{sy}}{3\mu_L}\delta\right) \tag{5.101}$$

$$\bar{v}_2 = -(1+\Lambda)\left(-\frac{7H_2}{60\mu_L}\delta^2 + \frac{\tau_{sy}}{5\mu_L}\delta\right) \tag{5.102}$$

The problem of solving equations (5.95) and (5.96) is apparently considerably easier. In addition, if the film flow is two dimensional, we can show that the analytical solutions can, under certain circumstances, be obtained through the use of the method of characteristics. This point is elaborated below.

Two-dimensional case

In the 2D case Equations (5.95) and (5.96) can be rewritten in a two-dimensional x-z coordinate system in the following form:

$$P_1(x,\delta,t)\frac{\partial\Lambda}{\partial t} + Q_1(x,\delta,t)\frac{\partial\Lambda}{\partial x} = R_1(x,\delta,t,\Lambda) \tag{5.103}$$

$$\frac{\partial\delta}{\partial t} + Q_2(x,\delta,t)\frac{\partial\delta}{\partial x} = R_2(x,\delta,t,\Lambda) \tag{5.104}$$

where

$$P_1 = -\frac{\Delta T \delta}{4}, \qquad Q_1 = \frac{\partial}{\partial \Lambda}(\bar{U}\delta), \qquad Q_2 = \frac{\partial}{\partial \delta}(\bar{u}\delta) \tag{5.105}$$

$$\begin{aligned} R_1 = {} & \frac{3\alpha\Lambda\Delta T}{\delta} - \frac{3+\Lambda}{4}\Delta T\frac{\partial \delta}{\partial t} - \frac{3+\Lambda}{4}\delta\frac{\partial \Delta T}{\partial t} \\ & - \frac{\partial(\bar{U}\delta)}{\partial \delta}\frac{\partial \delta}{\partial x} - \frac{\partial(\bar{U}\delta)}{\partial H_1}\frac{\partial H_1}{\partial x} - \frac{\partial(\bar{U}\delta)}{\partial \Delta T}\frac{\partial \Delta T}{\partial x} - \frac{\partial(\bar{U}\delta)}{\partial \tau_{sx}}\frac{\partial \tau_{sx}}{\partial x} \end{aligned} \tag{5.106}$$

$$R_2 = \frac{\dot{m}_v}{\rho_L} + \frac{\dot{m}_{net}}{\rho_L} - \frac{\partial(\bar{u}\delta)}{\partial H_1}\frac{\partial H_1}{\partial x} - \frac{\partial(\bar{u}\delta)}{\partial \tau_{sx}}\frac{\partial \tau_{sx}}{\partial x} \tag{5.107}$$

Equation (5.104) describes a hyperbolic wave traveling along the positive x direction. This equation is equivalent to the following pair of ordinary differential equations:

$$dt = \frac{dx}{Q_2(x,\delta,t)} = \frac{d\delta}{R_2(x,\delta,t,\Lambda)} \tag{5.108}$$

the first of which

$$\frac{dx}{dt} = Q_2(x,\delta,t) \tag{5.109}$$

represents a single family of characteristic lines on the x-t plane. If the initial data of (5.108) are given by

$$g_3(\delta, x) = 0 \quad \text{at } t = 0$$

then the analytical solution of (5.104) can be sought using a simple method proposed by Hildebrandt (1949). Accordingly, if

$$g_1(\delta,x,t) = d_1(\Lambda) \tag{5.110}$$

$$g_2(\delta,x,t) = d_2(\Lambda) \tag{5.111}$$

are two independent integrals of (5.108), then the elimination of x, δ, t from (5.110) and (5.111) yields a functional relation $G(d_1, d_2) = 0$, and the particular solution is

$$G[g_1(\delta,x,t), g_2(\delta,x,t), \Lambda] = 0 \tag{5.112}$$

This equation also yields the equation for δ of the form:

$$\delta = \delta(x,t,\Lambda) \tag{5.113}$$

Equation (5.113) contains an unknown variable Λ, an equation for which is obtained by substituting 5.113 into Equation (5.103) to yield:

$$\tilde{P}_1(x,\Lambda,t)\frac{\partial \Lambda}{\partial t} + \tilde{Q}_1(x,\Lambda,t)\frac{\partial \Lambda}{\partial x} = \tilde{R}_1(x,t,\Lambda) \tag{5.114}$$

This equation can be solved, using the same method as described above, to give:

$$\Lambda = \Lambda(x,t)$$

which is subsequently substituted into (5.113) to yield δ.

In most cases, however, analytical solutions are extremely difficulty to obtain and one has to resort numerical solutions. In the subsequent subsections, the numerical solution procedure of general film equations are described.

5.6.4 Discretisation of Film Equations

In this subsection, the depth-averaged film differential equations of mass, momentum and energy are discretised using the finite volume approach. Upon performing spatial and temporal integration, Equation (5.88) becomes:

$$\frac{1}{\Delta t}\int_t^{t+\Delta t}\left[\int_{\mathcal{A}_P}\left(\frac{\partial}{\partial t}(\phi\delta) + \frac{\partial}{\partial x}(g_\phi \bar{u}\phi\delta) + \frac{\partial}{\partial y}(h_\phi \bar{v}\phi\delta)\right) d\mathcal{A}_P\right] dt = (\tilde{S}_\phi)_P \tag{5.115}$$

where

$$(\tilde{S}_\phi)_P = \frac{1}{\Delta t}\int_t^{t+\Delta t}\left[\int_{\mathcal{A}_P} S_\phi d\mathcal{A}_P\right] dt \tag{5.116}$$

Here $\mathcal{A}_P$ is the area of a typical control volume as illustrated in Figure 5.1, which extends from the wall to the film surface. All the dependent variables and flow properties are located at the geometric center, (P) of the control volume. This practice, known as the 'non-staggered grid arrangement', minimises the amount of geometrical information required about the computational grid and facilitates efficient computer programming. But, care has to be taken in evaluating velocity values at the cell face, in order to avoid grid-scale oscillations of pressure (Rhie 1981). The treatment for this will be illustrated later.

Equation (5.115) can be rewritten as:

$$\frac{(\phi\delta)^n - (\phi\delta)^o}{\Delta t}\Delta x \Delta y + \frac{1}{\Delta t}\int_t^{t+\Delta t}[I_e - I_w + I_n - I_s]\, dt = \tilde{S}_\phi \tag{5.117}$$

in which the superscript ^{n} and ^{o} indicate, respectively, the values estimated at the new time and old time levels; and I_i, (i=e, s, w, n) are given by:

$$I_e = (g_\phi)_e F_c \phi_e, \quad I_w = (g_\phi)_w F_w \phi_w$$
$$I_n = (h_\phi)_n F_n \phi_n, \quad I_w = (h_\phi)_s F_s \phi_s \tag{5.118}$$

$$F_e = (\bar{u}\delta l)_e, \quad F_w = (\bar{u}\delta l)_w$$
$$F_n = (\bar{v}\delta l)_n, \quad F_s = (\bar{v}\delta l)_s \tag{5.119}$$

where l_i (i=e,s,w,n) denote the cell face lengths.

For temporal discretisation, the time averaging of a quantity F in the interval, Δt, may be approximated by

$$\frac{1}{\Delta t}\int_t^{t+\Delta t} F dt \approx \beta F^n + (1-\beta)F^o \tag{5.120}$$

in which $0 \leq \beta \leq 1$. Here we take $\beta = 1$, which corresponds to the fully implicit scheme.

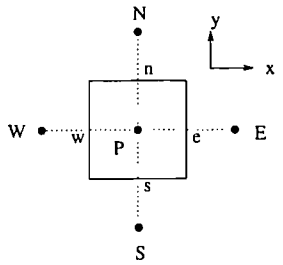


Figure 5.1: Layout of a typical control volume.

In the present study, the upwind difference scheme is employed to evaluate the convective fluxes at the cell faces because of its simplicity and obedience to the physical bounds on ϕ under all conditions. The latter is important, because Equation (5.115) does not contain second-order diffusion terms, which act to suppress non-physical oscillations generated by higher-order schemes. The first-order scheme also produces discretised equation forms that are easy to solve, but it can lead to numerical diffusion (Patankar 1980; Raithby 1976). Thus, care must be taken to minimise such diffusion at the cost of using fine meshes.

In the upwind differencing scheme, the convective cell face value is taken to be

that at the upstream node along the same coordinate line, e.g.

$$\phi_e = \begin{cases} \phi_P, \text{ if } F_e > 0 \\ \phi_E, \text{ if } F_e < 0 \end{cases} \tag{5.121}$$

Using the above expression and similar ones for the other faces, the discretised equation for the general film transport equation can be assembled as:

$$A_P \phi_P^n = \sum_C A_C \phi_C^n + A_P^o \phi_P^o + (\tilde{S}_\phi)_P \tag{5.122}$$

in which C stands for the neighbouring nodes of P; and the A coefficients are defined as follows:

$$\begin{aligned} A_E &= max[0, -(g_\phi)_e F_e] \\ A_W &= max[0, (g_\phi)_w F_w] \\ A_N &= max[0, -(h_\phi)_n F_n] \\ A_S &= max[0, (h_\phi)_s F_s] \end{aligned} \tag{5.123}$$

$$A_P^o = \frac{\delta^o \mathcal{A}_P}{\Delta t} \tag{5.124}$$

$$A_P = \sum_C A_C + [F_e(g_\phi)_e - F_w(g_\phi)_w + F_n(h_\phi)_n - F_s(h_\phi)_s] + \frac{(\delta)_P^n \mathcal{A}_P}{\Delta t} \tag{5.125}$$

The last term on the right side of Equation (5.125), can be evaluated using the following discretised continuity equation (corresponding to $\phi = 1$):

$$\frac{(\delta)_P^n \mathcal{A}_P - (\delta)_P^o \mathcal{A}_P}{\Delta t} + F_e - F_w + F_n - F_s = \tilde{S}_1 \tag{5.126}$$

where

$$\tilde{S}_1 = (\frac{\dot{m}_{net} + \dot{m}_v}{\rho_L})_P \mathcal{A}_P \tag{5.127}$$

Inserting (5.126) into (5.125) and making necessary rearrangement gives:

$$\begin{aligned} A_P = \sum_C A_C + A_P^o \phi_P^o + \tilde{S}_1 + \\ \{[g_\phi)_e - 1]F_e - [(g_\phi)_w - 1]F_w + [(h_\phi)_n - 1]F_n - [(h_\phi)_s - 1]F_s\} \end{aligned} \tag{5.128}$$

In the above expressions, the face values of g_ϕ, h_ϕ, and δ are evaluated as:

$$(g_\phi)_e = f_e\,(g_\phi)_E + (1 - f_e)\,(g_\phi)_P$$

$$
\begin{aligned}
(g_\phi)_w &= f_w (g_\phi)_W + (1 - f_w)(g_\phi)_P \\
(h_\phi)_n &= f_n (h_\phi)_N + (1 - f_n)(h_\phi)_P \\
(h_\phi)_s &= f_n (h_\phi)_S + (1 - f_s)(h_\phi)_P \\
\delta_e &= f_e \delta_E + (1 - f_e)\delta_P \\
\delta_w &= f_w \delta_W + (1 - f_w)\delta_P \\
\delta_n &= f_n \delta_N + (1 - f_n)\delta_P \\
\delta_s &= f_s \delta_S + (1 - f_s)\delta_P
\end{aligned}
\tag{5.129}
$$

$$
\begin{aligned}
f_e &= \frac{\Delta x_{e-P}}{\Delta x_{E-P}} = \frac{x_e - x_P}{x_E - x_P} \\
f_w &= \frac{\Delta x_{P-w}}{\Delta x_{P-W}} = \frac{x_P - x_w}{x_P - x_W} \\
f_e &= \frac{\Delta x_{n-P}}{\Delta x_{N-P}} = \frac{x_n - x_P}{x_N - x_P} \\
f_w &= \frac{\Delta x_{P-s}}{\Delta x_{P-S}} = \frac{x_P - x_s}{x_P - x_S}
\end{aligned}
\tag{5.130}
$$

Expressions of the above form are also used for the cell face values of pressure. The face values of the velocities are evaluated using the practice of Rhie and Chow (1983) which is to be described later.

Attention is now directed to the treatment of the source terms. The source term for the continuity equation is given in (5.127). If a source term contains ϕ explicitly, it can be evaluated based on the approach outlined by Patankar (1980). In this, the differential source term S_ϕ is assumed to be a quasi-linear function of ϕ:

$$S_\phi = S_\phi^I + S_\phi^{II}\phi \tag{5.131}$$

where it is required that

$$S_\phi^{II} < 0 \tag{5.132}$$

in order to obey the boundedness requirement to be discussed in Chapter 6.

In accordance with this, the expressions of S_ϕ^I and S_ϕ^{II} for variables $\bar{u}$, $\bar{v}$ and Λ are assembled in Table 5.2. Assuming that S_ϕ^I and S_ϕ^{II} remain constant during the time interval Δt, the integral source term in Equation (5.134) takes the following form:

$$\left(\tilde{S}_\phi\right)_P = \frac{1}{\Delta t}\int_t^{t+\Delta t}\int_{\mathcal{A}} \tilde{S}_\phi d\mathcal{A}dt \approx \tilde{S}_\phi^I + \tilde{S}_\phi^{II}\phi_P^n \tag{5.133}$$

Table 5.2: Definition of S_ϕ^I and S_ϕ^{II} in Equation (5.131)

ϕ	S_ϕ^I	S_ϕ^{II}
$\bar{u}$	$\frac{1}{\rho_L}\left(-\delta\frac{\partial p_L}{\partial x}+\tau_{sx}+\tilde{S}_{u,d}^L\right)+\bar{a}_x\delta$	$-\frac{\beta_1\mu_L}{\delta}$
$\bar{v}$	$\frac{1}{\rho_L}\left(-\delta\frac{\partial p_L}{\partial y}+\tau_{sy}+\tilde{S}_{v,d}^L\right)+\bar{a}_y\delta$	$-\frac{\beta_2\mu_L}{\delta}$
Λ	$2\frac{\partial\delta}{\partial t}+\frac{\partial}{\partial x}(F_2\bar{u}\delta)+\frac{\partial}{\partial y}(G_2\bar{v}\delta)-\frac{3\alpha}{\delta}$	$-\frac{3\alpha}{\delta}$

Insertion of (5.133) into (5.134) leads to

$$A_P^*\phi_P^n=\sum_C A_C\phi_C^n+A_P^o+\tilde{S}_\phi^I \tag{5.134}$$

where $A_P^*=(A_P-\tilde{S}_\phi^{II})$.

Hereafter, for the sake of simplicity, the superscript * for A_P and the overbars for the depth average velocity components will be omitted.

Finally, to enable evaluation of film surface temperatures at the grid nodes, it is necessary to cast Equation (5.13) into an algebraic equation. To this end, the following approximations are made:

$$\nabla T_L\approx\frac{\partial T_L}{\partial z};\quad \nabla T_G\approx\frac{\partial T_G}{\partial z} \tag{5.135}$$

Equation (5.135) is justified by the thin film assumption.

Thus, the liquid heat flux at the surface can be calculated by:

$$\begin{aligned}k_L\left.\frac{\partial T_L}{\partial z}\right|_s&=\frac{\partial T_L}{\partial\eta}\frac{\partial\eta}{\partial z}=k_L\frac{1}{\delta}\frac{\partial}{\partial\eta}\left(T_s+(T_s-T_W)\theta(\eta)\right)_s\\&=-k_L\frac{T_s-T_W}{\delta}(3+2\Lambda)\end{aligned} \tag{5.136}$$

The gas heat flux can be evaluated from Equation (3.67) as:

$$k_G\left.\frac{\partial T_G}{\partial z}\right|_s=K_{eff}\frac{T_G-T_W}{Y} \tag{5.137}$$

Here T_G is the gas temperature at a distance Y along the wall normal; and K_{eff} is defined in (3.69).

Upon applying to (5.13) a similar discretisation procedure to that employed for the geneal film transport equation, with the use of (5.136) (5.137), there results

$$(T_s)_P=(T_W)_P+(\dot{m}_v h_{fg})_P\left(\frac{\delta}{k_L(3+2\Lambda)}\right)_P$$

$$-\left(K_{eff}\frac{T_G-T_W}{Y}\right)_P\left(\frac{\delta}{k_L(3+2\Lambda)}\right)_P \tag{5.138}$$

5.6.5 Solution Procedure

The discretised film equations are solved by the following procedure, which will be embedded in the overall solution procedure including the gas-spray equations, to be described later in Chapter 6.

Predictor step

In this step, initial fields $\delta^{(1)}$, $\Lambda^{(1)}$ and $\left(u^{(1)}, v^{(1)}\right)$ are sought in the following sequence.

First, the implicit set of momentum equations of the following kinds are solved, using the initial or previous time step δ and C fields.

$$u_P^{(1)} = H_P(u_C^{(1)}) - D_1\Delta_x p_\sigma - D_1\Delta_x p_{imp} + A_P^{o'}u_P^o + \tilde{S}_u^{I'} \tag{5.139}$$

$$v_P^{(1)} = H_P(v_C^{(1)}) - D_2\Delta_y p_\sigma - D_2\Delta_y p_{imp} + A_P^{o'}v_P^o + \tilde{S}_v^{I'} \tag{5.140}$$

Here $H_P(\phi_C)$ is defined as:

$$H_P(\phi_C) = \frac{\sum_C \phi_C}{A_P}; \quad A_P^{o'} = \frac{A_P^o}{A_P}$$
$$D_1 = \frac{1}{\rho_L A_P^u}; \quad D_2 = \frac{1}{\rho_L A_P^v} \tag{5.141}$$

and p_σ and p_{imp} ($p_\sigma + p_{imp} = p_L$)are the capillary pressure and impingement pressure respectively; $\tilde{S}_u^{I'}$ and $\tilde{S}_v^{I'}$ are the source terms, after extraction of the pressure terms, divided by A_P; and Δ_x and Δ_y denote the pressure difference operator in the x and y directions, respectively. For example, $\Delta_x p_\sigma$ is a difference approximation of $\int_{\mathcal{A}_P}\delta\frac{\partial p_\sigma}{\partial x}d\mathcal{A}_P$, which, following the usual practice, can be evaluated as:

$$\int_{\mathcal{A}_P}\delta\frac{\partial p_\sigma}{\partial x}d\mathcal{A}_P = \int_x^{x+\Delta x}\int_y^{y+\Delta y}\delta\frac{\partial p_\sigma}{\partial x}dxdy \approx \delta_P\int_y^{y+\Delta y}[p_\sigma]_w^e dy \tag{5.142}$$

As an alternative, by performing integration by parts, the above term may be cast into the form:

$$\int_{\mathcal{A}_P}\delta\frac{\partial p_\sigma}{\partial x}d\mathcal{A}_P = \int_y^{y+\Delta y}[p_\sigma\delta]_w^e dy - \int_x^{x+\Delta x}\int_y^{y+\Delta y}p_\sigma\frac{\partial\delta}{\partial x}dxdy \tag{5.143}$$

The latter practice (.i.e. Equation (5.143)) enables more effective coupling between the pressure and δ, thus giving better numerical results, as confirmed by the numerical experiments carried out in this study.

Thus, we have

$$\Delta_x p_\sigma = \left[(p_\sigma\delta)_e\, l_e - (p_\sigma\delta)_w\, l_w - (p_\sigma)_P\,(\delta_e l_e - \delta_w l_w)\right]$$
$$\Delta_y p_\sigma = \left[(p_\sigma\delta)_n\, l_n - (p_\sigma\delta)_s\, l_s - (p_\sigma)_P\,(\delta_n l_n - \delta_s l_s)\right] \tag{5.144}$$

$$\Delta_x p_{imp} = \left[(p_{imp}\delta)_e\, l_e - (p_{imp}\delta)_w\, l_w - (p_{imp})_P\,(\delta_e l_e - \delta_w l_w)\right]$$
$$\Delta_y p_{imp} = \left[(p_{imp}\delta)_n\, l_n - (p_{imp}\delta)_s\, l_s - (p_{imp})_P\,(\delta_n l_n - \delta_s l_s)\right] \tag{5.145}$$

Here the face values of $p's$ and δ are evaluated according to (5.129).

Next, the data of $(u^{(1)},\ v^{(1)})$ obtained above are used to solve the discretised equation for δ, which is assembled based on the continuity equation (5.126) as:

$$A_P\delta_P^{(1)} = \sum_C A_C\delta_C^{(1)} + A_P^o\delta_P^o + S_1^{(1)} \tag{5.146}$$

where

$$A_E = max(0, -u_e), \quad A_W = max(0, u_w)$$
$$A_N = max(0, -u_n), \quad A_S = max(0, u_s) \tag{5.147}$$
$$A_P = \sum_C A_C + \frac{\mathcal{A}_P}{\Delta t} + [u_e - u_w + u_n - u_s]$$

Here it is clear that evaluation of the coefficients A's requires the expressions for the face velocities: $(u^{(1)})_i$ and $(v^{(1)})_i$ (i=e, s, w, n). In the collocated variable arrangement, these velocities need to be expressed in terms of the nodal velocities (in order to calculate the mass fluxes) and the neighbouring capillary pressures (to allow formulation of a suitable discretised film interface curvature equation, as will be described later). This is done by using the interpolation practice proposed by Rhie and Chow (1983). For instance, the u-momentum equation at cell face e and the v-momentum equation at cell face n (referring to Figure 5.1) are assembled as:

$$u_e^{(1)} = \overline{H_e(u_C^{(1)})} - \overline{(D_1)_e}\,(\Delta_x p_\sigma)_e\,\overline{(D_1)_e}\,(\Delta_x p_{imp})_e + \overline{A_p^{o'}u_P^o} + \overline{\tilde{S}_u^{I'}}$$
$$v_n^{(1)} = \overline{H_n(v_C^{(1)})} - \overline{(D_2)_n}\,(\Delta_y p_\sigma)_n\,\overline{(D_2)_n}\,(\Delta_y p_{imp})_n + \overline{A_p^{o'}v_P^o} + \overline{\tilde{S}_v^{I'}} \tag{5.148}$$

where the overbars denote the averaging form of Rhie and Chow (1983) on the nodal momentum coefficients appearing under them, e.g.

$$\overline{H_e(u_C^{(1)})} = f_e H_E(u_C^{(1)}) + (1 - f_e)H_P(u_C^{(1)})$$
$$\overline{(D_1)_e} = f_e\,(D_1)_E + (1 - f_e)\,(D_1)_P \tag{5.149}$$

and

$$(\Delta_x p_\sigma)_e = -l_e\sigma\left(\mathcal{C}_E^{(o)}\delta_E^{(o)} - \mathcal{C}_P^{(o)}\delta_P^{(o)} - \overline{\left(\mathcal{C}_P^{(o)}\right)}_e\left(\delta_E^{(o)} - \delta_P^{(o)}\right)\right) \tag{5.150}$$

$$(\Delta_y p_\sigma)_n = -l_n\sigma\left(\mathcal{C}_N^{(o)}\delta_N^{(o)} - \mathcal{C}_P^{(o)}\delta_P^{(o)} - \overline{\left(\mathcal{C}_P^{(o)}\right)}_e\left(\delta_N^{(o)} - \delta_P^{(o)}\right)\right) \tag{5.151}$$

$$(\Delta_x p_{imp})_e = l_e\left((p_{imp})_E^{(o)}\delta_E^{(o)} - (p_{imp})_P^{(o)}\delta_P^{(o)} - \overline{\left((p_{imp})_P^{(o)}\right)}_e\left(\delta_E^{(o)} - \delta_P^{(o)}\right)\right) \tag{5.152}$$

$$(\Delta_y p_{imp})_n = l_n\left((p_{imp})_N^{(o)}\delta_N^{(o)} - (p_{imp})_P^{(o)}\delta_P^{(o)} - \overline{\left((p_{imp})_P^{(o)}\right)}_e\left(\delta_N^{(o)} - \delta_P^{(o)}\right)\right) \tag{5.153}$$

The updated fields of $\delta^{(1)}$ and $(u^{(1)}, v^{(1)})$ are then used to evaluate the coefficients and source term in the discretised energy equation:

$$A_P\Lambda_P^{(1)} = \sum_C A_C\Lambda_C^{(1)} + A_P^o\Lambda_P^o + \tilde{S}_\Lambda^I \tag{5.154}$$

where

$$\begin{aligned}\tilde{S}_\Lambda^I &= 2\frac{\delta_P^{(1)}\mathcal{A}_P - \delta_P^o\mathcal{A}_P}{\Delta t} - \frac{3\alpha}{\delta_P^{(1)}}\mathcal{A}_P \\ &+ (F_2)_e u_e^{(1)}\delta_e^{(1)}l_e - (F_2)_w u_w^{(1)}\delta_w^{(1)}l_w \\ &+ (G_2)_n u_n^{(1)}\delta_n^{(1)}l_n - (G_2)_s u_s^{(1)}\delta_s^{(1)}l_s\end{aligned} \tag{5.155}$$

Solution of (5.154) yields the $\Lambda^{(1)}$ field.

Finally, the film surface temperature field T_s can be calculated from (5.138) as:

$$\begin{aligned}(T_s)_P^{(1)} &= (T_W)_P^{(1)} + (\dot{m}_v h_{fg})_P^{(o)}\left(\frac{\delta}{k_L(3+2\Lambda)}\right)_P^{(1)} \\ &- \left(K_{eff}\frac{T_G - T_W}{Y}\right)_P^{(1)}\left(\frac{\delta}{k_L(3+2\Lambda)}\right)_P^{(1)}\end{aligned} \tag{5.156}$$

This in turn enables the calculation of $\dot{m}_v$ field:

$$\dot{m}_v^{(1)} = \frac{Sh_r^{(o)}r}{\rho\mathcal{D}}\frac{\frac{P_{v,\infty}}{P_T} - \frac{P_{v,s}^{(1)}}{P_T}}{1 - \frac{P_{v,s}^{(1)}}{P_T}} \tag{5.157}$$

where $P_{v,s}^{(1)}$ is evaluated from the phase equilibrium condition (5.15) using $T_s^{(1)}$.

As the resulting velocity fields, $(u^{(1)}, u^{(1)})$ satisfy local momentum equations but not the continuity equation, the estimated dependent variables in this step are only a first approximation. They have to be corrected repeatedly until prespecified convergence criteria are satisfied, as illustrated below.

Corrector step

Main issues involved in the correctors are now elaborated for a particular corrector step, i.e., $(k-1)$-th corrector, at which the values of the variables are denoted by the superscript $^{(k)}$ $(k \geq 2)$.

To deal with capillary pressure, it is necessary to evaluate the curvature $\mathcal{C}$. This is done by deriving a discretised equation for it, thus avoiding the numerical problems of discretising second order differential terms, e.g., $\partial^2\delta/\partial x^2$ and $\partial^2\delta/\partial y^2$, on non-smooth data. This practice also helps achieve better accuracy. The starting point is the set of the discretised continuity and cell face velocity equations:

Continuity

$$\frac{\delta_P^{(k)}\mathcal{A}_P - \delta_P^{o}\mathcal{A}_P}{\Delta t} + \delta_e^{(k)}u_e^{(k)}l_e - \delta_w^{(k)}u_w^{(k)}l_e + \delta_n^{(k)}u_n^{(k)}l_n - \delta_s^{(k)}u_s^{(k)}l_s = S_1^{(k)} \tag{5.158}$$

Cell face velocities

$$\begin{aligned}
&\frac{\delta_e^{(k)}}{\delta_e^{(k-1)}}u_e^{(k)} = \overline{H_e(u_C^{(k-1)})} - \overline{(D_1)_e}\,(\Delta_x p_\sigma)_e^{(\mathcal{C}^k,\,\delta^{(k-1)})} \\
&-\overline{(D_1)_e}\,(\Delta_x p_{imp})^{(\delta^{(k-1)})} + \overline{\left(A_P^{o'}u_P^o\right)_e} + \overline{\left(\tilde{S}_u^{I^{k'}}\right)_e} \\
&\\
&\frac{\delta_n^{(k)}}{\delta_n^{(k-1)}}v_n^{(k)} = \overline{H_n(v_C^{(k-1)})} - \overline{(D_2)_n}\,(\Delta_y p_\sigma)_n^{(\mathcal{C}^k,\,\delta^{(k-1)})} \\
&-\overline{(D_2)_n}\,(\Delta_y p_{imp})^{(\delta^{(k-1)})} + \overline{\left(A_P^{o'}v_P^o\right)_n} + \overline{\left(\tilde{S}_v^{I^{k'}}\right)_n}
\end{aligned} \tag{5.159}$$

.....

.....

Here ..... denotes the omitted expressions for u_w and u_s similar to those of u_e and u_n; $(\Delta_x p_\sigma)_e^{(\mathcal{C}^k,\,\delta^{(k-1)})}$ is obtained from (5.150) by replacing $\delta^{(o)}$ with $\delta^{(k-1)}$ and $\mathcal{C}^{(o)}$ with $\mathcal{C}^{(k)}$. Similar explanations apply to other pressure difference terms.

For the purpose of deriving an equation for $\mathcal{C}$, $\mathcal{C}_P$ is first linked to δ_P, starting from integration of (5.6):

$$\int_{\mathcal{A}_P} \mathcal{C}\,d\mathcal{A}_P \approx -\int_{\mathcal{A}_P} \nabla\cdot\nabla\delta\,d\mathcal{A}_P \tag{5.160}$$

This can be approximated as:

$$\mathcal{C}_P\mathcal{A}_P = \left(\frac{\partial\delta}{\partial x}l\right)_w - \left(\frac{\partial\delta}{\partial x}l\right)_e + \left(\frac{\partial\delta}{\partial y}l\right)_s - \left(\frac{\partial\delta}{\partial y}l\right)_n \tag{5.161}$$

The derivatives of δ at the cell faces are evaluated using central differencing. For example, at cell face e, we have

$$\left(\frac{\partial\delta}{\partial x}\right)_e \approx \frac{\delta_E - \delta_P}{\Delta x_{E-P}} \tag{5.162}$$

Similar expressions hold for the other faces. Thus, upon substitution of these expressions into (5.161), there results

$$\delta_P^{(k)} = H(\delta_C^{(k-1)}) + \frac{\mathcal{C}_P\mathcal{A}_P}{b_P} \tag{5.163}$$

where

$$H(\delta_C) = \frac{\sum_C b_C\delta_C}{b_P} \tag{5.164}$$

and

$$\begin{aligned} b_E &= \frac{l_e}{\Delta x_{E-P}}, \qquad b_W = \frac{l_w}{\Delta x_{P-W}} \\ b_N &= \frac{l_n}{\Delta y_{N-P}}, \qquad b_S = \frac{l_s}{\Delta y_{P-S}} \\ b_P &= \sum_C b_C \end{aligned} \tag{5.165}$$

Insertion of (5.163) and(5.159) into the continuity equation (6.105) yields

$$B_P\mathcal{C}_P^{(k)} = \sum_C B_C\mathcal{C}_C^{(k)} + S_\mathcal{C}^{(k)} \tag{5.166}$$

where

$$\begin{aligned} B_E &= \delta_e\sigma l_e^{(k-1)}\overline{(D_1)_e}[(1-f_e)\delta_E^{(k-1)} + f_e\delta_P^{(k-1)}] \\ B_W &= \delta_w\sigma l_w^{(k-1)}\overline{(\Delta_1)_w}[(1-f_w)\delta_W^{(k-1)} + f_w\delta_P^{(k-1)}] \\ B_N &= \delta_n\sigma l_n^{(k-1)}\overline{(D_2)_n}[(1-f_n)\delta_N^{(k-1)} + f_n\delta_P^{(k-1)}] \\ B_S &= \delta_s\sigma l_s^{(k-1)}\overline{(D_2)_s}[(1-f_s)\delta_S^{(k-1)} + f_s\delta_P^{(k-1)}] \end{aligned} \tag{5.167}$$

$$B_P = \sum_C B_C + \frac{\mathcal{A}_P^2}{\Delta t b_P} \tag{5.168}$$

and

$$\begin{aligned} S_\mathcal{C}^{(k)} &= -\frac{H(\delta_C)\mathcal{A}_P}{\Delta t} + \frac{\delta_P^o\mathcal{A}_P}{\Delta t} + \tilde{S}_1^{(k)} \\ &- \left[\delta_e^{(k-1)}u_e' - \delta_w^{(k-1)}u_w' + \delta_n^{(k-1)}v_n' - \delta_s^{(k-1)}v_s'\right] \end{aligned} \tag{5.169}$$

in which

$$
\begin{aligned}
u_e' &= \overline{H_e(u_C^{(k-1)})} - \overline{(D_1)_e}\,(\Delta_x p_{imp})^{(\delta^{(k-1)})} + \overline{\left(A_P^{o^{k'}} u_P^o\right)_e} + \overline{\left(\tilde{S}_u^{I^{k'}}\right)_e} \\
u_w' &= \overline{H_w(u_C^{(k-1)})} - \overline{(D_1)_w}\,(\Delta_x p_{imp})^{(\delta^{(k-1)})} + \overline{\left(A_P^{o^{k'}} u_P^o\right)_w} + \overline{\left(\tilde{S}_u^{I^{k'}}\right)_w} \\
v_n' &= \overline{H_n(v_C^{(k-1)})} - \overline{(D_2)_n}\,(\Delta_y p_{imp})^{(\delta^{(k-1)})} + \overline{\left(A_P^{o^{k'}} v_P^o\right)_n} + \overline{\left(\tilde{S}_v^{I^{k'}}\right)_n} \\
v_s' &= \overline{H_s(v_C^{(k-1)})} - \overline{(D_2)_s}\,(\Delta_y p_{imp})^{(\delta^{(k-1)})} + \overline{\left(A_P^{o^{k'}} v_P^o\right)_s} + \overline{\left(\tilde{S}_v^{I^{k'}}\right)_s}
\end{aligned}
\tag{5.170}
$$

Equation (5.166) is solved to yield C data at the grid nodes, which are subsequently used to update the nodal velocity fields from:

$$u_P^{(k)} = H_P(u_C^{(k-1)}) - D_1\Delta_x p_\sigma - D_1\Delta_x p_{imp} + A_P^{o^{k'}} u_P^o + \tilde{S}_u^{I^{k'}} \tag{5.171}$$

$$v_P^{(k)} = H_P(v_C^{(k-1)}) - D_2\Delta_y p_\sigma - D_2\Delta_y p_{imp} + A_P^{o^{k'}} v_P^o + \tilde{S}_v^{I^{k'}} \tag{5.172}$$

Solution of the above equations yields the velocity field $u^{(k)}$, $v^{(k)}$, which, as evidenced by the above practice, satisfies more strictly the continuity equation.

The $\delta^{(k)}$ field is then obtained from the discretised equation:

$$A_P\delta_P^{(k)} = \sum_C A_C\delta_C^{(k)} + A_P^o\delta_P^o + S_1^{(k)} \tag{5.173}$$

Here the coefficients A's are evaluated base on the updated cell face velocities which are obtained by substituting $C^{(k)}$ field into Equation (5.159).

The new fields ($u^{(k)}$, $v^{(k)}$), and $\delta^{(k)}$ are then used to find $\Lambda^{(k)}$ field by solving the implicit set of equation:

$$A_P^{(k)}\Lambda_P^{(k)} = \sum_C A_C^{(k)}\Lambda_C^{(k)} + A_P^o\Lambda_P^o + S_\Lambda^{(k)} \tag{5.174}$$

The fields $T_s^{(k)}$ and $\dot{m}_v^{(k)}$ can be obtained using the expressions obtained respectively from (5.156) and (5.157) by replacing $^{(1)}$ with $^{(k)}$ and $^{(o)}$ with $^{(k-1)}$.

5.6.6 Test of the Solution Scheme

In order to assess the accuracy of the combined integral/finite volume method just described, it is first applied to test cases for which either partial or complete analytical solutions can be sought. These do not involve spray impingement.

(a) 2-D transient film condensation - In this case condensation of a vapour occurs on a vertical surface under conditions of negligible bulk motion and gas shear,

as illustrated in Figure 5.2. If local equilibrium is assumed, the set of governing equations reduce to the single member:

$$\frac{\partial \delta}{\partial t} + \frac{\rho_L g \delta^2}{\mu_L} \frac{\partial \delta}{\partial x} = \frac{k_L (T_S - T_w)}{h_{fg} \rho_L \delta} \tag{5.175}$$

which is subject to the following initial and boundary conditions:

$$t = 0, \quad \delta = 0 \qquad \text{for all t}$$

$$x = 0, \quad \delta = 0 \qquad \text{for all x}$$

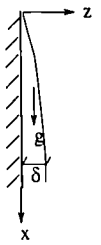


Figure 5.2: Schematic of transient film condensation

The above initial data constitute a Cauchy problem for the governing eqution 5.175, and the analytical solution can be obtained using the characteristic method outlined in Section 5.6.3. The result is

$$\delta = \begin{cases} \left[\dfrac{4k_L \mu_L (T_S - T_w) x}{\rho_L^2 g h_{fg}}\right]^{1/4} \left[\dfrac{t}{t^*}\right] & t \le t^*; \\ \left[\dfrac{4k_L \mu_L (T_S - T_w) x}{\rho_L^2 g h_{fg}}\right]^{1/4} & t \ge t^* \end{cases} \tag{5.176}$$

where $t^* = h_{fg} \mu_L x / k_L g (T_S - T_w)$ is the duration of the transient at a position x. Clearly, Equation (5.176) exhibits a discontinuous first derivative of the film thickness at $t = t^*$ where the film thickness reaches the steady-state value on the limiting characteristics.

Comparison between the numerical prediction and analytical solution is to be made of the film thickness variation with time at a particular location ($x = 1m$); and the following input data are used for both numerical and analytical solutions:

Numerical calculation of the above problem is performed using uniform grid and time step in the region $0 \le x \le 1$. First, sensitivity studies were conducted to determine the effects of the mesh size Δx and Δt on the steady state solution and

Table 5.3: Values of parameters in Equation (5.176)

Parameter	μ_L (Pas)	k_L (J/msK)	T_S (^0C)	T_w (^0C)	ρ_L (kg/m^3)	g (m/s^2)	h_{fg} (MJ/kg)
Value	1	0.15	500	0	840	9.81	1.92

the time taken to reach it. The relative error of steady film thickness at $x = 1m$ is plotted as a function of mesh size in Figure 5.3 for a fixed time step $\Delta t = 1s$. It can be clearly seen that better accuracy is achieved as the mesh size is reduced as would be expected. For the conditions examined, a mesh size of 10 cm or less gives an accuracy of better than 0.0001 (ie. 0.01%) which is quite good.

Figure 5.4 shows that the time taken to reach 99% of the steady state film thickness remains constant as the time step size, Δt, varies in the examined range:$0.01 \leq \Delta t \leq 10$. In this range of Δt, the case of $\Delta x = 0.05$ gives a value of 58s of the steady time whilst the case of Δx= 0.01 produces a lower value of $52s$ which is the same as that obtained analytically. Further evidence is provided in Figure 5.5 which shows that the curves depicting the film thickness variation with time for three time increments virtually coincide each other.

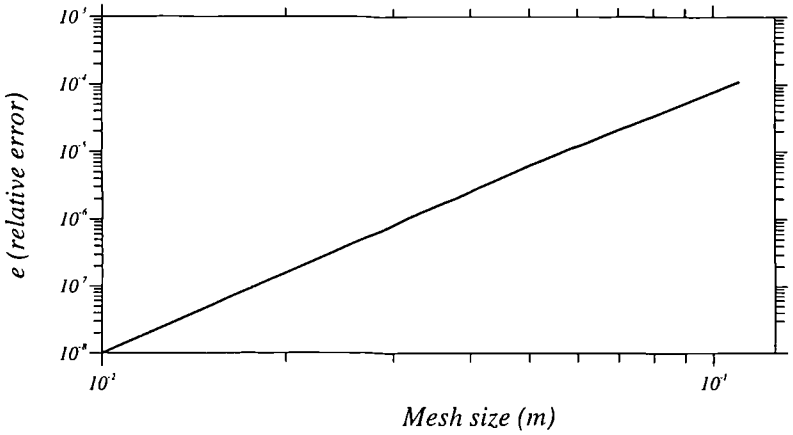


Figure 5.3: Variation with mesh size of the realative error of the steady film thickness between the numerical and analytical solutions

The numerical solution using grid and time increments of $\Delta x = 0.05m$ and $\Delta t = 1s$ respectively, is compared in Figure 5.6 with the analytical one for the film thickness variation with time at position $x = 1\,m$. The agreement is very good

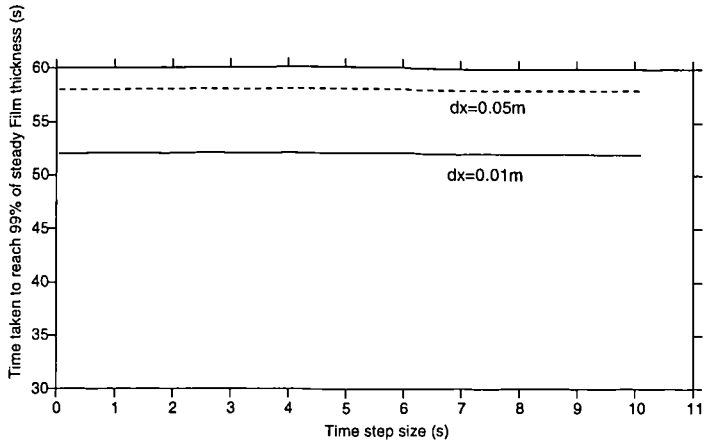


Figure 5.4: Time taken to reach 99% of the steady state value versus the time step size

except in the vicinity of the time at which the analytically-determined film thickness just reaches a steady state. Here the analytical solution shows a cusp, which arises from the discontinuous first derivative of the film thickness as discussed previously; in contrast the numerical solution displays a smooth transition from unsteady to steady state, which is more plausible.

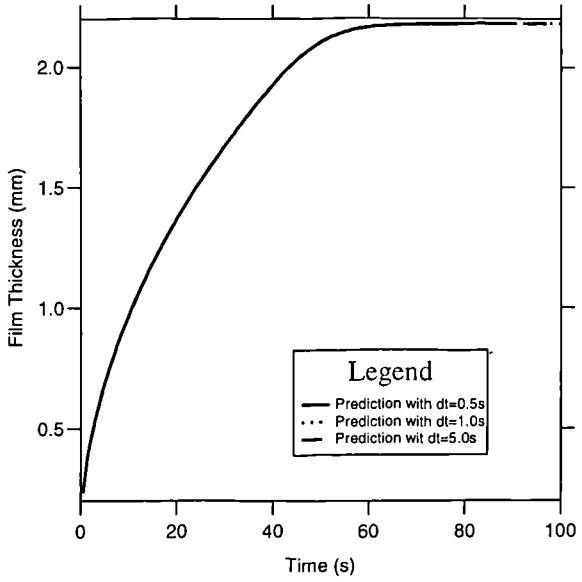


Figure 5.5: Numerical predictions of of film thickness at x=1 m with fixed mesh size (0.05m) and varied time step size: 0.05s, 1s, 5s.

(b) 3-D transient film condensation - Here we consider transient condensation on the interior of a circular tube of radius R inclined at an angle α to the vertical, under conditions such that local equilibrium model approximately applies:i.e. $K = 0.26$ and $K/Pr = 0.001$. Cylindrical coordinates centred on the tube are employed, with θ measured from the upper-most generator (see Figure 5.7). Gravity is the

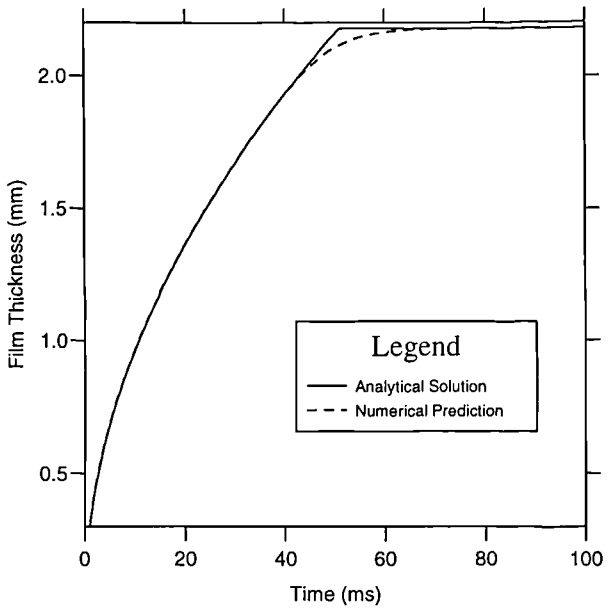


Figure 5.6: Comparison of numerical and analytical solutions of film thickness at x=1 m.

only external force applied on the film. The full equations are solved numerically, subject to the following initial and boundary conditions:

$$t = 0, \quad \delta = \delta_0 \qquad \text{for all z and } \theta$$

$$z = 0, \quad \delta = \delta_0 \qquad \text{for all t and } \theta$$

Here δ_0 is chosen to be very small, ie., 1 micron. The discretised equations are solved in the region: $0 \leq z \leq 1$, $0 \leq \theta \leq 2\pi$, using increments $dz = 0.02m$, $d\theta = 5^0$ and $dt = 10ms$, which are chosen based on sensitivity studies so that reasonable accuracy is maintained.

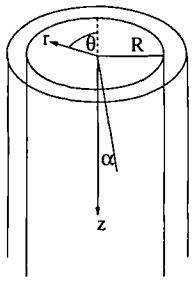


Figure 5.7: Coordinate system sketch

The numerical results obainted for $\alpha = 5^0$ are compared with analytical solutions obtained in the present study for the upper-most and lower-most generators $\theta = 0$ and $\theta = \pi$, using the following local equilibrium equation:

$$\frac{R\nu_L}{\delta^2 g}\frac{\partial \delta}{\partial t} + Rcot\alpha\frac{\partial \delta}{\partial z} + sin\theta\frac{\partial \delta}{\partial \theta} = \frac{ER}{\delta^3 sin\alpha} - \frac{1}{3}\delta sin\theta \tag{5.177}$$

where $E = k_f(T_s - T_w)\mu_L/\rho_L^2 h_{fg} g$.

The above equation indicates clearly that the term involving $\partial\delta/\partial\theta$ vinishes along the generators: $\theta = 0, \pi$. Thus, analytical solutions can be obtained using the characteristic method. They are:

$$\delta = \begin{cases} \delta_{st}(t/t_{st})^{1/2} & t \leq t_{st} \\ \delta_{st} & t \geq t_{st} \end{cases} \tag{5.178}$$

where

$$\delta_{st}^4 = \begin{cases} A + (\delta_0^4 - A)exp\left(-\frac{4}{3}\frac{z}{R}\tan\alpha\right) & \theta = 0; \\ (\delta_0^4 + A)exp\left(-\frac{4}{3}\frac{z}{R}\tan\alpha\right) - A & \theta = \pi \end{cases} \tag{5.179}$$

and

$$t_{st} = \begin{cases} \frac{\nu_L}{g}\left[\frac{3Rz\tan\alpha}{A - \delta_{st}^4}\right]^{1/2} & \theta = 0 \\ \frac{\nu_L}{g}\left[\frac{3Rz\tan\alpha}{A + \delta_{st}^4}\right]^{1/2} & \theta = \pi \end{cases} \tag{5.180}$$

Here $A = 3ER/sin\alpha$, δ_{st} is the steady state film thickness, and t_{st} is the time required to reach the steady state for the film thickness at postion z.

The comparisons are presented in Figure 5.8. Two features are noteworthy: Firstly, good agreement is obtained, except in the vicinity of the cusp, for reasons explained earlier. Secondly, since, as expected, the liquid has a tendency to settle towards the lower-most generator due to gravity, the film thickness at $\theta = \pi$ is consistently larger than at $\theta = 0$. This also explains why the film at $\theta = 0$ takes longer time to reach the steady state than at $\theta = \pi$.

(c) Verification of the criteria for local equilibrium - Earlier, the general conditions for the validity of the local equilibrium model were derived. These are now verified for a specific problem concerning again 2-D transient film condensation on a vertical plate, for which there are now gas shear forces at the interface. Conditions are chosen such that $K = 0.108$ and $K/Pr = 0.042$. In the analysis, the spatial region discretised is chosen to be $0 \leq x/l_0 \leq 1$ ($l_0 = 1m$ being a characteristic

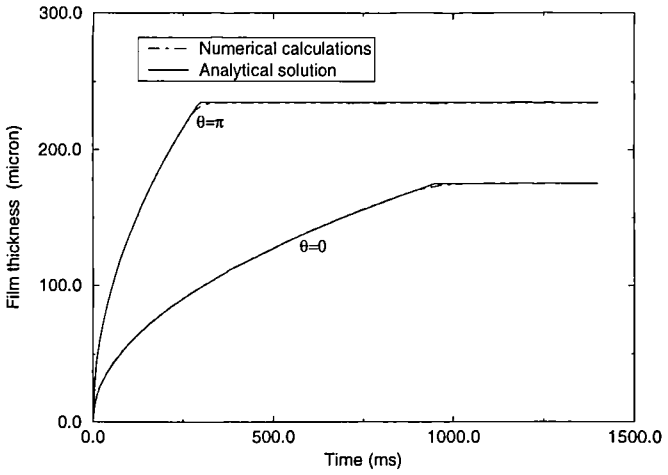


Figure 5.8: Numerical and analytical solutions of film thicknesses at z=1m and $\theta = 0,\ \pi$.

length), and the following transient inputs are used:

$$\tilde{\tau}_s(x,t) = \begin{cases} \dfrac{\tilde{t}}{\Delta\tilde{t}_r}\dfrac{\tilde{x}^{1/4}}{4} & t \le \Delta\tilde{t}_r; \\ \dfrac{\tilde{x}^{1/4}}{4} & t \ge \Delta\tilde{t}_r \end{cases} \tag{5.181}$$

and

$$\theta_s(t) = \begin{cases} 1 + \dfrac{1}{2}\dfrac{\tilde{t}}{\Delta\tilde{t}_r}\dfrac{\tilde{x}^{1/4}}{4} & t \le \Delta\tilde{t}_r; \\ 1.5 & t \ge \Delta\tilde{t}_r \end{cases} \tag{5.182}$$

in which all the parameters are in dimensionless form, as given below:

$$\begin{aligned} \tilde{\tau}_s(x,t) &= \frac{\tau_s}{\rho_L g \delta_N};\ \tilde{t} = t\left[\frac{g\delta_N^2}{\nu_L l_0}\right];\ \tilde{x} = x/l_0 \\ \theta_s &= \frac{T_s - T_w}{(T_s - T_w)_{t=0}};\ \delta_N = \left[\frac{4k_f\mu_L(T_s - T_w)l_0}{\rho_L^2 g h_{fg}}\right]^{1/4} \end{aligned} \tag{5.183}$$

$\Delta\tilde{x}$ and $\Delta\tilde{t}_r$ are chosen to be 0.02 and 0.1 respectively in the analysis.

In this case both the full boundary-layer type equations and the local equilibrium ones are solved numerically. Typical results are shown in Figures 5.9 and 5.10, where the equilibrium solutions are labelled 'quasisteady'.

Figure 5.9 compares variations with time of the dimensionless film thickness, $\tilde{\delta} = \delta/\delta_N$, at three locations, $\tilde{x} = 0.2, 0.6$, and 1.0. It is evident that, in each location,

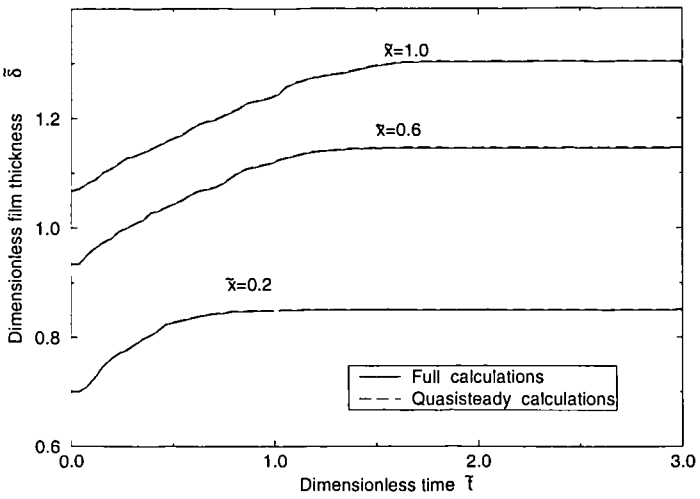


Figure 5.9: Variation of the dimensionless film thickness with time

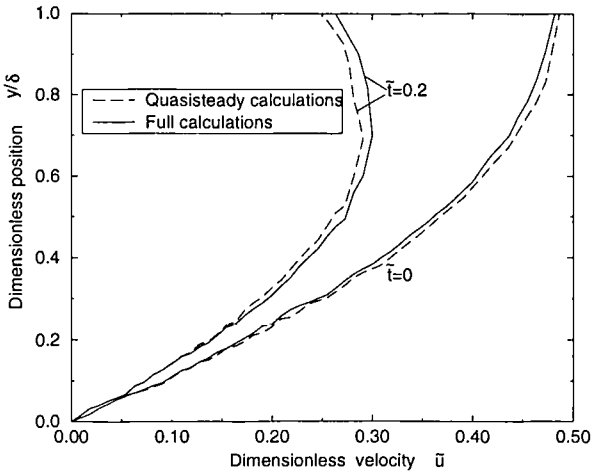


Figure 5.10: Dimensionless velocity distribution across film thickness

there is an excellent match of the film thickness variations obtained from both methods. However, the calculated dimensionless velocity profiles ($\tilde{u} = u\nu_L/g\delta_N^2$) at $\tilde{t} = 0.0$ and $\tilde{t} = 0.2$ for both cases exhibit small discrepancies, as evidenced in Figure 5.10. These are due to the fact that the parameters K and K/Pr used herein are not sufficiently small to absolutely satisfy the local equilibrium conditions.

It is thus clear that the calculations performed for this case do provide support for the conclusions on local equilibrium conditions.

Droplet spreading simulation - The final example, which is illustrated in Figure 5.11, is the spreading of an isothermal droplet on a solid surface, driven only by the capillary pressure, other forces being absent or negligible. The purpose is to see if the capillary pressure effect is predicted properly by the model.

Using cylindrical coordinates, the problem becomes two-dimensional because of axial symmetry. For the purpose of testing the numerical scheme, 'full' momentum equations are solved together with the interface mass continuity equations, despite the fact that the convective term in the momentum equations may be negligible.

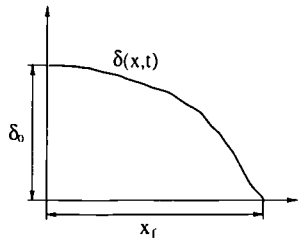


Figure 5.11: Schematic of drop spreading

The simulation starts from a drop which initially takes the shape of a spherical cap, with a volume of $0.12mm^3$, $\nu_L = 10.3cm^2/s$, $x_f = 1.40mm$ and $\delta_0 = 38\mu m$. The spatial and temporal discretised regions are: $0 \leq x \leq 10mm$, $0 \leq t \leq 10ms$, and the increments used are $\Delta x = 0.5mm$ and $\Delta t = 0.5ms$.

The numerical solution revealed that the scaled droplet thickness has a similarity behaviour in the sense that the normalised film thickness δ/δ_0 can be expressed as a single function of the scaled radial position x/x_f, i.e.,

$$\frac{\delta}{\delta_0} = f\left(\frac{x}{x_f}\right)$$

irrespective of the time level. This feature has also been confirmed by another source of data, as shown in Figure 5.12 which compares the calculations with the analytical

solution and experimental data of Diez et al (1993). The analytical solution was obtained by these authors using the lubrication theory which neglects convective terms in momentum equation. It can be seen that the present predictions are in very good agreement with both analytical and experimental data, indicating that the numerical modelling of the capillary pressure is reasonable.

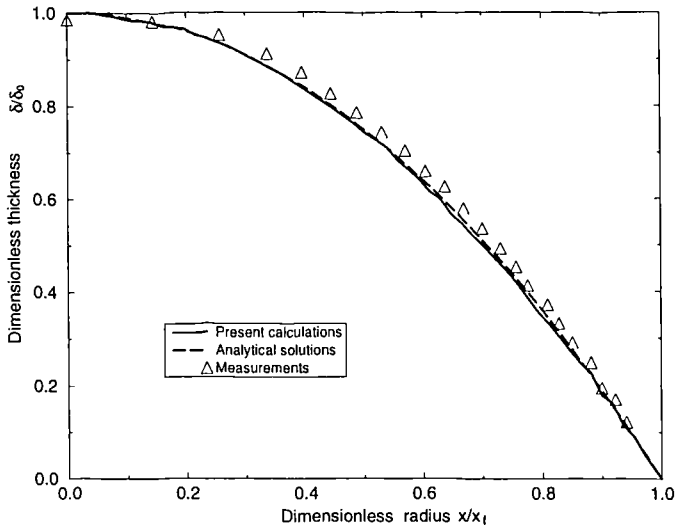


Figure 5.12: Dimensionless droplet spreading profile under the action of capillary pressure

5.7 Closure

In this chapter, a mathematical model of wall film flows has been formulated based on some simplifying assumptions. A major feature of this model is that it takes into account the effects on the film motion of the impingement pressure and tangential momentum imparted by the droplets as well as the gas shear force and capillary pressure. This allows better representation of the film spreading process, which is important in calculating film evaporation.

The general transport equations of wall film flow were established in the boundary layer framework, and the general criteria for them to reduce to local equilibrium equations were derived through an order of magnitude analysis. The full film equations were solved with an efficient numerical method which combines integral and finite-volume methods. This practice offers a particular advantage in that it avoids the need of using three-dimensional meshes which are subjected to modification from

time to time in the course of solution. With this scheme, the numerical solution of the three-dimensional film equations is performed in a two-dimensional framework, thereby substantially reducing the computational effort.

The formulation of the model was extended to film flows along a general curved surface, in terms of orthogonal curvilinear coordinate system. It is shown that under thin film assumptions, the curvature terms can be neglected in solving film equations.

A predictor-corrector numerical solution procedure was devised to solve the discretised film equations. To enable accurate modelling of capillary forces, a discretised equation for interface curvature is derived from discretised continuity and momentum equations. This also eliminates the need to use a higher order interpolation function for film thickness and thus also the inconvenience associated with this.

The numerical algorithm were tested for both two-dimensional and three-dimensional problems with analytical solutions. In all cases, the numerical solutions reproduce remarkablly well the analytical solutions.

Chapter 6

Numerical Solution Procedure

6.1 Introduction

We have now completed the assembly of the mathematical models involved in this study. These models are represented by highly nonlinear equations which do not admit an analytical solution. Hence, we seek numerical solution for them at a finite number of points in the flow domain. The purpose of this chapter is therefore to transform the mathematical models described in Chapters 3 and 4 into discretised equations, and to provide solution schemes for them.

Section 6.2 discusses the transformation of the continuum set of gas phase equations to a discrete set of algebraic equations. The discretised scheme employed is the finite-volume approach which involves a combination of formal integration of the differential equations over finite volumes or 'cells' and time.

In Section 6.3, the finite-difference technique is invoked to approximate droplet phase equations, along with the spray-related source terms.

Section 6.4 presents the EPISO-SPRAY algorithm whereby both sets of the discretised equations are assembled and solved. The solvers of the linear system of quations are subsequently highlighted in Section 6.5.

Implementation of boundary conditions is discussed in Section 6.6. The overall solution algorithm is outlined in Section 6.7.

6.2 Discretisation of Gas Phase Equations

A multitude of methods abound in the literature for discretising the continuum set of equations. These include typically finite difference, finite volume, finite element, spectral, panel and boundary element methods. In addition to these schemes there are many others as well as many variants within each approach.

The finite volume method, as used earlier in Chapter 5 for discretising film equations, involves the discretisation of integral equations and offers geometric flexibility in the choice of a grid and freedom in the determination of the functional representation of the flow field. This makes finite volume method quite popular in engineering applications, particularly in in-cylinder flow calculations. In this study, the finite-volume approach of Gosman et al. (1969) is adopted to discretise the gas phase equations by (i) integrating differential conservation equations over a finite volume and over a finite increment of time, Δt; and (ii) casting the so obtained integro-differential equations into algebraic form. For this purpose, the flow field or domain is subdivided into a finite number of contiguous, non-overlapping discrete volumes or 'cells' formed by coordinate surfaces. The cell volume should be large compared to the droplet diameter so as to avoid negative void fraction, but small compared to the scale of change of the average gas-phase properties in view of the accuracy requirement. Each cell encloses a grid point located at the cell centre, and the scalar quantities, i.e., ρ, P, θ, T, f, μ_{eff}, k, ϵ, are stored at each grid node (Figure 6.1). The velocity components are, however, stored at the cell faces (Figure 6.1) following a common practice, in order to ensure that velocity components satisfy simultaneously the continuity equations (from which the pressure-distribution is determined) and the momentum equations (Patankar 1980). This scheme is the so called 'staggard grid' scheme.

The notations used to indicate locations of the variables are shown in Figure 6.2; upper case letters P, E, W, N, S, D, and U denote the grid nodes, while lower case letters e, w, n, s, d and u indicate the cell surfaces.

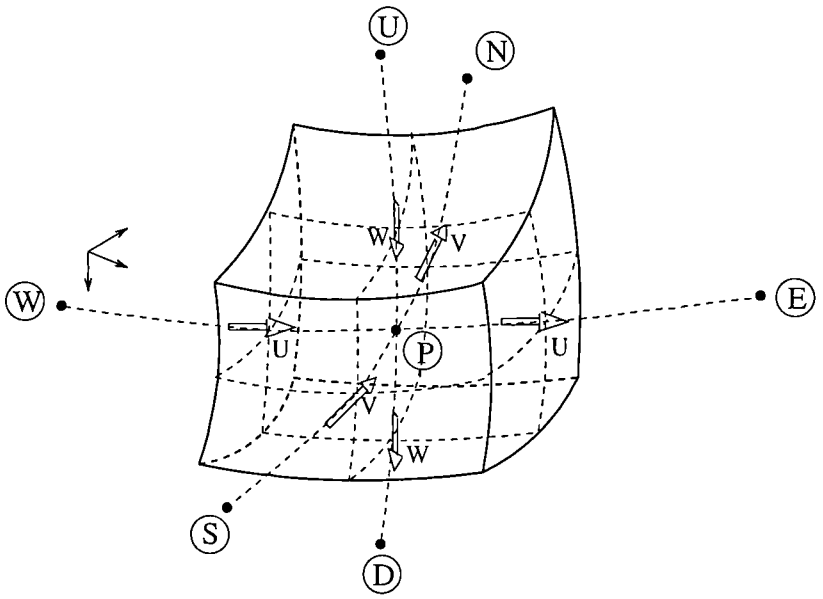


Figure 6.1: A typical scalar control volume

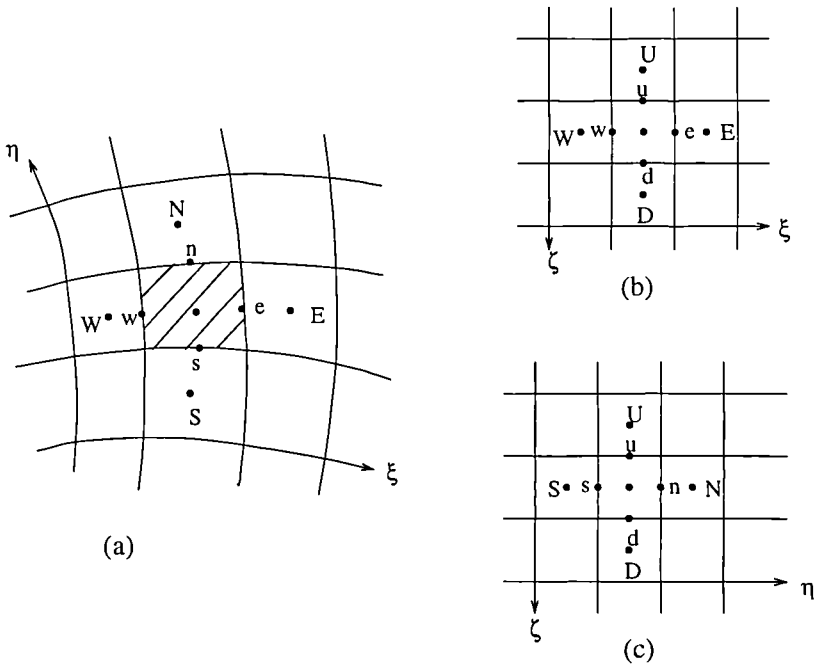


Figure 6.2: A typical control volume on three different planes

6.2.1 Discretisation of the General Scalar Transport Equations

Our focus here is on the following general scalar transport equations:

$$\frac{1}{\mathcal{V}}\frac{\partial}{\partial t}(\rho_b \mathcal{V}\phi) + \nabla \cdot (\rho_b \underline{V}_r \phi - \Gamma_\phi \theta \nabla \phi) = S_\phi + S_{\phi,d} \tag{6.1}$$

where ϕ stands for e_s, f, k, and ϵ.

The first step in discretising the above equation is to obtain its integral counterpart by applying the Gaussian divergence theorem (e.g. Begleris 1987; Tabrizi 1991) to the above equation for a control volume enclosing the node P (Figure 6.3), thus yielding:

$$\begin{aligned}
&\frac{1}{\Delta t}\int_t^{t+\Delta t}\left[\int_{\mathcal{V}_P}\frac{1}{\mathcal{V}_P}\frac{\partial}{\partial t}(\rho_b \mathcal{V}_P \phi)d\mathcal{V}\right]dt \\
&\qquad I \\
&+\frac{1}{\Delta t}\int_t^{t+\Delta t}\left[\int_a (\rho_b \underline{V}_r \phi - \Gamma_\phi \theta \nabla \phi)\cdot \underline{n} da\right]dt \\
&\qquad II \\
&= \frac{1}{\Delta t}\int_t^{t+\Delta t}\left[\int_{\mathcal{V}_P} S_\phi d\mathcal{V}\right]dt + \frac{1}{\Delta t}\int_t^{t+\Delta t}\left[\int_{\mathcal{V}_P} S_{\phi,d} d\mathcal{V}\right]dt
\end{aligned} \tag{6.2}$$

$$\qquad\qquad III \qquad\qquad\qquad IV$$

where $\underline{n}$ is the unit outward vector normal to the surface a of the control volume, and $\mathcal{V}_P$ is the cell volume.

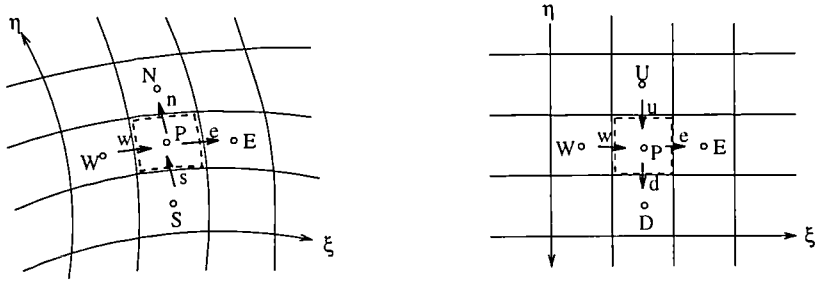


Figure 6.3: Control volume for scalar variables

The second step is to approximate the 'exact' equation (6.2) in order to cast it into an algebraic form. For clarity, attention here is directed to the first two terms, with the treatment of the last two terms left for the subsequent sections. We provisionally represent Terms III and IV, respectively, by:

$$(\hat{S}_\phi)_P = \frac{1}{\Delta t}\int_t^{t+\Delta t}\left[\int_{\mathcal{V}_P} S_\phi d\mathcal{V}\right]dt \tag{6.3}$$

$$\hat{S}_{\phi,d} = \frac{1}{\Delta t}\int_t^{t+\Delta t}\left[\int_{\mathcal{V}_P} S_{\phi,d}\, d\mathcal{V}\right] dt \tag{6.4}$$

Approximations of Terms I and II are now discussed in detail.

Term I is evaluated by assuming that the values at nodes represent averages over the control volume. This results in:

$$\begin{aligned} I &\approx \frac{1}{\Delta t}\int_t^{t+\Delta t}\left(\int_{\mathcal{V}_P}\frac{1}{\mathcal{V}_P}\left[\frac{\partial}{\partial t}(\rho_b \mathcal{V}_P \phi)\right]_P d\mathcal{V}\right) dt \\ &\approx \frac{(\rho_b\phi)_P^n \mathcal{V}_P^n - (\rho_b\phi)_P^o \mathcal{V}_P^o}{\Delta t} \end{aligned} \tag{6.5}$$

where the superscripts ^{n} and ^{o} denote the 'new' and 'old' time levels, respectively, seperated by the time interval, Δt.

Term II involves the surface integral of the total convective and diffusive fluxes of ϕ, which will be denoted by F for the simplicity. Then F can be expressed as:

$$\begin{aligned} F &= \int_a (\rho_b \underline{V}_r \phi - \Gamma_\phi \theta \nabla\phi)\cdot \underline{n} da \\ &\approx F_e - F_w + F_n - F_s + F_d - F_u \end{aligned} \tag{6.6}$$

where F_e, F_w, F_n, F_s, F_d, F_u stand, respectively, for the convection-diffusion flux of ϕ across the e, w, n, s, d and n cell faces of Figure 6.3. Using the Mean Value theorem, one can, for example, express the flux of ϕ across the e boundary as:

$$\begin{aligned} F_e &= \int_{a_e} (\rho_b U_r \phi - \Gamma_\phi \theta \frac{\partial\phi}{\partial\xi})_e da \\ &= (\rho_b U_r \phi a)_e - (\Gamma_\phi \theta \frac{\partial\phi}{\partial\xi})_e \end{aligned} \tag{6.7}$$

in which the subscript $_e$ denotes the value of the associated quantities averaged over the east cell face. This average value can be estimated by postulating that it assumes the value of the midpoint of the surface.

Evaluation of the first order difference term appearing in (6.7) is done by assuming a linear variation of ϕ between the adjacent cell nodes P and E, equivalent to a second-order central-difference approximation in Taylor series terms. Thus:

$$(\frac{\partial\phi}{\partial\xi})_e \approx \frac{\phi_E - \phi_P}{\xi_E - \xi_P} = \frac{\phi_E - \phi_P}{\Delta\xi_{E-P}} \tag{6.8}$$

which, when substituted into Equation (6.7), provides:

$$F_e = \dot{m}_e\left[\phi_e - \frac{\phi_E - \phi_P}{Pe_e}\right] \tag{6.9}$$

where

$$\dot{m}_e = (\rho_b U_r a)_e \tag{6.10}$$

is the main flow rate across the e boundary and Pe_e is the east cell boundary Peclet number that measures the ratio of convective and diffusive fluxes and is defined as:

$$Pe = \frac{(\rho U_r)_e \Delta\xi_{E-P}}{\Gamma_{\phi_e}} \tag{6.11}$$

The values of ρ, θ and Γ_{ϕ_e} at the e boundary are evaluated, through linear interpolation, from their values at cell nodes, P and E, as follows:

$$\begin{aligned} \rho_e &= (1-f_e)\rho_P + f_e\rho_E \\ \theta_e &= (1-f_e)\theta_P + f_e\theta_E \\ \Gamma_{\phi_e} &= (1-f_e)\Gamma_{\phi_P} + f_e\Gamma_{\phi_E} \end{aligned} \tag{6.12}$$

in which f_e is a linear interpolation factor specified by (see Figure 6.2)

$$f_e = \frac{\Delta\xi_{e-P}}{\Delta\xi_{E-P}} \tag{6.13}$$

Note that the parenthesis term in Equation (6.9) contains the cell face value, ϕ_e, the evaluation of which is important as it affects the consistency between the differential and discretised equations. In general, the values of ϕ at the cell faces (i.e. ϕ_e, etc.) can be determined using an interpolation or extrapolation involving the values of ϕ at one or more of the grid-point neighbours of the cell face. The choice of the geometric shape of the interpolation/extrapolation profiles dictate the type and the local order of accuracy, as will become clear shortly. Here, we use the interpolation/extrapolation scheme such that:

$$\phi_e - \frac{\phi_E - \phi_P}{Pe_e} = (1-\alpha_e)\phi_E + \alpha_e\phi_P \tag{6.14}$$

where the quantity α_e is the spatial difference factor, to be specified later when the interpolation scheme is detailed.

Hence, upon insertion of (6.14) into (6.9) ,the fluxes across the e boundary now read:

$$F_e = \dot{m}_e[(1-\alpha_e)\phi_E + \alpha_e\phi_P] \tag{6.15}$$

Similar expressions to the above hold for the fluxes across the other cell faces. A general expression can be written for all the fluxes as:

$$F_i = \begin{cases} \dot{m}_i[(1-\alpha_i)\phi_I + \alpha_i\phi_P] & \text{for } I = E, N, D \text{ and } i = e, n, d \\ \\ \dot{m}_i[\alpha_i\phi_I + (1-\alpha_i)\phi_P] & \text{for } I = W, S, U \text{ and } i = w, s, u \end{cases} \tag{6.16}$$

As a final step to the evaluation of term II, we approximate the time-average F_i in the interval, Δt, by

$$\frac{1}{\Delta t}\int_t^{t+\Delta t} F_i dt \approx \beta F_i^n + (1-\beta)F_i^o \tag{6.17}$$

where i denotes any cell surface, and the temporal difference factor β ($0 \leq \beta \leq 1$) is introduced to represent the relative contributions of the 'old' and 'new' time-level quantities in the finite volume equations. There are three common options regarding the specification of β: (i) $\beta = 0$ is referred to explicit scheme; (ii) $\beta = 1/2$ is the time-centred Crank-Nicolson scheme; and (iii) $\beta = 1$ corresponds to the fully implicit scheme (Roache 1982). In this study, the fully implicit scheme is adopted because it offers two major advantages. On the one hand, it ensures unconditional linear stability and boundedness even for arbitrary large time steps; while on the other hand, this scheme avoids the need to store and recalculate the 'old' set of coefficients (except for A_P^o) and is therefore more computationally efficient than any other case with $0 < \beta < 1$.

Insertion of $\beta = 1$ and making use of (6.5) to (6.17), term II of (6.2) becomes:

$$\begin{aligned} II &= \frac{1}{\Delta t}\int_t^{t+\Delta t} F dt \\ &\approx \frac{1}{\Delta t}\int_t^{t+\Delta t} (F_e - F_w + F_n - F_s + F_d - F_u) dt \\ &\approx \left\{ \sum_{\substack{i=e,n,d \\ I=E,N,D}} \dot{m}_i[(1-\alpha_i)\phi_I + \alpha_i\phi_P] \right. \\ &\qquad \left. - \sum_{\substack{i=w,s,u \\ I=W,S,U}} \dot{m}_i[(\alpha_i\phi_I + (1-\alpha_i)\phi_P] \right\}^n \end{aligned} \tag{6.18}$$

Substitution of (6.5) and (6.18) into (6.2) yields the discretised form of the general scalar equation as:

$$\frac{(\rho_b\phi)_P^n\mathcal{V}_P^n - (\rho_b\phi)_P^o\mathcal{V}_P^o}{\Delta t} + \left\{ \sum_{\substack{i=e,n,d \\ I=E,N,D}} \dot{m}_i[(1-\alpha_i)\phi_I + \alpha_i\phi_P] + \sum_{\substack{i=w,s,u \\ I=W,S,U}} \dot{m}_i[(\alpha_i\phi_I + (1-\alpha_i)\phi_P] \right\}^n = (\hat{S}_\phi)_P + (\hat{S}_{\phi,d})_P \tag{6.19}$$

The above equation can be expressed in a more compact form as:

$$A_P^n\phi_P^n = \sum_C A_C^n\phi_C^n + A_P^o\phi_P^o + (\hat{S}_\phi)_P + (\hat{S}_{\phi,d})_P \tag{6.20}$$

in which the summation is over the surrounding points E, W, N, S, D, U and the coefficients are defined as:

$$\begin{aligned} A_E^n &= \dot{m}_e^n(\alpha_e^n - 1) \quad , \quad A_W^n = \dot{m}_w^n\alpha_w^n \\ A_N^n &= \dot{m}_n^n(\alpha_n^n - 1) \quad , \quad A_S^n = \dot{m}_s^n\alpha_s^n \\ A_D^n &= \dot{m}_d^n(\alpha_d^n - 1) \quad , \quad A_U^n = \dot{m}_u^n\alpha_u^n \end{aligned} \tag{6.21}$$

$$A_P^n = \sum_C A_C^n + (\dot{m}_e - \dot{m}_w + \dot{m}_n - \dot{m}_s + \dot{m}_d - \dot{m}_u)^n + \frac{(\rho_b\mathcal{V})_P^n}{\Delta t} \tag{6.22}$$

$$A_P^o = \frac{(\rho_b\mathcal{V})_P^o}{\Delta t} \tag{6.23}$$

In Equation (6.22), the last term in the right hand side

$$\frac{(\rho_b\mathcal{V})_P^n}{\Delta t}$$

has to be evaluated from the discretised continuity equation in order to meet the requirement of consistency. The latter equation can be obtained by setting $\phi = 1$, $(\hat{S}_\phi)_P = 0$ and $(\hat{S}_{\phi,d})_P = (\hat{S}_{m,d})_P$ to yield:

$$\frac{(\rho_b\mathcal{V})_P^n - (\rho_b\mathcal{V})_P^o}{\Delta t} + (\dot{m}_e - \dot{m}_w + \dot{m}_n - \dot{m}_s + \dot{m}_d - \dot{m}_u)^n = (\hat{S}_{m,d})_P \tag{6.24}$$

Insertion of (6.24) into (6.22) enables the elimination of $\frac{(\rho_b\mathcal{V})_P^n}{\Delta t}$, thus yielding an discretised equation similar to (6.20) with new expression of A_P as follows (hereafter the superscript ^{n} of the coefficients is dropped for brevity):

$$A_P\phi_P^n = \sum_C A_C\phi_C^n + A_P^o\phi_P^o + (\hat{S}_\phi)_P + (\hat{S}_{\phi,d})_P \tag{6.25}$$

where

$$\begin{aligned} A_E &= \dot{m}_e(\alpha_e - 1) \quad , \quad A_W = \dot{m}_w\alpha_w \\ A_N &= \dot{m}_n(\alpha_n - 1) \quad , \quad A_S = \dot{m}_s\alpha_s \\ A_D &= \dot{m}_d(\alpha_d - 1) \quad , \quad A_U = \dot{m}_u\alpha_u \end{aligned} \tag{6.26}$$

$$A_P = \sum_C A_C + A_P^\circ + (\hat{S}_{m,d})_P \tag{6.27}$$

$$A_P^\circ = \frac{(\rho_b \mathcal{V})_P^\circ}{\Delta t} \tag{6.28}$$

We return now to the problem of specifying the spatial difference function α, which is introduced to express the values of the dependent variables at the cell faces of the control volume in terms of the neighbour nodal values by means of interpolation practices. If the number of computational cells tends to infinity, one would expect to get the 'exact' solution of the differential transport equation, irrespective of the interpolation practices used to evaluate the convective and diffusive fluxes. However, in practice one can only employ a finite number of cells, and it is then important to ensure that the solution of discretised equations satisfy certain important properties of the exact solution even on a coarse grid. The choice of α is therefore governed by the requirement that the discretised equations be consistent with the original equations. In particular, the discretised equations should exhibit the properties of conservation, boundedness and transportiveness, which are inherent in the exact solutions.

Here, conservation means that the net transport across the individual cell and solution domain boundaries should equal the total production/consumption by internal or external sources. This property is ensured if the flux across any cell face is uniquely represented in the discretised equations from the two adjacent control volumes. Boundedness implies that non-physical values, such as negative temperatures, should not be present in the solutions, while transportiveness means that, as the Peclet number is increased, the influence of the downstream nodes should be reduced (Roache 1982). Additionally, the discretised equation should also obey the criterion of stability which requires that the numerical errors diminish rather than grow as calculations are in progress.

A spatial interpolation scheme that possesses these desirable properties to a limitied extent is the hybrid central/upwind difference scheme of Spalding (1972). This scheme is obtained as the three-line asymptotic approximation to the exact ϕ variation taken from the solution of a simplified one-dimensional transport equation along a coordinate direction (Patankar 1980). According to this formulation, the spatial difference function α is specified to be:

$$\alpha_i = \begin{cases} 0 & , \text{ for } Pe_i < -\dfrac{1}{1-f_i} \\ 1 & , \text{ for } Pe_i > \dfrac{1}{f_i} \\ 1 - f_i + \dfrac{1}{Pe_i} & , \text{ for } -\dfrac{1}{1-f_i} \leq Pe_i \leq \dfrac{1}{f_i} \end{cases} \tag{6.29}$$

where i stands for any cell face and the f_i's are spatial weighting factors, e.g. (see Figure 6.3).

$$\begin{aligned} f_e &= \frac{\Delta\xi_{e-P}}{\Delta\xi_{E-P}} \quad , \quad f_w = \frac{\Delta\xi_{W-w}}{\Delta\xi_{W-P}} \\ f_n &= \frac{\Delta\eta_{n-P}}{\Delta\xi_{N-P}} \quad , \quad f_s = \frac{\Delta\xi_{S-s}}{\Delta\xi_{S-P}} \end{aligned} \tag{6.30}$$

It is not difficult to perceive that the basic idea behind formulation (6.29) is to apply the most appropriate of the two schemes– second-order central difference scheme (CD) and first-order upwind scheme (UD)– for the prevailing circumstances involving different ranges of grid Peclet number. In other words, the CD scheme is used for small values of the grid Peclet number, because central differencing is accurate and stable in this range of Peclet numbers, and the UD scheme which ignores the diffusion, is used for large values of the grid Peclet number where central differencing infringes the transportive property and becomes unstable (Roche 1982). It is also evident that Formulation (6.29) produces a continuous transition at the transition Peclet numbers, which, in the present case, are $Pe_i = 1/f_i$, and $-1/(1-f_i)$, so that the fluxes at these values, calculated by the CD and UD are equal.

Owing to the above desirable features, the hybrid-difference scheme is capable of producing accurate results for the entire range of grid Pe if the flow is aligned with the mesh. However, this scheme does nothing to alleviate numerical diffusion resulting from the non-alignment of flow and computing mesh, which is invariablely the case in multidimensional flows of engine circumstances. Thus for the latter situation, the hybrid scheme suffers from a certain level of inaccuracy. Although, some schemes have been proposed for the remedy of the numerical diffusion, they generally suffer from the propensity of producing numerical instability and unphysical solution. It is for this reason that the hybrid-difference scheme is employed in this study, despite its undesirable 'numerical diffusion'.

Before turning to the next subsection, let us divert our attention for a while to the introduction of a finite-volume related vector operator, ∇_{dif}, in order to facilitate the subsequent description. The operator,∇_{dif}, to be defined is associated with the well known operator,∇, which appears in the general transport equation (6.1). The former is defined here as:

$$\nabla_{\text{dif}} \cdot \underline{a} = \int_{\mathcal{V}_P} \nabla \cdot \underline{a}\, d\mathcal{V} = \sum_{\gamma} \underline{a} \cdot \underline{s}_{\gamma} \tag{6.31}$$

$$\nabla_{\text{dif}} \phi = \int_{\mathcal{V}_P} \nabla \phi\, d\mathcal{V} = \sum_{\gamma} \phi_{\gamma} \underline{s}_{\gamma} \tag{6.32}$$

where $\sum_{\gamma}$ is the summation for all faces of the cell enclosing the nodal point P; $\underline{a}$ stands for an arbitrary vector; ϕ denotes a general scalar; $\underline{s}_{\gamma}$ is the γ-th surface vector of the cell, which directs normally-outward to the cell face and has the cell face area as its magnitude; and ϕ_{γ} is the average value in the γ-th surface.

Using (6.31) and (6.32), we can evaluate the following nodal values:

$$(\nabla \phi)_P \approx \frac{\nabla_{\text{dif}} \phi}{\mathcal{V}_P} \tag{6.33}$$

$$(\nabla \cdot \underline{a})_P \approx \frac{\nabla_{\text{dif}} \cdot \underline{a}}{\mathcal{V}_P} \tag{6.34}$$

6.2.2 Discretisation of Momentum Equations

Although the general discretisation equation (6.25) holds for the scalar variables as well as velocities, special treatment is needed for the evaluation of the terms in Equation (6.25) for the particular case of velocities. This need arises from two

considerations. First, the control volumes for the velocities are displaced from the main node cells, due to the adoption of the staggered grid arrangement. Thus appropriate interpolation practices have to be introduced to ensure the continuity of fluxes across the cell boundaries and hence preserving conservation, as will be described below. Second, the pressure gradient appearing in the momentum source terms plays an important role in the solution of the momentum equations, which is unknown and needs obvious governing equation for itself. Provision is hence required to allow for the derivation of a pressure equation. For this purpose, the pressure gradient term is deliberately separated from the remaining gas-phase source terms and is treated specially.

To address the above problems in somewhat detail, our attention is focused on the U-momentum equation. We also adopt the convention that the labels of the velocities assume those of the grid nodes at which they point (Figures 6.4, 6.5 and 6.6). For a typical U-component control volume (Figure 6.4), the finite-volume approximation of the pressure gradient term is given by:

$$\frac{1}{\Delta t}\int_t^{t+\Delta t}\int_{\mathcal{V}_P} -\theta\frac{\partial P}{\partial \xi}d\mathcal{V}dt \approx -(\Delta\eta\Delta\zeta)_P \cdot \theta_P(P_e - P_w)$$
$$= -a_\xi \cdot \theta_P \Delta_\xi P \qquad (6.35)$$

where $a_\xi(=(\Delta\eta\Delta\zeta)_P)$ is the area of the main (or scalar) cell face on which U lies, and $\Delta_\xi P(=P_e - P_w)$ denotes the pressure difference acting on the U-control volume in the ξ-direction, so that equation (6.35) expresses the pressure force acting on the control volume in that direction.

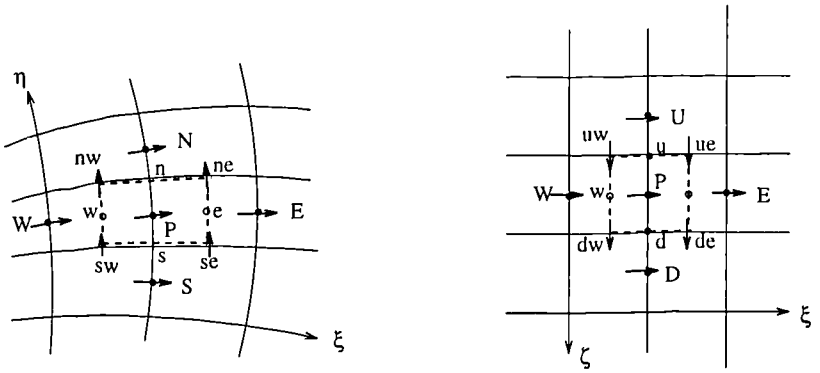


Figure 6.4: A typical control volume for U-velocity

Furthermore, the U-control volume is split between two scalar cells such that the

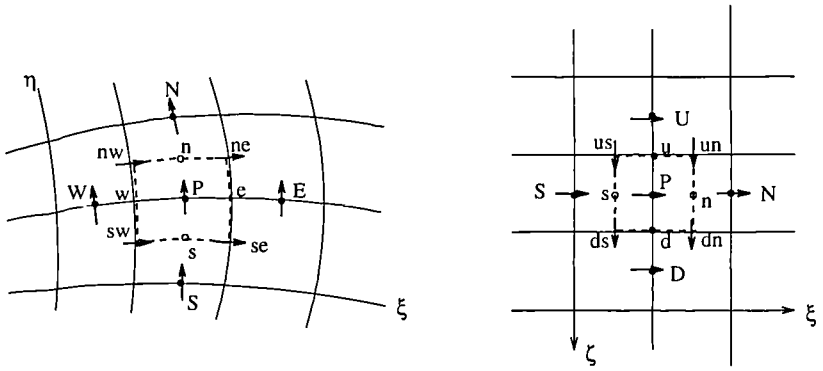


Figure 6.5: A typical control volume for V-velocity

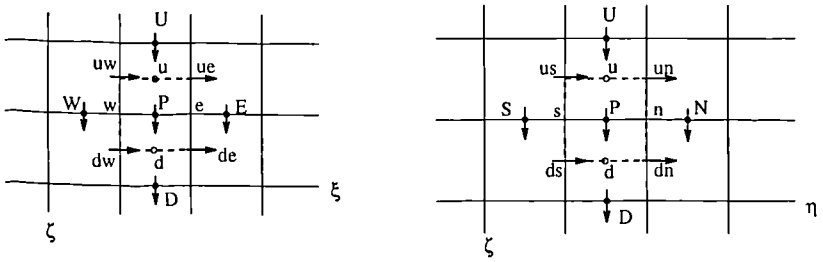


Figure 6.6: A typical control volume for W-velocity

coefficient A_P° can be represented by:

$$A_P^\circ = \frac{(\rho_b \mathcal{V})_P^\circ}{\Delta t} = \frac{[(\rho_b \mathcal{V})_e + (\rho_b \mathcal{V})_w]^\circ}{2\Delta t} \tag{6.36}$$

where $\mathcal{V}_e$ and $\mathcal{V}_w$ are, respectively, the volume of the east and west scalar cells. Hence, the discretised U-momentum equation is expressed as:

$$\begin{aligned} A_P U_P^n &= \sum_C A_C U_C^n - a_\xi \theta_P (P_e - P_w) + A_P^\circ U_P^\circ \\ &\quad + (\hat{S}_U)_P + \hat{S}_{U,d} \end{aligned} \tag{6.37}$$

where, $\hat{S}_{U,d}$ is the U-momentum exchange between the gas and the the droplets, $(\hat{S}_U)_P$ is the contribution of the remaining components of the gas phase source term, A_P° is defined as in Equation (6.36) and the coefficients A_P and A_C's are defined as in Equations (6.27) and (6.26) but with the cell boundary convection/diffusion flow rates calculated in somewhat different manner due to the staggering of the U-control volume. In particular, the mass flow rates across the e, n and d faces of the cell are given by:

$$\begin{aligned} \dot{m}_e &= (\rho_b)_e (\Delta\eta\Delta\zeta)_e \frac{(U_r)_P + (U_r)_E}{2} \\ \dot{m}_n &= (\rho_b)_{ne} (\Delta\xi\Delta\zeta)_{n-ne} V_{ne} + (\rho_b)_{nw} (\Delta\xi\Delta\zeta)_{n-nw} V_{nw} \end{aligned} \tag{6.38}$$

$$\dot{m}_d = (\rho_b)_{de}(\Delta\xi\Delta\eta)_{d-de}(W_r)_{de} + (\rho_b)_{dw}(\Delta\xi\Delta\eta)_{d-dw}(W_r)_{dw}$$

where

$$\begin{aligned}
(\rho_b)_{ne} &= f_{ne}(\rho_b)_{Ne} + (1-f_{ne})(\rho_b)_e \quad , \quad f_{ne} = \frac{\Delta\eta_{ne-e}}{\Delta\eta_{Ne-e}} \\
(\rho_b)_{nw} &= f_{nw}(\rho_b)_{Nw} + (1-f_{nw})(\rho_b)_w \quad , \quad f_{nw} = \frac{\Delta\eta_{nw-w}}{\Delta\eta_{Nw-w}} \\
(\rho_b)_{de} &= f_{de}(\rho_b)_{De} + (1-f_{de})(\rho_b)_e \quad , \quad f_{de} = \frac{\Delta\zeta_{de-e}}{\Delta\zeta_{De-e}} \\
(\rho_b)_{dw} &= f_{dw}(\rho_b)_{Dw} + (1-f_{dw})(\rho_b)_w \quad , \quad f_{dw} = \frac{\Delta\zeta_{dw-w}}{\Delta\zeta_{Dw-w}}
\end{aligned} \tag{6.39}$$

The diffusivities can also be obtained in the same manner as described above using linear or bilinear interpolation (see Begleris 1987).

Similar equations to (6.36) through (6.39) can be obtained for the V- and W-momentum equations, which read:

$$\begin{aligned}
A_P V_P^n = &\sum_C A_C V_C^n - a_\eta \theta_P (P_n - P_s) + A_P^o V_P^o \\
&+(\hat{S}_V)_P + \hat{S}_{V,d}
\end{aligned} \tag{6.40}$$

$$\begin{aligned}
A_P W_P^n = &\sum_C A_C W_C^n - a_\zeta \theta_P (P_d - P_u) + A_P^o W_P^o \\
&+(\hat{S}_W)_P + \hat{S}_{W,d}
\end{aligned} \tag{6.41}$$

As relative velocities are needed for the computation of mass fluxes through the cell faces, it is more efficient to rearrange the above discretised momentum equations so that the dependent variables are the velocities relative to the moving coordinate frame, $U_r = (U - U_g)$ and $W_r = (W - W_g)$, respectively, thus yielding:

$$\begin{aligned}
A_P (U_r)_P^n = &\sum_C A_C (U_r)_C^n - a_\xi \theta_P (P_e - P_w) \\
&+A_P^o (U_r)_P^o + (\hat{S}_{U_r})_P + \hat{S}_{U_r,d}
\end{aligned} \tag{6.42}$$

where

$$(\hat{S}_{U_r})_P = \hat{S}_U + \sum_C A_C (U_g)_C^n + A_P^o (U_g)_P^o - A_P (U_g)_P^n \tag{6.43}$$

$$\begin{aligned}
A_P (W_r)_P^n = &\sum_C A_C (W_r)_C^n - a_\zeta \theta_P (P_d - P_u) \\
&+A_P^o (W_r)_P^o + (\hat{S}_{W_r})_P + \hat{S}_{W_r,d}
\end{aligned} \tag{6.44}$$

where

$$(\hat{S}_{W_r})_P = \hat{S}_W + \sum_C A_C (W_g)_C^n + A_P^o (W_g)_P^o - A_P (W_g)_P^n \tag{6.45}$$

It should be noted that the need does not arise for a change of variable in the V-momentum equation (6.40), pertaining to the tangential direction, since the grid does not move in the η-direction.

Where necessary, the absolute velocities can be calculated from the relative velocities and the grid velocities which are given for the expanding/contracting and translating regions by equations (3.53) and (3.56), respectively.

6.2.3 Evaluation of Source Terms

Source term discretisation is also an important ingredient of the whole discretisation procedure, for it not only has a direct effect on the stability, boundedness and accuracy of the discrete counterpart of the original differential equations, but also, through its influence on the structure of the coefficient matrix of the algebraic systems, determines the accuracy and efficiency of the solution scheme employed. It is for this reason that this problem is paid a special attention here.

The source term S_ϕ is, in general, a non-linear function of ϕ. To effect discretisation, it is assumed that S_ϕ is linked to ϕ in a quasi-linear fashion:

$$S_\phi = s_P^\phi \cdot \phi + s_U^\phi \tag{6.46}$$

in which, the coefficients s_P^ϕ and s_U^ϕ are postulated to remain constant during the time interval, Δt. Thus term III of Equation (6.2) becomes:

$$\begin{aligned} (\hat{S}_\phi)_P &= \frac{1}{\Delta t} \int_t^{t+\Delta t} \int_{\mathcal{V}_P} S_\phi d\mathcal{V} dt \\ &= \frac{1}{\Delta t} \int_t^{t+\Delta t} \int_{\mathcal{V}_P} \left(s_P^\phi \phi + s_U^\phi \right) d\mathcal{V} dt \\ &\approx S_P^\phi \phi_P^n + S_U^\phi \end{aligned} \tag{6.47}$$

where

$$S_P^\phi = \int \mathcal{V}_P s_P^\phi d\mathcal{V}, \qquad \text{and} \qquad S_U^\phi = \int \mathcal{V}_P s_U^\phi d\mathcal{V}$$

To gain an appreciation of some restrictions on the choice of the coefficients s_P^ϕ and s_U^ϕ in Equation (6.46), we examine again the general discretised equation (6.25)

which is rewritten, with the use of (6.47), as:

$$(A_P - S_P^\phi)\phi_p^n = \sum_C A_C\phi_C^n + A_P^o\phi_P^o + S_U^\phi + \hat{S}_{\phi,d} \tag{6.48}$$

The above equation indicates clearly that when S_P^ϕ is positive, the coefficient of ϕ_P^n may become negative, leading to a violation of the boundedness requirement and thus possibly giving rise to instabilities and physically-unrealistic solutions (Pantankar 1980; Gosman and Issa 1984). On the contrary, a negative S_P^ϕ serves to (i) enhance boundedness, (ii)increase the diagonal dominance of the coefficient matrix, and (iii) promote stability and improve accuracy and efficiency of the solution.

On the other hand, if the source terms are large enough to dominate the discretised equations, as is true to the k and ϵ equations, the discretised equation (6.48) may be simplified to:

$$-S_P^\phi\phi_P \approx S_U^\phi \qquad \text{or} \qquad \phi_P \approx -\frac{S_U^\phi}{S_P^\phi} \tag{6.49}$$

Obviously, the ratio S_U^ϕ/S_P^ϕ must be properly bounded if ϕ_P is to be physically acceptable.

The above considerations make it clear that source discretisation should be performed in such a fashion as to ensure the satisfaction of the following two requirements: (a) the coefficients S_P^ϕ must be always be less or equal to zero ($S_P^\phi \leq 0$); and (b) The ratio, S_U^ϕ/S_P^ϕ, should itself be properly bounded.

In addition, S_U^ϕ must be always be positive for variable which are always positive (e.g. k and ϵ), as can be seen from (6.49).

In accord with the above requirements, source term coefficients s_P^ϕ, s_U^ϕ of Equation (6.46) for all variables are derived and given in Table 6.1 and 6.2 for the E/C and T regions, respectively.

Attention is now directed to the calculations of the integral source term coefficients (S_P^ϕ, S_U^ϕ) using the terms of (s_u^ϕ, s_P^ϕ) given in Table 6.1 and 6.2. Integration may involve surface and volume integrals, depending on the form of the term in question. In the following, we illustrate ways of handling these two types of integrals:

- Surface integrals arise from the terms that are exact differentials of a function, such as the stress contribution in the $s_U's$ of the momentum equations and

the pressure term in the energy equation. In such circumstances, the Gauss theorem is employed to convert the volume integrals to surface ones. Thus, for example, integration of the $\tau_{\xi\xi}$-contribution of the S_U^U of Table 6.2 gives:

$$\begin{aligned}
&\int_{\mathcal{V}_P} \frac{1}{\Delta\eta}\frac{\partial}{\partial\xi}\left\{\Delta\eta\left[\mu_{eff}\left(\frac{\partial}{\partial\xi}+2\mathcal{V}\frac{1}{\Delta\xi}\frac{\partial\Delta\xi}{\partial\eta}\right)\right]\right\}d\mathcal{V}\\
&=(\Delta\eta\Delta\xi)_e\left\{(\mu_{eff})_e\left[\frac{U_E-U_P}{\Delta\xi_{E-P}}+2\mathcal{V}_e\left(\frac{1}{\Delta\xi}\frac{\partial\Delta\xi}{\partial\eta}\right)_e\right]\right\}\\
&-(\Delta\eta\Delta\xi)_w\left\{(\mu_{eff})_w\left[\frac{U_P-U_W}{\Delta\xi_{P-W}}+2\mathcal{V}_w\left(\frac{1}{\Delta\xi}\frac{\partial\Delta\xi}{\partial\eta}\right)_w\right]\right\} \qquad (6.50)
\end{aligned}$$

- Volume integrals are associated with the terms which are not exact differential expressions. Evaluation of this type of integrals is pursued by invoking the postulation that the value of the term at the center of the cell prevails all over the cell volume. Thus, for example, we have:

$$\int_{\mathcal{V}_P} 2\mu_{eff}\theta\left(\frac{1}{r_2}\right)^2 d\mathcal{V}=\left[2\mu_{eff}\theta\left(\frac{1}{r_2}\right)^2\right]_P\mathcal{V}_P \qquad (6.51)$$

in which the curvature of ξ-coordinate line at node P, $(1/r_2)_P$, is obtained by interpolating the curvature on the east and west of P in the following manner (see Begleris 1987):

$$\left(\frac{1}{r_2}\right)_P=\frac{1}{2}\left[\left(\frac{1}{r_2}\right)_e+\left(\frac{1}{r_2}\right)_w\right] \qquad (6.52)$$

The reason for using interpolation scheme (6.52) instead of $(r_2)_P=1/2[(r_2)_e+(r_2)_w]$ is due to the fact that it is curvature and not radius of curvature that varies continuously for a continuously differentiable curve (Begleris 1987).

Table 6.1 Definition of Gas Source Term Coefficients S_P^ϕ and S_U^ϕ in Equation (6.46) for the Expanding/Contracting Region

ϕ	$-S_P^\phi(\geq 0)$	S_U^ϕ
W	0	$\frac{\partial}{\partial\zeta}[\mu_{eff}\theta\frac{\partial W}{\partial\zeta} - \frac{2}{3}(\rho_b k + \mu_{eff}\theta\nabla\cdot\underline{V})] + \frac{1}{\Delta\eta}\frac{\partial}{\partial\xi}(\mu_{eff}\theta\Delta\eta\frac{\partial U}{\partial\zeta}) + \frac{1}{\Delta\xi}\frac{\partial}{\partial\eta}(\mu_{eff}\theta\Delta\xi\frac{\partial V}{\partial\zeta})$ $\tau_{\zeta\zeta}$ – contribution $\tau_{\xi\zeta}$ – contribution $\tau_{\eta\zeta}$ – contribution
U	$(\frac{1}{\Delta\xi}\frac{\partial\Delta\xi}{\partial\eta})^2\mu_{eff}\theta$ $\tau_{\xi\eta}$/(radius of curvature) $+2(\frac{1}{\Delta\eta}\frac{\partial\Delta\eta}{\partial\xi})^2\mu_{eff}\theta$ $\tau_{\eta\eta}$/(radius of curvature) $+\frac{\rho_b}{2}[\lvert\frac{1}{\Delta\xi}\frac{\partial\Delta\xi}{\partial\eta}V\rvert - (-\frac{1}{\Delta\xi}\frac{\partial\Delta\xi}{\partial\eta}V)]$ Coriolis force contribution	$\frac{\partial}{\partial\zeta}[\mu_{eff}\theta\frac{\partial W}{\partial\xi} + \frac{1}{\Delta\eta}\frac{\partial}{\partial\xi}\{\Delta\eta[\mu_{eff}\theta(\frac{\partial U}{\partial\xi} + \frac{2V}{\Delta\xi}\frac{\partial\Delta\xi}{\partial\eta})]\}] - \frac{\partial}{\partial\xi}[\frac{2}{3}(\rho_b k + \mu_{eff}\theta\nabla\cdot\underline{V})]$ $\tau_{\xi\zeta}$ – contribution $\tau_{\xi\xi}$ – contribution $+\frac{1}{\Delta\xi}\frac{\partial}{\partial\eta}[\Delta\xi\mu_{eff}\theta(\frac{\partial V}{\partial\xi} - \frac{U}{\Delta\xi}\frac{\partial\Delta\xi}{\partial\eta} - \frac{V}{\Delta\eta}\frac{\partial\Delta\eta}{\partial\xi})] + \frac{1}{\Delta\xi}\frac{\partial\Delta\xi}{\partial\eta}[\mu_{eff}\theta(\frac{\partial V}{\partial\xi} + \frac{\partial U}{\partial\eta} - \frac{V}{\Delta\eta}\frac{\partial\Delta\eta}{\partial\xi})]$ $\tau_{\eta\zeta}$ – contribution $\tau_{\xi\eta}$/(radius of curvature) $+\frac{1}{\Delta\eta}\frac{\partial\Delta\eta}{\partial\xi}[-2\mu_{eff}\theta\frac{\partial V}{\partial\eta}] + \frac{1}{\Delta\eta}\frac{\partial\Delta\eta}{\partial\xi}(\rho_b V^2) + \frac{\rho_b}{2}[\lvert\frac{1}{\Delta\xi}\frac{\partial\Delta\xi}{\partial\eta}V\rvert + (-\frac{1}{\Delta\xi}\frac{\partial\Delta\xi}{\partial\eta}V)]U$ $\tau_{\eta\eta}$/(radius of curvature) centrifugal force Coriolis force contribution

Table 6.1 (continued)

ϕ	$-S_P^\phi(\geq 0)$	S_U^ϕ
V	$(\frac{1}{\Delta\eta}\frac{\partial\Delta\eta}{\partial\xi})^2\mu_{eff}\theta$ $\tau_{\eta\xi}$/(radius of curvature) $+2(\frac{1}{\Delta\xi}\frac{\partial\Delta\xi}{\partial\eta})^2\mu_{eff}\theta$ $\tau_{\xi\xi}$/(radius of curvature) $+\frac{\rho_b}{2}[\left\|\frac{1}{\Delta\eta}\frac{\partial\Delta\eta}{\partial\xi}U\right\| - (-\frac{1}{\Delta\eta}\frac{\partial\Delta\eta}{\partial\xi}U)]$ Coriolis force contribution	$\frac{\partial}{\partial\zeta}[\mu_{eff}\theta\frac{\partial W}{\partial\eta} + \frac{1}{\Delta\xi}\frac{\partial}{\partial\eta}\{\Delta\xi[\mu_{eff}\theta(\frac{\partial V}{\partial\eta} + \frac{2U}{\Delta\eta}\frac{\partial\Delta\eta}{\partial\xi})]\} - \frac{\partial}{\partial\eta}[\frac{2}{3}(\rho_b k + \mu_{eff}\theta\nabla\cdot\underline{V})]$ $\tau_{\eta\zeta}$ − contribution $\tau_{\eta\eta}$ − contribution $+\frac{1}{\Delta\eta}\frac{\partial}{\partial\xi}[\Delta\eta\mu_{eff}\theta(\frac{\partial U}{\partial\eta} - \frac{U}{\Delta\xi}\frac{\partial\Delta\xi}{\partial\eta} - \frac{V}{\Delta\eta}\frac{\partial\Delta\eta}{\partial\xi})] + \frac{1}{\Delta\eta}\frac{\partial\Delta\eta}{\partial\xi}[\mu_{eff}\theta(\frac{\partial V}{\partial\xi} + \frac{\partial U}{\partial\eta} - \frac{U}{\Delta\xi}\frac{\partial\Delta\xi}{\partial\eta})]$ $\tau_{\xi\eta}$ − contribution $\tau_{\xi\eta}$/(radius of curvature) $+\frac{1}{\Delta\xi}\frac{\partial\Delta\xi}{\partial\eta}[-2\mu_{eff}\theta\frac{\partial U}{\partial\xi}] + \frac{1}{\Delta\xi}\frac{\partial\Delta\xi}{\partial\eta}(\rho_b U^2) + \frac{\rho_b}{2}[\left\|\frac{1}{\Delta\eta}\frac{\partial\Delta\eta}{\partial\xi}U\right\| + (-\frac{1}{\Delta\eta}\frac{\partial\Delta\eta}{\partial\xi}U)]V$ $\tau_{\xi\xi}$/(radius of curvature) centrifugal force Coriolis force contribution
e_s	0	$-\theta\nabla\cdot(P\underline{V})$
k	$C_\mu\rho^2\theta k/\mu_{eff}$ $+\frac{2}{3}(\nabla\cdot\underline{V})^2\mu_{eff}\theta/k^0$ $+\frac{2}{3}\rho_b(\nabla\cdot\underline{V} + \|\nabla\cdot\underline{V}\|)/2$	$\mu_{eff}\theta g_t - \frac{2}{3}\rho_b k(\nabla\cdot\underline{V} - \|\nabla\cdot\underline{V}\|)/2 \quad (\geq 0)$

Table 6.1 (continued)

ϕ	$-S_P^\phi(\geq 0)$	S_U^ϕ
ϵ	$\frac{2}{3}C_\mu\mu_{eff}\theta(\nabla\cdot\underline{V})^2/k$ $+C_{\epsilon_2}\rho_b\epsilon/k$ $\{\mathcal{F}[\nabla\cdot\underline{V}]-\lvert\mathcal{F}[\nabla\cdot\underline{V}]\rvert\}/2$	$C_{\epsilon_1}C_\mu g_t\rho_b k+C_\mu\rho^2\theta k^2\{\mathcal{F}[\nabla\cdot\underline{V}]+\lvert\mathcal{F}[\nabla\cdot\underline{V}]\rvert\}/(2\mu_{eff})\quad(\geq 0)$

Remarks: Before linearising the S_k and S_ϵ in Table 3.3, they have been written, respectively, as:

$$S_k=\theta\mathcal{P}-\rho_b\epsilon-\frac{2}{3}\nabla\cdot\underline{V}(\rho_b k+\mu_{eff}\theta\nabla\cdot\underline{V})-\rho_b\epsilon=\mu_{eff}\theta g_t-\frac{2}{3}(\nabla\cdot\underline{V})^2\mu_{eff}\theta\frac{k}{k^o}-\frac{2}{3}\nabla\cdot\underline{V}\rho_b k-C_\mu\rho^2\theta\frac{k^2}{\mu_{eff}}$$

$$S_\epsilon=C_{\epsilon_1}\theta\mathcal{P}\frac{\epsilon}{k}-C_{\epsilon_1}\rho_b\frac{\epsilon^2}{k}+C_{\epsilon_3}\rho_b\epsilon\nabla\cdot\underline{V}=C_{\epsilon_1}C_\mu g_t\rho_b k+\mathcal{F}[\nabla\cdot\underline{V}]\rho_b\epsilon-\frac{2}{3}C_{\epsilon_1}\mu_{eff}\theta\frac{\epsilon}{k}(\nabla\cdot\underline{V})^2-C_{\epsilon_2}\rho_b\frac{\epsilon^2}{k}$$

where,

$$\mathcal{F}[\nabla\cdot\underline{V}]=\{(C_{\epsilon_3}-\frac{2}{3}C_{\epsilon_1})\nabla\cdot\underline{V}\}$$

and

$$\mathcal{F}[\nabla\cdot\underline{V}]\rho_b\epsilon=\frac{\mathcal{F}[\nabla\cdot\underline{V}]+\lvert\mathcal{F}[\nabla\cdot\underline{V}]\rvert}{2}C_\mu\rho^2\theta\frac{k^2}{\mu_{eff}}+\frac{\mathcal{F}[\nabla\cdot\underline{V}]-\lvert\mathcal{F}[\nabla\cdot\underline{V}]\rvert}{2}\rho_b\epsilon$$

Table 6.2 Definition of Gas Source Term Coefficients S_P^ϕ and S_U^ϕ in Equation (6.46) for the Translating Region

ϕ	$-S_P^\phi(\geq 0)$	S_U^ϕ
W	$2\mu_{eff}\theta(\frac{1}{r_2})^2$	$\frac{1}{\Delta\xi\Delta\eta}\frac{\partial}{\partial\zeta}\{\Delta\xi\Delta\eta[\mu_{eff}\theta(\frac{\partial W}{\partial\zeta}+\frac{2U}{r_1})]\}-\frac{\partial}{\partial\zeta}[\frac{2}{3}(\rho_b k+\mu_{eff}\theta\nabla\cdot\underline{V})]$
	$\tau_{\xi\xi}$/(radius of curvature)	$\tau_{\varsigma\varsigma}$ – contribution
	$+2\mu_{eff}\theta(\frac{\sin\beta}{r_3})^2$	$+\frac{1}{\Delta\eta\Delta\zeta}\frac{\partial}{\partial\xi}\{\Delta\eta\Delta\zeta[\mu_{eff}\theta(\frac{\partial U}{\partial\zeta}-\frac{W}{r_1}-\frac{U}{r_2})]\}+\frac{\partial}{\partial\eta}[\mu_{eff}\theta(\frac{\partial V}{\partial\zeta}-\frac{V\sin\beta}{r_3})]$
	$\tau_{\eta\eta}$/(radius of curvature)	$\tau_{\xi\varsigma}$ – contribution $\quad$ $\tau_{\eta\varsigma}$ – contribution
	$+\mu_{eff}\theta(\frac{1}{r_1})^2$	$+\frac{1}{r_2}[-2\mu_{eff}\theta\frac{\partial U}{\partial\xi}]+\frac{\sin\beta}{r_3}[-2\mu_{eff}\theta(\frac{\partial V}{\partial\eta}+\frac{U\cos\beta}{r_3})]$
	$\tau_{\varsigma\varsigma}$/(radius of curvature)	$\tau_{\xi\xi}$/(radius of curvature) $\quad$ $\tau_{\eta\eta}$/(radius of curvature)
	$+\frac{\rho_b}{2}[\lvert\frac{U}{r_1}\rvert-(-\frac{U}{r_1})]$	$+\frac{1}{r_1}\mu_{eff}\theta(\frac{\partial W}{\partial\xi}+\frac{\partial U}{\partial\zeta}-\frac{U}{r_2})+\frac{1}{r_2}\rho_b UU_r+\frac{\sin\beta}{r_3}\rho_b V^2+\frac{1}{r_1}\rho_b UW_g+\frac{r_b}{2}[\lvert\frac{U}{r_1}\rvert-(-\frac{U}{r_1})]W$
	Coriolis	$\tau_{\xi\varsigma}$/(radius of curvature) $\quad$ centrifugal $\quad$ Coriolis

Table 6.2 (continued)

ϕ	$-S_P^\phi(\geq 0)$	S_U^ϕ
U	$2\mu_{eff}\theta(\frac{1}{r_1})^2$	$\frac{1}{\Delta\eta\Delta\zeta}\frac{\partial}{\partial\xi}\{\Delta\eta\Delta\zeta[\mu_{eff}\theta(\frac{\partial U}{\partial\xi}+\frac{2W}{r_2})]\}-\frac{\partial}{\partial\xi}[\frac{2}{3}(\rho_b k+\mu_{eff}\theta\nabla\cdot\underline{V})]$
	$\tau_{\zeta\zeta}$/(radius of curvature)	$\tau_{\xi\xi}$ – contribution
	$+2\mu_{eff}\theta(\frac{\cos\beta}{r_3})^2$	$+\frac{1}{\Delta\xi\Delta\eta}\frac{\partial}{\partial\zeta}\{\Delta\xi\Delta\eta[\mu_{eff}\theta(\frac{\partial W}{\partial\xi}-\frac{W}{r_1}-\frac{U}{r_2})]\}+\frac{\partial}{\partial\eta}[\mu_{eff}\theta(\frac{\partial V}{\partial\zeta}-\frac{V\cos\beta}{r_3})]$
	$\tau_{\eta\eta}$/(radius of curvature)	$\tau_{\xi\zeta}$ – contribution $\quad$ $\tau_{\xi\eta}$ – contribution
	$+\mu_{eff}\theta(\frac{1}{r_2})^2$	$+\frac{1}{r_1}[-2\mu_{eff}\theta\frac{\partial W}{\partial\zeta}]+\frac{\cos\beta}{r_3}[-2\mu_{eff}\theta(\frac{\partial V}{\partial\eta}+\frac{W\sin\beta}{r_3})]$
	$\tau_{\xi\zeta}$/(radius of curvature)	$\tau_{\zeta\zeta}$/(radius of curvature) $\quad$ $\tau_{\eta\eta}$/(radius of curvature)
	$+\frac{\rho_b}{2}[\lvert\frac{W}{r_2}\rvert-(-\frac{W}{r_2})]$	$+\frac{1}{r_2}\mu_{eff}\theta(\frac{\partial W}{\partial\xi}+\frac{\partial U}{\partial\zeta}-\frac{W}{r_1})+\frac{1}{r_1}\rho_b WW_r+\frac{\cos\beta}{r_3}\rho_b V^2+\frac{1}{r_2}\rho_b WU_g+\frac{r_b}{2}[\lvert\frac{W}{r_2}\rvert-(-\frac{W}{r_2})]U$
	Coriolis	$\tau_{\xi\zeta}$/(radius of curvature) $\quad$ centrifugal $\quad$ Coriolis

Table 6.2 (continued)

ϕ	$-S_P^{\phi}(\geq 0)$	S_U^{ϕ}
V	$2\mu_{eff}\theta(\frac{1}{r_3})^2$	$\frac{\partial}{\partial\eta}[\mu_{eff}\theta(\frac{V}{\eta}+2\frac{W\sin\beta+U\cos\beta}{\rho_3})-\frac{2}{3}(\rho_b k+\mu_{eff}\theta\nabla\cdot\underline{V})]$
	$(\tau_{\eta\zeta}+\tau_{\xi\eta}$/(rad. of curvature)	$\tau_{\eta\eta}$/(radius of curvature)
		$+\frac{1}{\Delta\xi\Delta\eta}\frac{\partial}{\partial\zeta}[\Delta\xi\Delta\eta\mu_{eff}\theta(\frac{\partial W}{\partial\eta}-\frac{V\sin\beta}{r_3})]+\frac{1}{\Delta\eta\Delta\zeta}\frac{\partial}{\partial\xi}[\Delta\eta\Delta\zeta\mu_{eff}\theta(\frac{\partial U}{\partial\eta}-\frac{V\cos\beta}{r_3})]$
		$\tau_{\eta\zeta}$ – contribution $\quad$ $\tau_{\xi\eta}$ – contribution
	$+\frac{\rho_b}{2r_3}[\lvert W\sin\beta+U\cos\beta\rvert$	$+\frac{\sin\beta}{r_3}\mu_{eff}\theta(\frac{\partial V}{\partial\zeta}+\frac{\partial W}{\partial\eta})+\frac{\cos\beta}{r_3}\mu_{eff}\theta(\frac{\partial V}{\partial\xi}+\frac{\partial U}{\partial\eta})$
	Coriolis	$\tau_{\eta\zeta}$/(radius of curvature) $\quad$ $\tau_{\xi\eta}$/(radius of curvature)
	$-(-W\sin\beta-U\cos\beta)]$	$+\frac{\rho_b}{2r_3}[\lvert W\sin\beta+U\cos\beta\rvert+(-W\sin\beta-U\cos\beta)]V$
	Coriolis	Corilis
e_s	0	$-\theta\nabla\cdot(P\underline{V})$

Table 6.2 (continued)

ϕ	$-S_P^{\phi}(\geq 0)$	S_U^{ϕ}
k	as in Table 6.1	as in Table 6.1, with g_t taken from Table 3.4
ϵ	as in Table 6.1	as in Table 6.1, with g_t taken from Table 3.4

6.2.4 Final Form of Discretised Equations

Up to this point, a discretised set of gas-phase equations has been developed. As a summary, the final form of the discretised momentum and scalar equations can be written as:

$$\begin{aligned}(A_P - S_P^{\underline{V}})(\underline{V}_r)_P^n &= \sum_C A_C(\underline{V}_r)_C^n - \theta_P \nabla_{\text{dif}} P \\ &\quad + A_P^\circ(\underline{V}_r)_P^\circ + \hat{S}_U^{\underline{V}r} + \hat{S}_{\underline{V}_r,d} \end{aligned} \tag{6.53}$$

and

$$\begin{aligned}(A_P - S_P^{\phi})\phi_P^n &= \sum_C A_C\phi_C^n + A_P^\circ\phi_P^\circ \\ &\quad + \hat{S}_U^{\phi} + \hat{S}_{\phi,d} \end{aligned} \tag{6.54}$$

where $\nabla_{\text{dif}} P$ is evaluated from (6.32).

The next step is to develop a solution algorithm for the solution of the above equations. This is the topic of the Section 6.4, following the addressing of the approximation of spray-related terms and the droplet phase equations in the next section.

6.3 Discretisation of Droplet Equations

This section is concerned with the discretisation of the two-phase interaction terms and droplet equations, which are essentially ordinary differential equations. We need to pay particular attention to the following two issues: (i) determination of droplet time step, δt, and (ii) evaluation of local values, along the droplet trajectory, of the gas field variables appearing in the droplet equations. In what follows, the choice of droplet time step is first discussed. This is followed by a description of how to evaluate the local values of the gas-phase-related variables. Attention is then directed to the derivation of finite difference form of the droplet equations representing the conservation of mass, momentum and energy. Finally, evaluation is made of the droplet-related quantities involved in the gas phase equations.

6.3.1 Choice of Droplet Time Step

The scale of droplet time step, δt, used in the droplet computation has an important effect on the overall accuracy of both the gas-phase and the droplet calculations. Attempts should therefore be made to ensure the choice of appropriate δt. Some restrictions on δt can be perceived through the following considerations. First, a droplet cannot be allowed to travel more than one computational cell in one time step if it is to exchange mass, momentum and energy with all cells along its trajectory. This means that δt must be a small fraction of the residence time of the parcel in cell. Second, δt is not permitted to exceed the characteristic times scales associated with such processes as breakup and collision which characterise the evolution of droplet sizes and velocities, and droplet interactions with turbulent eddies, if these processes are to be properly represented. Thus, δt is limited by:

$$\delta t < (t_{r,c}, t_b, t_c, t_{int}) \tag{6.55}$$

where t_b, t_c are respectively, droplet breakup and collision time scale; t_{int} is the interaction time with turbulence; and the $t_{r,c}$ is the residence time of a droplet in a cell, which is defined by:

$$t_{r,c} = \frac{|\Delta \underline{L}|}{|\underline{U}_{d,r}|}$$

in which $\Delta \underline{L} = (\Delta\xi, \Delta\eta, \Delta\zeta)$ is the cell length vector defined by the arclengths in the ξ-, η- and ζ- directions.

Under the restriction of (6.55), it may well be the case that $\delta t < 1\mu s$—a time scale much smaller than the allowable time step size, Δt, for the solution of the gas-phase equations, since a fully-implicit scheme is adopted in the discretised equations (Section 6.2). For instance, in the near-injector region, one typically has $|\Delta \underline{L}| = 1mm$, and $|\underline{U}_{d,r}| = 100m/s$, which yields $t_{r,c} = 1\mu s$. Thus, it is not realistic to use the same time step sizes for both droplet and gas-phase calculations, since this would increase considerably the computation cost, especially for engine calculations which involves large three dimensional calculations. A judicious approach, as will be utilised in this study, is to distinguish δt from Δt, and to use a 'temporal subscycling' method in the droplet calculation. The basic idea here is to advance the droplet calculations using a subcycling step, δt, which satisfies the condition (6.55) and is a fraction of the overall time step, Δt. This method ensures reasonable accuracy of

droplet and gas-phase calculations while avoiding the additional computational cost arising from the practice which sets $\Delta t = \delta t$.

Further simplification can be made by omission of t_c and t_{int} in determining δt, as discussed by Tabrizi (1991) who cites some evidence to justify this treatment. Moreover, according to Tabrizi (1991), it is acceptable to use the following subcycling step:

$$\delta t_j = min\left(\frac{t_{r,c}}{10}, \frac{t_b}{10}\right) \tag{6.56}$$

6.3.2 Evaluation of the Local values of Gas-Phase-Related Variables

As evidenced by the droplet equations, the droplet calculations require the values of some gas field properties (e.g. temperature, velocities) along the trajectory of the droplet. At any particular time when droplet calculations are performed, it is often the case that the droplet position is not coincident to that of the grid point of the cell to which the droplet pertains, where the gas variables are stored. This gives rise to a problem as to how to evaluate the gas-phase properties at the droplet position. A simple way is to use the values of the gas phase at the grid node. This will however provoke non-negligible errors if the cell size is large or the droplet is located very close to the cell faces. An alternative, which is adopted in this study following Kralj (1995), is to employ a spatial interpolation which is represented by:

$$\phi^{i,j} = \phi^j(\underline{x}_d) = \phi^i_P + (\nabla\phi)^i_P \cdot (\underline{x}_P - \underline{x}^j_d) \tag{6.57}$$

where $\phi(\underline{x}_d)$ represents a general gas property at the droplet position $\underline{x}^j_d$ (here j refers to the value at the j-th subcycling time step; and $\underline{x}_P$ is the position vector of cell center in which the parcel temporarily resides. The superscript ^{i} denotes the values at the i-th overall time step. The nodal values of the gradient $(\nabla\phi)_P$ is calculated from (6.33).

6.3.3 Finite Difference Form of Droplet Equations

The droplet equations are all discretised into first-order difference form using the Eulerian implicit scheme, except for the droplet trajectory equations whose difference equation is explicit. They are give as follows.

Droplet Mass Equation

$$m_d^j \approx m_d^{j-1} + \dot{\mathcal{M}}\delta t_j \tag{6.58}$$

where

$$\dot{\mathcal{M}} = -2\pi D_d^{j-1}\left[\frac{\mathcal{D}_m Sh}{R_m(T+T_d)} P_T \ln\left(\frac{P_T - P_{v,\infty}}{P_T - P_{v,s}}\right)\right]^{j-1} \tag{6.59}$$

in which T is the gas temperature which is affected by the presence of the droplet and is specified from Equation (6.57).

Droplet Energy Equation (3.153)

$$T_d^j = \frac{1}{\tau_T^{j-1} + G^{j-1}\delta t_j}\left[G^{j-1}\delta t_j T^{j-1} + (\tau_T T_d)^{j-1} - \delta t_j\left(\frac{h_{fg}\tau_T}{\tau_v c_{p_d}}\right)^{j-1}\right] \tag{6.60}$$

where

$$G = \frac{z}{e^z - 1} \tag{6.61}$$

τ_v and τ_T are evaluated from (3.154) and (3.155), respectively.

Droplet Momentum Equation

$$\begin{aligned}\underline{U}_{d,r}^j \approx \underline{U}_{d,r}^{j-1} + \frac{1}{\tau_m^{j-1}}\left[\left(\underline{V}_r + \underline{V}_r''\right)^j - \underline{U}_{d,r}^j\right]\delta t_j \\ -\Delta\underline{V}_g^j + S_{\underline{U}_d,r}^{j-1}\delta t_j\end{aligned} \tag{6.62}$$

where, the momentum response time τ_m is given by (3.129), $\underline{V}_r$ and $\underline{V}_r''$ are respectively the mean and fluctuating components of the gas relative velocity; $\Delta\underline{V}_g^j = \underline{V}_g^j - \underline{V}_g^{j-1}$; and $S_{\underline{U}_{d,r}}$ contains terms representing the centrifugal and Coriolis effects and is given for the expanding/contracting and translating regions by Equations (3.133) and (3.134), respectively.

It should be noted that the droplet velocity $\underline{U}_{d,r}$ is resolved in the local coordinate frame attached to the cell to which it pertains. Thus, when a droplet moves from cell 1 at the (j-1)-th subcycling time step, to cell 2 which is a neighbouring cell of cell 1 at the j-th subcycling step, $\underline{U}_{d,r}^j$ and $\underline{U}_{d,r}^{j-1}$ may correspond to different local coordinate frames. An example is a two-dimensional case illustrated in Figure 6.7.

If this is the case, care must be taken to ensure that $\underline{U}_{d,r}^j$ and $\underline{U}_{d,r}^{j-1}$ are resolved in the same local coordinate frame. Failure to do this will take no account of the centrifugal and Coriolis effects and thereby provoke numerical errors where the mesh curvature is high, especially near or at the grid pole, which is (mathematically) a singular point. Thus in this study, for accuracy and consistency, the velocity $\underline{U}_{d,r}^{j-1}$

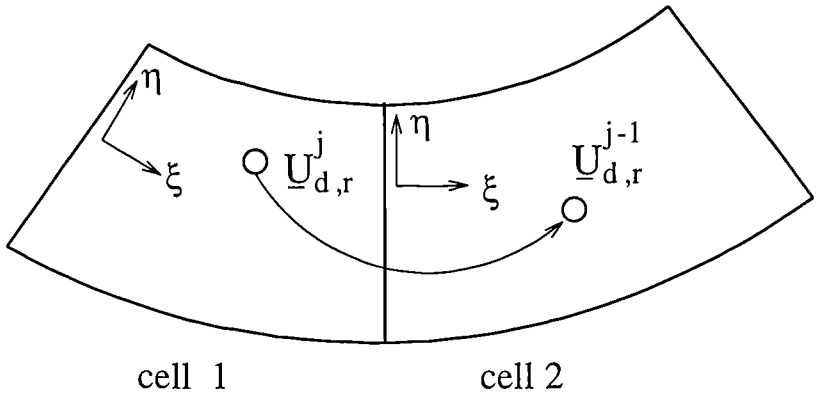


Figure 6.7: illustration of a droplet moving from one cell to another in one subcycling step, with both cells associated with different local coordinate frame

is always resolved in the same local coordinate frame as is $\underline{U}^{j}_{d,r}$. For this purpose, the following practice described by Tabrizi (1991) is adopted.

Let the moving droplet be resolved, at the (j-1)-th subcycling time step, in the local coordinate frame which has base vectors $(\underline{a}_1^{j-1}, \underline{a}_2^{j-1}, \underline{a}_3^{j-1})$; and at the j-th subcycling time step in the local coordinate frame with base vectors $(\underline{a}_1^{j}, \underline{a}_2^{j}, \underline{a}_3^{j})$. Thus, $\underline{U}^{j-1}_{d,r}$ can be resolved respectively along the above two sets of base vectors as:

$$\underline{U}^{j-1}_{d,r} = U^{j-1}_{d,r}\,\underline{a}_1^{j-1} + V^{j-1}_{d,r}\,\underline{a}_2^{j-1} + W^{j-1}_{d,r}\,\underline{a}_3^{j-1} \tag{6.63}$$

$$(\underline{U}^{j-1}_{d,r})^* = (U^{j-1}_{d,r})^*\underline{a}_1^{j} + (V^{j-1}_{d,r})^*\underline{a}_2^{j} + (W^{j-1}_{d,r})^*\underline{a}_3^{j} = \underline{U}^{j-1}_{d,r} \tag{6.64}$$

Noting that (6.63) and (6.64) represent the same vector, one can easily obtain the following relationships:

$$\begin{aligned}\left(U^{j-1}_{d,r}\right)^* = \Big\{\Big[&(U^{j-1}_{d,r}\cos\beta^{j-1} + W^{j-1}_{d,r}\sin\beta^{j-1})\cos\Delta\alpha \\ &+ V^{j-1}_{d,r}\sin\Delta\alpha\Big]\cos\beta^{j} \\ &-(W^{j-1}_{d,r}\cos\beta^{j-1} - U^{j-1}_{d,r}\sin\beta^{j-1})\sin\beta^{j}\Big\}\end{aligned}$$

$$\left(V^{j-1}_{d,r}\right)^* = V^{j-1}_{d,r}\cos\Delta\alpha - \left[U^{j-1}_{d,r}\cos\beta^{j-1} + W^{j-1}_{d,r}\sin\beta^{j-1}\right]\sin\Delta\alpha \tag{6.65}$$

$$\begin{aligned}\left(W^{j-1}_{d,r}\right)^* = \Big\{\Big[&\left(U^{j-1}_{d,r}\cos\beta^{j-1} + W^{j-1}_{d,r}\sin\beta^{j-1}\right)\cos\Delta\alpha \\ &+ V^{j-1}_{d,r}\sin\Delta\alpha\Big]\sin\beta^{j} \\ &+ (W^{j-1}_{d,r}\cos\beta^{j-1} - U^{j-1}_{d,r}\sin\beta^{j-1})\cos\beta^{j}\Big\}\end{aligned}$$

In the above expressions, β is the angle between the ζ-direction and the axis of symmetry on the ξ-ζ plane (see Figure 3.2); and $\Delta\alpha$ is the angle between $\underline{a}_1^j$ and $\underline{a}_1^{j-1}$ or $\underline{a}_2^j$ and $\underline{a}_2^{j-1}$ on the ξ-η plane.

In the light of the above discussion, the droplet momentum difference equation (6.62) is rearranged to yield:

$$\underline{U}_{d,r}^j \approx \frac{\underline{U}_{d,r}^{j-1}\tau_m^{j-1} + (\underline{V}_r^{nj} + \underline{V}_r''^n)\delta t_j - \Delta\underline{V}_g^j\tau_m^{j-1}}{\tau_m^{j-1} + \delta t_j} \tag{6.66}$$

where the superscript * associated with $\underline{U}_{d,r}^{j-1}$ has been dropped, but it should be understood that its components are always defined by (6.65).

Droplet Trajectory Equation

$$\underline{x}_{d,r}^j = \underline{x}_{d,r}^{j-1} + \delta t_j \underline{U}_{d,r}^{j-1} \tag{6.67}$$

6.3.4 Evaluation of the Interaction terms

First of all, we start with the evaluation of the void fraction, θ, which appears in the gas phase equations. For any particular cell containing grid point P, the void fraction of this cell, θ_P, is calculated by summing up the contributions of all the droplets residing in this cell to yield:

$$\theta_P = 1 - \frac{1}{\mathcal{V}_P}\sum_k \left(\frac{M}{\rho}\right)_{d,k} \tag{6.68}$$

where $\sum_k$ is the summation over all the droplet parcels contained in the control volume, and the mass of the parcel k, $m_{d,k}$, is given by:

$$M_{d,k} = N_{d,k} m_{d,k} \tag{6.69}$$

in which, $N_{d,k}$ and $M_{d,k}$, are the number of droplets and mass of a droplet, respectively, in parcel number k.

It should be noted that the Lagrangian description presented here contains no provision for recognising the fact that the droplet parcel actually disperses over a volume which is larger than the liquid volume it contains, and the fact that even though the center of the droplet parcel is within one cell, it may have some droplets distributed in one or more neighbouring cells. It is thus possible that Equation (6.68) can produce a negative void fraction in situations where many parcels enter a given cell. Hence, practical provision in coding is needed to avoid this by choosing

the cell size to be large compared to the droplet sizes or by preventing too many droplets from entering one cell in the calculations.

Attention is now turned to the evaluation of the droplet source terms contributing to the gas phase equations by use of the temporal subcycling procedure.

The droplet mass source term, $S_{m,d}$, which appears in the gas phase continuity and fuel concentration equations, is evaluated as:

$$\hat{S}_{m,d} \approx -\frac{1}{\Delta t}\sum_k\sum_j\left[M_{d,k}^j - M_{d,k}^{j-1}\right] \tag{6.70}$$

where, Δt is the overall time step, $\sum_j$ is the summation over all the subcycling time steps, and the superscript ^{j} denotes the value at the j-th subcycling time step.

Similarly, we can obtain the discretised expressions for droplet energy source term, $S_{e,d}$, and momentum exchange term, $S_{\underline{V}_{r,d}}$, respectively, as follows:

$$\hat{S}_{e,d} \approx \frac{1}{\Delta t}\sum_k\sum_j\left[(Mc_pT)_{d,k}^j - (Mc_pT)_{d,k}^{j-1}\right] \tag{6.71}$$

and;

$$\hat{S}_{\underline{V}_{r,d}} \approx \frac{1}{\Delta t}\sum_k\sum_j\left[(M_d\underline{U}_{d,r})_k^j - (M_d\underline{U}_{d,r})_k^{j-1}\right] \tag{6.72}$$

Equation (6.72) can be rearranged, with the aid of (6.66), to yield:

$$\hat{S}_{\underline{V}_{r,d}} \approx \frac{1}{\Delta t}\sum_k\sum_j\left[\frac{M_{d,k}^j\left(\underline{U}_{d,r}^{j-1}\tau_m^{j-1} + (\underline{V}_r^{n,j} + \underline{V}_r''^{n}\delta t_j - \Delta\underline{V}_g^j\tau_m^{j-1}\right)}{\tau_m^j + \delta t_j} - \left(M_d\underline{U}_{d,r}\right)_k^{j-1}\right] \tag{6.73}$$

in which $\underline{V}_r^{n,j}$ is evaluated, according to (6.57), as:

$$\underline{V}_r^{n,j} = (\underline{V}_r)_P + (\nabla(\underline{V}_r))_P(\underline{x}_{d,k} - \underline{x}_P) \tag{6.74}$$

Using (6.74), Equation (6.73) can further be cast into

$$\hat{S}_{\underline{V}_{r,d}} = S_d^I(\underline{V}_r^n)_P + S_d^{II} \tag{6.75}$$

in which

$$S_d^I = -\frac{1}{\Delta t}\sum_k\sum_j\frac{\delta t_j M_{d,k}^j}{\tau_m^{j-1} + \delta t_j} < 0 \tag{6.76}$$

$$S_d^{II} = \frac{1}{\Delta t}\sum_k\sum_j\left\{(M_d\underline{U}_{d,r})_k^{j-1} - \frac{\delta t_j M_{d,k}^j}{\tau_m^{j-1} + \delta t_j}\left[(\nabla(\underline{V}_r))_P\cdot(\underline{x}_{d,k} - \underline{x}_P)\right] + \frac{M_{d,k}^j\left(\underline{U}_{d,r}^{j-1}\tau_m^{j-1} + \underline{V}_r''^{n}\delta t_j - \Delta\underline{V}_g^j\tau_m^{j-1}\right)_k}{\tau_m^{j-1} + \delta t_j}\right\} \tag{6.77}$$

From Expression (6.76), it can be seen that the droplet source term (Equation (6.73)) obtained in this study serves to increase the diagonal dominance of the coefficient matrix, thereby enhancing stability and accelerating the convergence rate of linear iterative solver.

6.4 The Numerical Algorithm

In the foregoing sections, governing equations for both gas and droplet phases have been discretised into algebraic quations. It remains now to assemble a solution procedure for them in order to solve for the grid point values of the dependent variables. Before this is pursued, however, it is illuminating to review briefly some features of the discretised equations.

Inspection of Equations (6.53) and (6.54) reveals that they are strongly non-linear and fully influenced by the droplet phase, as evidenced by the appearance of droplet-related source terms. There are interlinkages between different primitive variables, with the coupling between the pressure and velocities being the most strongest. The gas velocities enter every set of equations, implying the primary importance of calculations of the velocities (thus also pressures due to their strong coupling). Hence, special attention must be paid to the velocity-pressure coupling in devising a solution algorithm.

The discretised droplet-phase equations (6.58), (6.60), (6.66) and (6.67), although less complicated, are linked to the gas-phase properties.

A variety of numerical algorithms have emerged for solving the discretised gas phase equations. These algorithms can, in general, be categorised into two classes. The first class is referred to as the 'sequential' approach, which is characterised by sequential solution of the governing equations for the primitive flow variables. The second class is the fully-coupled approach, which solve all equations simultaneously. In the sequential approach, much attention is paid to the velocity-pressure coupling. Compared to the full-coupling approach, the sequential approach has less coupling between flow variables, which generally leads to slower convergence. However, the sequential approach has the important advantage that additional complexities—for example, chemical reaction—can easily be accommodated by simply adding species-balance equations to the stack. The overall run time increases since each governing

equation is solved independently, and the total storage requirements scale linearly with the number of equations solved. On the other hand, the computer and storage requirements escalate faster in a fully coupled solution strategy. Consequently, the sequential solution procedure has been favoured for numerical simulations of a broad range of fluid flow problems. The literature is now replete with sequential solution algorithms bearing such names as SIMPLE (Patankar & Spalding 1972), SIMPLER (Patankar 1981), SIMPLEC (Doormaal & Raithby 1984), FIMOSE (Latimer & Pollard 1985) and PISO (Issa 1986). All these schemes involve the use of predictor-corrector iteration schemes, but differ from one another in the manner in which the momentum and pressure equations are corrected.

The PISO algorithm provides a predictor-corrector scheme for the implicit solution of the set of algebraic equations. It has a distinct feature in that simultaneous solution of the momentum equations (usually using an iterative method) is necessary only in the predictor stage. In each corrector stage the velocities can be determined directly for each grid point via the corrected pressure field and the discretised momentum equations without solving simultaneous equations. It is this feature of PISO that makes it more efficient than other sequential solution algorithms, which, depending on the convergence rate, involve two or more sequences of iterative solution of each set of momentum algebraic equations. Some evidence to support this has been provided by Issa et al (1983), who disclosed that a saving in CPU time as large as tenfold was realized with PISO as compared to SIMPLER. In addition to its efficiency, PISO also retains the advantage that it is stable for large time steps. Because of the special advantages that PISO can offer, continuous efforts have been devoted to extend it to suit to in-cylinder flow calculations. The EPISO (standing for Engine PISO) algorithm was an extension of PISO by Gosman et al (1984), Tsui (1987) and Begleris (1987) to cope with only the in-cylinder gas flow calculations. This has been subsequently extended to include the Lagrangian spray description by some other investigators (eg. Tabrizi 1991) who coined the name EPISO-SPRAY (standing for Engine PISO with spray) for it. In this study the EPISO-SPRAY algorithm is further developed to allow for the the spray impingement and film dynamics to be accounted. The main strategies adopted in this algorithm are:

- First order linearisation of the non-linear equations (6.53) and (6.54) is performed by evaluating the coefficients and source terms using the prevailing

field values.

- The equations to be solved are factorised in one predictor step and a number of corrector steps. The number of corrector steps employed is determined by a prespecified convergence criterion. In the predictor step where a guessed pressure field is used, droplet properties, fuel vapor mass fraction, gas energy and velocities are predicted in an implicit manner. In each corrector step, the pressure equation, which is derived from a combination of discretised continuity and momentum equations, replaces the continuity relation, while the momentum equations retain their role for defining the velocity field, with both sets of equations suitably coupled. The pressure correction is performed first by solving the pressure equation. Following this, the field-dependent coefficients arising from the coupling and nonlinearity are updated to ensure mass conservation. Then the velocities are corrected based on the corrected pressures. These corrected velocities are subsequently used to yield the better prediction of the other flow variables.

- Provision is made to cope with the additional problem arising from the bulk pressure changes due to the piston motion and bulk mass change due to the valve openings. This is done by introducing a bulk-adjustment procedure consisting of a global correction of local pressure and densities in a way as to ensure overall conservation of mass and energy. The need for doing this stems from the recognition of the following facts: (i) the bulk pressure changes are generally large compared with the local spatial variations associated with the fluid motion, and care must be taken to ensure that the former do not swamp the latter; and (ii) when the valves are open and the process of mass flow through the valves is in progress, the discretised gas momentum equations involve open geometry boundary. In such circumstances, Neumann boundary conditions are imposed on the pressure corrections due to the staggered grid arrangement. For the pressure-based method employed here, the explicit enforecement of global mass conservation is important in order to maintain good convergence rates in solving the pressure equation.

The above points are now elaborated in detail.

6.4.1 Initial Bulk Adjustment Step

The piston motion and flow through the valves have a twofold effect on the fluid within the cylinder: globally, they act to compress or expand the bulk of fluid, causing a global change in the bulk gas pressure and density after a time step; while on a local basis, they induce inhomgeneities, setting up an in-cylinder velocity field. Accordingly, we account for the first effect by introducing a bulk adjustment step, as will be detailed in this subsection, to render correction of the average fluid pressure and density (thus also the temperature); while allowing the second effect to be addressed in the predictor-corrector solution procedure which will be described in the following subsections.

For simplicity, it can be assumed that the global compression/expansion leads to a uniform increase or decrease in local pressure and density. This is justifiable if the flow velocity through the valve is sufficiently small compared to the speed of sound, since under these circumstances, rapidly propagating pressure waves of small apmlitude tend to equilibrate the pressure and densities within the cylinder, at least in relation to their absolute levels. With this assumption, the old-time step local density ρ_m^o and pressure P_m^o at the m-th cell can be corrected as follows:

$$P_m^{o+} = P_m^o + P^+ \tag{6.78}$$

$$\rho_m^{o+} = \rho_m^o + \rho^+ \tag{6.79}$$

where the uniform global increments in pressure P^+ and density ρ^+ can be evaluated from the requirement that the overall mass and energy calculated based on the summation over all cells be equal to those estimated using global cylinder mass and energy equations, thus yielding:

$$\rho_{cyl}^n \sum_m \mathcal{V}_m^n \theta_m^n = \sum_m (\rho_m^o + \rho_m^+) \mathcal{V}_m^n \theta_m^n \tag{6.80}$$

$$\left(\frac{c_p}{R}\right)_{cyl} P_{cyl}^n \sum_m \mathcal{V}_m^n \theta_m^n = \left(\frac{c_p}{R}\right)_{cyl} \sum_m (P_m^o + P_m^+) \mathcal{V}_m^n \theta_m^n \tag{6.81}$$

which, after rearrangement, gives:

$$\rho^+ = \rho_{cyl}^n - \frac{\sum_m \rho_m^o \mathcal{V}_m^n \theta_m^n}{\mathcal{V}_{cyl,b}} \tag{6.82}$$

$$P^+ = P_{cyl}^n - \frac{\sum_m P_m^o \mathcal{V}_m^n \theta_m^n}{\mathcal{V}_{cyl,b}} \tag{6.83}$$

where $\mathcal{V}_m^n$ is the volume of cell m; $\sum_m$ denotes summation over all cells, and $\mathcal{V}_{cyl,b}^n = \sum_m \mathcal{V}_m^n \theta_m^n$ represents the cylinder bulk volume. The cylinder bulk density ρ_{cyl}^n and pressureP_{cyl}^n are evaluated from the time-discretized overall cylinder continuity and energy equations (see for example Begleris 1978) to yield:

$$\rho_{cyl}^n = \frac{\rho_{cyl}^o \sum_m \mathcal{V}_m^o \theta_m^o + \dot{m}_v \Delta t}{\sum_m \mathcal{V}_m^n \theta_m^n} \tag{6.84}$$

$$P_{cyl}^n = \frac{\left[\left(\frac{c_p}{R}\right)_{cyl} \mathcal{V}_{cyl,b}^o - \mathcal{V}_{cyl,b}^-\right] P_{cyl}^o + \left\{\left[\left(\frac{c_p}{R}\right)_{cyl} \frac{P_{cyl}^o}{\rho_{cyl}^o} + e_v\right] \dot{m}_v + \dot{Q}_b\right\} \Delta t}{\left(\frac{c_p}{R}\right)_{cyl} \mathcal{V}_{cyl,b}^o - \mathcal{V}_{cyl,b}^-} \tag{6.85}$$

where e_v is the specific internal energy, $\dot{m}_v$ denotes the mass flow rate through the valve, $\dot{Q}$ is the total heat transfer rate at the cylinder surface, and $\mathcal{V}_{cyl,b}^-$ is the time average cylinder bulk volume:$\mathcal{V}_{cyl,b}^- = (\mathcal{V}_{cyl,b}^n + \mathcal{V}_{cyl,b}^o)/2$.

The corresponding local temperature can then be calculated using the equation of state:

$$T_m^{o+} = \frac{P_m^{o+}}{R_{mix} \rho_m^{o+}} \tag{6.86}$$

and the local bulk density can be estimated, as a first approximation, to be:

$$(\rho_b)_m^{o+} = \rho_m^{o+} \theta_m^o \tag{6.87}$$

Finally, the local gas internal energy and turbulent viscosity can be updated to give:

$$(e_s^{(1)})_m = e_s(T_m^{o+}, f_m^o) \tag{6.88}$$

$$(\mu_t)_m = C_\mu \rho_m^{o+} \frac{(k_m^o)^2}{\epsilon_m^o} \tag{6.89}$$

6.4.2 The Predictor Step

In the predictor stage, a first estimate is made of the values of both droplet and gas field which are subject to the refinement in the corrector stage. The predictor of droplet field precedes that of the gas field in order to provide interaction source terms necessary for the gas phase calculations. Hereafter, we use superscript $^{(1)}$ to denote the values of any variable obtained at the end of the predictor step.

I. Droplet Predictor

The finite-diffenence droplet equations (6.58), (6.60), (6.66) and (6.67) are linearised using the prevailing droplet and gas fields. Then droplet calculations in the subcycling procedure are carried out in the following sequence:

(i) Breakup

In the near-nozzle region, droplets usually possess larger sizes and velocities. Therefore the aerodynamic-induced droplet breakup is important here. Thus, the breakup calculation precedes the droplet velocity calculation so that the change of droplet size is introduced in the evaluation of the droplet velocity described later.

To obtain the droplet size resulting from breakup the rate equation (3.169) is intergrated over the subcycling time step, δt_j, which is assumed to be a constant during τ_b. The assumption invoked here hinges on the fact that δt_j is chosen to be much smaller than τ_b ($\delta t_j \leq \tau_b/10$). Thus, we have:

$$D_d^j = D_d^{(1)j-1} \exp\left(-\frac{\delta t_j}{\tau_b^{o\,j-1}}\right) + \left(D_{d,stable}^{o\,j-1}\right)\left[1 - \exp\left(-\frac{\delta t_j}{\tau_b^{o\,j-1}}\right)\right] \tag{6.90}$$

where $D_{d,stable}$ and τ_b are given by (3.170) and (3.171) respectively.

(ii) Velocity

$$\underline{U}_{d,r}^{(1)j} \approx \frac{\underline{U}_{d,r}^{(1)j-1}\tau_m^{o\,j-1} + (\underline{V}_r^o + \underline{V}_r''^o)\delta t_j - \Delta\underline{V}_g^{(1)j}\tau_m^{o\,j-1}}{\tau_m^{o\,j-1} + \delta t_j} \tag{6.91}$$

where $\tau_m^{o\,j-1}$ is evaluated with the use of D_d^j:

$$\frac{1}{\tau_m^{o\,j-1}} = \frac{3}{4}C_D^{o\,j-1}\frac{\rho^{o+}}{\rho_d^{(1)j-1}}\frac{\left|\underline{V}_r^o - \underline{U}_{d,r}^{(1)j-1}\right|}{D_d^j} \tag{6.92}$$

in which the drag coefficient, C_D is given by the correlation (3.113).

(iii) Position

$$\underline{x}_{d,r}^{(1)j} = \underline{x}_{d,r}^{(1)j-1} + \delta t_j\,\underline{U}_{d,r}^{(1)j-1} \tag{6.93}$$

(iv) Mass

$$m_d^{(1)j} = m_d^{(1)j-1} + \dot{\mathcal{M}}^o\delta t_j \tag{6.94}$$

where the coefficient $\dot{\mathcal{M}}$ is calculated from (6.59).

(v) Temperature

The above-obtained D_d^j, $U_{d,r}^{(1)j}$ and $m_d^{(1)j}$ are used to calculate the droplet temperature, as follows:

$$T_d^{(1)j} = \frac{1}{\tau_T^{(1)j-1} + G^{(1)j-1}\delta t_j}\left[G^{(1)j-1}\delta t_j T^{(1)j-1} + (\tau_T T_d)^{(1)j-1} - \delta t_j \left(\frac{h_{fg}\tau_T}{\tau_v c_{p_d}}\right)^{(1)j-1}\right] \tag{6.95}$$

where the time scales τ_T and τ_v are estimated, respectively, from (3.155) and (3.154);and G is calculated from (6.61).

Once $T_d^{(1)j}$ is known, the droplet density $\rho_d^{(1)j}$ can be determined for a given fuel. This in turn leads to the determination of droplet size:

$$D_d^{(1)j} = \left(\frac{6}{\pi}\frac{m_d^{(1)j}}{\rho_d^{(1)j}}\right)^{1/3} \tag{6.96}$$

(vi) The interaction terms

The droplet mass, momentum and energy exchange terms as well as void fraction can then be determined from (6.70), (6.72), (6.71) and (6.68), using the above-determined values, $m_d^{(1)j}$, $\underline{U}_{d,r}^{(1)j}$, $T_d^{(1)j}$ and $\rho_d^{(1)j}$.

II. The Gas-phase Predictor Step

The above estimates of droplet fields together with the prevailing gas velocity, bulk-adjusted pressure and density fields are used to assemble and solve the algebraic equations for fuel mass fraction, energy and momentum in an implicit manner. The procedures are as follows:

Fuel vapor mass fraction:

$$A_P\,(m_f)_P^{(1)} = \sum_C A_C\,(m_f)_C^{(1)} + A_P^o\,(m_f)_P^o + \hat{S}_{m,d}^1 \tag{6.97}$$

where the droplet mass source term $\hat{S}_{m,d}^1$ is calculated from (6.70):

$$\hat{S}_{m,d}^1 = -\frac{1}{\Delta t}\sum_k \sum_j \left[M_{d,k}^{(1)j} - M_{d,k}^{(1)j-1}\right] \tag{6.98}$$

Energy:

$$A_P e_{s,P}^{(1)} = \sum_C A_C e_{s,C}^{(1)} + S_U^{e(l)} + \hat{S}_{e,d}^{(1)} \tag{6.99}$$

where

$$\hat{S}_{e,d}^{(1)} = \frac{1}{\Delta t} \sum_k \sum_j \left[(Mc_pT)_{d,k}^{(1)j} - (Mc_pT)_{d,k}^{(1)j-1} \right] \tag{6.100}$$

and:

$$S_U^{e(1)} = -\theta_P^{(1)} \left\{ \left[aU^o \frac{P^o + P^{(l)}}{2} \right]_w^e + \left[aV^o \frac{P^o + P^{(l)}}{2} \right]_s^n + \left[aW^o \frac{P^o + P^{(l)}}{2} \right]_u^d \right\} \tag{6.101}$$

Upon solving for $e^{(1)}$, the temperature $T^{(1)}$ is obtained from:

$$e^{(1)} = C_{v_{mix}} T^{(1)} \tag{6.102}$$

Momentum

$$\begin{aligned} A_P^{(1)} (\underline{V}_r)_P^{(1)} &= \sum_C A_C (\underline{V}_r)_C^{(1)} - \theta_P \nabla_{\text{dif}} P \\ &\quad + A_P^o (\underline{V}_r)_P^o + \hat{S}_U^{\underline{V}_r(1)} + \hat{S}_d^{II(1)} \end{aligned} \tag{6.103}$$

where

$$A_P^{(1)} = A_P - S_P^{\underline{V}} - S_d^{I(1)} \tag{6.104}$$

Equation (6.103) can be solved to yield the velocity field, $\underline{V}_r^{(1)}$, which satisfies the local momentum equations (for the assumed prevailing fields) but not the continuity equation.

6.4.3 The Corrector Step

The droplet and gas fields obtained in the predictor step are only first approximations. They have to be corrected repeatedly until prespecified convergence criteria are satisfied. The main issues involved in the correctors are now elaborated for a particular corrector step, i.e., the $(l-1)$-th corrector step, at which the values of the variables are marked by the superscript $^{(l)}$ $(l \geq 2)$.

The droplet corrector procedure is similar to that of the predictor, and the same sequence can be followed. Moreover, the same equations as (6.90) to (6.96) can be written except that the superscript $^{(1)}$ and $^{(o)}$ are replaced by $^{(l)}$ and $^{(l-1)}$.

Attention is now focused on the gas corrector procedure. An essential issue of gas-phase corrector is to ensure adequate satisfaction of both continuity and momentum equations. This is attempted by first correcting the pressure field and then velocity fields and other relevant variables. Pressure correction is based on an implicit pressure equation derived from combination of the discretised continuity and momentum equations, which are given, respectively, by:

Continuity:

$$\frac{\left(\rho_b^{(l)}\mathcal{V}^n\right)_P - \left(\rho_b\mathcal{V}\right)_P^{\circ}}{\Delta t} + \nabla_{\text{dif}} \cdot \left(\rho_b^{(l)}\underline{V}_r^{(l)}\right) = \hat{S}_{m,d}^{(l)} \tag{6.105}$$

Momentum:

$$\begin{aligned}\left(\frac{A_P^{(l)}}{\rho_{b,P}^{(1)}}\right)\rho_{b,P}^{(l)}(\underline{V}_r)_P^{(l)} &= \sum_C A_C(\underline{V}_r)_C^{(l-1)} - \theta_P^{(l)}\nabla_{\text{dif}}P \\ &\quad + A_P^{\circ}(\underline{V}_r)_P^{\circ} + \hat{S}_U^{\underline{V}_r^{(l)}} + \hat{S}_d^{II^{(l)}}\end{aligned} \tag{6.106}$$

To obtain the pressure equation, we insert (6.106) into (6.105) and make use of the relation:

$$\rho_b^{(l)} = \frac{P^{(l)}\theta^{(l)}}{R_{mix}T^{(l-1)}} \tag{6.107}$$

This provides:

$$A_P^{p^{(l)}}P_P^{(l)} = \sum_C A_C^{p^{(l)}}P_C^{(l)} + S_U^{p^{(l)}} \tag{6.108}$$

where

$$\begin{aligned}A_E^{p^{(l)}} &= \left(\frac{\rho_b^{(1)}a^2\theta^{(l)}}{A_P^{(l)}}\right)_e \quad ; \qquad A_W^{p^{(l)}} = \left(\frac{\rho_b^{(1)}a^2\theta^{(l)}}{A_P^{(l)}}\right)_w \\ A_N^{p^{(l)}} &= \left(\frac{\rho_b^{(1)}a^2\theta^{(l)}}{A_P^{(l)}}\right)_n \quad ; \qquad A_S^{p^{(l)}} = \left(\frac{\rho_b^{(1)}a^2\theta^{(l)}}{A_P^{(l)}}\right)_s \\ A_D^{p^{(l)}} &= \left(\frac{\rho_b^{(1)}a^2\theta^{(l)}}{A_P^{(l)}}\right)_d \quad ; \qquad A_U^{p^{(l)}} = \left(\frac{\rho_b^{(1)}a^2\theta^{(l)}}{A_P^{(l)}}\right)_u \\ A_P^{p^{(l)}} &= \sum_C A_C^{p^{(l)}} + \frac{\theta^{(l)}}{R_{mix}T^{(l-1)}} + \frac{\mathcal{V}_P^n}{\Delta t}\end{aligned} \tag{6.109}$$

and:

$$\begin{aligned}S_U^{p^{(l)}} &= -\nabla_{dif} \cdot \left(\frac{\rho_{b,P}^{(1)}}{A_P^{(l)}}\left[\sum_C A_C(\underline{V}_r)_C^{(l-1)} + A_P^{\circ}(\underline{V}_r)_P^{\circ} + \hat{S}_U^{\underline{V}_r^{(l)}} + \hat{S}_d^{II^{(l)}}\right]\right) \\ &\quad + \hat{S}_{m,d}^{(l)} + \frac{\left(\rho_b\mathcal{V}\right)_P^{\circ}}{\Delta t}\end{aligned} \tag{6.110}$$

Once the pressure equation (6.108) is solved to yield the pressure field, $P^{(l)}$, the density field is updated using the local continuity equation to yield:

$$\begin{aligned}\rho_b^{(l)} &= \frac{\Delta t}{\mathcal{V}_P^n}\left\{\hat{S}_{m,d}^{(l)} + \frac{(\rho_b \mathcal{V})_P^o}{\Delta t}\right. \\ &\quad -\nabla_{dif}\cdot\left(\frac{\rho_{b,P}^{(1)}}{A_P^{(l)}}\left[\sum_C A_C(\underline{V}_r)_C^{(l-1)} - \theta^{(l)}\nabla_{\text{dif}}P^{(l)}\right.\right. \\ &\quad \left.\left.\left. + A_P^o(\underline{V}_r)_P^o + \hat{S}_U^{\underline{V}_r^{(l)}} + \hat{S}_d^{II^{(l)}}\right]\right)\right\} \qquad (6.111)\end{aligned}$$

The purpose of doing this is to enforce more strict satisfaction of mass conservation, thereby achieving a better convergence rate.

With the updated density field, $\rho_b^{(l)}$, together with the pressure field, $P^{(l)}$, the velocity field can be corrected from Equation (6.106) to yield $\underline{V}_r^{(l)}$.

The vapor mass fraction and energy equations are then corrected by solving the implicit set of equations:

$$A_P\,(m_f)_P^{(l)} = \sum_C A_C\,(m_f)_C^{(l)} + A_P^o\,(m_f)_P^o + \hat{S}_{m,d}^{(l)} \qquad (6.112)$$

and

$$A_P e_{s,P}^{(l)} = \sum_C A_C e_{s,C}^{(l)} + S_U^{e^{(l)}} + \hat{S}_{e,d}^{(l)} \qquad (6.113)$$

where $S_U^{e^{(l)}}$ is given by:

$$\begin{aligned}S_U^{e^{(l)}} &= -\theta_P^{(l)}\left\{\left[aU^{(l)}\frac{P^o + P^{(l)}}{2}\right]_w^e + \left[aV^{(l)}\frac{P^o + P^{(l)}}{2}\right]_s^n\right. \\ &\quad \left. + \left[aW^{(l)}\frac{P^o + P^{(l)}}{2}\right]_u^d\right\}\end{aligned}$$

Finally, the temperature field, $T^{(l)}$, is obtained from

$$e_s^{(l)} = c_{v_{mix}} T^{(l)}$$

6.4.4 Impingement Calculations

Before the impingement calculations are commerced it is necessary to resolve the gas and droplet velocity vectors into the components tangential and normal to the

wall. Thus we write:

$$\underline{V} = (U, V, W) = (u_G, v_G, w_G) \tag{6.114}$$

$$\underline{U}_d = (U_d, V_d, W_d) = (u_d, v_d, w_d) \tag{6.115}$$

where U, V, W and U_d, V_d, W_d are the original gas and droplet velocity components respectively; and the new velocity components u_G, v_G and u_d, v_d are in the directions tangential to the wall surface,and w_G and w_d are in the direction normal to the wall surface. These new components are in accord with the orthogonal coordinate system chosen for the film flow calculations.

With the new gas and droplet velocity components determined, the gas impingement pressure can first be calculated as:

$$\Delta p_G = \theta \, \frac{1}{2} \rho^{(q)} w_G^2 \tag{6.116}$$

where the superscript $^{(q)}$ stands for the last corrector number.

Then the droplet Weber and Laplace number are computed as:

$$We_n = \frac{\rho_L^{(q)} w_d^2 D_d^{(q)}}{\sigma}, \qquad La = \frac{\rho_L^{(q)} \sigma D_d^{(q)}}{\mu_L^2}$$

Once the values of We_n and La are obtained, the transition criteria established in Chapter 4 can be used to determine which impingement regime will occur. And calculations are then performed of the post-impingement characteristics for each individual regime, as described below:

(i) Adhesion

Here the impinging droplet simply adds to the built-up of local film thickness, causing an increment of the local film thickness which is given by:

$$\Delta\delta = \frac{M_d}{\rho_L^{(q)} a_{wl}} \tag{6.117}$$

where M_d the total mass of the impinging droplet parcel, and a_{wl} is the local wall area of the grid cell in which the impinging droplet resides.

Also, upon impingement the normal velocity of the droplet is destroyed and this imposes an increment of impact pressure on the local film. This is expressed by:

$$\Delta p_d = (1 - \theta) \frac{1}{2} \rho_L^{(q)} w_d^2 \tag{6.118}$$

in which θ is the void fraction of the cell containing the impinging droplet.

For the same reason, the tangential momentum lost by the impinging droplet provides a source of tangential momentum to the wall film, given by:

$$\Delta S^L_{u,d} = M_d(u_d - \bar{u}); \quad \Delta S^L_{v,d} = M_d(v_d - \bar{v}) \tag{6.119}$$

where $\bar{u}$ and $\bar{v}$ are depth-average film velocity components.

(ii) Bounce

The rebounding velocity components are determined from:

$$u_{dR} = \frac{5}{7}u_d \tag{6.120}$$

$$v_{dR} = \frac{5}{7}v_d \tag{6.121}$$

$$w_{dR} = -ew_d \tag{6.122}$$

where the restitution coefficient is evaluated from (4.13).

The contributions to the film momentum equations by the rebounding droplet are evaluated from:

$$\Delta p_d = (1-\theta)\frac{1}{2}\rho_L^{(q)}\left(w_d^2 - w_{dR}^2\right) \tag{6.123}$$

$$\Delta S^L_{u,d} = M_d(u_d - u_{dR}) \tag{6.124}$$

$$\Delta S^L_{v,d} = M_d(v_d - v_{dR}) \tag{6.125}$$

(iii) Splash

The post-impingement parameters for the two new secondary droplet parcels resulting from splashing in this regime are calculated in the following sequence:

(a) The mass ratio is evaluated as:

$$r_m = \frac{m_s}{m_I} = \begin{cases} 0.2 + \gamma(0.8 - 0.2), & \text{for dry wall} \\ 0.2 + \gamma(1.2 - 0.2), & \text{for wetted wall} \end{cases} \tag{6.126}$$

where γ is a random number uniformly distributed over the interval [0,1]. Equation (6.126) enables the determination of the mass ratio r_m, which in turn allows the evaluation of the mass of each secondary droplet parcel, i.e., $m_s/2$.

(b) The number of secondary droplets N is calculated from the number correlation (4.20) given in Chapter 4.

(c) The Sizes of Secondary droplets D_1, D_2 are determined by:

$$N_1 D_I^3 = \frac{r_m}{2} D_I^3 \tag{6.127}$$

$$N_2 D_I^3 = \frac{r_m}{2} D_I^3 \tag{6.128}$$

where N_1 and N_2 are calculated as:

$$N_1 = \gamma N, \quad N_2 = N - N_1 \tag{6.129}$$

Here γ is also a random number in the interval (0,1).

(d) The velocities of the two secondary droplet parcels, $\underline{U}_1 = (u_{d1}, v_{d1}, w_{d1})$ and $\underline{U}_2 = (u_{d2}, v_{d2}, w_{d2})$, are estimated from equations (4.21) through (4.28).

Upon determining the above quantities, the contributions of the splashing droplets to the film momentum equations are estimated as:

$$\Delta p_d = (1-\theta)\frac{1}{2}\rho_L^{(q)}\left(w_d^2 - \frac{r_m}{2}\left[w_{d1}^2 + w_{d2}^2\right]\right) \tag{6.130}$$

$$\Delta S_{u,d}^L = M_d u_d - \frac{1}{2} m_s (u_{d1} + u_{d2}) - (M_d - m_s)\bar{u} \tag{6.131}$$

$$\Delta S_{v,d}^L = M_d v_d - \frac{1}{2} m_s (v_{d1} + v_{d2}) - (M_d - m_s)\bar{v} \tag{6.132}$$

The local film thickness is increased, due to deposition of a portion of mass of the splashing droplet, by an amount:

$$\Delta\delta = \frac{M_d - m_s}{\rho_L^{(q)} a_{wl}} \tag{6.133}$$

6.4.5 Final Bulk Adjustment Step

On termination of the corrector step, the final pressure field, P^*, and density field, ρ^* are obtained which satisfy both local continuity and momentum conservation equations. Before accepting P^* and ρ^* as the field values for pressure and density at the new time level, however, it is necessary to adjust them once again to preserve overall mass and energy conservation. The purpose of this is to account for the fact that there is a minor infrigement of the overall conservation equations due to the assigned finite convergence criterion and the machine roundoff errors. Thus, a

global adjustment similar to the initial one is performed as:

$$P_m^n = P_m^* + P^{++} \tag{6.134}$$

$$\rho_m^n = \rho_m^* + \rho^{++} \tag{6.135}$$

where uniform global increment in pressure P^{++} and density ρ^{++} are given by:

$$\rho^{++} = \rho_{cyl}^n - \frac{\sum_m \rho_m^* \mathcal{V}_m^n \theta_m^n}{\mathcal{V}_{cyl,b}} \tag{6.136}$$

$$P^{++} = P_{cyl}^n - \frac{\sum_m P_m^* \mathcal{V}_m^n \theta_m^n}{\mathcal{V}_{cyl,b}} \tag{6.137}$$

The corresponding local temperature can then be calculated using the equation of state:

$$T_m^n = \frac{P_m^{*+}}{R_{mix}\rho_m^{*+}} \tag{6.138}$$

and the local bulk density can be estimated as:

$$(\rho_b)_m^n = \rho_m^{*+}\theta_m^n \tag{6.139}$$

6.4.6 The $k-\epsilon$ Predictor-Corrector Procedure

We now proceed to address the solution of the k and ϵ equations. A PISO-type predictor-corrector scheme is also used for this purpose. In this, the transportive coupling is implicit only in the predictor step, and in the correctors the coupling between k and ϵ is essentially local. This yields the possibility of an algebraic solution of the corrector equations for each cell.

To obtain the specific form of the discretized $k-\epsilon$ equations,the differential source terms of the $k-\epsilon$ equations in Table 6.1 are integrated to yield:

$$\begin{aligned}
-S_P^k &= C_\mu \left(\frac{\rho\rho_b\mathcal{V}k}{\mu_{eff}}\right)_P + \frac{2}{3}\left[\frac{\mu_{eff}\theta\mathcal{V}(\nabla\cdot\underline{V})^2}{k}\right]_P + \frac{2}{3}\left(\rho_b\mathcal{V}D^+\right)_P \\
S_U^k &= \left(\mu_{eff}\theta\mathcal{V}g_t\right)_P - \frac{2}{3}\left(\rho_b\mathcal{V}D^-k\right)_P \\
-S_P^\epsilon &= C_{\epsilon_2}\left(\frac{\rho_b\mathcal{V}\epsilon}{k}\right)_P + \frac{2}{3}C_{\epsilon_1}\left[\frac{\mu_{eff}\theta\mathcal{V}(\nabla\cdot\underline{V})^2}{k}\right]_P \\
&\quad - \left(C_{\epsilon_3} - \frac{2}{3}C_{\epsilon_1}\right)\left(\rho_b\mathcal{V}D^+\right)_P \\
S_U^\epsilon &= C_{\epsilon_1}C_\mu\left(\rho_b\mathcal{V}g_tk\right)_P + C_\mu\left(C_{\epsilon_3} - \frac{2}{3}C_{\epsilon_1}\right)\left(\frac{\rho\rho_b\mathcal{V}D^-k^2}{\mu_{eff}}\right)_P
\end{aligned} \tag{6.140}$$

where $\mathcal{V}_P$ is the cell volume, g_t denotes the strain rate part of turbulence generation $\mathcal{P}$ divided by $(\mu_{eff}\theta)$ (see Table 3.3 and 3.4), and the terms D^- and D^+ are given by:

$$\begin{aligned} D^- &= min(\nabla \cdot \underline{V}, 0) = \tfrac{1}{2}(\nabla \cdot \underline{V} - |\nabla \cdot \underline{V}|) \quad (\leq 0) \\ D^+ &= max(\nabla \cdot \underline{V}, 0) = \tfrac{1}{2}(\nabla \cdot \underline{V} + |\nabla \cdot \underline{V}|) \quad (\geq 0) \end{aligned}$$

By reference to the discretised general scalar equation (6.54), the discretised k and ϵ equations can be written, with the aid of the above relations, as:

$$(A_P^k + A_P^{k+})k_P^n = \sum_C A_C^k k_C^n + A_P^o k_P^o + (\mu_{eff}\theta\mathcal{V}g_t)_P^n - \frac{2}{3}\left(\rho_b \mathcal{V}^n D^+ k^n\right)_P \quad (6.141)$$

where

$$A_P^{k+} = C_\mu \left(\frac{\rho\rho_b\mathcal{V}k}{\mu_{eff}}\right)_P^n + \frac{2}{3}\left[\frac{\mu_{eff}\theta\mathcal{V}(\nabla \cdot \underline{V})^2}{k}\right]_P^n + \frac{2}{3}\left(\rho_b \mathcal{V}^n D^+\right)_P \quad (6.142)$$

$$A_P^k = \sum_C A_C^k + A_P^o + \hat{S}_{m,d}^n \quad (6.143)$$

and:

$$\begin{aligned} (A_P^\epsilon + A_P^{\epsilon+})\epsilon_P^n = {} & \sum_C A_C^\epsilon \epsilon_C^n + A_P^o \epsilon_P^o + C_{\epsilon_1} C_\mu \left(\rho\mathcal{V}g_t k\right)_P^n \\ & + C_\mu \left(C_{\epsilon_3} - \frac{2}{3}C_{\epsilon_1}\right)\left(\frac{\rho^n \rho_b^n \mathcal{V}^n D^- \left(k^n\right)^2}{\mu_{eff}}\right)_P \end{aligned} \quad (6.144)$$

where

$$\begin{aligned} A_P^{\epsilon+} &= C_{\epsilon_2}\left(\frac{\rho_b\mathcal{V}\epsilon}{k}\right)_P^n + \frac{2}{3}\left[\frac{\mu_{eff}\theta\mathcal{V}(\nabla \cdot \underline{V})^2}{k}\right]_P^n \\ &\quad - \left(C_{\epsilon_3} - \frac{2}{3}C_{\epsilon_1}\right)\left(\rho_b \mathcal{V}^n D^+\right)_P \\ A_P^\epsilon &= \sum_C A_C^\epsilon + A_P^o + \hat{S}_{m,d}^n \end{aligned} \quad (6.145)$$

It is evident that the above k and ϵ equations are strongly coupled through their source terms. To achieve sequential calculations, the predictor-corrector scheme employed here provides a way of efficiently decoupling the k and ϵ equations in the predictor, while in the correctors it utilizes a linearisation strategy which yields a quadratic corrector for the k and ϵ, as detailed below.

The $k-\epsilon$ predictor step

In the predictor stage, the turbulent fields to be solved are labelled by superscript $^{(1)}$, and the k and ϵ equations are split into the following fashion:

$$\left[A_P^k + \left(A_P^{k+}\right)^o\right] k_P^{(1)} = \sum_C A_C^k k_C^{(1)} + A_P^o k_P^o + \left(\mu_{eff}^o \theta^n \mathcal{V}^n g_t^n\right)_P - \frac{2}{3}\left(\rho_b^n \mathcal{V}^n D^+ k^o\right)_P \tag{6.146}$$

where A_P^k is given by Equation (6.143), and $\left(A_P^{k+}\right)^o$ is obtained with the field evaluated at the old time values of k and μ_{eff} in Equation (6.142), i.e.:

$$\left(A_P^{k+}\right)^o = C_\mu \left(\frac{\rho^n \rho_b^n \mathcal{V}^n k^o}{\mu_{eff}}\right)_P + \frac{2}{3}\left[\frac{\mu_{eff}^o \theta^n \mathcal{V}^n \left(\nabla \cdot \underline{V}^n\right)^2}{k}\right]_P + \frac{2}{3}\left(\rho_b \mathcal{V}^n D^+\right)_P \tag{6.147}$$

and:

$$\left[A_P^\epsilon + \left(A_P^{\epsilon+}\right)^o\right] \epsilon_P^{(1)} = \sum_C A_C^\epsilon \epsilon_C^{(1)} + A_P^o \epsilon_P^o + C_{\epsilon_1} C_\mu \left(\rho_b^n \mathcal{V}^n g_t^n k^{(1)}\right)_P + C_\mu \left(C_{\epsilon_3} - \frac{2}{3} C_{\epsilon_1}\right)\left(\frac{\rho^n \rho_b^n \mathcal{V}^n D^- \left(k^{(1)}\right)^{2^o}}{\mu_{eff}}\right)_P \tag{6.148}$$

where

$$\left(A_P^{\epsilon+}\right)^o = C_{\epsilon_2}\left(\frac{\rho_b^n \mathcal{V}^n \epsilon^o}{k^{(1)}}\right)_P + \frac{2}{3}\left[\frac{\mu_{eff}^o \theta^n \mathcal{V}^n \left(\nabla \cdot \underline{V}^n\right)^2}{k^{(1)}}\right]_P - \left(C_{\epsilon_3} - \frac{2}{3} C_{\epsilon_1}\right)\left(\rho_b \mathcal{V}^n D^+\right)_P \tag{6.149}$$

The linearized equations (6.146) and (6.148) are implicit in $k^{(1)}$ and $\epsilon^{(1)}$. They are solved in sequence of first k and then ϵ. The resulting fields $k^{(1)}$ and $\epsilon^{(1)}$ are then employed t calculate μ_t:

$$\mu_t = C_\mu \rho^n \frac{\left(k^{(1)}\right)^2}{\epsilon^{(1)}}$$

The $k-\epsilon$ corrector step

In the $(l-1)$-th corrector $(l \geq 2)$, the equations governing $k^{(l)}$ and $\epsilon^{(l)}$ fields are expressed, respectively, in terms of $k^{(l-1)}$ and $\epsilon^{(l)}$ together with the prevailing gas

and droplet fields. This leads to the following explicit split form of the k and ϵ equations:

$$\begin{aligned} A_P^{k(l)} k_P^{(l)} &= \sum_C A_C^k k_C^{(l)} + A_P^o k_P^o + C_\mu \left(\rho_b^n \mathcal{V}^n g_t^n k^o\right)_P \frac{k_P^{(l)}}{\epsilon_P^{(l)}} \\ &\quad - \left[\left(\rho_b^n \mathcal{V}^n\right)_P + \frac{2}{3}\left(\rho_b^n \mathcal{V}^n D^+ \frac{k^o}{\epsilon^o}\right)_P\right] \epsilon_P^{(l)} - \frac{2}{3}\left(\rho_b^n \mathcal{V}^n D^- k^o\right)_P \end{aligned} \tag{6.150}$$

where

$$A_P^{k(l)} = A_P^k + \frac{2}{3} C_\mu \left[\rho_b^n \mathcal{V}^n \frac{k^o}{\epsilon^o} \left(\nabla \cdot \underline{V}^n\right)^2\right]_P \tag{6.151}$$

and:

$$\begin{aligned} A_P^{\epsilon(l)} \epsilon_P^{(l)} &= \sum_C A_C^\epsilon \epsilon_C^{(l)} + A_P^o \epsilon_P^o + C_{\epsilon_1} C_\mu \left(\rho_b^n \mathcal{V}^n g_t^n k^o\right)_P \\ &\quad - \left[C_{\epsilon_2}\left(\rho_b^n \mathcal{V}^n\right)_P - \left(C_{\epsilon_3} - \frac{2}{3} C_{\epsilon_1}\right)\left(\rho_b^n \mathcal{V}^n D^+ \frac{\epsilon^o}{\epsilon^o}\right)_P\right] \frac{\left(\epsilon_P^{(l)}\right)^2}{k_P^{(l)}} \\ &\quad - \left(C_{\epsilon_3} - \frac{2}{3} C_{\epsilon_1}\right)\left(\rho_b^n \mathcal{V}^n D^- \epsilon^o\right)_P \end{aligned} \tag{6.152}$$

where

$$A_P^{\epsilon(l)} = A_P^k + \frac{2}{3} C_{\epsilon_1} C_\mu \left[\rho_b^n \mathcal{V}^n \frac{k^o}{\epsilon^o} \left(\nabla \cdot \underline{V}^n\right)^2\right]_P \tag{6.153}$$

In the above equations, use has been made of the relation $\mu_t^o = C_\mu \rho^n \left(k^o\right)^2 / \epsilon^o$ for the elimination of the turbulent viscosity.

Further manipulation of Equations (6.150) and (6.152) will result in the following algebraic form of equations:

$$k_P^{(l)} = \left(\frac{\alpha_1 + \alpha_2 \epsilon_P^{(l)}}{\alpha_3}\right) \epsilon_P^{(l)} \tag{6.154}$$

$$\alpha_2 \left(\epsilon_P^{(l)}\right)^2 + (\alpha_1 - A_1\alpha_2 + A_2\alpha_3)\epsilon_P^{(l)} - (A_1\alpha_1 + A_3\alpha_3) = 0 \tag{6.155}$$

where, the sets of coefficients (A_1, A_2, A_3) and (α_1, α_2, α_3) are given, respectively by:

$$\begin{aligned} A_1 &= \frac{C_\mu \left(\rho_b^n \mathcal{V}^n g_t^n k^o\right)_P}{A_P^{k(l)}} \\ A_2 &= \frac{\left[\left(\rho_b^n \mathcal{V}^n\right)_P + \frac{2}{3}\left(\rho_b^n \mathcal{V}^n D^+ \frac{k^o}{\epsilon^o}\right)_P\right]}{A_P^{k(l)}} \\ A_3 &= \frac{\left[\sum_C A_C^k k_C^{(l-1)} + A_P^o k_P^o - \frac{2}{3}\left(\rho_b^n \mathcal{V}^n D^- k^o\right)_P\right]}{A_P^{k(l)}} \end{aligned} \tag{6.156}$$

and:

$$\begin{aligned} \alpha_1 &= A_3 \\ \alpha_2 &= (B_2 - A_2) \\ \alpha_1 &= (B_1 - A_1 + B_3) \end{aligned} \tag{6.157}$$

where

$$\begin{aligned} B_1 &= \frac{C_{c_1} C_\mu \left(\rho_b^n \mathcal{V}^n g_t^n k^o\right)_P}{A_P^{\epsilon(l)}} \\ B_2 &= \frac{\left[C_{\epsilon_2}\left(\rho_b^n \mathcal{V}^n\right)_P - \left(C_{\epsilon_3} - \frac{2}{3}C_{\epsilon_1}\right)\left(\rho_b^n \mathcal{V}^n D^{+\frac{k^o}{\epsilon^o}}\right)_P\right]}{A_P^{\epsilon(l)}} \\ B_3 &= \frac{\left[\sum_C A_C^\epsilon \epsilon_C^{(l-1)} + A_P^o \epsilon_P^o + \left(C_{\epsilon_3} - \frac{2}{3}C_{\epsilon_1}\right)\left(\rho_b^n \mathcal{V}^n D^- \epsilon^o\right)_P\right]}{A_P^{\epsilon(l)}} \end{aligned} \tag{6.158}$$

Equation (6.155) is of quadratic form and implicit in $\epsilon_P^{(l)}$. It can be proved that $\epsilon_P^{(l)}$ (see Tabriz 1991) always has one positive root which is:

$$\epsilon_P^{(l)} = \frac{-(\alpha_1 - A_1\alpha_2 + A_2\alpha_3) + \sqrt{(\alpha_1 - A_1\alpha_2 + A_2\alpha_3)^2 + 4\alpha_2(A_1\alpha_1 + A_3\alpha_3)}}{2\alpha_2} \tag{6.159}$$

The corrector values of the turbulent kinetic energy $k_P^{(l)}$ is then obtained from (6.154). Up to this point, it is quite clear that $k_P^{(l)}$ and $\epsilon_P^{(l)}$ can be obtained cell by cell without solving simultaneous equations.

Finally, the turbulent viscosity can be obtained from:

$$\mu_t = C_\mu \rho^n \frac{\left(k^{(l)}\right)^2}{\epsilon^{(l)}} \tag{6.160}$$

6.4.7 Computation of Wall Film

Wall film calculations follow the gas-phase turbulence calculations. The solution procedure described in Subsection 5.6.5, together with the droplet source terms evaluated in Subsection 6.4.4, are employed for this purpose.

6.5 Solution of The Linear Algebraic Equations

In the EPISO-SPRAY algorithm described in Section 6.4, both predictor and corrector steps generated a set of simultaneous equations for each variable. The members

of each set can be written as:

$$A_P\phi_P = \sum A_C\phi_C + S \tag{6.161}$$

or in matrix form:

$$\widehat{A}\,\widehat{\phi} = \widehat{S} \tag{6.162}$$

where $\widehat{A}$ is a square seven-diagonal matrix of order $N = N_I \times N_j \times N_k$, where N_i, N_j and N_k are the number of interior grid points in the solution domain in the ξ-, η- and ζ- directions respectively. $\widehat{\phi}$ is a constant column matrix.

Some main features of the coefficient matrix, $\widehat{A}$ can be listed below:

1. $\widehat{A}$ is sparce in the sense that it has a large proportion of zero elements, because each node is connected only to a few (six for the present case) neighbouring nodes. Moreover, the non-zero elements are located in a well-defined order below and above the principal diagonal due to the use of an ordered indexing system that avoids triple subscript notation (Smith 1978).

2. $\widehat{A}$ is real and its diagonal elements are all positive, whilst its off-diagonal elements are non-positive. Furthermore, $\widehat{A}$ is strictly disgonally dominant, i.e.,

$$D_m > |C_m| + |E_m| + |B_m| + |F_m| + |G_m| + |H_m|, \quad 1 \leq m \leq N \tag{6.163}$$

(N is the equation number)

3. In the case of pressure correction equations, $\widehat{A}$ is positive definite–symmetric and strictly diagonally-dominant with positive real diagonal entries. [1]

The above properties may serve as a guide to our choice of the methods for solving simultaneous linear algebraic equations. There are two solution procedures for linear algebraic equations: direct and indirect (or iterative) methods. Direct methods always provide a solution in a single pass but can become prohibitively expensive as

[1] A real matrix, $\widehat{B}$, is called positive definite if the corresponding quadratic form, $\widehat{X^T} \cdot \widehat{B} \cdot \widehat{X}$, is greater than zero for every non-zero real vector $\widehat{X}$ ($\widehat{X^T}$ denotes the transpose of $\widehat{X}$)

the problem size increases. Iterative methods are, in general, more suitable for well-ordered, diagonally-dominant and large sparse matrices, like $\widehat{A}$ of Equation (6.162), as far as computer storage is concerned. This is because that iterative method offers an option of storing only those elements that lie on the non-zero diagonals, thereby requiring much less computer storage compared to its counterpart - direct methods. Additionally, the former tend to be self-correcting and hence tend to minimise round-off errors (Martin 1966; Brameller et al. 1976). It is for this reason that iterative methods are employed in this study to solve linear algebraic equations. In particular, the following two well-known solvers are utilised: the strongly-implicit Stone solver and the Conjugate Gradient Solver. The main features of these two solvers are outlined below.

6.5.1 The Stone Solver

The Stone Solver (Stone 1968) is essentially a strongly implicit iterative procedure (SSIP), which involves preconditioning the coefficient matrix $\widehat{A}$ to achieve efficiency. This method is employed here to solve linear implicit sets of systematic equations with non-symmetric coefficient matrices.

In SSIP, the preconditioning of the coefficient matrix $\widehat{A}$ is achieved by adding an auxiliary term, $\widehat{\delta A}$, to each side of Equation (6.162), so that the original system is changed to :

$$\left(\widehat{A} + \widehat{\delta A}\right)\widehat{\phi} = \widehat{\delta A}\,\widehat{\phi} + \widehat{S} \tag{6.164}$$

The associated iteration procedure takes the form:

$$\left(\widehat{A} + \widehat{\delta A}\right)\widehat{\phi^{(\nu+1)}} = \widehat{\delta A}\,\widehat{\phi^{(\nu)}} + \widehat{S} \tag{6.165}$$

or

$$\left(\widehat{A} + \widehat{\delta A}\right)\Delta\widehat{\phi^{(\nu)}} \approx \widehat{\gamma^{(\nu)}} \tag{6.166}$$

where ν is the iteration counter, $\Delta\widehat{\phi^{\nu}}$ is the correction to be made to the values of $\widehat{\phi^{\nu}}$ in order to obtain the new values $\widehat{\phi^{(\nu+1)}}$, and $\widehat{\gamma^{(\nu)}}$ is the residual vector given by:

$$\widehat{\gamma^{(\nu)}} = \widehat{S} - \widehat{A}\,\widehat{\phi^{(\nu)}} \tag{6.167}$$

If the process (6.167) converges, then the sequence $\widehat{\phi^{(\nu)}}$ has a limit which satisfies the original set, $\widehat{A}\,\widehat{\phi} = \widehat{S}$.

The key to SSIP lies in the choice of the preconditioning matrix $\widehat{\delta A}$, which, according to Stone (1968), shoud satisfy the following requirements:

- The matrix $(\widehat{A} + \widehat{\delta A})$ can be fatorised as:

$$\widehat{A} + \widehat{\delta A} = \widehat{L}\,\widehat{U} \tag{6.168}$$

  where $\widehat{L}$ and $\widehat{U}$ are, respectively, lower and upper triangular matrices of very simple form and are of the same order as Matrix $\widehat{A}$. Moreover, it is required that the arithmetic involved in (6.168) is much less than the standard $\widehat{L}\,\widehat{U}$ decomposition of $\widehat{A}$.

- The elements of $\widehat{L}$ and $\widehat{U}$ are easily calculated.

- $\| \widehat{\delta A} \| \ll \| \widehat{A} \|$. This means that matrix $\widehat{\delta A}$ is only a small correction to $\widehat{A}$. (Here, the notation $\| \widehat{B} \|$ designates a norm of matrix $\widehat{B}$). In this case , $(\widehat{A} + \widehat{\delta A})$ becomes closer to $\widehat{A}$ (or, in other words, more 'implicit'), thus accelerating the convergence rate of the method.

6.5.2 Conjugate Gradient Solver

The well-known conjugate gradient (CG) method was first applied by Hestenes & Stiefel (1952) to solve a linear system such as (6.162) where $\widehat{A}$ is symmetric and positive definite. This method has now become the most prominent iterative method. A review of the historical background of CG is provided by Golub and O'Leary (1989). The basic idea behind The CG method is to solve an equivalent problem of minimising the functional

$$\begin{aligned} \mathcal{F}(\widehat{\phi}) &= \frac{1}{2}(\widehat{A\phi}, \widehat{\phi}) - (\widehat{S}, \widehat{\phi}) \\ &= \frac{1}{2}\widehat{\phi^T}\,\widehat{A\phi} - \widehat{\phi^T}\,\widehat{S} \end{aligned} \tag{6.169}$$

It is easy to verify that the gradient of the quadratic form (6.169) becomes zero at $\widehat{\phi} = \widehat{\xi}$ where $\widehat{A}\,\widehat{\xi} = \widehat{S}$. Therefore the solution to (6.162) is a critical point of $\mathcal{F}(\widehat{\phi})$. If $\widehat{A}$ is positive as well as symmetric, then this solution is a mininmum of $\mathcal{F}(\widehat{\phi})$, so (6.162) can be solved by finding an $\widehat{\phi}$ that minimises $\mathcal{F}(\widehat{\phi})$.

In order to find this minimum of (6.169), the CG scheme starts at an arbitrary point $\widehat{\phi^0}$ and then searches for the minimum point in an iterative fashion:

$$\widehat{\phi^{(\nu+1)}} = \widehat{\phi^{(\nu)}} + \alpha^{(\nu)} \widehat{p^{(\nu)}} \tag{6.170}$$

where ν is the iteration counter, $\widehat{p^{(\nu)}}$ is defined as a search direction, $\alpha^{(\nu)}$ is a scalar chosen to minimise the one dimensional function $\mathcal{F}(\widehat{\phi^{(\nu)}} + \alpha p^{(\nu)})$. Here, the determination of $\alpha^{(\nu)}$ is based on the residual vector, $\widehat{\gamma^{(\nu)}}$, defined by:

$$\widehat{\gamma^{(\nu)}} = \widehat{S} - \widehat{A}\,\widehat{\phi^{(\nu)}} \tag{6.171}$$

Equation (6.170) sets out to minimise the functional $\mathcal{F}$ in the direction $\widehat{p^{(\nu)}}$. If the search direction $\widehat{p^{(\nu)}}$ is chosen to be conjugate to each direction $\widehat{p^{(0)}}, \widehat{p^{(1)}}, ..., \widehat{p^{(\nu-1)}}$, i.e.,

$$\widehat{p^{(\nu)^T}}\,\widehat{A}\,\widehat{p^{(\lambda)}} = 0, \qquad \lambda = 0, 1, ..., \nu - 1 \tag{6.172}$$

the 'exact' solution to the system can be atained, in principal, in at most N iterations (N being the order of system (6.162)), given infinite floating point precision (Golub & Van Loan 1983). Despite this, there is still great concern about the convergence rate of the CG method. The reason is twofold. Firstly, accumulated floating point roundoff errors in practice cause the residual to gradually lose accuracy, and cancellation errors cause the search vectors to lose the condition of orthogonality of (6.172). To avoid this loss of conjugacy, the iterative step should be as small as possible. Secondly, for a large enough problem, it may not be feasible to run even N iterations.

Theoretical analysis has revealed that CG is quick if there are duplicated eigenvalues of the coefficient matrix $\widehat{A}$. Also, the convergence rate is faster when eigenvalues are clustered together than when they are evenly distributed between maximum and minimum eigenvalues. Thus, a variety of attempts have been made to improve the CG convergence rates by preconditioning the system (6.162) in the fashion:

$$\widehat{M^{-1}}\,\widehat{A}\,\widehat{\phi} = \widehat{M^{-1}}\,\widehat{S} \tag{6.173}$$

The choice of $\widehat{M}$ is such that eigenvalues of $\widehat{M}\,\widehat{A}$ are closer to each other. This can be intuitively interpreted as stretching the quadratic form (6.169) to make it

appear more spherical. It is generally accepted that CG should always be used with a preconditioner if possible. In this study, the most popular preconditioning method, referred to as ICCG method, will be used. ICCG is based on an incomplete Cholesky factorisation of $\widehat{A}$:

$$\widehat{A} = \widehat{L}\,\widehat{L^T} + \widehat{E} \tag{6.174}$$

where $\widehat{E}$ is an error matrix, and $\widehat{L}$ is a lower triangular matrix which might be restricted to have the same pattern of non zero elements as $\widehat{A}$. Then, $\widehat{L}\,\widehat{L^T}$ is used as a preconditioner. It should be noted, however, that ICCG is not always stable.

6.5.3 Convergence Criteria

An iterative process is terminated when a pre-specified convergence criterion is satisfied. The convergence criterion used in this study is the one based on the normalised absolute residual sum, defined with respect to general discretised equation as:

$$R_r^{\phi} = \sum_P \left| \sum_C A_C \phi_C^{(\nu)} + S - A_P \phi_P^{(\nu)} \right| \leq \lambda \cdot R_{ref}^{\phi} \tag{6.175}$$

where λ is a small preassigned number (usually of the order of 10^{-3}), and R_{ref}^{ϕ} is a normalisation factor whose value depends on both physical realism and experience.

6.6 Implementation of Boundary Conditions

This section deals with the numerical treatment of the boundary conditions. The main task is to modify the equations for those cells adjoining various boundaries, which have been described in Section 3.7, so as to reflect the boundary conditions in the discretised equations.

6.6.1 Wall Boundaries

An internal node labelled P, which adjoins a wall boundary as illustrated in Figure 6.8, has at least one fictitious neighbouring node (e.g. Node E in Figure 6.8) and a corresponding cell face coincident with the wall surface. Thus, the treatment of

wall boundaries involves two steps. Firstly, the linkage between the cell P and its fictitious neighbouring node(s) has to be removed from the discretised equation for the cell P. This can easily be achieved by setting the relevant A_C coefficients to zero. Secondly, the wall face values ϕ_W are related to the internal nodal values ϕ_P by the physical boundary conditions (such as no-slip condition and fluxes on the walls,etc.) which will be denoted here by $S_W^\phi(\phi_P, \phi_W)$. This differs from the case for the internal cell faces where the cell face values are linked to the internal nodal values through the use of interpolation functions as described in Section 6.2. The linkage function, S_W^ϕ, has to be appropriately incorporated into the discretised equation for the cell P—which is the major problem that has to be coped with in the implementation of wall boundaries. In this study, the relation $S_W^\phi(\phi_P, \phi_W)$ is treated as a 'fictitious source term', which, following the treatment of the real source term in Section 6.2.3, is linearised as:

$$S_W^\phi = \left(S_P^\phi\right)_W \phi_P + \left(S_U^\phi\right)_W \tag{6.176}$$

where $\left(S_P^\phi\right)_W$ (< 0) and $\left(S_U^\phi\right)_W$ represent the implicit and explicit contributions, respectively. Equation (6.176) is then absorbed into the real source terms of the discretised equation for the cell P in which the A_C coefficients associated with the fictitious in-wall nodes have been set to zero.

In the following, the form of S_W^ϕ and its linearisation for different dependent variables are presented.

Velocity Components

For normal velocity component, the fictitious source term S_W^ϕ is provided by the condition:

$$(\underline{V} - \underline{V}_W) \cdot \underline{n} = 0 \tag{6.177}$$

which enables the determination of the gas normal velocity components at the wall boundary cell face. Since Equation (6.177) presents no linkage between the internal nodal and boundary values, the corresponding momentum equations need no special treatment.

As for the tangential velocity components, the no slip condition is imposed by

setting S_W^ϕ to be the shear force, F_W:

$$F_W = \tau_w \cdot a_w \tag{6.178}$$

where, the resultant wall shear stress, τ_w, is given by Equation (3.66), and a_w is the cell area coincident with the wall (see, for example, Figure 6.8). F_W can be decomposed into components along the coordinates, and for the case shown in Figure 6.8, this is given by:

$$F_{\xi\eta} = \tau_{\xi\eta} \cdot a_w = -\mu_{eff} \frac{V_P - V_W}{Y_P} a_w \tag{6.179}$$

$$F_{\xi\zeta} = \tau_{\xi\zeta} \cdot a_w = -\mu_{eff} \frac{W_P - W_W}{Y_P} a_w \tag{6.180}$$

where subscripts P and W refer to the values at a near-wall point and on the wall, respectively, and μ_{eff} is obtained from Equation (3.68).

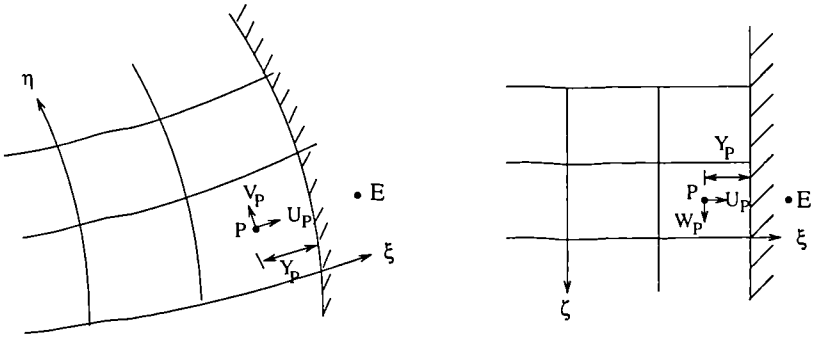


Figure 6.8: Diagram showing wall boundary

Equations (6.179) and (6.180) are then linearised according to Equation (6.176), as follows:

$$-S_P^v = \mu_{eff} \frac{a_w}{Y_P} \qquad S_U^v = \mu_{eff} \alpha_w \frac{V_W}{Y_P} \tag{6.181}$$

$$-S_P^w = \mu_{eff} \frac{a_w}{Y_P} \qquad S_U^w = \mu_{eff} \alpha_w \frac{W_W}{Y_P} \tag{6.182}$$

Energy

The thermal boundary conditions are imposed by treating the wall as a source/sink of energy whose flow rate is taken to be the fictitious source term, thus providing:

$$S^e = \dot{q}_w a_w = -K_{eff} \frac{T_P - T_W}{Y_P} a_w \tag{6.183}$$

where K_{eff} is calculated from equation (3.69), T_P and T_W are the temperature of the gas at point P adjacent to the wall and the wall temperature, respectively.

Linearisation of the above equation provides:

$$-S_P^e = \frac{K_{eff} a_W}{c_v Y_P} \quad , \quad S_U^e = K_{eff} a_W \frac{T_W}{Y_P} \tag{6.184}$$

The $k - \epsilon$ equations

The $k - \epsilon$ predictor and corrector sequence, introduced in the previous subsection, is employed here to obtain the values of k at near-wall nodes where ϵ is fixed according to Equation (3.73). Details of the procedure are given below:

The k predictor step

In the near wall region, the k equation is expressed in the following split fashion:

$$A_P^k k_P^{(1)} = \sum_C A_C^k k_C^{(1)} + A_P^o k_P^o + \mathcal{P}^n - \rho_P \epsilon_P^{(1)} \tag{6.185}$$

where the source terms are modified at the near wall nodes to conform to the Couette flow assumptions of subsection 3.7.1. Hence, the production term for the cell depicted in Figure 6.8, for example, is approximated by

$$\mathcal{P}^n = \left| \tau_{\xi\eta} \frac{V_P^n - V_W^n}{Y_P} \right| + \left| \tau_{\xi\zeta} \frac{W_P^n - W_W^n}{Y_P} \right| \tag{6.186}$$

and the sink term, $\rho^n \epsilon^{(1)}$, is replaced by equation (3.72):

$$\begin{aligned} C_\mu^{3/4} \rho^n \left(k^{(1)}\right)^{3/2} \frac{Y^+}{Y_P} \quad & \text{for} \quad Y^+ < 11.63 \\ C_\mu^{3/4} \rho^n \left(k^{(1)}\right)^{3/2} \frac{\ln(EY^+)}{k_v Y_P} \quad & \text{for} \quad Y^+ \geq 11.63 \end{aligned} \tag{6.187}$$

Moreover, the relevant A_C coefficients are set to zero because there is no transport normal to the wall in a Couette layer. Thus, the linearised equation (6.185) is solved with the aid of (6.186) and (6.187) to yield $k^{(1)}$ values near the wall.

The $\epsilon^{(1)}$ values are then obtained from equation (3.73), as follows:

$$\epsilon^{(1)} = C_\mu^{3/4} \frac{\left(k^{(1)}\right)^{3/2}}{k_v Y_P} \tag{6.188}$$

without solving the full ϵ transport equation. The above condition is imposed by setting:

$$\begin{aligned} S_U^{\epsilon} &= LC_{\mu}^{3/4}\frac{\left(k^{(1)}\right)^{3/2}}{k_v Y_P} \\ -S_U^{\epsilon} &= L \end{aligned} \tag{6.189}$$

where L is a very large number (e.g. $L = 10^{30}$).

The k corrector step

In the $(l-1)$-th corrector step ($l \geq 2$), the k equation is written in its split explicit form:

$$\begin{aligned} A_P^{k(l)} k_P^{(l)} &= \sum_C A_C^k k_C^{(l)} + A_P^o k_P^o + \left(\mu_{eff}^{(l)} \mathcal{V}^n g_t^n\right)_P \\ &\quad -\frac{2}{3}\left[\frac{\mu_{eff}^{(l)} \mathcal{V}^n \left(\nabla \cdot \underline{V}^n\right)^2}{k^o}\right]_P k_P^{(l)} - \frac{2}{3}\left(\rho^n \mathcal{V}^n D^+\right)_P k_P^{(l)} \\ &\quad -C_{\mu}\left(\rho^{n^2} \mathcal{V}^n\right)_P \frac{\left(k_P^{(l)}\right)^2}{\mu_{eff}^{(l)}} - \frac{2}{3}\left(\rho^n \mathcal{V}^n D^+ k^o\right)_P \end{aligned} \tag{6.190}$$

In the laminar sublayer ($Y^+ < 11.63$), where the effective viscosity equals the laminar viscosity, i.e.,$\mu_{eff} = \mu$, the above expression can be expressed in quadratic form:

$$a_1 \left(k_P^{(l)}\right)^2 + b_1 k_P^{(l)} + c_1 = 0 \tag{6.191}$$

where

$$\begin{aligned} a_1 &= C_{\mu}\left(\rho^{n^2}\frac{\mathcal{V}^n}{\mu}\right)_P \\ b_1 &= A_P^k + \frac{2}{3}\left(\rho^n \mathcal{V}^n D^+\right)_P + \frac{2}{3}\left[\frac{\mu \mathcal{V}^n \left(\nabla \cdot \underline{V}^n\right)^2}{k^o}\right]_P \\ c_1 &= -\left[\sum_C A_C^k k_C^{(l-1)} + A_P^o k_P^o + \left(\mu_{eff}^{(l)} \mathcal{V}^n g_t^n\right)_P - \frac{2}{3}\left(\rho^n \mathcal{V}^n D^- k^o\right)_P\right] \end{aligned} \tag{6.192}$$

The product of coefficients a_1 and c_1 is always negative as $a_1 > 0$ and $c_1 < 0$. Thus, the quadratic equation (6.191) has one positive root:

$$k_P^{(l)} = \frac{-b_1 + \sqrt{b_1^2 - 4a_1 c_1}}{2a_1} \tag{6.193}$$

$\epsilon_P^{(l)}$ for this region is then calculated from Equation (3.73) using $K_P^{(l)}$ obtained above.

In the inertial sublayer ($Y^+ \geq 11.63$), the effective viscosity is given by Equation (3.68) and reads:

$$\mu_{eff}^{(l)} = C_\mu^{3/4} \frac{\rho^n \left(k_P^{(l)}\right)^{1/2} k_v Y}{\ln(EY^+)} \tag{6.194}$$

Once more, the corrector k equation (6.190) is written in a quadratic form, as follows:

$$a_2 \left(k_P^{(l)}\right)^2 + b_2 k_P^{(l)} + c_2 = 0 \tag{6.195}$$

where

$$\begin{aligned}
a_2 &= A_P^k + \frac{2}{3}\left(\rho^n \mathcal{V}^n D^+\right)_P C_\mu^{3/4} \left[\frac{\rho^n \mathcal{V}^n \ln(EY^+)\left(k^o\right)^{1/2}}{k_v Y}\right]_P \\
b_2 &= -C_\mu^{1/4}\left[\frac{\rho^n \mathcal{V}^n g_t^n k_v Y}{\ln(EY^+)}\right]_P + \frac{2}{3} C_\mu^{1/4}\left[\frac{\rho^n \mathcal{V}^n \left(\nabla \cdot \underline{V}^n\right)^2 k_v Y}{\ln(EY^+)}\right]_P \\
c_2 &= -\left[\sum_C A_C^k k_C^{(l-1)} + A_P^o k_P^o + \left(\mu_{eff}^{(l)} \mathcal{V}^n g_t^n\right)_P - \frac{2}{3}\left(\rho^n \mathcal{V}^n D^- k^o\right)_P\right]
\end{aligned} \tag{6.196}$$

as $a_2 > 0$ and $c_2 < 0$, it follows that $a_2 c_2 < 0$ and the above equation has one positive root which reads:

$$k_P^{(l)} = \left[\frac{-b_2 + \sqrt{b_2^2 - 4a_2 c_2}}{2a_2}\right]^2 \tag{6.197}$$

In this sublayer, $\epsilon_P^{(l)}$ is obtained as before using the $k_P^{(l)}$ values.

6.6.2 Coordinate Pole/Axis

Symmetric Case

The present treatment of turbulent droplet dispersion makes it possible that droplets stray across the axis of symmetry. In this case, if the outcome of the trajectory equation (3.132) in the radial direction is that $\xi_{d,r}^n < 0$, the droplet is reflected back by setting

$$\xi_{d,r} = -\xi_{d,r}$$

and,

$$U_{d,r} = -U_{d,r}$$

.

Non-Symmetric Case

In a three-dimensional flow, neither the values of variables nor their gradients are known a priori at a pole. In this situation, the pole values of variables are calculated using area-weighted interpolations between surrounding nodal values, as illustrated below.

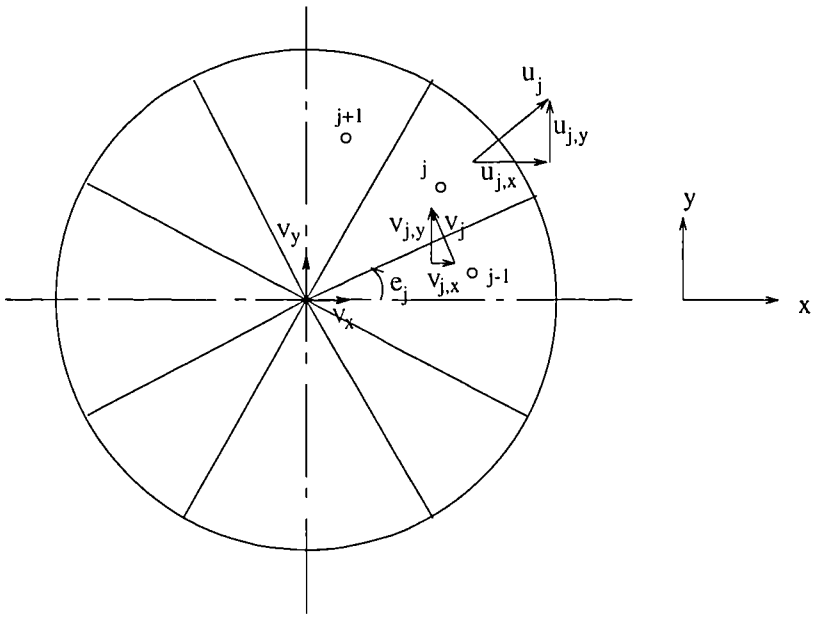


Figure 6.9: Diagram illustrating grid pole velocity

The velocities, U_j and V_j of the j-th cell adjoining the grid pole are each decomposed into their Cartesian components X- and Y-directions in Figure 6.9 to yield:

$$\begin{aligned} U_{j,X} &= U_j \cos\left(\frac{\theta_j + \theta_{j+1}}{2}\right) \\ U_{j,Y} &= U_j \sin\left(\frac{\theta_j + \theta_{j+1}}{2}\right) \end{aligned} \tag{6.198}$$

and

$$\begin{aligned} V_{j,X} &= V_j \sin\theta_j \\ V_{j,Y} &= V_j \cos\theta_j \end{aligned} \tag{6.199}$$

where θ_j denotes the polar angle of the 'south ' face of the j-scalar cell. Assuming that the contribution of U_j and V_j on the grid pole velocity are proportional to the diametrical a_j and $(a_{j-1} + a_j)/2$, respectively, the Cartesian velocity components (V_X, V_Y) at the grid pole can be determined by the following area-weighted

interpolation between surrounding cell velocities:

$$\begin{aligned} V_x &= \frac{1}{\sum_j a_j}\left[\sum_j V_{j,X} a_j + \sum_j V_{j,X}\left(\frac{a_{j-1}+a_j}{2}\right)\right] \\ V_y &= \frac{1}{\sum_j a_j}\left[\sum_j V_{j,Y} a_j + \sum_j V_{j,Y}\left(\frac{a_{j-1}+a_j}{2}\right)\right] \end{aligned} \tag{6.200}$$

These velocities are resolved back into the ξ and η directions to provide the necessary component values which, for example, take the form of:

$$(U_j)_{pole} = V_x \cos\left(\frac{\theta_j + \theta_{j+1}}{2}\right) + V_y \sin\left(\frac{\theta_j + \theta_{j+1}}{2}\right) \tag{6.201}$$

The velocity component along the pole is simply calculated as an area-weighted mean, as follows:

$$(W)_{pole} = \frac{1}{\sum_j a_j}\left(\sum_j W_j a_j\right) \tag{6.202}$$

The values of scalar variables at the pole are obtained in a similar manner to the w-velocity component above.

6.6.3 Cyclic (or Periodic) Boundaries

Treatment of cyclic boundaries (which were defined in subsection 2.8.5) is illustrated in conjunction with Figure 6.10 depicting two adjoining cells, A and B, on either side of a cyclic boundary. The discretised equation for cell A is:

$$\begin{aligned} A_{P,A}\phi_{P,A} = &\sum_{C\neq S} A_{C,A}\phi_{C,A} + A_{S,A}\phi_{S,A} + A^{\circ}_{P,A}\phi^{\circ}_{P,A} \\ &+ S^{\phi}_{U,A} + \hat{S}_{\phi,d}|_A \end{aligned} \tag{6.203}$$

while the one for cell B reads:

$$\begin{aligned} A_{P,B}\phi_{P,B} = &\sum_{C\neq N} A_{C,B}\phi_{C,B} + A_{S,B}\phi_{S,B} + A^{\circ}_{P,B}\phi^{\circ}_{P,B} \\ &+ S^{\phi}_{U,B} + \hat{S}_{\phi,d}|_B \end{aligned} \tag{6.204}$$

From Figure 6.10, it is evident that

$$\phi_{S,A} = \phi_{P,B}, \quad \text{and} \quad \phi_{N,B} = \phi_{P,A} \tag{6.205}$$

These values are not known a priori; rather, they form part of the matrix of un-

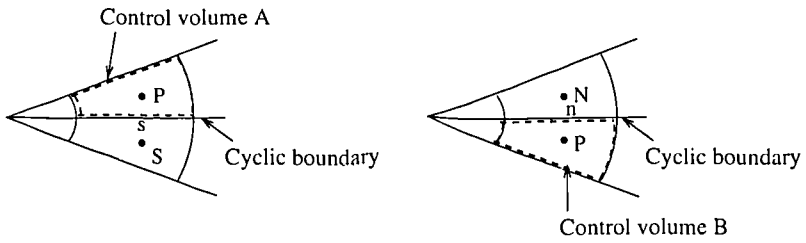


Figure 6.10: Diagram showing control volume at a cyclic boundary

knowns. In order to keep the banded form of the coefficient matrix of discretised equations intact, these cyclic boundary conditions are imposed in an explicit manner by absorbing such terms as $A_{S,A}\phi_{P,B}$ or $A_{NB}\phi_{P,A}$ into the source terms $S_{U,A}$ or $S_{U,B}$, respectively. Then, the above equations for cells A and B read:

$$\begin{aligned} A_{P,A}\phi_{P,A}^{\nu+1} &= \sum_{C\neq S} A_{C,A}\phi_{C,A}^{\nu+1} + A_{P,A}^{o}\phi_{P,A}^{o} \\ &\quad +(S_{U,A}^{\phi} + A_{S,A}\phi_{P,B}^{\nu}) + \hat{S}_{\phi,d}|_A \qquad (6.206) \\ A_{P,B}\phi_{P,B}^{\nu+1} &= \sum_{C\neq S} A_{C,B}\phi_{C,B}^{\nu+1} + A_{P,B}^{o}\phi_{P,B}^{o} \\ &\quad +(S_{U,B}^{\phi} + A_{S,B}\phi_{P,A}^{\nu}) + \hat{S}_{\phi,d}|_B \qquad (6.207) \end{aligned}$$

where superscripts ν and $\nu+1$ designate iteration indices (it has been implicitly assumed that an iterative solver is employed to solve the linear set of equations).

A droplet reaching cell B has an associated cell number, $d_{i,j,k}$, and its relative position in cell B is given by $(\xi_{d,r}, \eta_{d,r}, \zeta_{d,r})$. If, for example,

$$\eta_{d,r}|_B > \Delta\eta|_B$$

where $\Delta\eta|_B$ is the length of cell B in the circumferential (η-) direction. Then the droplet cell number is adjusted as $d_{i,j+1,k}$ such that it crosses the boundary to the adjoining cell.

6.6.4 Injector(s)

Sprays are introduced as 'blobs' from one or more injectors which may be placed in any desired direction. Each blob is assigned a size equal to the diameter of the injector from which it comes out, penetrating with the injection velocity whose magnitude , U_{inj}, is given by:

$$U_{inj} = \frac{4\Delta\dot{\mathcal{V}}}{\pi D_N^2} \qquad (6.208)$$

where $\dot{\mathcal{V}}$ is the volume of fuel injected per time step, and D_N is the nozzle exit diameter.

The velocity direction of the blob is perturbed around the injection direction, with the maximum perturbation limited by the semi-cone angle of the spray angle β.

Since the droplet velocities are resolved in the local orthogonal curvilinear frame in this study. It is necessary to obtain the components of the injection velocity in this local frame. For this purpose, a Cartesian coordinate system is defined such that its center coincides with the grid pole and its Z-axis coincides with the bowl axis. Moreover, we define by α_x and α_z the angles formed by the injection direction with the X- and Z-axes, respectively; and by α_g the angle between the radial grid line in which the injector is located and the X-axis (see Figure 6.11). It should be noted that α_g is a function of time, because the grid moves.

The injection direction can now be defined in the local Cartesian coordinates by the following two angles:

$$\begin{aligned} \alpha_1 &= f_1\beta \\ \alpha_2 &= f_2 2\pi \end{aligned}$$

where f_1 and f_2 are random numbers between zero and unity. Here, it is assumed that there is equal probability for all angles within this limits. The injection velocity components in the local Cartesian frame are therefore given by:

$$\begin{aligned} U_d^C &= U_{inj}\cos\alpha_1 \\ V_d^C &= U_{inj}\sin\alpha_1\cos\alpha_2 \\ W_d^C &= U_{inj}\sin\alpha_1\sin\alpha_2 \end{aligned} \tag{6.209}$$

The components of the injection velocity in the local orthogonal curvilinear frame are then obtained by employing the transformation relationship between the two coordinate frames:

$$\begin{aligned} U_d &= U_d^C\sin\alpha_z\cos(\alpha_x-\alpha_g) - V_d^C\sin(\alpha_x-\alpha_g) \\ &\quad -W_d^C\cos\alpha_z\cos(\alpha_x-\alpha_g) \\ V_d &= U_d^C\sin\alpha_z\cos(\alpha_x-\alpha_g) + V_d^C\cos(\alpha_x-\alpha_g) \end{aligned}$$

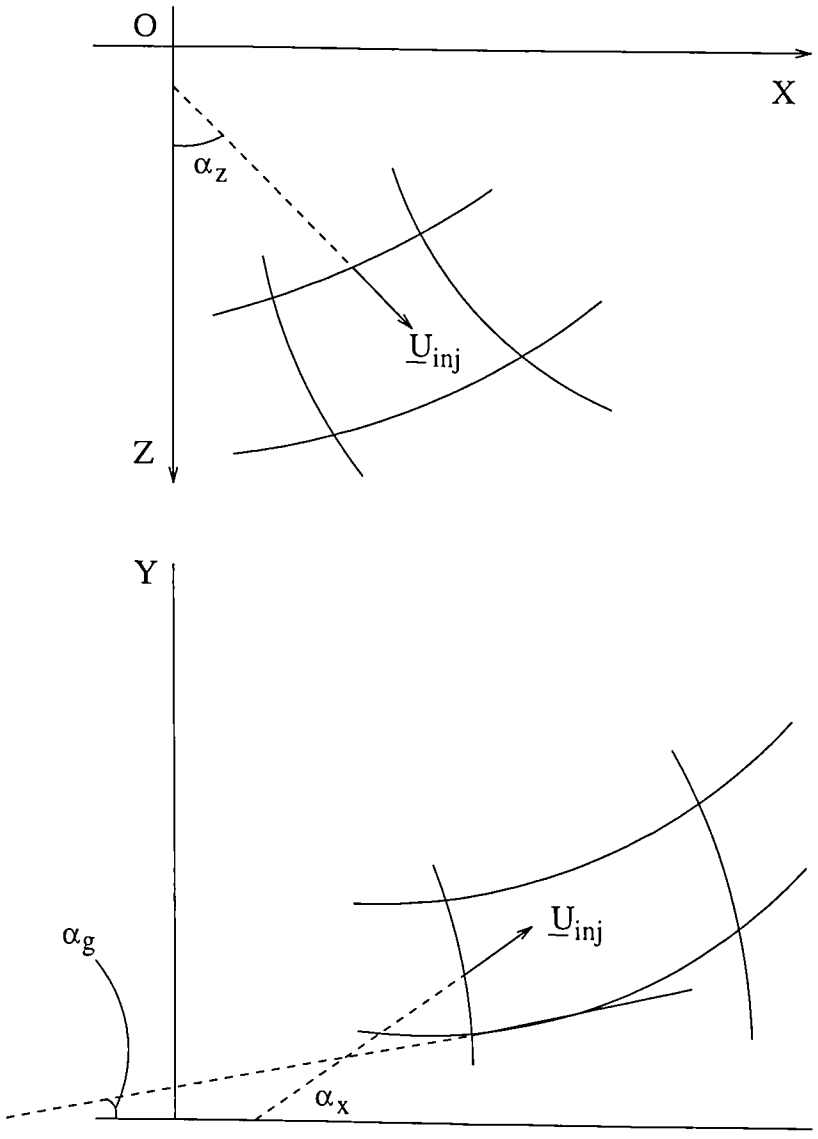


Figure 6.11: Diagram showing injection direction

$$-W_d^C \cos\alpha_z \sin(\alpha_x - \alpha_g) \tag{6.210}$$

$$W_d = U_d^C \cos\alpha_z + W_d^C \sin\alpha_z$$

where U_d^C, V_d^C and W_d^C are given by (6.209).

6.7 Outline of Overall Solution Procedure

Given the following parameters: (i) engine geometry and specifications; (ii) injector position in the combustion chamber; (iii) nozzle diameter; (iv) spray cone angle;(v) injection orientation; (vi)injection rate specification; and (vii) having generated the (time invariant) grid in the diametrical planes of the E/C and (where relevant) T regions, the calculations commence using prescribed initial conditions and march forward in finite time increments, Δt (or, equivalently, crank angle increments, $\Delta\theta$). The dependent variables are advanced during each time step in the following sequence.

1. *Piston Motion*

   The piston displacement from the cylinder head is given by (Tabrizi 1991):

   $$Z_p(\theta) = Z_c + \frac{S}{2}\left[1 - \cos\theta + \frac{2L_{cr}}{S}\left(1 - \sqrt{1 - \left(\frac{2L_{cr}}{S}\sin\theta\right)^2}\right)\right] \tag{6.211}$$

   where Z_c is the clearance distance at TDC, S is the stroke, θ is the crank angle measured from the TDC induction and L_{cr} is the connecting rod length. The piston velocity, $V_p(\theta)$, is then calculated as:

   $$V_p(\theta) = \frac{Z_p(\theta) - Z_p(\theta - \Delta\theta)}{Dt} \tag{6.212}$$

2. *Axial Grid Adjustment*

   The grid line velocities in the E/C and T regions are determined from Equations (3.51) and (3.55), respectively, and the axial grid configuration is adjusted to accord with the movement of the piston.

3. *Spray Introduction*

   N_p (specified by the user) parent droplet parcels (or blobs) are introduced at injector(s), with an initial size equal to the nozzle exit diameter. The velocities

of these blobs are calculated according to (6.210). Huh's atomisation model is then applied to each parent droplet parcel, enabling the prediction of the new droplet parcels detached from the blobs.

4. *Initial Bulk Adjustment*

   The local gas pressure, densities and temperatures are adjusted globally to the initial new time level values according to Equations (6.78) to (6.86)

5. *The Predictor Step*

   The droplet fields are first calculated to yield preliminary values of the sizes, velocities, positions, masses and temperatures, as well as the interaction terms such as the void fraction and exchange terms of mass, momentum and energy. Following this, the implicit vapour mass fraction, energy and momentum equations are solved using the initial gas field values and the prevailing droplet field information.

6. The Corrector Step

   First, the droplet fields are corrected using the most updated gas field values, which form the basis for the gas field correction. The latter corrector procedure starts with the calculation of the new pressure field, which is in turn used to obtain corrected velocities which obey continuity more strictly. The local continuity condition (6.111) is then invoked to update the density field. Finally, the vapor mass fraction and energy fields are corrected using Equations (6.112 and (6.113), respectively.

   The above described corrector step has to be repeated until the desired convergence requirement is satisfied.

7. *Impingement Calculations*

   At the last droplet corrector step, wall impingement calculations are introduced. For each impinging droplet, the Weber number and the Laplace number are first evaluated according to the computationally-simulated values of droplet size, velocity, and liquid properties. These are then used to determine the outcome of the impinging droplet by the transition criteria correlations derived in Chapter 4. Subsequently, the quantities representing the

post-impingement characteristics are computed using the relevant correlations provided in Chapter 4. Finally, the droplet source terms to film momentum equations are calculated.

8. *Final Bulk Adjustment*

   The gas pressure, density and temperature fields are adjusted to their new time level values according to (6.134) to (6.138)

9. *Computation of Turbulence*

   The turbulent kinetic energy k and its dissipation rate ϵ fields are also obtained using a predictor-corrector procedure. In the predictor step, the implicit equations (6.146) and (6.148) are solved to provide first estimates of k and ϵ. Refinement of these fields are then pursued in the corrector step in which calculations of $k^{(l)}$, $\epsilon^{(l)}$ are performed in the order of first $\epsilon^{(l)}$ by use of (6.155) and then $k^{(l)}$ according to (6.154). With both $k^{(l)}$ and $\epsilon^{(l)}$ known, the μ_t field can be calculated from (6.160).

10. *Calculation of Film Characteristics* Here a predictor-corrector procedure is again employed for computing δ, (u, v), Λ, T_s and $\dot{m}_v$ fields

11. *Droplet Collision*

    For each pair of droplet parcels, collision is calculated if they lie in the same computational cell and satisfy the condition described in Section 3.8.7. Modification of droplet sizes (due to coalescence) and the momentum and energy are conducted according to the post-collision treatments provided in Section 3.8.7.

The overall procedure then advances to the next time step and recommences from Step 1 again. A general flow chart is illustrated in Figure 6.12

6.8 Closure

In this chapter, a detailed discussion has been given of the discretisation scheme, the numerical algorithm and the equation solvers whereby finite number of values for

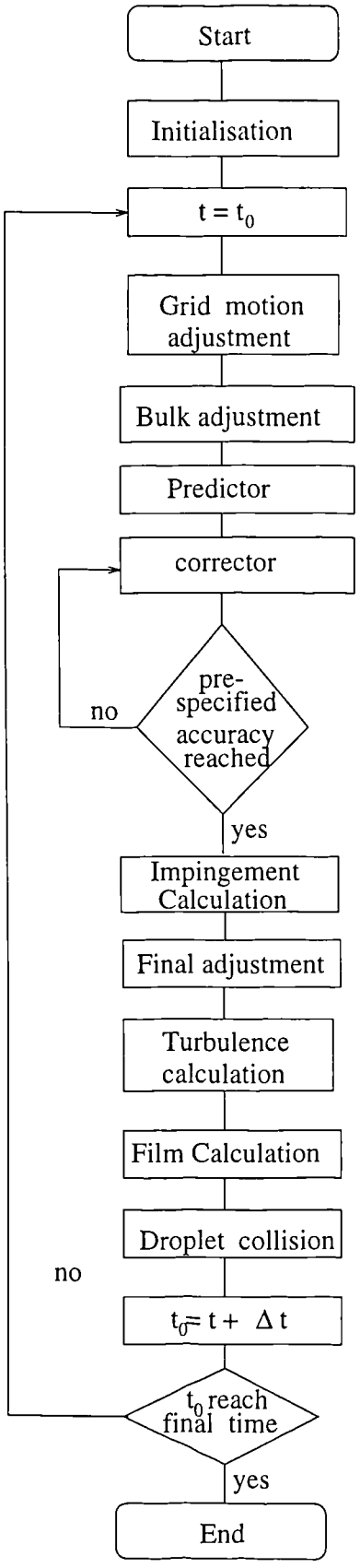


Figure 6.12: Illustration of flow chart

each dependent variables can be attained from the governing equations described in Chapter 3.

The finite volume technique has been invoked to discretise the gas phase equations, involving the use of staggered grid for the velocity components, and the hybrid-difference and fully implicit schemes for spatial and temporal discretisation, respectively.

In deriving the finite-difference equations of the droplet fields, special attention has been paid to the choice of time step and the evaluation of the gas field values along the droplet trajectories. The temporal subcycling procedure has been invoked to improve the overall accuracy, and a spatial interpolation practice has also been introduced in an attempt to make proper estimation of the gas variable values at the droplet locations. Each set of droplet difference equation is Euler implicit except for the trajectory equation.

The set of fully coupled non-linear differential equations governing the gas and droplet phases has been linearised and solved with the aid of EPISO-SPRAY algorithm which involves the factorisation of the discretised equations into a series of predictor-corrector steps. Two equation solvers have been employed for the solution of linear algebraic simultaneous equations: the SSIP solver for the fully-implicit of equations with non-symmetric coefficients and CG solver for the pressure equation.

Finally, the alterations to the difference equations required to handle boundary conditions have been discussed and an overview is provided of the overall solution procedure.

Chapter 7

Validation Studies

7.1 Introduction

In this chapter, we assess the performance of the impingement and film models developed in this study. This is achieved by applying a modified version of the EPISO-SPRAY code, which assembles all the methodologies described in Chapters 3, 4, 5 and 6, to the prediction of several spray impingement cases for which experimental data are available for comparison. These data were already discussed earlier in the review of Chapter 2.

Section 7.2 is devoted to an initial evaluation of the models against the normal spray impingement measurements of Katsura et al (1989) made in a quiescent pressure chamber at elevated pressure and room temperature. Here, the impingement calculation methods are first subject to preliminary sensitivity studies to examine the effects of grid density, time step size, and the number of droplet parcels introduced per unit time. The predicted results are then presented and compared with the measured data.

In Section 7.3, a subsequent assessment of the models is made by comparison with CNPM normal spray impingement experiments conducted for a test bomb at atmospheric conditions. This is followed by additional validation studies performed for normal spray impingement experiments of Harwell in Section 7.4, and those of Saito et al (1993) in Section 7.5. In both cases, the calculations are compared with the measured data on both the wall spray and film characteristics.

The models are then further assessed against CNPM oblique spray impingement

experiments in Section 7.6.

Finally, as a demonstration calculation, the models are applied, in Section 7.7, to the prediction of impingement events for a motored engine with a cylindrical bowl.

The chapter closes in Section 7.8 by highlighting the main findings and drawing conclusions from the aforementioned studies.

7.2 Comparison with Experiments of Katsura et al (1989)

7.2.1 Introduction

Katsura et al (1989) performed experiments in which sprays issuing from a single-hole nozzle were directed normally onto a flat wall at elevated pressure and room temperature. The pertinent injection and impingement conditions are summarised in Table 7.1 and Figure 7.1.

A laser light extinction method was employed to obtain photographs of spray patterns at different times, from which Katsura et al deduced wall spray radius, R_w, and wall spray height, H_w (see Figure 7.2 for their definitions). The proportion of the injected mass deposited on the wall was also measured after termination of the fuel injection when it reaches a steady state. However, no measurements were made of the wall film dynamics.

In addition, some parametric studies were made. The parameters varied include the ambient gas density and the nozzle-wall distance, hereafter referred to as the impingement distance. Here we perform similar computational studies of the effect of the latter parameter and compare the results with the measurements.

Before proceeding to the comparisons, a preliminary assessment of the prediction method is first carried out in order to establish grid, time step and droplet parcel introduction rate requirements for adequate numerical resolution. The basic case used here, which is referred to as Case N1, involves an impingement distance of 24mm. It is the only case for which the experimental photographs of wall spray patterns were provided.

To perform simulation, a cylindrical chamber with a radius of 40mm and a height

Table 7.1: Specification for Case N1

Impingement distance (mm)	20, 24, 30, 34
Gas Pressure (bar)	15
Gas Temperature (K)	293
Nozzle Diameter (mm)	0.3
Injection Duration (ms)	1.2
Injection Angle (Deg)	90
Fuel Injected (mm^3/pulse)	10.5
Fuel type	Diesel
Injection Schedule	Figure 7.1

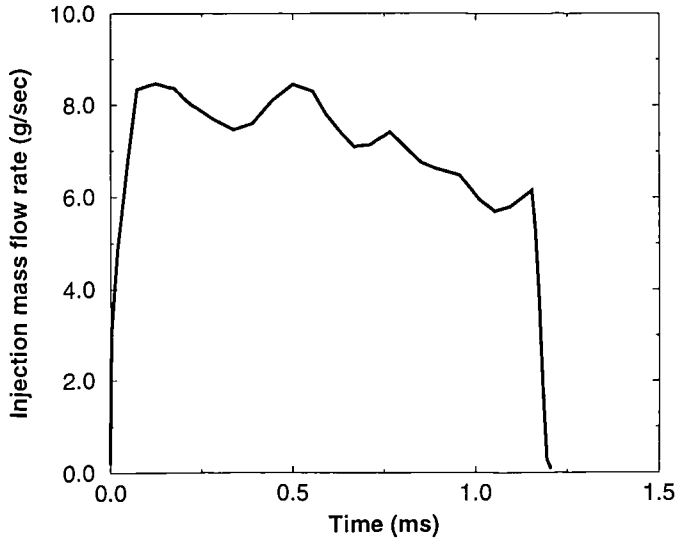


Figure 7.1: Fuel injection history for Case N1

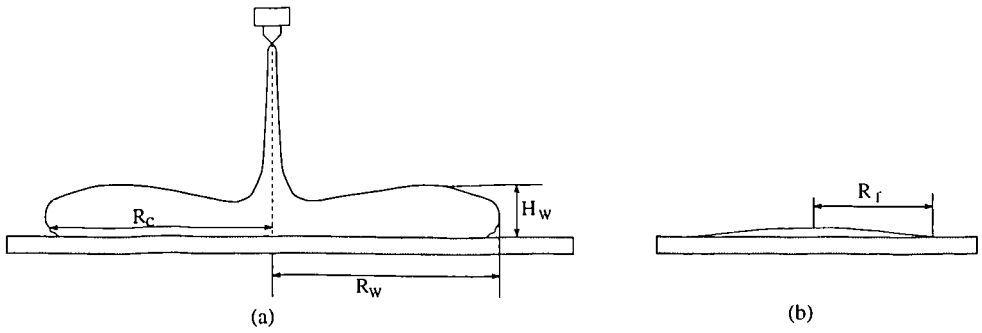


Figure 7.2: Diagrams showing definitions of (a) radii of wall spray R_w and spray cross section R_c, wall spray height H_w; (b)wall film radius R_f

of 44mm was considered. Because of axisymmetry, two-dimensional computational meshes are used throughout the computations in this section.

7.2.2 Preliminary Parametric Studies

In the following, we investigate the effects of grid density, computational time step size, and number of droplet parcels introduced per unit time, in order to provide a guide to the appropriate choices of these parameters which offer the best compromises between accuracy and economy.

(i) Effect of the grid density

Here we investigate the effect of the grid by changing the grid density while fixing the time step size and the number of computational droplet parcels introduced per unit time to portray the spray. The former is assigned a value of 2 μs based on the droplet trajectory analysis of Beshay (1985) which concludes that an accurate calculation of droplet behaviour necessitates the use of time steps less than $5\mu s$; and the latter is specified as 1000 parcels/ms.

The grid specification is as follows: in the axial direction, it expands uniformly from the smallest cell with an expansion factor of 1.03 for the first 15mm, and then contracts with a factor of 0.99 for the next 5mm or so, and finally it is uniformly spaced (size of 0.73mm) for the remaining 4mm near the wall in order to provide finer mesh in the near-wall region to allow for accurate calculations of (i) the high mean gas velocity gradients, and (ii) overall behaviour of dense wall spray resulting from impingement. In the radial direction, it is equally spaced for the first 6 mm

and thereafter uniformly expands by a factor of 1.045. The smallest cell is located adjacent to the nozzle exit and the centerline.

Different grid densities are obtained by decreasing the size of the smallest cell, which in turn has the effect of increasing the number of grid lines to cover the same computation domain.

The effect of the grid density can now be examined by inspecting Figures 7.3 and 7.4 which show the results for the predicted wall spray radius and adhered fuel ratio. Here the computed spray radius is defined as the radius of a cylindrical body which contains 99% of total spray liquid, with the impingement surface being the base; and the adhered fuel ratio is defined as the ratio of the cumulative mass of fluid adhering to the wall to the cumulative mass injected at a certain time. Figure 7.3 illustrates that reducing the axial spacing produces very little change in both the predicted wall spray radius and adhered fuel ratio. In contrast, the effect of reducing radial spacing is much stronger, as evidenced in Figure 7.4, from which it is clear that, when the radial size is reduced from 0.7 to 0.5, the wall spray radius exhibits a substantial increase whilst percentage of the adhered fuel ratio shows an appreciable reduction. However, further reducing the radial spacing from 0.5 to 0.4 does not cause significant changes in either quantity. Thus in the present study, the minimum cell size is taken to be (0.4×0.5) mm and, in particular, the results to be presented hereafter for Case N1 is obtained using the mesh illustrated in Figure 7.5 which contains 39 and 49 grid lines in the axial and radial directions, respectively.

(ii) Effect of time step size

The response of the predicted wall spray radius and adhered fuel ratio to the different time step sizes is displayed in Figures 7.6(a) and (b) respectively. The results are obtained using the same droplet parcel introduction rate (1000 parcels/ms) and time step sizes of 1, 2, 4, and 8μs, equivalent to Courant numbers (defined as $C_r = \dfrac{U_{inj}\Delta t}{\Delta x}$, where Δx is the minimum cell size), $C_r = 0.45$, 0.9, 1.8, and 3.6.

It is clear from the figure that halving C_r from 3.6 to 1.8 causes a noticeable reduction in the wall spray radius but only a slight increase in the adhered fuel ratio. However, further halving of C_r successively from 1.8 to 0.45 produces little change in either quantity but of course increases the computational cost. Therefore, in all subsequent axisymmetric spray calculations a Courant number of 0.7 (equivalent to

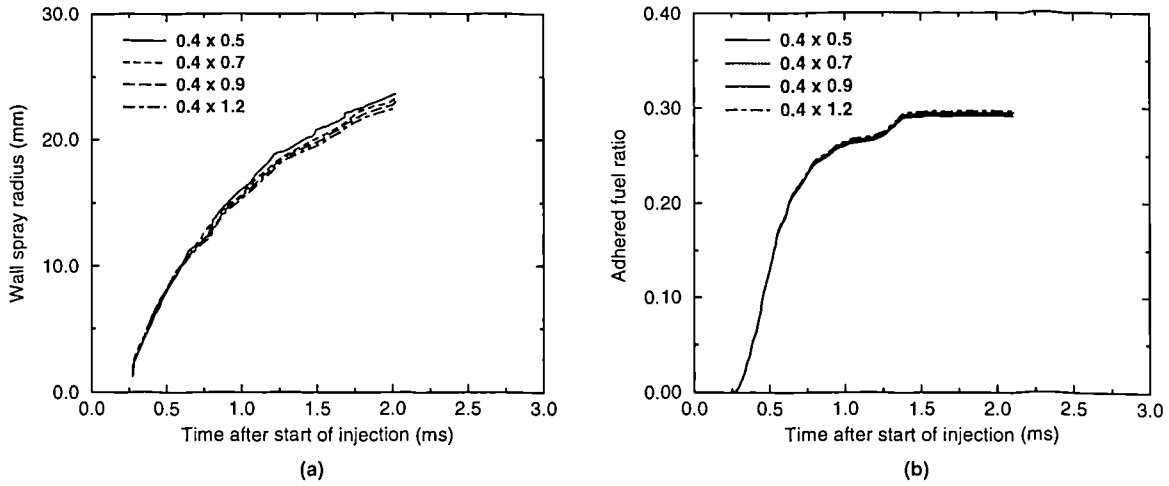


Figure 7.3: Effects of grid density change in axial direction on (a) wall spray radius; (b) adhered fuel ratio

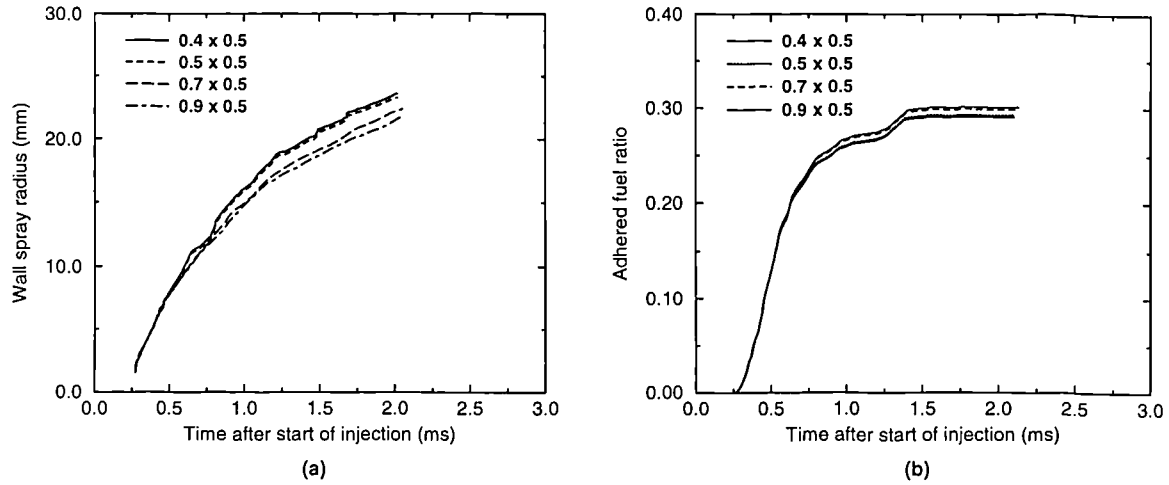


Figure 7.4: Effects of grid density change in radial direction on (a) wall spray radius; (b) adhered fuel ratio

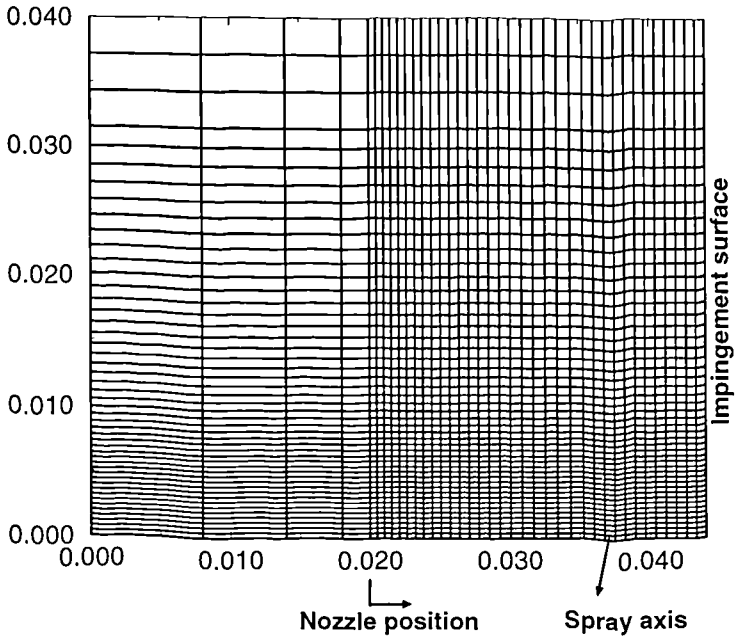


Figure 7.5: Grid scheme used for Case N1.

a time step size of 2 μs) for the chosen mesh will be used.

(iii) Effect of the number of droplet parcels

Figures 7.7(a) and (b) show that both the wall spray radius and adhered fuel ratio are not sensitive to the increase of the parcel introduction rate from 500 to 2000 parcels/ms. Thus, in all subsequent spray computations presented in this study, an introduction rate of 1000 droplet parcels/ms is employed.

7.2.3 Presentation of Results

Figure 7.8 presents the predicted spray patterns at three different times for Case N1, which may be compared with corresponding experimental image-processed spray patterns from Katsura et al (1989) in the same figure. The measured and predicted spray patterns show the same trends and are in good agreement. We can see a clear wall spray structure, comprised mainly of rebounding and secondary droplets resulting from splashing, penetrating outward as time goes on. A common feature of these patterns is that the spray is most dense close to the wall. A close examination of this figure reveals that the predicted and measured wall spray volumes are quite close at each time; but the computed wall spray extent is moderately underpredicted

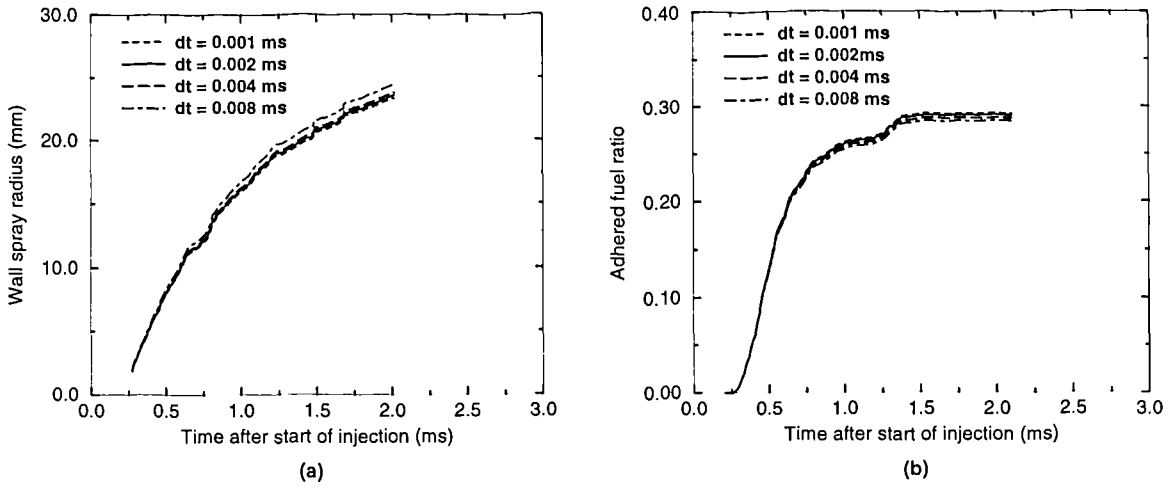


Figure 7.6: Effects of time step size on (a) wall spray radius; (b) adhered fuel ratio

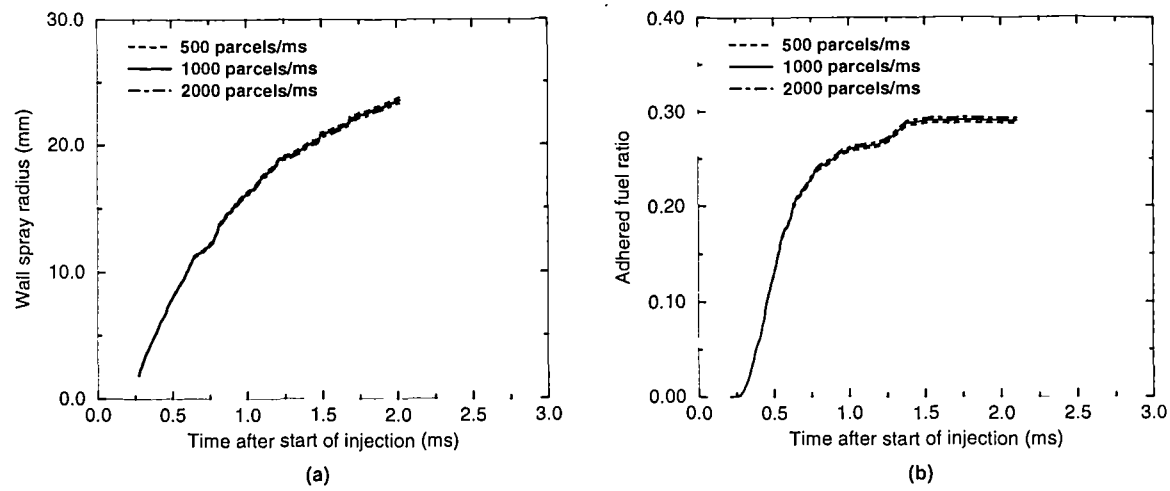


Figure 7.7: Effect droplet parcel introduction rate (a) wall spray radius; (b) adhered fuel ratio

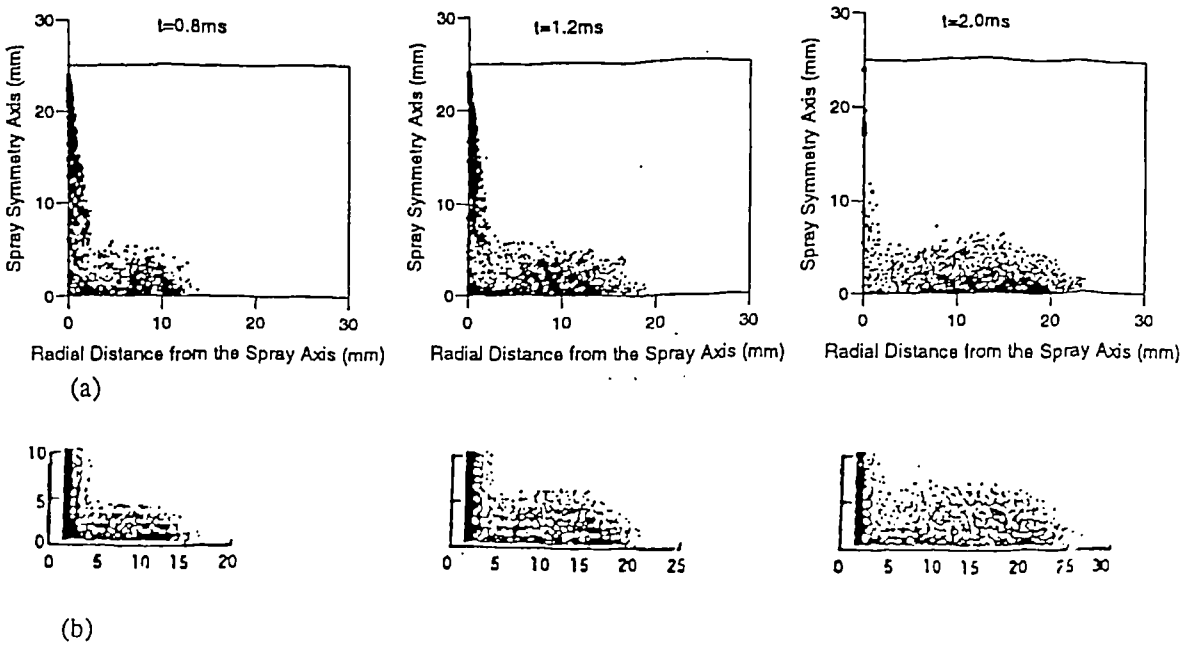


Figure 7.8: Spray pattern development for Case N1:(a) predictions and (b) image processed spray pattern by Katsura et al (1989)

in the radial direction and overpredicted in the normal direction. This can be seen more clearly from Figure 7.9(a), which compares, respectively, the measured and predicted variations with time of wall spray radius (as defined in the preceding subsection) and height. Here the spray height is computationally defined as the normal distance from the wall to the height above which less than 1% of the total droplets lie in the zone outside the spray cone.

The above-observed difference for wall spray may be due in part to the fact that all the droplets in each parcel are computationally located at a single point, whereas in reality they would be dispersed in a cloud. Also, small droplets have strong light-scattering and obscuration properties which are not represented in the plots depicting the predictions.

Also compared in Figure 7.9 are the predicted and measured temporal variations of the wall spray radius and height for three other cases corresponding respectively to the impingement distances: Z=20, 30, 34mm (see plots (b), (c) and (d) in the figure). The overall agreement is fairly good between the measurements and calculations in each case, although there are consistent discrepancies in that: calculations overestimate the spray height and underestimate the spray radius. A more detailed

discussion concerning the differences between each plot in Figure 7.9 will be made later.

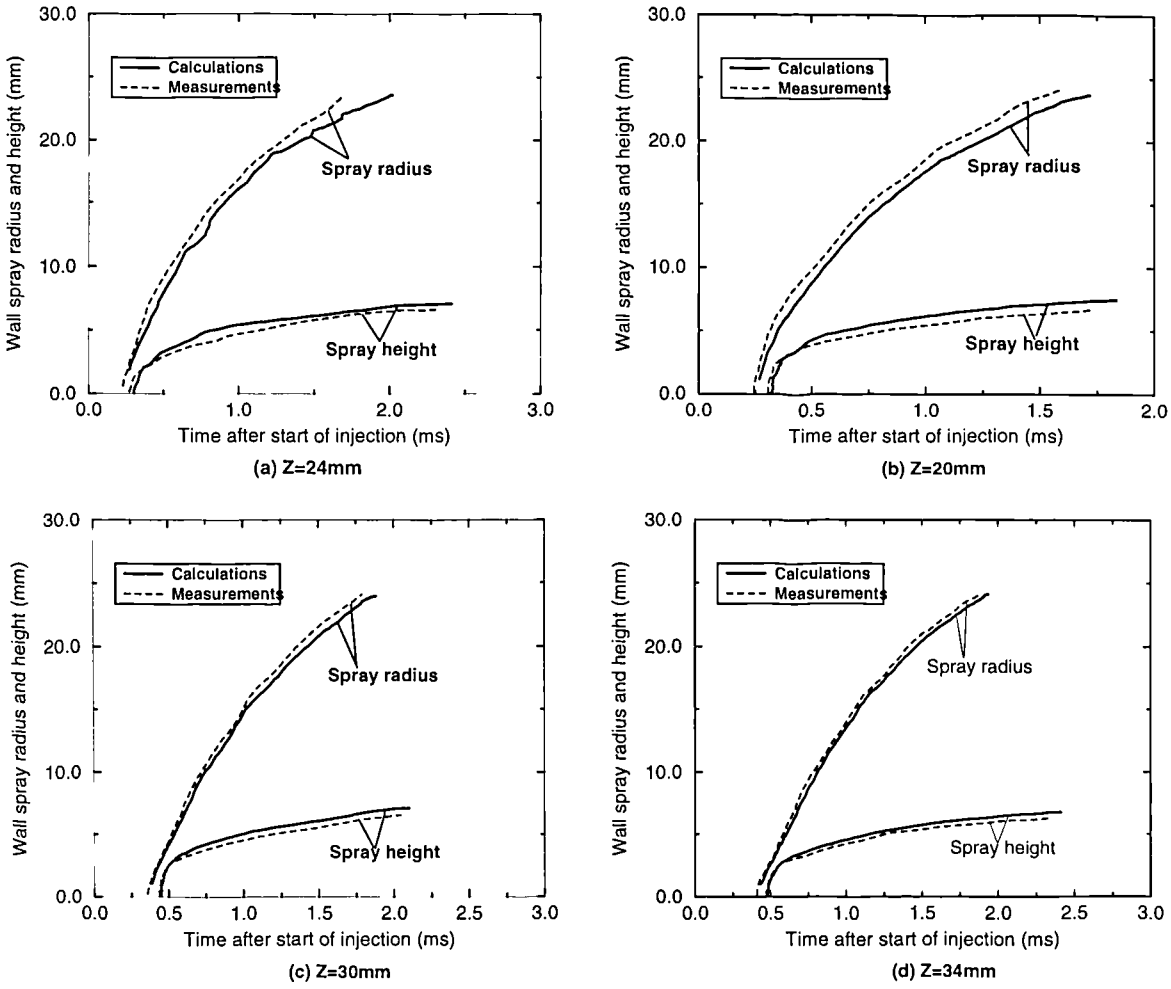


Figure 7.9: Predicted and measured temporal evolution of wall spray radius and height for four different impingement distances: (a) Z=24mm, (b)Z=20mm, (c) Z=30mm, and (d) Z=34mm.

Evidence of continuous fuel deposition after start of impingement is indicated in Figure 7.10(a), which contains the predicted temporal evolution of the adhered fuel ratio, $m_d(t)/m_{inj}(t)$, for all four impingement distances. We observe that this quantity is initially a monotonically increasing function of time, which, as expected, gradually reaches a steady-state value. Experimental data were provided for these steady-state values in all four cases, and are shown as symbols in the figure. Fairly close agreement is obtained between the calculated and measured steady-state values, although the predictions overestimate the measurements.

It can be noted that in each curve of Figure 7.10(a) there exists a cusp at the time corresponding to the end of fuel injection, immediately after which the adhered fuel ratio increases very rapidly. This can be explained as follows. The deposited mass ratio at time t is evaluated in our calculation from the total mass deposited, $m(t)_d$, divided by the total mass injected ,$m(t)_{inj}$, at that time. Both $m(t)_d$ and $m(t)_{inj}$ increase monotonically with time till the end of injection. However, immediately after the end of fuel injection, the deposited mass $m(t)_d$ continues to increase for a short while at a comparable rate as before, whilst the injected mass $m(t)_{inj}$ remains constant, causing a rapid local increase of the adhered fuel ratio. A short time later, at the time when all the injected droplets reach the near-wall region, the quantity $m(t)_d$ also begins to reach a constant value. This also causes the adhered fuel ratio to reach a steady state value, as evidenced in Figure 7.10(a).

The predicted film thickness distributions along the radial distance at different times for Case N1 is displayed in Figure 7.10(c) (no measured data are available for comparison). Here we can see clear mass accumulation around the film periphery in the course of film spreading. This local mass accumulation is due to the combined effects of local flow deceleration at the film edges and the relatively larger local radial film velocities in the impingement zone due to the pressure increase there. It is also evident that the film thickness in the impingement zone decreases with time, indicating that droplet mass flux is not enough to offset the loss caused by spreading. In addition, the peak film thickness observed in this figure is below $15\mu m$, which is linked in part to the fact that total injected fuel volume is small (only $10.5mm^3$) so that the fuel volume on the wall is also low .

The effect of the impingement distance on the wall spray characteristics can now be investigated by comparing all the plots in Figure 7.9 and the curves in 7.10(a). There are common trends in that: the wall spray radius and height both decrease as the impingement distance Z is increased. This may be explained by the fact that the larger the distance, the less the impact energy the impinging droplets possess, due to momentum loss caused by longer interaction with the gas prior to their impingement. As a consequence, as the impingement distance is increased, more arriving droplets

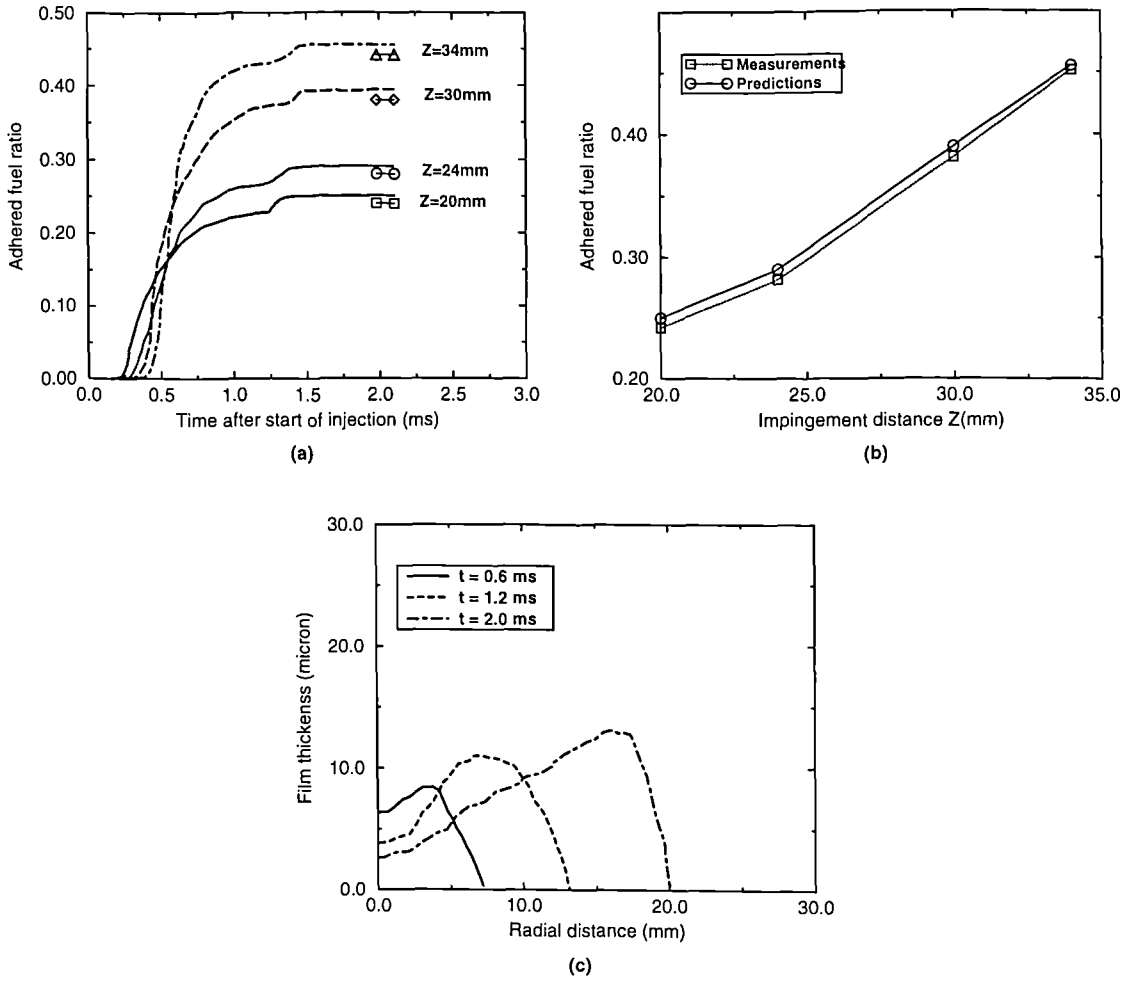


Figure 7.10: Results on (a) temporal evolution of adhered fuel ratio for all four impingement distance; (b) variation with the impingment distance Z of the steady-state adhered fuel ratio; and (c) film thickness spatial distributions for Case N1 at three times after start of injection (note the greatly expanded ordinate scale).

would 'spread' on the wall instead of 'splashing' upon hitting the wall, causing more fuel deposition. This is clearly indicated in Figure 7.10(a), from which we see that the steady-state value of the adhered fuel ratio increases substantially from around 25% to about 45% when Z is increased from 24 to 34mm. A correlation between this steady-state value and the impingment distance Z is directly illustrated in Figure 7.10(b) which suggests that the relation is approximately linear (at least in the region $24 \leq Z \leq 34$).

7.3 Comparison with CNPM Normal Spray Impingement Experiments

Description of Experiments

Normal spray impingement experiments were performed by Coghe et al (1992) in a quiescent chamber where a fuel spray, introduced from a single-hole nozzle, impinges normally onto a flat plate, under the conditions characterised in Table 7.2 and Figure 7.11.

Table 7.2: Specification for Case N2

Impingement distance (mm)	25
Gas Pressure (bar)	1
Gas Temperature (K)	293
Nozzle Diameter (mm)	0.25
Injection Duration (ms)	3.4
Injection Angle (Deg)	90
Fuel Injected (mm^3/pulse)	36
Fuel type	Diesel
Injection Schedule	Figure 7.11

As already mentioned in Chapter 2, in this case (hereafter referred to as Case N2), the phase PDA technique was employed to measure the following local wall spray characteristics: (a) droplet peak normal velocities versus time at specific locations in the near-wall region; (b) ensemble-averages over 1ms duration of droplet diameter,

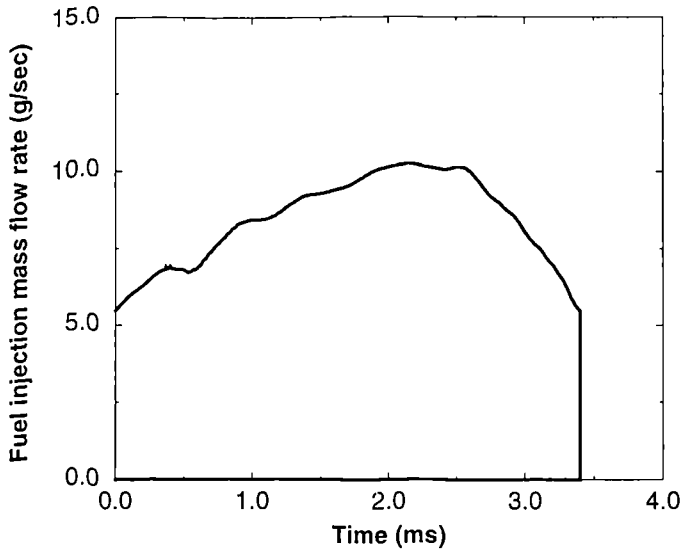


Figure 7.11: Fuel injection history for Case N2

normal and tangential velocities at 14mm from stagnation point and various heights from the wall surface. These are to be compared with our calculations.

Presentation of the results

The calculated results using the present impingement model will now be shown for Case N2. Plots (a) to (c) in Figure 7.12 display the computed details of the spray structures at 3 different times after the start of injection. Unlike Case N1, where the gas density is 15 times larger, here the wall spray is less compact due to the much smaller ambient gas resistance, and we can find more isolated droplets outside the main body of the wall spray. But the wall spray shape development is similar to that of Case N1. In this case, we can also find that the wall spray consists mostly of smaller droplets (with green color in the figure) due to splashing; and that the spray is most dense in the near-wall region.

Figure 7.12(d) shows the predicted droplet field using the conventional 'stick' model, which may be compared with those just discussed, e.g. Figure 7.12(b). Here by contrast, we can see no wall spray structure in the plot outside the free spray cone region. This is because this simple model here does not reflect the physics of the bounce and splash regimes.

The present predictions may be better understood by reference to the the cal-

culated gas velocity fields at corresponding times shown in Figures 7.13(a), (b) and (c). Each of these reveals a wall jet eminating radially outward from the spray impingement region, near the tip of which there is a vortex. This leading vortex structure has also been noted by Coghe et al(1991) in their experiments. It can also be seen that the vortex becomes progressively radially stretched at the later stages.

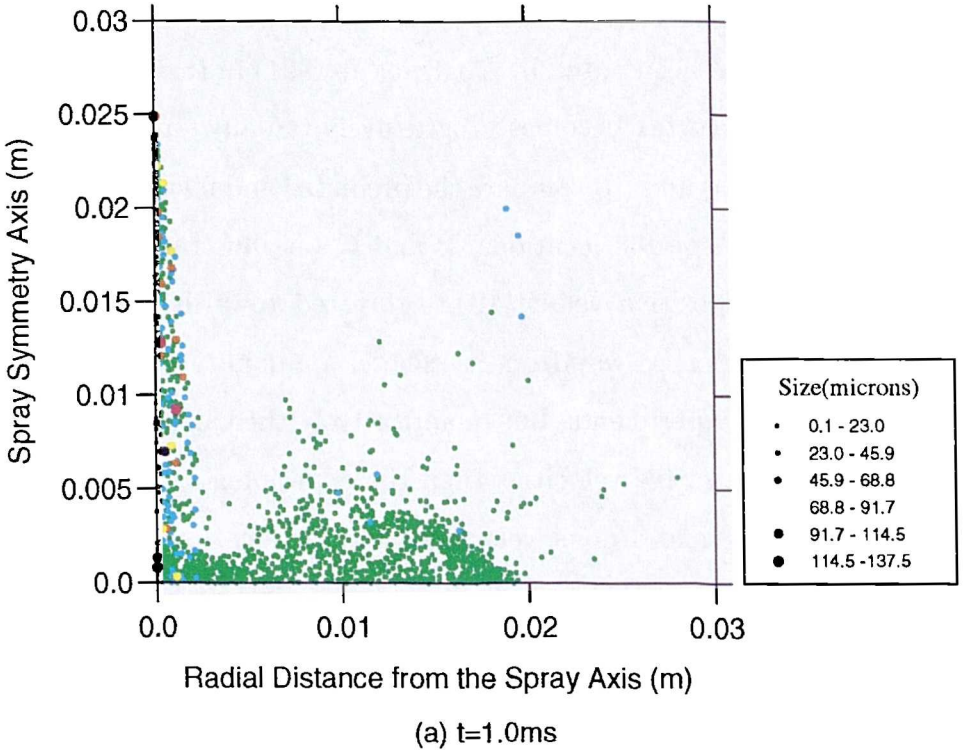
Figures 7.14(a) and (b) compare the predicted and measured droplet peak normal velocities at two specific locations, P and Q (as illustrated in Figure 7.12(d)), for Case N2. The positive velocities are directed towards the impingement surface and the negative ones away from it. There is a qualitative agreement between the predictions and experiments, but quantitatively the calculations tend to give larger magnitudes of negative velocities than the experiments. In these calculations, the peak negative normal droplet velocities at these locations were found always to be those of the secondary droplets resulting from splashing.

Figures 7.15 and 7.16 show respectively the predicted and measured local mean tangential and normal droplet velocity components, and the mean droplet diameter at 14 mm from stagnation point for Case N2, plotted against height above the wall surface (line fg in Figure 7.12(d)). The 'local mean value' referred to here is experimentally determined as local ensemble-average over 1ms duration, while it is computationally defined as the arithmetic value for all droplets identified in the mesh cell which encloses the measurement position, in the same period. For example, the mean droplet size is mathematically represented as

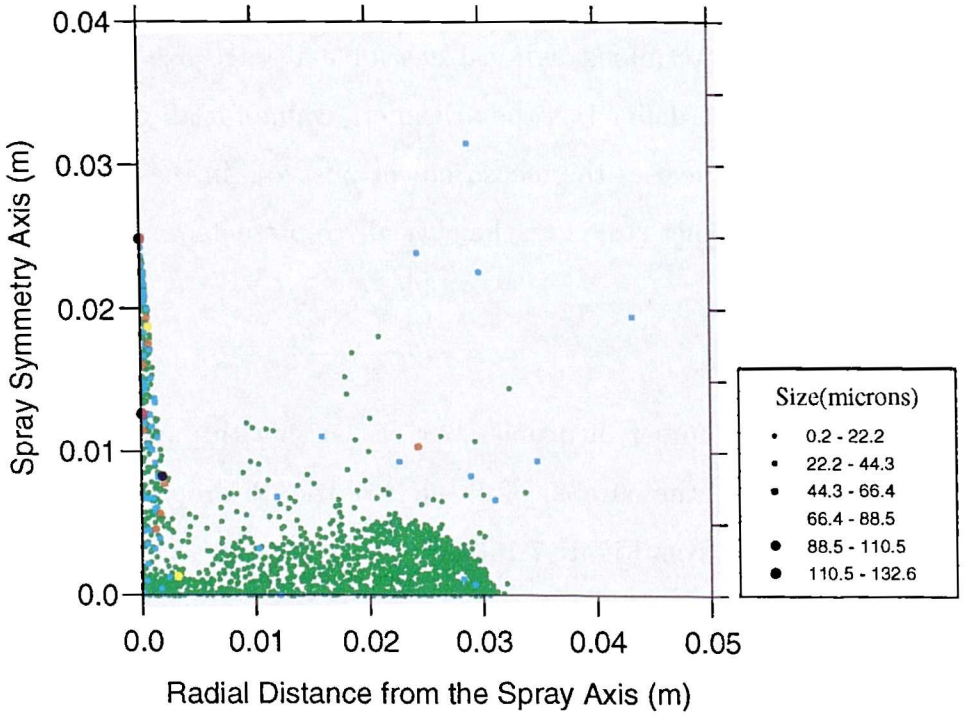
$$\bar{d} = \frac{\sum_{i=1}^{K} N_i d_i}{\sum_{i=1}^{K} N_i}$$

where K is the number of droplet parcels passing through the cell over the time interval, and N_i is the number of droplets of the ith droplet parcel.

It can be seen from Figure 7.15(a) that both the measured and predicted droplet mean tangential velocities show the same trend of variation with distance from the wall: they increase with the height in the region very close to the wall, reach a maximum value at around 1.5mm height, and then monotonically decrease. Quantitative discrepancies are evident in the near-wall region, particularly around the location of the maximum value, where a peak difference of about 15 m/s is observed. However good agreement can be seen in the region further away.

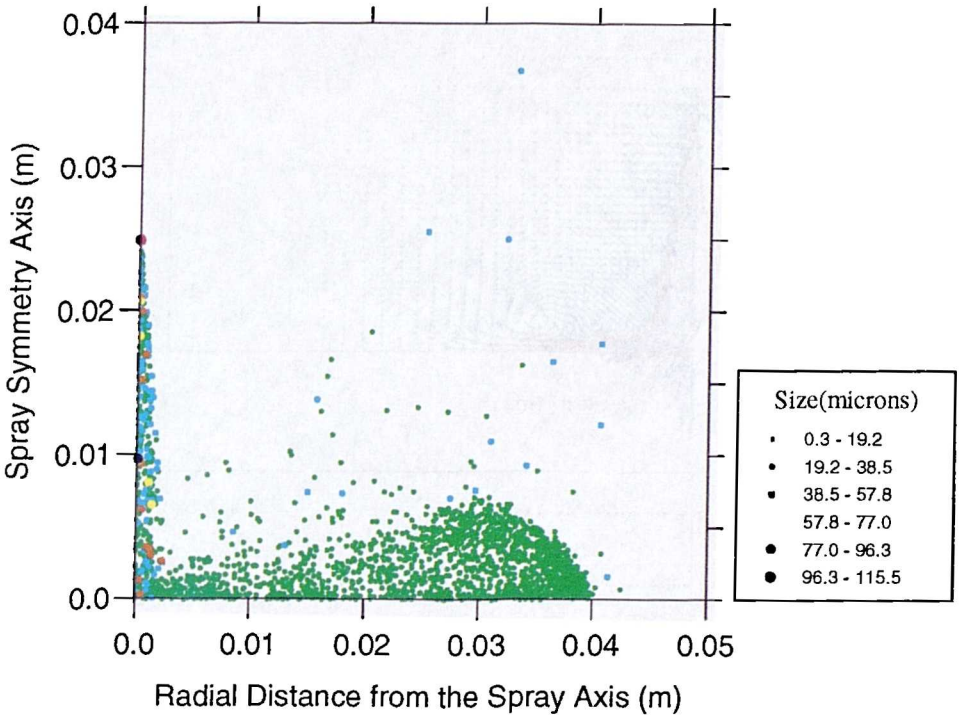


(a) t=1.0ms

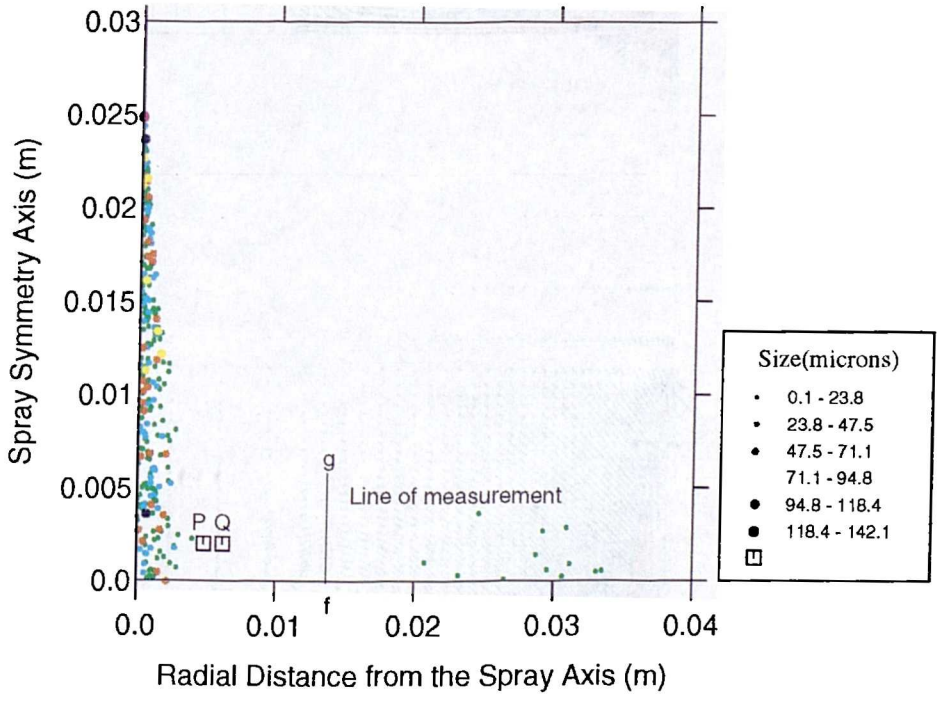


(b) t=2.0ms

Figure 7.12: Predicted development of spray patterns for Case N2



(c) t=3.0ms



(d)Spray predictions with 'Stick' model(t=2.0ms)

Figure 7.12 Continued

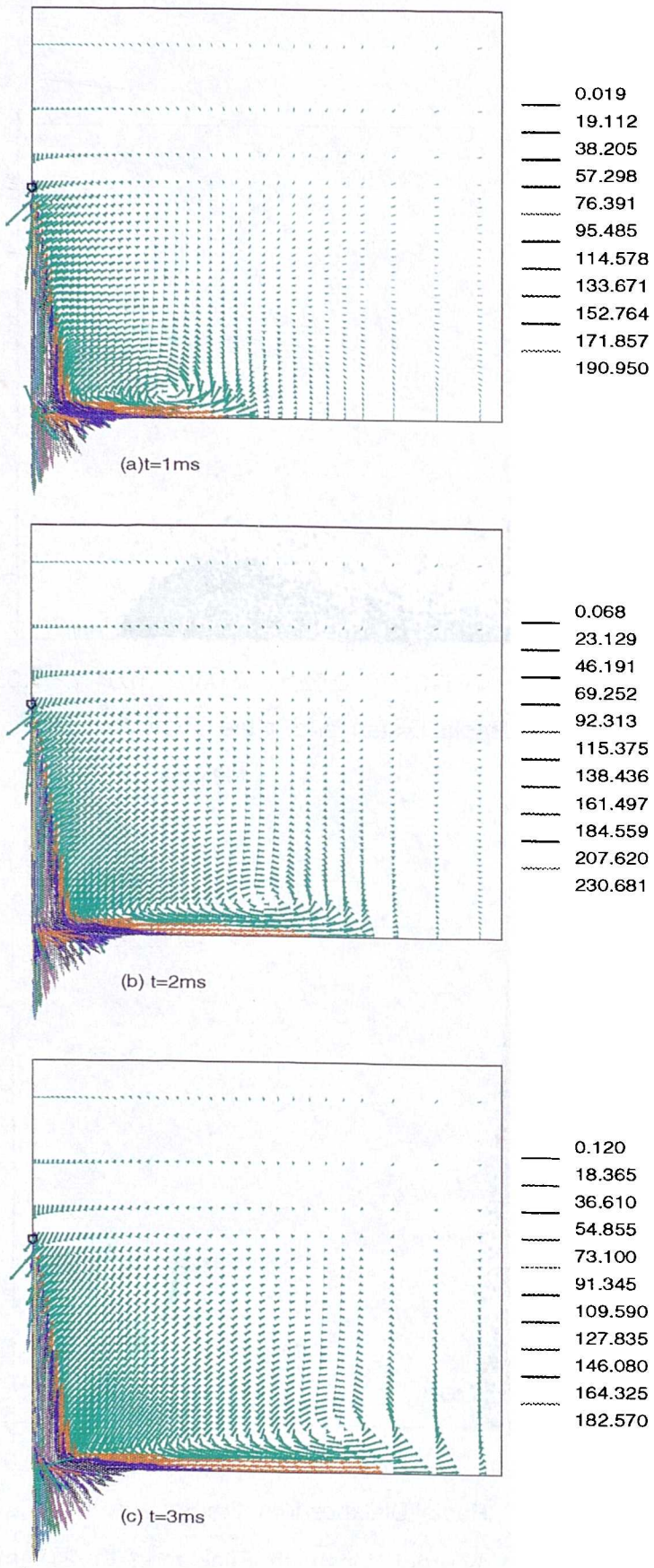


Figure 7.13: Predicted development of gas velocity fields for Case N2.

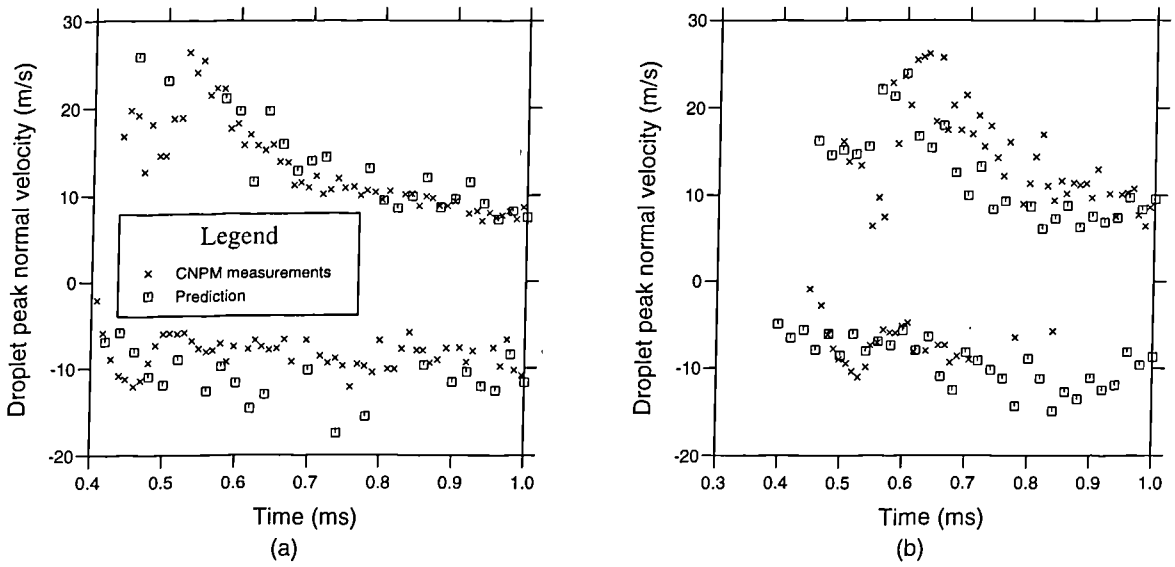


Figure 7.14: Comparison between the predicted and measured droplet peak normal velocities for Case N2 at two locations which are all 2mm height from plate, but differ in radius from the spray axis: (a) r=5mm and (b) r=6mm

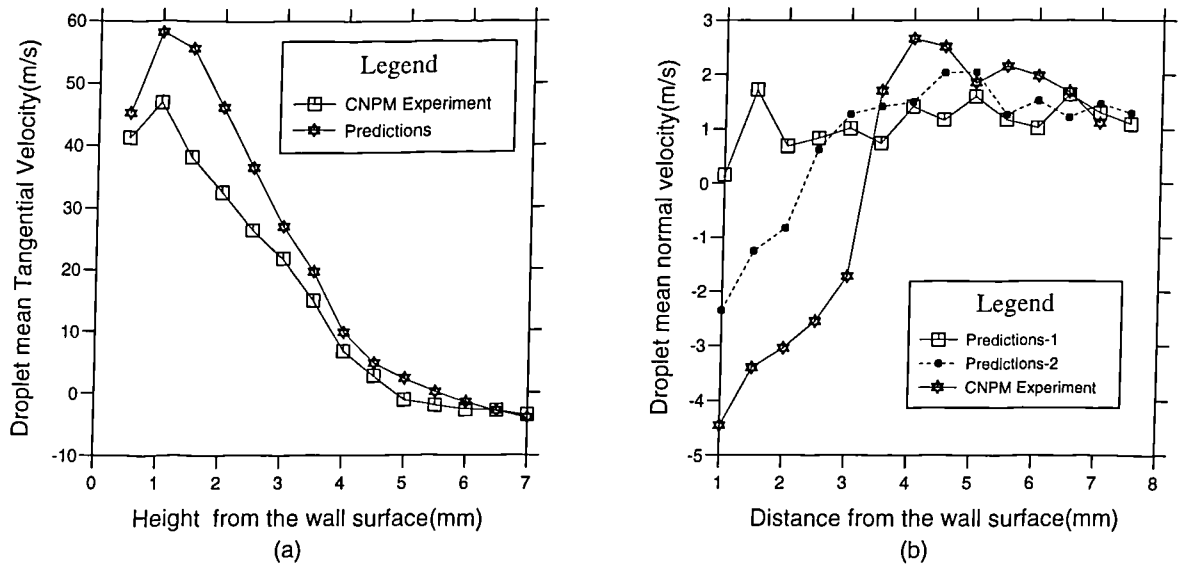


Figure 7.15: Predicted and measured variations with height above the wall for Case N2 of (a) droplet mean tangential velocity; and (b) mean normal velocity at 14mm radius away from the spray axis.

As for the normal velocities Figure 7.15(b), two different predictions are compared with the experimental data. For 'Predictions-1', Saffman lift forces in the near-wall region were ignored. It can be seen that the results differ appreciably from the measurements, especially in the region very close to the wall, where the predictions show droplets moving towards the wall (positive normal velocities) whilst the measurements display the reverse trend. However, when Saffman forces are included for droplets forming the wall spray, we obtain 'Predictions-2' which exhibit better qualitative agreement as evidenced in Figure 7.15(b). However, there is still appreciable quantitative discrepancy in the near-wall region for the negative velocities. One possible explanation for this could be that there may exist another kind of lift force, induced by turbulent bursts, as noted by Cleaver and Yates (1973). Such bursts act to move the fluid very rapidly away from the wall and and thus may exert a lift force much larger than the Saffman force. Since this bursting behavior is yet not fully understood, it is not possible to model the effect here.

In Figure 7.16(a), one can see a clear opposed behavior of the predicted and measured mean droplet diameter variation with height. The measurements show larger mean droplet sizes close to the wall and smaller ones away from it, whereas the converse is true for the predictions, although the peak values of the sizes for both cases are close. To investigate the reasons for the above discrepancies, sensitivity studies were performed. Shown in Figure 7.16(b) are the results obtained from three cases:(1) with Saffman lift forces; (2)with the splash regime ignored, and all the splashing droplets treated as bouncing ones; (3) with permanent coalescence assumed to be the only outcome of the collisions between the droplets forming the wall spray, irrespective of the collision conditions. The results all show the same qualitative behavior as the predictions in Figure 7.16(a). Generally, Case 2 produces the largest droplet sizes, as a consequence of ignoring secondary atomisation. Additional sensitivity studies were also carried out by assigning different fixed values to the secondary droplet sizes, velocities and ejection angles for splash regime, but no exception to the above-predicted trends was found. The findings here suggest that, if experimental errors are assumed to be small, there may be other mechanisms responsible for the discrepancies which are not accounted for in the calculations. Some possibilities are:

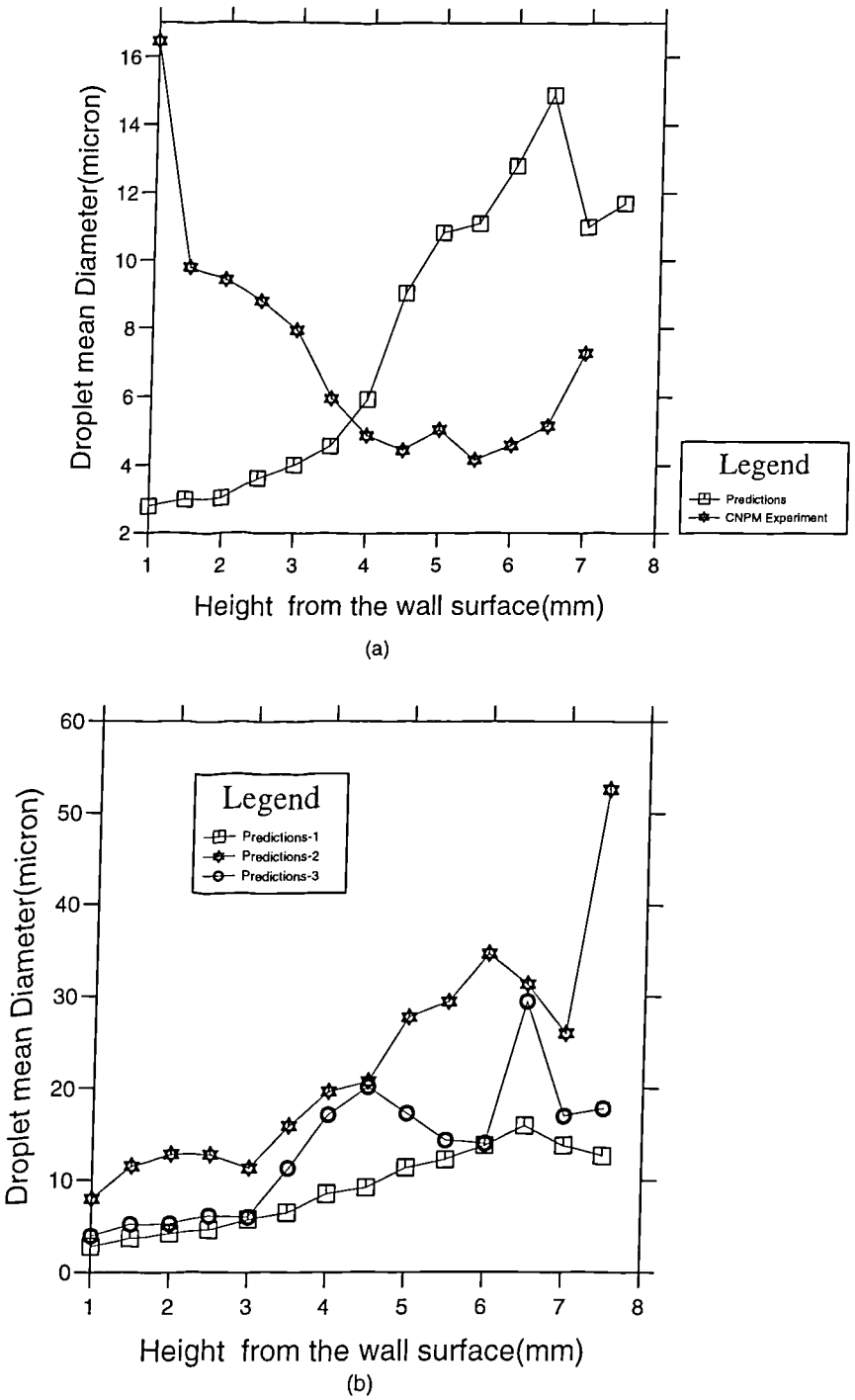


Figure 7.16: Predicted mean diameter variation with the height above the wall surface at 14mm radius away from the spray axis (Case N2): (a) without Saffman lift forces; (b) predictions with three other practices: (1) with Saffman lift forces included, (2)only bounce and stick regimes assumed, and (3)coalescence assumed to occur for all binary collisions of droplets in the wall spray.

- Break-up resulting from high energy droplet-droplet collision. This mechanism is not accounted in our droplet-droplet model. In the impingement zone where the droplets are highly concentrated, the ejected splashing droplets and the arriving droplets from the nozzle are likely to collide with very high relative velocities, thus causing another kind of secondary break-up. Such break-up will introduce some smaller droplets in the upper-edge of the wall spray, which will probably remain in the periphery region afterwards due to the gas flow, and the displacement by the droplets below them. This collision-induced break-up will also contribute to the modification of the whole droplet size distribution and evolution as time elapses.

- As the wall spray is very dense in the near-wall region, further forces may have non-negligible effects on the droplet motion. These include Saffman and Magnus lift forces , as well as turbulent bursts mentioned earlier. Magnus lift forces are associated with droplet rotation, and it was observed by Ghadiry(1978) that the secondary droplets resulting from splashing do have appreciable rotation speed. In addition, the effects of random fluctuations of gas velocity may warrant the inclusion of the Basset correction force which corrects for temporal variations in the relative velocity(cf. Hansell et al 1992).

- The effect of neighbouring droplets on the droplet impingement dynamics. This is also expected to influence droplet impingement outcomes and post-impingement characteristics and thus also droplet size distribution.

Finally, for interest, some simulation results for wall film characteristics are shown in Figure 7.17(a) and (b). The former presents the predicted variation with time of the adhered fuel mass ratio, which behaves in a similar manner to those observed in the experiments of Katsura et al (1989). It increases initially and reaches a steady state value of around 45% shortly after the end of injection. Shown in Figure 7.17(b) are the predicted spatial distributions of film thickness at three times after start of injection. Here, like in Case N1, we observe similar features in that it spreads outward continuously as time goes on and the peak film thickness (which is here observed to be always below $20\mu m$) appears near the film edge, which is again indicative of local film mass accumulation there.

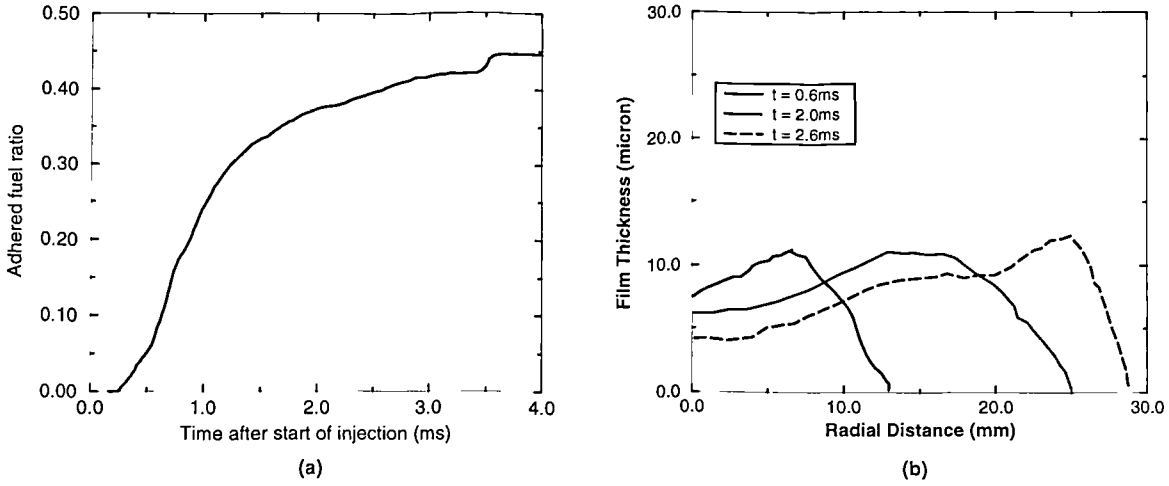


Figure 7.17: Prediction for Case N2 of (a) temporal evolution of adhered fuel ratio; (b) film thickness distributions at three times after start of injection

7.4 Comparison with Harwell Experiments

Description of Experiments

The experimental studies conducted in Harwell byEreautet al (1992), of normal spray impingement in a pressure chamber, produced some useful data for the validation of the present computational models. They measured the spray cross-section radii, R_c, at different heights above the wall, and the wall film radius,R_f: both were obtained using a laser sheet technique. The definitions of R_c and R_f are illustrated in Figure 7.2.

In these experiments, fuel sprays were injected from a single-hole nozzle with a diameter of 3mm . The nozzle is positioned 50mm away from a flat plate onto which the spray impinges. A total volume of $40mm^3$ Diesel fuel was injected in a single pulse (corresponding to a time period of 2.4 ms), according to the injection schedule depicted in figure 7.18. Two sets of ambient gas conditions were investigated: (a) atmospheric temperature (293K) and pressure (1 bar); and (b) elevated temperature (473K) and pressure (20 bar). For the convenience of subsequent discussions, we refer these as Cases N3 and N4 respectively.

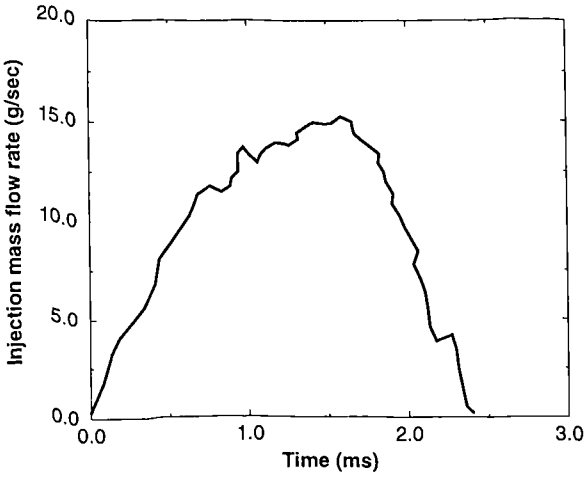


Figure 7.18: Injection history of Harwell experiments

Presentation of Results

Results for atmospheric gas conditions (Case N3) are shown in Figures 7.19(a) and (b) The former compares the predicted and measured film radius variation with time at 20^0C gas temperature, and 1bar gas pressure. The solid line represents the prediction by the present film model, while the broken line denotes that using the static film model which does not consider the film spreading but traces the position furthest from the spray axis where mass deposition occurs. The present model, being capable of simulating film spreading behavior, produces good agreement with the measurements and capture the trend that the film radius increases monotonically and nearly linearly with time, although the calculated result has a slightly smaller slope. The static film model, however, gives substantial under-prediction because it ignores film motion. This indicates clearly the importance of appropriate film modelling.

Figure 7.19(b) shows the variation with time of the calculated spray section radius R_c at 2mm height, compared with measurements. Here R_c is defined, similar to the definition of spray radius, as the radius of a cylindrical body which contains 99% of the total fuel liquid available in the region above the spray section (which is parallel to the flat plate), and has this section as its base and spray axis its symmetry line.

Here the agreement is less good than that of Figure 7.19(a), probably due to

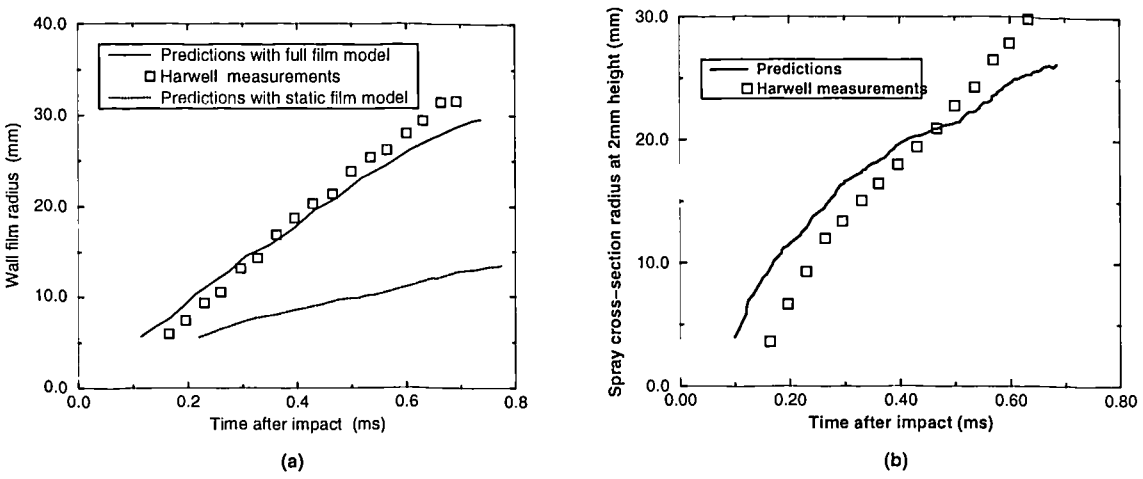


Figure 7.19: Comparison between predicted and measured temporal variations for Case N3 of (a) wall film radius; and (b) spray cross-section radius at 2mm height above the wall.

the fact that the predicted wall spray contains a number of isolated droplets, which makes it difficult for the computationally-defined spray section radius to always represent the actual radius which is perceived in the visualisation studies. However, for the case of elevated gas temperature(200^0C) and gas pressure(20bar) (Case N4) where spray is more compact (due to the increase of ambient gas resistance) and the computationally-defined radius is probably more representative to that of the visualisation, the predicted spray-section radiii at 2mm and 4mm heights from the surface both show satisfactory agreement with experiments, as exhibited in Figures 7.19(a) and (b).

Figure 7.21 compares, for Case N4 (elevated pressure and temperature), the predicted and measured temporal variations of film radius. Again the agreement is not bad but, as can be seen from the figure, the experimental data show a dip commencing at around 0.2ms after the impact. This seems to be unusual, since the film radius should be an increasing, or at least a non-decreasing, function of time during the spreading stage, when fuel is continuously impinging on the wall. The behaviour here might be due to experimental error.

Figures 7.22 (a) and (b) show respectively for Cases N3 and N4 the predicted spatial film thickness distributions at various times (no measurements are available).

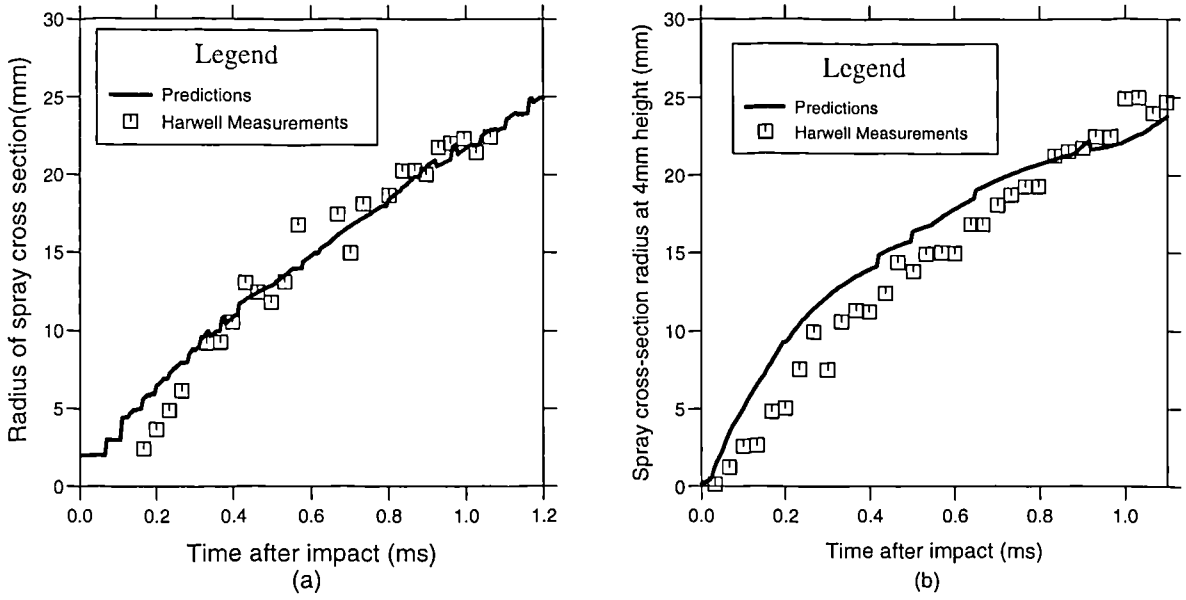


Figure 7.20: Comparison between predicted and measured variations with time of spray cross-section radius at (a) 2mm and (b) 4mm above the wall for Case N4

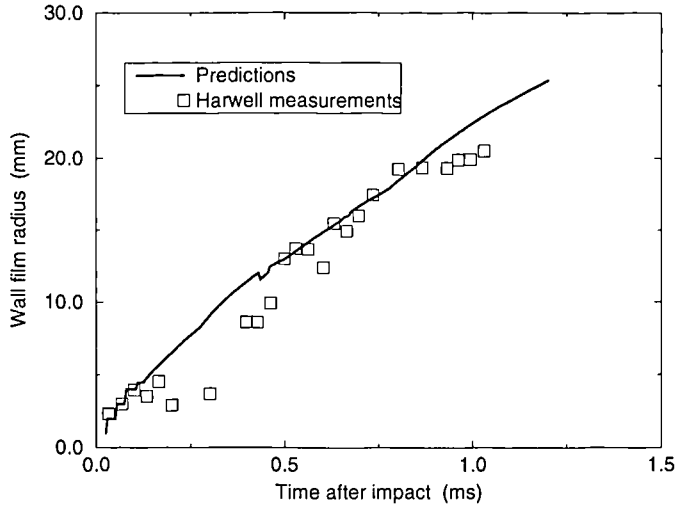


Figure 7.21: Comparison between predicted and measured variations with time of film radius for Case N4

Both plots show again the common features that have been revealed in the previous calculations.

It is also noteworthy from Figure 7.22 that the film thickness is invariably lower in Case N3, as a consequence of the much higher gas temperature. This is due to two mechanisms. First, the higher pressure enhances droplet breakup induced by aerodynamic forces, reducing the sizes of the arriving droplets and thus also mass deposition. Second, strong vaporisation of the film and droplets also reduces mass deposition. This can be seen from Figure 7.23(a) which compares the predicted temporal variations of adhered fuel ratio for both cases. It is clear from the figure that this ratio is substantially lower in Case N4 than in Case N3. In particular, final value of the ratio in Case N4 is about 40%, whilst in Case N3 it is around 60%.

Evidence of film evaporation can also be seen in Figure 7.23(b), which shows the predicted temporal evolution of the mass ratio between the cumulative film mass evaporated and the cumulative mass deposited. We observe that this quantity increases monotonically with time and reaches a value of about 27% at 2ms after the start of impingement.

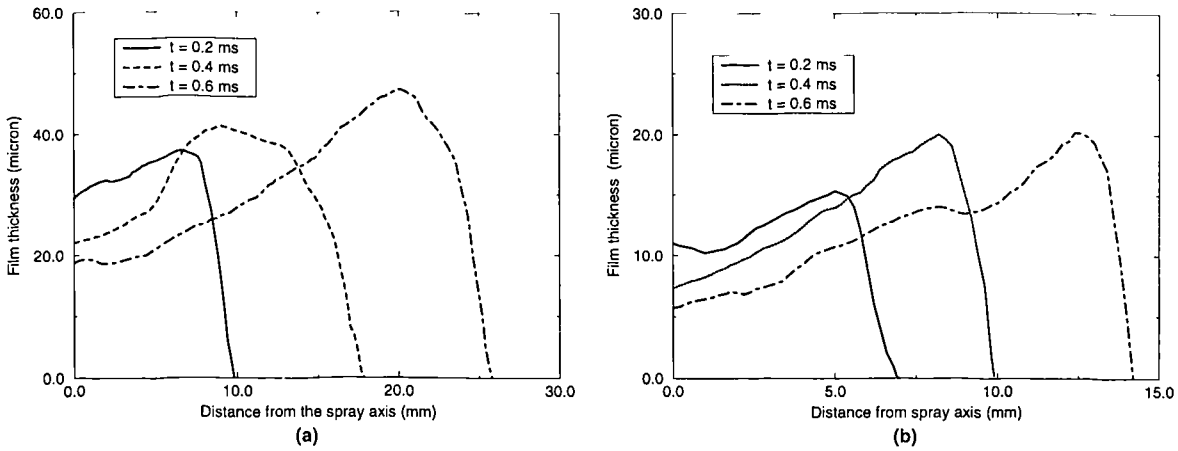


Figure 7.22: Predicted film thickness distributions at different times after start of impingement for (a) Case N3 and (b) Case N4

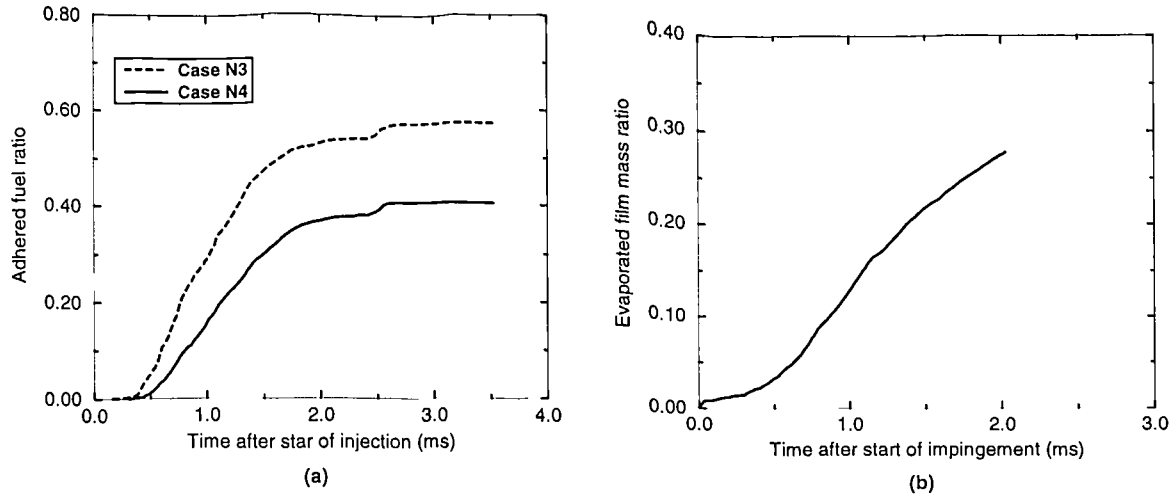


Figure 7.23: Predicted temporal variations of (a) adhered fuel mass ratio for Cases N3 and N4; (b) evaporated film mass percentage for Case N4

7.5 Comparison with Experiments of Saito et al

Description of Experiments

As discussed in Chapter 2, Saito et al (1993) performed spray impingement experiments in a pressure chamber under injection conditions closely approximating those in Diesel engines. The spray was injected from a single-hole nozzle with a constant injection pressure, under experimental conditions characterised in Table 7.3. Measurements were made of both wall spray and film characteristics using high speed photographs. These include: (i) the final adhered fuel ratio after the end of injection (transient data for this quantity were not measured due to experimental difficulty); (ii) the wall spray radius and height as functions of time; and (iii) temporal variations of wall film radius and mean film thickness.

Presentation of Results

Comparisons are first made with wall spray radius and height, shown in Figure 7.24(a) and (b) respectively (note that there were no data for wall spray radius for Case N6). Very good agreement is observed for spray radius and moderate agreement exists for spray height. Moreover, the predictions capture the trend that the higher the injection pressure, the larger the spray radius and height, all other

Table 7.3: Specifications for Experiments of Saito et al (Cases N5, N6, N7)

Case No.	N5	N6	N7
Wall Distance(mm)	25	25	25
Gas Pressure(bar)	21	21	21
Gas Temperature(K)	293	293	293
Nozzle Diameter(mm)	0.25	0.25	0.25
Injection Duration(ms)	2.85	2.1	1.425
Injection Angle(Deg.)	90	90	90
Fuel Injected(mm^3/pulse)	35	35	35
Fuel	Diesel	Diesel	Diesel
Injection Pressure	$30MPa$	$55MPa$	$120MPa$

conditions being the same. This is not difficult to understand, since at high injection pressure, the droplets in the wall spray generally possess larger tangential velocities due to the increased gas velocities, and higher normal velocities due to more intense splashing.

Figure 7.25 displays variations of adhered fuel ratios with time for three different constant injection pressures, namely, $30MPa$ (Case N5), $55MPa$ (Case N6) and $120MPa$ (Case N7). Again there are two features that are reminiscent of those observed in earlier calculations. First, as expected, the adhered fuel ratio in each case initially increases with time and gradually reaches a steady-state value after termination of injection. The calculated steady state values for all three cases are also in close agreement with the measured ones, which are shown in Figure 7.25(a) as symbols. Second, a cusp appears in each curve at the time corresponding to the end of fuel injection, immediately after which there is a local rapid increase in the adhered fuel ratio due to the reasons explained earlier.

Another noteworthy feature in Figure 7.25(a) is that as the injection pressure is increased, the adhered fuel ratio (and thus also the average film thickness) are reduced. In particular, the final ratio is decreased by about 20% when the injection pressure is increased from $30MPa$ to $120MPa$. The variation of the steady-state ratio with the injection pressure is displayed in Figure 7.25(b).

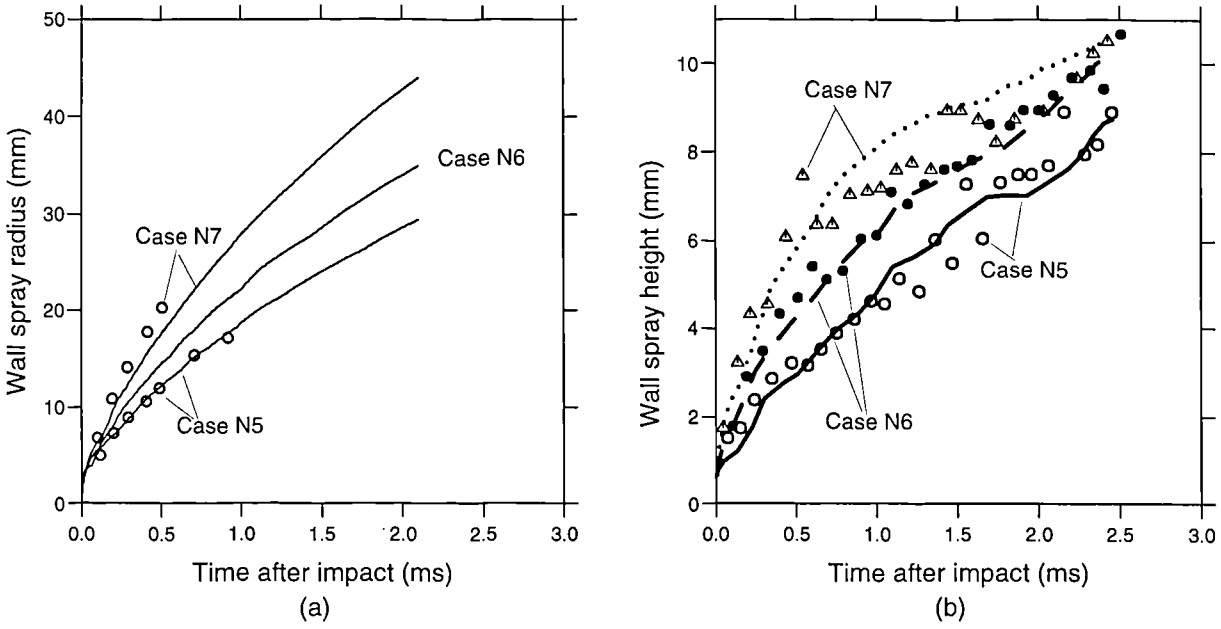


Figure 7.24: Comparison between predicted and measured (a) wall spray radius and (b) wall spray height

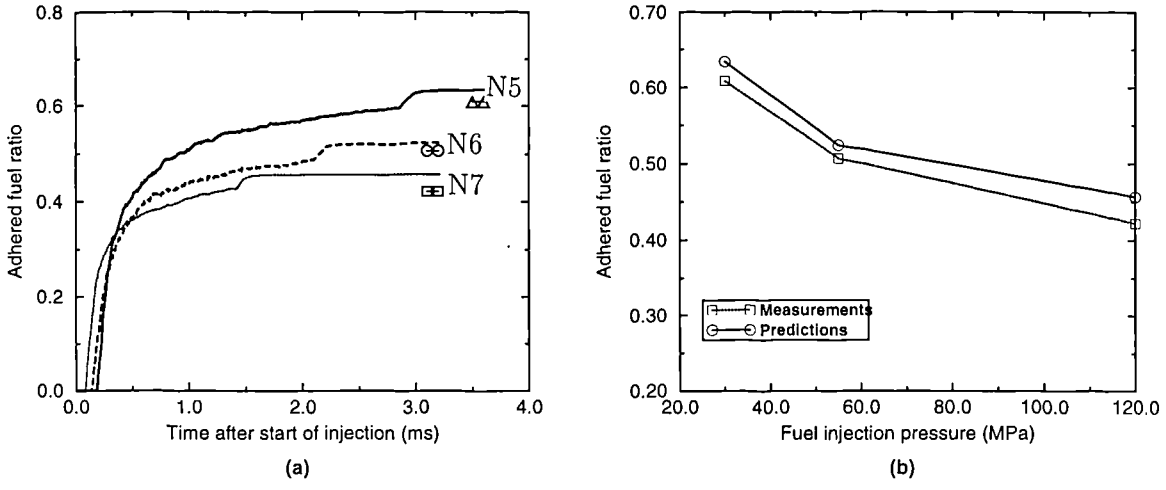


Figure 7.25: (a) Predicted variation with time (curves in the figure) of adhered fuel ratio for Cases N5, N6 and N7 (the open symbols stand for experimental data for steady value); and (b) predicted and measured steady state adhered fuel ratio versus fuel injection pressure.

The above-observed effects of fuel injection pressure on the adhered fuel ratio may be explained by two facts. Firstly, as is confirmed in our calculations, higher injection pressures result in better fuel atomisation so that the sizes of arriving droplets at the impingement region are generally smaller. As a consequence of this, more droplets with smaller sizes are carried away directly by the gas flow in the near-wall region without hitting the wall at all, thereby resulting in less fuel deposition. Secondly, at higher injection pressures, impingement-induced secondary atomisation for the larger droplets is enhanced due to the higher impact energy and consequently more liquid is entrained away by the more violent gas jet, which also exhibits a stronger vortex structure (not shown).

The next comparisons are made with measured wall film characteristics, for Cases N5 and N7. Figures 7.26(a) and (b) show respectively the calculated and experimental variations with time of film radius and mean film thickness. The latter is here defined as the total film volume divided by the surface area it covers. Very good agreement is observed for film radius and satisfactory results are also obtained for the film thickness. The predictions clearly reproduce well the experimental behavior that, as the injection pressure is increased, the film spreads faster whilst the mean film thickness becomes smaller. The reasons for this are almost self-evident, since a higher injection pressure results in larger droplet and gas impingement velocities which in turn promote faster film spreading. This fact, together with the earlier observation that higher injection pressure causes less mass deposition, serves to explain the above thickness behavior.

Displayed in Figures 7.27(a) and (b) are respectively the predicted film thickness distributions at four different times for Cases N5 and N7 respectively (again there are no measurements to compare with). Here again we see the usual trends. However, in Figure 7.27(b) the peak value of film thickness is, unlike in the other cases, reducing with time, probably because the film spreading rate is faster in this case.

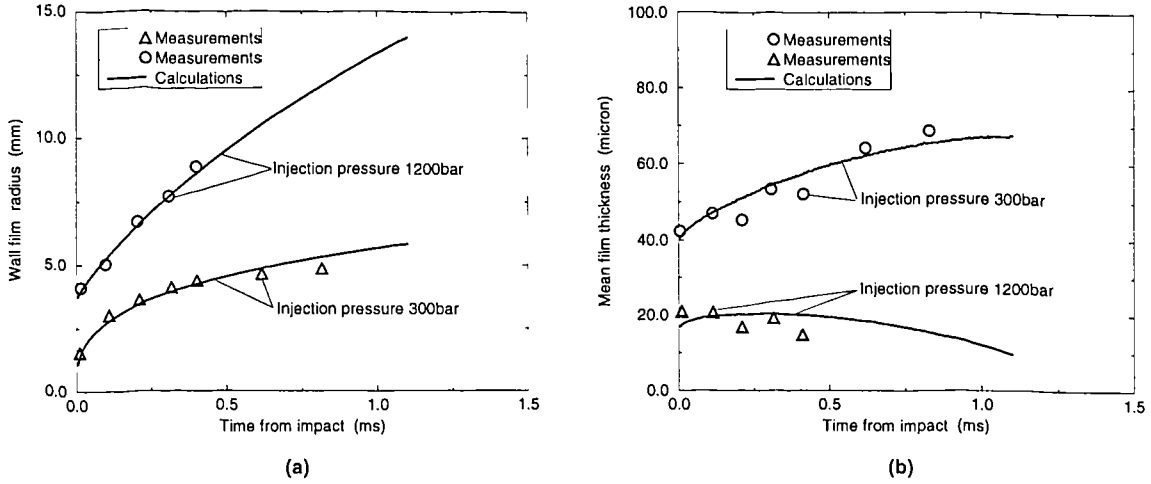


Figure 7.26: Calculated and measured variation with time for Case N5 and N7 of (a) film radii; and (b) mean film thickness

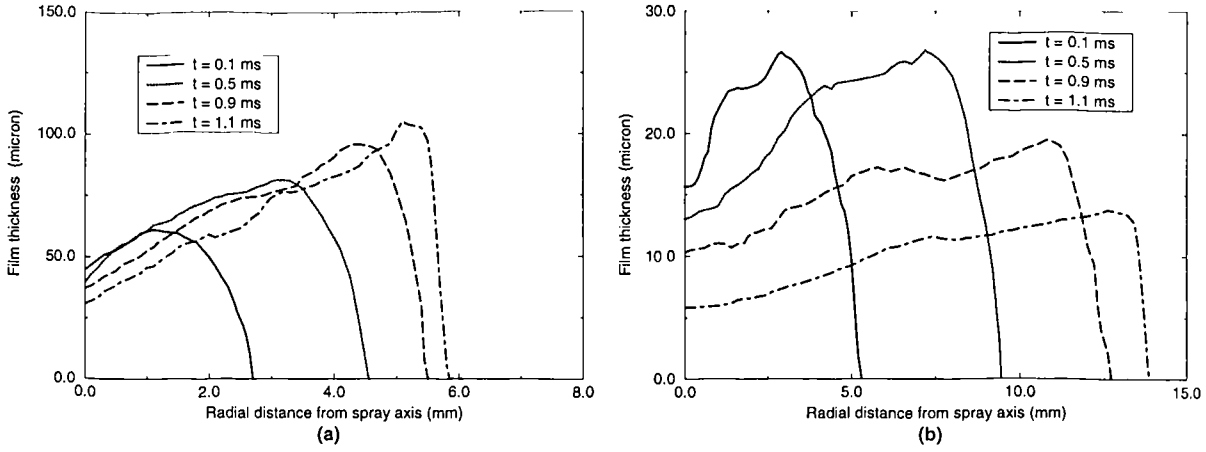


Figure 7.27: Predicted film thickness distributions at different times for (a) Case N5 and (b) Case N7

7.6 Comparison with CNPM Oblique Spray Impingement Experiments

Description of the Experiments

Coghe et al (1992) also performed oblique spray impingement experiments in cylindrical chambers, using the same nozzle and injection conditions as those in their normal impingement experiments (see Section 7.2). Figures 7.31(a) and (b) illustrate the two new cases, denoted respectively as Cases O1 and O2. In Case O1, the spray was directed obliquely at an angle of 45^0 onto the bottom surface of the chamber, and measurements were made only of ensemble-averaged droplet sizes and velocities in the near-wall region.

In Case O2, the spray was directed at an inclination angle of 60^0 onto a vertical cylindrical surface, and measurements were made of film thickness characteristics. These include: film volume over a selected wall patch, film thickness temporal profiles at some specific locations, and film thickness spatial distributions over the wall patch. There are however, no experimental data on wall spray characteristics in this case.

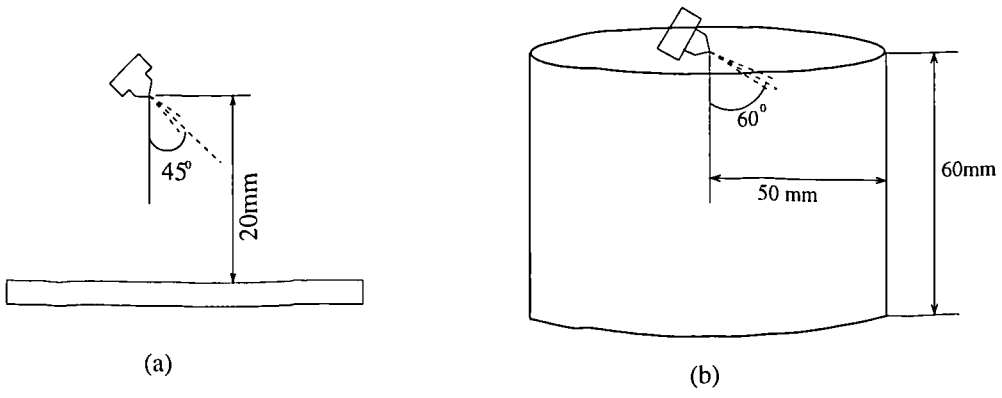


Figure 7.28: Schematics of CNPM oblique impingement cases.

Details of Simulation

Calculations are performed for both cases in three dimensional cylindrical computational domains, and the nozzle is positioned 10mm away from the top of the chamber in both cases. In case O1, a domain of 100mm radius and 30mm height is divided

into a number of cells by a grid containing $79 \times 27 \times 25$ planes in the radial, circumferential and axial directions, respectively. This grid is illustrated in Figures 7.29(a) and (b) for plan view and elevated view respectively. In order to have optimal numerical accuracy, a smaller grid spacing in the circumferential direction is arranged in the right half of the chamber as can be seen in Figure 7.29(b), because it is in this region where the fuel spray develops.

In Case O2, the calculation domain is 50mm in radius and 70mm in height. The grid employed is depicted in Figure 7.30, which has $49 \times 27 \times 59 = 78057$ nodes in the radial, circumferential and axial directions, respectively. The grid spacing in the circumferential direction is arranged in the same manner as in Case O1.

The time step size and droplet parcel number introduction employed here are the same as in normal spray impingement cases.

Presentation of the Results

Figures 7.31 shows the spray patterns for Case O1. Wall sprays can be seen in both the upstream and downstream regions, stretching away in opposite directions and at different speeds. The downstream wall spray height and radius are larger than the upstream ones. This can be explained by the fact that the momentum of the spray is predominantly downstream after impingement. Another feature of the wall sprays is that they contain mostly small droplets formed by secondary atomisation (note that droplet sizes are scaled with colours in the figure). Also, the downstream wall spray exhibits a vortex-like shape near the leading edge, induced by the gas flow.

Comparisons are made in Figures 7.32(a), (b) and (c) with experimental data for the mean tangential and normal velocities and mean droplet sizes, respectively, along a vertical line (labelled mn in Figure 7.31(a)) which is 14 mm downstream from the stagnation point(see also Figure 7.31(a)). Virtually, the same trends as those for Case N2 are obtained, i.e., good agreement for the mean tangential droplet velocity (see plot(a)); but appreciable differences for the normal velocities in the region close to the wall, particularly when the Saffman forces are not included (plot(b)); and opposing behaviour for the predicted and measured mean droplet sizes (plot(c)). Here improvement is again seen for the droplet mean normal velocities when the lift

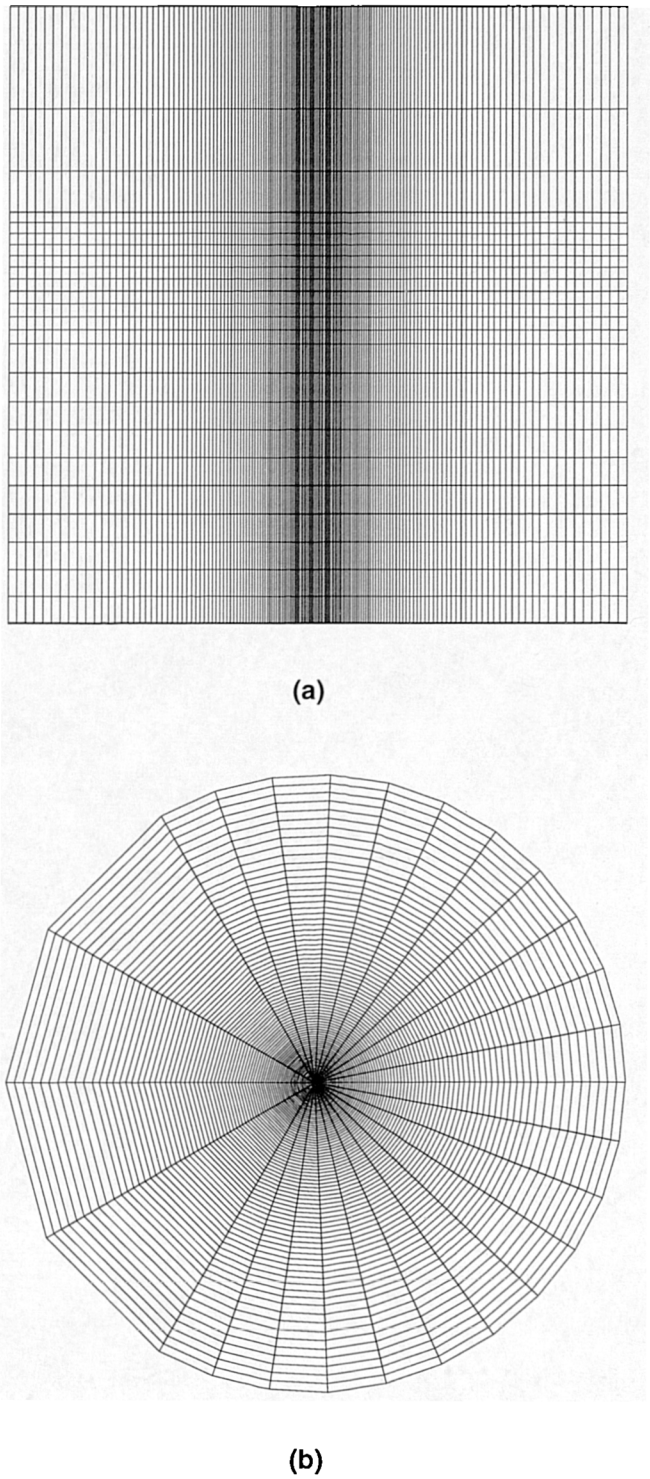


Figure 7.29: Computational mesh used for Case O1: (a) elevated view (b) plan view

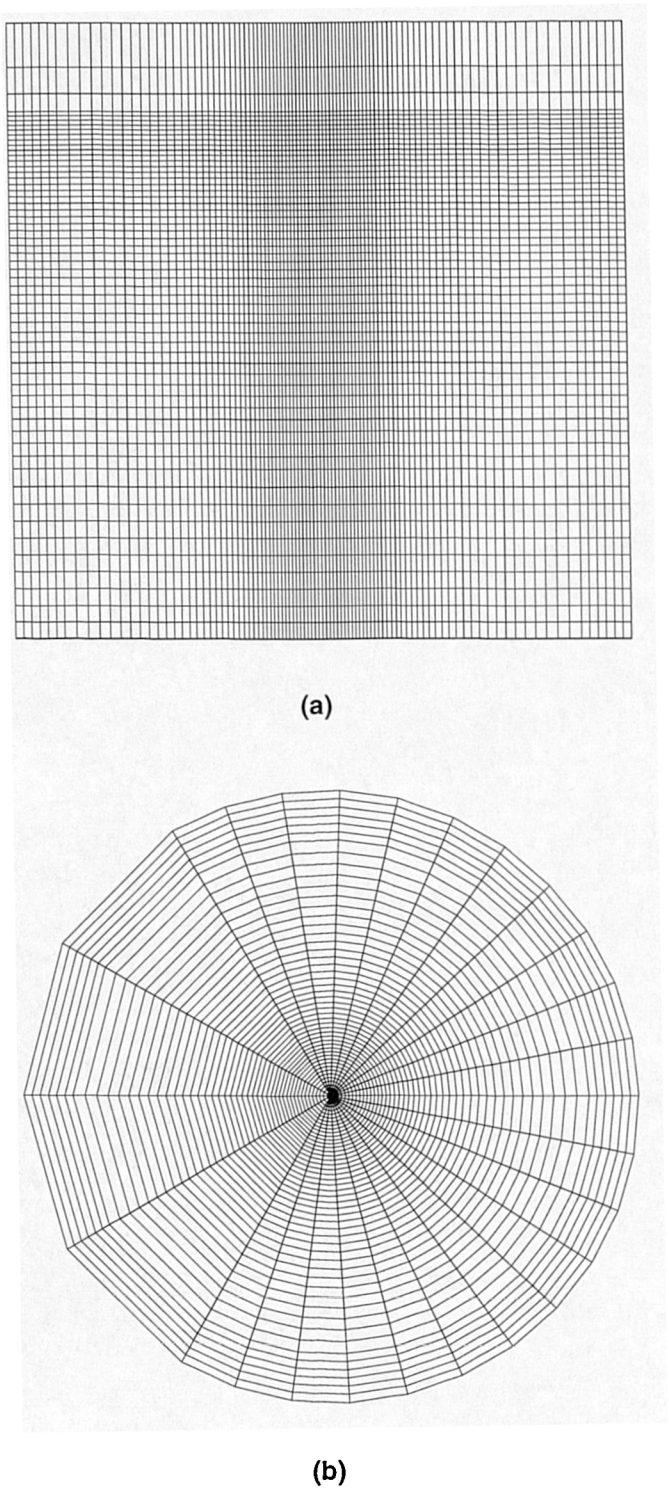


Figure 7.30: Computational mesh used for Case O2: (a) elevated view (b) plan view

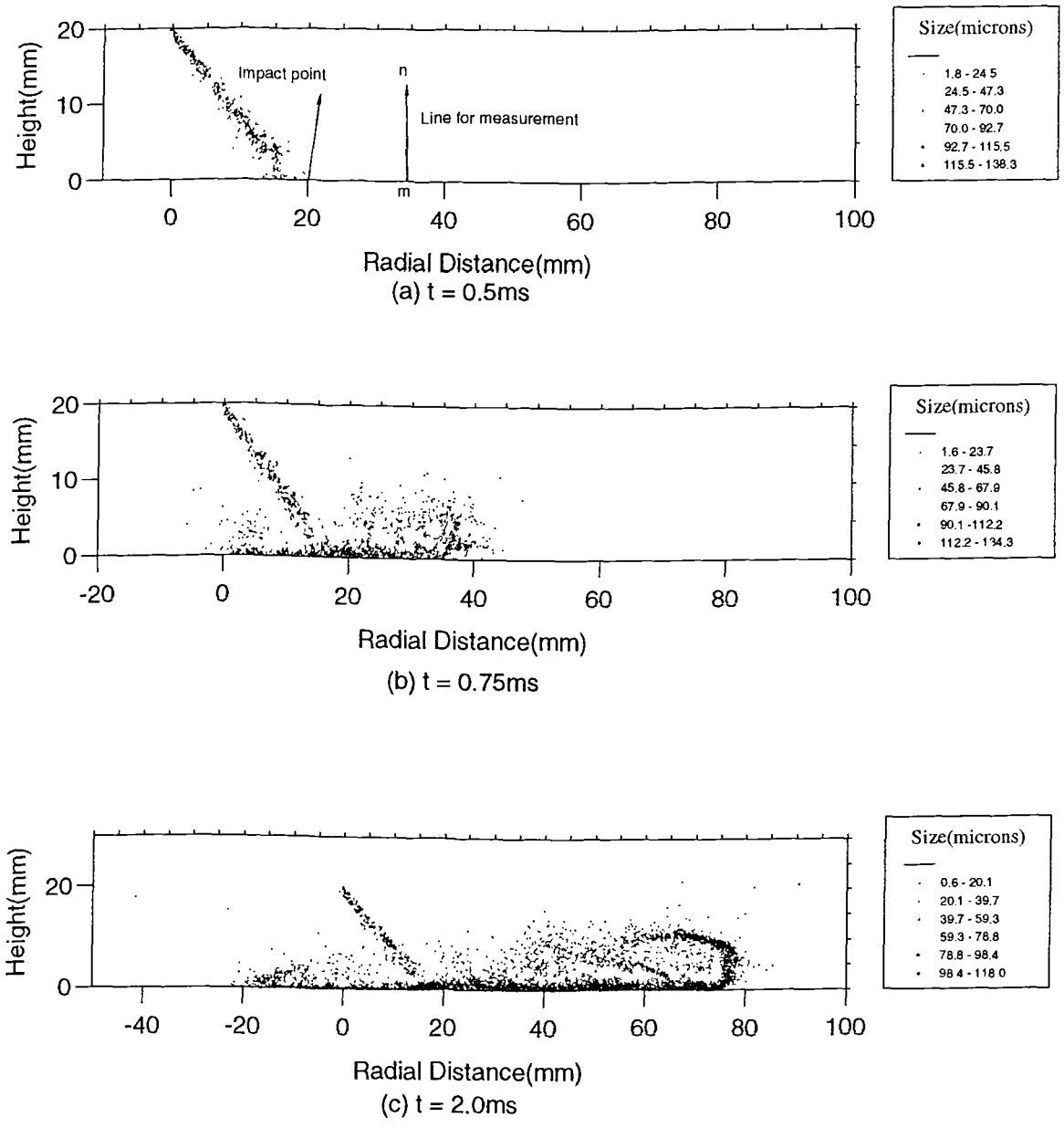


Figure 7.31: Predicted development of spray patterns for Case O1

forces are included, emphasising their importance in the near-wall region.

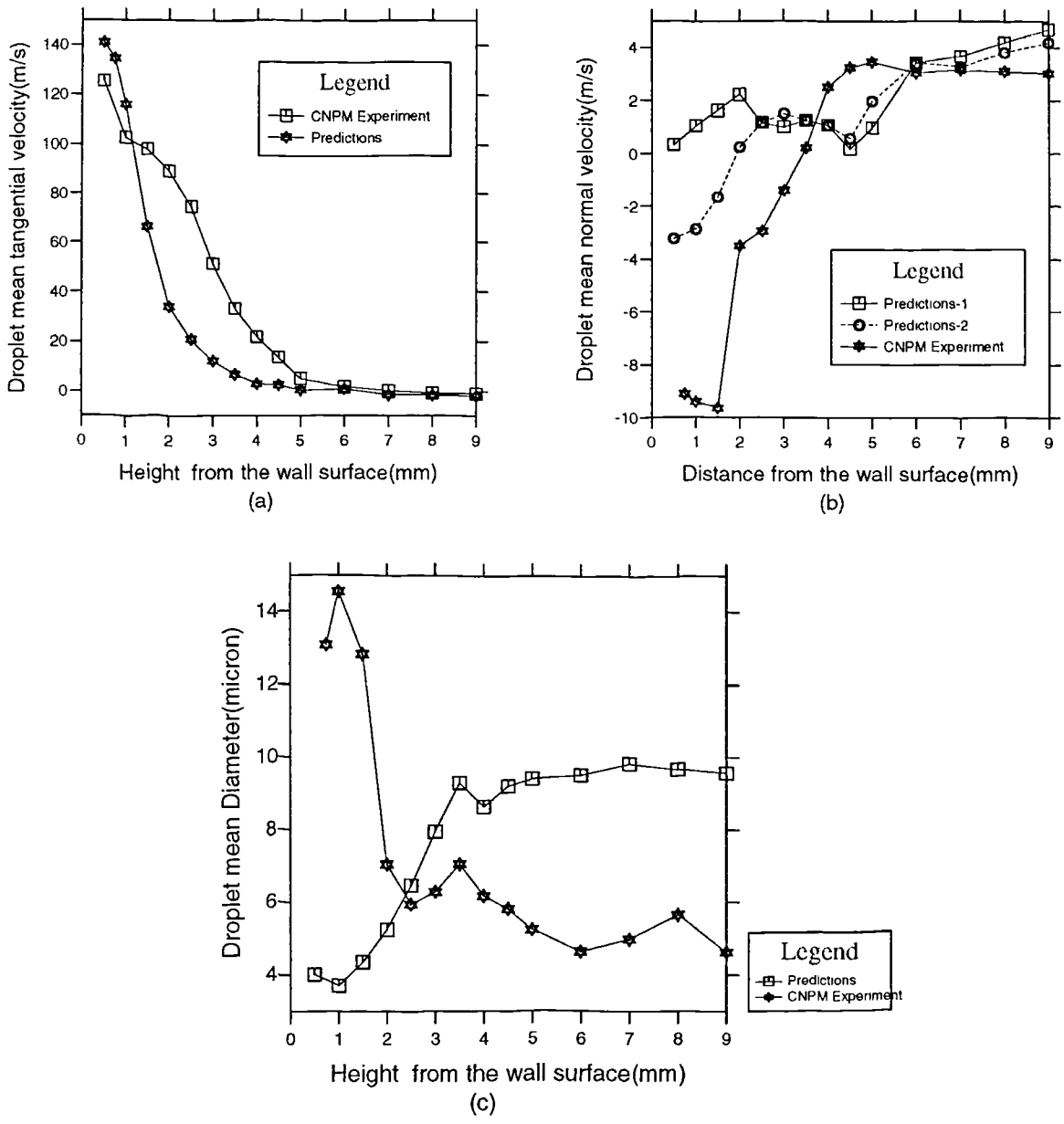


Figure 7.32: Predicted and measured variations with height above the wall surface for Case O1 of (a) droplet mean tangential velocity; (b) droplet mean normal velocity; and (c) droplet mean size at 14mm radius away from the spray axis.

Figure 7.33(a) presents the predicted configurations of the moving contact line of the wall film (which is the line delimiting the wall area covered by the film) at three times after start of injection. Here two expected physical characteristics are indicated clearly in this figure. First, wall film spreads outward in all directions as time goes on. Second, the film, like the wall spray, spreads faster downstream, which

explains why the area covered by the film exhibits an elliptic shape at all stages. The corresponding predicted film thickness profiles along the incidence line can be seen in Figure 7.33(b) for the same three times as in Figure 7.33(a). The incidence line here denotes the line of intersection of the impingement surface with a plane, formed by the spray axis and the line through the nozzle which is perpendicular to the impact surface. Also evident in the figure is that local film mass accumulation occurs around the edges in both the upstream and downstream for the reasons explained earlier. The maximum film thickness observed here is below $20\mu m$.

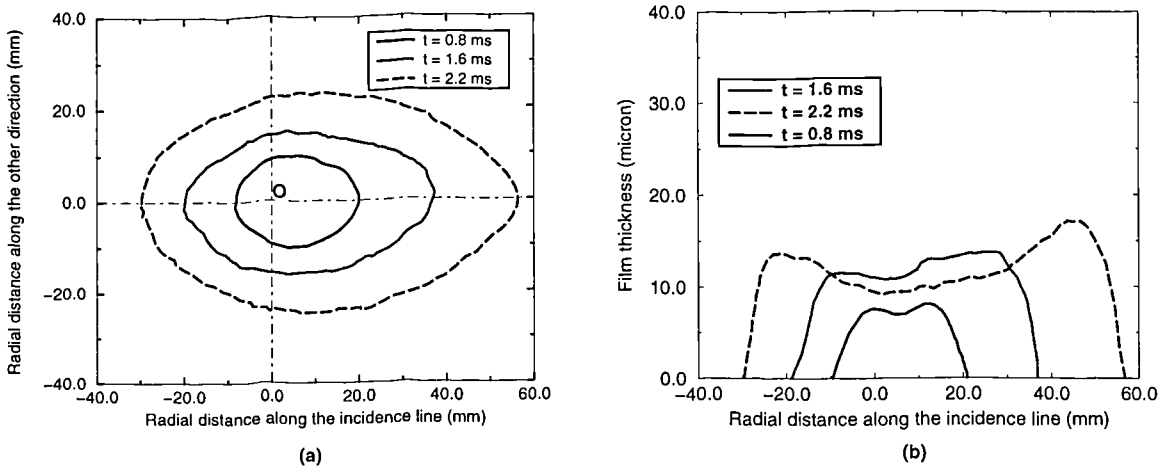


Figure 7.33: Predictions for Case O1 at three times of (a) wall film patches (note that point O in the figure denotes the stagnation point); and (b) wall film thickness spatial profiles along the incidence line.

Attention is now turned to the results for Case O2. Figure 7.34 depicts the spray patterns at two times, which exhibit similar structure to that of Case O1, although wall spray here looks more compact. This may be due to the fact that wall impingement distance in this case is more than twice as large as Case O1, so that when droplets reach the wall they have less impact energy. This in turn causes more fuel deposition and less kinetic energy for the rebounding and splashing droplets.

Figure 7.35 compares the measured and predicted variation with time of the volume of liquid deposited on the wall patch ABCD, which covers an area of $30\times30mm^2$ of the cylindrical impingement surface, as shown in Figure 7.36. The measured wall film volume is obtained as summation of the film volumes over 144 equal subareas,

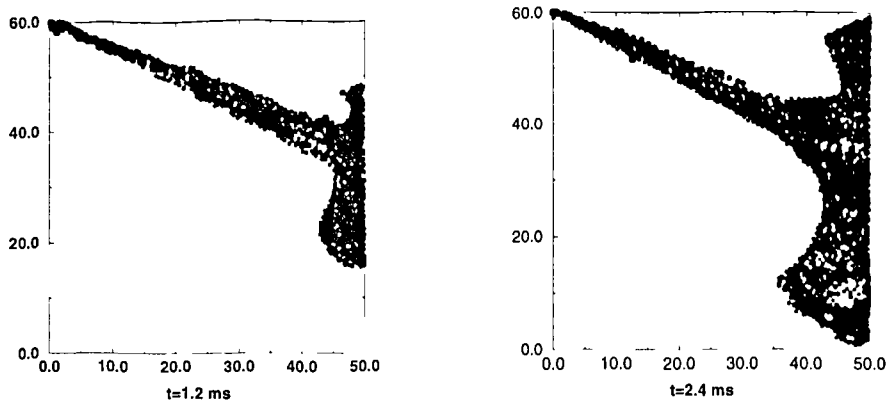


Figure 7.34: Predicted spray patterns at two times after start of injection for Case O2

each with an area of $6.25mm^2$, and the predicted film volume is obtained, in a similar manner, as summation of the calculated film volumes over the mesh cells covering the specified wall patch. Good agreement between the predictions and the measurements from the onset of spray impingement to around 5.4ms after start of injection. The measurement shows a constant non-zero film volume even before impingement. This is probably due to experimental error.

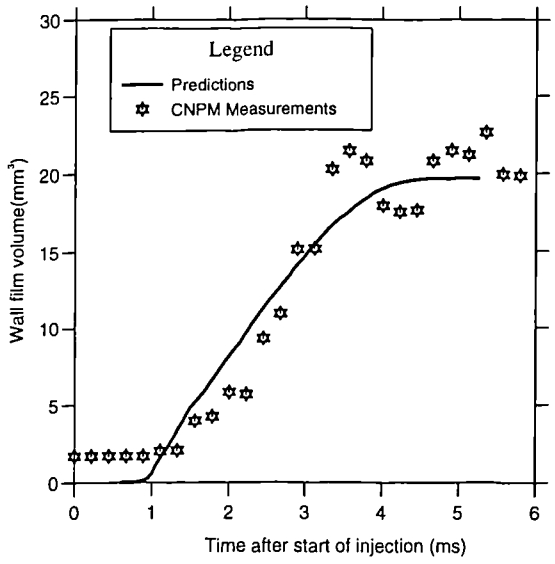


Figure 7.35: Predicted and measured variation with time of film volume wall patch (Case O2).

Figures 7.37(a)-(d) show for Case O2 predictions and measurements of local film thickness variation with time at four locations a, b, c, d inside the area of impact of

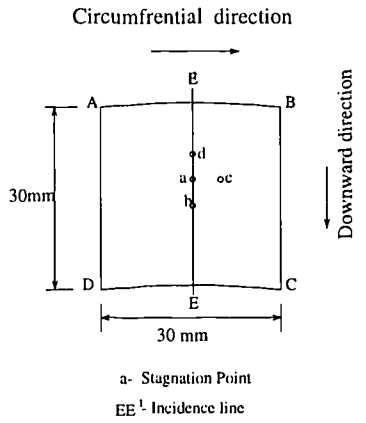


Figure 7.36: Wall patch of film thickness measurements.

the free spray cone (see Figure 36). Here point a is the nominal stagnation point, defined as the intersection between the injection hole axis with the impact surface. Points b and d are situated, along the incidence line, downstream and upstream respectively of the stagnation point. Point c lies in the line which is perpendicular to the incidence line and passes through the stagnation point. The latter three points are all 2.5 mm equal distant from point a.

A common feature of these plots is that the predictions generally show smaller film thickness at the early stage (from the instant of impact up to 2ms after start of injection), particularly in the period immediately after impact. It can further be noted that the predictions show an expected continuous increase of film thickness as mass deposition increases; whereas the measurements produce values which are almost constant or show slight variations. The latter case is particularly obvious in Figure 7.37(a) (at stagnation point), where the film thickness is seen to be a constant value of about $16\mu m$ in the time interval from 1ms to 3.4 ms(the end of injection). This is difficult to explain, as the continuous mass deposition and impact pressure effects would almost certainly cause a dynamic variation of film thickness at this position. The explanation may lie in experimental error , especially in view of the fact that uncertainties do arise when the measured film thickness value is less than about $20\mu m$. Such uncertainties are believed to be caused by the width of laser beam used in the measurement technique, as pointed out by Ereat at al (1992).

In the period that follows, from around 2 to 5ms after start of injection (ASI), reasonable agreement can be observed between the predictions and measurements, both of which show moderate variation of film thickness with time. However, shortly

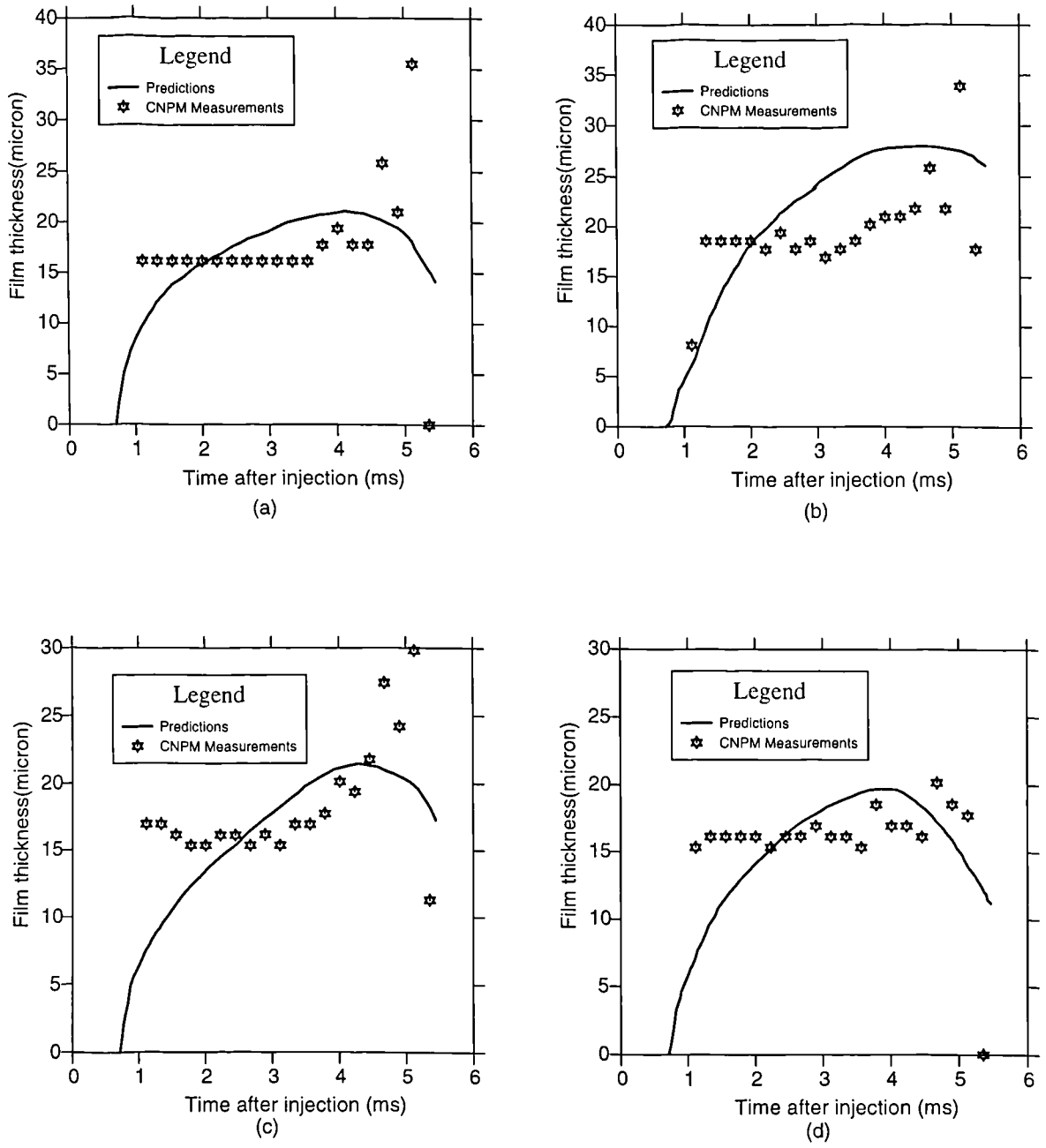


Figure 7.37: Predicted and measured variation with time of film thickness at (a) point a; (b) point b; (c) point c; and (d) point d which are located on the selected wall patch (Case O2).

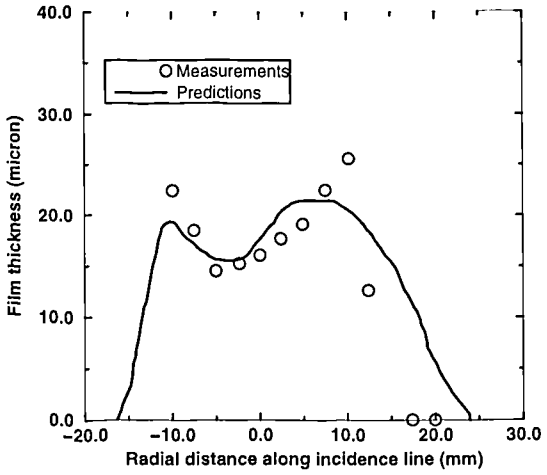


Figure 7.38: Predicted and measured film thickness distribution along the incidence line at 2.23ms after start of injection for Case O2.

after about 5ms ASI, the measured film thickness exhibits a rapid increase (except at point d) and then an abrupt decrease; while the predicted film thickness undergoes a relatively smoother variation. This experimental behaviour is also difficult to understand, as a rapid change in local film thickness could only result either from a rapid mass deposition or from a rapid local film motion (note that evaporation is negligible in this case). The former condition is obviously not applicable, because by this stage the spray injection has ceased for 1.5ms. For the same reason impingement pressure and gas drag effects must be smaller than at earlier stages.

Figure 7.38 presents the distribution of film thickness along the incidence line at 2.23 ms after start of injection. The calculated data cover the whole film extent, whereas the measured data are only for a limited part. We can see that the predictions reproduce reasonably well the general trends of the experimental data, especially in the impingment zone. However, substantial discrepancies exist at around 10mm from the stagnation point in both directions, where the measured film thickness is significantly larger than predicted.

7.7 Wall Interaction Predictions for a Research Engine

Description

The engine examined was employed by Gutmann (1993) at IMH in Munich in his photographic studies of spary wall impingement occuring inside the piston bowl of a Diesel engine under motoring conditions. The engine, as illustrated in Figure 7.39, has a cylindrical bowl and a single-hole injector which is off-centered from the symmetry axis. The pertinent dimensions and operating conditions are given in Table 7.4, and the fuel mass injection history is presented in Figure 7.40. Swirl (clockwise when viewed from the top) was generated within the chamber during injection, giving a solid-body velocity distribution.

The main experimental results obtained are photographs through a window in the cylinder head of the spray patterns at different crank angles after start of injection, and the spray tip penetration.

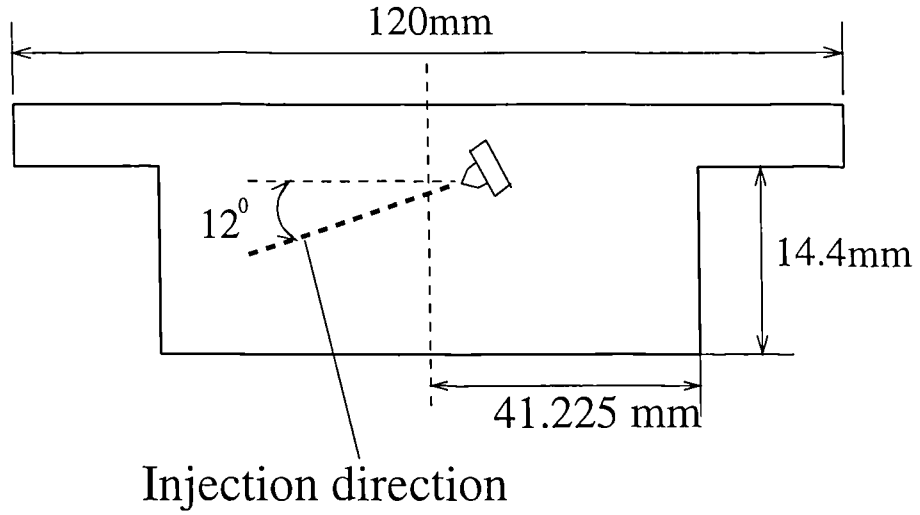


Figure 7.39: Schematic of the engine used by Guttman (1993)

Details of Simulation

The engine simulation was commenced at BDC, with the in-cylinder gas at 25^0C temperature and 1 bar pressure, rotating about the cylinder axis as a solid body (assumed in the absence of any other information) at a speed of 3480 RPM. The computational grid used in our calculations consists of 41 × 27 × 29= 32103 nodes in the radial, circumferential and axial directions, respectively. The grid arrangement

Table 7.4: Engine Specifications

Engine Speed(rmp)	1200
Bore Diameter(mm)	120
Engine Stroke(mm)	120
BDC Swirl Ratio	2.9
Bowl Diameter(mm)	82.45
Bowl Depth(mm)	14.4
Compression Ratio	16
Nozzle Diameter(mm)	0.28
Nozzle Length(mm)	1.4
Fuel	20% water/diesel emulsion (modelled as n-dodecane)
Fuel Delivered	$32(mm^3/\text{pulse})$
Injection Timing	14^0 BTDC - 2^0ATDC

is illustrated in elevation and plan views in Figures 7.41(a) and (b) respectively.

The sprays was directed towards the bowl side wall at an inclination of 12^0 to the cylinder head (see Figure 7.39), and the injected droplet sizes and velocities were calculated using the atomisation model of Huh and Gosman (1991) (see Section 2.8.1).

The calculations for the 166^0 CA period from BTDC to the start of injection at 14^0 before top dead center were performed using a computational time step of 1^0 CA which, according to previous experience (see, for example, Ahmadi-Befrui (1985)), is believed to provide adequate temporal resolution; and thereafter up to 15^0 after TDC a time step of $1/20^0$ CA was used to allow for accurate modelling of gas/spray interactions. During injection, 10 droplet parcels were introduced per time step.

Presentation of the Results

The measured and calculated spray tip penetration are shown in Figure 7.42. The calculated tip position is here taken to be the axial extent (measured along the

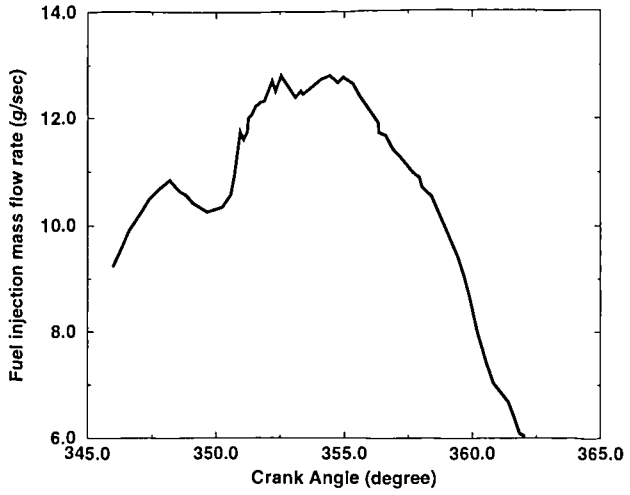


Figure 7.40: Fuel injection history for engine case

nozzle axis) of the region containing 99% of the liquid, and is compared with the perceived tip position in the experiments, as deduced from the photographs. The predicted spray penetrates faster than the experimental one at the early injection stage and falls below later, just before the tip hits the wall. These discrepancies can be due to uncertainties in aspects of the spray models such as atomisation, drop breakup and drop-drop collision. There may also be experimental uncertainties in recording the injection pressure schedules, which in turn are empirically converted into a fuel flow rate schedule in the calculations. In addition, the fuel used in the experiments is a water/diesel mixture, which has different surface tension and viscousity than those of n-dodecane used in the calculations, and hence different behaviour in breakup, coalescing and vapourising.

The predicted overall spray characteristics are illustrated in Figures 7.43 to 7.44. Figure 7.43 depicts details of droplet sizes and spray evolution, visualised in an integrated side view, at three times during injection period. There is a core region of relative large droplets near the nozzle, resulting from the initial breakup into 'blobs' which have a size equal to the nozzle exit diameter. In contrast to this, droplets are seen to be smaller near the spray tip or close to the wall, due to evaporation, droplet breakup, and wall impingement. Shown in Figure 7.44 are the corresponding top views, which may be compared with the experimental photographs. Here it can be noted that after wall impingement, the predicted wall spray shows the same trend as

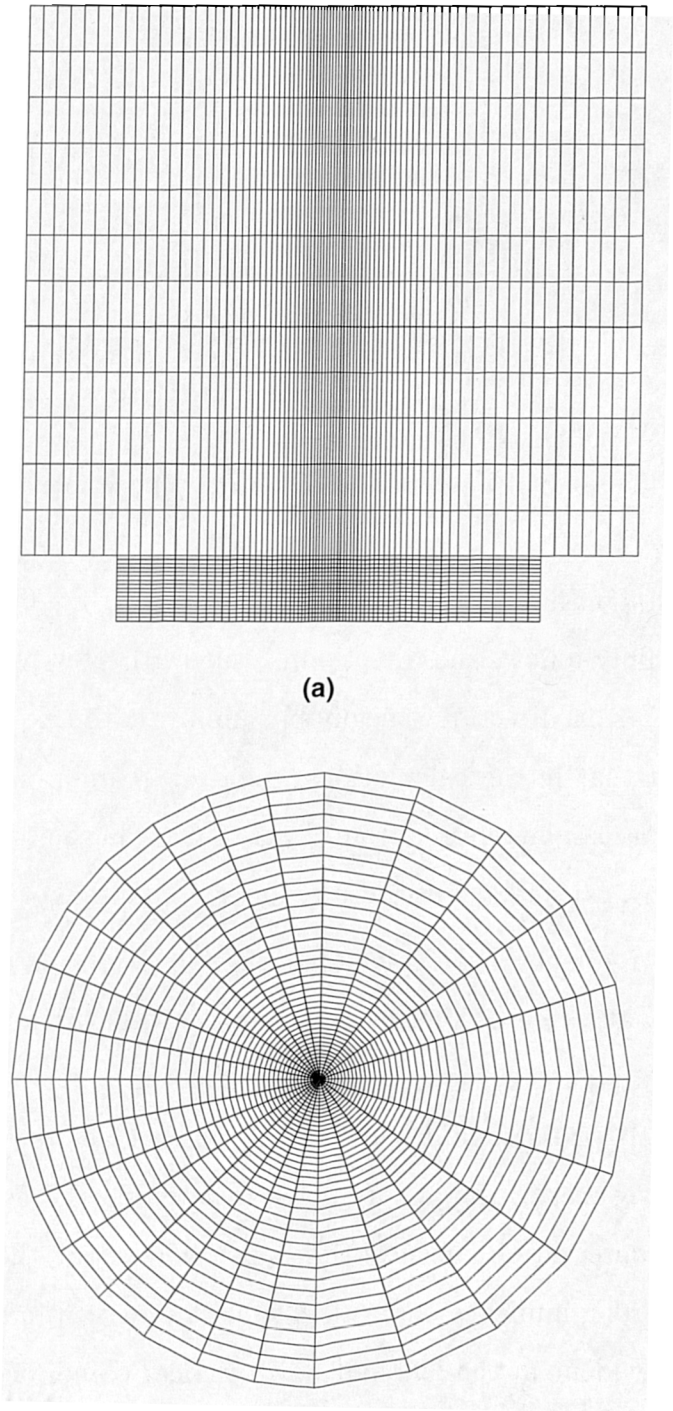


Figure 7.41: Computational mesh used for Case O1: (a) elevation view (b) plan view

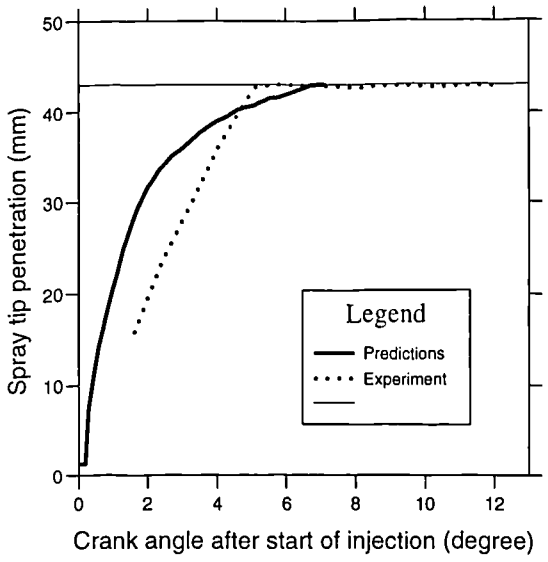
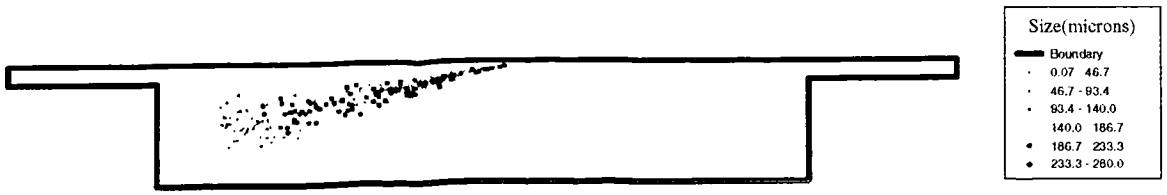


Figure 7.42: Predicted and measured spray tip penetration versus CA for engine case

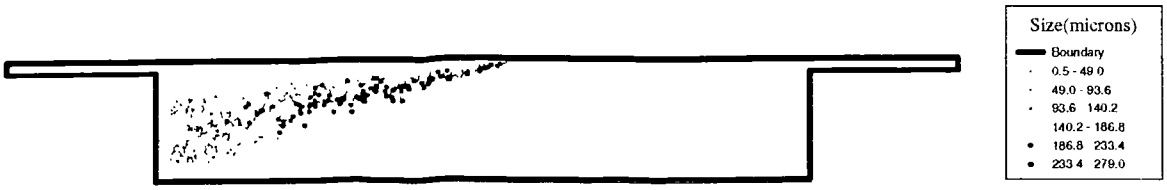
experiments, both indicating a strong effect of swirling flow on the wall spray whose motion mainly follows the direction of the swirl. However, the predicted spread in the counter-swirl direction is negligible, unlike that in experiments. This may be due to the fact that in the calculations, the droplet impingement velocities are under-predicted, as can be inferred from Figure 7.42. Thus fewer splash events occur in the calculations, causing a substantially lower population of backward-moving droplets.

Figure 7.45 shows the calculated gas velocity fields in a vertical plane through spray axis at three different crank angles; while Figure 7.46 presents those in a diametrical plane through the spray stagnation point which is around 4mm above the piston bowl bottom. Figure 7.46 displays a clear swirl flow, the effect of which becomes stronger as the piston moves towards the TDC, reflecting the angular momentum conservation effect as the squish flow enters the bowl. The injected spray exerts a strong influence on gas fields, as can be seen in Figure 7.45, where a strong vortex is evident in the left half bowl vertical plane, because of the injected spray and wall impingement. Note also that in Figure 7.45, a clear squish flow is observed, moving toward the bowl center before TDC.

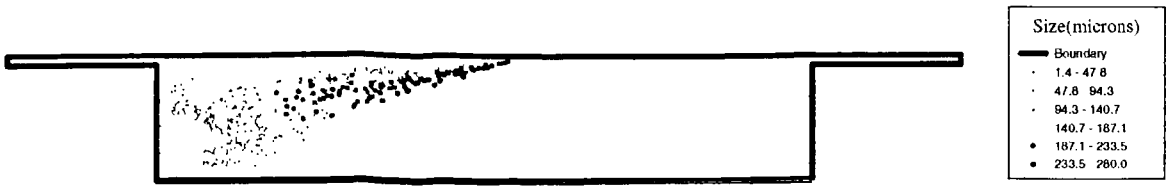
The spray-related disturbance in gas fields can also be seen in the plots of relative turbulence intensity (defined as $u'/\bar{V}_p$, where $u' = \sqrt{k}$ and the mean piston speed is $\bar{V}_p = 4.8m/s$) displayed in Figure 7.47. It is evident that the turbulence levels induced by the injected spray are greater than those induced by squish. This is



(a) CA = 4 degree ASI



(b) CA = 8 degree ASI



(c) CA = 12 degree ASI

Figure 7.43: Side view of predicted spray patterns

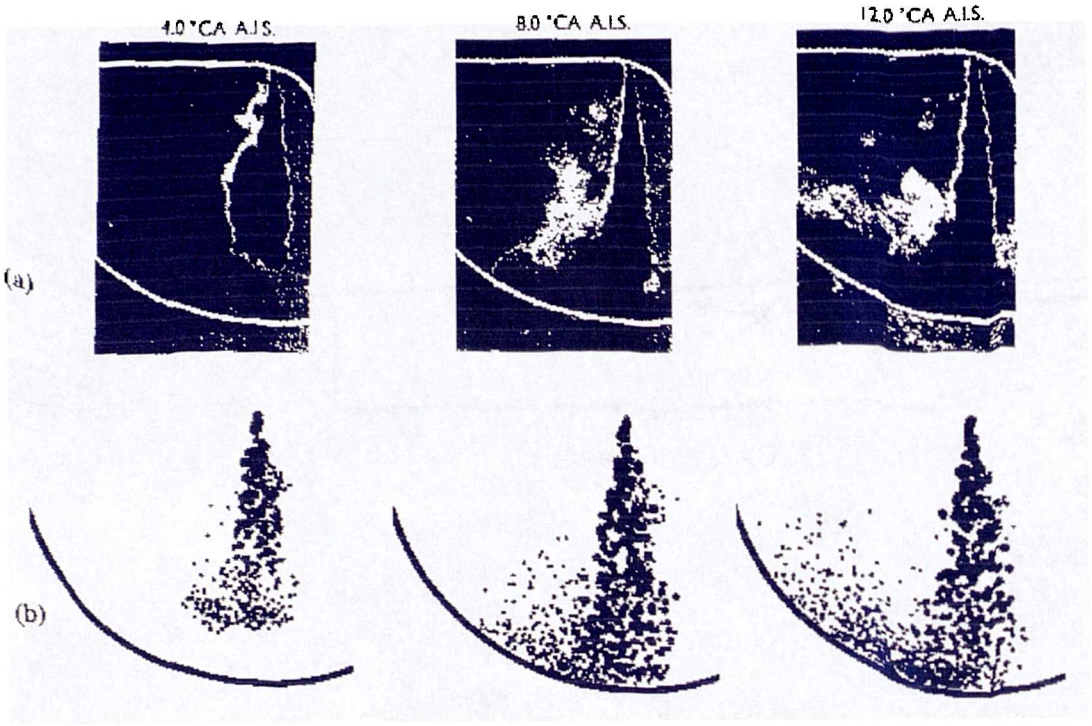


Figure 7.44: Spray pattern (top view) development for engine case: (a) IMH high speed Schileren-photographs; and (b) predictions.

because the spray generates local mean velocity gradients via entrainment and displacement processes, thus intensifying the turbulence generation rate which varies as the square of the mean gradients. A closer inspection of these plots reveals another feature : the region of spray-induced turbulence expands as the spray penetrates, with peak levels occurring near the nozzle.

Figure 7.48 depicts the contours of fuel vapor mass fraction in an axial plane at three crank angles. There is clear evidence of the vapour spreading as the spray penetrates outward. In particular, there is fuel vapour impingement on the side wall of piston bowl at later stages, which is a consequence of the spray-wall interaction.

We now direct our attention to the predicted wall film characteristics including mean wall film thickness, film volume and the shape of film patch, which are of interest, but for which in this case no measurements are available.

Figure 7.49 shows the variation with time of the predicted film volume on bowl side wall for calculations with and without the impingement model. It can be seen that for both cases, the deposited fuel mass increases monotonically with time. In

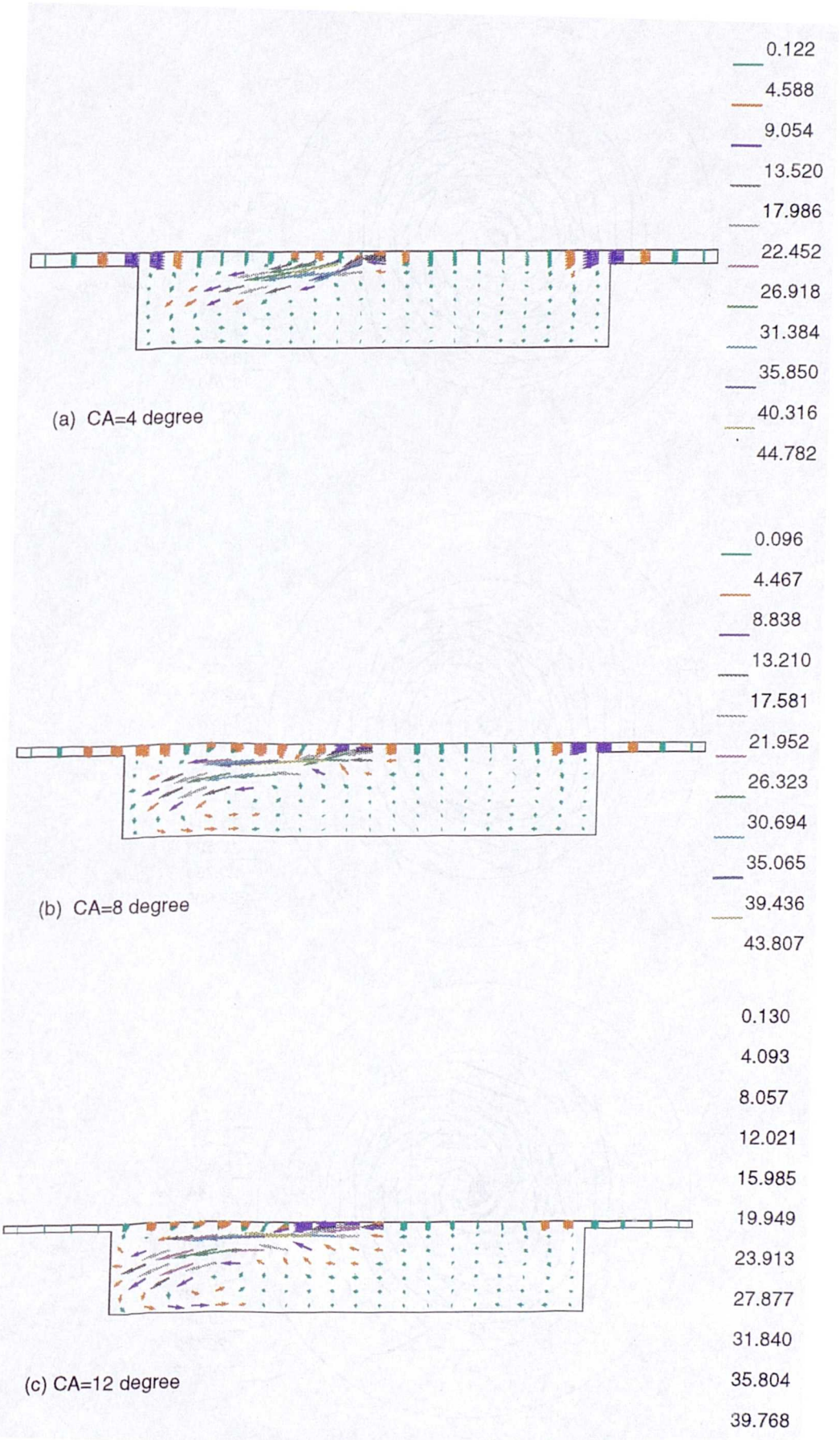


Figure 7.45: Calculated gas velocity fields in a vertical plane through spray axis for the engine case

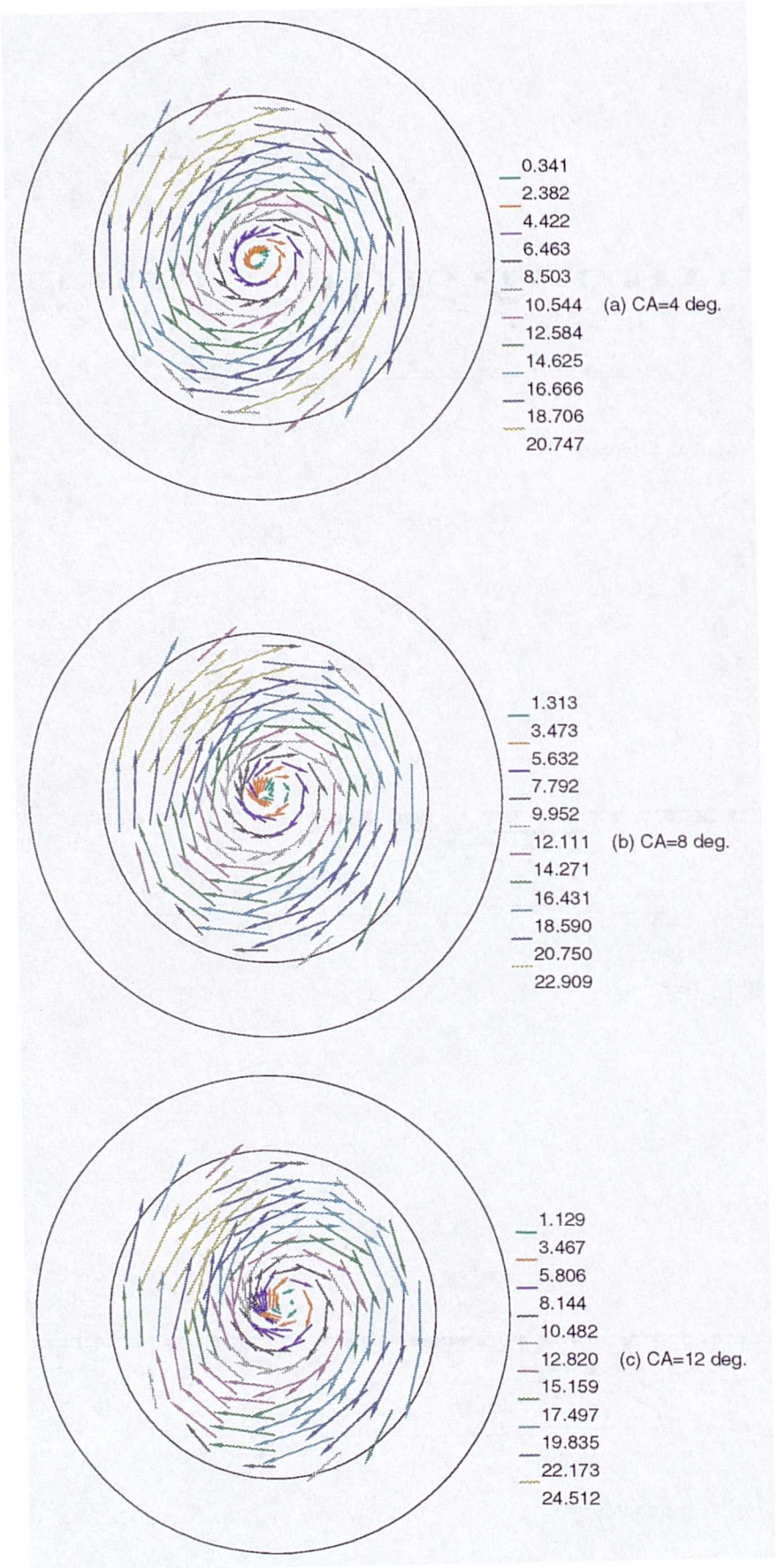
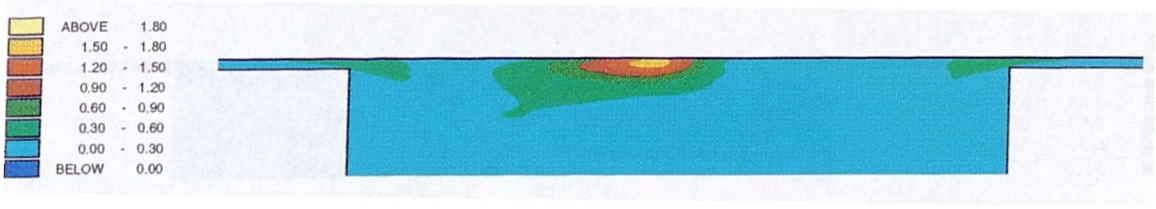
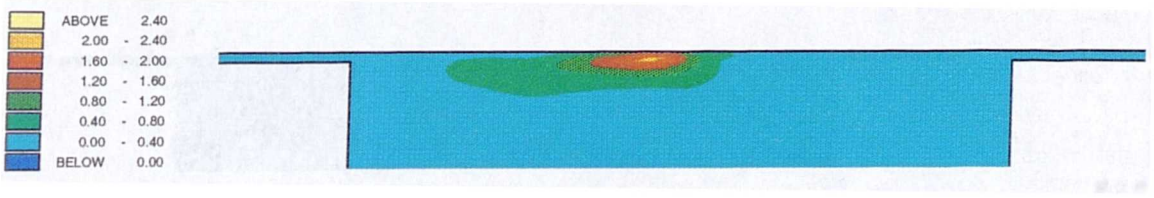


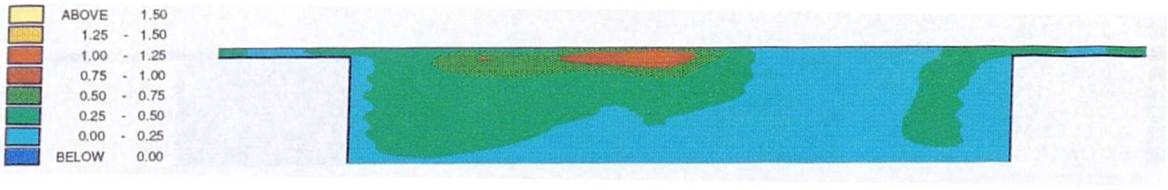
Figure 7.46: Calculated gas velocity fields in a diametrical plane through the spray stagnation point (4mm above the bowl bottom) for engine case



(a) CA = 4 degree ASI

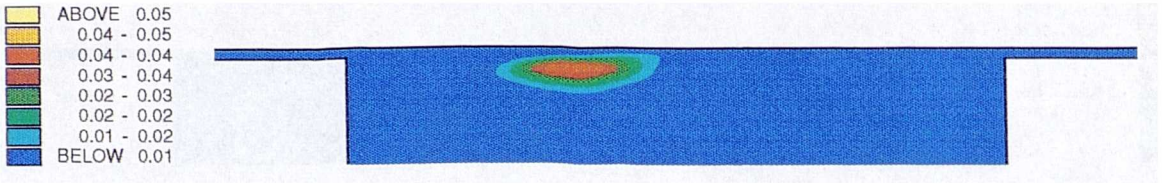


(b) CA = 8 degree ASI

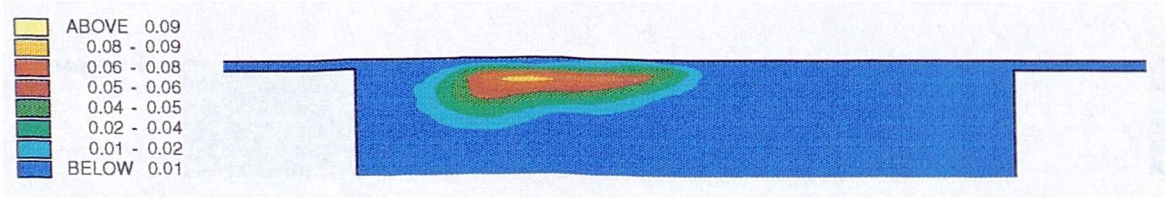


(c) CA = 12 degree ASI

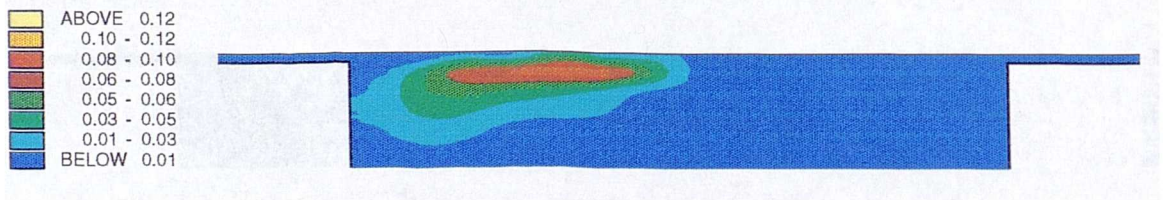
Figure 7.47: Predicted relative turbulent intensity contours in an axial plane through spray axis for engine case



(a) CA = 4 degree ASI



(b) CA = 8 degree ASI



(c) CA = 12 degree ASI

Figure 7.48: Predicted vapour concentration contours in an axial plane through spray axis for engine case

the case where the impingement model is switched off, and all the droplets that hit the wall are assumed to adhere, the deposited mass is clearly over-predicted as a consequence of ignoring all the splashing and rebounding droplets. Under the conditions investigated, the maximum deposited mass is around 60% of the total injected mass for the case without the impingement model and 45% for the case with the model.

Based on the predicted volume of liquid deposited on the wall, the mean film thickness as a function of time can readily be estimated by dividing the film volume by the area of film patch. The results obtained using both static and full film models are displayed in Figures 7.50(a) and (b), respectively. In the former case where the film is assumed static, the area of film patch is evaluated from the locations of the impinging droplets which deposit mass; whereas in the latter case the film area is calculated. Both figures reveal a common trend that the mean film thickness for the subcase without the impingement model grows larger than with the impingement model at later stages after the start of injection. This is because in the former case droplet mass deposition is over-predicted, as all the droplets which reach the wall are assumed to form the film. Another feature which can be noted is that the mean film values in Figure 7.50(a) are typically twice as large as those in Figure 7.50(b) at later stages. This is because that in the former figure the area covered by the wall film does not increase while it does in the latter figure where film is allowed to spread on the wall. Also, it can be seen that the peak value of mean film thickness predicted without the impact model is around 30% larger than with the impact model.

Evidence of wall film spreading in all directions as time goes on can be seen in Figure 7.51, which depicts the evolution of wall area covered by the film at two times, plotted as projections into a flat plane. In particular, the spreading is most significant in the swirling direction (positive circumferential direction in the plot) due to gas drag forces. This feature is evidenced in the figure by the fact that wall film occupies much larger area and spreads much faster on the right side of the incidence line (i.e.,vertical dashed line in the plot).

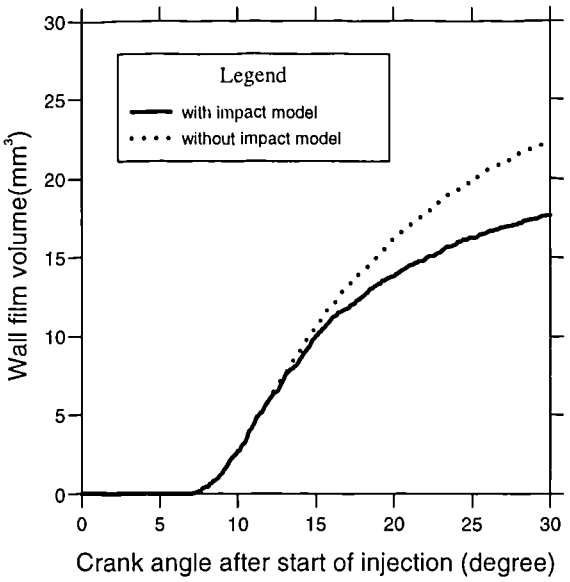


Figure 7.49: Predicted variation with time of deposited fuel volume on the bowl wall for engine case.

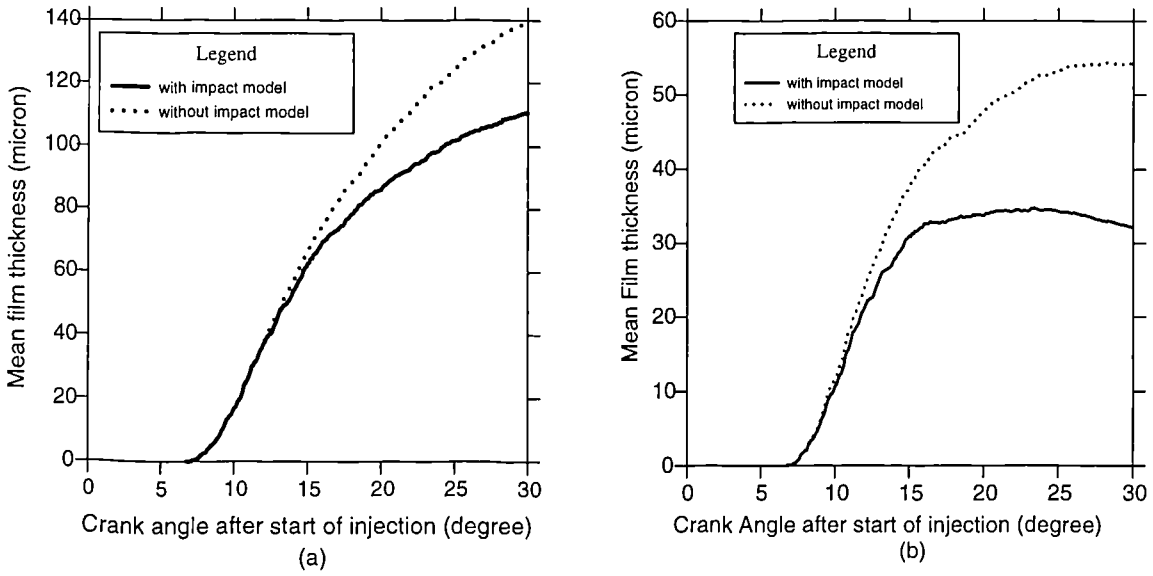


Figure 7.50: Predicted variations with time of mean film thickness for engine case with (a) static film model; and (b)full film model

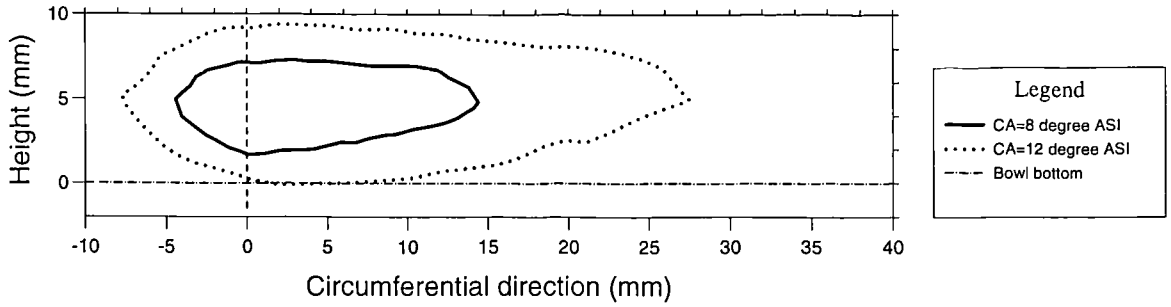


Figure 7.51: Predicted shapes of wall film patch on circumference of cylindrical bowl for engine case.

7.8 Closure

In this chapter, validation studies have been performed for the impingement and wall film models developed in this study. The main findings and conclusions are highlighted as follows.

First, preliminary tests were carried out to determine suitable grid densities, time step sizes and the introduction rates of the droplet parcels that ensure both adequate numerical resolution and efficiency.

Second, four sources of experimental data concerning normal spray impingement were employed to test the models. Here detailed comparisons were made with measurements of the following two kinds:

- *Quantities representing wall spray characteristics.* These range from the global parameters, such as: wall spray pattern, wall spray radius and height, radii of spray cross section at different heights above the wall; to the local parameters, including mean droplet velocities as a function of time at different locations in the near-wall region, and droplet velocity profiles. The conditions investigated involve ambient and elevated pressures and temperatures. In all cases, the predictions compared reasonably well with the measured data on the above-mentioned global quantities, and in some cases very good agreement was achieved for spray radius and height; moderate agreement was obtained for local droplet mean tangential and normal velocities and it was noted that

the inclusion of Saffman forces for the droplets within the wall spray results noticeable improvement in the agreement between predicted and measured normal mean droplet velocities in the region immediately close to the wall.

However, there is an opposed qualitative behaviour between the measured and predicted local mean droplet sizes in the near-wall region for CNPM normal spray impingement case (Case N2). Sensitivity studies were conducted in an attempt to understand the reasons for such discrepancies. It was found that, changing impingment modelling in different ways does not remove these opposed trends; and, accordingly, some other mechanisms, which have not been accounted in the available spray models, were suggested as potentially responsible for these discrepancies.

- *Quantities representing wall film characteristics.* These include: percentage of the fuel deposited on the wall, wall film radius, and mean film thickness. Both calculations and measurements show satisfactory agreement for these quantities. In addition, other features of wall films that were not measured were also calculated and the predicted behaviour shows the expected trends. In particular, a common feature that has been confirmed in all cases is that there is local mass accumulation around the film edge at the later stages of film spreading .

Further assessments of the models were then performed against the CMPM oblique spray impingement experiments which involved two different cases. The results obtained reveal the following features:

- The wall spray produced by oblique spray impingement divides into two parts which moves in both the upstream and downstream respectively, at different speeds.The downstream wall spray radius and height (thus also the dispersed wall spray volume) are invariably larger than those upstream. This feature has also been confirmed by the experimental photographs of Ereat et al (1992), for a similar situation.

- Similar conclusions to the CNPM normal impingement case can be drawn concerning the comparison between the measured and predicted variations

with height above the wall for Case O1 of local mean droplet tangential and normal velocities, and mean droplet sizes. The necessity of including Saffman forces in order to obtain good agreement is again highlighted.

- The predicted wall film patch exhibits an elliptic shape. Its temporal evolution shows that wall film also penetrates faster in the downstream, which is consistent with the above-mentioned feature for the wall spray.

- The predicted film thickness profiles also exhibit local mass accumulation near the film edges in both up- and down- stream directions. The maximum film thickness is observed to occur downstream.

- In Case O2, good agreement exists between predicted and measured wall film volume, as a function of time. The predicted wall film thickness distribution along the incidence line also shows reasonable agreement in the impingement zone and the regions immediately outside of it. The predicted film thickness temporal behaviour at some specific locations shows the expected trends, although there are substantial differences. Possible reasons for the discrepancies were discussed. These include potential experimental errors.

Lastly, impingment calculations were made for a motored research engine with a cylindrical bowl in which a spray was injected into a swirling flow and impinges with the side wall of the piston bowl. Comparisons with experimental data on spray tip penetration and wall spray patterns (viewed from the top) show moderate agreement; and the predicted wall film characteristics show interesting and expected behaviour. In addition, some insight into the two-way interactions between the spray and the in-cylinder flow under motoring conditions were provided. Some important features unveiled by the calculations are:

- The spray exerts on the gas motion a strong effect in that the injection process entrains substantial air into the spray plume and accelerates it in the direction of injection with the consequence of intense turbulence generation. The spray-generated turbulence levels are comparable to and, sometimes even greater than, thoses produced by squish.

- The 'heavier' droplets (with larger sizes) are able to hit the bowl wall , while the 'lighter' ones (with smaller sizes) are carried tangentially by the swirling gas.

- The swirling flow has a strong effect on the wall spray development and wall film spreading, as indicated by the fact that both the wall spray and film penetrate much faster in the direction of swirl.

- The inclusion of the present impingment and film models produces results on film characteristics which are quite different from those obtained without these models. In particular, the maximum mass deposition is overpredicted by 15% and the peak mean film thickness by around 30% when the present impact model is switched off. On the other hand, the mean film thickness predicted by the simple static film model is nearly twice as high as that evaluated by the present model. This suggests the necessity of using suitable impingement and wall film models in calculating spray impingement events occurring in Diesel engine combustion chambers.

Chapter 8

Closure

In this chapter, a summary is presented of major achievements and findings of the present study and some proposals are made for future work.

8.1 Main Achievements

In the preceding chapter, the present impingement and film modelling has been assessed and applied, and main findings have been outlined in the last section. It is thus only necessary here to summarise the main achievements of the present work; these are as follows

1. *The development of a computer model for spray impingment simulation.* This model, which possesses several novel features as compared with the impingement models developed earlier by other researchers, can now be applied to the prediction of spray impingment events occurring inside the combustion chambers of any kind of engines. In particular, as is currently being done by a major engine manufacture, it can be employed, in a cost-effective way, to perform parametric studies in order to improve substantially the design of very small DI Diesel engines, which inevitably involve spray impingement. Such studies would allow the determination of the optimal operating conditions and bowl geometries that enable full use of the advantages offered by spray impingement while minimising the negative effects associated with it (see the discussion in Chapter 1).

The model can also be applied to spray impingment simulation in other circumstances, although slight modifications may be needed for the parameters (e.g. A_s in Equation (4.2)) used in some of the critical Weber numbers when different wall surface roughness and temperature are involved. An example is provided by the work of Currle (1996) who applied the present model to the prediction of water spray impingment inside the ventilation system of a passenger car. The calculated impingement characteristics were found to be in satisfactory agreement with the measurements.

2. *The provision of a complete mathematical model for wall films formed by impinging sprays.* This model, which is particularly attractive in its numerical efficiency (i.e. avoiding three dimensional calculations and any special procedure for film interface tracking) and novel treatment of capillary force, has been demonstrated to be suitable for the simulation of engine wall film dynamics in a wide range of applications. Its capabilities of predicting accurately 'conventional' problems (as special cases) such as film condensation/evaporation, and 'slow' droplet spreading on the surface driven only by the capillary force, have also been proved in the test calculations performed in Chapter 5. In view of the advanced nature of solution scheme, the film model is also expected to be applicable to the simulation of the post-impingment spreading of a single droplet (whose size should be below 1 mm in order to justify thin film assumptions) upon its impact onto a wall, as has been done by Fukai et al (1993) who performed three-dimensional calculations which are rather complicated(see the discussion in Chapter 2).

3. *The extensive literature survey performed in this study on droplet and spray impingements, film flow, and other related spray phenomena, has improved the current understanding of these processes.* The available data on droplet impingment processes are rather scattered and each single source of data does not allow for the useful conclusions to be drawn. The present review has, for the first time ,analysed the findings in great detail and integrated them in a way that allows (i) identification of full range of important parameters influencing the impingement processes; (ii)construction of an overall map on

various impingement regimes and the associated transition criteria; and (iii) establishment of a preliminary knowledge on post-impingement characteristics for each regime.

In addition, in the light of the recent literature findings on other spray processes such as atomisation, droplet breakup and collisions, droplet drag correlations (see the discussions in relevant places of Chapter 3), a useful evaluation has been made of the existing spray models on the above. In particular, a mistake and inconsistency associated with the conventional droplet breakup model of Reitz and Diwakar (1986) has been analysed and it is suggested that this model can be improved by introducing a certain statistical procedure.

8.2 Suggestions for Future Work

The following are suggested as profitable areas for future work:

Impingement modelling

The present impingment model is based largely on the data and correlations for isolated water drops impinging on walls at atmospheric conditions. As a consequence, the effects of the following kinds are ignored: (i) neighbouring impinging droplets; (ii) elevated gas pressure and temperature; and (iii) range of fluid properties. There is therefore a need to properly account these effects in the future when experimental data become available.

At high gas pressure and temperature conditions, an additional effect, namely, the vapour layer surrounding each impinging droplet, has to be introduced in the modelling because this may tend to modify the impingement outcome and thus also film behaviour, as pointed out in Chapter 2. This task, of course, relies experimental investigations which should be conducted in the future.

The need also exists to quantify the effect of the gas boundary layer characteristics in the near-wall region, which are important according to the review in Chapter 2.

Another future challenge relates to the need of further improving the present regime transition criteria. This includes the quantification of the effects of more

parameters, such as impact angle and gas boundary characteristics, and the use of appropriate statistical procedures since there are no sharp boundaries between different regimes.

Modelling of post-impingment characteristics can be refined if correlations on size and velocity distributions of secondary droplets can be made available either through experiments or theoretical analysis. This also poses substantial future challenges.

Film modelling

In the first instance, the present film modelling should be extented to cover turbulent films which may be important in port-injection applications where the gas shear may be very strong and the film thickness is relatively larger due to continuous mass accumulation of many cycles.

Secondly, strong gas shear may also result in surface wave break up and therefore droplet entrainment. As this phenomenon affects the total film mass flux in and out from the film interface and thus also the momentum exchange between the film and the other two phases - droplets and gas, it is important to have a model to address these effects. The basic issue here is to derive mathematical equations that tell us: (i) at what conditions will the entrainment occur; (ii) how to evaluate the droplet mass flux due to entrainment; and (iii) how to predict film momentum change caused by entrainment.

Thirdly, we also need to address the problem of film separation at sharp corners, which occurs in port-injection applications when wall film enters into the combustion chamber. The main challenge here is to model subsequent motion, expansion, and/or possible breakup of the liquid which has separated from the wall and has interfaces at both upper and lower sides.

Another important need is to develop a film evaporation model which allows for multicomponent fuels and accounts for the effect of high ambient pressure. There is a major challenge here when the film evaporates at supercritical pressure. The critical point for a mixture depends strongly upon the composition and critical pressure values can be greater for a mixture than for any of its components (cf. Shuen et al 1992). Therefore, certain portions of the field can be supercritical while other portions are subcritical even when the pressure is uniform. Accurate modelling

of these depends on the approximations employed for the equation of the state and for the thermodynamic properties.

On the numerical side, the use of the upwind difference scheme for the discretisation and the choice of general orthogonal coordinate system for the representation of film equations, although satisfactory for the purposes of this thesis, could certainly be improved by using composite and bounded high order difference schemes and unstructured meshes. Research on this aspect will certainly increase the utility of the present methodology.

Spray modelling

It is obvious that, in simulating spray impingement events, the impingement outcome is largely determined by the conditions of arriving droplets (e.g. sizes, velocities, and temperatures), which in turn are determined by the spray models of atomisation, evaporation, droplet breakup, and droplet binary collisions. Thus, it is also necessary to refine these models in order to improve the accuracy of impingement modelling, as outlined below.

- There is a major need to develop a predictive capability for the primary atomisation process which, besides accounting for nozzle internal flow turbulence and aerodynamic disturbances, should provide provision for the phenomenon of cavitation. This will allow more accurate predictions of the spray cone angle, initial droplet sizes and velocities.

- Further effort is needed to reduce the empiricism in calculating droplet breakup time and the constants used for the breakup criteria, as they directly influence the predictions. Since these parameters are found to be scattered in a wide range (see discussion in Chapter 3), there may be additional variables that affect them; thus there is also a need to identify and introduce these variables into the relevant equations.

- Additional provision should be made in the droplet collision model to allow (i) collision-induced breakup ; and (ii) mass exchange between two colliding droplets after separation following their collision. Also, the regime transition

criteria should be refined in the light of experimental data of fuel droplets (eg. those of Jiang et al 1992).

- The correlations for the droplet drag coefficient should be modified to account for the effects of (i) droplet deformation; (ii) neighbouring droplets; and (iii) the presence of a wall (which is especially important for droplets within the wall spray) in the light of the experimental data discussed in Chapter 3. In particular, (i) and (ii) are two opposing effects, with the former increasing the drag and the latter reducing it, they should therefore be considered simultaneously.

Appendix A

Relations between Density-Weighted and Unweighted average quantities

In this appendix, the set of expressions (3.16) which relate the Reynolds and Favre average quantities is derived in details.

According to the Reynolds averaging, the instantaneous value of a variable, ϕ, and in particular the bulk gas density, ρ_b, can be decomposed, as follows:

$$\phi = \bar{\phi} + \phi' \tag{A.1}$$

$$\rho_b = = \bar{\rho}_b + \rho_b' \tag{A.2}$$

Multiplication of (A.1) by (A.2) and application of the Reynolds averaging definition to the product yield:

$$\overline{\rho_b \phi} = \bar{\rho}_b \tilde{\phi} + \overline{\rho_b' \phi'} \tag{A.3}$$

On the other hand, ϕ can be decomposed according to the Favre averaging as:

$$\phi = \tilde{\phi} + \phi'' \tag{A.4}$$

in which

$$\tilde{\phi} = \frac{\overline{\rho_b \phi}}{\bar{\rho}_b} \tag{A.5}$$

With the above definitions, the derivation of relationships (3.16) are detailed below:

1. The division of (A.3) by $\bar{\rho}_b$ and use of (A.5) yield:

$$\tilde{\phi} = \bar{\phi} + \frac{\rho_b' \phi'}{\bar{\rho}_b} \tag{A.6}$$

From (A.6) it is apparent that when $\rho' = 0$, we have

$$\tilde{\phi} = \bar{\phi} \tag{A.7}$$

Substitution of ϕ from (A.4) into (A.6) gives:

$$\phi = \bar{\phi} + \frac{\overline{\rho_b' \phi}}{\bar{\rho}_b} + \phi'') \tag{A.8}$$

Application of Reynolds averaging to (A.8) results in:

$$\bar{\phi}'' = -\frac{\overline{\rho_b' \phi'}}{\bar{\rho}_b} \tag{A.9}$$

2. Multiplication of (A.8) by ρ_b and application of Reynolds averaging to the product provide:

$$\overline{\rho_b \phi} = \bar{\rho}_b \bar{\phi} + \overline{\rho_b' \phi'} + \overline{\rho_b \phi''} \tag{A.10}$$

Upon use of (refavg-app-3), the above relationship becomes:

$$\overline{\rho_b \phi''} = 0 \tag{A.11}$$

3. Multiplication of (A.2) by (A.4) and averaging the product by use of Reynolds averaging procedure yield:

$$\overline{\rho_b \phi} = \bar{\rho}_b \tilde{\phi} + \bar{\rho}_b \bar{\phi}'' + \overline{\rho_b' \phi''} \tag{A.12}$$

Substitution of (A.5) into the above produces:

$$\bar{\rho} \bar{\phi}'' = -\overline{\rho_b' \phi''} \tag{A.13}$$

4. Finally,the relationship (A.9) can be written as:

$$\bar{\rho}_b \bar{\phi}'' = -\overline{\rho_b' \phi'} \tag{A.14}$$

Use of (A.13) in the above gives:

$$\overline{\rho_b' \phi''} = \overline{\rho_b' \phi'} \tag{A.15}$$

Appendix B

Order of Magnitude Analysis of Film Momentum Equations

The purpose of this appendix is to provide justification, through an order of magnitude analysis, for the use of boundary-layer type equations in wall film flow, given the condition that the film thickness is very 'thin'. For clarity, we only focus on the following full momentum equations:

$$\frac{\partial u}{\partial t}+u\frac{\partial u}{\partial x}+v\frac{\partial u}{\partial y}+w\frac{\partial u}{\partial z} = -\frac{\partial p}{\partial x}+\nu_L\left(\frac{\partial^2 u}{\partial x^2}+\frac{\partial^2 u}{\partial y^2}+\frac{\partial^2 u}{\partial z^2}\right) \quad \text{(B.1)}$$

$$\frac{\partial v}{\partial t}+v\frac{\partial v}{\partial x}+v\frac{\partial v}{\partial y}+w\frac{\partial v}{\partial z} = -\frac{\partial p}{\partial y}+\rho a_y+\nu_L\left(\frac{\partial^2 v}{\partial x^2}+\frac{\partial^2 v}{\partial y^2}+\frac{\partial^2 v}{\partial z^2}\right) \quad \text{(B.2)}$$

$$\frac{\partial w}{\partial t}+v\frac{\partial w}{\partial x}+v\frac{\partial w}{\partial y}+w\frac{\partial w}{\partial z} = -\frac{\partial p}{\partial y}+\rho a_y+\nu_L\left(\frac{\partial^2 w}{\partial x^2}+\frac{\partial^2 w}{\partial y^2}+\frac{\partial^2 w}{\partial z^2}\right) \quad \text{(B.3)}$$

If δ_0 and l_0 represent typical film thickness and longitudinal dimension respectively, then the scaling parameter, $e = \delta_0/l_0$, is small under the assumption of very thin film thickness, i.e.

$$e = \delta_0/l_0 \ll 1 \quad \text{(B.4)}$$

It is well known that the time scale during which a fluid particle spends near the body is represented by the ratio l_0/U_0, where U_0 stands a typical reference velocity in the longitudinal direction; whereas the time required for viscous effects to spread across the film thickness is of the order δ_0^2/ν_L (ν_L being the film kinematic viscosity). It follows that the viscous effects can spread across the film if the diffusion time is shorter than the residence time:

$$\frac{\delta_0}{\nu_L} < \frac{l_0}{U_0} \quad \text{(B.5)}$$

Hence

$$eRe_L < 1 \tag{B.6}$$

where Re_L is the Reynolds number based on the characteristic film thickness and film longitudinal velocity:

$$Re_L = \frac{\delta_0 U_0}{\nu_L}$$

To enable the comparison of the magnitudes of the various terms in Equations (B.1) through (B.3), the following dimensionless variables (all of which are ensured to be of the order of unity) are introduced:

$$\begin{aligned} (\bar{x}, \bar{y}, \bar{z}, \bar{t}) &= (\frac{x}{l_0}, \frac{y}{l_0}, \frac{z}{\delta_0}, \frac{tU_0}{l_0}) \\ (\bar{u}, \bar{v}, \bar{w}, \bar{p}) &= (\frac{u}{U_0}, \frac{v}{U_0}, \frac{w}{U_0 e}, \frac{p}{\rho_L U_0^2}) \end{aligned} \tag{B.7}$$

Substitution of (B.7) into (B.1) through (B.3) yields:

$$\frac{\partial \bar{u}}{\partial \bar{t}} + \bar{u}\frac{\partial \bar{u}}{\partial \bar{x}} + \bar{v}\frac{\partial \bar{u}}{\partial \bar{y}} + \bar{w}\frac{\partial \bar{u}}{\partial \bar{z}} = -\frac{\partial \bar{p}}{\partial \bar{x}} + \frac{1}{eRe_L}\left(\frac{\partial^2 \bar{u}}{\partial \bar{x}^2}e^2 + \frac{\partial^2 \bar{u}}{\partial \bar{y}^2}e^2 + \frac{\partial^2 \bar{u}}{\partial \bar{z}^2}\right) \tag{B.8}$$

$$\frac{\partial \bar{v}}{\partial \bar{t}} + \bar{u}\frac{\partial \bar{v}}{\partial \bar{x}} + \bar{v}\frac{\partial \bar{v}}{\partial \bar{y}} + \bar{w}\frac{\partial \bar{v}}{\partial \bar{z}} = -\frac{\partial \bar{p}}{\partial \bar{y}} + \frac{1}{eRe_L}\left(\frac{\partial^2 \bar{v}}{\partial \bar{x}^2}e^2 + \frac{\partial^2 \bar{v}}{\partial \bar{y}^2}e^2 + \frac{\partial^2 \bar{v}}{\partial \bar{z}^2}\right) \tag{B.9}$$

$$e^2\left(\frac{\partial \bar{w}}{\partial \bar{t}} + \bar{u}\frac{\partial \bar{w}}{\partial \bar{x}} + \bar{v}\frac{\partial \bar{w}}{\partial \bar{y}} + \bar{w}\frac{\partial \bar{w}}{\partial \bar{z}}\right) = -\frac{\partial \bar{p}}{\partial \bar{z}} + \frac{e}{Re_L}\left(\frac{\partial^2 \bar{w}}{\partial \bar{x}^2}e^2 + \frac{\partial^2 \bar{w}}{\partial \bar{y}^2}e^2 + \frac{\partial^2 \bar{w}}{\partial \bar{z}^2}\right) \tag{B.10}$$

Retaining the terms of orders 1 and e in (B.8) to (B.10), we come to the following boundary-layer type equations:

$$\frac{\partial \bar{u}}{\partial \bar{t}} + \bar{u}\frac{\partial \bar{u}}{\partial \bar{x}} + \bar{v}\frac{\partial \bar{u}}{\partial \bar{y}} + \bar{w}\frac{\partial \bar{u}}{\partial \bar{z}} = -\frac{\partial \bar{p}}{\partial \bar{x}} + \frac{1}{eRe_L}\frac{\partial^2 \bar{u}}{\partial \bar{z}^2} \tag{B.11}$$

$$\frac{\partial \bar{v}}{\partial \bar{t}} + \bar{u}\frac{\partial \bar{v}}{\partial \bar{x}} + \bar{v}\frac{\partial \bar{v}}{\partial \bar{y}} + \bar{w}\frac{\partial \bar{v}}{\partial \bar{z}} = -\frac{\partial \bar{p}}{\partial \bar{y}} + \frac{1}{eRe_L}\frac{\partial^2 \bar{v}}{\partial \bar{z}^2} \tag{B.12}$$

$$\frac{\partial \bar{p}}{\partial \bar{z}} = 0 \tag{B.13}$$

Bibliography

[1] ADAM, J. R., LINDBLAND, N. R., and HENDRICKS, C. D. 1968 The collision, coalescence and disruption of water drops. *J. Appl. Phys.*, **39**, 5173-5180.

[2] AHMADI-BEFRUI, B 1985 Analysis of flow evolution in the cylinders of motored reciprocating engines. PhD Thesis, University of London.

[3] AITCHINSON, J., and BROWN, J. A. C. 1957 The log-normal distribution. *Cambridge University Press.*

[4] ALLEN, R. F. 1975 The role of surface tension in splashing. *J. Colloid Interface Sci.*, **51**, 350-351.

[5] ALLEN, R. F. 1988 The mechanism of splashing. *J. Colloid Interface Sci.*, **124**, 309-316.

[6] ALLOCA, L.,AMATO, U., BERTOLI, C. and CORCIONE, F. E. 1990 Comparison of models and experiments for diesel fuel sprays. In Int. Symp. on Diagnostics and Modelling of Combustion in I C Engines, pp. 225-261.

[7] AMSDEN, A. A., RAMSHAN, J. D., O'ROURKE, P. J., and DUKOWICZ, J. K. 1985 A computer program for two-and three-dimensional fluid flows with chemical reactions and fuel sprays. *Los Almos Report*, No. LA-10245-MS.

[8] ANNAMALAI, K. and RYAN, W. 1992 Interactive processes in gasification and combustion. Part I: Liquid drop arrays and clouds. *Prog. Energy Combust. Sci.*, **18**,221-295.

[9] ARAKI, K., MORIYAMA, A. 1982 Deformation behavior of a liquid droplet impinging on a hot surface. in *Int. Conf. on Liquid Atomisation and Spray Systems(ICLASS-82)*

[10] ARCOUMANIS, D. and CHANG, J. C. 1993 Heat transfer between a heated plate and impinging transient diesel spray. *Experiments in Fluids,***16**, 105-119.

[11] ARKHIPOV, V. A., RATANOV, G. S. and TROFIMOV, V. F. 1978 Experimental investigation of the interaction of colliding droplets. *J. Appl. Mech. Tech. Phys. U.S.S.R.,* **2**, 201-205.

[12] ARKHIPOV, V. A., VASENIN, I. M., and TROFIMOV, V. F., 1983 Stability of colliding drops of ideal liquid. *Tomsk. Translated from Zh, Prikl. Mekh. Tekh. Fiz.* **3**, 95-98.

[13] ASHGRIZ, N. and GIVI, P. 1987 Binary collision dynamics of fuel droplets. *Int J. Heat and Fluid Flow,* **8**, 205-210

[14] ASHGRIZ, N. and GIVI, P. 1989 Coalescence efficiencies of fuel droplets in binary collisions. *Int Commun. Heat Mass Transfer,* **16**, 11-20.

[15] ASHGRIZ, N. and POO, J. Y. 1990 Coalescence and separation in binary collisions of liquid drops. *J. Fluid Mech.,* **221**, 183-204.

[16] ASSANIS, D. N. and HEYWOOD, J. B. 1986 Development and use of computer simulation of the turbocompounded Diesel system for engine performance and components heat transfer studies. SAE Paper 860329.

[17] BACH, P. and HASSAGER, O. 1985 An algorithm for the use of the Lagrangian specification in Newtonian fluid mechanics and applications to free surface flow. *J. Fluid Mech.* **152**, 173-190.

[18] BAJPAI, P. K., PAMKRISHNA, D. and PROKOP, A. 1988 A coalescence redispersion model for drop size distributions in an agitated vessel. *Chem. Engng. Sci.,* **31**, 913-920.

[19] BANKOFF, S. G. 1971 Stability of liquid flow down a heated inclined plane. *Int. J. Heat Mass Transfer* **14**, 377-385.

[20] BEGLERIS, P. B. 1987 Three-dimensional flow predictions in motored Diesel engines. PhD Thesis, University of London.

[21] BELKIN, H. H., MAcLEOD, A. A., MONRAD, C. C., and ROTHFUS, R. R. 1959 *AIChE J.* **5**,245.

[22] BENJAMIN, T. B. 1957 Wave formation in laminar flow down an inclined plane. *J. Fluid Mech.,* **2**, 554-574.

[23] BENNEY, D. J. 1966 Long waves on liquid films. *J. Math. and Phys.* **45**, 150-155.

[24] BESHAY, K. R. 1985 Computer modelling of Diesel spray dispersion and evaporation. PhD Thesis, University of London

[25] BESHKOV, V. N. and BOYADZHIEV, K. B. 1974 Laminar flow of thin liquid films. *J. Eng. Phys.,* **27**, 1266-1269.

[26] BRIFFA, F. E. J. 1981 Transient drag in sprays. *18th Int. Symp. on Combustion, the Combustion Institute*, 307-319.

[27] BINNIE, A. M. 1957 *J. Fluid Mech.* **2**, 551.

[28] BINNIE, A. M. 1959 *J. Fluid Mech.* **5**, 561.

[29] BONACINA, C., COMINI, G. and GIUDICE, S. D. 1975 Evaporation of atomised liquids on hot surface *Lett. Heat Mass Transfer* **2**, 401-406.

[30] BORISOV, A. A. et al 1970 Amplification of weak shock waves in a hot two-phase liquid-gas system. *Zh. Prikl. Mekh. Tekh. Fiz., No.1*,168-173.

[31] BRACCO, F. V. 1985 Modelling of engine sprays. *SAE Paper 850394.*

[32] BRADLEY, S. G. and STOW, C. D 1978 Collisions between liquid drops. *Phil. Trans. R. Soc. Lond. A***287**, 635-675.

[33] BRAMELLER, A., ALLAN, R. N., and HAMAM, Y. M. 1976 Sparsity. *Pitman Publishing.*

[34] BRAUER, H. 1956 Strömung und Wärmeübergang bei Rieselfilmen. *VDI (Ver. Deut. Ingr.)-Forschungsheft* **457**.

[35] BRAZIER-SMITH, P. R., JENINGS, S. G. and LATHAM, J. 1972 The interaction of falling water drops: coalescence. *Proc. R. Soc. Lond.-A,* **326**, 393-408.

[36] BRENNER, H. 1961 The slow motion of sphere through a viscous fluid towards a plane surface. *Chem. Engng Sci* **16**, 242-251.

[37] BRESSLER, R. 1960 Untersuchung des Wärmeüberganges in einem Dünnschichtver dampfer. *Forschungsber. Landes Nordrhein-Westfalen* **770**.

[38] BRODKEY, R.S 1967 The phenomena of fluid motions. *Addison-Wesley, Reading, MA.*

[39] BROWN, H. 1976 Energy in our future. *Ann. Rev. Energy.*, **1**, 1-36.

[40] BROWN, P. S. 1985 An implicit scheme for efficient solution of the coalescence/collision breakup equation. *J. Comput. Phys.*, **58**, 417-431.

[41] BURELBACH, J. P., BANKOFF, S. G. and DAVIS, S. H. 1988 Nonlinear stability of evaporating/condensing liquid films. *J. Fluid Mech.*, **195**, 563-494.

[42] CASTMAN, R. A. 1932 The mechanism of the atomisation accompanying solid injection. NACA Report 440.

[43] CHANDRA, S. and AVEDISIAN, C. T. 1991 On the collision of a droplet with a solid surface. *Proc. R. Soc. Lond.-A*, **432**, 13-41.

[44] CHANDRA,S. and AVEDISIAN, C. T. 1992 Observations of droplet impinging on a ceramic porous surface. *Int. J. Heat Mass Transfer.*, **35**, 2377-2388.

[45] CHEHROUDI, B., ONUMA, Y., CHEN, S.-H., and BRACOO, F. V. 1985 On the intact core of full-cone sprays. *SAE Paper 850126*

[46] CHIEN, K. Y. 1982 Predictions of channel and boundary layer flows with a low Reynolds number turbulence model. *AIAA J.*, **20**, 33-38.

[47] CHIEN, S. and IBELE, W. 1964 Pressure drop and liquid film thickness of two-phase annular and annular-mist flows. *Trans Am Soc MEch Engrs, Series C, J Heat Transfer,* **86**, 80-96.

[48] CHING, B., GOLAY, M. W. and JOHNSON, T. J. 1984 Droplet impacts upon liquid surfaces. *Science,* **226**(4674), 535-537.

[49] CHOI, K. J. and LEE, H. J. 1992 Experimental studies on the dynamics and evaporation of tandem liquid droplets in a hot gas flow. *Int. J. Heat Mass Transfer,* **35**, 2921-2929.

[50] CHUNG, P. M. 1963 Unsteady laminar film condensation on vertical plate. *ASME J. Heat Transfer,* **85**, 63-70.

[51] CLEAVER, J. W. and YATES, B. 1973 Mechanism of detachment of colloidal particles from a flat substrate in a turbulent flow. *J. Colloid Interface Sci.*, **44**, 464-474.

[52] COGHE, A. et al 1991, 1993 Private communications.

[53] COX, R. G. and BRENNER, H. 1967 The slow motion of a sphere through a viscous fluid towards a plane surface-II. Small gap widths,including inertial effects. *Chem. Engng. Sci.,* **22**, 1753-1777.

[54] CRAIK, A. D. D. 1966 Wind-generated waves in thin liquid films. *J. Fluid Mech.* **26**, 369-392.

[55] CUMO, M. and FARELLO, G. E. 1967 Heated wall-droplet interaction for two-phase flow heat transfer in liquid deficient region. *Symp. on Two Phase Flow Dynamics, EINDHOVEN*, II, 1325-1357.

[56] CUNNINGHAM, E. 1910 On the velocity of steady fall of spherical particles through fluid medium. *Proc R. Soc. Lond. A* **83**, 357-365.

[57] CURRLE, J. 1996 Simulation of the two phase flow in the waterbox of a HVAC system. *SAE Paper* 960962.

[58] DAHNEKE, B. 1974 Diffusion deposition of particles. *J. Colloid Interface Sci.* **48**, 520-522.

[59] DANDY; D. S., and DWYER, H. H. 1990 A sphere in shear at finite Reynolds number: effect of shear on particle lift, drag, and heat transfer. *J. Fluid Mech.* **216**, 381-410.

[60] DAVIS, E. J., CHEREMISINOFF, N. P., and SAMBASIVAN, G. 1978 Heat and momentum transfer analogies for two-phase transfer stratified and annular flows. in *Two-phase Transport and Reactor Safety,* **2**, *Hemisphere, New York*, 577-608.

[61] DEB, S., YAO, S. C. 1989 Analysis on film boiling heat transfer of impacting sprays. *Int. J. Heat Mass Transfer,* **32**, 2099-2112.

[62] DE GENNES, P. G. 1985 Wetting: statics and dynamics. *Rev. of Mordern Phys.* , **57**,827-863.

[63] DELHAYE, J. M. 1974 Jump conditions and entropy sources in two-phase systems. Local instant formulation. *Int. J. Multiphase Flow* **1**, 395-409.

[64] DICKERSON, R. A. and COULTAS, T. A. 1966 Breakup of droplets in an accelerating gas flow. *AIAA Paper, No. 611*

[65] DIEZ, J. A., GRATTON, R., THOMAS, L.P. and MARINO, B. 1994 Laplace pressure driven drop spreading. *Phys. Fluids,* **6**, 24-33, 1994.

[66] DOBRAN, F. 1983 Hydrodynamic and heat transfer analysis of two-phase annular flow with a new liquid film model of turbulence. *Int. J. Heat Mass Transfer* **26**, 1159-1171.

[67] DOORMAAL, J. P. VAN & RUITHBY, G. D. 1984 Enhancement of the SIMPLE method for predicting incompressible fluid flows. *Numer. Heat Transfer,* **7**, 147-163.

[68] DUBROVSKII, V. V., PODVYSOTSKII, A. M. and SHRAIBER, A. A. 1991 Experimental investigation of drop fragmentation by aerodynamic forces. *J. Appl. Mech. and Tech. Phys.,* **32**, 734-740.

[69] DUKLER, A. E. 1960 Fluid mechanics and heat transfer in vertical falling-film systems. *Chem. Engng Prog. Symp. Ser.,* **56**, 1-10.

[70] DUSSAN, V. E. B. and DAVIS, S. H. 1974 On the motion of a fluid-fluid interface along a solid surface. *J. Fluid Mech.,* **65** 71-95.

[71] DWYER, H. A. and SANDERS, B. R. 1984 Detailed computation of unsteady droplet dynamics. *20th Int. Symp. on Combustion,* 1743-1749.

[72] EISENKLAN, P., ARUNACHALAM, S. A., and WESTON, J. A. 1967 Evaporation rates and drag resistance of burning drops. *In: Proc. 11th Symp. (Int.) on Combustion*, 715-728, Butterworths, London.

[73] EL WAKIL, M. M., UGEHARA, O. A. and MYERS, P. S. 1954 A theoretical investigation of the heating-up period of injected fuel droplets vapourising in air. *NACA TN 3179.*

[74] ENGEL, O. G. 1955 Water drop collisions with solid surfaces. *J. Res. Nat. Stds.* **54**, 281-298.

[75] ENGEL, O. G. 1958 Fragmentation of water drops in the zone behind an air shock. *J. Res Natn. Bur. Stand.* **60**, 245-280.

[76] EREAUT, P. R., GOVER, M. D. and SHAND, A. M. 1992 Private communication.

[77] FAETH, G. M. 1977 Current studies of droplet and liquid combustion. *Progress in Energy and combustion Science* **3**, 191-224.

[78] FAETH, G. M. 1983 Evaporation and combustion of sprays. *Prog. Energy Combustion Sci.* **9**, 1-76.

[79] FAETH, G. M. 1990 Structure and atomisation properties of dense turbulent sprays. *Twenty-Third Symposium(International) on Combustion, The Combustion Institute*, 1345-1352.

[80] FAVRE, A. 1969 Statistical equations of turbulent gases. *Problems of Hydrodynamics and Continuum Mechanics, SIAM*, 231-266.

[81] FAXEN, H. 1923 Die Bewegun einer Starren Kugel Langs der Achse eines mit Zaher Flussigkeit getullten Rohres. *Arkiv. Mat. Astron. Fys.* **17**, 1-28.

[82] FLECKHAUS, D., HISHIDA,D. and MAEDA, M. 1987 Effect of laden solid particle on the turbulent flow structure of a ruound jet. *Exp. Fluids,* **5**,323.

[83] FRIEDMAN, S. J. and MILLER, C. O. 1941 *Ind. Eng. Chem.* **33**, 885.

[84] FROSSLING, N. 1938 On the evaporation of falling droplets. *Gerlands beitr. Geophys.* **52**,170-216.

[85] FUJIMOTO, H., SAITO, M., MINOURA, A., KATSURA, N., CHO, I. Y. and SEDA, J. 1988 Characteristics of a Diesel spray impinging on a flat wall. *Proc. of ICLASS-88,* Sendai, Japan.

[86] FUKAI, J., ZHAO, Z., POULIKAKOS, D., MEGARIDIS, C. M., MIYATAKE, O. 1993 Modeling of the deformation of a liquid droplet impinging upon a flat surface. *Phys. Fluids A,* **5**, 2588-2599.

[87] FULFORD, G. D. 1962 Gas-liquid flow in an inclined channel. PhD Thesis, University of Birmingham.

[88] FYALL, H. A. 1967 Single impact studies of rain erosion. *Proc. 2nd Meers Con. Rain Erosion and Allied Phen.* **2**, 328-354.

[89] GEL'FAND, B. E. , GUBIN, S. A., and KOGARKO, S. M. 1974 Varieties of droplet breakup in shock waves and their characteristics. *Inzh.-Fiz. Zh.,* **27**, 119-126.

[90] GHADIRI, H. 1978 Raindrop impact, soil splash and cratering. PhD Thesis, University of Reading

[91] GHADIRI, H. and PAYNE, D. 1979 Rain drop impact and soil splash. In: R. Lal & D. J. Greenland (Eds), Soil Physical properties and crop production in the tropics. J. Wiley, Chichester, 95-104.

[92] GILLESPIE, D. T. 1975 An exact method for numerically simulating the stochastic coalescence process in a cloud. *J. Atmos. Sci.*, **32**, 1977-1989.

[93] GILLESPIE, D. T. and LIST, R. 1979 Effects of collision-induced breakup on drop size distributions in steady state rainshafts. *Pure appl. Geophys.*, **117**, 599-626.

[94] GILLESPIE, T. and RIDEAL, E. 1955 On the adhesion of drops and particles on impact at solid surfaces.II. *J. Colloid Sci.*, **10**, 281-298.

[95] GJEVIK, B. 1970 Occurrence of finite-amplitude surface waves on falling liquid films. *Phys. Fluids* **13**, 1918-1925.

[96] GLUSHKOV, V. I. 1975 Interaction between liquid droplets and a solid wall. *In : Povysheniye effectivnosti transport gaya (Improving the efficiency of gas trasport)*, Moscow, 90-98.

[97] GOLDSMITH, M. and PENNER, S. S. 1954 On the Burning of Single Drops of Fuel in an Oxidizing Atmosphere. *J. Propul.* **24**,245-251.

[98] GOLUB, G. H. and VAN LOAN, C. F. 1983 Matrix computations. *North Oxford Academic*, Oxford.

[99] GOLUB, G. H., and O'LEARY, D. P. 1989 Some history of the conjugate gradient and Lanczos algorithms:1948-1976, *SIAM Review* **31**, 50-102.

[100] GOOD, R. J. 1992 Contact angle, wetting , and adhesion: a critical review. *J. Adhesion Sco. Technol.*, **6**(12), 1269-1302.

[101] GOSMAN, A. D., PUN, W. H., RUNCHAL, A. K., SPALDING, D. B. and WOLFSHTEIN, M. 1969 Heat and mass transfer in recirculating flows. *Academic Press.*

[102] GOSMAN, A.D and IOANNIDES, E. 1981 Aspects of computer simulation of liquid-fuelled combustors. *AIAA Paper 81-0323.*

[103] GOSMAN, A. D., TSUI, Y. Y. and WATKINS, A. P. 1984 Calculations of three-dimensional air motion in model engines. *SAE Paper 840229*

[104] GOUSSIS, D. and KELLY, R. E. 1985 Effects of viscosity variation on the stability of film flow down heated or cooled inclined surfaces: Long-wavelength analysis. *Phys. Fluids* **28**, 3207-3214

[105] GRANT, G. and TABAKOFF, W. 1975 Erosion prediction in turbomachinery resulting from environmental solid particles. *J. Aircraft* **12**, 471-478.

[106] GREENE, G. A., IRVINE,T. F., GYVES, T. and SMITH, T. 1993 Drag relationships for liquid droplets setting in a continuous liquid. *AIChE J.,* **39**(1), 37-41.

[107] GREENBERG, J. B., ALBAGLI, D. and TAMBOUR, Y. 1986 An opposed jet quasi-monodisperse spray diffusion flame. *Combust. Sci. Technol.,* **50**, 225-270.

[108] GREGORY, P. H., GUTHRIE, E. J., and BUNCE, M. E. 1959 Experiments on splash dispersal of fungus spores. *J. Gen. Microbiol.* **20**, 328-354.

[109] GRIGULL, U. 1952 *Forsch. Gebiete Ingenieurw.* **18**, 10

[110] GRISSOM, W. M. and WIERUM, F. A. 1981 Liquid spray cooling of a heated surface. *Int. J. Heat Mass Transfer,* **24**, 261-271.

[111] GUKHMAN, A. A., VDYNETS, A. Z., ROZHDESTVENSKII, A. V. and BRAZHNIKOV, S. M. 1985 Features of heat transfer in the impact of a drop against a hot surface. *J. Eng. Phys.,* **49**,1178-1180.

[112] GUNN, R. 1965. Collision characteristics of freely falling water drops. *Science,* **150**, 695-701.

[113] Gutmann, M. 1993 Private communication.

[114] HAENLEIN, A. 1932 Disintegration of a liquid jet. *NACA TN 659*

[115] HANRATTY, T. J. and ENGEN, J. M 1957 Interaction between a turbulent air stream and a moving water surface. *AIChE J.* **3**, 299-304.

[116] HANRATTY, T. J. and HERSHMAN, A. 1961 *AIChE J.* **7**, 488.

[117] HANRATTY, T. J. and WOODMANSEE, D. E. 1970 Stability of the interface for a horizontal air-liquid flow. *Symp. on Two-phase Flow, Exter, June 1965*, Paper A1.

[118] HANSELL, D., KENNEDY, I. M. and KOLLMANN, W. 1992 A simulation of particle dispersion in a turbulent jet. *Int. J. multiphase Flow,* **18**(4), 559-576.

[119] HARLOW, F. H., and AMSDEN A. A. 1975 Numerical calculation of multiphase fluid flow. *J. Compt. Phys.* **17**, 19-52.

[120] HARLOW, F. H. & SHANNON, J. P. 1967 The splash of a liquid drop. *J. Appl. Phys.*, **38**, 3855-3866.

[121] HESTENES, M. R. and STIEFEL, E. 1952 Methods of conjugate gradients for solving linear systems, *J. Res. Nat. Bureau Stand.* **49**, 409-403

[122] HETSRONI, G. and SOKOLOV, M. 1971 Distribution of mass, velocity and intensity of turbulence in a two-phase jet. *J. Appl. Mech.* **38**, 315.

[123] HEWITT, G. F. 1961 Analysis of annular two-phse flow: Application of the Dukler analysis to vertical flow in a tube. *UKAEA Rep. AERE-R-3690.*

[124] HEWITT, G. F. and HALL-TAYLOR, N. S. 1970 *Annular Two-Phase Flow.* Academic Press, London.

[125] HICKMAN, K. 1952 Studies in high vacuum evaporation. Part III: surface behavior in the pot still. *Ind. Engng Chem.* **44**, 1892-1902.

[126] HILDEBRANDT, F. B. 1949 Advanced Calculus for Engineers. Prentice-Hall, Inc., New York, 368-378.

[127] HINZE, J. O. 1955 Fundamentals of the hydrodynamic mechanics of splitting in dispersion processes. *AIChE J.*, **1**, 289-295.

[128] HINZE, J. O 1975 Turbulence. McGraw-Hill, New York.

[129] HIROYASU, H., SHIMIZU, M. and ARAI, M. 1982 The breakup of high speed jet in a high pressure gaseous atmosphere. *ICLASS-82, Paper No. 2.5*,p69.

[130] HOCKING, L. M. 1976 A moving fluid interface on a solid surface. *J. Fluid Mech.*, **76**, 801-817.

[131] HOOGENDOOM, C. J. and HORD, R. den 1974 Leidenfrost temperature and heat transfer coefficients for water spras impinging on a hot surface. *Proc. 5th Int. Heat Transfer Conf.* Tokyo.

[132] HOPF, L. 1910 *Ann. Physik* **32**, 777.

[133] HORTON, R. E., LEACH, H. R., and van VLIET, R. 1934 *Trans. Am. Geophys. Union* **15**, 393. HOULT et al. 1988

[134] HSIANG, L.-P. and FAETH, G. M. 1992 Near-limit drop deformation and secondary breakup. *Int. J. Multiphase Flow,* **18**, 635-652.

[135] HSIANG, L.-P. and FAETH, G. M. 1993 Drop properties after secondary breakup. *Int. J. Multiphase Flow,* **19**, 721-735.

[136] HU, S. and KINTNER, R. C. 1955 The fall of single liquid drops through water. *AIChE J.,* **1**, 42.

[137] HUANG, Y. C., HAMMITT, F. G., and YANG, W. H. 1973 *J. Fluids Eng.* **95**, 276-294.

[138] HUH, K. Y. and GOSMAN A. D. 1991 A phenomenological model of Diesel spray atomisation. *Int. Conf. Multiphase Flows*, Tsukuba, Japan.

[139] HUH, C. and SCRIVEN, L. E. 1971 Hydrodynamic model of steady movement of a solid/liquid/fluid contact line. *J. Colloid Interface Sci.* **35**, 85-101.

[140] HUANG, A. and JOSEPH, D. D. 1992 Instability of the equilibrium of a liquid below its vapor between horizontal heated plates. *J. Fluid Mech.,* **252**, 235-247.

[141] HUTCHINSON, P. and WHALLEY, P. B. 1973 A possible characterisation of entrainment in annular flow. *Chem. Engng. Sci* **28**, 974.

[142] HWANG, CHI-CHUAN, and WENG, C-I. 1988 Nonlinear stability analysis of film flow down a heated or cooled inclined plane with viscosity cariation. *Int. J. Heat Mass Transfer.,* **31**, 1775-1784.

[143] HYROYASU, H., SHIMIZU, M., and ARAI, M. 1982 The breakup of a high speed jet in a high pressure gaseous environment. *ICLASS-82, University of Wisconsin, Madison, WI*

[144] IDOUM, A., PACKER, J. P., WALLACE, F. T. and CHARLTON, S. J. 1985 An experimental and analytical study of jet impingement and wall jets in high swirl D.I diesel engines using the hydraulic analogy. *SAE Paper 850263.*

[145] INADA, S., MIYASAKA, Y., SAKAMOTO, K. and HOJO, K. 1988 Liquid-solid contact state and fluctuation of the vapor film thickness of a drop impinging on a heated surface. *J. Chem. Engng. Japan.* **21**, 463-468.

[146] INGEBO, R. D 1956 Drag coefficient for droplets and spheres in clouds accellerating in airstream. *NACA TN 3762*

[147] ISHII, M. and GROLMES, M. A. 1975 Inception criteria for droplet entrainment in two-phase concurrent film flow. *AIChE. Jl* **21**, 308

[148] ISHIHARA, T., IWAGAKI, Y., and ISHIHARA, Y. 1952 *Mem. Fac. Eng. Kyoto Univ.* **14**, 83.

[149] ISHIHARA, T., IWAGAKI, Y., and IWASA, Y. 1961 *Trans. Am. Soc. Civil Engrs.* **26**, 548.

[150] ISSA. R. I. 1986 Solution of the implicitly discretised fluid flow equations by operator splitting. *J. Comput. Phys,* **62**, 40-65.

[151] ISSA, R. I., GOSMAN, A. D., and WATKINS, A. P. 1983 The computation of compressible and incompressible recirculating flows by a non-iterative implicit scheme. *Report FS/83/8, Mech. Eng. Dept., Imperial College*

[152] JAYARANTNE, D. W. and MASON, B. J. 1964 The coalescence and bouncing of water drops at an air/water interface. *Proc. R. Soc. Lond.-A,* **280**, 545-565.

[153] JAYATILLAKA, C. L. V. 1966 The influence of Prandtl number and surface roughness on the resistance of the laminar sublayer to momentum and heat transfer. Imperial College, Mechanical Engineering Department, Report TWF/R/2.

[154] JHONS, R. J. R. 1980 Prediction of flow in diesel engine cylinders. PhD Thesis, University of London.

[155] JIANG, Y. J., UMERNURA, A. and LAW, C. K. 1992 An experimental investigation on the collision behavior of hydrocarbon droplets. *J. Fluid Mech.,* **234**, 171-190.

[156] JONES, W. P 1979 Models for turbulent flows with variable density and combustion. *VKI Lecture series-2.*

[157] JONES, W. P. and LAUNDER, B. E. 1973 The calculation of low-Reynolds-number phenomena with a two equation model of turbulence. *Int. J. Heat Mass Transfer* **16**, 1119-1130.

[158] JORDAN, D W. 1954 *Brit. J. Appl. Phys.* **3**, 194.

[159] KALLIO, G. A. 1989. Wall-impact velocities of particles in the turbulent boundary layer. presented at the 3rd Int. Symp. on Gas-Solid Flows, La Jolla, CA.

[160] KAMEI, S. and OISHI, J. 1955 *Mem. Fac. Eng. Kyoto University,* **17**, 277.

[161] KAMIMOTO, T., TAKAHASHI, H, KOBAYASHI, H. and MATSUKO, S. 1982 Convective heat transfer of an impinging diesel flame in a rapid compression machine. *SAE Paper* 821035

[162] KAMIMOTO, T., KOMORI, S., NOH, S. H. and ENOMOTO, Y. 1992 Effects of flame motion and temperature on local wall heat transfer in a rapid compressive expansion machine simulating diesel contribution. *SAE Paper* 922208 KAPITSA 1951

[163] KAPITZA, P. L. 1948 Wave flow of thin viscous fluid layers. *Zh. Eksp. Teor. Fiz.* **18**, 3-28.

[164] KARIMI, E. R. 1989 High-speed photography of fuel spray and combution events in a production diesel engine and combustion bomb. *Proc. I. MEch. Eng. (C372/012).*

[165] KATAOKA. I. and ISHII, M. 1982 Mechanism and correlation of droplet entrainment and deposition in annular two-phase flow. *ANL-82-4L1.*

[166] KATAOKA, I., ISHII, M. and MISHIMA, K. 1983 Generation of size distribution of droplets in annular two-phase flow. *Trans. ASME:J. Fluids Engng* **105**, 230-238.

[167] KATSURA, N., SAITO, M., SENDA, J. and FUJIMOTO, H. 1989 Characteristics of a diesel spray impinging on a flat wall *SAE Paper* No. 890264.

[168] KAWAMURA, K., SAITO, A. 1993 Analysis of impinging spray characteristics under high-pressure fuel injection. (2nd report, modeling for impinging spray) *Trans. Jap. Soc. Mech. Engrs. B***59**, 3290-3295.

[169] KAZENIN, D. A. and MAKEEV, A. A. 1987 Collision of drops with a surface in conditions of film boiling, taking account of the temperature dependence of the vapor properties. *High Temperature,* **25**(2), 234-239.

[170] KENDALL, G. E. and Rohsenow, W. M 1978 Heat transfer to impacting drops and post critical heat flux dispersed flow. *Heat Transfer Laboratory 85694-100*, Massachusetts Institute of Technology, March.

[171] KIM, I., ELGHOBASHI; S. E., and SIRIGNANO; W. A. 1992 Three dimensional flow computation for two interacting, moving droplets. *Preprint 92-0343*, AIAA 30th Aerospace Sciences Meeting, Reno, NV.

[172] KLEE, A. and TREYBAL, R. E. 1956 Rate of rise or fall of liquid drops. *AIChE J.*, **2**, 444.

[173] KOCAMUSTAFAOGULLARI, G. 1985 Two-fluid modelling in analyzing the interfacial stability of liquid film flows. *Int. J. Multiphase Flow,* **11**, 63-89.

[174] KOLPAKOV, A. V., ROMANOV, K. V., and TITOVA, E. I. 1985 Calculation of the rebound condition for colliding drops of sharply different sizes. *Kolloidn. Zh.*, **47**, 953.

[175] KOH, J. C. Y. 1961 An integral treatment of two-phase boundary layer in film condensation. *ASME J. Heat Transfer,* **83**, 359-362.

[176] KRALJ, C. 1995 Numerical simulation of Diesel spray process. PhD Thesis, University of London.

[177] KREZECZKOWSKI, S. A. 1980 Measurement of liquid droplet disintegration mechanisms. *Int. J. Multiphase Flow,* **6**, 227-239.

[178] KROEGER, C. A. 1986 A neat methonal direct injection combustion system for heavy duty applications. *SAE Paper 861169*

[179] KUNIYOSHI, H., YAMAMOTO, H., FUJIMOTO, H. and SATO, G. T. 1980 Investigation of the characteristics of diesel fuel spray(third paper: impinging on a flat plate). *J. of M.E.S.J.,* **15**, 57-64.

[180] KUTATELADZE, S. S. and STYRIKOVICH, M. A. 1958 Hydraulics of Gas-Liquid Systems. Gosénergoizdat, Moscow, 1958; translated by U.S Dept. Commerce, Office Tech. Serv., Washington, D. C. 1960.

[181] KUTATELADZE, S. S. 1972 Elements of the hydrodynamics of gas liquid system. *Fluid Mech - Sov. Res.* **1**, 29.

[182] LABEISH, V. G. and PIMENOV, A. G. 1984 Experimental study of heat transfer between a hot wall and impinging drops. *J. Eng. Phys* **47**, 1400-1406.

[183] LABUNTSOV, D. A. 1956 *Teploenerg.* No. 12. 47.

[184] LAI, R. J. and SHEMDIN, O. H. 1974 Laboratory study of the generation of spray over water. *J. Geophys. Res.* **79**, 3055-3063.

[185] LAMB, H. *Hydrodynamics.* Dover, New York, 1932.

[186] LANGMUIR, I. 1948 The production of rain by a chain reaction in cumulous clouds at temperatures above freezing. *J. Meteor.* **5**, 175-192.

[187] LATIMER,B. R. and POLLARD, A. 1985 Comparison of pressure-velocity coupling solution algorithms. *Numer. Heat Transfer,* **8**,635-652.

[188] LAUNDER, B. E. and SPALDING, D. B. 1972 Lectures in Mathematical Models of Turbulence. *Academic Press, London.*

[189] LEE, D. W. and SPENCER, R. C. 1932 Preliminary photomicrographic studies of fuel sprays. *NACA Tech. Note 424*

[190] LEE, D. W. and SPENCER, R. C. 1933 Photomicrographic studies on fuel spray. *NACA Tech. Note 454*

[191] LEGER, L. and JOANNY, J. F. 1992 Liquid spreading. *Rep. Prog. Phys.,* **55**, 431-486.

[192] LEFEBVRE, A. H. 1989 Atomisation and Sprays. Hemisphere Publishing Corporation.

[193] LEVICH, V. G. 1948 *Zh. Fiz. Khim.* **22**,721.

[194] LEVICH, V. G. 1962 Physico-chemical Hydrodynamics. *Prentice-Hall, Englewood Cliffs, New Jersey.*

[195] LEVIN, Z. and HOBBS, P. V. 1971 Splashing of water drops on solid and wetted surfaces: hyseodynamics and charge separation. *Phil. Trans. Roy. Soc. Lond.-A,* **269**, 555-585.

[196] LEVY, Y. and LOCKWOOD, F. C. 1981 Velocity measurement in a particle-laden turbulent free jet. *Combust. Flame,* **40**, 333.

[197] LIBBY, P. A. and WILLIAMS, F. A. 1980 Fundamental aspectsof turbulent reacting flows (Eds P. A. Libby & F. A. Williams), Topics in Applied Physics, Springer-Verlag.

[198] LIU, A. B. MATHER, D., and REITZ, R. D. 1993 Modelling the effects of drop drag and breakup on fuel sprays. SAE paper 930072.

[199] LOEHR, K. F., LASEK, A. 1990 Splashing of drops. *Arch. Mech.,* **42**, 507-513.

[200] LOW, T. B. & LIST, R. 1982a Collision, coalsence and breakup of raindrops. Part I: Experimentally established coalescence efficiencies and fragment size distribution in breakup. *J. Atomos Sci.,* **39**(7), 1591-1606.

[201] LOW, T. B. & LIST, R. 1982b Collision, coalsence and breakup of raindrops. Part II: Parametrisation of fragment size distribution. *J. Atomos Sci.,* **39**(7), 1607-1618.

[202] MACKLIN, W. C. and HOBBS, P. V. 1969 Subsurface phenomena and the splashing of drops on shallow liquid. *Science,* **166**, 107-108.

[203] MAKINO, K. and MICHIYOSHI, I. 1984 The behaviour of a water droplet on heated surfaces. *Int. J. Heat and Mass Trans.* **27**, 781-791.

[204] MARTIN, D. W. 1966 Linear Algebraic Equations. in *Numerical Analysis - An Introduction (ed. J. Walsh), Academic Press.*

[205] MAUDE, A. D. 1961 End effects in a falling-sphere viscometer. *Br. J. Appl. Phys.* **12**, 293.

[206] MATSUI, Y. and SUGIHARA, K. 1986 Sources of hydrocarbon emissions from a small direct injection diesel engines. *J. SAE Review,* **7** 4-11.

[207] MATSUMOTO, S. and SAITO, S. 1970 Monte Carlo simulation of horizontal pneumatic conveying based on the rough wall model *J. Chem. Engng. Japan,* **3**, 223-230.

[208] McGINNIS, F. K. and HOLMAN, J. P. 1969 Individual droplet heat-transfer rate for splattering on hot surface. *Int. J. Heat Mass Transfer,* **12**, 95-108.

[209] MEDJESKI, J. 1976 Soldification of droplets on a cold substrate. *Int. J. Heat Mass Transfer* **19**, p1009.

[210] MEURER, J. S. 1956 Evaluation of reaction kinetics eliminates diesel knock. The M combustion system of man. *SAE Trans.,* **64**,250-268.

[211] MIESSE, C. C. 1955 Correlation of experimental data on the disintegration of liquid jets. *Ing. Eng. Chem.,* **47**, 1690-1701.

[212] MIRAZ, R. 1991 Studies of diesel spray interacting with cross-flow and solid boundaries. PhD Thesis, University of Manchester, Faculty of Technology.

[213] MODARRESS, D. , TAN, H., and ELGHOBASHI, S. 1984 Two-component LDA measurement in a two-phase turbulent jet. *AIAA J.,* **22**, 624.

[214] MOUREAU, J. C. L., BOLLE, L. and GIOT, M. 1979 Influence of the droplet size distribution on the spray cooling efficiency. *Two-Phase Momentum, Heat and Mass Transfer,* **1**, 171-184.

[215] MULHOLLAND, J. A., SRIVASTAVA, R. K. and WENDT,J. O. L. 1988 Influence of droplet spacing on drag coefficient in nonevaporating, monodisperse streams. *AIAA J.,* **26**, 1231-1237.

[216] MUTCHLER, C. K. 1967 Parameters for describing raindrop splash. *J. Soil. and Water Cons.,* **22**, 91-94.

[217] MUTCHLER, C. K. 1970 The size, travel and composition of droplets formed by water drop splash on thin water layers. PhD Thesis, University of Minnuesota.

[218] MUTCHLER, C. K. 1971 Splash droplet production by waterdrop impact. *Water Resources Research,* **7**, 1024-1030.

[219] NABER, J. D., ENRIGHT, B. and FARRELL, P. 1988 Fuel impingement in a direct injection diesel engine. *SAE Paper 881316*

[220] NABER, J. D. and FARRELL, P. V. 1993 Hydrodynamics of droplet impingement on a heated surface. *SAE Paper 930919.*

[221] NABER, J. D. and REITZ, R. D. 1988 Modelling engine spray/wall impingement. *SAE Paper No. 880107.*

[222] NAKAGAWA, T. 1983 On characteristics of the water-particle velocity in a plunging breaker. *J. Fluid Mech.* **126**, 251-268.

[223] NAKAYAMA, A., KOYAMA, H. and OHSAWA, S.-I. 1982 An integral method in laminar film condensation on plane and axisymmetric bodies. em Letters in Heat and Mass Transfer, **9**, 443-453.

[224] NAKAYAMA, A. and KOYAMA, H. 1984 An approximate method for laminar film condensation in nonuniform gravity. *Int. Comm. Heat Mass Transfer,* **11**, 105-113.

[225] NAKAYAMA, A. and KOYAMA, H. 1986 An integral procedure for a two-phase boundary in laminar film condensation. *Int. J. Multiphase Flow,* **12**, 135-144.

[226] NAMBIAR, D. K. R., KUMAR, R., DAS, T. R. and GANDHI, K. S. 1992 A new model for the breakage frequency of drops in turbulent stirred dispersions. *Chem. Engng. Sci.,* **47**, 2989-3002.

[227] NISHIO, S. and HIRATA, M. 1978 Study on the Leidenfrost temperature-2nd report, behavior of liquid-solid contact surace and Leidenrtost temperature. *Trans. Japan Soc. Mech. Engrs.,* **44**(380), 1335-1346.(in Japanese)

[228] NUSSELT, W. 1916 Die obserflächenkondensation des Wasserdampfes. *Zeitschrift des Vereines Deutscher Ingenieure* **60**, 541-569.

[229] OHNESORGE, W. 1936 Formation of drops by nozzles and the breakup of liquid jets. *Z. Angew. Math. Mech.,* **16**, 355-358.

[230] ORMANCEY, A. and MARTINON, J. 1984 Prediction of particle dispersion in turbulent flows. *Physicochem Hydrodynam.* **5**, 229-244.

[231] O'ROURKE, P. J.1981 Collective drop effects on vaporising liquid sprays. PhD Thesis, University of Princeton, USA.

[232] O'ROURKE, P. J. and AMSDEN, A. A. 1987 The TAB method for numerical calculation of spray droplet break-up. *SAE 872089.*

[233] O'Rourke, P. J. and Bracco, F. V. 1980 Modelling of drop interactions in thick sprays and a comparison with experiment. In *Stratified Charge Automotive Engines Conf.* IMechE.

[234] ÖZDEMIR, I. B,. 1991 Impingement of single and two-phase jets on unheated and heated flat plates. *Ph. D Thesis*, University of London.

[235] PADDY, J. F. 1992 Spreading, wetting, and contact angles. *J. Adhesion Sci. Technol.,* **6**(12), 1347-1358.

[236] PALATNIK, I. B. 1981 Dust clusters with venturi tube coagulators [in Russian]. Nauka, Alma-Ata.

[237] PALMER, H. J. 1976 The hydrodynamic stability of rapidly evaporating liquids at reduced pressure", *J. Fluid Mech.* **75**, 487-511.

[238] PARK, R. W. 1970 Behaviour of water drops colliding in humid nitrogen. PhD Thesis, Department of Chemical Engineering, The University of Wisconsin.

[239] PATANKAR, S. V. 1980 Numerical Heat Transfer and Fluid Flow, Hemisphere, Washington. D.C.

[240] PATANKAR, S.V. 1981 A calculation procedure for two dimensional elliptic situations. *Numer. Heat Transfer,* **4**, 409-425.

[241] PATANKAR, S.V. & SPALDING, D. B. 1972 A calculation procedure for heat, mass and momentum transfer in three dimensional parabolic flows. *Int. J. Heat Mass Transfer,* **15**,987-1806.

[242] PEDERSEN, C. O. 1967 The dynamics and heat transfer characteristics of water droplets impinging upon a heated surface. PhD Thesis, Carnegie Institute of Technology.

[243] PEDERSEN, C. O. 1970 An experimental study of the dynamic behavior of heat transfer characteristics of water droplets impinging upon a wetted surface. *Int. J. Heat Mass Transfer,* **13**, 369-381.

[244] PHINNEY, R. E. 1973 The breakup of a turbulent liquid jet in a Gaseous atmosphere. *J. Fluid Mech.,* **60**, 689-701.

[245] PILTCH, M. and ERDMAN, C. A. 1987 Use of breakup time data and velocity history data to predict the maximum size of stable fragments for acceleration-induced breakup of a liquid drop. *Int. J. Multiphase Flow,* **13**, 741-757.

[246] PODVYSOTSKY, A. M. and SHRAIBER, A. A. 1984 Coalescence and breakup of drops in two-phase flows. *Int. J. Multiphase Flow,* **10**, 195-209.

[247] POPPER, J., ABUAF, N., and GESTRONI, G. 1974 Velocity measurements in a two-phase turbulent jet. *Int. J Multphase Flow,* **1**, 715.

[248] PORTALSKI, S. 1960 The mechanism of flow in wetted wall colmns. PhD Thesis, University of London.

[249] POVAROV, D. A. SHAL'NEV, K. K., NAZAROV, O. I. and SHALOVASOV, I. A. 1975 Collision of droplets with a moving plane surface. *Sov. Phys. Dokl.* **20**, 782-783.

[250] RABIN, E., SCHALLENMULLER, A. R. , and LOWHEAD, R. B. 1960 Displacement and scattering of propellant droplets. *HFOSR TR-60-75.*

[251] RAITHBY, G. D. 1976 A critical evaluation of upstream differencing applied to problems involving fluid flow. *Comp. Meth. Appl. Mech. Eng.* **9**, 75.

[252] RAJU, M. S. and SIRIGNANO, W. A. 1990 Interaction between two vaporising droplets in an intermediate Reynolds number flow. *Phys. Fluids. A* **2**, 1780-1796.

[253] RANGER, A. A. and NICHOLLS, J. A. 1969 Aerodynamic shattering of liquid drops. *AIAA J.* **7**, 285-290.

[254] RANZ, W. E. 1956 On sprays and spraying. Engineering Rescarch Bulletin No. 65, the Pennsylvania State Universtity.

[255] RANZ, E. W. 1958 Some experiments on orifice sprays. *Canadian Journal of Chemical Engineering,* **36**, 175-181.

[256] RANZ, W. E., and MARSHALL, W. R. 1952 Evaporation from drops. *Chem. Eng. Prog.* **48**, Part I,141-146; Part II, 173-180.

[257] REINECKE, W. G. and WALDMAN, G. D. 1970 A study of drop breakup behind strong shocks with applications to flight. AVCO Report AVSD-0110-70-RR, May 1970.

[258] REITZ, R. D. 1978 Atomisation and other breakup regimes of a liquid jet. PhD Dissertation 1375-T, Princeton Univ.

[259] REITZ, R. D. 1987 Modelling atomisation and processes in high-pressure vapourising sprays. *Atomisation and Spray Technology,* **3**, 309-337.

[260] REITZ, R. D. and BRACCO, F.V. 1984 Encyclopedia of Fluid Mechanics (N. P. Cheremisinoff Ed.), Vol. III, Chapt. 11.

[261] REITZ, R. D. and DIWAKAR, R. 1986 Effect of drop breakup on fuel sprays. *SAE Paper No. 860469.*

[262] REITZ, R. D. and DIWAKAR, R. 1987 Structure of high-pressure fuel sprays. *SAE Paper 870598.*

[263] REUNKSIZBULUT, M. and YUEN, M. C. 1983 Numerical study of droplet evaporation in a high-temperature stream. *J. Heat Transfer,* **105**, 389-397.

[264] REYNOLDS, W. C. 1980 Modelling of fluid motions in engines: An introductory overview. in *Combustion Modelling in Reciprocating Engines. (eds. J. N. Mattavi and C. A. Amann), Plenum Press.*

[265] RHIE, C. M. 1981 A numerical study of the flow past an isolated air foil with separation. PhD Thesis, University of Illinois at Urbana-Chapmain.

[266] RHIE, C. M., and CHOW, W. L. 1983 A numerical study of turbulent flow past an isolated airfoil with trailing edge separation. *AIAA J.* **21**, 1523-1532.

[267] ROACHE, P. J. 1982 Computational Fluid Dynamics, Revised printing, Hermosa Publishers, N.M.

[268] ROCHESTER, M. C. and BRUNTON, J. H. 1974 Surface pressure distribution during impingement. *the 4th International Conference on Rain Erosion and Related Phenomena*, 371-393, *Meersburg, The Federal German Republic*

[269] RODRIGUEZ, F. and MESLER, R. 1985 Some drops don't splash. *J. Colloid Interface Sci.,* **106**(2), 347-352.

[270] ROSE, J. W. 1980 Approximate equations for forced-convection condensation in the presence of a non-condensing gas on a flat plate and horizontal tube", *Int. J. Heat and Mass Transfer,* **23**, 539-546.

[271] ROWE, P. N. and HENWOOD, G. A. 1961 Drag forces in a hydraulic model of a fluidized bed: Part I. *Trans. Inst. Chem. Eng.* **39**, 43-54.

[272] RUFF, G. A., SAGAR, A. D. and FAETH, G. M. 1989 Structure and mising properties of pressure-atomised sprays. *AIAA J.,* **27**, 901-908.

[273] RUFF, G. A. and FAETH, G. M. 1990 *AIAA Paper No. 90-0464*

[274] RYLEY, D. J. and BENNETT-COWELL, B. N. 1967 The collision behaviour of steam-borne water drops. *Int. J. Mech. Sci* **9**, 817-833.

[275] RYLEY, D. J. and WOOD, M. R: 1966 Thermodynamics and Fluid Mechanics Group Convention. *J. Mech Eng., Paper 1*, Liverpool.

[276] SAFFMAN, P. G. 1965 The lift on a small sphere in a slow sheer flow. *J. Fluid Mech.,* **22**, 385-400.

[277] SAFFMAN, P. G. 1968 Corrigendum to the lift on a small sphere in a slow shear flow. *J. Fluid Mech.,* **31**, 624.

[278] SAFFMAN, P. G. and TURNER, J. S. 1956 On the collision of drops in turbulent clouds. *J. Fluid Mech.,* **1**, 16-30.

[279] SAITO, A., KAWAMURA, K., WATANABE, S., TAKAHASHI, T. and NAOYUKI, T. 1993 Analysis of impinging spray characteristics under high-pressure fuel injection. (1st report, measurements of impinging spray characteristics) *Trans. Jap. Soc. Mech. Engrs. B***59**, 3290-3295.

[280] SAKANE, A., HAMAMOTO, Y. and SUMIMOTO, T. 1988 Behavior of a spray impinging on a wall. *Journal-Marine Engineering Society, B.,* **54**, 1861-1865.

[281] SATCUNANATHAN, S. 1968 Evaporation rates of liquid droplets evaporating in the spheroidal state on a hot surface. *J. Mechanical Eng. Sci.* **10**,438-441.

[282] SAVEANU, T., IBANESCU, I. and VASILIU, M. 1962 *Rev Chim. (Bucharest)* **13**, 589.

[283] SAVIC, P and BOULT, G. T. 1957 Heat transfer and Fluid Mechanics Institute, California Institute of Technology, 43-84.

[284] SCHEELE G, F, MEISTER, B. J. 1968 *AIChE J.,* **14**, 9

[285] SCHOTLAND, R. M 1960 Experimental results relating to the coalescence of water drops with water surfaces. *Discuss Faraday Soc.* **30**, 72-77.

[286] SEKI, M., KAWAMURA, H. and SANOKAWA, K. 1978 Transient temperature profile of a hot wall due to an impinging liquid droplet. *ASME J. Heat Transfer,* **100**, 167-169.

[287] SHIBUYA, I. 1951 *Rept. Inst. High Speed Mech.*, Tohoku Univ., **1**, 17

[288] SHIKHMURZAEV, Yu. D. 1991 Spreading flow of a viscous liquid over a solid surface. *Sov. Phys. Dokl.,* **36**, 749-752.

[289] SHIN, Y., CHENG, W. K, and HEYWOOD, J. B 1994 Liquid gasoline behavior in the engine cylinder of a SI engine. *SAE Paper* No. 941872.

[290] SHRAYBER, A. A., PODVYSOTSKY, A. M. and KHELEMSKIY, S. L. 1992 Effect of viscosity on the rate of mass transfer in impingement of droplets on a wetted wall. *Fluid Mechanics Research,* **21** (2), 6-9.

[291] SHUEN, J. S., YANG, V., and HSIAO, C. C. 1992 Combustion of liquid fuel droplets in supercritical conditions. *Combustion and Flame.* **89**, 299-319.

[292] SIMMONS, H. C. 1977 The correlation of drop-size distributions in fuel nozzle sprays. *J. Eng. Power,* **99**, 309-319.

[293] SIWOŃ,B. 1988 The behavior of a liquid film while gas-liquid spray is directed onto a flat surfacc. *FLUCOME 2nd Int. Symp.*, Sheffield, 535-539.

[294] SIWÓN, B. and ENNAOUI, M. 1991 Calculating hydrodynamics problems for a liquid film flowing radially on a flat horizontal surface. *Int. J. Num. Meths. in Fluids,* **13**, pp. 655-666.

[295] SLATTERY, J. C. 1967 Genaral balance equation for a phase interface. *Ind. Engng Chem. Fund.***6**, 108-115.

[296] SMITH, G. D. 1978 Numerical solution of partial differential equations: Finite difference methods. *Clarendon Press.*

[297] SPALDING, D. B 1953 The combustion of liquid fuels. *Forth Symp. (International) on Combustion. , Willisams & Wilkins*, Baltimore, 847-864.

[298] SPALDING, D. B 1955 Some Fundamentals of Combustion, *Academic Press*, New York; Butterworths Scientific Publications, London.

[299] SPALDING, D. B. 1972 A novel finite difference formulation for differential expression involving both first and second derivatives. *Int. J. Num. Meth. Eng.* **4**, 551-559.

[300] SPARROW, E. M. and GREGG, J. L. 1959 A boundary-layer treatment of laminar-film condensation. *ASME J. Heat Transfer,* **81**, 13-18.

[301] SPARROW, E. M. and SIEGEL, R. 1959 Transient film condensation. *ASME J. Applied Mechanics,* **81**, 120-121.

[302] SPINDLER, B. 1982 Linear stability of liquid films with interfacial phase change. *Int. J. Heat mass Transfer*, **25**, 161-173.

[303] STERLING, A. M. and SLEICHER, C. A. 1975 The instability of capillary jets. *J. Fluid Mech.,* **68**, 477-495.

[304] STOKES, G. G. 1901 Scientific Papers, University Press, Cambridge.

[305] STONE, H. L. 1968 Iterative solution of implicit approximations of multidimensional differential equations. *SIAM. J. Num Anal.* **5**, 530.

[306] STOW, C. D. and HADFIELD, M. G. 1981 An experimental investigation of fluid flow resulting from the impact of a water drop with an unyielding dry surface. *Proc. R. Soc. Lond.-A,* **373**, 419-441.

[307] STOW, C. D. and STAINER, R. D. 1977 The physical products of a splashing water drop. *Journal of the Meteorological Society of Japan,* **55**, 518-531.

[308] SUGAWARA, S. 1990 Droplet deposition and entrainment modelling based on the three-fluid model. *Nuclear Engineering and Design* **122**, 67-84.

[309] TABRIZI, B. S. 1991 Three-dimensional Diesel spray predictions in combustion chamber flows. PhD Thesis, University of London.

[310] TAKEUCHI, K., SENDA, J. & SATo, Y. 1982 Experimental studies on the behavior of a small droplet impinging upon a hot surface. In: *Int. Conf. on Liquid Atomisation and Spray System (ICLASS-82)*

[311] TAMBOUR, Y. 1985 Coalescence of vapourising kerosene fuel sprays in a turbulent jet. *Combust. Flame,* **60**, 15-28.

[312] TAMURA, Z. and TANASAWA, Y. 1959 Evaporation and combustion of a drop contacting with a hot surface. *Proceedings of the 7th International symposium on combustion*, 509-522.

[313] TAN, N. T., KLEVTSOV, A. V. and CHILIKIND, N. V. 1989 The theory of deformation of a droplet on a horizontal surface. *Thermal Engineering,* **36**(10), 572-574.

[314] TAYLOR, D. H. and WALSHAM, B. E. 1970 Combustion process in medium-speed diesel engine. *Proc. I. Mech. Eng*

[315] TENNEKES, H. and LUMLEY, J. L. 1980 A First Course in Turbulence. MIT Press.

[316] TESHIROGI, N. 1975 Combustion control Diesel engines by heated surfaces. Doctor of Engineering Thesis, University of Tokyo, Japan.

[317] TRAPAGA, G. and SZEKELY, J. 1991 Mathematical modeling of the isothermal impingement of liquid droplets in spraying processes. *Metall. Trans. B,* **22**,901-914.

[318] TSUJI, Y., MORIKAWA, Y., TANAKA, T., KARIMINE, K. and NISHIDA, S. 1988 Measurement of axisymmetric jet laden with coarse particles. *Int. J Multiphase Flow,* **14**,565.

[319] UEDA, T. 1979 Droplet entrainment rate and droplet diameter in annular two-phase flow. *JSME* **45**, 127-135.

[320] UEDA, T., ENOMOTO, T. and KANETSUKI, M. 1979 Heat transfer characteristics and dynamic behavior of saturated droplets impinging on a heated vertical surface. *Bulletin of the JSME,* 22, 724-732.

[321] UEDA, T. and NOSE, S. 1974 Studies of liquid film flow in two-phase annular and annular - mist flow regions; Part 2, Upflow in a vertical tube. *Bull. Japan. Soc. Mech Engrs,* **17**, 614-624.

[322] UEDA, T. and TANAKA, T. 1974 Studies of liquid film flow in two-phase annular and annular - mist flow regions; Part 1, Downflow in a vertical tube. *Bull. Japan. Soc. Mech Engrs,* **17**, 603-613.

[323] UNSAL, M. and THOMAS, W. C. 1978 Linearised stability analysis of film rupture. *ASME Journal of heat transfer,*,**100**, 629-634.

[324] VAN ROSSUM, J. J. 1959 Experimental investigation of horizontal films. *Chem. Engng. Sci.* **11**,35.

[325] VOUYOUCALOS, S. 1961 Effect of surface roughness and hydrolysis on mass transfer. MSc Thesis, University of Birmingham.

[326] WACHTERS, L. H. J. and WESTERLING, N. A. J. 1966 The heat transfer from a hot wall to impinging water drops in the spheroidal state. *Chem. Engng. Sci.,* **21**, 1047-1056.

[327] WALLIS, G. B. 1962 The onset of droplet entrainment in annular gas-liquid flow. *62 GL 127, General Electric.*

[328] WALLIS, G. B. 1969 One dimensional two-phase flow, McGraw Hill.

[329] WALZEL, P. 1980 Zerteilgrenze beim tropfenprall. *Chem.-Ing.-Tech.,* **52**,338-339.

[330] WANG, C. S. and STREET, R. L. 1978 Measurements of spray at an air-water interface. *Dyn. Atmos. Oceans* **2**,141-152.

[331] WATKIN, A. P. 1977 Flow and heat transfer in piston/cylinder assemblies. PhD Thesis, University of London.

[332] WATKINS, A. P. and WANG, D. M. 1990 A new model for diesel spray impaction on walls and comparison with experiment. In *Int. Symp. on Diagnostics and Modelling of Combustion in I C Engines*, Kyoto, 243-248.

[333] WENGLARZ, R. A. 1982 Boundary layer effects on impingement and erosion. *Proc. 17th Annunal Cavitation and Poly-Phase Flow Forum*, ASME Fluids Eng. Conf., St. Lousis, June 7-11.

[334] WHITE, F. M. 1979 Fluid Mechanics. McGraw-Hill Kogakushi Limited.

[335] WIERZBA, A. 1990 Deformation and breakup of liquid drops in a gas stream at nearly critical Weber numbers. *Experiments in Fluids,* **9**, 59-64.

[336] WILKES, J. O. and NEDEERMANN, R. M. 1962 *Chem. eng. Sci.* **17**, 177.

[337] WILLIAMS, F. A. 1962 Progress in spray-combustion analysis. Eighth Intern. Symp. on Combustion, Williams and Wilkins Co. Baltimore, 50-69.

[338] WILLIAMS, F. A. 1976 Fundamentals of oil combustions. *Prog. Energy Combust. Sci.,* **2**, 167-179.

[339] WILSON, S. D. R. 1974 Flow of a liquid film down a slightly inclined tube. *AIChE J.,* **20**, 408-410.

[340] WILSON, S. D. R. 1976 Unsteady and two-dimensional flow of a condensate film. *ASME J. Heat Transfer,* **98**, 313-315.

[341] WOLF, R. S. 1988 A study of diesel heat transfer distribution using a rapid compression machine. PhD Thesis, Massachusetts Institute of Technology.

[342] WOLF, R. S., CHENG, W. K. 1989 Heat transfer characteristics of impinging diesel sprays. *SAE Paper* 890439

[343] WOODMANSEE, D. F. and HANRATTY, T. J. 1969 Mechanism for the removal of droplets from a liquid surface by a parallel air flow. *Chem. Engng Sci* **24**, 299-307.

[344] WORTHINGTON, A. M. 1876 On the forms assumed by drops of liquids falling vertically on a horizontal plate. *Proc. Roy. Soc. Lond.,* **25**, 261-271.

[345] WORTHINGTON, A. M. 1908 A study of splashes. *Longmans Green and Co., New York*

[346] WORTHINGTON, A. M. 1877 A second paper on the forms assumed by drops of liquids falling vertically on a horizontal plate. *Proc. Roy. Soc. Lond.,* **25**, 498-503.

[347] WORTHINGTON, A. M. 1882 On impact with liquid surfaces. *Proc. Roy. Soc. Lond.,* **34**, 217-230.

[348] WRIGHT, A. C. 1986 A physically-based model of the dispersion of splash droplets ejected from a water drop impact. *Earth Surface Processes and Landforms,* **11**, 351-367.

[349] XIONG, T. Y. and YUEN, M. C. 1991 Evaporation of a liquid droplet on a hot plate. *Int. J. Heat Mass Transfer.,* **34**, 1881-1894.

[350] YAO, S. C. and CAI, K. Y. 1985 Dynamics and heat transfer of drops impacting on a hot surface at small angles. *Proceedings of the 3rd International conference on liquid atomisation and spray systems, Imperial College, London, ICLASS-85*, VII/B/1-11.

[351] YARIN, A. L. and ORON, A. 1993 Capillary instability of thin liquid film on a cylinder. *Phys. Fluids A,* **5**, 91-98.

[352] YIH, C.-S. 1954 *Proc. 2nd U. S. Natl. Congr. Appl. Mech.*, 623-628.

[353] YIH, C.-S. 1963 Stability of liquid flow down an inclined plane. *Phys. Fluids*, **6**, 321-334.

[354] YOUNG, T. 1805 An essay on the cohesion of fluids. *Phil. Trans. R. Soc. Lond.* **95**,65-87.

[355] YUEN, M. C. and CHEN, L. W. 1976 On the drag of evaporating liquid droplets. *Combust. Sci. Technol.,* **14**, 147-154.

[356] YULE, A. J. and FILIPOVIC, I. 1992 On the break-up times and lengths of diesel sprays. *Int. J. Heat and Fluid Flow,* **13**, 197-202.

[357] ZHAVORONKOV , N. M., MALYUSOV, O. A. & MALAFEEV, N. A. 1951 *Khim Prom.*, 240.

[358] ZHBANKOVA, S. L. and KOLPAKOV, A. V. 1991 Collision of water drops with a plane water surface. *Fluid Dyn.,* **25**, 470-473.

[359] ZHIVAĬKIN, L. Ya., and VOLGIN, B. V. 1961 *Zh. Prikl. Khim.* **34**, 1236.

[360] ZOTIKOV, I. A. and BRONSKII, L. N. 1962 *Inzh. Fiz. Zh. Akad. Nauk Belornssk.* **5**, 10.

[361] ZUBER, N. 1962 On the atomisation and entrainment of liquid films in shear flow. *62 GL 153, General Electric.*